



## Durham E-Theses

---

### *Exploring the impact of self-assembly pathways on the structures and properties of small-molecule gels*

JONES, CHRISTOPHER,DAVID

#### How to cite:

---

JONES, CHRISTOPHER,DAVID (2017) *Exploring the impact of self-assembly pathways on the structures and properties of small-molecule gels*, Durham theses, Durham University. Available at Durham E-Theses Online: <http://etheses.dur.ac.uk/12115/>

#### Use policy

---

The full-text may be used and/or reproduced, and given to third parties in any format or medium, without prior permission or charge, for personal research or study, educational, or not-for-profit purposes provided that:

- a full bibliographic reference is made to the original source
- a [link](#) is made to the metadata record in Durham E-Theses
- the full-text is not changed in any way

The full-text must not be sold in any format or medium without the formal permission of the copyright holders.

Please consult the [full Durham E-Theses policy](#) for further details.

---

Academic Support Office, Durham University, University Office, Old Elvet, Durham DH1 3HP  
e-mail: [e-theses.admin@dur.ac.uk](mailto:e-theses.admin@dur.ac.uk) Tel: +44 0191 334 6107  
<http://etheses.dur.ac.uk>

# **Exploring the impact of self-assembly pathways on the structures and properties of small-molecule gels**



**Christopher D. Jones**

Department of Chemistry  
Durham University  
2017

This thesis is submitted in partial fulfilment of the requirements  
for the degree of  
*Doctor of Philosophy*

# Exploring the impact of self-assembly pathways on the structures and properties of small-molecule gels

**Christopher Jones, Durham University**

Gels based on low-molecular-weight gelators (LMWGs) often consist of highly extended sheets or fibrils, which fuse or intertwine to produce a sample-spanning network. The aim of this investigation was to gain insight into such hierarchical processes by characterising a variety of urea-based LMWGs, and modelling the impact of key structural features on the outcome of self-assembly.

Self-assembly of bis(urea) LMWGs often produces chains of urea-urea hydrogen bonds known as  $\alpha$  tape motifs. One series of bis(urea)s with a sterically hindered spacer vary greatly in their gelation abilities, and form single crystals comprising a diverse range of  $\alpha$  tape networks. Molecular dynamics simulations suggest that gels arise when crystal growth is outcompeted by the spontaneous scrolling of isolated lamellar assemblies. Thus, gelation is mainly associated with species that self-assemble into asymmetric lamellae, which undergo scrolling due to the differing forces exerted by the upper and lower faces.

Even small changes to a self-assembly pathway can dramatically alter the resulting material. Photoisomerisation of bis(urea)s with terminal salicylidene-aniline (anil) moieties requires that the surface imine groups of crystalline lamellae can freely rotate, and is inhibited when gelation or co-crystallisation results in a less optimal molecular arrangement. Likewise, the anion affinities and aggregate microstructures of five isomeric linear tris(urea)s depend strongly on their spacer configurations. Although these molecules are not effective LMWGs, more extended oligo(urea)s can deliver higher gelation capacities. Remarkably, one achiral pentakis(urea) self-assembles into amyloid-like braided helices that may be chirally enriched by a template material. In addition, the tris(urea) analogue of this compound can form interfacial "lily pad" metallogels under vapour-diffusion conditions, demonstrating a novel mode of self-assembly with potential applications in metal sequestration. Building on these results could lead to supramolecular material with more complex microstructures and stimuli-responsive functionalities, and aid our understanding of the hierarchical self-assembly processes observed in biological systems.



# Table of contents

<b>1</b>	<b>Introduction</b>	
1.1	Key characteristics of supramolecular gels	1
1.2	Sol-gel and gel-sol transitions	4
1.3	Exploring the self-assembly landscape	16
1.4	Rheological characterisation	22
1.5	Optical signatures of gel formation	35
1.6	Photoinduced conformational changes	46
1.7	Bond-forming processes in gels	56
1.8	Conclusions and outlook	70
1.9	References	71
<b>2</b>	<b>Scrolling of supramolecular lamellae in the hierarchical self-assembly of fibrous gels</b>	
2.1	Background	82
2.2	Results and discussion	
2.2.1	Synthesis and structural categorisation	86
2.2.2	Non-solvated assemblies	88
2.2.3	Solvated assemblies	90
2.2.4	Gelation behaviour	93
2.2.5	Lamellar self-assembly	97
2.2.6	Scrolling behaviour	100
2.2.7	Schematic model	106
2.3	Conclusions	108
2.4	References	109
<b>3</b>	<b>Stick or twist: the role of surface packing in the photoreactivity of switchable gelators</b>	
3.1	Background	112
3.2	Results and discussion	
3.2.1	Synthesis and crystallisation	115
3.2.2	Crystal structures	115
3.2.3	Gelation behaviour	120
3.2.4	Photoreactivity of crystals	125
3.2.5	Photoreactivity of gels	131
3.3	Conclusions	136
3.4	References	137
<b>4</b>	<b>Bis(urea) gelators: a designer's guide</b>	
4.1	Background	139
4.2	Results and discussion	

<b>4.2.1</b>	Synthesis and crystallisation	144
<b>4.2.2</b>	Structural trends	145
<b>4.2.3</b>	Gelation behaviour	155
<b>4.2.4</b>	Scrolling pathways	163
<b>4.3</b>	Conclusions	168
<b>4.4</b>	References	168
<b>5</b>	<b>Targeting gelation over crystallisation in the self-assembly of linear tris(urea)s</b>	
<b>5.1</b>	Background	171
<b>5.2</b>	Results and discussion	
<b>5.2.1</b>	Synthesis	173
<b>5.2.2</b>	Self-assembly behaviour	177
<b>5.2.3</b>	Solution-state conformations	185
<b>5.3</b>	Conclusions	190
<b>5.4</b>	References	191
<b>6</b>	<b>Braid helices and lilypad gels: controlling hierarchical self-assembly over a range of length-scales</b>	
<b>6.1</b>	Background	194
<b>6.2</b>	Results and discussion	
<b>6.2.1</b>	Synthesis	197
<b>6.2.2</b>	Gelation behaviour	198
<b>6.2.3</b>	Helix braiding	203
<b>6.2.4</b>	Lilypad gels	212
<b>6.3</b>	Conclusions	222
<b>6.4</b>	References	223
<b>7</b>	<b>Closing remarks</b>	
<b>7.1</b>	Conclusions	226
<b>7.2</b>	Future work	227
<b>8</b>	<b>Experimental</b>	
<b>8.1</b>	Compositional analysis	229
<b>8.2</b>	Single-crystal X-ray diffraction	230
<b>8.3</b>	Powder X-ray diffraction	232
<b>8.4</b>	Rheometry	232
<b>8.5</b>	Microscopy	233
<b>8.6</b>	NMR spectroscopy	233
<b>8.7</b>	UV-vis and FT-IR spectroscopy	234
<b>8.8</b>	Computational work	235
<b>8.9</b>	Synthesis	237

8.10	References	264
9	Appendices	
9.1	Derivations	265
9.2	CSD survey	272
9.3	Conference presentations	282

## Abbreviations

<b>ACQ</b>	Aggregation-caused (fluorescence) quenching
<b>AFM</b>	Atomic force microscopy
<b>AIEE</b>	Aggregation-induced enhanced emission
<b>Anil</b>	<i>N</i> -salicylidene-aniline
<b>CD / LD</b>	Circular dichroism / linear dichroism
<b>CDI</b>	1,1'-carbonyldiimidazole
<b>CGC</b>	Critical gelator concentration
<b>CSD</b>	Cambridge Structural Database
<b>DFT</b>	Density functional theory
<b>DSC</b>	Differential scanning calorimetry
<b>DTE</b>	Dithienylethene
<b>ESI-MS</b>	Electrospray ionisation mass spectrometry
<b>ESIPT</b>	Excited-stated intramolecular proton transfer
<b>FT-IR</b>	Fourier-transfer infrared spectroscopy
<b>ICP-MS</b>	Inductively coupled plasma mass spectrometry
<b>LMWG</b>	Low-molecular-weight gelator
<b>MD</b>	Molecular dynamics
<b>MLG</b>	Molecular logic gate
<b>MM</b>	Molecular mechanics
<b>NMR</b>	Nuclear magnetic resonance
<b>OPV</b>	Oligo( <i>p</i> -phenylenevinylene)
<b>P-XRD</b>	Powder X-ray diffraction
<b>SAM</b>	Self-assembled monolayer
<b>SANS</b>	Small-angle neutron scattering
<b>SC-XRD</b>	Single-crystal X-ray diffraction
<b>SEM</b>	Scanning electron microscopy
<b>TEM</b>	Transmission electron microscopy
<b>TGA</b>	Thermogravimetric analysis
<b>TICT</b>	Twisted intramolecular charge transfer
<b>UV-vis</b>	Ultraviolet-visible spectroscopy
<b>XPS</b>	X-ray photoelectron spectroscopy

# Symbols

<b><math>A_{\text{mol}}</math></b>	Average area of lamellae per molecule
<b><math>c, c_0</math></b>	Gelator concentration and critical gelator concentration (CGC)
<b><math>\gamma</math></b>	Surface energy of simulated crystallite face
<b><math>\gamma_{\text{sol}}, \gamma_{\text{vap}}</math></b>	Surface energies of gel-sol and gel-vapour interfaces
<b><math>d_{\text{layer}}</math></b>	Average spacing of lamellae in single-crystal structure
<b><math>D_f</math></b>	Fractal dimension
<b><math>E</math></b>	Energy of lilypad gel; sum of gravitational and surface energies
<b><math>\Delta E_{\text{U-Cl}}</math></b>	DFT energy change due to formation of a urea-chloride complex
<b><math>\Delta E_{\text{U-U}}</math></b>	DFT energy change due to intramolecular urea-urea interaction
<b><math>E_{\text{tot}}</math></b>	Total simulated crystallite energy from MD simulations
<b><math>E_{\text{bulk}}, E_{\text{face}}</math></b>	Bulk (per layer) and surface energies of simulated crystallite
<b><math>f</math></b>	Distance from surface to centre of lilypad gel as a fraction of $R$
<b><math>f_{\text{start}}, f_{\text{end}}</math></b>	Values of $f$ when gel growth begins ( $V = 0$ ) and when $V = V_{\text{end}}$
<b><math>g</math></b>	Acceleration due to gravity
<b><math>G, G', G''</math></b>	Shear, storage and loss moduli
<b><math>K_{11}</math></b>	Equilibrium constant for formation of 1:1 host-guest complex
<b><math>\mu^*</math></b>	Dynamic viscosity
<b><math>n</math></b>	Power-law exponent (e.g. in rheological expressions)
<b><math>N</math></b>	Number of layers in simulated crystallite
<b><math>\rho_{\text{gel}}, \rho_{\text{sol}}</math></b>	Densities of lilypad gel and surrounding sol
<b><math>R</math></b>	Radius of sphere bounding the immersed surface of a lilypad gel
<b><math>\sigma</math></b>	Applied stress
<b><math>\tau</math></b>	Estimated average lamella thickness in single-crystal structure
<b><math>T_g</math></b>	Temperature of system during gelation ( $T_g < T_{\text{gel}}$ )
<b><math>T_{\text{gel}}</math></b>	Gelation temperature; highest temperature of sol-gel transition
<b><math>T_{\text{melt}}</math></b>	Degelation temperature; lowest temperature of gel-sol transition
<b><math>\phi_A, \phi_B</math></b>	Torsion angles for specifying anil rotations in MM models
<b><math>\phi_1, \phi_2</math></b>	Torsion angles describing <i>m</i> -xylylene spacer geometry
<b><math>V</math></b>	Volume of lilypad gel; $V_{\text{end}}$ is the volume at the end of growth
<b><math>V_{\text{mol}}</math></b>	Average volume per molecule in single-crystal structure
<b><math>\omega</math></b>	Angular frequency of oscillatory stress

## Figures and tables

<b>Fig. 1</b>	Levels of structure in a hierarchical gel	3
<b>Fig. 2</b>	Gel-sol and sol-gel transitions of <b>1.1</b>	4
<b>Fig. 3</b>	Variation of gel structure and strength with $T_g$	6
<b>Fig. 4</b>	Heat-induced gelation of <b>1.2</b> with guanidine chloride	9
<b>Fig. 5</b>	Changes in fluorescence of <b>1.3</b> during gel formation	10
<b>Fig. 6</b>	Sonication-induced morphological changes in gels of <b>1.4</b>	11
<b>Fig. 7</b>	Henry nitroaldol reactions in gels of <b>1.5</b>	14
<b>Fig. 8</b>	Cryo-SEM micrographs of <b>1.6</b> metallogels after shaking	16
<b>Fig. 9</b>	SEM micrographs of <b>1.7</b> gels after heating and sonication	18
<b>Fig. 10</b>	Sonication-induced self-assembly of <b>1.8</b>	20
<b>Fig. 11</b>	Self-assembly pathways of <b>1.9</b> after heating and sonication	20
<b>Fig. 12</b>	Sonication-induced vesicle-to-fibre transitions	22
<b>Fig. 13</b>	Strain-sweep behaviour of toluene gels of <b>1.10</b>	24
<b>Fig. 14</b>	Effect of surfactant on the aggregation of <b>1.7</b>	27
<b>Fig. 15</b>	Iodine sequestration via phase separation of <b>1.11</b> gels	29
<b>Fig. 16</b>	Self-repair of <b>1.12</b> metallogels	30
<b>Fig. 17</b>	Sound-induced LD in <b>1.13</b> sols before and after illumination	33
<b>Fig. 18</b>	Fluorescence of <b>1.14</b> in gels and sols	34
<b>Fig. 19</b>	Energy levels in J- and H-aggregates	36
<b>Fig. 20</b>	UV-vis spectra of <b>1.15</b> solutions at varying temperatures	38
<b>Fig. 21</b>	Thermoreversible excimer emission of <b>1.16</b> and ACQ effect	40
<b>Fig. 22</b>	Interconversion of J and H aggregates of <b>1.17</b>	42
<b>Fig. 23</b>	$T_{\text{melt}}$ and spin-crossover temperatures in iron(II) metallogels	45
<b>Fig. 24</b>	Photoinitiation of gelation in a protected peptide	47
<b>Fig. 25</b>	Reversible photolithography in gels of azobenzene <b>1.18</b>	50
<b>Fig. 26</b>	Light-induced hierarchical self-assembly of <b>1.19</b>	51
<b>Fig. 27</b>	Reversible swelling of mixed hydrogels of <b>1.20</b> and <b>1.21</b>	52
<b>Fig. 28</b>	Isodesmic and ring-chain self-assembly of stilbene <b>1.22</b>	54
<b>Fig. 29</b>	Switching response of <b>1.23</b> and resulting emission changes	56
<b>Fig. 30</b>	Stokes shifts in solutions and gels of ESIPT-active <b>1.24</b>	57
<b>Fig. 31</b>	Energy level diagram for isomerisation of <b>1.25-1.27</b>	58

<b>Fig. 32</b>	Thermally induced colour changes in gels of <b>1.28</b>	62
<b>Fig. 33</b>	Optical changes in gels of <b>1.29</b> after heating and cooling	62
<b>Fig. 34</b>	Phase and colour changes in <b>1.30</b> gels due to photoisomerisation	64
<b>Fig. 35</b>	Changes in fluorescence upon ring-opening of DTE compound <b>1.31</b>	66
<b>Fig. 36</b>	Localised gel formation due to zonal illumination of <b>1.32</b> in toluene	67
<b>Fig. 37</b>	Logic-gating behaviour in gels of <b>1.33</b>	68
<b>Fig. 38</b>	Logic-gating behaviour of multiaddressable MLG <b>1.34</b>	69
<b>Fig. 39</b>	Typical stages in the hierarchical self-assembly of fibrous gels	85
<b>Fig. 40</b>	Common topologies of lamellar $\alpha$ -tape networks	88
<b>Fig. 41</b>	Hydrogen bonding network in structure <b>I</b>	89
<b>Fig. 42</b>	Parallel and antiparallel $\alpha$ -tapes in structures <b>II</b> and <b>III</b>	89
<b>Fig. 43</b>	Lamellar bis(urea) networks in dihydrate of <b>2.2</b> , structure <b>IV</b>	90
<b>Fig. 44</b>	Major supramolecular motifs in picoline solvates of <b>2.3</b>	91
<b>Fig. 45</b>	Comparison of $\alpha$ -tape orientations in structures <b>VIII</b> , <b>IX</b> and <b>X</b>	92
<b>Fig. 46</b>	Determination of CGC in nitrobenzene gels of <b>2.3</b>	94
<b>Fig. 47</b>	Effect of concentration on crystallisation of <b>2.3</b> in wet nitrobenzene	95
<b>Fig. 48</b>	SEM images of nitrobenzene and nitromethane gels of <b>2.3</b>	96
<b>Fig. 49</b>	Stress and frequency sweep profiles of nitrobenzene gels of <b>2.3</b>	96
<b>Fig. 50</b>	$G'$ changes during formation and collapse of nitrobenzene gel of <b>2.3</b>	97
<b>Fig. 51</b>	Plots to determine surface energies of model structure <b>II</b> crystallites	99
<b>Fig. 52</b>	Face-indexed single crystal of structure <b>II</b>	100
<b>Fig. 53</b>	Lamellae from structures <b>I-IX</b> after 1500 ps MD simulations	102
<b>Fig. 54</b>	Energies and hydrogen bond populations of simulated lamellae	103
<b>Fig. 55</b>	Scrolling of pseudo-lamellar $\alpha$ -tape networks from structure <b>X</b>	104
<b>Fig. 56</b>	Folding of asymmetric lamellae before and after equilibration	105
<b>Fig. 57</b>	Schematic diagram of lamellar deformations during gelation	107
<b>Fig. 58</b>	Schematic energy plot to explain monodispersity of gel fibrils	108
<b>Fig. 59</b>	Isomerisation pathways of anils	113
<b>Fig. 60</b>	Comparison of hydrogen bonding in structures <b>XIII</b> and <b>XIV</b>	117
<b>Fig. 61</b>	Comparison of crystals formed by <b>3.1a</b> , structures <b>XII</b> and <b>XV</b>	117
<b>Fig. 62</b>	Comparison of bis(urea) lamellae in structures <b>XVI-XIX</b> .	119
<b>Fig. 63</b>	SEM images of anil gels and aggregates	121
<b>Fig. 64</b>	PXRD data for dried anil gels	122

<b>Fig. 65</b>	Rheometric data and photographs of anil gels	123
<b>Fig. 66</b>	Avrami plot for gelation of 1,2-dichlorobenzene by 0.1% (w/v) <b>3.2c</b>	124
<b>Fig. 67</b>	Photographs of photochromic responses in solid anils <b>3.3b</b> and <b>3.3a</b>	125
<b>Fig. 68</b>	DRUV spectra for solid anils after irradiation with UV light	126
<b>Fig. 69</b>	DFT energies of model anils in $S_0$ and $S_1$ states	127
<b>Fig. 70</b>	Arrangements of anil groups on crystal surfaces	129
<b>Fig. 71</b>	MM energy profiles for rotations of anil groups on crystal surfaces	130
<b>Fig. 72</b>	UV-vis spectra of anil solids, solutions and gels	132
<b>Fig. 73</b>	Stacking motifs in salicylaldehyde crystal structures	134
<b>Fig. 74</b>	Crystal structure of co-crystal <b>XXII</b> and MM energy for anil rotation	135
<b>Fig. 75</b>	Frequencies of urea conformers and interactions in CSD	140
<b>Fig. 76</b>	Distribution of lattice parameters in mono(urea) structures	142
<b>Fig. 77</b>	Frequency of key structural motifs in mono(urea) structures	143
<b>Fig. 78</b>	Asymmetric lamellae in bis(urea) structures	148
<b>Fig. 79</b>	Symmetric lamellae in bis(urea) structures	149
<b>Fig. 80</b>	Non-lamellar bis(urea) structures	150
<b>Fig. 81</b>	Different $\alpha$ -tape topologies in bis(urea) structures	151
<b>Fig. 82</b>	Torsion angles specifying conformation of bis(urea) spacer	152
<b>Fig. 83</b>	Bis(urea)s with methylated <i>m</i> -xylylene spacer in the literature	153
<b>Fig. 84</b>	DFT energies and observed torsion angles of bis(urea) spacer	153
<b>Fig. 85</b>	Plot of observed torsion angles between urea groups	154
<b>Fig. 86</b>	Rheometric data and photographs of bis(urea) gels	158
<b>Fig. 87</b>	SEM images of bis(urea) xerogels	159
<b>Fig. 88</b>	SEM images of bis(urea) precipitates and nitrobenzene xerogels	159
<b>Fig. 89</b>	Polar and non-polar lamellar stacking in crystal structures	161
<b>Fig. 90</b>	Surface energies of bis(urea) crystallites from MD simulations	162
<b>Fig. 91</b>	PXRD data for crystals and xerogels of <b>4.1d</b>	163
<b>Fig. 92</b>	Solid-state $^{13}\text{C}$ NMR spectra for crystals and xerogels of <b>4.1a-d</b>	164
<b>Fig. 93</b>	Final frames from MD simulations of non-scrolling bis(urea) lamellae	165
<b>Fig. 94</b>	Effect of lamellar thickness on maximum curvature	166
<b>Fig. 95</b>	Energy profiles and final morphologies of scrolling lamellae	167
<b>Fig. 96</b>	Coupling agents for urea and amide synthesis	174
<b>Fig. 97</b>	Urea-urea interactions in diamine structures <b>XLIV-XLVI</b>	176



<b>Fig. 98</b>	Rheometric data and photographs of tris(urea) gels	179
<b>Fig. 99</b>	SEM images of non-gel-forming tris(urea) aggregates	180
<b>Fig. 100</b>	SEM images of fibrous gels and gelatinous precipitates of tris(urea)s	181
<b>Fig. 101</b>	PXRD data and simulated structure of tris(urea) aggregates	183
<b>Fig. 102</b>	FT-IR spectra for as-synthesised tris(urea)s	184
<b>Fig. 103</b>	Model compounds for DFT studies of urea interactions	185
<b>Fig. 104</b>	DFT results for tris(urea)s with intramolecular hydrogen bonds	187
<b>Fig. 105</b>	DFT results for tris(urea)-chloride complexes	188
<b>Fig. 106</b>	Comparison of DFT energies for urea-urea and urea-chloride bonds	189
<b>Fig. 107</b>	<sup>1</sup> H NMR titration data of tris(urea)-chloride complex formation	190
<b>Fig. 108</b>	Rheometric data and photographs of pentakis(urea) gels	199
<b>Fig. 109</b>	SEM images of precipitates and gels of <b>6.1a</b> and <b>6.1b</b>	200
<b>Fig. 110</b>	TEM and AFM images of helical fibres in gels of <b>6.1b</b>	201
<b>Fig. 111</b>	PXRD data for aggregates of <b>6.1a</b> and <b>6.1b</b>	202
<b>Fig. 112</b>	Branching in networks of braided helical fibrils	204
<b>Fig. 113</b>	Braid word representation of nested double helices	205
<b>Fig. 114</b>	SEM images of crossings between heterochiral helices	206
<b>Fig. 115</b>	SEM images of different braiding patterns in gels of <b>6.1b</b>	208
<b>Fig. 116</b>	Origin of structural complexity in even-stranded heterochiral braids	209
<b>Fig. 117</b>	CD spectra and SEM images of chiral and racemic fibre networks	210
<b>Fig. 118</b>	SEM image of chiral gel and mechanism of chiral amplification	211
<b>Fig. 119</b>	Microscope image of lilypad gel growth via colloidal self-assembly	213
<b>Fig. 120</b>	Photographs of typical stages in lilypad gel development	214
<b>Fig. 121</b>	Geometric model of lilypad gel for energy analysis	215
<b>Fig. 122</b>	Schematic plot for estimating surface energies of lilypad gels	217
<b>Fig. 123</b>	Energy profiles for lilypad gels of increasing volume	218
<b>Fig. 124</b>	FT-IR spectrum and SEM image of lilypad gel	220
<b>Fig. 125</b>	XPS spectra of lilypad gel in Ni 2p and C 1s regions	220
<b>Fig. 126</b>	TGA data for lilypad gel and SEM and PXRD results after pyrolysis	221
<b>Table 1</b>	Examples of photoresponsive functionalities in LMWGs	49
<b>Table 2</b>	Crystallographic data for compounds <b>2.1-2.3</b>	87
<b>Table 3</b>	Crystallographic data for compounds <b>3.1a-d</b>	116

<b>Table 4</b>	Crystallographic data for anil-based structures	118
<b>Table 5</b>	Results of gelation trials for anils <b>3.2a-d</b> , <b>3.3a-d</b> , <b>3.4a-c</b> and <b>3.5</b>	120
<b>Table 6</b>	Crystallographic data for co-crystal <b>XXII</b> and salicylaldehydes	133
<b>Table 7</b>	Crystallographic data for bis(urea) structures	146
<b>Table 8</b>	Results of gelation trials for bis(urea)s	156
<b>Table 9</b>	Crystallographic data for diamines <b>5.1b-d</b>	176
<b>Table 10</b>	Results of gelation trials for tris(urea)s <b>5.4a-e</b>	179
<b>Table 11</b>	Braid words of allowed braids with two, three and four strands	207

## Statement of copyright

The copyright of this thesis rests with the author. No quotation from it should be published without the author's prior written consent and information derived from it should be acknowledged.

## Declaration

This work has not been submitted in substance for any other degree or award at this or any other university or place of learning, nor is being submitted concurrently in candidature for any degree or other award. Crystallographic data for structures **VII**, **XIX**, **XXX** and **XL** were collected and processed by Dr Dmitry Yufit and Dr Andrei Batsanov at station I19 of the Diamond Light Source synchrotron. Single-crystal structures **XIII**, **XIV**, **XVIII**, **XXVI** and **XLIV** were also obtained by Dr Dmitry Yufit, and structures **IX**, **XV**, **XX**, **XXII**, **XXVII**, **XXVIII** and **XXXVI** by Dr Stuart Kennedy. Solid-state NMR, TEM, ICP-MS, and the PXRD experiments in Chapter 3 were performed by Dr David Apperley, Dr Budhika Mendis, Dr Chris Ottley and Mr Gary Oswald respectively. XPS spectra were collected by Dr Aled Lewis (Swansea University) and processed by the author. Scripts for the preparation of GROMACS topology files and the analysis of torsion energies in Materials Studio were supplied by Dr Martin Walker and Mr Charl Bezuidenhout (Stellenbosch University) respectively. The synthesis and characterisation of compounds **5.1** and **5.7** (Chapter 5) was performed by Mr Henry Simmons, who also assisted in the acquisition of AFM images for Chapter 6. All other results are the product of independent work and investigation by the author.

## Publications

“Gels with sense: supramolecular materials that respond to heat, light and sound”, C. D. Jones and J. W. Steed, *Chem. Soc. Rev.*, 2016, **45**, 6546-6596.

“Scrolling of supramolecular lamellae in the hierarchical self-assembly of fibrous gels”, C. D. Jones, S. R. Kennedy, M. Walker, D. S. Yufit and J. W. Steed, submitted.

## Funding

This work and all associated publications was funded by the Engineering and Physical Sciences Research Council (EPSRC) *via* a Doctoral Scholarship, grant 1374655.

## Acknowledgements

The best advice I was given when beginning my PhD went something along the lines of the Thomas Huxley quote: “try to learn something about everything and everything about something.” In that sense, being invited to join the group of Jonathan Steed was a stroke of luck: I couldn’t have asked for a more knowledgeable supervisor, and will always be grateful for his help and encouragement over the last three years.

The second best piece of advice I received was to make good use of my expert co-workers. Kathi Edkins, in particular, must be recognised for her constant support during the writing of this document. I am extremely grateful to Andrea Perrin, Rachael Lee, Stuart Kennedy, Andrei Batsanov and Dmitry Yufit for their invaluable contributions to my single-crystal X-ray diffraction work, and to Kaiqiang Liu and Henry Simmons for bearing some of the brunt of my synthetic work. I must also acknowledge Yu-Ting (Helen) Hsu, Hannah Bolt, Helen Mason, Andy Beeby, and my brother Daniel Jones for training in spectroscopic methods; Budhika Mendis and Leon Bowen for providing expert electron microscopy support; and Gary Oswald, David Apperley, Raquel Belda-Vidal, Juan Aguilar Malavia, Jackie Moseley, Chris Ottley and Aled Lewis for their assistance in acquiring spectroscopic and diffraction data. I am greatly appreciative to the Thompson group, and Richard Thompson and Stephen Boothroyd especially, for offering free access to their laboratory and patiently overseeing my AFM imaging and rheometry work. Finally, I would like to thank Martin Walker, Kate Horner, Valentina Erastova and Charl Bezuidenhout for their in-depth instruction in computational techniques, without which much of my project would not have been possible.

Outside the laboratory, my fondest memories will be of hurtling through the sky with my good friends at the Skydive Academy, Peterlee. Skydiving has offered a haven away from the stress of failed experiments, and I owe much of my remaining sanity to Chloé Smith, Daniel Osborne, Henry Simmons, Kieran Hogan, Joe Brinn, Lucia Gray and the other members of Durham University Freefall Club (DUFFC). I am grateful, too, for the many travel opportunities that I have enjoyed in the course of my studentship. In particular, I would like to thank Lian Hutchings, Len Barbour and Marike du Plessis for organising my three-month trip to Stellenbosch University, and everyone in the Barbour group for making my stay in South Africa such an enjoyable experience.

This work is dedicated to my parents, Stephen and Suzanne Jones, whose wise words and unwavering support I value most of all.

# 1. Introduction

## 1.1 Key characteristics of supramolecular gels

Gels are an important component of many human technologies, both modern and ancient. Natural gels of pectin, gelatine and agar have been utilised in food products since medieval times. Today, gels are also found in products such as lubricants, adhesives, soaps, cosmetics, medical implants and explosives.<sup>1</sup> The diverse and widespread application of gels may be attributed to their unique physical properties: like conventional solids, gels are able to support weight and retain their shape, yet they exhibit fluid-like behaviour under stress and can be moulded, printed and injected as required.<sup>2</sup>

A gel is defined by IUPAC<sup>3</sup> as “a colloidal network that is expanded throughout its whole volume by a fluid.” Gels may be formed from water,<sup>4</sup> organic solvents<sup>5</sup> or ionic liquids<sup>6</sup> and are termed hydrogels, organogels and ionogels accordingly. Gels in which the fluid phase is a gas, meanwhile, are termed aerogels. In general, liquid constitutes the vast majority of the material’s mass. The solid network, in which the liquid is encapsulated, consists of fibrous aggregates of polymers<sup>7</sup> or small molecules, commonly referred to as low-molecular-weight gelators (LMWGs).<sup>8</sup> It is worth noting that the definition of a gel does not require that a material be commonly identified as such. Indeed, this family of materials arguably encompasses even complex biological systems lacking the archetypal appearance of a gel, such as cytoskeletons, blood clots, microbial colonies and swollen cellular tissues.

Although it is normal practice to identify a gel by visual inspection, there are a number of other, more quantifiable physical properties that are typically exhibited by materials of this type. The popular inversion test, in which a gel is characterised by its resistance to flow in an upturned vial, delivers a positive result for the majority of gels but is difficult to apply consistently due to the dependency of the outcome on the size and composition of the container.<sup>9</sup> Furthermore, the test is poorly suited to the identification of weak and partial gels and may yield false positive results if applied to viscous liquids, suspensions and strongly adhered solids. A more reliable approach is to categorise materials based on their

rheological behaviour.<sup>10</sup> Gels undergo characteristic changes when subjected to tensile and compressive stresses but are more often identified based on their responses to oscillatory shear. In a typical experiment, the strain of a gel should vary only weakly with frequency and exhibit a similar phase to the imposed stress. Furthermore, the strain should increase dramatically if the stress exceeds the yield point of the material, defined as the threshold value beyond which liquefaction takes place.

Historically, discoveries of new gelators have relied heavily on serendipity. However, burgeoning interest in the patterns of interactions between molecules has led to an improved understanding, at the molecular level, of the factors contributing to gel formation.<sup>11, 12</sup> Particular pairs of functional groups that assemble into robust supramolecular synthons may be deliberately incorporated into a small molecule<sup>13</sup> or polymer<sup>14</sup> to target aggregates with the desired morphology. In gels, strongly hydrogen-bonding moieties such as ureas and amides are often exploited to generate fibrous structures,<sup>15, 16</sup> though species containing aromatic rings or extended lipophilic moieties may also produce suitable architectures.<sup>5</sup>

One potentially useful feature of supramolecular gels is their sensitivity to chemical stimuli. Hydrogen-bonding motifs are strongly influenced by pH, so supramolecular gels often collapse or dissolve when an acid or base is added.<sup>17-21</sup> A gel-sol transition is not, however, the only response that can arise from stimulation of a gel. Changes in gel structure may also affect properties such as colour,<sup>22</sup> fluorescence,<sup>23</sup> viscosity,<sup>24</sup> conductivity<sup>25</sup> or magnetic susceptibility.<sup>26, 27</sup> Furthermore, it is possible for gelator molecules to rearrange into an alternative aggregate, such as another gel,<sup>28-34</sup> a non-gel micellar phase,<sup>35-37</sup> or a precipitate of crystals<sup>38, 39</sup> or amorphous solid.<sup>29, 35, 40-43</sup> The susceptibility of supramolecular gels to large-scale structural changes can be attributed to the metastable nature of their constituent assemblies. Whilst gelation is often kinetically favoured over competing crystallisation processes, molecules remain sufficiently mobile to access alternative minima in the self-assembly landscape, allowing more thermodynamically favourable materials to arise following small changes to the aggregate environment.

To target a gel with a desirable microstructure or functional property, it is necessary to understand how the structure of an LMWG influences the arrangement of molecules in the resulting assemblies. As noted by Estroff and Hamilton, the formation of a fibrous gel can be represented as a hierarchical process, beginning with the growth of one- or two-dimensional assemblies through supramolecular polymerisation (step 1).<sup>4</sup> Scrolling or intertwining of these assemblies affords larger fibrils (step 2), which further aggregate to generate the final gel network (step 3). By analogy with the levels of organisation in folded peptides,<sup>44</sup> the products of steps 1, 2 and 3 may be termed primary, secondary and tertiary structures respectively (Fig. 1). The primary structure of a gel describes the connectivity, symmetry and dimensionality of supramolecular motifs, and can often be reliably modelled on patterns of hydrogen bonding and  $\pi$ -stacking in the gelator crystal structure(s).<sup>45</sup> However, it is more challenging to track the evolution of such assemblies into well-defined secondary structures, or to describe the architecture of an observed gel fibre at a molecular level. In many cases, it is only possible to probe these stages of gel development indirectly, via their effects on aggregate morphology and bulk rheological and optical characteristics.

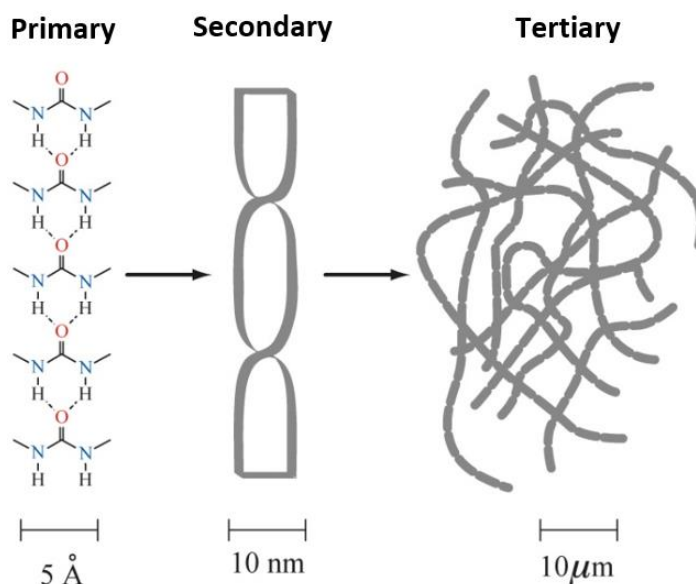


**Fig. 1** Schematic illustration of the levels of structure in a supramolecular gel, with scale bars indicating typical dimensions of the assemblies involved. Primary structure is represented by the  $\alpha$  tape motif, a continuous array of urea-urea hydrogen bonds frequently observed in gels of urea-based LMWGs. Image adapted from ref. 4 with permission. Copyright 2004 American

Chemical Society.

## ■ Gel-sol and sol-gel transitions

Owing to the labile nature of supramolecular interactions, LMWGs can often undergo reversible interconversion between gel and sol states. Such switchable behaviour may also be induced by physical stimuli such as changes in heat, light and mechanical forces. For example, Liu *et al.* reported that gels of azobenzene dendron **1.1** in polar solvents may be obtained through either ultrasound treatment or thermal cycling, and disrupted by heating, shaking, or UV illumination (Fig. 2).<sup>46</sup> Unlike chemical changes, these stimuli can be applied remotely and non-invasively, potentially allowing for rapid cycling between different gel and sol phases without contamination or degradation of the active material.

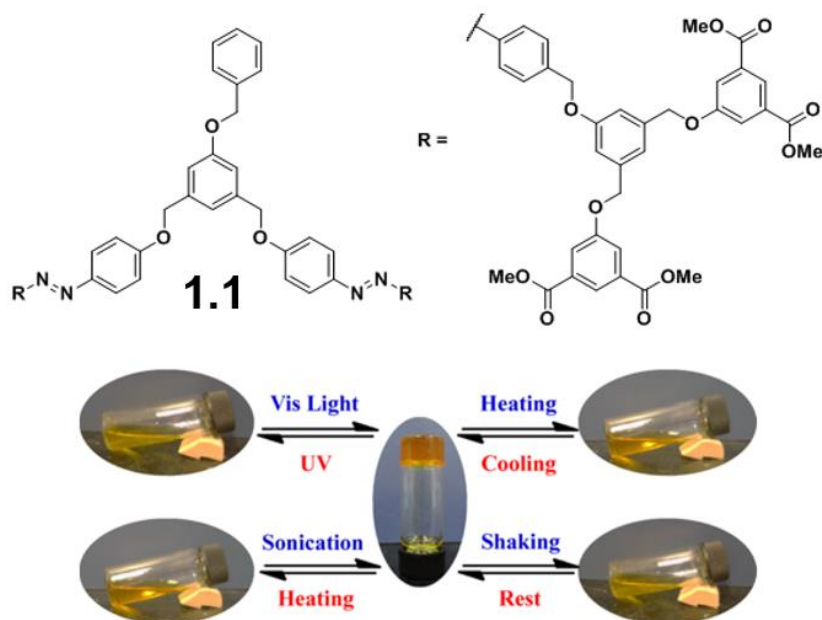


**Fig. 2** Gel-sol and sol-gel transitions of a multiaddressable dendron **1.1** in 2-methoxyethanol.

Image adapted with permission from ref. 46. Copyright 2012 American Chemical Society.

The majority of reported supramolecular gels are thermoreversible in nature. Typically, gelation takes place when a solution of the LMWG is cooled beyond the gelation temperature  $T_{\text{gel}}$ , and can be reversed by heating the material above a melting temperature  $T_{\text{melt}}$ .<sup>47, 48</sup> In rare cases, however, a thermoreversible gel may be obtained by raising, rather than lowering, the temperature: the gel is “heat-set” and dissolves upon cooling.<sup>29, 49-56</sup> Reversible heat-setting is often the result of an entropically-favoured molecular transformation. For example, a metallopolymer reported by de Hatten *et al.* forms a reversible gel at 140 °C due



to a ligand-exchange reaction, in which the material dissociates into free trioctylphosphine-copper(I) complexes and neutral organic polymers that can more readily aggregate.<sup>54</sup> Likewise, Kuroiwa *et al.* created a gel by heating a cobalt(II) coordination polymer to induce an octahedral-to-tetrahedral transition, with concomitant release of the triazole ligand.<sup>56</sup> The entropic drive for gelation may also be provided by the aggregation process itself. Although the gelator experiences a loss of disorder during self-assembly, this can be offset by an increase in the entropy of a polar solvent, which must form ordered solvation shells while the compound remains in solution. An effect of this nature is commonly displayed by partly or wholly hydrophobic species such as  $\beta$ -cyclodextrin, calixarenes and non-polar peptides, and can be enhanced by the addition of kosmotropic salts such as lithium chloride.<sup>50, 57, 58</sup>

A comprehensive summary of the influence of heating on gel formation can be found in a recent review by Li and Liu.<sup>59</sup> Crucially, the stability of a gel has been shown to depend on the number of junctions between the constituent fibres.<sup>60</sup> In some gels, fibres become entangled, physically crossing over each other to form transient junctions.<sup>61</sup> Alternatively, self-assembly may proceed in multiple directions such that fibres are connected via rigid branch points, known as permanent junctions.<sup>62</sup> Gels containing permanent junctions are typically stronger than those containing only transient junctions,<sup>60, 63, 64</sup> as quantified by their storage moduli and yield points.<sup>65</sup> Indeed, introducing covalent or robust intermolecular crosslinks between gel fibres is an established method for preventing disassembly of the aggregate state.<sup>66</sup> Branching may also affect the size, volume and connectivity of pores and, in gels of conductive materials such as poly(thiophene)s<sup>67</sup> and iodine-doped tetrathiafulvalenes,<sup>68</sup> facilitate electron transport through the fibre network.

Formation of permanent junctions is highly dependent on gelator concentration.<sup>69</sup> At low levels of supersaturation, branching is limited and occurs mainly on the slowly growing side-faces of fibres. By contrast, highly supersaturated solutions favour extensive branching from both the side and tip surfaces.<sup>70</sup> Raising the level of supersaturation in a gelator solution can serve to enhance the mechanical strength and thermal stability of the gel produced.

However, increased supersaturation results in more frequent nucleation, giving rise to a larger number of separate networks connected only by transient junctions (Fig. 3).<sup>71</sup> In addition, fibres with many permanent junctions may form dense spherulites, in which close packing of branches prevents the interpenetration of adjacent networks.<sup>72</sup> To maximise the stability and strength of a gel, supersaturation must therefore be carefully controlled to establish an optimum balance between nucleation, fibre growth and branching.<sup>63, 73</sup>

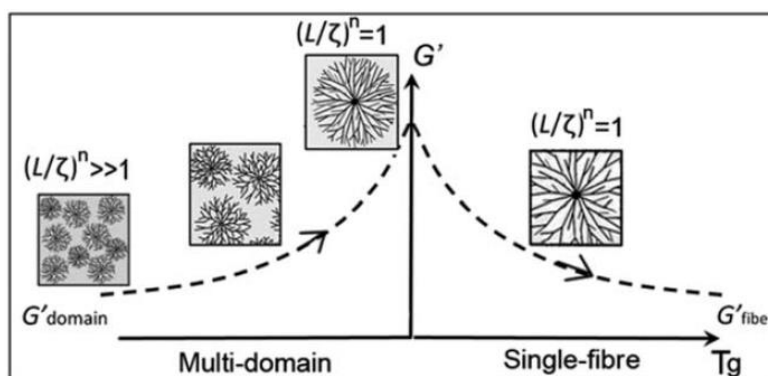


**Fig. 3** Schematic plot showing the variation of network structure and storage modulus,  $G'$ , with  $T_g$ , the temperature of the gelling solution (where  $T_g < T_{gel}$ ).  $(L/\zeta)^n$  is the ratio of the gel volume to the volume of a single fibre-growth domain. Gel strength is maximised at levels of supersaturation giving small numbers of highly branched spherulites. Image adapted from ref. 63 with permission from The Royal Society of Chemistry.

Supersaturation varies in proportion to the solubility of the gelator. If solubility increases with temperature in a typical fashion, cooling a gelling solution raises the level of supersaturation and increases the mass of fibres and degree of branching in the final material.<sup>62, 70, 72</sup> Branching can also be promoted by subjecting the solution to a higher rate of cooling.<sup>64, 74</sup> It has been proposed that crystalline ordering is lost at permanent junctions, and that accelerated cooling facilitates this mismatch by reducing the time available for self-assembly.<sup>62</sup> This theory was explored by Lam *et al.* in a study of the gelation kinetics of 12-hydroxystearic acid in mineral oil under non-isothermal conditions.<sup>75</sup> Intriguingly, at cooling rates below 5 K/min, fibres in a 2.5 wt.% solution exhibit nearly constant persistent lengths of 90–100  $\mu\text{m}$  and fractal dimensions of approximately 1.0, indicative of extremely limited branching. At higher cooling rates, however, the persistence length is reduced to 20–40  $\mu\text{m}$  and branching becomes more prevalent, producing fractal dimensions in the range 1.1–1.4.

Fourier-transform infrared (FT-IR) analysis reveals that increased branching coincides with divergence in the formation rates of supramolecular synthons. Whereas hydrogen bonding by hydroxyl groups scales in proportion to gel formation, the rate of carboxyl dimerization plateaus at cooling rates above 5 K min<sup>-1</sup>, suggesting that molecules under these conditions are forced to interact in a suboptimal fashion.

To fully understand the mechanism of a gel's formation, the kinetics of self-assembly must be quantitatively assessed.<sup>76</sup> In an isodesmic process, wherein successive stages of aggregation are similarly favoured, the rate of growth is constant near the start of gelation but falls thereafter. Conversely, the existence of a significant induction period suggests that nucleation and early propagation steps occur more slowly than subsequent growth. Mathematical models have been developed to describe and distinguish between these regimes, but characterisation of real systems may be complicated by changes in kinetic behaviour over time or under varying conditions. For example, Jonkheijm *et al.* found that an oligo(*p*-phenylenevinylene) (OPV) in cooled alkane solutions undergoes isodesmic self-assembly to form small disordered nuclei, before developing into larger helical structures via a cooperative nucleation-elongation pathway.<sup>77</sup>

The stability of a reversible self-assembled aggregate may generally be gauged from the maximum temperature at which it forms. In a gel, this threshold temperature  $T_{\text{gel}}$  is variously defined as the point at which the material becomes more opaque, experiences a marked increase in elastic modulus, becomes capable of supporting a ball bearing at its surface or resists flow under gravity when the container is inverted. The onset of the reverse transitions is associated with the melting temperature of the gel,  $T_{\text{melt}}$ , but this value can vary depending on the temperature at which gelation is performed,  $T_{\text{f}}$ . Thus,  $T_{\text{melt}}$  is more reliably defined as the point at which  $T_{\text{f}}$  converges with the observed melting temperature, and can be obtained by linear extrapolation of measurements at  $T_{\text{f}} \ll T_{\text{melt}}$  on a Hoffman-Weeks plot. Malik *et al.* adopted this approach in a study of gel formation by a synthetic tripeptide in 1,2-dichlorobenzene, and found that the initial rate of gelation, approximated as the reciprocal of  $t_{\text{gel}}$ , exhibits a

thermal dependency characteristic of fibrillar crystallisation.<sup>78</sup> Specifically, the logarithm of  $t_{\text{gel}}$  scales linearly with the ratio of  $T_{\text{melt}}$  to the product of  $T_f$  and the degree of undercooling,  $(T_{\text{melt}} - T_f)$ . It is worth noting, however, that this thermodynamic model does not fully capture the complexity of the gelation process. Turbidity measurements and microscopic observations indicate that gelation is preceded by a process of spinoidal decomposition, in which the solvent and peptide undergo spontaneous demixing to produce separate liquid phases. Furthermore, it is suspected that crystallisation involves the complexation of four solvent molecules by each molecule of tripeptide, as gels with this composition exhibit the largest melting enthalpies per mass of gelator.

The value of  $T_{\text{gel}}$  is largely determined by the strength of the supramolecular interactions in the material, and is thus highly sensitive to the structure of the gelator. Indeed,  $T_{\text{gel}}$  may be affected substantially by differences in enantiomeric excess,<sup>79, 80</sup> chain length<sup>15, 46, 81, 82</sup> or even the positions of functional groups.<sup>83-85</sup> It is interesting to note that varying a simple molecular characteristic such as polarity, solubility or flexibility can lead to marked changes in nucleation and growth processes. For example, Rogers *et al.* found that while 6-, 8-, 10-, 12- and 14-hydroxystearic acids form gels easily in mineral oil, isomers hydroxylated in the 2 and 3 positions typically afford a small number of large, fibrous crystals.<sup>84</sup> This difference was explained in terms of the rate of crystal formation: separating the hydroxyl and carboxylate groups increases the activation barrier to nucleation, as it becomes more entropically costly to direct both polar functionalities towards the face of a growing crystallite.

Another factor governing the stability of a gel is the concentration of the gelling solution. Typically, the value of  $T_{\text{gel}}$  increases with concentration above the critical gelator concentration (CGC) until a saturation value is reached. Given that the onset of gelation depends on the solubility of the gelator, the stability of the final material is largely dictated by the solvent present. However, it may be possible in some cases to alter the solubility of a compound, and thus the value of  $T_{\text{gel}}$ , without the use of a different solvent. The chaotropic salt guanidinium chloride was shown by Nebot *et al.* to increase the aqueous solubility of bolaamphiphile gelator **1.2**, but the guanidinium-amide interactions responsible

for this effect are weakened by heating (Fig. 4).<sup>86</sup> Thus, addition of the salt to a solution of **1.2** above its usual CGC affords a heat-set gel with an elastic modulus that varies inversely with temperature. Such gels are only kinetically stable at room temperature, and may thus be utilised for the release of entrapped small molecules in a slow and controllable fashion.

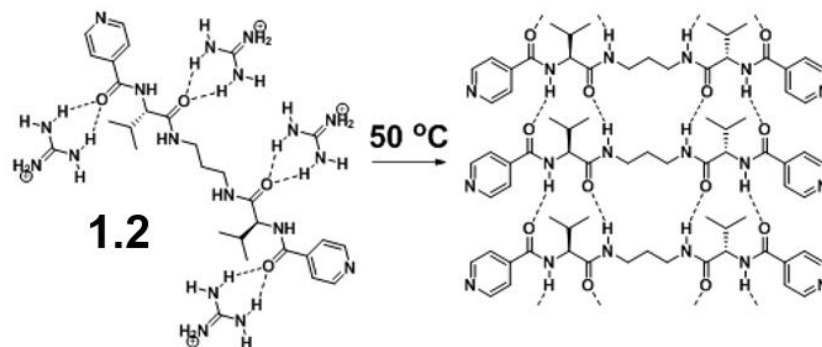


**Fig. 4** Example of heat-induced gelation triggered by the loss of hydrogen bonding interactions with a chaotropic cation. Image adapted with permission from ref. 86. Copyright 2014 John Wiley and Sons.

Gelator concentration may also influence the rate of gel formation. Malik *et al.* found that the reciprocal of gelation time,  $t_{\text{gel}}^{-1}$ , scales approximately as the square root of concentration in excess of the CGC.<sup>78</sup> Whilst the proposed link to percolation theory is highly tentative, this formula usefully captures the effect of supersaturation on the kinetics of self-assembly, and demonstrates how additives and solvents that produce a change in CGC may inhibit or accelerate the gelation process. It is important to note, however, that the temperature dependency of the CGC does not fully account for the impact of solvent on gelation rate. For example, the dihydrazide gelator **1.3** was shown by Zhang *et al.* to gel chloroform far more rapidly than toluene, even though it is substantially less soluble in the latter above 20 °C (Fig. 5).<sup>87</sup> Furthermore, increasing the temperature of the chloroform system leads to more transparent gels with higher  $T_{\text{melt}}$  values and lower rates of formation, whereas gelation in toluene is accelerated by heating and always produces an opaque material of high thermal stability. Attempts to estimate the fractal dimensionality,  $D_f$ , of the gels from dynamic fluorescence data are of uncertain validity as the claimed correspondence with the Dickinson model of gelation<sup>88</sup> is not clearly justified. Nonetheless, a somewhat<sup>89</sup> more robust analysis based on the Avrami equation<sup>90</sup> suggests that  $D_f$  values of the chloroform gels increase slightly as the temperature is raised. In toluene, meanwhile,  $D_f$  values rise sharply partway

through the gelation process and scale dramatically with temperature, with representative maxima of 1.7 and 3.0 at 5 and 35 °C respectively. These changes suggest that the aggregates in both systems become more interconnected with increasing temperature, and in toluene form via a two-stage process, undergoing one-dimensional growth before assembling into more densely packed fibrous bundles.

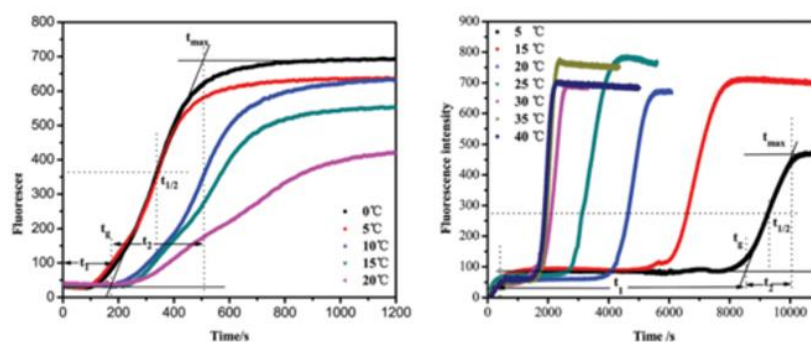
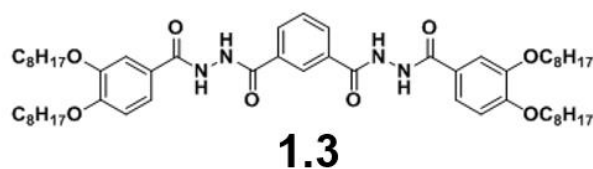


**Fig. 5** Changes in fluorescence of **1.3** during gel formation in chloroform (left) and toluene (right). The time for gelation to begin ( $t_1$ ) and reach completion ( $t_2$ ) are both shorter in chloroform below 20 °C. However, the rate of gelation increases with temperature in toluene, whilst in chloroform it decreases. Image adapted from ref. 87 with permission from The Royal Society of Chemistry.

Although the environment of a gelator can influence both the rate of aggregation and mode of self-assembly, correlations between the gelation time and physical properties of a gel are not always straightforward. Cholesterol-polyoxometalate hybrids were found by Su *et al.* to form gels comprising branched and intertwining ribbons in 17:3 toluene-DMF mixtures, and shorter, straighter assemblies at higher toluene concentrations.<sup>91</sup> Whilst increasing the concentration of toluene, a relatively poor solvent, initially reduces gelation time, volume fractions beyond 0.9 result in less rapid gel formation. By contrast, both fibre length and gel strength increase with toluene concentration. Similarly divergent trends in gelation kinetics and gel stability were described by Rohner *et al.*, in a study of 1:1 toluene gels of phenylethylamine and a range of peptide carboxylic acids.<sup>92</sup> The least soluble peptides exhibited the lowest CGC values and gelation times as expected, but converted to sols at roughly the same

temperature as more soluble analogues, due to a tendency for more enthalpically favoured structures to exhibit larger entropies of dissociation.

There has been some progress in predicting the outcomes of gelation experiments from the known physical properties of the gelator and solvent. In one notable study, Xu *et al.* showed that for gels containing solvents with comparable solubility parameters,  $T_{\text{gel}}$  correlates well with the solvent's viscosity and molecular volume.<sup>93</sup> In addition, it has been shown that molecules are more likely to gel a given solvent if they display large enthalpies and entropies of dissolution,<sup>94</sup> and strongly favour low-dimensionality assemblies in crystal-structure predictions.<sup>45</sup> However, even in systems with simple compositions and calculable bulk properties, accurate estimation of a gel's thermal behaviour is often made difficult by complex, heat-induced changes at the molecular scale. A good illustration of the effect of molecular transformations on gel stability was provided by Ke *et al.*<sup>36</sup> Alternating treatments with heat and ultrasound cause aggregates of **1.4** in THF-water to interconvert between vesicular and gel-forming fibrous structures, due to a reversible transition between two U-shaped conformations of the LMWG (Fig. 6).

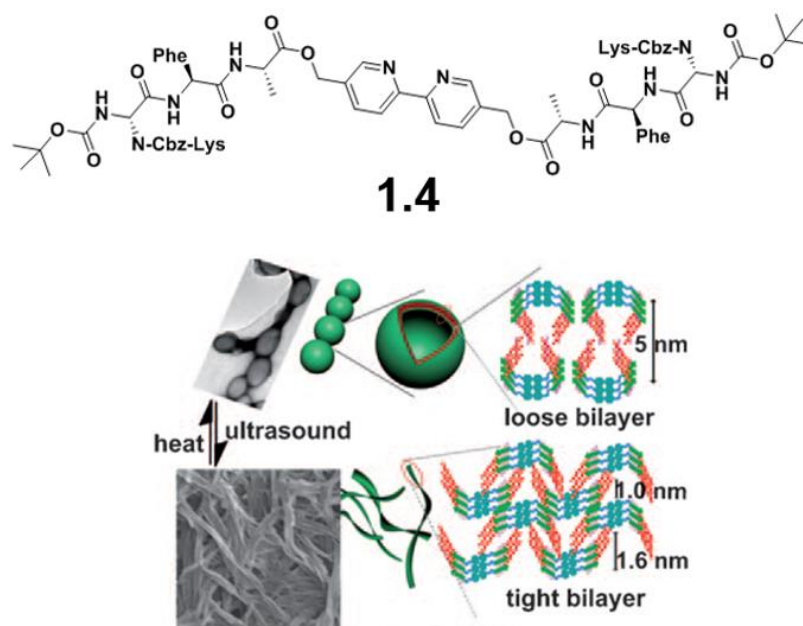


**Fig. 6** SEM images and schematic representations of the morphological transitions induced by heating and sonication of **1.4** in THF-water. Shown right are the proposed packing modes of the gelator in its different conformations. The bipyridine core, drawn in blue, is connected to the tripeptide chains (red) via alkyl ester groups (green). Image reproduced with permission from ref. 36. Copyright 2011 John Wiley and Sons.

Further variability in gel characteristics may arise if self-assembly can produce a range of products. The influence of even subtle changes in supramolecular interactions was strikingly demonstrated by Zhou *et al.*, who reported that a chiral calix[4]arene diamine gels cyclohexane if heated in the presence of D-2,3-dibenzoyltartaric acid but exhibits the reverse behaviour if the L-isomer is used.<sup>95</sup> Gelation in the second case is attributable to the formation of fibres with a lamellar structure, while heat-setting in the alternative system occurs because mismatched interactions between the co-gelators favour discrete, egg-shaped vesicles at lower temperatures. Discrimination between aggregate morphologies is thought to arise because cooling strengthens and shortens intermolecular interactions and thus promotes curvature in growing lamellae, to optimise packing of the chiral species. It should be noted that such dramatic changes in self-assembly outcome can also be achieved by mixing a chiral gelator with the enantiomeric species. According to one general mechanism, known as the chiral bilayer effect, an enantiopure amphiphile forms more stable micellar gels than the corresponding racemate, because crystallisation of the latter can more readily preserve the head-head and tail-tail interactions of the micelle assemblies.<sup>96</sup>

In the competition between self-assembly pathways, kinetic effects are especially important. Thus, an effective method for controlling the aggregation outcome is through variation in the rate of change in temperature. Murata *et al.* demonstrated that rapidly cooling solutions of an azobenzene-linked cholesteryl gelator produces right-handed helices, whereas gradual cooling favours left-handed structures.<sup>97</sup> The chirality of the rapidly cooled system may be inverted by gentle heating, but the reverse transition cannot occur without dissolution of the gel. It may be deduced that the right-handed aggregate is a kinetically favoured but metastable state, which persists only if the cooling rate exceeds the rate of formation of the thermodynamic product.

A more common consequence of gel metastability is collapse of the material due to crystallisation.<sup>39, 45, 98-100</sup> This change in phase may involve a salting-out process,<sup>101, 102</sup> rearrangement of hydrogen bonds<sup>45, 98, 103</sup> or recombination of labile metal-ligand interactions.<sup>104, 105</sup> The relative stabilities of products are often highly sensitive to the environment of the gelator, and in particular the solvent,



which in some multicomponent systems might be temperature-dependent. For example, Vidyasagar and Sureshan report a series of carbohydrate-derived gelators with 1,3-diol motifs that can interact to form linear supramolecular assemblies.<sup>106</sup> Remarkably, aggregation in petrol containing fewer moles of water than gelator affords a strong gel made up exclusively of non-hydrated fibres, while increasing the water concentration beyond one equivalent results in hydrated crystals with no concomitant gel. Although the authors do not explore the effect of temperature, it is feasible that the balance between gelation and crystallisation could be tuned by gradual evaporation of the more volatile co-solvent, or through heat-induced dehydration of a water-containing additive. Comparable dynamic control of the aggregation process has been realised in phase-separating colloidal suspensions, which may afford a kinetically trapped gel material before coalescing into a more compact equilibrium arrangement.<sup>107</sup>

The mechanism of degelation may also exhibit unexpected complexity. A common observation is that the temperature of the gel-sol transition exceeds  $T_{\text{gel}}$ , due to the kinetic stability of the aggregate state.<sup>108-111</sup> Breakup of the gel may be preceded by interconversion of polymorphic assemblies, with relative stabilities dictated by the structure of the gelator and the solvent being gelled. Such transformations need not reflect the pathway of self-assembly during formation of the gel. Indeed, differential scanning calorimetry studies by Čaplar *et al.* found that one series of isomeric chiral alkylamides can undergo as many as three endothermic transitions upon heating, but often display fewer exothermic transitions when cooled.<sup>85</sup> The temperatures of the transitions rarely coincide, and are strongly affected by even small changes in the polarity of the solvent, or the ionisation state or enantiopurity of the gelator. This behaviour is typical of a chiral amphiphilic gelator that can access a range of bilayer arrangements, the energies of which vary subtly in accordance with the symmetry, packing efficiency and chemical environment of the self-assembled molecules.

Many applications of supramolecular gels are dependent on the reversibility of gel-sol and sol-gel transitions. However, while thermoreversibility in small-molecule gels is common, such materials do not always form a simple gelator solution upon heating.<sup>112</sup> Wang *et al.* described a gel that appears to dissolve at a

temperature  $T_{\text{clear}}$ , but retains residual nuclei up to a significantly higher temperature  $T_{\text{soln}}$ .<sup>70</sup> When the system is heated to between  $T_{\text{clear}}$  and  $T_{\text{soln}}$  and cooled, the surviving nuclei facilitate regelation, resulting in a higher-than-expected value of  $T_{\text{gel}}$ . Penaloza *et al.* similarly found, via FT-IR, fluorescence microscopy and small-angle X-ray scattering experiments, that the amphiphilic gelator *N*-palmitoyl-Gly-Gly-Gly-His trifluoroacetate forms fibrous aggregates in both the gel and sol states.<sup>113</sup> Notably, the presence of such intact structures in a sol may lead to the development of new aggregates, with the result that cycles of gel formation and destruction cannot be repeated indefinitely.<sup>29, 35</sup>

Where ready interconversion between gel and sol states is possible, supramolecular materials may be usefully employed as temporary catalyst supports.<sup>114, 115</sup> Small-molecule gels have been successfully utilised in the *in situ* preparation of gold, palladium and platinum nanoparticles for use in a range of liquid- and gas-phase processes. Moreover, a number of studies have shown that gelation can be used to boost the catalytic activity of gelators themselves. For example, Rodríguez-Llansola *et al.* reported that gelator **1.5** can effectively catalyse Henry nitroaldol reactions only in the gel state, wherein interactions between L-proline residues serve to enhance the basicity of the material (Fig. 7).<sup>116</sup> Inducing dissolution of the gel was found to reduce both conversion and

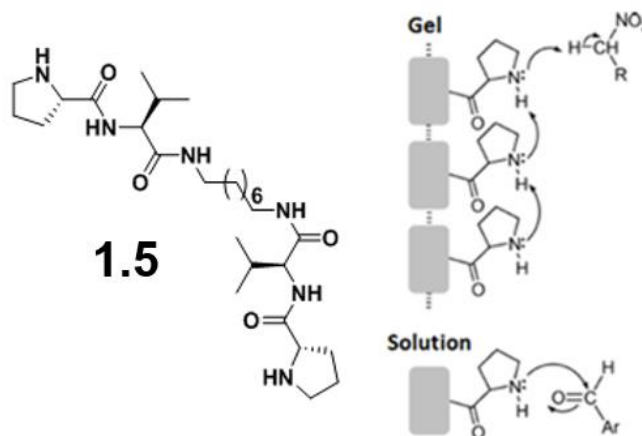


**Fig. 7** Structure of L-proline-based gelator **1.5** and reaction schemes illustrating the dominant reaction pathways in its gels and sols. Proton transfer between proline residues in the gel promotes deprotonation of the nitroalkane reagent, which may subsequently react with an aldehyde to yield a nitroaldol product. In solution, the catalyst is considerably less basic and thus acts as a soft nucleophile, directly attacking the aldehyde to form an imine. Further reactions lead to nitroalkenes and dinitroalkanes as products. Images adapted with permission from ref. 116. Copyright 2009 American Chemical Society.

selectivity: a rise in temperature from 5 to 50 °C was needed to match the reaction rate in the gel, and the yields of side-reactions, such as nitroalkene generation, were markedly increased.

The formation of a gel might alternatively lead to a fall in catalytic turnover. Bachl *et al.* illustrated such an effect in the photooxidation of 1-(4-methoxyphenyl)ethanol by riboflavin acetate.<sup>117</sup> When carried out within a gel, the reaction progressed at a rate 30-60% lower than in a non-stirred solution, and utilising the flavin catalyst as a co-gelator led to deactivation by almost 90%. Notwithstanding these limitations, the use of gels as reaction media did offer some benefits: the catalyst was protected from photodegradation, and in one case the reaction could be conducted without the proton-transfer agents needed in solution. The study additionally demonstrates the advantages of supramolecular gels over many other solid supports. In particular, the transparency of gels permits light-mediated reactions to be performed, and the ability to induce gel-sol transitions allows for easy recycling of the catalyst and gelator.

Switchable gelation has been exploited in a number of other applications. Due to their large surface areas, fibrous gels can serve as supports for catalytic particles, enzymes or quantum dots, or as tuneable media for controlling crystallisation and nanofabrication processes.<sup>39, 118-124</sup> Precipitation in a gel may deliver materials with unusual crystal structures or particle morphologies, which can subsequently be collected by simply dissolving the gel and filtering. Polymer gels exhibiting sol-gel transitions have also proven useful in medical products. In particular, a compound which forms a heat-set hydrogel near the temperature of the body (37 °C) may be administered to a patient as a liquid, but thereafter develop into a functional material with solid-like properties. As described in thorough reviews by Moon *et al.* and Hirst *et al.*, gels of this type have been used in controllable drug delivery systems, internal wound dressings and biocompatible scaffolds to replace, and aid the regeneration of, damaged tissues.<sup>125, 126</sup>

### 1.3 Exploring the self-assembly landscape

Where self-assembly is kinetically disfavoured, a mechanical stimulus may be employed to overcome the activation barrier or offer access to more viable aggregation pathways. The products of such processes may differ significantly from materials obtained by conventional thermal treatments. Indeed, agitation may be the only method by which a gel can be obtained. Piepenbrock *et al.* found that bis(urea) **1.6** forms strong gels in the presence of copper(II) bromide if the solution is shaken, but otherwise affords only viscous solutions (Fig. 8).<sup>127</sup> Cryo-SEM studies indicate that aggregates in the original sol consist mainly of straight, unbranched fibres. Upon shaking, however, the density of interconnections is increased, as shearing the coordination polymer fibres results in their rapid recombination into more highly entangled configurations.<sup>59</sup>

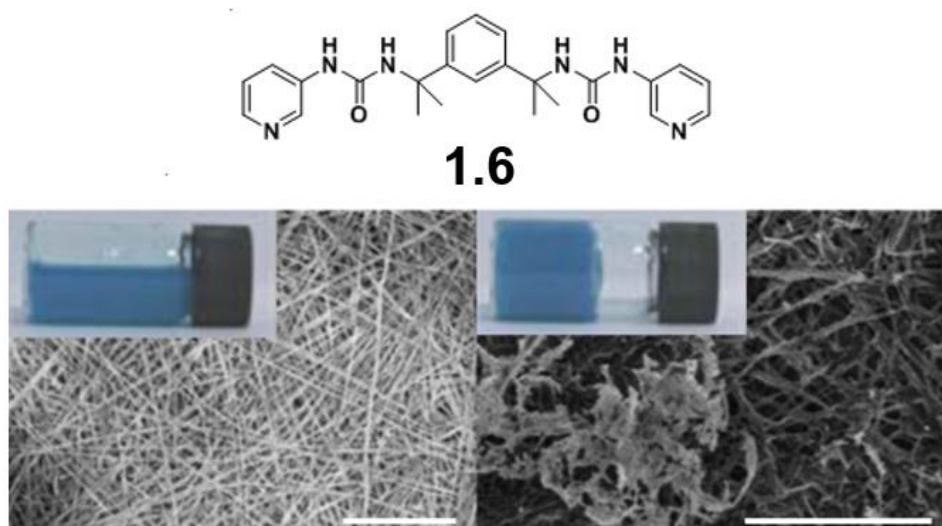


**Fig. 8** Cryo-SEM images of **1.6** and 0.3 equivalents of copper(II) bromide in methanol, before (left) and after (right) shaking. Scale bars represent 1 and 2  $\mu\text{m}$  respectively. Inset are images of the bulk materials, illustrating the shear-induced sol-gel transition. Images adapted from ref. 127 with permission from The Royal Society of Chemistry.

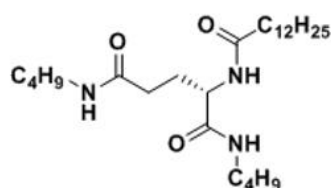
The use of a mechanical stimulus to induce a kinetically disfavoured self-assembly process does not preclude thermoresponsive behaviour in the resulting material. This principle was illustrated in a study by van Herpt *et al.*, profiling the gelation behaviour of a carbazole-based bis(urea).<sup>112</sup> Although gels in DMSO cannot be obtained by thermal cycling, they may be formed in less than a minute when solutions of the gelator are vigorously shaken. The gels are destroyed by heating but, intriguingly, reform upon cooling if the temperature remains below

75 °C. The presence of secondary aggregates in the heated sol is reflected in the NMR signals of the gelator, which are diminished by slow relaxation in the gel state and only fully recover above 80 °C. It is suspected that the dissolved structures are the initial products of self-assembly and serve as intermediates for the reversible formation of larger gel fibres. Agitation may initiate this process by fragmenting nascent fibres to create additional sites for secondary nucleation. Alternatively, the mechanical input may act as a driving force for convection, which has been shown in similar shear regimes to lead to self-accelerating particle coagulation.<sup>128</sup> Ultrasonication, or exposure to sound waves with frequencies of 1 MHz or higher, is another stimulus often employed in the preparation of supramolecular materials. Within a typical laboratory sonication bath,<sup>129</sup> propagation of ultrasound through a sample solution generates transient bubbles of vapour which undergo abrupt implosion, or cavitation, under the pressure of the surrounding liquid.<sup>130, 131</sup> Kinetic<sup>132</sup> and sonoluminescence<sup>133</sup> studies suggest that the short timescale of cavitation may lead to local temperatures of up to 5000 K and pressures of several hundred atmospheres. Energy from cavitation is released in the form of shockwaves and jets which may fragment nearby particles, or cause them to melt and fuse through high-speed collisions.<sup>134</sup> Perhaps surprisingly, self-assembly can take place in such an environment,<sup>135-137</sup> and may even proceed at a lower concentration, higher temperature or faster rate than would be possible under milder conditions.<sup>138-140</sup> Moreover, the resulting aggregates may prove unusual, with structures or physical properties that would be difficult to achieve by other methods.

Many routine uses of ultrasound exploit its capacity to break up and dissolve materials that are resistant to thermal treatment. It is interesting to note that such solubilisation can, under certain circumstances, prove instrumental to gelation. In one study, Anderson *et al.* exploited sonication to partially dissolve the highly insoluble compounds uric acid and melamine in water, allowing the materials to re-aggregate as a stable co-gel.<sup>141</sup> Similarly, Baddeley *et al.* attributed the sonication-induced gelation of one pyridine-cored bis(urea) in alcohols to the dissolution of “imperfect” assemblies, which may thereafter reassemble into a fibrous product.<sup>142</sup> The application of ultrasound provides a driving force for

equilibration, so that aggregates can evolve into the thermodynamic product in spite of kinetic competition from alternative pathways.

Sonication may further promote gelation through its effects on nucleation.<sup>139, 143, 144</sup> Under ambient conditions, aggregation typically involves the development of a relatively small number of nuclei into dense, highly branched spherulites through gradual sequestration of the dissolved gelator. Exposure to ultrasound, however, fragments and disperses the initial aggregates to create a much larger population of nuclei, resulting in vastly accelerated fibre growth. Because separate assemblies propagate independently, they experience a less supersaturated environment on average and mature into smaller, less branched and more interpenetrated spherulites that are better suited to gel formation (Fig. 9). Wang *et al.* exploited this phenomenon in gels of **1.7** to reduce the CGC from 2.0 to 0.5% (w/v) and increase gel strength by up to three orders of magnitude relative to thermally generated materials.<sup>144</sup> The degree of branching, average fibre diameter and thermodynamic stability of the sonogels could be tuned via the temperature or concentration, or by varying the duration or power of the mechanical stimulus.<sup>112, 138, 145</sup>



**1.7**

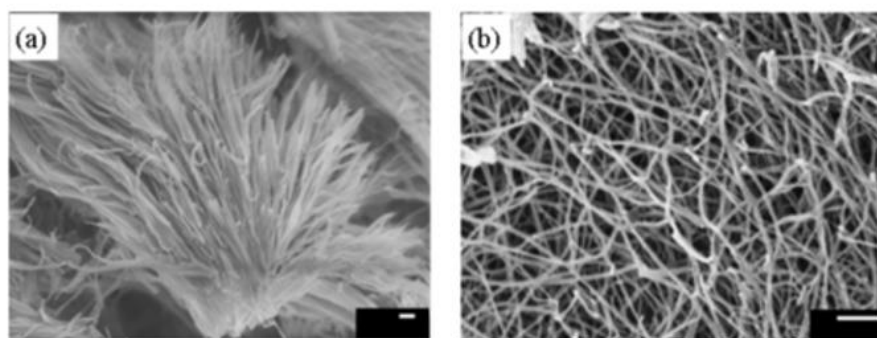


**Fig. 9** SEM micrographs (scale bars 500 nm) of propylene glycol gels of **1.7** after a heating-cooling cycle (a) and with additional ultrasound treatment (b). An increase in gel strength after sonication is associated with a conversion from highly branched spherulites to thicker and less interconnected fibres. Image reproduced with permission from ref. 144. Copyright 2009

American Chemical Society.

The microstructures of sonogels are often markedly different from those of aggregates generated by other mechanical processes. As a result of the more extreme conditions experienced by the material, a gel produced by sonication typically exhibits particles with clearer signs of fragmentation. For example, Bardelang *et al.* found that sonicated crystals of a TEMPO-based compound are smaller and more effectively gelating than those subjected to shaking or stirring.<sup>146</sup> Likewise, metallo gels reported by Weng *et al.* are strengthened by vigorous shaking or sonication, due to the progressive breakup and fusion of globular particles upon exposure to shear forces.<sup>147</sup> By contrast, Teunissen *et al.* describe gels of a urethane-functionalized ditopic ureidopyrimidone, which become stronger only after stirring the system for several hours.<sup>148</sup> Infrared and NOESY NMR experiments suggest that lateral stacking of the initial linear assemblies is obstructed by urethane-ureidopyrimidone interactions, but prolonged agitation causes these kinetically trapped structures to dissociate, allowing for the formation of larger aggregates linked by a continuous network of urethane-urethane motifs.

Unlike more gentle mechanical stimuli, sonication may induce changes in the local environment of a molecule sufficient to dramatically alter its structure. One possible outcome is a conformational change, which might influence the ability of the molecule to engage in supramolecular interactions. In one of the earliest reports of sonogelation by an LMWG, Naota and Koori showed that the chiral palladium(II) complex **1.8** converts from a clothes-peg-like conformation to a more open structure, permitting the self-assembly of continuous,  $\pi$ - $\pi$  stacked chains (Fig. 10).<sup>149</sup> Gelator **1.9**, similarly, was found by Liu *et al.* to twist under sonication, forcing the central naphthalimide ring into the plane of the platinum(II)-terpyridyl head group (Fig. 11).<sup>150</sup> While the original molecules form vesicles bounded by hydrophilic head groups, aggregates of the new conformer consist of extended bilayers, with outwardly oriented cholesteryl groups creating a hydrophobic interface. Such particle-to-fibre transitions have been demonstrated in a wide range of supramolecular materials, and are of particular interest in peptide-based systems, where unfolding can give rise to the cross- $\beta$  sheet assemblies implicated in amyloid aggregation.<sup>44, 151</sup>

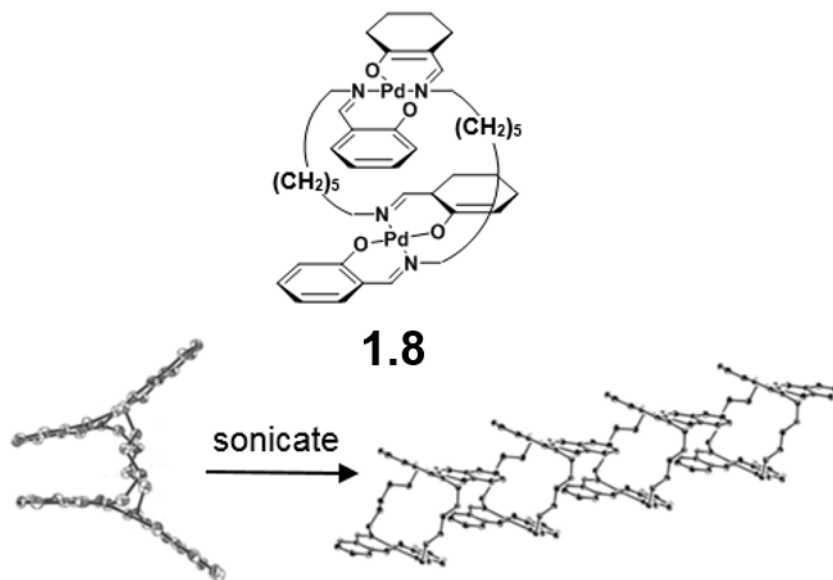


**Fig. 10** Sonication of **1.8** in a range of organic solvents induces conversion from a clothes-peg conformation to a more open structure, which can undergo  $\pi$ - $\pi$  stacking to form extended assemblies. The packing arrangement shown is part of the X-ray crystal structure of an analogous complex, in which imine nitrogen atoms are linked by chains of six methylene groups. Image adapted with permission from ref. 149. Copyright 2005 American Chemical Society.

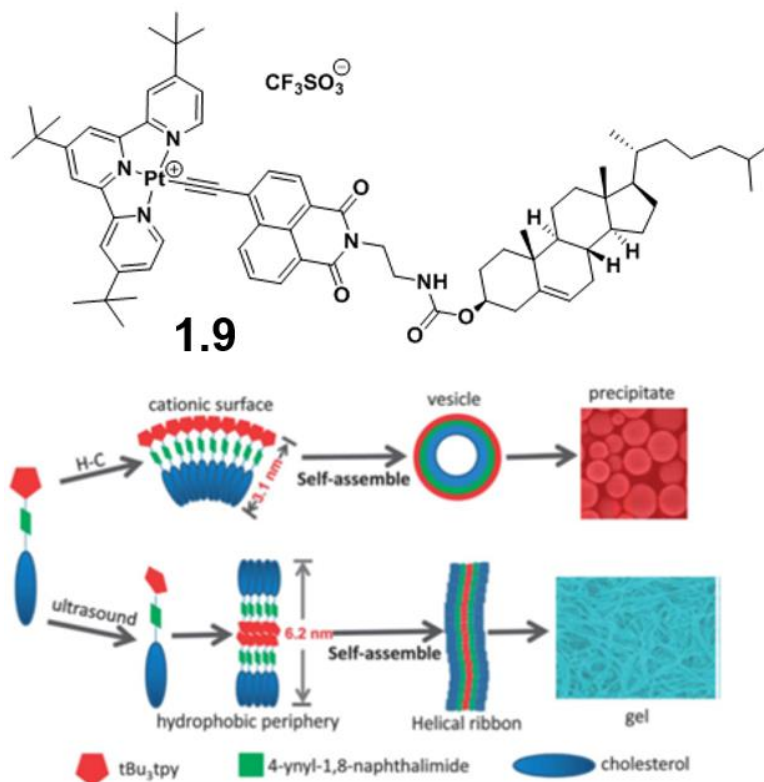


**Fig. 11** Schematic representation of the self-assembly mechanism of platinum(II) complex **1.9**.

Heating and cooling (H-C in diagram) produces a vesicular precipitate, but a conformational change induced by sonication allows for closer interactions between cationic head-groups to give ribbon-like fibres. Image reproduced from ref. 150 with permission from The Royal Society of Chemistry.



In addition to driving conformational changes, ultrasound may facilitate the breaking and rearrangement of labile bonds. Interactions involving metals are often relatively weak and thus particularly susceptible to scission. Paulusse *et al.* have studied the effects of sonication on a number of coordination polymer systems, and describe the generation of reactive fragments which can exchange ligands, cyclise or recombine to create mixtures of new species.<sup>152, 153</sup> A report by Zhang *et al.* similarly linked the sheet-to-fibre transformation of a coordination polymer to a rearrangement of the constituent zinc(II) complexes, from tetrahedral to see-saw configurations.<sup>154</sup> Paradoxically, sonication may also result in the strengthening of interactions. Work by Komiya *et al.* exemplifies this phenomenon: the platinum-based analogue of complex **1.8** forms weakly associated and non-emissive vesicular assemblies in solution, but exposure to ultrasound results in phosphorescent fibrous gels, due to conversion of the parent aggregates into structures with strong  $\pi$ - $\pi$  and metal-metal interactions.<sup>155</sup>

Other changes in aggregate morphology are often attributable to the disruption of hydrogen bonds. An increase in the propensity for non-covalent bonding may facilitate a transition from discrete self-assembled systems to more continuous architectures. For example, Wang *et al.* found that sonication-induced gelation of cyclohexane by (*R*)-*N*-Fmoc-octylglycine occurs alongside an increase in fibre branching and shifts in the FT-IR spectrum of the system, which could reflect a switch from  $R_1^1(7)$  and  $C(5)$  interactions to  $C(4)$  motifs.<sup>156</sup> Similarly, Deng *et al.* reported that tripodal tris(urea)s form dimeric aggregates in acetonitrile solutions, but reassemble under ultrasound to give gels comprising  $\alpha$ -tape motifs.<sup>157</sup> Sonication may also influence binding to solvent molecules, leading to changes in gelator solubility or the solvation capacity of an aggregate.<sup>127, 145</sup> In a study by Park and Kim, concerning the gelation of a 2'-deoxyadenosine derivative in water, an effect of this nature was cited to explain the conversion of needle-like precipitates to interconnected fibres upon sonication.<sup>158</sup> It is proposed that hydroxyl radicals solubilise the gelator by converting it to a more hydrophilic oxidised species, but subsequent reduction causes the solution to become supersaturated, leading to the rapid formation of an amorphous gel.

Although the molecular effects of ultrasound may serve to initiate self-assembly, the morphologies of the final aggregates more typically reflect the large-scale physical impacts of cavitation events. Constructive processes, such as the fusion of discrete particles into sheets and fibres, are sometimes observed (Fig. 12),<sup>138</sup> but these are frequently accompanied by signs of exposure to extreme conditions, such as a decrease in particle size<sup>145, 159, 160</sup> or loss of crystallinity. More generally, the application of stress to a gel often induces a transition between solid- and liquid-like properties, culminating in fracture, plastic deformation and near-total liquefaction. This strain behaviour may be associated with other, non-mechanical responses such as AIE effects, and can be tuned, like many gel properties, through careful optimisation of the gelator structure and its aggregation environment.

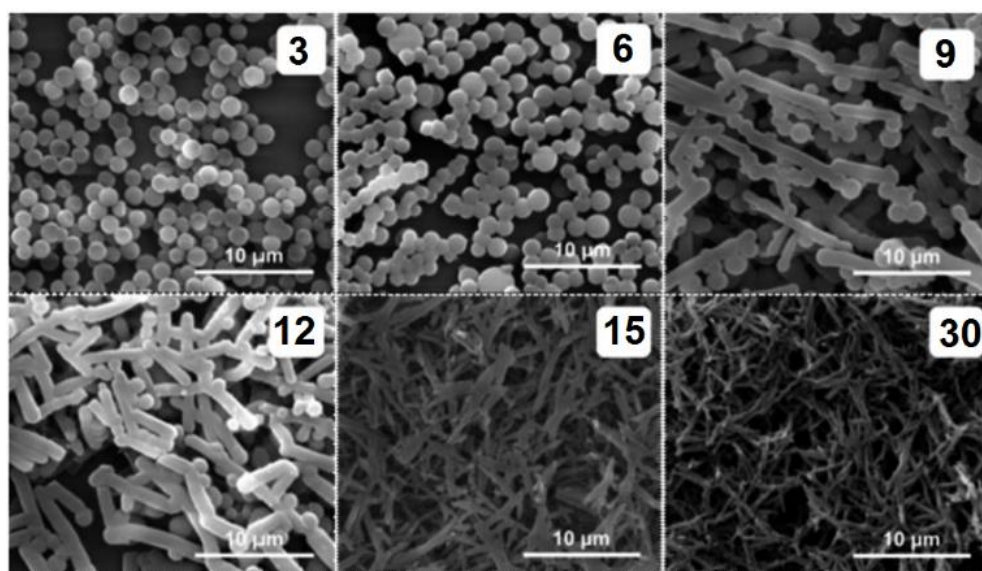


**Fig. 12** SEM images (after drying) of a cholesteryl calix[4]arene in isopropanol, illustrating the changes in morphology during sonication to form a fibrous gel. Numbers (inset) indicate the number of minutes for which samples were agitated. Fusion of vesicles appears to reach completion after 15 minutes. Image adapted from ref. 138 with permission from The Royal Society of Chemistry.

## 1.4 Rheological characterisation

In many applications, the usefulness of a gel is dictated by its behaviour on exposure to a mechanical stimulus. Changes in bulk properties are commonly probed by means of an oscillatory shear experiment, in which a sample is sandwiched between two plates and subjected to a periodic rotational stress.<sup>161</sup>

The shear modulus  $G$ , defined as the ratio of shear strain to shear stress, can be resolved into an in-phase component  $G'$  and out-of-phase component  $G''$ , corresponding to elastic and dissipative deformations respectively. In a typical gel, the storage modulus  $G'$  exceeds the loss modulus  $G''$  by an order of magnitude and remains roughly constant up to the yield stress,  $\delta$ , at which the material begins to flow. The behaviour in the vicinity of  $\delta$  may be indicative of the mechanism by which gel disruption arises. Hyun *et al.* suggest that an increase in  $G'$  could be due to the formation of close-packed aggregates, while an increase in  $G''$  signifies the breakup of such structures as they align with the direction of shear.<sup>162</sup> The latter effect, termed weak strain overshoot, is common among gels containing crystals and other discrete particles, and frequently implicated in complex mechanoresponsive behaviours.<sup>163</sup> For example, Piepenbrock *et al.* observed that weak strain overshoots in silver(I) metallo gels of a pyridyl-functionalised bis(urea) correlate with larger  $G'$  values, lower yield stresses and higher densities of silver nanoparticles, and may be enhanced by UV irradiation or increased silver loadings.<sup>164</sup> Yu *et al.*, meanwhile, noted that a rise in  $G''$  during the shear-induced collapse of a toluene gel of **1.10** coincides with the fragmentation of nano-ring structures, which can reassemble on resting to restore the original gel network (Fig. 13).<sup>165</sup>

The dependency of rheological parameters on the gelator concentration,  $c$ , may also be instructive. Between the CGC,  $c_0$ , and the point of saturation, pre-shear  $G'$  and  $\delta$  usually change in accordance with the power law expression  $(c - c_0)^n$ , or  $c^n$  if  $c \gg c_0$ . Shih *et al.* propose that the exponent  $n$  in colloidal gels will depend on whether the interactions between aggregate flocs are weaker than, or comparable to, those of the floc interior.<sup>166</sup> In the former case, termed the weak-link regime,  $n$  is dictated solely by the fractal dimension of the floc network and is typically greater than unity. In the strong-link regime, meanwhile, an additional dependency on the fractal dimension of the internal floc structure causes  $\delta$  and  $c$  to become negatively correlated, whilst  $G'$  scales with powers of  $c$  higher than those of the weak-link regime. Sangeetha *et al.* applied this theory to gels of a cationic bile acid derivative in aqueous sodium chloride, and found that the system undergoes a transition from weak-link to strong-link behaviour as the

gelator concentration rises.<sup>167</sup> The value of  $\delta$  reaches a maximum at the transition point, as expected, but the rate of change in  $G'$  undergoes a surprising increase, due to a substantial reduction in the fractal dimension. Such marked rheological variation can result from dramatic changes in the size or connectivity of a gel's constituent particles. For example, Xu *et al.* observed that gels of a nitrobenzoxadiazole-containing cholesteryl derivative in THF-methanol and pyridine-methanol mixtures become stronger with increasing concentration of the gelator or methanol antisolvent, due to a transition from narrow fibrous aggregates to dense spheroidal particles several micrometres in diameter.<sup>168</sup>

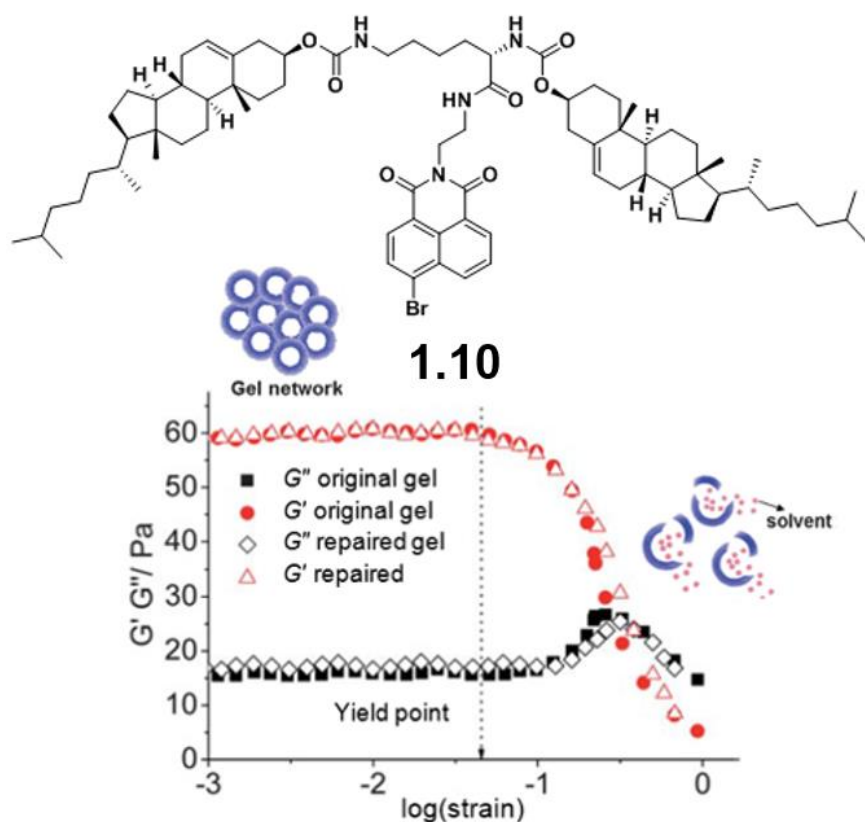


**Fig. 13** Strain-sweep plots for a 0.86 wt.% gel of **1.10** in toluene at 25 °C, before and after self-repair. Resting of the gel after disruption leads to complete restoration of its original rheological properties. As represented schematically, the increase in  $G''$  near the yield point of the gel coincides with fragmentation of nano-ring structures under the imposed stress. Image adapted from ref. 165 with permission from The Royal Society of Chemistry.

Not all gels are well described by the model of colloidal aggregation. Whereas  $G'$  in floc-based networks commonly conforms to a power law with  $n > 3$ , particularly in the strong-link regime, many small-molecule gels exhibit  $G'$  vs.  $c$  plots that are almost exactly quadratic.<sup>10</sup> Values of  $\delta$  also increase with  $c$  but at

somewhat lower rates, with exponents  $n$  in the vicinity of 1.5. Such behaviour is characteristic of a cellular network made up of stiff rods with fixed points of interconnection, wherein  $G'$  scales linearly with the Young's modulus,  $E_s$ , of the load-bearing struts.<sup>169</sup> By fitting this model to the rheological profiles of chiral bis(urea) organogels, and assuming the gel fibres to be equal in density to the corresponding single crystals, Lloyd *et al.* were able to estimate values for  $E_s$  in the range 1–2 GPa.<sup>170</sup> Helical nanofibres of a tripodal tris(urea) were found by Stanley *et al.* to exhibit similar mechanical properties, but in this system the mechanism of gel collapse in the region of  $\delta$  was also considered.<sup>171</sup> Noting that the observed values of  $\delta$  are an order of magnitude lower than expected if failure occurs through elastic buckling, it was proposed that fibre networks collapse via plastic deformation, with individual fibres displaying a plastic yield stress on the order of 1 MPa. Plastic failure in gels is generally marked by a large increase in strain deviating from the linear elastic stress-strain relationship, and involves non-recoverable processes such as the fracturing of crystallites and breakage of permanent fibre junctions. Strain is concentrated in the mostly weakly connected regions of the fibres and may be accompanied by twisting or untwisting of the affected fibrils, weakening of the intermolecular bonds between fibrils and an increasing abundance of solvent-aggregate interactions.<sup>172, 173</sup> In consequence, the value of the plastic yield stress is usually dependent on the solvent, level of crystallinity and dimensions of fibres and their constituent fibrils.

Both floc-based and cellular materials can be described by a spherulitic model of aggregate growth. Continuous fibre networks arise if fibre branching by secondary nucleation vastly outpaces the primary nucleation of additional spherulites, whereas flocs are observed if the rates of the two processes are similar in magnitude. In both cases, the strength of the resulting material may be controlled via adjustments to the fibre dimensions and connectivities. By simulating spherulitic networks of interconnected rigid rods, Shi *et al.* derived a power law relationship between  $G'$  and the ratio  $L/R$ , where  $L$  is the length of a rod between branch points and  $R$  its cross-sectional radius.<sup>60</sup> The exponent of this relationship was estimated as -1.7, indicating that  $G'$  may be dramatically enhanced by increasing either the density of network junctions or the thickness

of the component rods. In floc-based networks, an increase in the number of weak interparticle junctions offsets increasing spherulite density to produce a more gradual scaling of  $G'$ , but changing the aggregation environment to favour more frequent branching remains an effective strategy for maximising gel strength.<sup>73</sup> A promising approach is to add surfactants to the gelator solution to modify the surface energies of growing fibres. Chen *et al.* found that gels of 2,3-di-*n*-decyloxyanthracene in DMSO display smaller and more highly branched spherulites in the presence of the non-ionic surfactant polyethylene glycol *t*-octyl-phenyl ether (Triton X-100), whilst another non-ionic surfactant sorbitan monolaurate (Span 20) produces larger, more weakly branched spherulites comparable to a continuous fibrous network.<sup>174</sup> NMR studies suggest that the alkyl chains of Span 20 associate with those on the sides of gel fibres to promote branching along their length, whereas Triton X-100 interacts with fibre tips and primary nucleation sites to facilitate the initiation and peripheral branching of isolated flocs. Both surfactants serve to enhance  $G'$  at low concentrations, but addition of Span 20 in larger quantities may produce the opposite result, due to excessive loss of the extended branches needed for effective interpenetration of the fibre networks.

The presence of surfactants is just one of a number of factors that can be harnessed to modify gel strength. Tang *et al.* showed that floc-based propylene glycol gels of **1.7** can be weakened by Span 20, which suppresses spherulitic growth by confining branch points to the periphery of primary fibres (Fig. 14).<sup>175</sup> At high concentrations, however, the surfactant additive forms spherical micelles, which act as nucleation sites for spherulites to produce an increase in  $G'$ . In the same system, Yuan *et al.* increased spherulite size by raising the temperature, but were also able to limit the number of spherulites along one axis by inducing gelation within a narrow glass cell.<sup>63</sup> While  $G'$  initially scales with average spherulite separation,  $\zeta$ , to the power of just 0.12, imposing a gap of 0.85 mm leads to a fourfold increase beyond 70 °C, the temperature at which  $\zeta$  and the gap width become comparable in size.  $G'$  rises until 80 °C but falls at higher temperatures due to an increasing dependency on the branch separation  $L$ , which varies in inverse proportion to the supersaturation.<sup>176</sup>

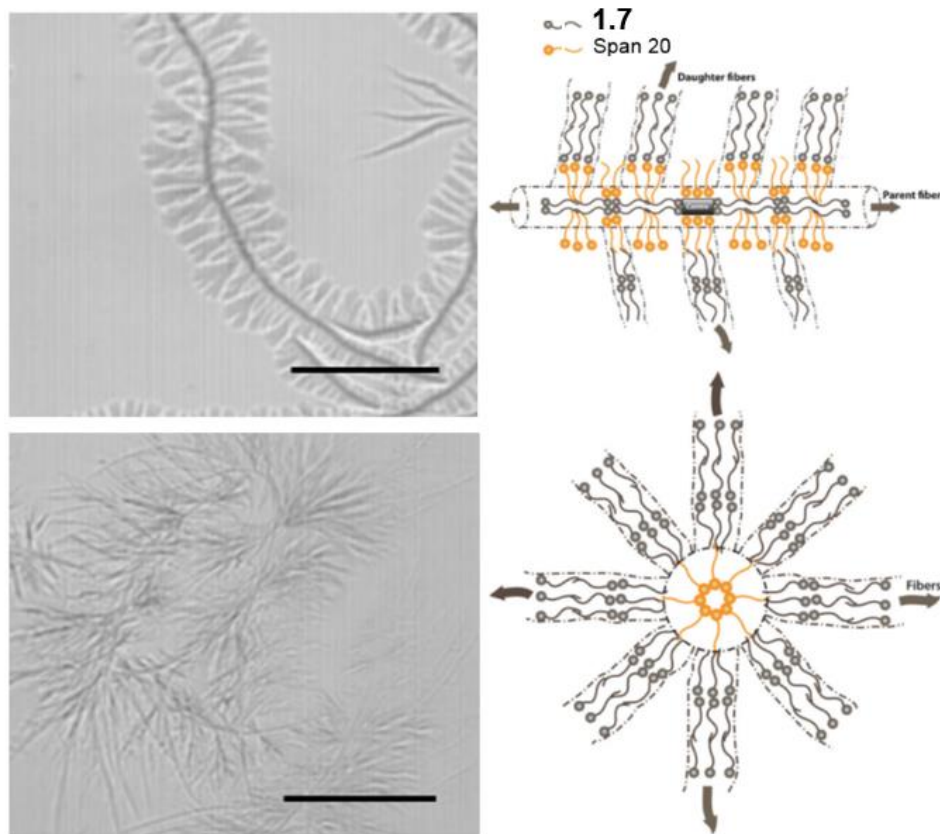


**Fig. 14** Optical microscope images (scale bar 100  $\mu\text{m}$ ) and schematic diagrams illustrating the effect of the surfactant Span 20 on the aggregation of gelator **1.7** in propylene glycol. Below the critical micelle concentration (CMC) of Span 20, the surfactant promotes branching of the gel fibres to produce a comb-like topology (upper images). Micelles of Span 20, meanwhile, act as nucleation sites for fibre growth, producing spherulitic aggregates (lower images). Images adapted with permission from ref. 175. Copyright 2009 John Wiley and Sons.

Deformation of a soft material under stress does not occur instantaneously, but over a finite timescale linked to its viscosity,  $\mu$ .<sup>177</sup> Viscosity under steady shear is defined as the ratio of shear stress  $\sigma$  to shear strain  $\dot{\gamma}$ . In oscillatory shear experiments, meanwhile, it is customary to define a complex viscosity,  $\mu^*$ , equal to the magnitude of  $G$  divided by the frequency  $\omega$ . The viscosity of a Newtonian fluid is constant with respect to both  $\dot{\gamma}$  and  $\omega$  and obeys the Cox-Merz rule, adopting the same value irrespective of the stress regime. In non-Newtonian fluids such as gels, however,  $\mu$  and  $\mu^*$  are variable and may therefore violate the Cox-Merz rule under certain conditions. It is generally true for gels below their yield point  $\delta$  that  $G'' \ll G'$ , and the Kramers-Kronig relation further asserts that  $G''$  scales as the rate of change of  $G'$  with  $\omega$ .<sup>178</sup> Thus,  $G'$  should remain almost constant over a wide range of  $\omega$ , resulting in a roughly inverse relationship between  $\mu^*$  and  $\omega$ . A more accurate analysis reveals that  $G'$  increases with  $\omega$  in

an approximate power law relationship, with an exponent equal to the ratio  $G''/G'$ .<sup>179</sup> Classically cellular gels of 12-hydroxystearic acid in toluene, dodecane and nitrobenzene were shown by Terech *et al.* to conform to this trend, exhibiting exponents in the range 0.02–0.09.<sup>10</sup> The associated negative correlation between  $\mu^*$  and  $\omega$  is termed shear-thinning behaviour and may be ascribed to alignment of fibres along the axis of stress. It is important to note that increased flow at higher rates of shear need not correspond to yielding of the material: provided the stress does not exceed  $\delta$ , the magnitude of strain remains almost unaltered and deformation of the material is predominantly elastic and reversible. The greater-than-linear reduction in viscosity with increasing flow rate is particularly useful in materials such as lubricants and dyes for inkjet printing, which are required to flow under temporary high-shear conditions but otherwise display solid-like properties.

Following mechanical disruption, the aggregates in a gel may reassemble into a new solid or viscoelastic material. Reconstruction of a gel in response to macroscale fracturing is often referred to as self-healing, and is fairly common among metallogels and other materials supported by labile covalent bonds and/or dynamic supramolecular motifs.<sup>180, 181</sup> Shi *et al.* prepared self-healing hybrid gel films with conductivities up to  $12 \text{ S m}^{-1}$  by freeze-drying phytic acid hydrogels and impregnating the resulting aerogels with acetonitrile solutions of a gelating zinc(II)-terpyridyl coordination cage.<sup>182</sup> The gels become more resistive if cut or stretched but rapidly return to their original state on resting, allowing a circuit to be broken and reconnected in less than one minute. Likewise, Sahoo *et al.* found that the dicyclohexylammonium salt of Boc-protected L-glycine forms a robust double-stranded hydrogen bonded network in nitrobenzene, affording a fibrous gel that can be cut and fused together with limited loss of tensile strength.<sup>183</sup> Interestingly, any change in the gelator composition results in a marked reduction in both the strength of the gel and its self-healing ability, as other amino acids and ammonium cations favour an alternative tape-like supramolecular network that is less well suited to gel formation.

Recovery of a gel can also occur in response to shaking, shearing or sonication, which lead to microscale fracturing in the bulk of the material. Self-healing of this



nature may partly result from surface tension and buoyancy forces, especially if the gel is surrounded by an immiscible liquid phase. For example, Yan *et al.* found that heptane gels of the ferrocene-containing cholesteryl compound **1.11**, dispersed in an aqueous iodine solution with shaking, efficiently absorb and entrap the iodine before reforming an easily isolable gel at the air-solvent interface (Fig. 15).<sup>184</sup> More generally, the bulk regeneration of a gel can be attributed to the renewal of junctions between fibres, and may be observed following an oscillatory shear experiment as a gradual increase in  $G'$  and reduction in strain. Gels that respond to stresses in excess of  $\delta$  by undergoing progressive shear-thinning over time, but tend towards their initial solid-like state after removal of the stress, may be referred to as thixotropic materials.<sup>185-187</sup> The magnitude of a thixotropic response may be modified with the use of additives that interact strongly with the gelator,<sup>187</sup> or by altering the aggregation environment or type of stress applied. In one notable study, co-gels of a pyridyl bis(urea) with dicarboxylic acids were found by Liu and Steed to reform after mechanical disruption, but become non-thixotropic upon exposure to heating, high pH or prolonged sonication.<sup>188</sup>



**Fig. 15** Heptane gels of **1.11** are disrupted by shaking but reform on resting, providing an effective method for extracting iodine from an aqueous solution. The gels are thermoreversible and may also be disrupted irreversibly through oxidation with ceric ammonium nitrate, producing a colour change from orange-brown to green. Image adapted with permission from ref. 184. Copyright 2015 Elsevier.

A further complication in the design of thixotropic gels is the possibility of material fatigue. Non-recoverable strain increases with the magnitude of the applied stress and can be attributed to the loss or weakening of fibre junctions or large-scale changes in aggregate morphology. For instance, Lloyd *et al.* observed that interconnections between fibres in a chiral bis(urea) gel become thinned after shearing and self-repair, resulting in a  $G'$  value 45% lower than that of the parent material.<sup>170</sup> It is worth noting that the self-healing capacity of a gel may not be correlated with its initial resistance to mechanical disruption. In one study, Terech *et al.* showed that a decane gel of 12-hydroxystearic acid deforms ten times more slowly than a DMF gel of terpyridyl ligand **1.12** and nickel(II) chloride but exhibits strain recovery of just 32%, compared with 72% in the metal-containing system (Fig. 16).<sup>189</sup> The thermodynamic stability of a gel is of particular importance since fragmented assemblies may be sequestered by competitive modes of aggregation, preventing the reestablishment of lost transient junctions under dynamic conditions.<sup>190</sup>

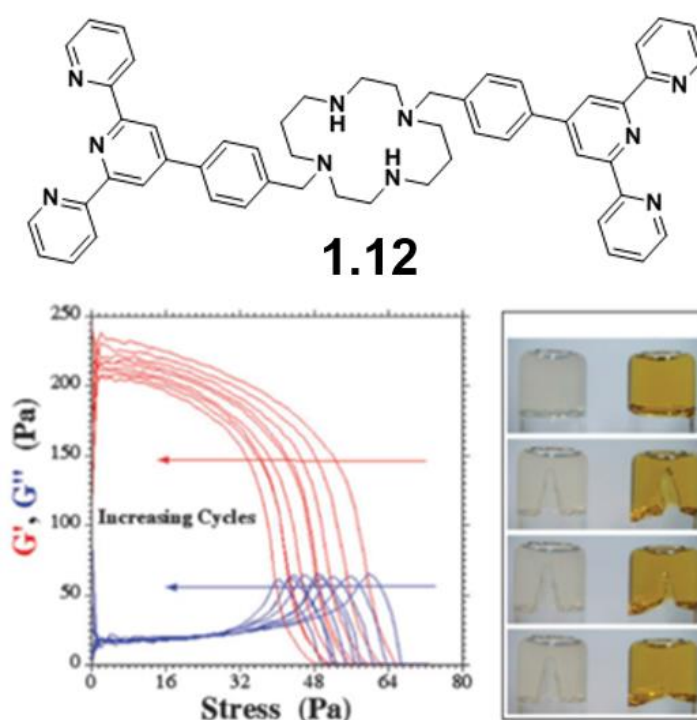


**Fig. 16** Stress-sweep plots for a DMF gel of **1.12** (40 mM) and two equivalents of nickel(II) chloride over multiple cycles of disruption and recovery. The gel recovers after fracturing within 48 hours (right) but a decane gel of 12-hydroxystearic acid with the same storage modulus does not exhibit self-healing behaviour (centre). Images adapted from ref. 189 with permission from the PCCP Owner Societies.

The strength of a gel does not always decrease upon the application of stress. Stiffening may arise at stresses less than  $\delta$  if these lead to increased jamming, close packing or crosslinking of aggregates.<sup>191</sup> Compression stiffening is implicated in the behaviour of certain biological tissues,<sup>192</sup> and could be reproduced synthetically by exploiting feedback between the density of crosslinks and their rate of formation. A computational study by Yashin *et al.* showed that coupling the Belousov-Zhabotinsky reaction with a gel-based ruthenium(II)-terpyridyl catalyst might be a promising strategy, since the proportion of metal sites undergoing reduction and crosslinking would increase upon compression of the material.<sup>193</sup> The magnitude of the effect would largely be dictated by the concentration of fibres and could thus be usefully modulated by triggering a deswelling response. Such rheological sensitivity to particle density mirrors that of biological materials such as blood clots, which consist of a fibrous fibrin network with entrapped cells and platelets. Materials of this type soften under compression in the manner of a classical polymer network<sup>194</sup> but exhibit stiffening behaviour if water is lost, increasing the density of the fibre network.<sup>195</sup> Stiffness perturbations are thought to play an important role in cellular development, signalling and disease processes, as changes to the characteristic rheological properties of tissues can strongly influence the shapes, motilities, growth rates and differentiation pathways of constituent cells.<sup>196-198</sup>

Gels of fibrous biological macromolecules such as fibrin, actin and collagen may also display stiffening behaviour if subjected to extensional stresses exceeding a critical value,  $\sigma_c$ .<sup>199, 200</sup> Stress stiffening can be attributed to a transition between entropic and enthalpic stretching and is typically characterised by a power-law scaling of  $G$  with  $\sigma$ , tending towards a maximum exponent of 1.5.<sup>201</sup> Though common in biomaterials, stress stiffening is rarely observed in synthetic gels as the requirement for semi-flexible fibres, or a persistence length comparable to the distance between junctions, is difficult to satisfy.<sup>202</sup> Nonetheless, biomimetic stiffening behaviour was realised by Jaspers *et al.* in a range of hydrogels comprising polyisocyanopeptides with peripheral tri(ethylene glycol) substituents.<sup>203</sup> The materials display dimensions comparable to those of neurofilaments but can access substantially higher  $G$  values with stiffening over a

wider range of stresses. Furthermore, the gels are heat-set and display unprecedented marginal properties close to  $T_{\text{gel}}$ , transitioning from viscous fluids to solid-like elastic networks in response to extremely small applied forces. Stress stiffening may be tuned, like other rheological properties, through variation of the gelation conditions. Both pre-shear  $G$  and  $\sigma_c$  scale roughly quadratically with concentration and exponentially with temperature, whilst the rate of change of  $G$  with  $\sigma$  increases slowly and linearly as the material is heated.

Stiffening of a gel under a directional mechanical stimulus may be partly due to alignment of fibres with the applied force. Indeed, shear may induce gelation by converting coiled fibres into extended bundles suitable for incorporation into a three-dimensional network. Pappas *et al.* demonstrated that short, curved nanofibres of the tripeptides  $^{\text{D}}\text{FFD}$  and  $^{\text{D}}\text{FFI}$  can be converted to bundles of parallel nanofibres through directional sonication, resulting in strong gels with pronounced supramolecular chirality.<sup>204</sup> Alignment of nanofibres in solution may also be induced by audible (20 Hz to 20 kHz) sound waves, or within the high-shear flows of a printing nozzle or liquid vortex. The susceptibility of an aggregate to alignment and the magnitude of the resulting optical effects can in some cases be controlled by exploiting other stimuli-induced responses, such as the isomerisation of a photoreactive switch. Velocity gradients generated by 120 Hz sound at an amplitude of 13.5 Pa were found by Hotta *et al.* to orient nanofibres of a DTE-containing bis(urea) in *n*-hexane, but the resulting linear dichroism (LD) signal spans UV and visible frequencies only if the closed DTE isomer is used.<sup>205</sup> More strikingly, the azobenzene derivative **1.13** produces a strong sound-induced LD signal in cyclohexane solutions of its *trans* form but becomes LD silent when isomerised, due to fragmentation of the fibrous aggregates into non-orientable spheroidal particles (Fig. 17).<sup>206</sup>

The symmetry of fibres can be similarly influenced by anisotropic stress. Net chirality in assemblies of achiral or racemic molecules commonly results from chiral impurities, trace enantiomeric enrichment of the parent solution<sup>207-209</sup> or the aggregation phenomenon known as the Adam effect,<sup>210</sup> in which heating or mechanical disturbance causes a chiral material to evolve from a small, non-statistical population of primary nuclei.<sup>211-213</sup> However, there is some evidence to

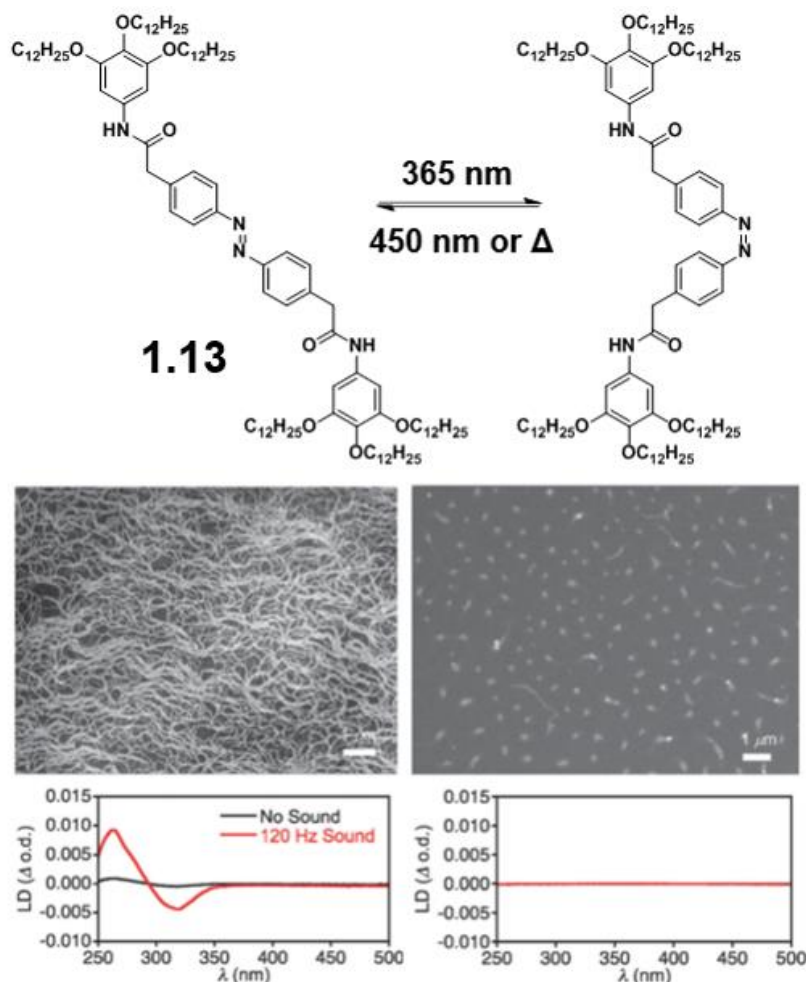


**Fig. 17** SEM micrographs of air-dried samples of *trans*-**1.13** (left) and *cis*-**1.13** (right) from cyclohexane, and LD spectra with and without 120 Hz sound (amplitude 13.5 Pa). Image adapted from ref. 206 with permission from The Royal Society of Chemistry.

suggest that stirring can itself template the assembly of helical fibres, producing a bias in handedness dependent on the sense of rotation of the liquid medium.<sup>214, 215</sup> For example, Escudero *et al.* showed that J-aggregated bilayers of a sulfonated porphyrin can undergo folding above a critical width, producing different CD signals depending on the stirring direction.<sup>216</sup> Ultrasound, meanwhile, was utilised by Azeroual *et al.* to disrupt helical stacks of an achiral foldamer, allowing it to reassemble into homochiral fibres in the presence of the chiral template diethyl tartrate.<sup>217</sup> It is important to note that the spectroscopic methods used to identify supramolecular chirality are subject to experimental artefacts which may exaggerate or invert the apparent anisotropy.<sup>218</sup> In addition, deflection of liquid by the vessel walls produces vortical flows in opposing directions, so the resulting mechanoresponsive behaviour may prove container-dependent and difficult to control.<sup>219</sup>

Microstructural and rheological transitions are not the only stress-induced responses that a gel may exhibit. Mechanical stimuli can affect the wettability of an aggregate post-drying, as well as optical properties such as colour, opacity and emissivity. For example, Dou *et al.* found that ultrasound-induced gelation of **1.14** in DMF is associated with a shift in fluorescence wavelength from green to yellow (Fig. 18), while grinding of the dry material triggers a piezochromic transition from orange to yellow.<sup>143</sup> Like changes in aggregate morphology, optical effects can vary with the nature and duration of the applied stimulus. In a study of cholesterol-appended ferrocene gelator, Liu *et al.* found that sonication of a transparent cyclohexane gel results in a viscous opaque suspension, whereas shaking or heating the material produces a transparent solution.<sup>220</sup> Komiya *et al.*, meanwhile, observed that sonicating the platinum analogue of complex **1.8** for three seconds in cyclohexane affords weakly phosphorescent gels, which exhibit stronger emissions and more intense metal-ligand charge-transfer absorption bands after prolonged exposure to ultrasound.<sup>155</sup> Although NMR spectra indicate that complete aggregation occurs regardless of sonication time, the extended treatment appears to produce thicker bundles of fibres, in which increased ordering and rigidity of molecules diminishes the rate of non-radiative relaxation.

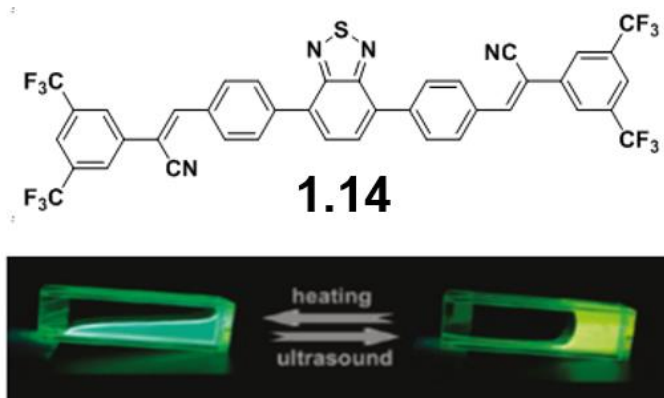


**Fig. 18** Fluorescence of **1.14** in DMF under 365 nm light, after treatment with heat (left) and ultrasound (right). Image reproduced with permission from ref. 143. Copyright 2011 American Chemical Society.

The ability to undergo multiple reversible transformations on exposure to external stimuli is crucial if gels are to function as smart devices, with properties that can be adjusted *in situ* to suit a range of operating environments. Of particular interest are gels that react differently depending on the type of stimulus or the processing history of the material. Optical effects are commonly

associated with gel-sol and sol-gel transitions but may also occur in the absence of a phase change, due to swelling effects, spin transitions or the direct interconversion of supramolecular assemblies. Thus, LMWGs incorporating chromophore functionalities can often switch between a variety of gel forms, responding to different combinations of physical inputs in a visual, non-destructive and orthogonal fashion.

## 1.5 Optical changes in supramolecular gels

It has long been known that aggregation can lead to substantial changes in the optical properties of a material. The mechanisms responsible for these phenomena may be subdivided according to their spectroscopic outcomes. In supramolecular assemblies, it is usual to compare the frequencies of absorption signals in the solid state with the corresponding frequencies in solution. A red-shift is termed a bathochromic effect and attributed to J-aggregation, while a blue-shift, or hypsochromic effect, is indicative of H-aggregation.

Molecules produce colour largely by absorption of photons, which causes electrons to be promoted from their ground state  $S_0$  to an excited state  $S_1$ .<sup>221</sup> These are singlet configurations, as the number of antiparallel electron spins is maintained during the excitation. In a coloured organic compound, the highest occupied orbital of  $S_0$  is typically a filled  $\pi$  bonding or non-bonding MO, while that of  $S_1$  is a low-lying  $\pi^*$  MO with single occupancy. Fluorescence occurs when, following an  $S_1 \leftarrow S_0$  transition, an excited molecule returns to the  $S_0$  state and releases its excess energy in the form of a photon. Alternatively, an electron may relax non-radiatively, releasing energy as heat via internal conversion. The balance between radiative and non-radiative deactivation in a molecule is largely determined by its electronic structure, but may also be influenced by environmental factors. For example, heating usually reduces fluorescence by promoting quenching effects such as molecular vibrations and solvent collisions.<sup>222</sup>

Although  $S_0$  and  $S_1$  are quantised, the energy of a transition can vary over a wide range, as each electronic state is coupled to molecular vibrations to produce a ladder of quantised vibronic energy levels. As a result, molecular absorption and

emission spectra display broad continuous signals, with maxima arising from the most favourable vibronic transitions. Since electrons may relax non-radiatively to lower vibrational states after a transition, and the  $S_1 \rightarrow S_0$  transition need not involve the ground vibrational state of  $S_0$ , absorption spectra span higher energies than the corresponding emission spectra. This separation in energy, as measured between the global maxima of the two spectra, is termed the Stokes shift. Like absorption frequency, the Stokes shift can be significantly affected by aggregation: in particular, H-aggregation tends to increase the shift observed, while J-aggregation produces shifts of low or even zero magnitude.

An explanation for aggregation effects was first proposed by Kasha,<sup>223</sup> who noted that dimerisation replaces each vibronic state with one higher in energy and another lower (Fig. 19).<sup>224</sup> These energy levels correspond to the two possible configurations of transition dipoles in the dimer. Crucially, electrons are only promoted to states in which the transition dipoles are aligned in-phase. If arrangements of this type are lowest in energy,  $S_1 \leftarrow S_0$  transitions in the dimer require less energy than in the monomer, and the material exhibits bathochromic behaviour. A hypsochromic effect, by contrast, arises when out-of-phase pairing is favoured. Fluorescence primarily involves the most stable  $S_1$  vibronic energy level which, in H-aggregates, corresponds to an out-of-phase state. Electrons promoted to an in-phase state must therefore relax non-radiatively before emission, producing a large Stokes shift.

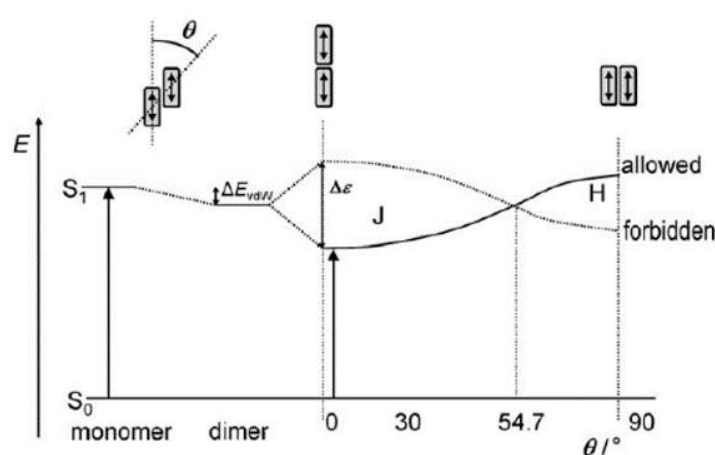


**Fig. 19** Schematic diagram showing the variation in energy of the allowed and forbidden  $S_1$  states as the angle between molecules,  $\theta$ , is varied. Note that splitting does not affect  $\Delta E_{\text{vib}}$ , the average energy of dimer states relative to the monomer. Image reproduced with permission from ref. 224. Copyright 2011 John Wiley and Sons.



Given that the allowed transitions in a dimer are dictated by the orientations of the monomer dipoles, the optical characteristics of the system must be closely linked to the mode of self-assembly. For rod-like molecules, bathochromic effects tend to result from strong end-to-end interactions, while hypsochromic effects require a side-on molecular arrangement. Less ideal structures, in which molecules are tilted or offset relative to their neighbours, may exhibit both J- and H-type absorption (Fig. 19).<sup>224</sup> These relationships are highly robust, and applicable even to extended aggregates such as supramolecular polymers. Thus, any stimulus that alters the packing of molecules in a material is likely to alter its spectroscopic properties.

In general, gelators exhibit the most pronounced optical changes when moving between solution and the solid state. It is thus unsurprising that many thermal chromic responses are associated with sol-gel or gel-sol transitions. For example, Yao *et al.* reported that merocyanine dye **1.15** forms supramolecular polymers with distinctive blue-shifted absorption signals (Fig. 20).<sup>225</sup> The polymers are stabilised by dipolar  $\pi$ - $\pi$  stacking motifs and bundle together at high concentration to generate interconnected gel fibres. However, in the presence of solvents more polar than alkanes such as THF, the molecules assemble into dimers and monomers, producing absorption maxima at higher wavelengths. Intriguingly, polymers formed in the moderately polar solvent trichloroethene are metastable, so undergo a chromic transition through gradual disassembly into smaller clusters. This transition occurs over a period of days below 30 °C, but may be greatly accelerated by heating: in accordance with an Arrhenius-type relationship, the rate roughly doubles for an increase in temperature of 7-9 °C.

Another example of a thermoresponsive gel with variable absorption was provided by Das *et al.*<sup>28</sup> In non-polar solvents, dialkoxynaphthalene and naphthalene-diimide derivatives form co-gels in which the different naphthalene moieties are stacked in an alternating fashion. Since the frontier orbitals of the  $\pi$  systems differ greatly in energy, aggregation is associated with the formation of intensely absorbing charge-transfer complexes. The co-gels appear bright red or orange at 0 °C but assume permanent yellow colorations when warmed to room temperature, due to separation of the gelators into single-component gels. The

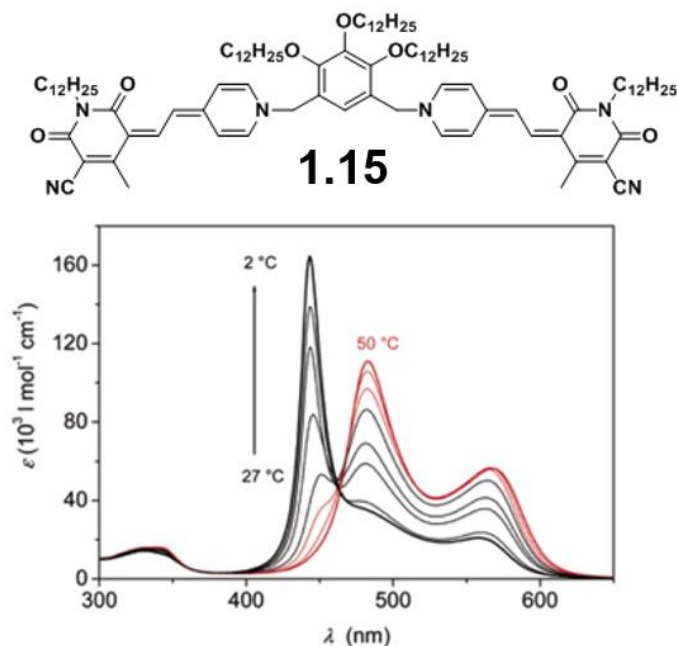


**Fig. 20** UV-vis absorption spectra of **1.15** in a mixture of THF and methylcyclohexane over a range of temperatures. Maxima at 440, 490 and 570 nm are attributed to polymers, dimers and monomers of **1.15** respectively. Image adapted with permission from ref. 225. Copyright 2004 American Chemical Society.

thermal dependency of the process is characteristic of a supramolecular material that is kinetically favoured but lacks thermodynamic stability. Thus, the study illustrates how rate-controlled gel formation can produce a material that is preconfigured to display thermochromic behaviour, due to the metastability of the self-assembled states.

Thermally induced structural changes can also affect fluorescence. Emission responses involving  $\pi$ - $\pi$  interactions are particularly common, as stacking of aromatic rings may lead to exchange of excitation energy between neighbouring  $\pi$  systems. Energy transfer may occur through dipole-dipole interactions (the Förster mechanism) or, in materials displaying very small  $\pi$ - $\pi$  separations, direct orbital overlap (the Dexter mechanism). Both the Förster and Dexter processes quench the fluorescence of the donor system by providing non-radiative pathways for electron relaxation. The acceptor, meanwhile, becomes more strongly emissive, typically fluorescing at a lower frequency than the unquenched donor.

Excitation energy transfer can be modulated by varying the separation or orientation of the interacting  $\pi$  systems. Praveen et al. demonstrated this

principle by incorporating rhodamine, a charge acceptor, into a dodecane-chloroform gel of an OPV.<sup>226</sup> Förster transfer induces the rhodamine to fluoresce at 625 nm, while quenching the gelator signal at 530-570 nm. Raising the temperature, however, leads to the disappearance of the rhodamine emissions and re-emergence of the gelator signal at 450 nm. The blue-shift in the fluorescence of the gelator results from disaggregation of the gel fibres, accompanied by loss of dipole-dipole coupling and divergence of the S0 and S1 states. Evidently, disassembly of the material acts as a switch for the donor-acceptor interaction, triggering a reversible and thermally controllable chromic response.

The study by Praveen *et al.* demonstrates the effects of  $\pi$ - $\pi$  coupling on the wavelength and intensity of a fluorescence signal. While self-assembly often serves to strengthen such interactions, the mobility and conformational freedom of the aggregating species are greatly reduced. An excited molecule in solution may dissipate its energy through vibrations, rotations or intermolecular collisions. By contrast, the components of a supramolecular polymer are restricted to a small range of positions and geometries, and relatively isolated from the surrounding solvent molecules. Aggregation reduces the ability of electrons to relax via non-radiative pathways, so the lifetime of the excited state is extended and the efficiency of radiative deactivation markedly increased. This phenomenon, sometimes referred to as aggregation-induced enhanced emission (AIEE), occurs in a variety of supramolecular gel systems and is the subject of a number of recent reviews.<sup>23, 227</sup>

Clearly, AIEE can only take effect if the systems responsible for fluorescence are formed or retained during aggregation. Even minor structural changes can lead to a pronounced alteration of the emission spectrum. For example, fluorescence of pyrene moieties at wavelengths of 450-500 nm is indicative of dimerization, as  $\pi$ - $\pi$  stacking of these groups generates an emissive excited-state complex, or excimer.<sup>228</sup> Aggregation commonly promotes excimer formation by reducing the separation of the pyrenyl species,<sup>111, 229-231</sup> but the opposite effect – sometimes termed aggregation-caused quenching, or ACQ – may occur under some circumstances.<sup>41, 227, 232</sup> In pyrene-based aggregates, ACQ arises when  $\pi$

systems self-organise into a non-overlapping arrangement, such that the bonding interactions of the excimer are no longer possible. The lack of  $\pi$ - $\pi$  coupling may be compensated for by a strengthening of other interactions such as the hydrogen bonds of **1.16** (Fig. 21)<sup>41, 232, 233</sup> or, if steric constraints allow for a range of packing modes, an increase in entropy.<sup>234</sup>

ACQ frequently occurs during the self-assembly of highly conjugated molecules. Indeed, non-emissivity appears to be a general feature of H-aggregates, in which serial face-to-face stacking of  $\pi$  systems is a common structural motif. According to the theory of Kasha,<sup>223</sup> fluorescence in these materials is disfavoured because the most populated  $S_1$  states correspond to out-of-phase dipole configurations, which typically exhibit small  $S_1 \rightarrow S_0$  transition moments. Quenching increases with the size of the  $\pi$ - $\pi$  stacked arrays and may thus be used to monitor the growth of self-assembled aggregates.<sup>99</sup> Exceptions may arise, however, where electrons can access weakly coupled triplet states to dissipate energy in the form of phosphorescent emissions.<sup>235</sup> Intersystem crossing between singlet and triplet states is promoted by the presence of heavy atoms such as Pt<sup>155, 235</sup> and Br,<sup>236</sup> and leads readily to radiative relaxation when coupled with AIEE effects.

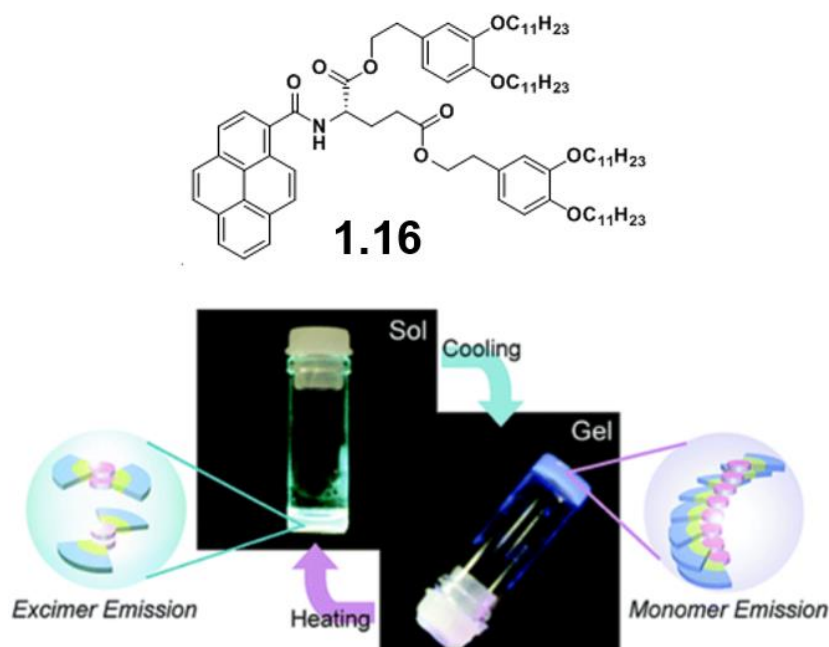


**Fig. 21** Thermoreversible excimer emission of **1.16**. Gelation produces an ACQ effect because the close  $\pi$ - $\pi$  stacking of the excimer cannot occur in the hydrogen-bonded structure of the gel.

Image adapted with permission from ref. 232. Copyright 2007 American Chemical Society.

A factor more commonly responsible for emission enhancement is the displacement of  $\pi$  systems from the ideal face-to-face stacking arrangement. Rösch *et al.* have shown that torsion angles as small as  $10^\circ$  are sufficient to enable strong fluorescence in merocyanine dyes, which otherwise behave as classical H-aggregates.<sup>237</sup> Similarly, Cigáň *et al.* reported that H-aggregates of one bicyclic system are emissive because the molecules are offset to minimise separation of the electron-rich and electron-deficient rings.<sup>238</sup> If the relative displacement of rings is very large, an assembly of  $\pi$  systems may even display the enhanced fluorescence, small Stokes shift and red-shifted absorption characteristic of a J-aggregate.<sup>224</sup> The occurrence of J-aggregation in gels is often strongly dependent on the presence of directional interactions other than  $\pi$ - $\pi$  stacking. For example, Ajayaghosh and Praveen found that OPV derivatives terminated with one or more hydroxyl groups give gels with J-aggregate structures, whereas derivatives terminated with cholesteryl esters produce H-aggregate materials.<sup>239</sup>

The balance between H- and J-aggregation may be influenced by environmental changes, such as exposure to heating or sonication,<sup>240</sup> variation in the solvent<sup>241-243</sup> or addition of a strongly binding additive.<sup>244</sup> According to Würthner *et al.*,<sup>224</sup> the synthetic route is particularly important when aggregation is governed by non-directional van der Waals interactions, as in the stacking of pseudoisocyanine dyes. In some cases, the self-assembly pathway may lead to a product which is kinetically favoured but thermodynamically unstable, such that the optical properties of the system may continue to evolve even after the material has formed.<sup>28, 245, 246</sup> This effect was exemplified in a study by Lohr *et al.*, wherein a helical H-aggregate of a chiral bis(merocyanine) dye was found to convert over time to a different H-aggregate comprising more twisted fibres.<sup>247</sup> As expected, the rate of the rearrangement process is controllable by heating: the initial aggregate is almost completely lost after 7000 min at  $20^\circ\text{C}$ , but may be trapped for weeks if the temperature is lowered.

Direct conversion between J- and H-aggregates can also be achieved. Cho *et al.* reported that carboxylated porphyrin **1.17** forms hypsochromic metallogels when sonicated in the presence of palladium(II) ions, but these break up into bathochromic aggregates when heated above  $T_{\text{gel}}$ , and further disassemble to

give monomeric species at 60 °C (Fig. 22).<sup>240</sup> The reverse process, conversion from J- to H-aggregates, can be induced through subsequent sonication of the sol. Switching between phases is associated with changes in both colour and fluorescence: the thermally generated metallo gel is green and exhibits the non-emissivity typical of H-aggregates, whereas the J-aggregate is red and more strongly fluorescent than both the original gel and the dissolved monomer. Although the metallo gel displays a highly amorphous sheet-like morphology, the J-aggregate adopts the form of cubic crystals, affording an X-ray structure in which the expected staggered molecular arrangement is clearly visible.

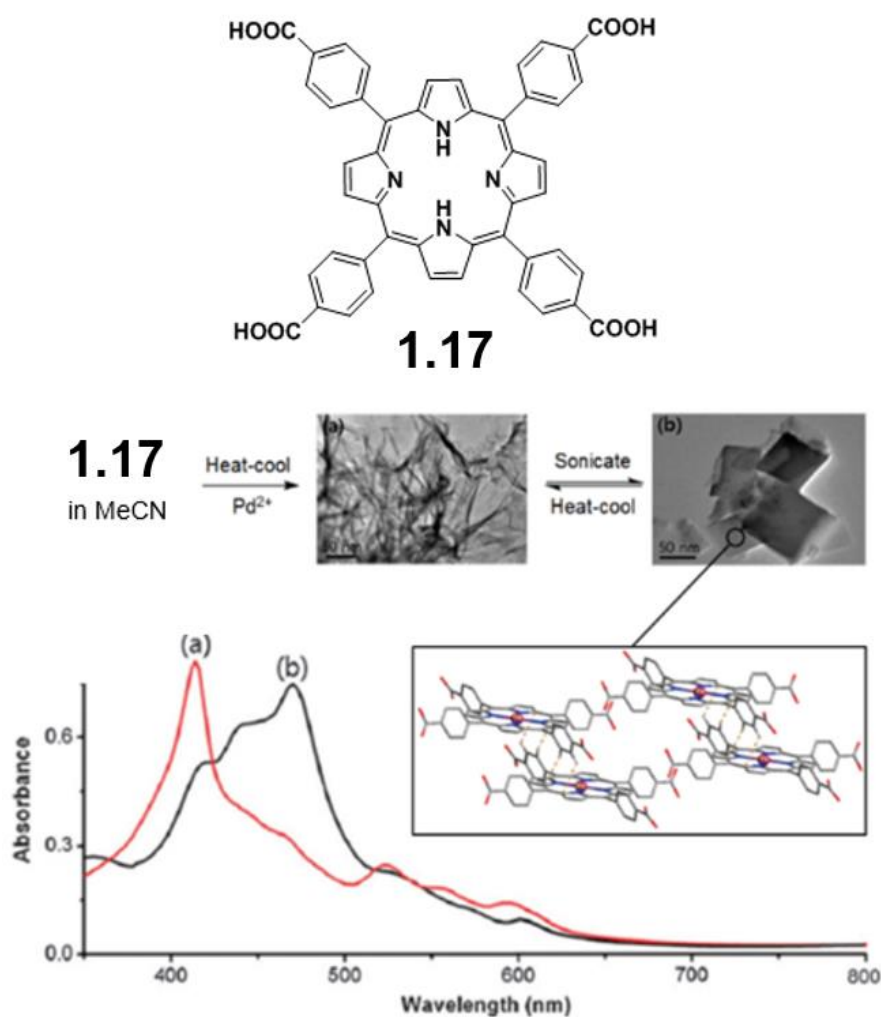


**Fig. 22** Thermal formation of H-aggregated gel (a) from palladium(II) porphyrin complex **1.17** in acetonitrile, and the subsequent sonication-induced conversion to J-aggregates (b). The UV-vis absorption spectra of the two aggregates are shown. Inset is the X-ray crystal structure of **1.17** obtained in DMF. Images adapted from ref. 240 with permission from the Centre National de la Recherche Scientifique (CNRS) and The Royal Society of Chemistry.

The optical properties of gels may be further modulated through swelling effects. The thermally induced collapse of a gel can dramatically reduce its transparency,<sup>43, 248</sup> and may also be harnessed to control the structural colour of suspended particles or pores.<sup>249</sup> In one study, close-packed silica beads were used to template an optical diffraction grating consisting of a porous poly(*N*-isopropylacrylamide) (pNIPA) gel, the dimensions of which could be varied under pH or temperature control to emit any colour in the visible spectrum.<sup>250</sup> Swelling may additionally be associated with changes in aggregate morphology, which can in turn affect the colour or fluorescence of a material. For example, hydrogels based on a pyrenyl conjugate of phenylalanine were shown by Nanda *et al.* to contain helical fibres between 30 and 55 nm in diameter and emit strongly at 398 and 489 nm under neutral conditions.<sup>17</sup> By contrast, gels at pH 14 contain non-helical tape-like fibres 80 to 210 nm in width and are far less emissive at 398 nm, due to greater incorporation of monomeric pyrene groups into excimer assemblies.

Even if swelling does not induce optical transitions in the gel itself, such changes may result from the uptake or expulsion of a visible guest. The rate of diffusion of a guest into or out of the material is dictated by the size of the guest and the density and flexibility of the gel network. Sutton *et al.* demonstrated that hydrogels of Fmoc-phenylalanine prepared by a gradual decrease in pH can freely release even a 20 kDa fluorescently labelled dextran 5 nm in diameter.<sup>251</sup> Fmoc-tyrosine, however, is less ionised at the point of gelation and capable of stronger hydrogen bonding interactions, so produces stronger gels with less labile fibre junctions. Accordingly, the diffusion rates of 358 Da Naphthol Yellow and 676 Da Direct Red were found to be lower by 8 and 84% respectively, and a 4 kDa dextran 2 nm in diameter showed no appreciable diffusion whatsoever. Willis-Fox *et al.* exploited such restrictions in solute transport to establish localised concentrations of a poly(fluorene) conjugated polyelectrolyte (CPE) in a matrix of diureasils, polymeric bis(urea)s crosslinked via terminal triethoxysilane moieties.<sup>252</sup> Whilst adding CPEs to the diureasils during their sol-gel preparation caused them to be uniformly distributed throughout the material, swelling a preformed diureasil film in a CPE solution produced a dense layer of the

fluorophore within 12-14  $\mu\text{m}$  of the surface. Confining a guest to the surface of diureasil films may improve their performance as luminescent solar concentrators for photovoltaic devices, by reducing their cost and minimising losses in efficiency due to self-absorption effects.<sup>253</sup>

A more esoteric consequence of restricted diffusion in gels is the emergence of complex, wave-like patterns within the solute distributions. Convection in liquid systems, driven by heat, light or an electric potential, can produce remarkably ordered dissipative structures including rolls, dendrites and pseudo-crystalline lattices.<sup>254</sup> Spatiotemporal patterns responsive to chemical interactions, however, are possible only if the transport rates of reagents are substantially mismatched. Effects of this nature, known as Turing instabilities, have been realised through the multicomponent reaction of iodide, chlorite, malonic acid and starch in acidic polymer hydrogels.<sup>255</sup> Interaction of the iodine product with both the polymer network and starch indicator dramatically lower its diffusion coefficient, generating standing wave oscillations in the reagent concentrations to establish a three-dimensional lattice of coloured spots. Similar reaction-diffusion coupling in gel-phase Belousov-Zhabotinsky reactions can break the symmetry of the initial reagent distributions to produce spots, bands and spiral waves.<sup>256</sup> An important feature of such instabilities is that they are sensitive not only to the reagent concentrations and container geometry but also to environmental inputs such as heat, light, mechanical disturbances and even gravity.<sup>257</sup> Patterns may be controlled by varying catalytic activity with gradients in temperature, pH or illumination, or through controlled swelling of a gel with suitable stimuli-responsive characteristics. Observations of these artificial systems could offer insight into comparable diffusion-limited patterning of biological systems, which has been implicated in symmetry-breaking cellular differentiation during tissue morphogenesis and embryo development.<sup>258</sup>

Additional environmental sensitivity is possible in gel networks containing d- or f-block metals.<sup>259-262</sup> Heating or cooling may alter the coordination environment of a metal, potentially inducing gel disassembly and/or a chromic response.<sup>54, 56</sup> For certain metals, the change in coordination may occur via a spin-crossover mechanism, wherein a high-spin configuration of electrons converts to



a low-spin state. Transitions of this type have been reported in gels comprising iron(II) complexes of triazole ligands.<sup>27, 263</sup> Reversible conversion from diamagnetic low-spin to paramagnetic high-spin states is typically marked by a loss of colour and substantial increase in magnetic susceptibility. Spin-crossover temperatures are roughly constant in a given solvent, but stress-strain moduli and melting temperatures vary with gelator concentration (Fig. 23). Thus, the mechanical properties of the gels may be adjusted to suit a particular application, without reducing the efficacy of the desired switching response.

Electronic transitions may also affect the covalent structure of a gelator. The resulting molecule may pack and interact differently to its precursor, leading to changes in the stability, morphology and physical characteristics of the aggregate. Provided the reactive group responds to a specific stimulus and undergoes a well-defined transformation, it may be utilised as a molecular switch to convert between materials in a rapid and quantitative manner. The mechanisms and applications of such switches will be outlined in the following section.

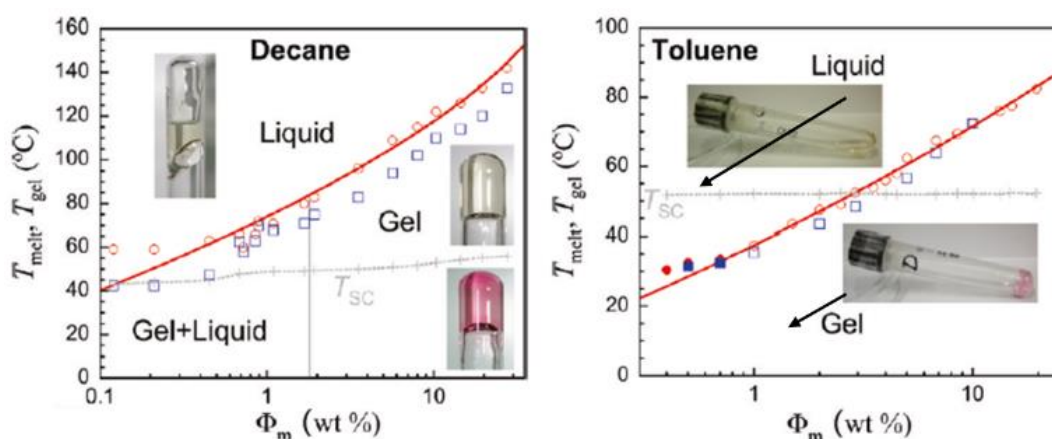


**Fig. 23** Pseudo phase-diagrams of an iron(II)-triazole complex in decane and toluene. The measured  $T_{\text{gel}}$  value at each gelator concentration,  $\Phi_m$ , is marked in blue squares and the melting temperature,  $T_{\text{melt}}$ , in red circles. Empty and full symbols denote gels prepared by cooling to 20 °C and 1 °C respectively. The recorded spin-crossover temperature,  $T_{\text{SC}}$ , is shown in grey. Spin-crossover clearly leads to a change from pink to colourless in both solvents, while heating above  $T_{\text{melt}}$  produces a colourless sol. Images adapted with permission from ref. 27.

Copyright 2010 American Chemical Society.

## 1.6 Photoinduced conformational changes

Changes in molecular conformation are a common phenomenon in supramolecular materials. Flexible gelators can often access a number of packing modes with comparable energies, in which bond angles vary but the connectivity of atoms remains fixed. One such transformation, reported by Ke *et al.* and involving a change in the relative orientation of tripeptide chains around a bipyridine core, was mentioned in section 2.1 (Fig. 6).<sup>36</sup> Yan *et al.* invoked a similar process to rationalise the heat-setting of a nickel(II) metallogel of a bis(terpyridine) cyclam, noting that conversion of the U-shaped ligand to a more linear conformation would allow neighbouring coordination polymers to form bundle-like assemblies.<sup>51</sup> In these and many other systems, molecular deformation is associated with the growth or break-up of the gel network, but it is not unusual for a gelator to produce a different fibrous material in each conformational state. For example, Wu *et al.* found that the molecular arrangement of a cholesteryl gelator in *p*-xylene gels varies according to the gelation procedure.<sup>264</sup> Molecular-geometry calculations suggest that molecules in gels obtained by thermal treatment display a straightened conformation with relatively little intramolecular hydrogen-bonding, whereas those in gels generated by sonication are bent in order to maintain the intramolecular interactions. This structural variation, though slight, translates to stark differences in the morphology and surface wettability of the aggregates formed.

Further conformational control can be achieved by altering the molecular structure of the gelator. One approach, which mimics the enzymatic processes governing self-assembly in biological systems,<sup>265</sup> is to incorporate a labile moiety that inhibits folding of the molecule into a gel-forming conformation. Haines *et al.* employed this strategy in the development of a synthetic 20-residue peptide that forms hydrogels on exposure to UV light.<sup>266</sup> In the absence of protecting groups, the molecule adopts a  $\beta$ -hairpin structure that can self-assemble laterally through the formation of intermolecular hydrogen bonds, and facially through the association of hydrophobic faces. Protection of a cysteine residue with an  $\alpha$ -carboxy-2-nitrobenzyl group, however, results in a random coil conformation unsuited to the formation of an extended supramolecular network. It is proposed

that introduction of a charged residue on the valine-rich face disrupts hydrophobic interactions and provides steric hindrance to disfavour the formation of intramolecular hydrogen bonds. Deprotection can be achieved in just 30 minutes with a hand-held UV lamp, and affords hydrogels at basic pH with rheological properties comparable to those of a fresh unprotected peptide gel (Fig. 24). This photo-initiation methodology, sometimes referred to as caging, is preferable to the use of a photoreactive additive since it may be executed without significantly perturbing the pH of the system, and yields a by-product that has little effect on the strength or biocompatibility of the resulting gel.

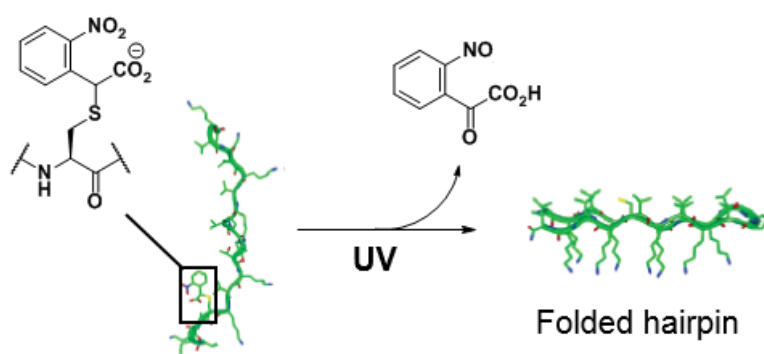


**Fig. 24** Protection of a cysteine residue in a 20-residue peptide prevents the formation of a fibrous gel. Upon UV illumination, the protecting group is removed as a molecule of 2-nitrosoglyoxylic acid, allowing the peptide to fold into a  $\beta$ -hairpin structure. Subsequent stacking of hairpins affords a network of fibrils. Image adapted with permission from ref. 266. Copyright 2005 American Chemical Society.

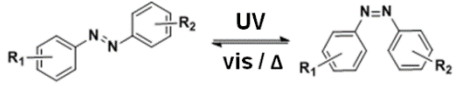
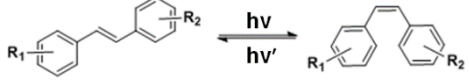
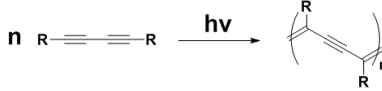
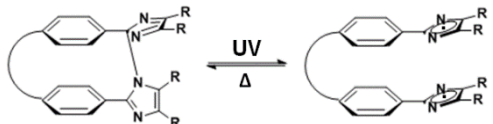
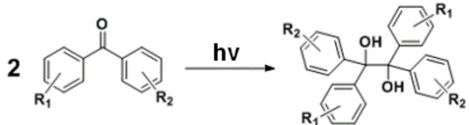
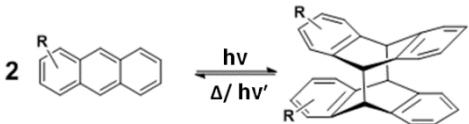
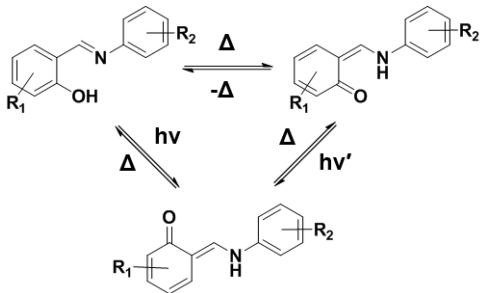


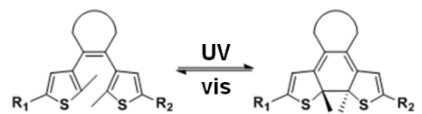
Photocleavage of a gelator precursor represents an effective and elegant method for initiating a self-assembly process, but is impractical in systems that cannot be suitably functionalised or must be capable of reverting *in situ* to their original state. A more popular strategy is to exploit functional groups that remain intact upon illumination, but undergo switching between two or more rigid conformations. As a means of controlling gel properties, the use of species with intramolecular switching behaviour offers a number of advantages. Many popular reactive groups can tolerate a wide range of temperatures and solvents, and may be easily integrated into existing classes of gelator without greatly diminishing their propensity for gelation. Switching often occurs only in response to particular sets of stimuli and may thus be triggered as required, without affecting other sensitive functionalities present in the material. Finally, in many cases, a switching response may be tailored to suit a particular application: it may be made rapid

and quantitative, or targeted to a product state with the required optical, mechanical and reactive properties.<sup>8, 30, 267, 268</sup>

Many different molecular switches have been incorporated into LMWGs, but common patterns of reactivity may be identified (Table 1). *Cis-trans* isomerisations are particularly popular, as they deliver a reversible conversion between two well-defined and chemically similar states that are both conformationally locked. Transformations of this type are most frequently realised in gels through the use of the azobenzene group, which is isomerised from the *trans* form to the *cis* by UV radiation near 360 nm in wavelength. The reverse reaction can normally proceed to completion in a few hours at room temperature, but it may also be facilitated by visible light, with optimal wavelengths ranging from 430 to 450 nm.<sup>269</sup>

One use of the azobenzene switch is to produce a marked optical response. The *trans-cis* reaction occurs with a loss of absorbance near 360 nm and the emergence of  $\pi$ - $\pi^*$  and  $n$ - $\pi^*$  bands, at 290 and 460 nm respectively. Isomerisation in the solid state typically leads to a photostationary state in which 30–50% of the switch adopts a *cis* configuration, but higher yields are possible if the product becomes kinetically trapped. Moriyama *et al.* achieved such an effect in a bis(amide) gelator by irradiating a dichloromethane solution of the *trans* form with UV light whilst rapidly evaporating the solvent.<sup>270</sup> In the recovered solid, UV-vis spectra displayed a 3:1 excess of the *cis* form, significantly exceeding the yield achieved in a comparable closed system.

*Cis-trans* isomerisations may also affect the structure or stability of a gel. Given that most azobenzene-based systems strongly favour a *trans* configuration under ambient conditions, it is perhaps unsurprising that the majority of gelators discovered produce gels in this form. Conversion to a *cis* configuration dramatically alters the shape of a molecule, which can be accommodated in the solid state only through substantial rearrangement of surrounding molecules. Such changes leave some aggregates morphologically unaltered, but their effect in a gel is often to induce dissolution of the material. Fibrous DMSO gels of tripodal azobenzene **1.18**, for example, were found to undergo gel-sol transitions when irradiated with UV light, even though the spherical structures formed in aqueous THF remain intact following isomerisation (Fig. 25).<sup>271</sup> The breakdown of aggregates may result in a simple solution of the constituent compounds. However, it is also possible for new, smaller assemblies to be generated, as illustrated

Reaction class	Example	Equation
<b>Trans-cis (E-Z) isomerisation</b>	Azobenzene	
	Stilbene	
<b>Polymerisation</b>	Diacetylene	
<b>Dimerisation</b>	Imidazole	
	Benzophenone	
<b>Cycloaddition</b>	Anthracene	
<b>Tautomerisation</b>	N-salicylidene aniline (anil)	
<b>Electrocyclic reaction</b>	Spiropyran	
	Dihydroindolizine	
	Dithienylethene (DTE)	

**Table 1** Examples of photoresponsive functionalities that have been incorporated into LMWGs. R groups indicate common derivatisation patterns but are not exhaustive.

by Yagai *et al.* in a study of the melamine derivative **1.19**.<sup>269</sup> In cyclohexane solutions, the molecule in its *trans* form co-assembles with a substituted barbiturate to form columnar stacks of rosette-like structures, but UV irradiation causes these to decompose into single rosettes, with *trans*-to-*cis* conversions of just 16% giving rise to a 50% decrease in aggregate size (Fig. 26). Light-induced gel-sol transitions may be exploited, like their thermal counterparts, for the controlled release of drugs and other encapsulated species,<sup>272</sup> and are uniquely suited to applications requiring remote or localised degelation, or where changes in temperature are difficult to accomplish.

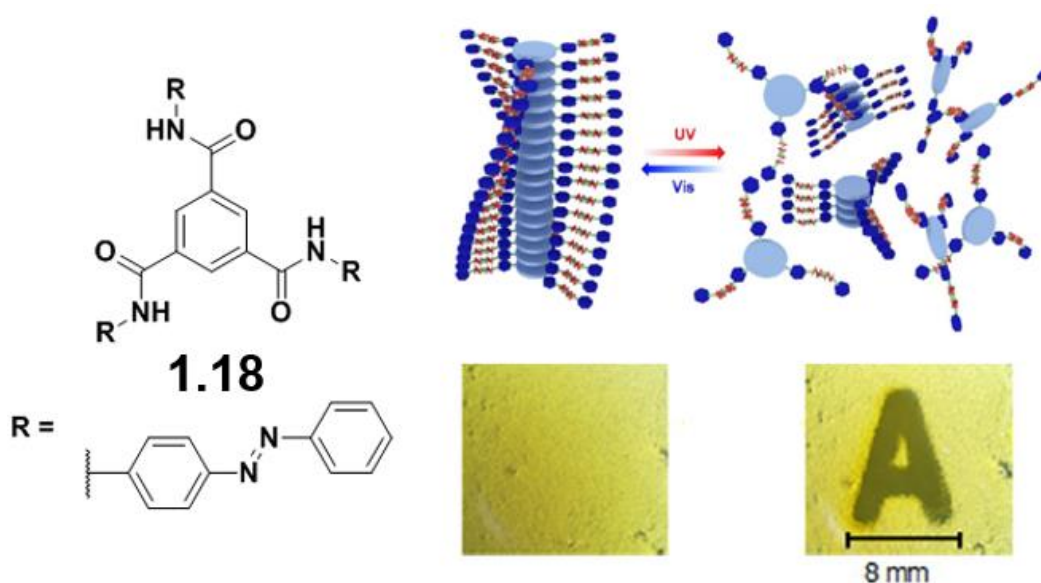


**Fig. 25** Gels of **1.18** in DMSO consist of stacked assemblies of the tripodal gelator. The schematic diagram illustrates disassembly of the fibrils upon *trans*-*cis* isomerisation of the azobenzene groups. Localised UV illumination allows for well-resolved and reversible photolithography of a gel sample (bottom). Image adapted with permission from ref. 271. Copyright 2013 American Chemical Society.

In addition to altering the conformation of a molecule, a *cis*-*trans* isomerisation may strongly alter its polarity. The C-shaped *cis* form of an azobenzene compound tends to be more polar than the S-shaped *trans*,<sup>273</sup> so a gel-sol transition may lead to precipitation if the material is based on a non-polar solvent.<sup>274</sup> In some cases, the kinetic stability of the precipitate may even prevent regeneration of the original aggregates by a *cis*-*trans* reaction.<sup>275</sup> Where the *trans* form is soluble in a non-polar solvent, however, conversion to the *cis* form may provide the reduction in solubility necessary for gelation to occur. Delbecq *et al.* illustrated this principle in solutions of a salt derived from 12-hydroxystearic acid and an azobenzene-containing primary amine.<sup>276</sup> A gel forms readily

in toluene and undergoes a typical gel-sol transition upon UV irradiation, but in chloroform the compound exhibits the opposite behaviour, converting from a solution to a gel as the concentration of the *cis* structure increases. It is interesting to note that the formation of the chloroform gel is short-lived, since the azobenzene gelator reverts to its more stable *trans* configuration over time. Assemblies that dissociate in this manner, if not sustained by a continuous supply of energy, have attracted interest as temporary catalyst supports and crystallisation media, and as analogues for biological polymers that form under similar non-equilibrium conditions.<sup>277</sup>

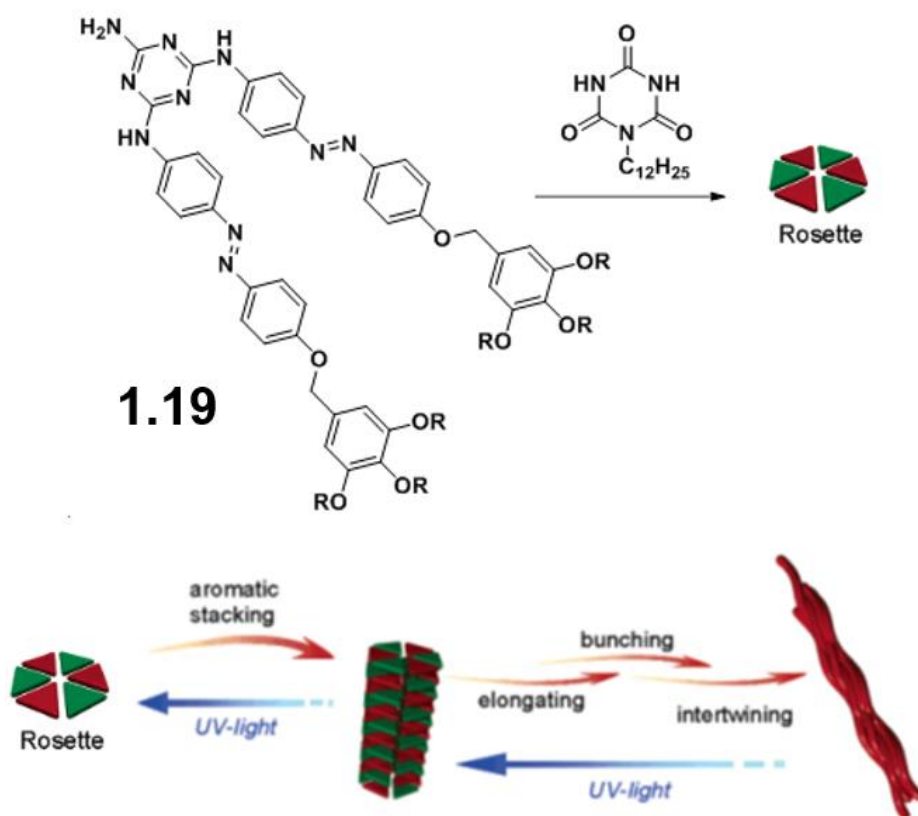


**Fig. 26** Hierarchical self-assembly of **1.19** with a substituted barbiturate. Hydrogen bonding gives rise to rosette structures, but  $\pi$ - $\pi$  stacking into elongated columns is possible only in the *trans* configuration. Image adapted with permission from ref. 269. Copyright 2005 American Chemical Society.

Changes in polarity can be harnessed to effect sol-gel and gel-sol transitions, but they may also be utilised to modulate the interactions of an aggregate with the surrounding solvent. Such surface modifications may induce swelling or contraction of a gel, as the capacity to encapsulate bulk liquid depends strongly on the energy of the solvent-gel interface. The greater ability of *cis*-azobenzene groups to interact with polar solvents was beautifully demonstrated by Seki *et al.*, who found that Langmuir monolayers of an azobenzene-based polymer can be made to expand across an air-water interface by

exposure to UV radiation.<sup>278</sup> Conversely, Borré *et al.* reported that zinc(II) metallogels of an azobenzene-functionalised terpyridyl ligand undergo deswelling of 85% upon isomerisation and, due to the limited solubility of the product, fail to return to their swollen state.<sup>180</sup> It is worth noting that whilst light-induced volume transitions may resemble those achieved through heating, the microstructural changes involved in these processes can greatly differ. Xie *et al.* reported that mixed hydrogels of the dendron gelator **1.20** and azobenzene derivative **1.21** undergo thermally reversible deswelling when stored at 20 °C, but return to a swollen state upon isomerisation of the photoreactive species (Fig. 27).<sup>279</sup> Although heating and irradiation produce swollen gels that are comparable in appearance, the latter affords fibres that are significantly wider and more twisted, and greatly diminishes the supramolecular chirality of the parent material.

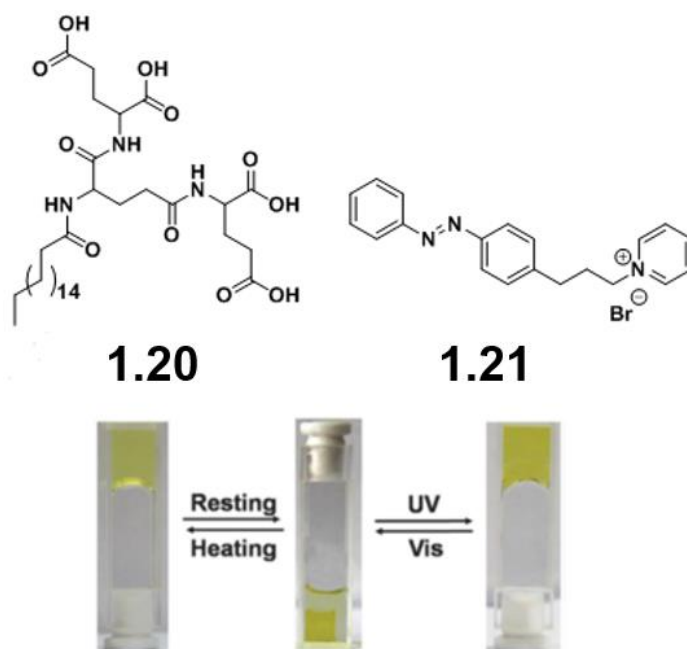


**Fig. 27** Reversible deswelling and swelling transitions of a mixed hydrogel of **1.20** and **1.21**, on resting and after exposure to UV light. Image reproduced from ref. 279 with permission from The Royal Society of Chemistry.

To design a gel in which azobenzene isomerisation is rapid and high-yielding, the environment of the switchable groups within the aggregate must be considered. Since the azobenzene moiety is small, its direct interactions are only occasionally important for stability,<sup>280</sup> but it may facilitate more extensive  $\pi$ - $\pi$  stacking by providing a conjugated bridge between planar aromatic functionalities. It is therefore common for azobenzene-based gelators to assemble into H-aggregates, in which molecules are closely packed and, due to strong coupling between the aligned dipoles, non-



emissive.<sup>223</sup> The lack of vacant space in such materials strongly disfavours transformations that involve large conformational changes. Consequently, reaction of the azobenzene switch in the gel state may be far slower than in solution, or require initiation by light of relatively high intensity.<sup>281, 282</sup> To avoid these limitations, gelators have been constructed wherein hydrogen-bonding groups and non-planar, aliphatic frameworks favour the self-assembly of aggregates without  $\pi$ - $\pi$  stacking.<sup>275</sup> A molecule with these properties was shown by de Loos *et al.* to promote thermal *cis-trans* switching of an azobenzene-containing bis(urea) in co-gels of 1-butanol.<sup>283</sup> Indeed, the rate of isomerisation in gels was found to exceed that in solution, and could be further enhanced by utilising enantiomers of matching chirality in the self-assembly process.

When used as molecular switches, azobenzene groups exhibit a number of drawbacks. Conversion of the *trans* form to the *cis* cannot reach completion, and usually proceeds with quantum yields below 30%. Furthermore, thermal relaxation to the *trans* form tends to occur within hours of irradiation, even if the transition is discouraged by strong interactions in the aggregate state. These problems cannot be addressed easily whilst retaining the azobenzene moiety, but they may be eliminated entirely by the use of an alternative molecular switch, the stilbene group. Like azobenzene compounds, stilbenes undergo photoisomerisation between *cis* and *trans* configurations. However, the reactions display relatively high conversions and quantum yields, and thermal relaxation is precluded under ambient conditions by a large activation barrier, allowing the *cis* and *trans* isomers to be stored and characterised separately without risk of compositional change.<sup>284</sup>

A good example of aggregation controlled by stilbene switching was provided by Xu *et al.*<sup>284</sup> Irradiation by light at 387 nm induces quantitative conversion of **1.22** from the *E* form to the *Z*, while light at 360 nm triggers the reverse reaction. The compound can form fibrous aggregates in either form, but the mechanism of self-assembly is different for the two configurations (Fig. 28). A linear correlation between viscosity and concentration in solutions of the *E* form suggests that fibre growth occurs by isodesmic polymerisation, in which monomers are added to the end of a chain at a rate independent of its current length. The *Z* form, meanwhile, displays a discontinuity in the slope of its viscosity-concentration profile, indicating that linear fibres develop from cyclic intermediates via a ring-chain polymerisation pathway. Interestingly, only fibres of the *E* form are found to give rise to a stable gel. It is proposed that the extended

conformation of the *E* form promotes the propagation of a one-dimensional supramolecular polymer, and the planarity of the molecules enables  $\pi$ - $\pi$  stacking to give a three-dimensional network. By contrast, the C-shape of the *Z* form favours the formation of cyclic structures, and unidirectional  $\pi$ - $\pi$  stacking is hindered by the proximity of the molecule's bulky side-chains, which prohibits the aromatic moieties from adopting a co-planar arrangement.

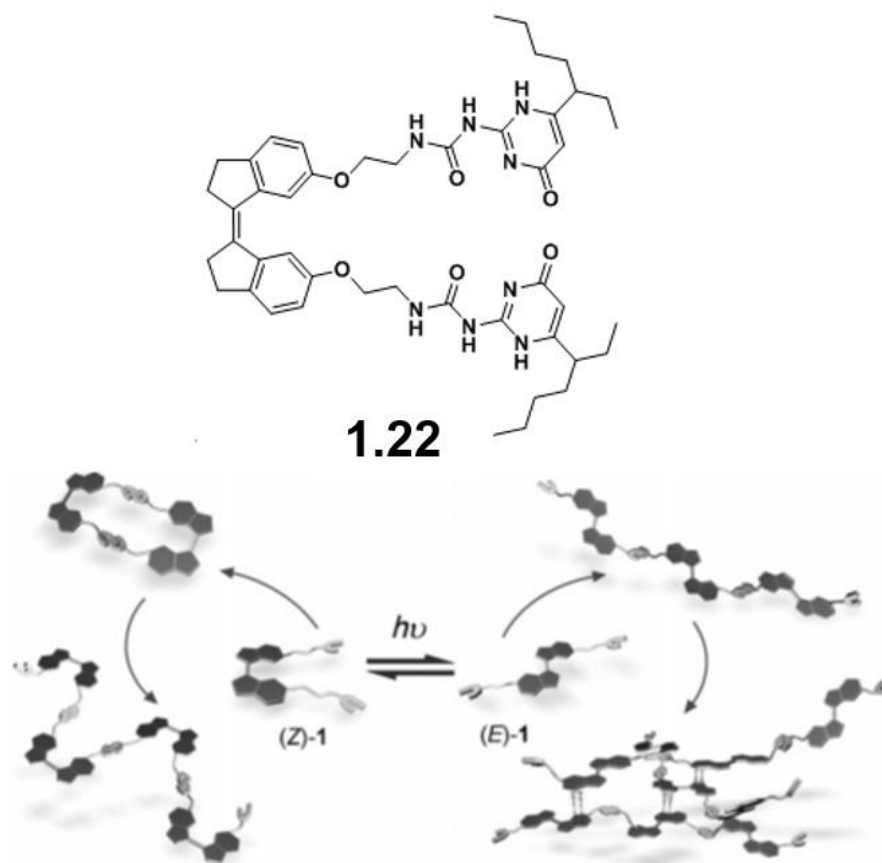


**Fig. 28** Schematic representation of the self-assembly mechanism of stilbene **1.22**. The compound in its *E* form undergoes isodesmic polymerisation to give a fibrous gel network. The *Z* form, however, aggregates via a two-stage ring-chain pathway and cannot form gels, due to a lack of  $\pi$ - $\pi$  stacking between fibres. Image adapted with permission from ref. 284. Copyright 2013 John Wiley and Sons.

As in azobenzene-based systems, the effect of molecular switching in a stilbene gelator depends on how the rest of the molecule interacts before and after the conformational change. Miljanić *et al.* reported that solutions of a stilbene oxamide-derivative in its *Z* form undergo gelation upon irradiation with 250-520 nm light, due to the lower solubility of the compound in its *E* configuration.<sup>285</sup> A similar effect was observed by Chen *et al.* in a study of a dibenzosuberane-based helicene, but in this case the compound forms a sol only if the concentrations of the *M* and *P* configurations are comparable, and acts as a gelator if either isomer is present in significant excess.<sup>286</sup>

Conversion of the *M* isomer to the *P* transforms one fibrous assembly to another via an intermediate vesicular phase, and can be controlled by adjusting the irradiation wavelength within the range 270–335 nm. It is suspected that linear aggregates form through complementary interactions between molecules of like chirality, whereas the competitive pairing of opposite enantiomers favours more cyclic supramolecular motifs, leading to discrete structures that are unsuited to the development of an extended gel network.

The stability of the stilbene moiety in its two configurations permits its use in situations that demand a predictable and long-lived response. For example, Matsumoto *et al.* utilised an alkene switch similar to a stilbene to achieve rapid and controlled release of nanobeads, bacteria and large molecules from a glycolipid-based hydrogel.<sup>287</sup> In the absence of UV irradiation, the gel fibres were found to act as a barrier to diffusion, limiting the efflux of one model compound, vitamin B<sub>12</sub>, to 7.8% over three hours. Changes in fluorescence during switching may also be harnessed to provide tuneable contrast in bio-imaging applications. Zhu *et al.* demonstrated that irradiation of cyanostilbene **1.23** with UV light can shift fluorescence from yellow to blue, even when using cervical cancer (HeLa) cells as a medium for the dye (Fig. 29).<sup>288</sup> The initial colour is attributed to emissions from the naphthalimide moiety, while the increase in wavelength results from an enhancement of the cyanostilbene fluorescence during the photo-induced *Z-E* isomerisation. Computational studies suggest that the *E* form is more emissive because steric hindrance prevents the formation of a stable excited species, known as a twisted intramolecular charge transfer (TICT) state, in which radiative relaxation is disfavoured. Prevention of TICT states is a common mechanism for the amplification of fluorescence during switching reactions,<sup>288, 289</sup> and can occur more generally through aggregation, contributing to the AIEE phenomena previously outlined.<sup>23</sup>

Notwithstanding their useful characteristics, stilbene-based molecular switches exhibit a number of significant limitations. In some cases, neighbouring functionalities may inhibit isomerisation of the alkene group, or promote the irreversible formation of cyclic species. Overlap in the absorption bands of the *E* and *Z* forms may render selective interconversion impossible, with mixtures of products arising even under monochromatic irradiation.<sup>288, 290</sup> Furthermore, the reaction necessitates a large conformational change which may be strongly disfavoured in the solid state. Problems

of this nature arise frequently in materials that deliver switchable behaviour by means of a *cis-trans* isomerisation. Indeed, to achieve a response that is rapid, reversible and high-yielding, it might be preferable to trigger changes in the connectivity of a molecule, whilst only moderately altering its overall conformation.

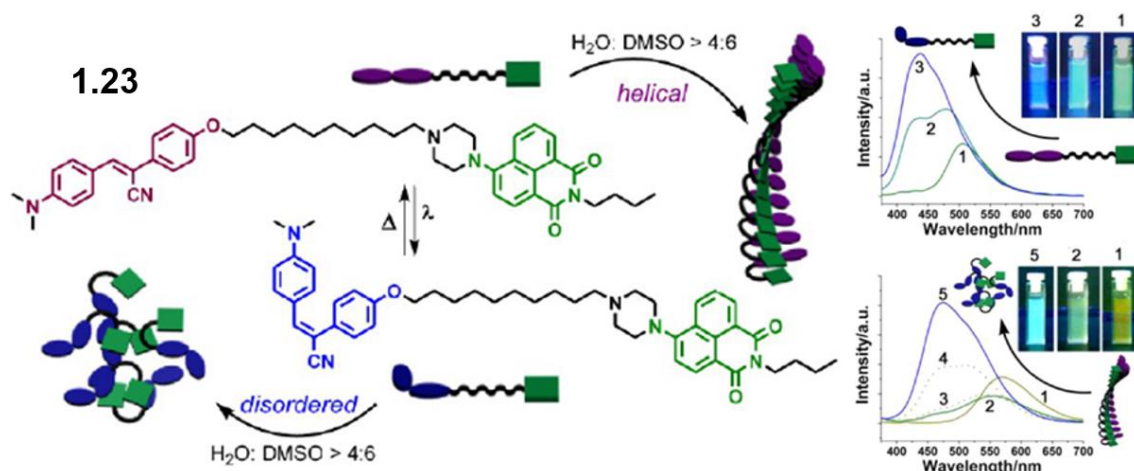


**Fig. 29** Switching response of the cyanostilbene **1.23**, and schematic representations of the self-assembled structures in mixtures of dimethylsulfoxide (DMSO) and water. UV-vis spectra of THF solutions (upper right), in which self-assembly does not occur, show a shift in emission towards lower wavelengths when the initial species (1) is irradiated for 3h (2) or 6h (3) at 254 nm. Aggregates of the Z form (lower right) in aqueous DMSO (1) undergo a similar change when irradiated for 2h (2), 3h (3), 5h (4) or 8h (5) at 365 nm. In both cases, cyanostilbene fluorescence is amplified during the Z-E transition due to prevention of TICT states in the E form. Image adapted with permission from ref. 288. Copyright 2013 American Chemical Society.

## ■ Bond-forming processes in gels

Synergistic switching of closely packed molecules can take place more readily if it involves only minor atomic displacements. In practice, the species to be coupled must be fixed in a reactive configuration by non-covalent interactions or, in the case of intramolecular reactions, a fortuitous conformation. One possibility is the transfer of a proton between two basic functionalities involved in a cyclic hydrogen bonding motif. Such reactions are appealing for their reversibility, relatively weak impact on molecular conformation and, in many instances, reliable responsiveness to pH control.

A common mechanism for tautomerisation in gels is excited-state intramolecular proton transfer (ESIPT).<sup>291</sup> Reactions of this type arise when the most stable tautomer of a molecule in its ground state can relax to another form following excitation by light. ESIPT is frequently characterised by a large Stokes

shift, since some of the energy gained by absorption is dissipated non-radiatively when proton transfer takes place. For example, although **1.24** emits strongly in DMF at wavelengths close to the absorption maximum at 360 nm, a second emission maximum occurs at the much higher wavelength of 541 nm (Fig. 30).<sup>292</sup> The red-shifted fluorescence is attributable to the keto form of the compound, generated by proton transfer from the phenolic oxygen to the nitrogen of the benzoxazole group. Interestingly, gelation in DMF-toluene mixtures produces a hypsochromic shift and substantially enhances both the intensity and lifetime of the fluorescence, with emissions due to the keto form most strongly affected. These observations are consistent with a structure comprising  $\pi$ - $\pi$  stacked planar molecules, in which the stages of ESIPT – excitation, proton transfer and radiative relaxation – can readily take place (Fig. 31).

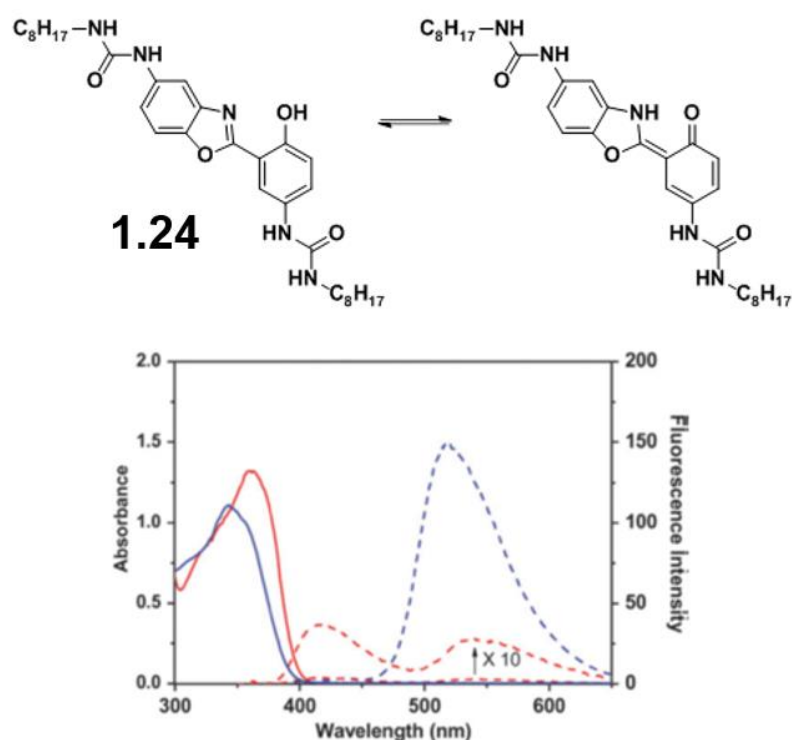


**Fig. 30** Absorbance (solid lines) and fluorescence (dashed lines) spectra of **1.24** in DMF solution (red lines) and after aggregation in 1:58 (v/v) DMF-toluene (blue lines). Image adapted from ref. 292 with permission from The Royal Society of Chemistry.

In general, ESIPT in the solid state demands that tautomerisation occur without prohibitive changes in conformation. Hydrogen bonding groups, such as the amide moieties in **1.25a**, may promote ESIPT by stabilising close intramolecular arrangements of base and acid functionalities. Indeed, crystal structure predictions by Qian *et al.* suggest that amide-amide and  $\pi$ - $\pi$  stacking interactions

in **1.25a** are aligned, favouring tape-like assemblies of close-packed planar molecules with strong intramolecular hydrogen bonding motifs.<sup>293</sup> In practice, the compound is weakly emissive in solution but forms highly fluorescent fibrous gels in mixtures of THF and cyclohexane. A large Stokes shift of 137 nm, and lack of emission bands closer to the absorption maximum, indicate the materials are strongly ESIPT-active, as expected.

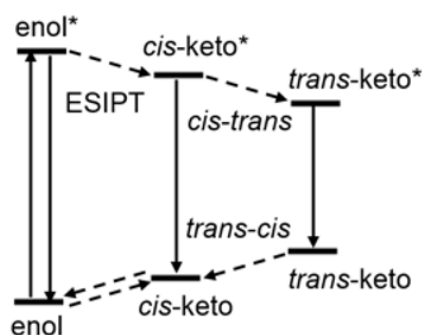
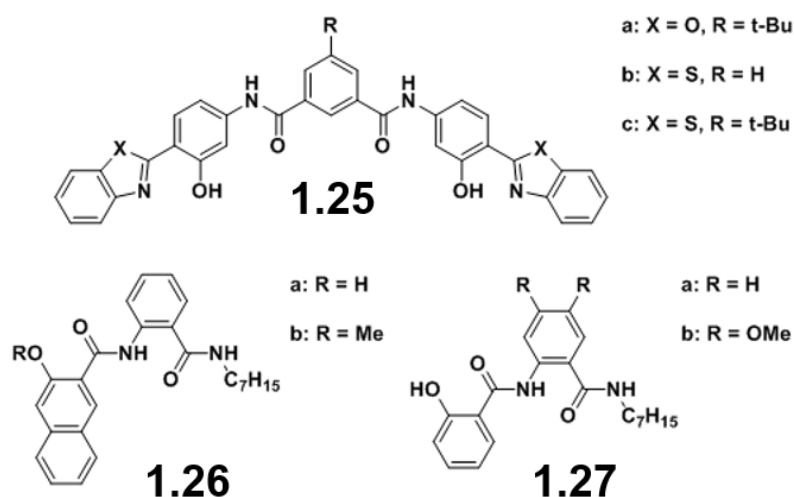


**Fig. 31** Schematic energy level diagram for a general anil-like compound, of which **1.26a**, **1.27a** and **1.27b** are examples. Dashed and solid arrows indicate non-radiative and potentially radiative transitions respectively.

When designing a gelator with ESIPT properties, it is important to note that even small changes in the substituents, including the tautomerising moieties themselves, may strongly influence the mode of self-assembly. By methylating the phenol group of gelator **1.26a**, Nayak sought to generate an analogue incapable of ESIPT activity.<sup>294</sup> The fluorescence spectrum of the product **1.26b** consists of a single strong resonance between 360 and 410 nm, and is indeed simpler than that of **26a**, which displays signals from the enol and keto species at 390-450 and 500-575 nm respectively. However, whilst **1.26a** forms gels in dodecane and cyclohexane at concentrations as low as 0.25 wt.%, **1.26b** gives rise

to needle-shaped crystals, suggesting that the intramolecular hydrogen bond of **1.26a** is crucial for the growth of an extended fibrous network. By contrast, replacing the naphthanilide moiety of **1.26a** with a salicylanilide end group does not greatly alter either the CGC or range of solvents gelled. The salicylanilide analogue **1.27a** also produces similar absorption spectra in its solutions and gels, but is notably emissive only at wavelengths ascribable to the keto tautomer, since the energy barrier for ESIPT is relatively low.<sup>295</sup>

Although derivatisation of a gelator can lead to drastic changes in its aggregation properties, it is not uncommon for its ESIPT responsiveness to be preserved. For instance, powder X-ray diffraction (P-XRD) studies indicate that dodecane gels of **1.27a** and its dimethoxylated derivative **1.27b** are structurally dissimilar: whereas the former displays the (*h* 0 0) reflections and short cell axis typical of interdigitated lamellae, the latter is best characterised as a hexagonal columnar assembly, with reciprocal *d*-spacings in the ratio 1:√3:2.<sup>295</sup> Both compounds are effective gelators at concentrations of 0.2 wt.%, but while gels of **1.27a** are opaque due to the presence of rod-like aggregates several micrometres thick, those of **1.27b** are transparent and consist of entangled, flexible fibres only 100 nm in diameter. Despite these differences, the two systems give rise to similar unimodal emission spectra, signifying complete enol-keto conversion in their excited states.

The robustness of ESIPT behaviour illustrates the stability of intramolecular hydrogen bonding motifs in the presence of varying intermolecular interactions. Nonetheless, it is worth noting that the features of ESIPT are seldom wholly independent of the mode of self-assembly. The importance of supramolecular effects was strikingly demonstrated by Qian *et al.*, in a study of two benzothiazole-containing compounds with ESIPT activity.<sup>296</sup> Aggregation in THF-water mixtures gives rise to AIEE effects in both **1.25b** and **1.25c**, but the quantum efficiency of proton transfer is increased only in the *t*-butylated system. It was proposed that **1.25b** forms an H-aggregate in which net excitation of the enol is reduced, though overall fluorescence is enhanced due to tilt in the aryl groups along the  $\pi$ - $\pi$  stacking axis. Molecules of **1.25c**, meanwhile, are forced by steric constraints to adopt a head-to-tail arrangement, delivering a highly emissive J-aggregate that suppresses relaxation of the excited enol back to its ground state.

Evidently, control of ESIPT in a gel can be accomplished by adjusting either the structures of the gelator molecules or the interactions between them. Since intramolecular proton transfer tends to alter the shape of a molecule only slightly, molecular packing within a self-assembled material is rarely affected by the ESIPT process itself. However, switching between gels with different ESIPT capabilities can occur if the gelator contains a molecular switch capable of larger conformational changes. N-salicylidene-anilines, or anils, are well suited to such applications, as they can typically undergo a *cis-trans* isomerisation in addition to tautomerisation.<sup>297</sup> ESIPT involves the thermally interconvertible enol and *cis-keto* isomers, but irradiation of either form with UV light results in a short-lived *trans-keto* compound, in which proton transfer between the basic nitrogen and oxygen atoms can no longer take place.

One advantage of the switching responses in anils is their orthogonality: by stimulating the enol form with heat or light, it is possible to separately target the *cis-* or *trans-keto* products.<sup>297</sup> Each step in the switching response of anils is associated with a different chromic response. Heating a solid anil typically results in yellow or orange coloration, owing to increased diffuse reflectance in the range 400–500 nm.<sup>298-300</sup> This transition is usually attributable to a rise in the concentration of the *cis-keto* tautomer, but it may also occur in the absence of tautomerisation through thermally induced broadening of absorption bands.<sup>301</sup> In the *trans-keto* system, diffuse reflectance is augmented at higher wavelengths still, producing materials with a dark orange or red appearance. Fluorescence is possible in all states, but is generally dominated by contributions from the *cis-keto* isomer, which is by far the least susceptible to non-radiative  $\pi^* \rightarrow \pi$  transitions.<sup>298</sup> The emissions of solid anils are often amplified due to the increased stability of the *cis-keto* structure, alongside more general AIEE effects such as J-aggregation, restricted conformational freedom and the prevention of TICT states.<sup>302</sup>

A further notable characteristic of anils in the solid state, and crystals in particular, is their variable susceptibility to isomerisation. Anils prone to tautomerisation upon heating are more likely to adopt planar conformations, which localise electron density on the nitrogen atom by minimising  $\pi$ - $\pi$  overlap with the adjacent aniline ring.<sup>297</sup> Light-reactive anils, conversely, are typically non-



planar and loosely packed, to accommodate the pedal-like motion of molecules undergoing *cis-trans* transformations.<sup>303</sup> These opposing structural trends underlie the oft-cited rule that thermo- and photochromic responses of solid anils are mutually exclusive. It has been noted, however, that the behaviour of anils in disordered materials such as gels is sometimes less strongly constrained. For example, Hadjoudis *et al.* found that an anil derived from 1-adamantylamine, which is purely thermochromic when crystalline, can undergo photochromic switching after forming a supramolecular inclusion complex with  $\beta$ -cyclodextrin.<sup>304</sup> The cavity of the macrocycle is sufficiently large for the *cis-trans* isomerisation to occur, and also prolongs the lifetimes of the two most stable *cis*-keto conformers, producing a bimodal resonance in the compound's emission spectrum.

A variety of anils and similar moieties, such as 2-(2'-hydroxyphenyl)benzothiazoles,<sup>296</sup> 3-hydroxy-2-naphthanilides<sup>294</sup> and 2-hydroxynaphthylidene acetohydrazides<sup>305</sup> have been successfully incorporated into LMWGs. Gelation has been found to amplify fluorescence by as much as three orders of magnitude, whilst still allowing chromic transitions to take place.<sup>306-308</sup> Furthermore, thermal disassembly of a gel provides an additional mechanism through which the optical properties of the system may be controlled. The interplay between aggregation and stimuli-responsiveness was demonstrated in a study by Chen *et al.*, which found that the intense yellow colour of **1.28** in cyclohexane gels can be turned off by either a decrease in temperature or a heat-induced gel-sol transition (Fig. 32).<sup>307</sup> Similarly, Zang *et al.* reported that gels of **30** display greater fluorescence at 77 K than under ambient conditions, even though the yellow colour of the *cis*-keto isomer is greatly diminished by cooling (Fig. 33).<sup>309</sup>

It is clear that functionalities capable of intramolecular proton transfer may confer responsiveness to a range of chemical and physical stimuli. However, where switching must substantially alter the mechanical properties of a material, groups that can undergo larger structural changes are usually better suited to the task. A popular strategy is to employ reactions that produce stable bonds between preorganised molecules in the solid state. Examples of irreversible photo-induced transformations that are possible in gels include the pinacol

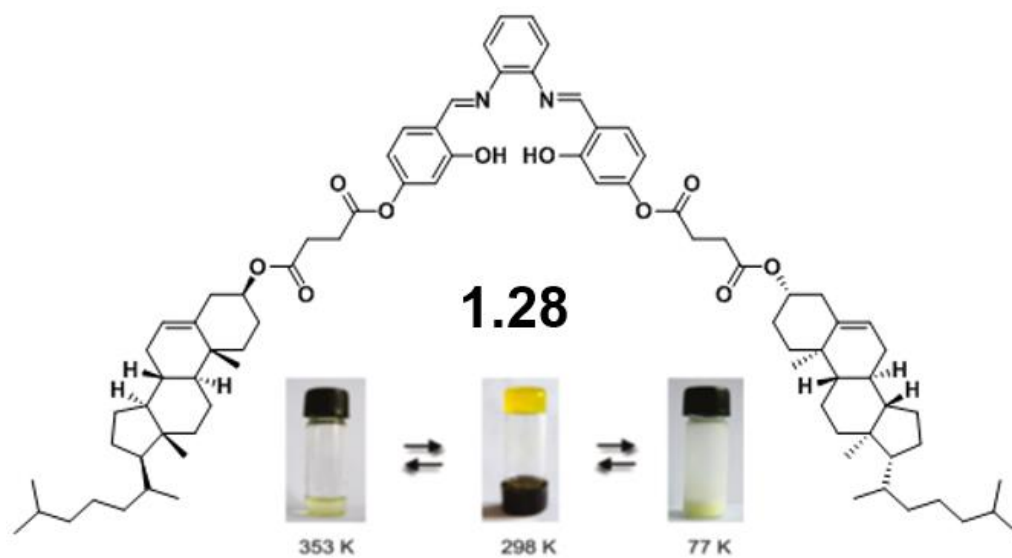


**Fig. 32** The yellow colour of **1.28** in cyclohexane gels can be diminished by cooling, or heating to induce a gel-sol transition. Image adapted with permission from ref. 307. Copyright 2009 American Chemical Society.

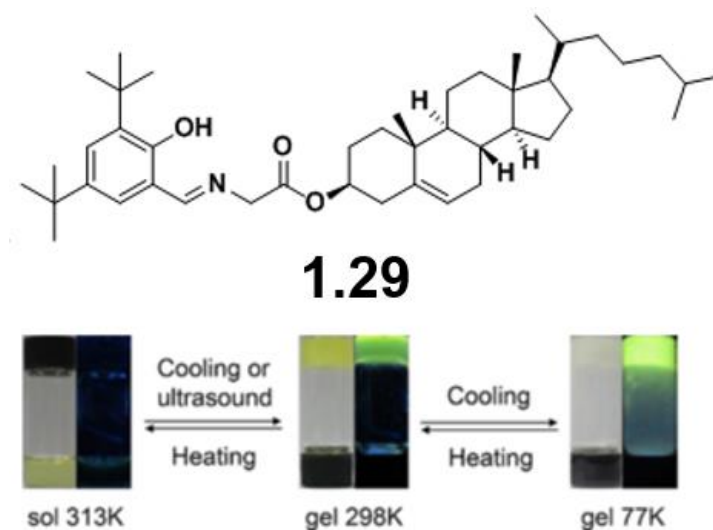


**Fig. 33** Cooling an ethanol gel of **1.29** leads to a loss of yellow colour accompanied by a large increase in emissivity. Heated solutions of the gelator are non-emissive and less strongly coloured than the parent gel. Image adapted with permission from ref. 309. Copyright 2013 Elsevier.

reaction,<sup>310</sup> polymerisation of diacetylenes<sup>311</sup> and the cascade reactions of 1,3,4-oxadiazoles with styrenes.<sup>312</sup> Reversible coupling, meanwhile, has been achieved via the radical-mediated dimerisation of imidazoles<sup>313</sup> and, more commonly, cycloadditions of reactive  $\pi$  systems such as anthracenes,<sup>314, 315</sup> cinnamates<sup>316</sup> and coumarins.<sup>317</sup> Where reactions establish new covalent bonds, they might naively be expected to generate a more robust material, but instances of decreased stability and even spontaneous gel-sol transitions have been reported. For

example, Ayabe *et al.* found that irradiation of an anthracene-based gel leads to breakdown of the fibrous network, due to the inability of the non-planar products to maintain the  $\pi$ - $\pi$  stacking in the original network.<sup>315</sup>

Bond-forming processes in a gel can produce a wide variety of useful optical and mechanical transitions; indeed, even irreversible reactions such as diacetylene coupling may generate a material with reversible responsive behaviour.<sup>311</sup> However, the use of these transformations in molecular switches is hampered by the need for preorganisation of the reacting moieties. To alleviate this problem, switching may be achieved by means of an electrocyclic process, in which bonding occurs between orbitals that are already linked via an extended  $\pi$  system.<sup>318</sup> One species capable of such a reaction is the dihydroindolizine group. Ahmed *et al.* showed that an LMWG containing this motif can form a gel in polar solvents but undergoes a reversible ring opening under UV irradiation, yielding the betaine structure in the form of a red-coloured sol.<sup>319</sup>

Other molecular motifs that display light-induced electrocyclic reactions include spiropyrans, spirooxazines, naphthopyrans and benzopyrans, otherwise known as chromenes. All of these compounds undergo ring opening within a six-membered heterocycle to generate a new double bond and a ketone, enol or phenol moiety.<sup>318</sup> The products contain fewer  $sp^3$  sites than the reactants so tend to adopt a more planar conformation, allowing for increased conjugation and the emergence of new optical absorption bands in the range 570-750 nm. A sol-gel transition may occur due to the possibility of increased  $\pi$ - $\pi$  stacking,<sup>320, 321</sup> and other effects requiring close interactions between conjugated systems, such as Förster transfer<sup>322</sup> or the formation of donor-acceptor complexes,<sup>320</sup> may also be observed. The sensitivity of supramolecular assemblies to such changes in packing was illustrated by Qiu *et al.* in a study of a spiropyran linked to a di-D-alanine moiety.<sup>320</sup> While the closed-form spiropyran **1.30** is non-gelating, UV irradiation of this compound in aqueous solution generates a merocyanine species, which can form dark red fibrous gels at low pH (Fig. 34). In addition to visible light, which induces regeneration of the closed-ring system, the gels may be disrupted by one equivalent of vancomycin, a large chiral molecule capable of strong hydrogen bonding interactions. Intriguingly, however, this ligand-guest response does not occur if the gelator is based on the L enantiomer of alanine rather than the D. It is evident that binding of the guest demands a particular combination of hydrogen

bonds and  $\pi$ - $\pi$  stacking interactions, which can compete with those in the gel assembly only if the merocyanine gelator exhibits a complementary structure.

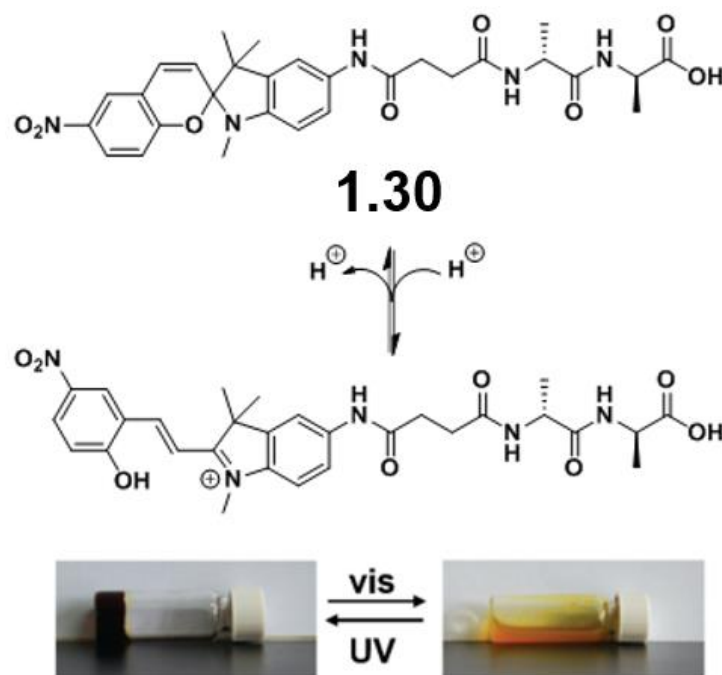


**Fig. 34** Acidic aqueous sols of **1.30** undergo sol-gel transition on exposure to UV light, and assume a dark red colour due to increased absorbance between 450 and 550 nm. Irradiating the gel with visible light (> 400 nm) reverses the transition. Image adapted from ref. 320 with permission from The Royal Society of Chemistry.

A drawback of many electrocyclic reactions is that their products are short-lived under ambient conditions. Although the lifetime of a photoresponse in the gel state may exceed that in solution by as much as two orders of magnitude, significant loss of product typically occurs within minutes, making such systems unsuitable for information storage over extended periods of time.<sup>323, 324</sup> An electrocyclic switch exhibiting more stable photo-induced transitions is the dithienylethene (DTE) moiety. DTE groups convert to a closed-ring structure upon exposure to UV light, and can persist in this form for months and even years at room temperature.<sup>325</sup> Ring closure is usually reversible by visible light, but one or both parts of this reaction cycle may be inhibited depending on the nature of the groups around the DTE core.<sup>326</sup> In a comparison of DTEs based on cyclopentenes and maleimides, Herder *et al.* found the latter to be highly resistant to photo-induced ring closure, and were able to attribute this effect to stable TICT states and small LUMO coefficients on the atoms to be coupled.<sup>289</sup> By contrast, dithiocyclopentenes and fluorinated derivatives deliver reliable and reversible

photochemical reactions, and are thus a popular target for investigations of molecular switches in the gel state.

Ring closure of a DTE reduces the flexibility of the molecule, so may favour gelation by lowering the entropic cost of aggregation. However, the reaction also generates two  $sp^3$  sites and forces the substituents at these sites to be oriented out of the plane of the molecule. The effects of such changes were demonstrated by Yagai *et al.* in a study of the DTE gelator **1.31**.<sup>327</sup> In the closed form, the compound forms non-fluorescent solutions in methylcyclohexane, but ring opening under 600 nm light produces a highly fluorescent gel within one minute. Molecular modelling suggests that the photoproduct can self-assemble into ordered  $\pi$ - $\pi$  stacked aggregates, with efficient migration of excitation energy leading to strong emissivity (Fig. 35). The closed species, however, forms only disordered structures, as the steric hindrance of methyl groups prevents close  $\pi$ - $\pi$  interactions between DTE moieties. Indeed, aggregation of the open form is so favourable that ring opening in the gel-sol system is only partially reversible, unless the reaction is conducted within a thin film to prevent molecules from accessing their optimum packing arrangement.

Changes in aggregation induced by closure of a DTE system were also identified by Hotta *et al.*<sup>205</sup> The open isomer of a DTE-containing bis(urea) was found to be soluble in chloroform but form fibrous H-aggregates upon gradual dilution with hexane. The suspended assemblies undergo over 90% conversion to the closed form when treated with UV light, producing a purple solution of needle-like nanofibres with a 60% enlargement in mean hydrodynamic radius. Irradiation of the chloroform solution, however, delivers a slightly lower yield of the isomerised species, and subsequent self-assembly gives rise to nanoparticles instead of fibrous aggregates. It is proposed that the close-packed molecular arrangement in assemblies of the open isomer forces ring closure to proceed in a cooperative fashion, such that each resulting nanofibre comprises only one enantiomer of the closed molecule. In solution, meanwhile, the (*R,R*) and (*S,S*) enantiomers are formed in equal quantities and remain mixed on aggregation, forming disordered assemblies with no preferred axis of growth. As in most DTE systems, the aggregates are stable under ambient conditions, but may be interconverted through cycles of UV and visible light with no significant degradation of their responsive behaviour.

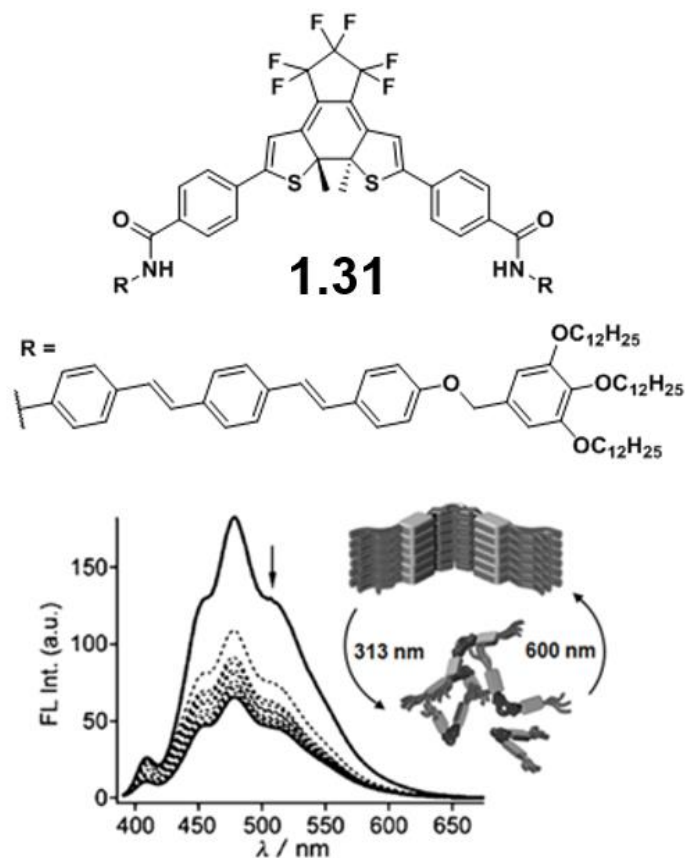


**Fig. 35** Closed form of DTE-OPV conjugate **1.31**, schematic representations of the molecular packing in the open (top) and closed (bottom) forms, and changes in fluorescence upon ring closing in methylcyclohexane. Due to the strong  $\pi$ - $\pi$  interactions within aggregates of the open isomer, conversion to the closed form is limited to 6%, but even this yield is sufficient to reduce the intensity of emissions by 36%. Image adapted with permission from ref. 327. Copyright 2013 John Wiley and Sons.

A particular benefit of DTE groups is that isomerisation often occurs at a high rate, even in the solid state. Rapid switching of a DTE was strikingly demonstrated by de Jong *et al.*, in work aimed at achieving sol-gel switching in a spatially controlled manner.<sup>328</sup> Photolithography by gel-gel and gel-sol transitions is frequently reported,<sup>287, 329-333</sup> but similarly localised formation of a gel from a solution is difficult, since aggregation must outpace the transport of material away from the irradiated area. Nonetheless, UV irradiation of **1.32** in toluene produced bands of material in the shape of a photomask, with spacings as small as 5  $\mu\text{m}$  capable of being resolved (Fig. 36). Optical density measurements indicate that the gelator concentration in the aggregated regions can exceed that of the non-irradiated solution by a factor of 20, owing to entrapment of the compound following the ring closing reaction. It can be seen that photoinduced aggregation serves to sequester the gelator within the irradiated regions, allowing concentration gradients to be established that mirror the variation in light intensity.

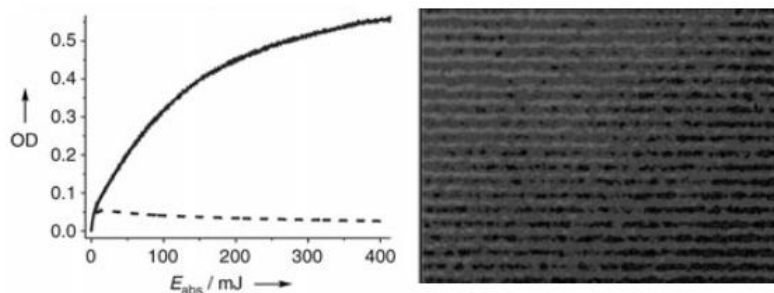
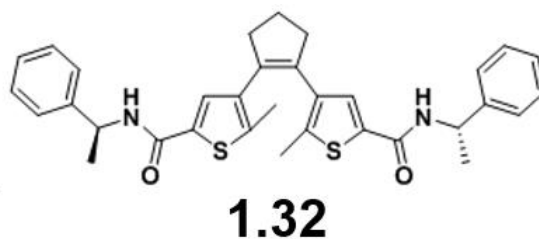


**Fig. 36** Optical density of a toluene gel of **1.32** during ring closure with uniform (dashed line) and localised (solid line) UV illumination, as a function of total adsorbed energy  $E_{\text{ads}}$ . Bands of gel reproducing the shape of a photomask grating are shown. Images adapted with permission from ref. 328. Copyright 2005 John Wiley and Sons.

A further advantage of DTEs is that fluorescence may be induced by wavelengths of light that have no effect on the bonding framework. For example, Xiao *et al.* reported a pyridyl DTE gelator that can be converted quantitatively to the closed- and open-ring structures by irradiation at 365 and 620 nm respectively.<sup>330</sup> Fluorescence of the closed system occurs at 623 nm and can be excited by light at 470 nm, to which both forms of the compound are almost completely inert. The open form, by contrast, is only weakly emissive above 500 nm. Consequently, recording the emission spectrum of the system provides a reliable and non-invasive measure of its current composition, without risk of conversion to an alternative state. This non-destructive readout ability would be a useful feature in a chemical data-storage device, an application with which DTEs – with their quantitative, long-lasting and fatigue-resistant switching response – are clearly highly compatible.<sup>325, 334</sup>

Another potential use for the DTE group is as a component of a molecular logic gate, or MLG. Like their electronic counterparts, MLGs deliver an output signal in the presence of a particular combination of inputs, in accordance with a predefined set of Boolean operations.<sup>335</sup> A tetrakis-amide gelator developed by Xue *et al.*, for instance, acts as an XNOR gate in DMSO-water mixtures, losing its fluorescence at 650 nm if fluoride ions are present without acid, or *vice versa*.<sup>336</sup> Gel-sol transitions and absorbance at 450 nm, meanwhile, behave in the manner of an INHIBIT gate, in that they occur only in response to acid in the absence fluoride. The ability of MLGs to deliver multiple outputs means

that they may perform series of logical operations that would normally require a combination of logic gates, potentially allowing chemical systems to be modulated *in situ* without the use of invasive devices. Control of this nature was demonstrated by Komatsu *et al.*, in a study of the hydrogelator **1.33** (Fig. 37).<sup>337</sup> Concentrated solutions of **1.33** in its *cis* form are converted to gels of the *trans* form by visible light, but at lower concentrations acid or calcium ions must also be present for gelation to occur. By varying the makeup of the gel and the input stimuli, sol-gel and gel-sol transitions may be induced in accordance with four different Boolean operators, allowing entrapped compounds to be released under specific environmental conditions.

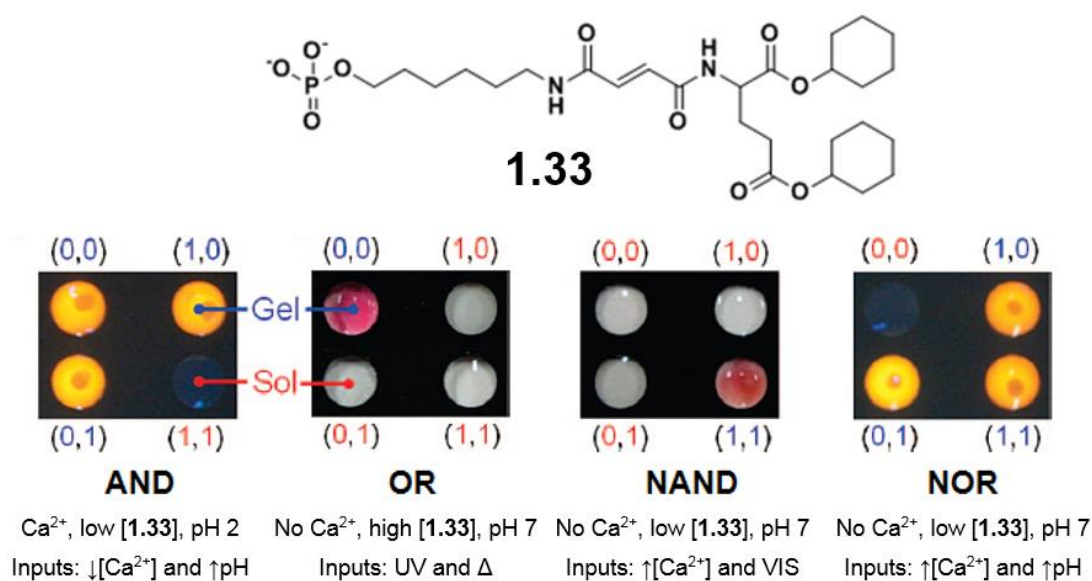


**Fig. 37** Alkene gelator **1.33** and images illustrating gel-sol transitions under different conditions. Gels are stained with a rhodopsin complex (AND and NOR gates) or vitamin B<sub>12</sub> (OR and NAND gates) which are released in the sol state. Gels are formed from the alkene in its *trans* state, provided the system exhibits high [**1.33**], high [Ca<sup>2+</sup>] and/or low pH. In the logic gates above, inputs are marked “1” if applied and “0” if not, and coloured blue or red to signify gelation or dissolution respectively. Δ indicates heating above  $T_{melt}$ ; UV, a *trans-cis* transition induced by a xenon lamp with no filter; VIS, a *cis-trans* transition induced by white light above 350 nm; ↑[Ca<sup>2+</sup>], addition of aqueous CaCl<sub>2</sub>; ↓[Ca<sup>2+</sup>], addition of EDTA, a chelating agent; and ↑pH, addition of aqueous ammonia to reach pH 8. Image adapted with permission from ref. 337. Copyright 2009 American Chemical Society.

Chemically addressable MLGs could be useful in applications requiring a single switching event, such as sensing and drug delivery. However, cycles of writing and erasing in data-storage systems necessitate repeatable responses, which may only be achieved through the use of MLGs with exclusively non-invasive inputs. An elegant solution is to incorporate two or more different switchable groups into the same species. This approach is exemplified by compound **1.34**, reported by Andréasson *et al.*, which



contains cyclisable DTE and fulgimide moieties and displays a remarkable array of logic-gating behaviour (Fig. 38).<sup>338</sup> The two molecular switches in the molecule can be induced to undergo ring opening and closing in an orthogonal fashion, with each combination of isomers producing a characteristic pattern of absorption and fluorescence signals. In consequence, **1.34** can, as a single molecule, perform most of the basic Boolean operations, and may even function as a keypad lock, due to the dependency of certain outputs on the order in which photonic inputs are applied.

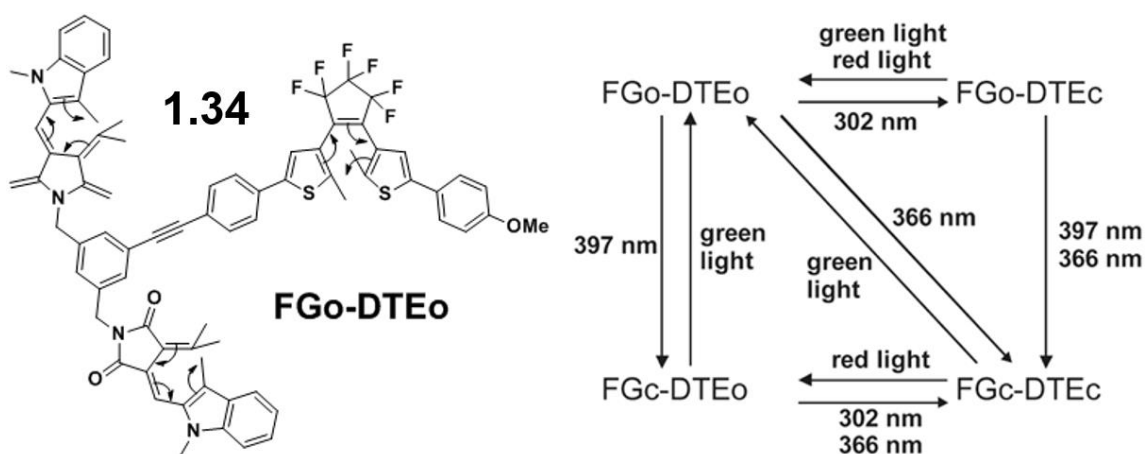


**Fig. 38** Different wavelengths of UV light can induce ring closure of the DTE and fulgimide moieties in **1.34** either separately or in combination (curly arrow mechanisms shown). The reverse reactions are triggered by red and/or green light. Since the state of one switchable group affects the inputs needed to trigger switching of the other, the system can display a wide range of logic-gating behaviour.

Much of the versatility of LMWGs stems from their ability to access a range of molecular arrangements with diverse chemical and physical properties. Precise navigation of this self-assembly landscape is crucial to the development of complex hierarchical structures in biological systems. In order to realise this level of control in synthetic materials, it is necessary to circumvent thermodynamic aggregation by adjusting the self-assembly environment to favour alternative kinetic pathways. Many of the successes so far have relied on chemical strategies, such as varying the pH, altering the composition of a solvent mixture or adding a reactive species to continuously replenish kinetically unstable structures. The advent of smart gelators with multiaddressable behaviour will greatly expand this toolkit, allowing materials to adapt autonomously to changing demands, or assemble piecewise into intricate heterogeneous nanostructures with useful biomimetic functionalities.

## 1.8 Conclusions and outlook

Supramolecular gels represent a unique and versatile platform for the development of responsive materials with real-world applications. In contrast to many polymeric gelators, LMWGs often form thermoreversible gels in a wide range of organic solvents, and can be synthesised and modified with relative ease. By exploiting these properties, systems may be engineered to deliver drugs, bind pollutants or catalyse reactions, and even mimic the complex dynamic properties of biological machinery, such as intracellular filaments, muscle tissue and sensory receptors.

A further limitation of current gelator design is that it relies on an incomplete model of gel formation. Self-assembly of small groups of molecules has been thoroughly investigated, and the microstructures of gel systems are also well documented. More poorly defined are the processes via which idealised supramolecular assemblies - which can be likened to the primary structure of a peptide - evolve into the fibres, lamellae and vesicles constituting its tertiary structure. Nucleation, growth and folding of aggregates are often governed by environmental factors such as temperature, pH and solvent, and thus represent the earliest manifestation of stimuli-responsive behaviour in any gel system. The ability to computationally predict the dominant aggregation pathway would lead to more robust methods of gelator design, free of the empiricism and serendipity necessitated by our current level of understanding.

There is much to be gained from the emergence of smart gels with rationally designed characteristics. An obvious advantage of such materials is that they may be controlled remotely and non-invasively, to minimise unwanted effects on supported materials such as cells, crystals or catalytic particles. When used as reaction vessels and growth media, smart gels could provide a confined environment with tuneable interactions to influence transport, adhesion and coalescence of the guest. However, in contrast to biological matrices and even other synthetic porous materials, small-molecule gels are often uniform in composition and constructed from disordered networks of polydisperse aggregates. To produce more specific binding and more strongly influence guest behaviour, gels must be designed with surfaces that are chemically or microstructurally complementary to the target adsorbate. Enhanced control of the gel-crystal interface might be achieved in mixed-gelator systems by

orchestrating the sequential self-assembly of components with orthogonal stimuli. Alternatively, swelling or dissolution of the gel, induced by heat or illumination, could generate surface patterns of ridges and channels, to modulate the area available for binding or the speed and directionality of guest diffusion.

It is clear that smart gels will continue to play an important role in the development of novel multifunctional nanomaterials. Innovations based on stimuli-sensitive LMWGs promise to revolutionise existing technologies and enable a new generation of exciting applications, in which the properties of a gel can be tuned in response to varying real-time conditions. As archetypal examples of self-assembled systems, small-molecule gels will serve to inspire and inform new models of supramolecular aggregation and provide a test bed for bottom-up approaches to material design. Furthermore, improved mechanistic understanding of stimuli-induced behaviour will create the foundation for more intelligent gel-based devices, and offer insight into the complex and interdependent responses of their biological counterparts.

## 1.9 References

1. Y. Osada and K. Kajiwara, *Gels Handbook: Applications*, Academic Press, 2001.
2. K. Nishinari, *Prog. Colloid Polym. Sci.*, 2009, **136**, 87-94.
3. J. Alemán, A. V. Chadwick, J. He, M. Hess, K. Horie, R. G. Jones, P. Kratochvíl, I. Meisel, I. Mita, G. Moad, S. Penczek and R. F. T. Stepto, *Pure Appl. Chem.*, 2007, **79**, 1801-1827.
4. L. A. Estroff and A. D. Hamilton, *Chem. Rev.*, 2004, **104**, 1201-1217.
5. P. Terech and R. G. Weiss, *Chem. Rev.*, 1997, **97**, 3133-3159.
6. J. Le Bideau, L. Viau and A. Vioux, *Chem. Soc. Rev.*, 2011, **40**, 907-925.
7. M. Suzuki and K. Hanabusa, *Chem. Soc. Rev.*, 2010, **39**, 455-463.
8. J. W. Steed, *Chem. Commun.*, 2011, **47**, 1379-1383.
9. S. R. Raghavan and B. H. Cipriano, *Molecular Gels*, Springer, 2006.
10. P. Terech, D. Pasquier, V. Bordas and C. Rossat, *Langmuir*, 2000, **16**, 4485-4494.
11. J. H. van Esch, *Langmuir*, 2009, **25**, 8392-8394.
12. P. Dastidar, *Chem. Soc. Rev.*, 2008, **37**, 2699-2715.
13. J. G. Hardy, A. R. Hirst, I. Ashworth, C. Brennan and D. K. Smith, *Tetrahedron*, 2007, **63**, 7397-7406.
14. T. Rossow, S. Hackelbusch, P. van Assenbergh and S. Seiffert, *Polym. Chem.*, 2013, **4**, 2515-2527.
15. N. Zweep, A. Hopkinson, A. Meetsma, W. R. Browne, B. L. Feringa and J. H. van Esch, *Langmuir*, 2009, **25**, 8802-8809.
16. M. de Loos, B. L. Feringa and J. H. van Esch, *Eur. J. Org. Chem.*, 2005, 3615-3631.
17. J. Nanda, A. Biswas and A. Banerjee, *Soft Matter*, 2013, **9**, 4198-4208.
18. S. Ray, A. K. Das and A. Banerjee, *Chem. Mater.*, 2007, **19**, 1633-1639.
19. D. Schmaljohann, *Adv. Drug Deliv. Rev.*, 2006, **58**, 1655-1670.
20. K. Sugiyasu, N. Fujita, M. Takeuchi, S. Yamada and S. Shinkai, *Org. Biomol. Chem.*, 2003, **1**, 895-899.
21. P. Rajamalli and E. Prasad, *Org. Lett.*, 2011, **13**, 3714-3717.

22. P. Xie and R. B. Zhang, *J. Mater. Chem.*, 2005, **15**, 2529-2550.
23. Z. J. Zhao, J. W. Y. Lam and B. Z. Tang, *Soft Matter*, 2013, **9**, 4564-4579.
24. J. M. J. Paulusse and R. P. Sijbesma, *Angew. Chem. Int. Edit.*, 2006, **45**, 2334-2337.
25. A. Heller, *Curr. Opin. Chem. Biol.*, 2006, **10**, 664-672.
26. Y. Wu, Y. Hirai, Y. Tsunobuchi, H. Tokoro, H. Eimura, M. Yoshio, S. Ohkoshi and T. Kato, *Chem. Sci.*, 2012, **3**, 3007-3010.
27. P. Grondin, O. Roubeau, M. Castro, H. Saadaoui, A. Colin and R. Clérac, *Langmuir*, 2010, **26**, 5184-5195.
28. A. Das, M. R. Molla, B. Maity, D. Koley and S. Ghosh, *Chem. Eur. J.*, 2012, **18**, 9849-9859.
29. Y. H. Hou, F. F. Xin, M. J. Yin, L. Kong, H. C. Zhang, T. Sun, P. Y. Xing and A. Y. Hao, *Colloids Surf., A*, 2012, **414**, 160-167.
30. X. Y. Yang, G. X. Zhang and D. Q. Zhang, *J. Mater. Chem.*, 2012, **22**, 38-50.
31. Y. Qiao, Y. Y. Lin, Z. Y. Yang, H. F. Chen, S. F. Zhang, Y. Yan and J. B. Huang, *J. Phys. Chem. B*, 2010, **114**, 11725-11730.
32. L. W. Yan, Y. Xue, G. Gao, J. B. Lan, F. Yang, X. Y. Su and J. S. You, *Chem. Eur. J.*, 2010, **16**, 2250-2257.
33. X. D. Yu, Q. A. Liu, J. C. Wu, M. M. Zhang, X. H. Cao, S. Zhang, Q. Wang, L. M. Chen and T. Yi, *Chem. Eur. J.*, 2010, **16**, 9099-9106.
34. C. Wang, D. Q. Zhang and D. B. Zhu, *J. Am. Chem. Soc.*, 2005, **127**, 16372-16373.
35. S. S. Song, R. H. Dong, D. Wang, A. X. Song and J. C. Hao, *Soft Matter*, 2013, **9**, 4209-4218.
36. D. M. Ke, C. L. Zhan, A. D. Q. Li and J. N. Yao, *Angew. Chem. Int. Edit.*, 2011, **50**, 3715-3719.
37. S. N. Qu, L. J. Wang, X. Y. Liu and M. Li, *Chem. Eur. J.*, 2011, **17**, 3512-3518.
38. P. Jana, S. Maity, S. K. Maity, P. K. Ghorai and D. Haldar, *Soft Matter*, 2012, **8**, 5621-5628.
39. D. Braga, S. d'Agostino, E. D'Amen and F. Grepioni, *Chem. Commun.*, 2011, **47**, 5154-5156.
40. P. Y. Xing, S. Y. Li, F. F. Xin, Y. H. Hou, A. Y. Hao, T. Sun and J. Su, *Carbohydr. Res.*, 2013, **367**, 18-24.
41. N. Yan, Z. Y. Xu, K. K. Diehn, S. R. Raghavan, Y. Fang and R. G. Weiss, *Langmuir*, 2013, **29**, 793-805.
42. C. D. Dou, D. Li, H. Z. Gao, C. Y. Wang, H. Y. Zhang and Y. Wang, *Langmuir*, 2010, **26**, 2113-2118.
43. S. Kiyonaka, K. Sugiyasu, S. Shinkai and I. Hamachi, *J. Am. Chem. Soc.*, 2002, **124**, 10954-10955.
44. A. W. P. Fitzpatrick, G. T. Debelouchina, M. J. Bayro, D. K. Clare, M. A. Caporini, V. S. Bajaj, C. P. Jaroniec, L. C. Wang, V. Ladizhansky, S. A. Müller, C. E. MacPhee, C. A. Waudby, H. R. Mott, A. De Simone, T. P. J. Knowles, H. R. Saibil, M. Vendruscolo, E. V. Orlova, R. G. Griffin and C. M. Dobson, *Proc. Natl. Acad. Sci. U.S.A.*, 2013, **110**, 5468-5473.
45. D. J. Adams, K. Morris, L. Chen, L. C. Serpell, J. Bacsá and G. M. Day, *Soft Matter*, 2010, **6**, 4144-4156.
46. Z. X. Liu, Y. Feng, Z. C. Yan, Y. M. He, C. Y. Liu and Q. H. Fan, *Chem. Mater.*, 2012, **24**, 3751-3757.
47. L. Feng and K. A. Cavicchi, *Soft Matter*, 2012, **8**, 6483-6492.
48. A. R. Hirst, I. A. Coates, T. R. Boucheteau, J. F. Miravet, B. Escuder, V. Castelletto, I. W. Hamley and D. K. Smith, *J. Am. Chem. Soc.*, 2008, **130**, 9113-9121.
49. S. C. Wei, M. Pan, K. Li, S. J. Wang, J. Y. Zhang and C. Y. Su, *Adv. Mater.*, 2014, **26**, 2072-2077.
50. P. Y. Xing, T. Sun, S. Y. Li, A. Y. Hao, J. Su and Y. H. Hou, *Colloids Surf., A*, 2013, **421**, 44-50.
51. M. H. Yan, S. K. P. Velu, M. Marechal, G. Royal, J. Galvez and P. Terech, *Soft Matter*, 2013, **9**, 4428-4436.
52. J. J. Wu, M. L. Cao, J. Y. Zhang and B. H. Ye, *RSC Adv.*, 2012, **2**, 12718-12723.

53. F. F. Xin, H. C. Zhang, B. X. Hao, T. Sun, L. Kong, Y. M. Li, Y. H. Hou, S. Y. Li, Y. Zhang and A. Y. Hao, *Colloids Surf., A*, 2012, **410**, 18-22.
54. X. de Hatten, N. Bell, N. Yufa, G. Christmann and J. R. Nitschke, *J. Am. Chem. Soc.*, 2011, **133**, 3158-3164.
55. Y. Y. Li, J. A. Liu, G. Y. Du, H. Yan, H. Y. Wang, H. C. Zhang, W. An, W. J. Zhao, T. Sun, F. E. Xin, L. Kong, Y. M. Li, A. Y. Hao and J. C. Hao, *J. Phys. Chem. B*, 2010, **114**, 10321-10326.
56. K. Kuroiwa, T. Shibata, A. Takada, N. Nemoto and N. Kimizuka, *J. Am. Chem. Soc.*, 2004, **126**, 2016-2021.
57. J. A. Foster and J. W. Steed, *Angew. Chem. Int. Edit.*, 2010, **49**, 6718-6724.
58. D. J. Pochan, J. P. Schneider, J. Kretsinger, B. Ozbas, K. Rajagopal and L. Haines, *J. Am. Chem. Soc.*, 2003, **125**, 11802-11803.
59. J. L. Li and X. Y. Liu, *Adv. Funct. Mater.*, 2010, **20**, 3196-3216.
60. J. H. Shi, X. Y. Liu, J. L. Li, C. S. Strom and H. Y. Xu, *J. Phys. Chem. B*, 2009, **113**, 4549-4554.
61. W. T. Xu, H. W. Tang, H. Y. Lv, J. Li, X. L. Zhao, H. Li, N. Wang and X. N. Yang, *Soft Matter*, 2012, **8**, 726-733.
62. X. Y. Liu, P. D. Sawant, W. B. Tan, I. B. M. Noor, C. Pramesti and B. H. Chen, *J. Am. Chem. Soc.*, 2002, **124**, 15055-15063.
63. B. Yuan, X. Y. Liu, J. L. Li and H. Y. Xu, *Soft Matter*, 2011, **7**, 1708-1713.
64. M. Lescanne, A. Colin, O. Mondain-Monval, F. Fages and J. L. Pozzo, *Langmuir*, 2003, **19**, 2013-2020.
65. G. Schramm and G. Haake, *A practical approach to rheology and rheometry*, Haake Karlsruhe, 1994.
66. J. R. Moffat, I. A. Coates, F. J. Leng and D. K. Smith, *Langmuir*, 2009, **25**, 8786-8793.
67. G. M. Newbloom, K. M. Weigandt and D. C. Pozzo, *Macromolecules*, 2012, **45**, 3452-3462.
68. X. J. Wang, L. B. Xing, W. N. Cao, X. B. Li, B. Chen, C. H. Tung and L. Z. Wu, *Langmuir*, 2011, **27**, 774-781.
69. G. Tan, V. T. John and G. L. McPherson, *Langmuir*, 2006, **22**, 7416-7420.
70. R. Y. Wang, X. Y. Liu, J. Narayanan, J. Y. Xiong and J. L. Li, *J. Phys. Chem. B*, 2006, **110**, 25797-25802.
71. X. Y. Liu, *J. Phys. Chem. B*, 2001, **105**, 11550-11558.
72. J. L. Li, B. Yuan, X. Y. Liu and H. Y. Xu, *Cryst. Growth Des.*, 2010, **10**, 2699-2706.
73. J. L. Li, B. Yuan, X. Y. Liu, R.-Y. Wang and X. G. Wang, *Soft Matter*, 2013, **9**, 435-442.
74. M. A. Rogers and A. G. Marangoni, *Langmuir*, 2009, **25**, 8556-8566.
75. R. Lam, L. Quaroni, T. Pederson and M. A. Rogers, *Soft Matter*, 2010, **6**, 404-408.
76. D. H. Zhao and J. S. Moore, *Org. Biomol. Chem.*, 2003, **1**, 3471-3491.
77. P. Jonkheijm, P. van der Schoot, A. Schenning and E. W. Meijer, *Science*, 2006, **313**, 80-83.
78. S. Malik, S. K. Maji, A. Banerjee and A. K. Nandi, *J. Chem. Soc., Perkin Trans. 2*, 2002, 1177-1186.
79. T. Nakagawa, M. Amakatsu, K. Munenobu, H. Fujii and M. Yamanaka, *Chem. Lett.*, 2013, **42**, 229-231.
80. D. A. S. Grahame, C. Olauson, R. S. H. Lam, T. Pedersen, F. Borondics, S. Abraham, R. G. Weiss and M. A. Rogers, *Soft Matter*, 2011, **7**, 7359-7365.
81. A. Pal and J. Dey, *Langmuir*, 2013, **29**, 2120-2127.
82. M. O. M. Piepenbrock, G. O. Lloyd, N. Clarke and J. W. Steed, *Chem. Commun.*, 2008, **23**, 2644-2646.
83. S. Abraham, Y. Q. Lan, R. S. H. Lam, D. A. S. Grahame, J. J. H. Kim, R. G. Weiss and M. A. Rogers, *Langmuir*, 2012, **28**, 4955-4964.
84. M. A. Rogers, S. Abraham, F. Borondics and R. G. Weiss, *Cryst. Growth Des.*, 2012, **12**, 5497-5504.
85. V. Čaplar, L. Frkanec, N. S. Vujičić and M. Žinić, *Chem. Eur. J.*, 2010, **16**, 3066-3082.
86. V. J. Nebot, J. J. Ojeda-Flores, J. Smets, S. Fernández-Prieto, B. Escuder and J. F. Miravet, *Chem. Eur. J.*, 2014, **20**, 14465-14472.

87. C. X. Zhang, T. R. Zhang, N. Ji, Y. Zhang, B. L. Bai, H. T. Wang and M. Li, *Soft Matter*, 2016, **12**, 1525-1533.
88. E. Dickinson, *J. Chem. Soc., Faraday Trans.*, 1997, **93**, 111-114.
89. J. Málek, *Thermochim. Acta*, 2000, **355**, 239-253.
90. M. Avrami, *J. Chem. Phys.*, 1939, **7**, 1103-1112.
91. M. M. Su, H. K. Yang, L. J. Ren, P. Zheng and W. Wang, *Soft Matter*, 2015, **11**, 741-748.
92. S. S. Rohner, J. Ruiz-Olles and D. K. Smith, *RSC Adv.*, 2015, **5**, 27190-27196.
93. H. Q. Xu, J. Song, T. Tian and R. X. Feng, *Soft Matter*, 2012, **8**, 3478-3486.
94. M. L. Muro-Small, J. Chen and A. J. McNeil, *Langmuir*, 2011, **27**, 13248-13253.
95. J. L. Zhou, X. J. Chen and Y. S. Zheng, *Chem. Commun.*, 2007, 5200-5202.
96. J. H. Fuhrhop, P. Schnieder, J. Rosenberg and E. Boekema, *J. Am. Chem. Soc.*, 1987, **109**, 3387-3390.
97. K. Murata, M. Aoki, T. Suzuki, T. Harada, H. Kawabata, T. Komori, F. Ohseto, K. Ueda and S. Shinkai, *J. Am. Chem. Soc.*, 1994, **116**, 6664-6676.
98. K. A. Houton, K. L. Morris, L. Chen, M. Schmidtman, J. T. A. Jones, L. C. Serpell, G. O. Lloyd and D. J. Adams, *Langmuir*, 2012, **28**, 9797-9806.
99. B. Roy, P. Bairi and A. K. Nandi, *Soft Matter*, 2012, **8**, 2366-2369.
100. Y. J. Wang, L. M. Tang and J. Yu, *Cryst. Growth Des.*, 2008, **8**, 884-889.
101. I. Kapoor, E. M. Schön, J. Bachl, D. Kühbeck, C. Cativiela, S. Saha, R. Banerjee, S. Roelens, J. J. Marrero-Tellado and D. D. Díaz, *Soft Matter*, 2012, **8**, 3446-3456.
102. G. O. Lloyd and J. W. Steed, *Soft Matter*, 2011, **7**, 75-84.
103. G. H. Li, Y. Y. Hu, J. F. Sui, A. X. Song and J. C. Hao, *Langmuir*, 2016, **32**, 1502-1509.
104. C. D. Jones, J. C. Tan and G. O. Lloyd, *Chem. Commun.*, 2012, **48**, 2110-2112.
105. P. Byrne, G. O. Lloyd, L. Applegarth, K. M. Anderson, N. Clarke and J. W. Steed, *New J. Chem.*, 2010, **34**, 2261.
106. A. Vidyasagar and K. M. Sureshan, *Angew. Chem. Int. Edit.*, 2015, **54**, 12078-12082.
107. L. J. Teece, J. M. Hart, K. Y. N. Hsu, S. Gilligan, M. A. Faers and P. Bartlett, *Colloids Surf., A*, 2014, **458**, 126-133.
108. W. Li, Y. L. Guo, P. He, R. Yang, X. G. Li, Y. Chen, D. H. Liang, M. Kidowaki and K. Ito, *Polym. Chem.*, 2011, **2**, 1797-1802.
109. Y. L. Chen, Y. X. Lv, Y. Han, B. Zhu, F. Zhang, Z. S. Bo and C. Y. Liu, *Langmuir*, 2009, **25**, 8548-8555.
110. S. K. Samanta, A. Pal and S. Bhattacharya, *Langmuir*, 2009, **25**, 8567-8578.
111. P. Babu, N. M. Sangeetha, P. Vijaykumar, U. Maitra, K. Rissanen and A. R. Raju, *Chem. Eur. J.*, 2003, **9**, 1922-1932.
112. J. T. van Herpt, M. C. A. Stuart, W. R. Browne and B. L. Feringa, *Langmuir*, 2013, **29**, 8763-8767.
113. D. P. Penalzoza, A. Shundo, K. Matsumoto, M. Ohno, K. Miyaji, M. Goto and K. Tanaka, *Soft Matter*, 2013, **9**, 5166-5172.
114. D. D. Díaz, D. Kühbeck and R. J. Koopmans, *Chem. Soc. Rev.*, 2011, **40**, 427-448.
115. B. Escuder, F. Rodríguez-Llansola and J. F. Miravet, *New J. Chem.*, 2010, **34**, 1044-1054.
116. F. Rodríguez-Llansola, B. Escuder and J. F. Miravet, *J. Am. Chem. Soc.*, 2009, **131**, 11478-11484.
117. J. Bachl, A. Hohenleutner, B. B. Dhar, C. Cativiela, U. Maitra, B. König and D. Díaz Díaz, *J. Mater. Chem. A*, 2013, **1**, 4577-4588.
118. C. Ruiz-Palomero, S. R. Kennedy, M. L. Soriano, C. D. Jones, M. Valcárcel and J. W. Steed, *Chem. Commun.*, 2016, **52**, 7782-7785.
119. A. Cayuela, S. R. Kennedy, M. L. Soriano, C. D. Jones, M. Valcárcel and J. W. Steed, *Chem. Sci.*, 2015, **6**, 6139-6146.
120. A. Dawn, K. S. Andrew, D. S. Yufit, Y. X. Hong, J. P. Reddy, C. D. Jones, J. A. Aguilar and J. W. Steed, *Cryst. Growth Des.*, 2015, **15**, 4591-4599.
121. D. K. Kumar and J. W. Steed, *Chem. Soc. Rev.*, 2014, **43**, 2080-2088.
122. D. B. Amabilino and J. Puigmarti-Luis, *Soft Matter*, 2010, **6**, 1605-1612.

123. J. A. Foster, M. O. M. Piepenbrock, G. O. Lloyd, N. Clarke, J. A. K. Howard and J. W. Steed, *Nat. Chem.*, 2010, **2**, 1037-1043.
124. L. A. Estroff, L. Addadi, S. Weiner and A. D. Hamilton, *Org. Biomol. Chem.*, 2004, **2**, 137-141.
125. H. J. Moon, D. Y. Ko, M. H. Park, M. K. Joo and B. Jeong, *Chem. Soc. Rev.*, 2012, **41**, 4860-4883.
126. A. R. Hirst, B. Escuder, J. F. Miravet and D. K. Smith, *Angew. Chem. Int. Edit.*, 2008, **47**, 8002-8018.
127. M. O. M. Piepenbrock, N. Clarke and J. W. Steed, *Soft Matter*, 2010, **6**, 3541-3547.
128. A. Zaccone, H. Wu, D. Gentili and M. Morbidelli, *Phys. Rev. E*, 2009, **80**, 051404.
129. G. J. Price, M. Ashokkumar, M. Hodnett, B. Zequiri and F. Grieser, *J. Phys. Chem. B*, 2005, **109**, 17799-17801.
130. G. Cravotto and P. Cintas, *Chem. Soc. Rev.*, 2006, **35**, 180-196.
131. K. S. Suslick and G. J. Price, *Annu. Rev. Mater. Sci.*, 1999, **29**, 295-326.
132. J. Rae, M. Ashokkumar, O. Eulaerts, C. von Sonntag, J. Reisse and F. Grieser, *Ultrason. Sonochem.*, 2005, **12**, 325-329.
133. E. B. Flint and K. S. Suslick, *Science*, 1991, **253**, 1397-1399.
134. S. J. Doktycz and K. S. Suslick, *Science*, 1990, **247**, 1067-1069.
135. D. Bardelang, *Soft Matter*, 2009, **5**, 1969-1971.
136. G. Cravotto and P. Cintas, *Chem. Soc. Rev.*, 2009, **38**, 2684-2697.
137. E. Blanco, L. Esquivias, R. Litrán, M. Piñero, M. Ramírez-del-Solar and N. de la Rosa-Fox, *Appl. Organomet. Chem.*, 1999, **13**, 399-418.
138. X. Q. Cai, Y. Wu, L. Y. Wang, N. Yan, J. Liu, X. H. Fang and Y. Fang, *Soft Matter*, 2013, **9**, 5807-5814.
139. M. M. Zhang, L. Y. Meng, X. H. Cao, M. J. Jiang and T. Yi, *Soft Matter*, 2012, **8**, 4494-4498.
140. Y. B. He, Z. Bian, C. Q. Kang, R. Z. Jin and L. X. Gao, *New J. Chem.*, 2009, **33**, 2073-2080.
141. K. M. Anderson, G. M. Day, M. J. Paterson, P. Byrne, N. Clarke and J. W. Steed, *Angew. Chem. Int. Edit.*, 2008, **47**, 1058-1062.
142. C. Baddeley, Z. Q. Yan, G. King, P. M. Woodward and J. D. Badjić, *J. Org. Chem.*, 2007, **72**, 7270-7278.
143. C. D. Dou, D. Chen, J. Iqbal, Y. Yuan, H. Y. Zhang and Y. Wang, *Langmuir*, 2011, **27**, 6323-6329.
144. R. Y. Wang, X. Y. Liu and J. L. Li, *Cryst. Growth Des.*, 2009, **9**, 3286-3291.
145. Y. Cao, L. M. Tang, Y. J. Wang, B. Y. Zhang and L. K. Jia, *Chem. Lett.*, 2008, **37**, 554-555.
146. D. Bardelang, M. Giorgi, V. Hornebecq, A. Stepanov, E. Rizzato, M. B. Zaman, G. Chan, O. Ouari and P. Tordo, *RSC Adv.*, 2012, **2**, 5605-5609.
147. W. Weng, J. B. Beck, A. M. Jamieson and S. J. Rowan, *J. Am. Chem. Soc.*, 2006, **128**, 11663-11672.
148. A. J. P. Teunissen, M. M. L. Nieuwenhuizen, F. Rodríguez-Llansola, A. R. A. Palmans and E. W. Meijer, *Macromolecules*, 2014, **47**, 8429-8436.
149. T. Naota and H. Koori, *J. Am. Chem. Soc.*, 2005, **127**, 9324-9325.
150. K. Y. Liu, L. Y. Meng, S. L. Mo, M. M. Zhang, Y. Y. Mao, X. H. Cao, C. H. Huang and T. Yi, *J. Mater. Chem. C*, 2013, **1**, 1753-1762.
151. S. Maity, P. Kumar and D. Haldar, *Soft Matter*, 2011, **7**, 5239-5245.
152. J. M. J. Paulusse, D. J. M. van Beek and R. P. Sijbesma, *J. Am. Chem. Soc.*, 2007, **129**, 2392-2397.
153. J. M. J. Paulusse, J. P. J. Huijbers and R. P. Sijbesma, *Chem. Eur. J.*, 2006, **12**, 4928-4934.
154. S. Y. Zhang, S. J. Yang, J. B. Lan, Y. R. Tang, Y. Xue and J. S. You, *J. Am. Chem. Soc.*, 2009, **131**, 1689-1691.
155. N. Komiya, T. Muraoka, M. Iida, M. Miyanaga, K. Takahashi and T. Naota, *J. Am. Chem. Soc.*, 2011, **133**, 16054-16061.
156. Y. B. Wang, C. L. Zhan, H. B. Fu, X. Li, X. H. Sheng, Y. S. Zhao, D. B. Xiao, Y. Ma, J. S. Ma and J. N. Yao, *Langmuir*, 2008, **24**, 7635-7638.

157. C. Deng, R. Fang, Y. F. Guan, J. L. Jiang, C. Lin and L. Y. Wang, *Chem. Commun.*, 2012, **48**, 7973-7975.
158. S. M. Park and B. H. Kim, *Soft Matter*, 2008, **4**, 1995-1997.
159. D. M. Ke, C. L. Zhan, X. Li, X. Wang, Y. Zeng and J. N. Yao, *J. Colloid Interface Sci.*, 2009, **337**, 54-60.
160. W. G. Weng, J. B. Beck, A. M. Jamieson and S. J. Rowan, *J. Am. Chem. Soc.*, 2006, **128**, 11663-11672.
161. J. Lyklema, *Fundamentals of Interface and Colloid Science: Particulate Colloids*, Morgan Kaufmann, 2005.
162. K. Hyun, S. H. Kim, K. H. Ahn and S. J. Lee, *J. Non-Newtonian Fluid Mech.*, 2002, **107**, 51-65.
163. K. Hyun, J. G. Nam, M. Wilhelm, K. H. Ahn and S. J. Lee, *Rheol. Acta*, 2006, **45**, 239-249.
164. M. O. M. Piepenbrock, N. Clarke and J. W. Steed, *Soft Matter*, 2011, **7**, 2412-2418.
165. X. D. Yu, X. H. Cao, L. M. Chen, H. C. Lan, B. Liu and T. Yi, *Soft Matter*, 2012, **8**, 3329-3334.
166. W. H. Shih, W. Y. Shih, S. I. Kim, J. Liu and I. A. Aksay, *Phys. Rev. A*, 1990, **42**, 4772-4779.
167. N. M. Sangeetha, S. Bhat, A. R. Choudhury, U. Maitra and P. Terech, *J. Phys. Chem. B*, 2004, **108**, 16056-16063.
168. Z. Y. Xu, J. X. Peng, N. Yan, H. Yu, S. S. Zhang, K. Q. Liu and Y. Fang, *Soft Matter*, 2013, **9**, 1091-1099.
169. L. J. Gibson and M. F. Ashby, *Proc. R. Soc. London, A*, 1982, **382**, 43-49.
170. G. O. Lloyd, M. O. M. Piepenbrock, J. A. Foster, N. Clarke and J. W. Steed, *Soft Matter*, 2012, **8**, 204-216.
171. C. E. Stanley, N. Clarke, K. M. Anderson, J. A. Elder, J. T. Lenthall and J. W. Steed, *Chem. Commun.*, 2006, **30**, 3199-3201.
172. S. Paavilainen, J. L. McWhirter, T. Rog, J. Jarvinen, I. Vattulainen and J. A. Ketoja, *Nord. Pulp Paper Res. J.*, 2012, **27**, 282-286.
173. A. Gautieri, M. J. Buehler and A. Redaelli, *J. Mech. Behav. Biomed. Mater.*, 2009, **2**, 130-137.
174. J. Y. Chen, B. Yuan, Z. Y. Li, B. Tang, E. Ankers, X. G. Wang and J. L. Li, *Langmuir*, 2016, **32**, 1171-1177.
175. S. K. Tang, X. Y. Liu and C. S. Strom, *Adv. Funct. Mater.*, 2009, **19**, 2252-2259.
176. J. L. Li, X. Y. Liu, R. Y. Wang and J. Y. Xiong, *J. Phys. Chem. B*, 2005, **109**, 24231-24235.
177. M. Djabourov, K. Nishinari and S. B. Ross-Murphy, *Physical Gels from Biological and Synthetic Polymers*, Cambridge University Press, 2013.
178. N. W. Tschoegl, *The Phenomenological Theory of Linear Viscoelastic Behaviour: An Introduction*, Springer-Verlag, 2012.
179. P. Sollich, *Phys. Rev. E*, 1998, **58**, 738-759.
180. E. Borré, J. F. Stumbé, S. Bellemin-Laponnaz and M. Mauro, *Angew. Chem. Int. Edit.*, 2016, **55**, 1313-1317.
181. T. Ozdemir and F. Sozmen, *RSC Adv.*, 2016, **6**, 10601-10605.
182. Y. Shi, M. Wang, C. B. Ma, Y. Q. Wang, X. P. Li and G. H. Yu, *Nano Lett.*, 2015, **15**, 6276-6281.
183. P. Sahoo, R. Sankolli, H. Y. Lee, S. R. Raghavan and P. Dastidar, *Chem. Eur. J.*, 2012, **18**, 8057-8063.
184. J. L. Yan, J. Liu, H. R. Lei, Y. Kang, C. Zhao and Y. Fang, *J. Colloid Interface Sci.*, 2015, **448**, 374-379.
185. G. W. Huang, Q. L. Yu, M. R. Cai, F. Zhou and W. M. Liu, *Adv. Mater. Interfaces*, 2016, **3**, 10.
186. Q. L. Yu, D. M. Li, M. R. Cai, F. Zhou and W. M. Liu, *Tribol. Lett.*, 2016, **61**, 16.
187. A. Dawn, T. Shiraki, H. Ichikawa, A. Takada, Y. Takahashi, Y. Tsuchiya, L. T. N. Lien and S. Shinkai, *J. Am. Chem. Soc.*, 2012, **134**, 2161-2171.
188. K. Q. Liu and J. W. Steed, *Soft Matter*, 2013, **9**, 11699-11705.
189. P. Terech, M. H. Yan, M. Maréchal, G. Royal, J. Galvez and S. K. P. Velu, *Phys. Chem. Chem. Phys.*, 2013, **15**, 7338-7344.



190. P. Bartlett, L. J. Teece and M. A. Faers, *Phys. Rev. E*, 2012, **85**, 021404.
191. C. S. O'Hern, L. E. Silbert, A. J. Liu and S. R. Nagel, *Phys. Rev. E*, 2003, **68**, 011306.
192. K. Pogoda, L. Chin, P. C. Georges, F. J. Byfield, R. Bucki, R. Kim, M. Weaver, R. G. Wells, C. Marcinkiewicz and P. A. Janmey, *New J. Phys.*, 2014, **16**, 075002.
193. V. V. Yashin, O. Kuksenok and A. C. Balazs, *J. Phys. Chem. B*, 2010, **114**, 6316-6322.
194. A. S. van Oosten, M. Vahabi, A. J. Licup, A. Sharma, P. A. Galie, F. C. MacKintosh and P. A. Janmey, *Sci. Rep.*, 2016, **6**, 19270.
195. O. V. Kim, R. I. Litvinov, J. W. Weisel and M. S. Alber, *Biomaterials*, 2014, **35**, 6739-6749.
196. U. S. Schwarz and S. A. Safran, *Rev. Mod. Phys.*, 2013, **85**, 1327-1381.
197. P. A. Janmey and R. T. Miller, *J. Cell Sci.*, 2010, **124**, 9-18.
198. I. Levental, P. C. Georges and P. A. Janmey, *Soft Matter*, 2007, **3**, 299-306.
199. H. Kang, Q. Wen, P. A. Janmey, J. X. Tang, E. Conti and F. C. MacKintosh, *J. Phys. Chem. B*, 2009, **113**, 3799-3805.
200. M. L. Gardel, J. H. Shin, F. C. MacKintosh, L. Mahadevan, P. Matsudaira and D. A. Weitz, *Science*, 2004, **304**, 1301-1305.
201. J. R. Blundell and E. M. Terentjev, *Macromolecules*, 2009, **42**, 5388-5394.
202. R. H. Pritchard, Y. Y. Huang and E. M. Terentjev, *Soft Matter*, 2014, **10**, 1864-1884.
203. M. Jaspers, M. Dennison, M. F. J. Mabesoone, F. C. MacKintosh, A. E. Rowan and P. H. J. Kouwer, *Nat. Commun.*, 2014, **5**, 5808.
204. C. G. Pappas, P. Frederix, T. Mutasa, S. Fleming, Y. M. Abul-Haija, S. M. Kelly, A. Gachagan, D. Kalafatovic, J. Trevino, R. V. Ulijn and S. Bai, *Chem. Commun.*, 2015, **51**, 8465-8468.
205. Y. Hotta, S. Fukushima, J. Motoyanagi and A. Tsuda, *Chem. Commun.*, 2015, **51**, 2790-2793.
206. Y. Hotta, S. Suiko, J. Motoyanagi, H. Onishi, T. Ihozaki, R. Arakawa and A. Tsuda, *Chem. Commun.*, 2014, **50**, 5615-5618.
207. H. M. M. ten Eikelder, A. J. Markvoort, T. F. A. de Greef and P. A. J. Hilbers, *J. Phys. Chem. B*, 2012, **116**, 5291-5301.
208. W. L. Noorduin, T. Izumi, A. Millemaggi, M. Leeman, H. Meekes, W. J. P. Van Enckevort, R. M. Kellogg, B. Kaptein, E. Vlieg and D. G. Blackmond, *J. Am. Chem. Soc.*, 2008, **130**, 1158-1159.
209. L. Pérez-García and D. B. Amabilino, *Chem. Soc. Rev.*, 2002, **31**, 342-356.
210. J. W. Steed and J. L. Atwood, *Supramolecular Chemistry*, John Wiley & Sons, 2013.
211. Y. Saito and H. Hyuga, *Rev. Mod. Phys.*, 2013, **85**, 603-621.
212. Z. El-Hachemi, J. Crusats, J. M. Ribó and S. Veintemillas-Verdaguer, *Cryst. Growth Des.*, 2009, **9**, 4802-4806.
213. D. K. Kondepudi, R. J. Kaufman and N. Singh, *Science*, 1990, **250**, 975-976.
214. J. Crusats, Z. El-Hachemi and J. M. Ribó, *Chem. Soc. Rev.*, 2010, **39**, 569-577.
215. D. B. Amabilino, *Nat. Mater.*, 2007, **6**, 924-925.
216. C. Escudero, J. Crusats, I. Díez-Pérez, Z. El-Hachemi and J. M. Ribó, *Angew. Chem. Int. Edit.*, 2006, **45**, 8032-8035.
217. S. Azeroual, J. Surprenant, T. D. Lazzara, M. Kocun, Y. Tao, L. A. Cuccia and J. M. Lehn, *Chem. Commun.*, 2012, **48**, 2292-2294.
218. M. Wolffs, S. J. George, Ž. Tomović, S. C. J. Meskers, A. P. H. J. Schenning and E. W. Meijer, *Angew. Chem. Int. Edit.*, 2007, **46**, 8203-8205.
219. A. Tsuda, M. A. Alam, T. Harada, T. Yamaguchi, N. Ishii and T. Aida, *Angew. Chem. Int. Edit.*, 2007, **46**, 8198-8202.
220. J. Liu, P. L. He, J. L. Yan, X. H. Fang, J. X. Peng, K. Q. Liu and Y. Fang, *Adv. Mater.*, 2008, **20**, 2508-2511.
221. B. Valeur, *Molecular fluorescence: principles and applications*, John Wiley & Sons, 2013.
222. E. J. Bowen and J. Sahu, *J. Phys. Chem.*, 1959, **63**, 4-5.
223. M. Kasha, *Radiat. Res.*, 1963, **20**, 55-70.
224. F. Würthner, T. E. Kaiser and C. R. Saha-Möller, *Angew. Chem. Int. Edit.*, 2011, **50**, 3376-3410.

225. S. Yao, U. Beginn, T. Gress, M. Lysetska and F. Würthner, *J. Am. Chem. Soc.*, 2004, **126**, 8336-8348.
226. V. K. Praveen, S. J. George, R. Varghese, C. Vijayakumar and A. Ajayaghosh, *J. Am. Chem. Soc.*, 2006, **128**, 7542-7550.
227. Y. N. Hong, J. W. Y. Lam and B. Z. Tang, *Chem. Soc. Rev.*, 2011, **40**, 5361-5388.
228. K. Char, C. W. Frank, A. P. Gast and W. T. Tang, *Macromolecules*, 1987, **20**, 1833-1838.
229. B. Chen, K. L. Liu, Z. X. Zhang, X. P. Ni, S. H. Goh and J. Li, *Chem. Commun.*, 2012, **48**, 5638-5640.
230. P. Rajamalli and E. Prasad, *Soft Matter*, 2012, **8**, 8896-8903.
231. X. D. Xu, J. Zhang, X. D. Yu, L. J. Chen, D. X. Wang, T. Yi, F. Y. Li and H. B. Yang, *Chem. Eur. J.*, 2012, **18**, 16000-16013.
232. Y. Kamikawa and T. Kato, *Langmuir*, 2007, **23**, 274-278.
233. T. Kato and K. Tanabe, *Chem. Lett.*, 2009, **38**, 634-639.
234. S. Yamane, Y. Sagara and T. Kato, *Chem. Commun.*, 2013, **49**, 3839-3841.
235. T. Cardolaccia, Y. J. Li and K. S. Schanze, *J. Am. Chem. Soc.*, 2008, **130**, 2535-2545.
236. S. Alex, M. C. Basheer, K. T. Arun, D. Ramaiah and S. Das, *J. Phys. Chem. A*, 2007, **111**, 3226-3230.
237. U. Rösch, S. Yao, R. Wortmann and F. Würthner, *Angew. Chem. Int. Edit.*, 2006, **45**, 7026-7030.
238. M. Cigáň, J. Donovalová, V. Szöcs, J. Gašpar, K. Jakusová and A. Gáplovský, *J. Phys. Chem. A*, 2013, **117**, 4870-4883.
239. A. Ajayaghosh and V. K. Praveen, *Acc. Chem. Res.*, 2007, **40**, 644-656.
240. Y. Cho, J. H. Lee, J. Jaworski, S. Park, S. S. Lee and J. H. Jung, *New J. Chem.*, 2012, **36**, 32-35.
241. C. Wang, C. J. Berg, C. C. Hsu, B. A. Merrill and M. J. Tauber, *J. Phys. Chem. B*, 2012, **116**, 10617-10630.
242. V. Kumar, G. A. Baker and S. Pandey, *Chem. Commun.*, 2011, **47**, 4730-4732.
243. P. C. Xue, Y. Zhang, J. H. Jia, D. F. Xu, X. F. Zhang, X. L. Liu, H. P. Zhou, P. Zhang, R. Lu, M. Takafuji and H. Ihara, *Soft Matter*, 2011, **7**, 8296-8304.
244. S. Yagai, Y. Nakano, S. Seki, A. Asano, T. Okubo, T. Isoshima, T. Karatsu, A. Kitamura and Y. Kikkawa, *Angew. Chem. Int. Edit.*, 2010, **49**, 9990-9994.
245. V. Karunakaran, D. D. Prabhu and S. Das, *J. Phys. Chem. C*, 2013, **117**, 9404-9415.
246. M. A. Drobizhev, M. N. Sapozhnikov, I. G. Scheblykin, O. P. Varnavsky, M. Van der Auweraer and A. G. Vitukhnovsky, *Chemical Physics*, 1996, **211**, 455-468.
247. A. Lohr, M. Lysetska and F. Würthner, *Angew. Chem. Int. Edit.*, 2005, **44**, 5071-5074.
248. K. Haraguchi, T. Takehisa and S. Fan, *Macromolecules*, 2002, **35**, 10162-10171.
249. D. Buenger, F. Topuz and J. Groll, *Prog. Polym. Sci.*, 2012, **37**, 1678-1719.
250. K. Ueno, K. Matsubara, M. Watanabe and Y. Takeoka, *Adv. Mater.*, 2007, **19**, 2807-2812.
251. S. Sutton, N. L. Campbell, A. I. Cooper, M. Kirkland, W. J. Frith and D. J. Adams, *Langmuir*, 2009, **25**, 10285-10291.
252. N. Willis-Fox, A. T. Marques, J. Arlt, U. Scherf, L. D. Carlos, H. D. Burrows and R. C. Evans, *Chem. Sci.*, 2015, **6**, 7227-7237.
253. A. Kaniyoor, B. McKenna, S. Comby and R. C. Evans, *Adv. Opt. Mater.*, 2015, 444-456.
254. M. Cross and H. Greenside, *Pattern Formation and Dynamics in Nonequilibrium Systems*, Cambridge University Press, 2009.
255. V. Castets, E. Dulos, J. Boissonade and P. Dekepper, *Phys. Rev. Lett.*, 1990, **64**, 2953-2956.
256. J. M. Köhler and S. C. Müller, *J. Phys. Chem.*, 1995, **99**, 980-983.
257. W. Hanke, M. Sieber, P. Spencer, J. Schwertner and V. M. F. de Lima, *Microgravity Sci. Technol.*, 2009, **21**, 239-246.
258. N. Tompkins, N. Li, C. Girabawe, M. Heymann, G. B. Ermentrout, I. R. Epstein and S. Fraden, *Proc. Natl. Acad. Sci. U.S.A.*, 2014, **111**, 4397-4402.
259. J. H. Jung, J. H. Lee, J. R. Silverman and G. John, *Chem. Soc. Rev.*, 2013, **42**, 924-936.
260. A. Y. Y. Tam and V. W. W. Yam, *Chem. Soc. Rev.*, 2013, **42**, 1540-1567.

261. M. O. M. Piepenbrock, G. O. Lloyd, N. Clarke and J. W. Steed, *Chem. Rev.*, 2010, **110**, 1960-2004.
262. J. W. Steed, *Chem. Soc. Rev.*, 2009, **38**, 506-519.
263. T. Fujigaya, D. L. Jiang and T. Aida, *Chem. Asian J.*, 2007, **2**, 106-113.
264. J. C. Wu, T. Yi, T. M. Shu, M. X. Yu, Z. G. Zhou, M. Xu, Y. F. Zhou, H. J. Zhang, J. T. Han, F. Y. Li and C. H. Huang, *Angew. Chem. Int. Edit.*, 2008, **47**, 1063-1067.
265. Z. Yang, G. Liang and B. Xu, *Acc. Chem. Res.*, 2008, **41**, 315-326.
266. L. A. Haines, K. Rajagopal, B. Ozbas, D. A. Salick, D. J. Pochan and J. P. Schneider, *J. Am. Chem. Soc.*, 2005, **127**, 17025-17029.
267. J. J. Zhang, Q. Zou and H. Tian, *Adv. Mater.*, 2013, **25**, 378-399.
268. X. Z. Yan, F. Wang, B. Zheng and F. H. Huang, *Chem. Soc. Rev.*, 2012, **41**, 6042-6065.
269. S. Yagai, T. Nakajima, K. Kishikawa, S. Kohmoto, T. Karatsu and A. Kitamura, *J. Am. Chem. Soc.*, 2005, **127**, 11134-11139.
270. M. Moriyama, N. Mizoshita and T. Kato, *Bull. Chem. Soc. Jpn.*, 2006, **79**, 962-964.
271. S. Lee, S. Oh, J. Lee, Y. Malpani, Y. S. Jung, B. Kang, J. Y. Lee, K. Ozasa, T. Isoshima, S. Y. Lee, M. Hara, D. Hashizume and J. M. Kim, *Langmuir*, 2013, **29**, 5869-5877.
272. Z. L. Pianowski, J. Karcher and K. Schneider, *Chem. Commun.*, 2016, **52**, 3143-3146.
273. Y. P. Wu, S. Wu, X. J. Tian, X. Wang, W. X. Wu, G. Zou and Q. J. Zhang, *Soft Matter*, 2011, **7**, 716-721.
274. X. Ran, H. T. Wang, P. Zhang, B. L. Bai, C. X. Zhao, Z. X. Yu and M. Li, *Soft Matter*, 2011, **7**, 8561-8566.
275. N. Koumura, M. Kudo and N. Tamaoki, *Langmuir*, 2004, **20**, 9897-9900.
276. F. Delbecq, N. Kaneko, H. Endo and T. Kawai, *J. Colloid Interface Sci.*, 2012, **384**, 94-98.
277. J. Boekhoven, A. M. Brizard, K. N. K. Kowligi, G. J. M. Koper, R. Eelkema and J. H. van Esch, *Angew. Chem. Int. Edit.*, 2010, **49**, 4825-4828.
278. T. Seki, H. Sekizawa and K. Ichimura, *Polym. J.*, 1999, **31**, 1079-1082.
279. F. Xie, L. Qin and M. H. Liu, *Chem. Commun.*, 2016, **52**, 930-933.
280. R. Reuter and H. A. Wegner, *Chem. Commun.*, 2013, **49**, 146-148.
281. S. Yagai, T. Karatsu and A. Kitamura, *Langmuir*, 2005, **21**, 11048-11052.
282. K. Uchida, S. Yamaguchi, H. Yamada, M. Akazawa, T. Katayama, Y. Ishibashi and H. Miyasaka, *Chem. Commun.*, 2009, 4420-4422.
283. M. de Loos, J. van Esch, R. M. Kellogg and B. L. Feringa, *Angew. Chem. Int. Edit.*, 2001, **40**, 613-616.
284. J. F. Xu, Y. Z. Chen, D. Y. Wu, L. Z. Wu, C. H. Tung and Q. Z. Yang, *Angew. Chem. Int. Edit.*, 2013, **52**, 9738-9742.
285. S. Miljanić, L. Frkanec, Z. Meić and M. Žinić, *Eur. J. Org. Chem.*, 2006, **5**, 1323-1334.
286. C. T. Chen, C. H. Chen and T. G. Ong, *J. Am. Chem. Soc.*, 2013, **135**, 5294-5297.
287. S. Matsumoto, S. Yamaguchi, S. Ueno, H. Komatsu, M. Ikeda, K. Ishizuka, Y. Iko, K. V. Tabata, H. Aoki, S. Ito, H. Noji and I. Hamachi, *Chem. Eur. J.*, 2008, **14**, 3977-3986.
288. L. L. Zhu, X. Li, Q. Zhang, X. Ma, M. H. Li, H. C. Zhang, Z. Luo, H. Agren and Y. L. Zhao, *J. Am. Chem. Soc.*, 2013, **135**, 5175-5182.
289. M. Herder, M. Utecht, N. Manicke, L. Grubert, M. Pätzelt, P. Saalfrank and S. Hecht, *Chem. Sci.*, 2013, **4**, 1028-1040.
290. S. Miljanić, L. Frkanec, Z. Meić and M. Žinić, *Langmuir*, 2005, **21**, 2754-2760.
291. J. E. Kwon and S. Y. Park, *Adv. Mater.*, 2011, **23**, 3615-3642.
292. T. H. Kim, M. S. Choi, B. H. Sohn, S. Y. Park, W. S. Lyoo and T. S. Lee, *Chem. Commun.*, 2008, 2364-2366.
293. Y. Qian, S. Y. Li, Q. Wang, X. H. Sheng, S. K. Wu, S. Q. Wang, J. Li and G. Q. Yang, *Soft Matter*, 2012, **8**, 757-764.
294. M. K. Nayak, *J. Photochem. Photobiol., A*, 2011, **217**, 40-48.
295. M. K. Nayak, B. H. Kim, J. E. Kwon, S. Park, J. Seo, J. W. Chung and S. Y. Park, *Chem. Eur. J.*, 2010, **16**, 7437-7447.
296. Y. Qian, S. Y. Li, G. Q. Zhang, Q. Wang, S. Q. Wang, H. J. Xu, C. Z. Li, Y. Li and G. Q. Yang, *J. Phys. Chem. B*, 2007, **111**, 5861-5868.

297. E. Hadjoudis and I. M. Mavridis, *Chem. Soc. Rev.*, 2004, **33**, 579-588.
298. F. Robert, P. L. Jacquemin, B. Tinant and Y. Garcia, *CrystEngComm*, 2012, **14**, 4396-4406.
299. D. A. Safin, K. Robeyns and Y. Garcia, *CrystEngComm*, 2012, **14**, 5523-5529.
300. D. A. Safin, K. Robeyns and Y. Garcia, *RSC Adv.*, 2012, **2**, 11379-11388.
301. G. K. Pierens, T. K. Venkatachalam, P. V. Bernhardt, M. J. Riley and D. C. Reutens, *Aust. J. Chem.*, 2012, **65**, 552-556.
302. M. M. Cai, Z. Q. Gao, X. H. Zhou, X. P. Wang, S. F. Chen, Y. Z. Zhao, Y. Qian, N. E. Shi, B. X. Mi, L. H. Xie and W. Huang, *Phys. Chem. Chem. Phys.*, 2012, **14**, 5289-5296.
303. J. Harada, H. Uekusa and Y. Ohashi, *J. Am. Chem. Soc.*, 1999, **121**, 5809-5810.
304. E. Hadjoudis, K. Yannakopoulou, S. D. Chatziefthimiou, A. Paulidou and I. M. Mavridis, *J. Photochem. Photobiol., A*, 2011, **217**, 293-298.
305. J. S. Xie, C. J. Chen, X. X. Ma and J. C. Wu, *Inorg. Chem. Commun.*, 2016, **65**, 41-44.
306. S. Datta and S. Bhattacharya, *Chem. Commun.*, 2012, **48**, 877-879.
307. P. Chen, R. Lu, P. C. Xue, T. H. Xu, G. J. Chen and Y. Y. Zhao, *Langmuir*, 2009, **25**, 8395-8399.
308. P. Xue, R. Lu, G. Chen, Y. Zhang, H. Nomoto, M. Takafuji and H. Ihara, *Chem. Eur. J.*, 2007, **13**, 8231-8239.
309. L. B. Zang, H. X. Shang, D. Y. Wei and S. M. Jiang, *Sens. Actuators, B*, 2013, **185**, 389-397.
310. H. Koshima, W. Matsusaka and H. T. Yu, *J. Photochem. Photobiol., A*, 2003, **156**, 83-90.
311. S. Ampornpun, S. Montha, G. Tumcharern, V. Vchirawongkwin, M. Sukwattanasinitt and S. Wacharasindhu, *Macromolecules*, 2012, **45**, 9038-9045.
312. F. Dumur, E. Contal, G. Wantz, T. N. T. Phan, D. Bertin and D. Gigmès, *Chem. Eur. J.*, 2013, **19**, 1373-1384.
313. M. Takizawa, A. Kimoto and J. Abe, *Dyes Pigm.*, 2011, **89**, 254-259.
314. A. Dawn, N. Fujita, S. Haraguchi, K. Sada, S. Tamaru and S. Shinkai, *Org. Biomol. Chem.*, 2009, **7**, 4378-4385.
315. M. Ayabe, T. Kishida, N. Fujita, K. Sada and S. Shinkai, *Org. Biomol. Chem.*, 2003, **1**, 2744-2747.
316. G. C. Kuang, Y. Ji, X. R. Jia, Y. Li, E. Q. Chen, Z. X. Zhang and Y. Wei, *Tetrahedron*, 2009, **65**, 3496-3501.
317. H. T. Yu, H. Mizufune, K. Uenaka, T. Moritoki and H. Koshima, *Tetrahedron*, 2005, **61**, 8932-8938.
318. V. I. Minkin, *Chem. Rev.*, 2004, **104**, 2751-2776.
319. S. A. Ahmed, Z. Moussa, S. Y. Al-Raqa and S. N. Alamry, *J. Phys. Org. Chem.*, 2009, **22**, 593-606.
320. Z. J. Qiu, H. T. Yu, J. B. Li, Y. Wang and Y. Zhang, *Chem. Commun.*, 2009, **23**, 3342-3344.
321. S. A. Ahmed, X. Sallenave, F. Fages, G. Mieden-Gundert, W. M. Müller, U. Müller, F. Vögtle and J. L. Pozzo, *Langmuir*, 2002, **18**, 7096-7101.
322. Q. Chen, D. Q. Zhang, G. X. Zhang, X. Y. Yang, Y. Feng, Q. H. Fan and D. B. Zhu, *Adv. Funct. Mater.*, 2010, **20**, 3244-3251.
323. V. I. Minkin, *Russ. Chem. Rev.*, 2013, **82**, 1-26.
324. G. Berkovic, V. Krongauz and V. Weiss, *Chem. Rev.*, 2000, **100**, 1741-1753.
325. M. Irie, *Chem. Rev.*, 2000, **100**, 1685-1716.
326. R. Göstl, B. Kobin, L. Grubert, M. Pätzelt and S. Hecht, *Chem. Eur. J.*, 2012, **18**, 14282-14285.
327. S. Yagai, K. Ishiwatari, X. Lin, T. Karatsu, A. Kitamura and S. Uemura, *Chem. Eur. J.*, 2013, **19**, 6971-6975.
328. J. J. D. de Jong, P. R. Hania, A. Pugžlys, L. N. Lucas, M. de Loos, R. M. Kellogg, B. L. Feringa, K. Duppen and J. H. van Esch, *Angew. Chem. Int. Edit.*, 2005, **44**, 2373-2376.
329. J. Eastoe, M. Sánchez-Dominguez, P. Wyatt and R. K. Heenan, *Chem. Commun.*, 2004, 2608-2609.
330. S. Z. Xiao, Y. Zou, M. X. Yu, T. Yi, Y. F. Zhou, F. Y. Li and C. H. Huang, *Chem. Commun.*, 2007, 4758-4760.
331. A. Shumburo and M. C. Biewer, *Chem. Mater.*, 2002, **14**, 3745-3750.

332. Q. Chen, Y. Feng, D. Q. Zhang, G. X. Zhang, Q. H. Fan, S. N. Sun and D. B. Zhu, *Adv. Funct. Mater.*, 2010, **20**, 36-42.
333. M. Moriyama, N. Mizoshita, T. Yokota, K. Kishimoto and T. Kato, *Adv. Mater.*, 2003, **15**, 1335-1338.
334. H. Tian and S. J. Yang, *Chem. Soc. Rev.*, 2004, **33**, 85-97.
335. J. Andréasson and U. Pischel, *Chem. Soc. Rev.*, 2010, **39**, 174-188.
336. P. C. Xue, R. Lu, J. H. Jia, M. Takafuji and H. Ihara, *Chem. Eur. J.*, 2012, **18**, 3549-3558.
337. H. Komatsu, S. Matsumoto, S. Tamaru, K. Kaneko, M. Ikeda and I. Hamachi, *J. Am. Chem. Soc.*, 2009, **131**, 5580-5585.
338. J. Andréasson, U. Pischel, S. D. Straight, T. A. Moore, A. L. Moore and D. Gust, *J. Am. Chem. Soc.*, 2011, **133**, 11641-11648.

## 2. Scrolling of supramolecular lamellae in the hierarchical self-assembly of fibrous gels

### 2.1 Background

Increasing interest in LMWGs as alternatives to polymeric materials can be partly attributed to a growing understanding of their gelation mechanisms. With the aid of empirical structure-property relationships,<sup>1</sup> crystal engineering principles<sup>2</sup> and spectroscopic insights,<sup>3</sup> it is now possible to tune the physical properties of a wide variety of supramolecular gels. However, predicting the self-assembly behaviour of a potential LMWG *a priori* remains a challenge.<sup>4</sup> LMWGs can be designed in a modular fashion by incorporating functional groups known to give rise to fibrous assemblies, but the resulting gels may be affected in surprising ways by even small modifications to the gelator, solvent or preparation method. For example, gel formation may depend on the enantiopurity of a chiral molecule,<sup>5</sup> the relative orientations of hydrogen bonding motifs,<sup>6</sup> the cooling rate of the gelling solution<sup>7</sup> and the properties of peripheral functional groups. Among gelators with an uneven balance of hydrogen bond donor and acceptor groups, the concentration of water in the organic solvent is of particular importance due to the possible formation of hydrated solid forms.<sup>8-11</sup> Hydration may limit the potential for gel formation by offering access to higher-symmetry packing modes with more optimal arrangements of hydrogen bonding motifs.<sup>12</sup>

Competition between gelation and crystallisation processes is a key feature of many LMWG systems. A gel often consists of microcrystals with a high aspect ratio,<sup>13</sup> and even non-crystalline gels may form alongside a non-gelating crystalline phase or undergo crystallisation with the passage of time.<sup>14-16</sup> Although the crystal structure of a gelator might offer some indication of how molecules interact in the gel phase,<sup>17, 18</sup> the assumption of a structural relationship between the two materials is not always justified.<sup>19</sup> Nonetheless, it is likely that the dominant supramolecular motifs in crystals are preserved in the corresponding gels, and play a central role in determining the materials' optical, microstructural and rheological characteristics.<sup>20</sup> Indeed, Anderson *et al.* found that the lowest-energy calculated structures for hydrated co-crystals of uric acid and melamine closely reproduce the PXRD patterns of the corresponding sonogels, and feature

the most stable hydrogen bonding motifs identified through *ab initio* calculations.<sup>18</sup>

The likelihood of gelation is often strongly dependent on the solvent environment. Solvent molecules may co-assemble with an LMWG to produce gel aggregates with enhanced thermodynamic stability.<sup>21</sup> Additionally, solvation effects in the precursor sol may favour gelation by promoting self-assembly of the necessary supramolecular motifs. For example, carboxylic acid dimer synthons may form more readily in the absence of competing hydrogen bonding species,<sup>22</sup> and the self-association of hydrophobic moieties may be strengthened by the use of a more polar solvent.<sup>23</sup> Owing to the large surface areas of nanoscale particles, a nascent gel aggregate may outcompete nuclei of higher bulk stability through stabilising interactions with the surrounding solvent.<sup>24</sup> Similarly, solvation of growing surfaces may lead to large differences in their relative surface energies, producing the anisotropic growth conditions required for gel formation.<sup>25</sup>

It is clear that predicting gel formation by LMWGs requires a detailed understanding of their behaviour in solution. Information regarding the local environment and conformations of gelator molecules may be obtained from NMR and other spectroscopic experiments,<sup>26, 27</sup> and the growth of a percolated gel network may be monitored via changes in fluorescence or rheological properties.<sup>28</sup> Nascent aggregates can sometimes be visualised *in situ* by optical methods, or deposited onto a solid substrate for analysis by atomic force and electron microscopies. Furthermore, solution-state assemblies may be probed by small-angle neutron scattering (SANS), with data fitting to ascertain their average size, shape, periodic structure and fractal dimension. In exceptional cases, it is possible to gain insight into hierarchical self-assembly processes, such as the bundling of peptide fibrils to form amyloid aggregates<sup>29</sup> or the thickening and elongation of cylindrical gel fibres comprising lamellar assemblies of bis(urea)s.<sup>30, 31</sup> However, such results are time-consuming to obtain and offer limited assistance in the design and optimisation of LMWGs, since it is difficult to link experimental outcomes to the behaviour of gelators on a molecular scale.

To acquire a more detailed understanding of gel formation, it is necessary to develop detailed computational models of the self-assembly process. Provided the system is well-parameterised and the force-field carefully chosen, molecular

dynamics (MD) simulations can replicate the key results of more accurate but computationally expensive calculation techniques. MD studies have been used to map the phase diagrams of peptides,<sup>32</sup> lipids<sup>33</sup> and polysaccharides,<sup>34</sup> as well as generalised polymers,<sup>35, 36</sup> rod-shaped molecules<sup>37, 38</sup> and colloidal particles.<sup>39, 40</sup> The simulations capture the formation of experimentally observable structures such as  $\beta$  sheets and phospholipid bilayers, and provide realistic illustrations of their interactions with solvents, ions and biologically important additives. As well as accurately reproducing measurable physical properties, such as CGCs, phase transition temperatures and packing coefficients, MD models have been used to probe less accessible parameters, including surface tensions, self-diffusion coefficients and molecular conformations.<sup>33, 41, 42</sup> Furthermore, some studies have yielded useful predictions. For instance, simulations of a triblock amphiphilic peptide highlight the potential for  $\beta$ -sheets to stack in a perpendicular fashion, producing soluble dimeric assemblies that could actively participate in neurological pathologies such as Alzheimer's disease.<sup>32</sup>

To accurately describe a supramolecular system and extract physically meaningful results, it is typically necessary to model several thousand molecules over a timeframe of tens or even hundreds of nanoseconds. Owing to the prohibitive expense of performing atomistic MD simulations on this scale, systems are usually simplified by constructing a coarse-grained representation of the molecules involved. A coarse-grained model may be parameterised to precisely mimic particular characteristics of a smaller atomistic simulation. Moreover, controlling the number of degrees of freedom in the system may allow for more general investigations into the roles of certain key parameters, such as molecular length, curvature and charge separation. A drawback of this approach is that it limits the ability to accommodate changes in molecular properties, and may therefore lack predictive power when extrapolating beyond the conditions of the model validation. In addition, it is rarely possible to emulate the nucleation and growth of complex hierarchical aggregates, which may occur over inaccessible timescales or rely on supramolecular interactions that are poorly addressed by the chosen force-field.

An alternative method of simplification is to base the initial configuration on a preformed motif or supramolecular assembly.<sup>43</sup> The primary aim of this



investigation was to model the development of fibrous gels from lamellar networks of hydrogen bonded molecules. It was speculated that supramolecular assemblies in solution could preserve the general features of the corresponding single-crystal structures. Thus, crystals based on layers of hydrogen bonded molecules are likely to arise from the stacking of similar lamellae in solution, and MD simulations of these assemblies may reveal how alternative fibrous aggregates and hence gels can form. Evidence of lamellar structures in bis(urea) gels and comparable tape-like aggregates has been obtained via a number of experimental techniques, including SANS, PXRD and scanning tunnelling microscopy.<sup>30</sup> A reasonable hypothesis is that isolated lamellae undergo spontaneous scrolling to form fibrous nuclei, which are subsequently enlarged by propagation of the scrolled sheet or accretion of unscrolled assemblies (Fig. 39). Comparable scrolling has been observed in a number of materials comprising asymmetric lamellar structures, including asbestos chrysotile and crystalline polymers such as poly(ethylene),  $\gamma$ -poly(vinylidene fluoride) and Nylon 66.<sup>44</sup>

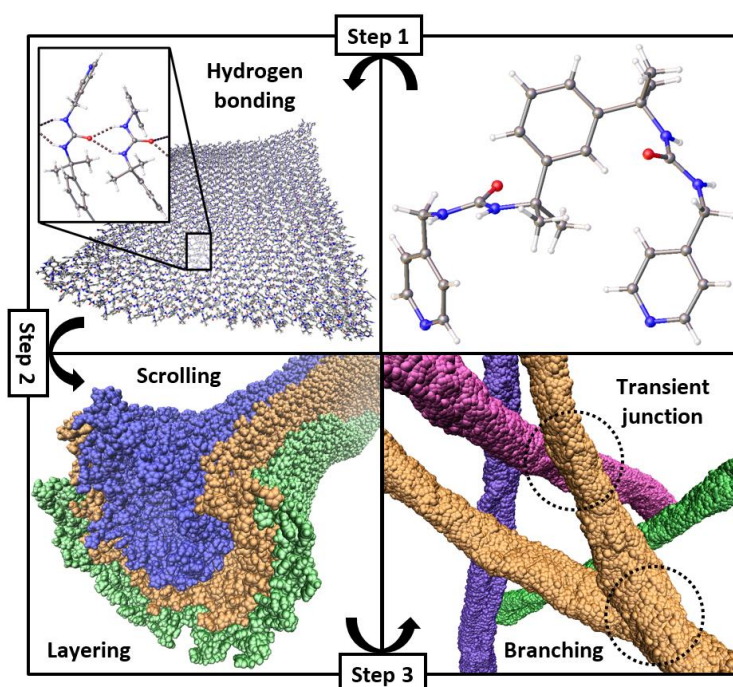
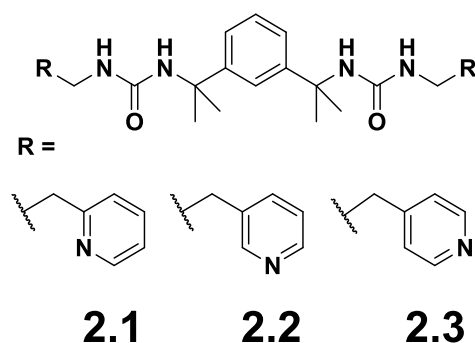


**Fig. 39** Typical stages in the hierarchical self-assembly of fibrous gels. Molecules assemble into lamellar networks (step 1) which subsequently undergo scrolling and layering to form extended fibrils (step 2). These fibrils further entangle to generate a sample-spanning aggregate network (step 3). Fibrils may be connected physically via transient junctions or undergo branching to form permanent junctions. Images of scrolled lamellae and gel fibrils are constructed from frames of MD simulations in VMD.<sup>45</sup>

To test the validity of the scrolling model, the crystal structures of three representative isomeric bis(urea)s with picolyl end groups, **2.1-2.3**. Bis(urea)s frequently

form linear arrays of urea-urea hydrogen bonds known as  $\alpha$ -tape motifs, which can link molecules into a range of topologically distinct one-, two- and three-dimensional networks.<sup>46-49</sup> Owing to the limited flexibility of the sterically bulky spacer, species derived from 1,3-bis(1-isocyanato-1-methylethyl)benzene tend to crystallise readily and often exhibit highly unusual  $\alpha$ -tape topologies.<sup>50</sup> Compounds **2.1-2.3** are of particular interest since they typically form lamellar structures which are highly compatible with gel formation. Moreover, as in the extensively studied 3-pyridyl analogue,<sup>51-53</sup> the presence of multiple competing hydrogen bond acceptors allows for a diverse range of self-assembly outcomes. The multiple polymorphs and solvates of each compound offer insight into the potential supramolecular assemblies that may form in solution, and provide useful starting points for simulating lamellae in the early stages of gel formation.

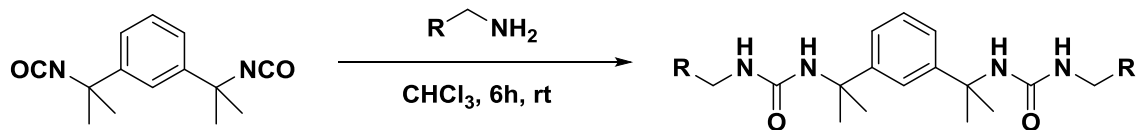


## 2.2 Results and discussion

### 2.2.1 Synthesis and structural categorisation

Compounds **2.1-2.3** were synthesised by adding a diisocyanate to a chloroform solution of excess picolylamine. The compounds form good-quality single crystals when recrystallized from polar solvents (Table 2). In most cases, the structures consist of layers of molecules linked by a two-dimensional network of  $\alpha$ -tapes. The topologies of these lamellar assemblies are categorised by assigning a common letter to molecules sharing a pair of tapes (Fig. 40). For example, for bis(urea)s adopting a “brick wall” arrangement, in which alternating rows of molecules are tape-sharing, the repeat unit of each  $\alpha$ -tape is denoted [AB]. All lamellar bis(urea) crystal structures so far reported display one of just two network topologies: [AB] and [AABB]. However, the suitability of lamellae for gel formation also depends on their symmetry and morphology, which may be strongly perturbed by changes to the molecular structure or solvent environment. It is noted that although crystals of compounds **1a-c** generally exhibit similar

supramolecular motifs, altering the configuration of the picolyl group can greatly affect the interactions between lamellae and the favourability of solvate formation.



	<b>2.1 (I)</b>	<b>2.2 (II)</b>	<b>2.2 (III)</b>	<b>2.2·2H<sub>2</sub>O (IV)</b>
<b>Formula</b>	C <sub>26</sub> H <sub>32</sub> N <sub>6</sub> O <sub>2</sub>	C <sub>26</sub> H <sub>32</sub> N <sub>6</sub> O <sub>2</sub>	C <sub>26</sub> H <sub>32</sub> N <sub>6</sub> O <sub>2</sub>	C <sub>26</sub> H <sub>36</sub> N <sub>6</sub> O <sub>4</sub>
<b>Formula weight</b>	460.57	460.57	460.57	496.61
<b>Space group</b>	<i>P</i> 2 <sub>1</sub>	<i>P</i> 2 <sub>1</sub> 2 <sub>1</sub> 2 <sub>1</sub>	<i>Pbca</i>	<i>P</i> 2 <sub>1</sub> / <i>c</i>
<b><i>a</i> / Å</b>	11.1606(17)	9.3865(12)	12.1736(15)	20.9540(16)
<b><i>b</i> / Å</b>	9.0613(14)	11.4758(14)	9.2491(12)	15.2334(12)
<b><i>c</i> / Å</b>	12.6316(19)	23.407(3)	43.427(5)	18.0568(14)
<b><math>\alpha</math> / °</b>	90	90	90	90
<b><math>\beta</math> / °</b>	101.436(5)	90	90	110.150(3)
<b><math>\gamma</math> / °</b>	90	90	90	90
<b><i>V</i> / Å<sup>3</sup></b>	1252.1(3)	2521.3(5)	4889.7(10)	5411.0(7)
<b><i>Z</i></b>	2	4	8	8
<b><i>D</i><sub>calc</sub> / g cm<sup>-3</sup></b>	1.222	1.213	1.251	1.219
<b><i>R</i><sub>int</sub></b>	0.0711	0.1270	0.1571	0.1615
<b><i>R</i><sub>1</sub> [<i>I</i> ≥ 2σ (<i>I</i>)]</b>	0.0615	0.0533	0.0881	0.1202
<b>w<i>R</i><sub>2</sub> [all data]</b>	0.1660	0.1150	0.1960	0.3240
	<b>2.3·(C<sub>6</sub>H<sub>7</sub>N) (V)</b>	<b>2.3·0.5(C<sub>6</sub>H<sub>7</sub>N) (VI)</b>	<b>2.3·0.5(C<sub>6</sub>H<sub>7</sub>N) (VII)</b>	<b>2.1·0.5PhNO<sub>2</sub>·0.25H<sub>2</sub>O (VIII)</b>
<b>Formula</b>	C <sub>32</sub> H <sub>39</sub> N <sub>7</sub> O <sub>2</sub>	C <sub>58</sub> H <sub>71</sub> N <sub>13</sub> O <sub>4</sub>	C <sub>58</sub> H <sub>71</sub> N <sub>13</sub> O <sub>4</sub>	C <sub>116</sub> H <sub>140</sub> N <sub>26</sub> O <sub>13</sub>
<b>Formula weight</b>	553.70	1014.27	1014.27	2106.53
<b>Space group</b>	<i>P</i> 2 <sub>1</sub>	<i>P</i> -1	<i>I</i> 2/ <i>a</i>	<i>P</i> 2 <sub>1</sub> / <i>c</i>
<b><i>a</i> / Å</b>	9.2277(6)	15.1050(18)	16.000(14)	15.2876(11)
<b><i>b</i> / Å</b>	11.2568(7)	18.340(2)	36.172(3)	35.975(3)
<b><i>c</i> / Å</b>	15.1469(9)	20.543(2)	20.309(2)	20.6493(15)
<b><math>\alpha</math> / °</b>	90	88.283(3)	90	90
<b><math>\beta</math> / °</b>	105.978(2)	76.761(3)	106.865(4)	103.288(3)
<b><math>\gamma</math> / °</b>	90	89.450(3)	90	90
<b><i>V</i> / Å<sup>3</sup></b>	1512.59(16)	5537.1(11)	11248.6(18)	11052.4(14)
<b><i>Z</i></b>	2	4	8	4
<b><i>D</i><sub>calc</sub> / g cm<sup>-3</sup></b>	1.216	1.217	1.198	1.266
<b><i>R</i><sub>int</sub></b>	0.0690	0.1020	0.0876	0.0898
<b><i>R</i><sub>1</sub> [<i>I</i> ≥ 2σ (<i>I</i>)]</b>	0.0487	0.0848	0.0665	0.0587
<b>w<i>R</i><sub>2</sub> [all data]</b>	0.1098	0.2147	0.1983	0.1367
	<b>2.3·1.25PhNO<sub>2</sub>·0.25H<sub>2</sub>O (IX)</b>	<b>2.3·2MeNO<sub>2</sub> (X)</b>	<b>2.3·2MeCN (XI)</b>	
<b>Formula</b>	C <sub>134</sub> H <sub>155</sub> N <sub>29</sub> O <sub>19</sub>	C <sub>28</sub> H <sub>38</sub> N <sub>8</sub> O <sub>6</sub>	C <sub>28</sub> H <sub>38</sub> N <sub>8</sub> O <sub>6</sub>	
<b>Formula weight</b>	412.64	582.66	542.68	
<b>Space group</b>	<i>P</i> -1	<i>Fdd</i> 2	<i>Fdd</i> 2	
<b><i>a</i> / Å</b>	15.6876(10)	29.2830(14)	28.9722(16)	
<b><i>b</i> / Å</b>	18.4655(12)	34.2175(16)	34.2485(19)	
<b><i>c</i> / Å</b>	22.7146(14)	12.0618(6)	12.1561(7)	
<b><math>\alpha</math> / °</b>	82.8733(19)	90	90	
<b><math>\beta</math> / °</b>	87.1357(18)	90	90	
<b><math>\gamma</math> / °</b>	83.168(2)	90	90	
<b><i>V</i> / Å<sup>3</sup></b>	6478.6(7)	12085.8(10)	12061.9(12)	
<b><i>Z</i></b>	2	16	16	
<b><i>D</i><sub>calc</sub> / g cm<sup>-3</sup></b>	1.269	1.281	1.195	
<b><i>R</i><sub>int</sub></b>	0.1135	0.0597	0.0636	
<b><i>R</i><sub>1</sub> [<i>I</i> ≥ 2σ (<i>I</i>)]</b>	0.0935	0.0676	0.0426	
<b>w<i>R</i><sub>2</sub> [all data]</b>	0.2904	0.1777	0.0927	

**Table 2** Summary of crystallographic data for compounds **2.1-2.3**.

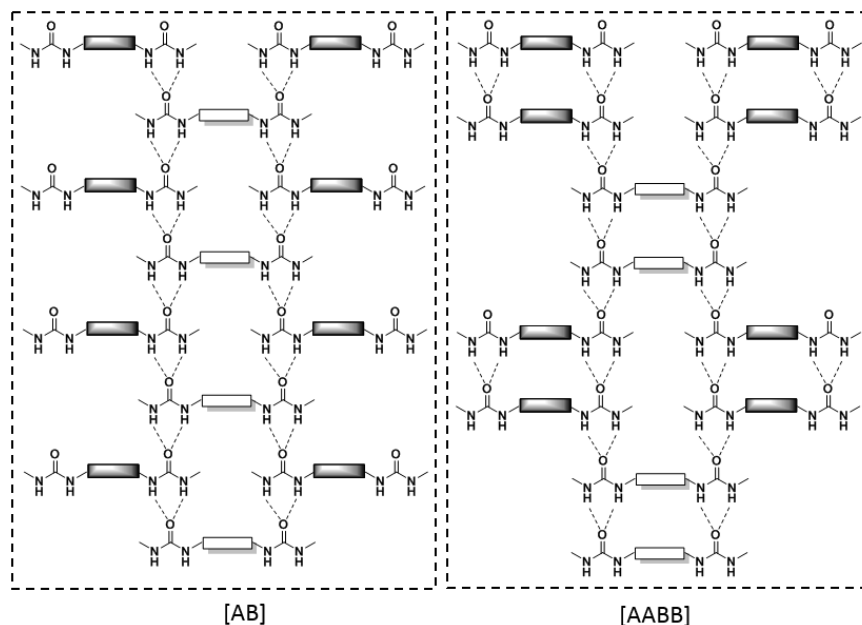


**Fig. 40** The two most common topologies of lamellar  $\alpha$ -tape networks. Within each  $\alpha$ -tape, molecules are labelled with a common letter if they are also connected via a second  $\alpha$ -tape. These “tape-sharing” bis(urea)s are represented schematically as white (A) or black (B) spacers linking two urea moieties, with dashed lines indicating hydrogen bonds.

### 2.2.2 Non-solvated assemblies

In their non-solvated crystal structures, compounds **2.1** and **2.2** both display an [AB] molecular arrangement with one bis(urea) molecule in the asymmetric unit. However, the morphologies of the lamellar networks differ due to the variable ability of picolyl groups to form hydrogen bonds. In crystals of structure **I**, obtained by recrystallisation of **2.1** from nitromethane or 3-picoline, the disordered spacer of the bis(urea) is nearly parallel to the lamellar plane. Thus, lamellae are relatively thin, with an interlayer spacing  $d_{\text{layer}}$  of 7.553(1) Å and lamellar area  $A_{\text{mol}}$  of 83.55(2) Å<sup>2</sup> per molecule. This packing mode is favoured because the bis(urea)s do not form the common  $R_2^1(6)$  urea-urea motifs,<sup>54</sup> but instead interact via single urea-urea and picolyl-urea hydrogen bonds (Fig. 41). The resulting  $R_2^1(11)$  motifs force the picolyl and urea groups to lie in roughly the same plane, with no significant interactions between neighbouring lamellae. Such an arrangement of hydrogen bonds is not possible in crystals of **1b** and **1c**, as it is not geometrically feasible for the nitrogen atoms of 3- and 4-picolyl groups to approach the hydrogen bond donors of adjacent urea-urea motifs.

The geometry of a bis(urea) lamella may also be influenced by the symmetry of the  $\alpha$ -tape network. In non-solvated crystals of compound **2.2**, the

configuration of  $\alpha$ -tapes depends on the solvent used for crystallisation. Structure **II** was crystallised from an acetonitrile solution and comprises  $\alpha$ -tapes in the relatively common antiparallel arrangement (Fig. 42(a)). There are no other significant supramolecular motifs within each lamellar bis(urea) network. However, pairs of lamellae are linked by bifurcated urea-urea-picolylic hydrogen bonds, which lead to pronounced asymmetry in the  $R_2^1(6)$  urea-urea motifs. Since molecules are not constrained to lie in the plane of the  $\alpha$ -tape network, the bis(urea) assemblies are thicker than those in structure **I** and more highly interdigitated, with  $d_{\text{layer}} = 11.704(2)$  Å and  $A_{\text{mol}} = 53.86(1)$  Å<sup>2</sup>.

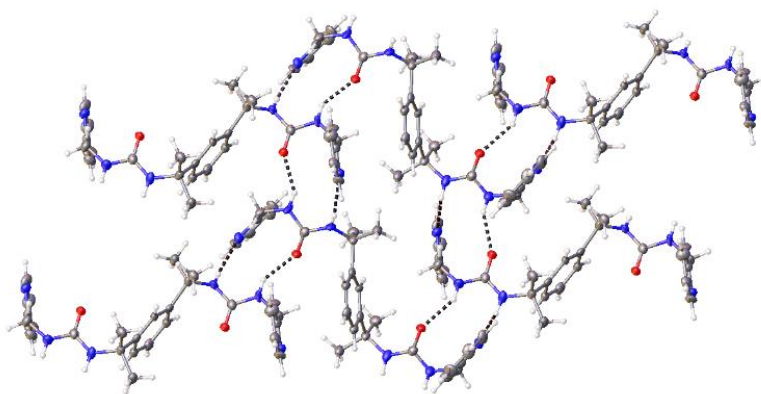


**Fig. 41** Lamellar hydrogen bonding network in structure **I**, viewing down the normal axis of the lamellar plane. Molecules of **2.1** are linked by urea-urea and picolylic-urea interactions (dashed lines). Disorder in the spacer between urea groups is omitted for clarity.

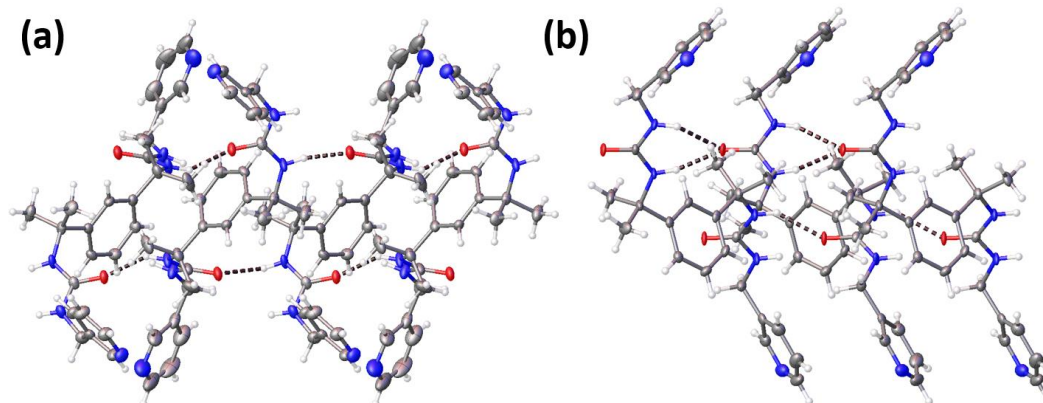


**Fig. 42** Lamellar networks in the non-solvated polymorphs of **2.2**, viewing along the lamellar planes and perpendicular to the  $\alpha$ -tapes. Adjacent  $\alpha$ -tapes are antiparallel in structure **II** (a) and syn-parallel in structure **III** (b).

A second polymorph of **2.2** (structure **III**) was crystallised from nitrobenzene. Owing perhaps to competitive solvent-urea hydrogen bonding during the self-assembly process, the material does not exhibit any significant picolylic-urea interactions. In addition, the structure consists of polar  $\alpha$ -tape networks, in which

all interconnected urea groups exhibit the same orientation (Fig. 42(b)). It has been suggested that syn-parallel tapes are less favourable than antiparallel networks as a result of destabilising dipole interactions between neighbouring ureas.<sup>55</sup> However, examination of bis(urea) crystal structures in version 5.37 of the Cambridge Structural Database<sup>56</sup> (CSD) reveals that around 40% of bis(urea)s with urea-urea interactions exhibit a parallel intramolecular conformation of urea groups (Section 9.2, Table 3). Indeed, while structure **III** lacks the additional hydrogen bonding of structure **II**, its density is 3% higher due to more efficient interdigitation of neighbouring lamellae ( $d_{\text{layer}} = 10.857(2) \text{ \AA}$ ,  $A_{\text{mol}} = 56.30(1) \text{ \AA}^2$ ). It appears that each polymorph of **2.2** represents a different compromise, providing a stable balance between the competing demands of picolyl-urea hydrogen bonding and crystal packing efficiency.

### 2.2.3 Solvated assemblies

By crystallising as solvates, compounds **2.1-2.3** can acquire a more balanced ratio of hydrogen bond donors to acceptors.<sup>57</sup> Solvate formation may result in increased structural disorder, reduced crystallographic symmetry or a more complex  $\alpha$ -tape topology.<sup>12</sup> For example, recrystallization of **2.2** from wet methanol produced poor-quality single crystals of a dihydrate system (structure **IV**). The structure displays an [AABB] network of  $\alpha$ -tapes and there is slight disorder in one of the four symmetry-independent picolyl groups. Likewise, of the four water molecules in the asymmetric unit, only three can be precisely located. The ordered water molecules form a linear trimer, and bridge adjacent lamellae via one urea-water and two picolyl-water hydrogen bonding motifs (Fig. 43).

Solvate formation by compounds **2.1-2.3** is not restricted to solvents that are strong hydrogen bond donors. Indeed, compound **2.3** forms crystalline solvates with both 3- and 4-picoline, guests that are unable to engage in strong hydrogen bonding with the picolyl end groups. The 4-picoline solvate (structure **V**) consists of an [AB]  $\alpha$ -tape network, with an asymmetric unit containing one molecule each of the solvent and bis(urea). One NH group in half of the urea groups forms a hydrogen bond with the picoline guest molecule (Fig. 44(a)), but the picolyl end groups of the bis(urea) are not involved in any significant supramolecular motifs. By contrast, crystallisation of **2.3** from 3-picoline affords two concomitant

polymorphic solvates that both exhibit interacting picolyl moieties. In structure **VI**, [AABB] bis(urea) lamellae are arranged as bilayers linked by picolyl-picolyl  $\pi$ - $\pi$  stacking motifs (Fig. 44(b)). In structure **VII**, bis(urea) molecules are organised into an unprecedented [AAAABBBB] network, and there is one example each of picolyl-urea and solvent-urea hydrogen bonding (Fig. 44(c)).

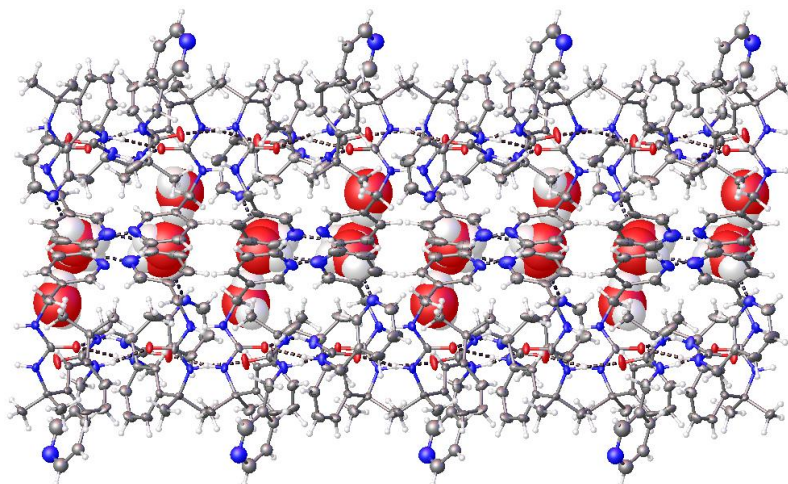


**Fig. 43** A pair of lamellar networks in the dihydrate of **2.2**, structure **IV**, viewing along the lamellar planes and perpendicular to the  $\alpha$ -tapes. Hydrogen-bonded water trimers (shown in space-filling representation) link pairs of lamellae via interactions with the pendant picolyl groups. Disorder in the picolyl groups and the fourth water molecule in the asymmetric unit are omitted for clarity.

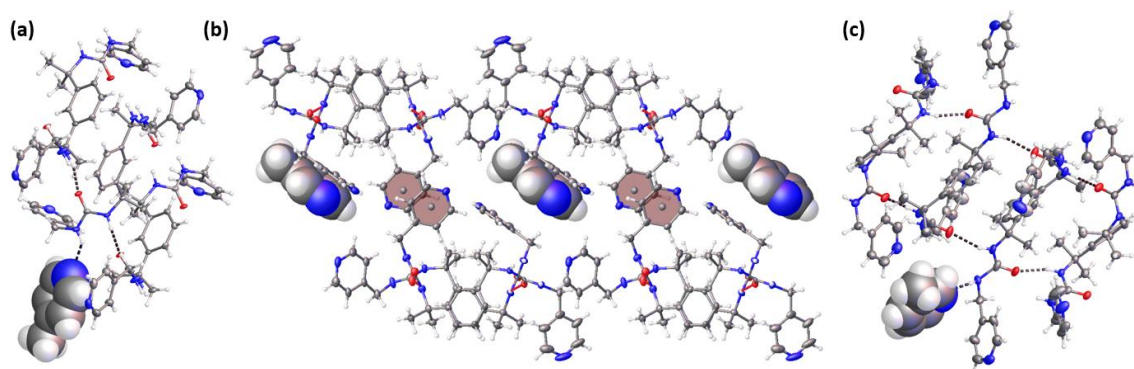


**Fig. 44** Major supramolecular motifs in the picoline solvates of **2.3**: (a) hydrogen bonding between 4-picoline and a urea group in structure **V** (N-N distance 3.200(4) Å); (b) solvent-picolyl and picolyl-picolyl  $\pi$ - $\pi$  stacking in structure **VI** (centroid separations 3.848(2) and 3.799(4) Å and plane-to-plane angles of 8.95(13) and 0.0° respectively); (c) hydrogen bonding between 3-picoline and a urea group in structure **VII** (N-N bond distance 3.1330(2) Å), showing the unusual subunit of four tape-sharing molecules. Solvent is shown in a space-filling representation and the centroids and mean planes of  $\pi$ - $\pi$  stacked rings are marked. Additional solvent molecules in structures **VI** and **VII** and the extensive end-group disorder in structure **VII** are omitted.

Optimisation of hydrogen bonding and crystal close packing is sometimes best achieved through the formation of a ternary crystal structure. Nitrobenzene solvates of **2.1** and **2.3** (structures **VIII** and **IX** respectively) may be crystallised



from wet nitrobenzene, and both systems incorporate molecules of water in addition to the main crystallisation solvent. The two structures both comprise lamellar bis(urea) networks bridged by picolyl-water hydrogen bonds. Furthermore, the asymmetric units of both structures are unusually large: in addition to four bis(urea) molecules and one molecule of water, there are two symmetry-independent nitrobenzene molecules in structure **VIII** and five in structure **IX**. Despite these similarities, the molecular arrangements of the crystals are starkly different. Tape networks in structure **VIII** exhibit an [AAAABBBB] topology, and the faces of the lamellae are symmetry equivalent, even though the picolyl groups of each bis(urea) molecule are oriented in the same direction (Fig. 45(a)). Lamellae in structure **IX**, meanwhile, consist of [AABB] repeat units, in which half of the tape motifs are fragmented into discrete tetramers of interacting ureas (Fig. 45(b)). The missing urea-urea hydrogen bonds are replaced with picolyl-urea interactions which, due to the asymmetric arrangement of bis(urea) molecules, are confined to one side of the lamellar network. Likewise, most of the bis(urea) molecules adopt a roughly C-shaped conformation, such that one face of the lamella accommodates three quarters of the picolyl end groups.

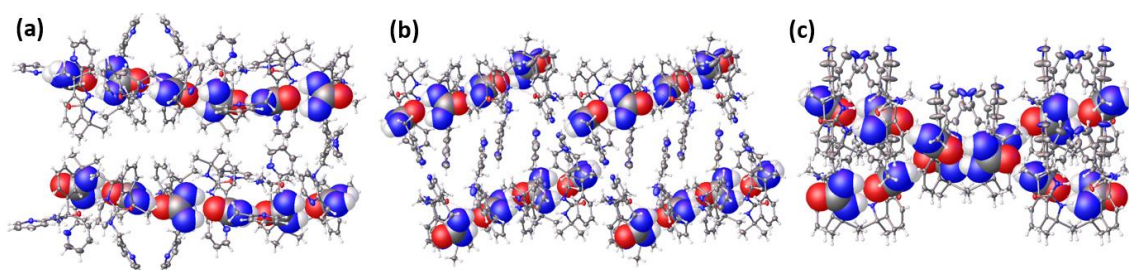


**Fig. 45** Varying orientations of  $\alpha$ -tapes, viewing down  $a$ : (a) antiparallel  $\alpha$ -tapes in two lamellae of structure **VIII**; (b) fragmented tape motifs in two lamellae of structure **IX**; (c) non-parallel  $\alpha$ -tapes in structure **X**. For clarity, solvent is omitted and only half of the urea groups are shown in a space-filling representation.

Fragmentation of  $\alpha$ -tape motifs generates “free” NH and carbonyl groups that can interact with bis(urea)s in adjacent tape networks. In structure **IX**, matching faces of neighbouring lamellae are linked by bifurcated picolyl-urea-picolyl hydrogen bond motifs. It is evident, however, that an alternative polar (head-to-tail) stacking of lamellae would allow for the formation of additional urea-urea hydrogen bonds. Arrangements of this type are observed in the isostructural



nitromethane and acetonitrile solvates of **2.3** (structures **X** and **XI** respectively). The structures may be viewed as stacks of [AABB] lamellae in which half of the  $\alpha$ -tapes have been fragmented, allowing the urea groups to interact with those of neighbouring lamellae to produce a three-dimensional network (Fig. 45(c)). Every bis(urea) molecule forms a pair of urea-urea motifs with one of its neighbours. However, no two non-adjacent molecules are tape-sharing, because the tapes formed by each bis(urea) are aligned with different diagonals of the (100) face. To the best of our knowledge, non-parallel  $\alpha$ -tapes have never been observed in a bis(urea) system and are almost unprecedented among related compound classes. Indeed, an extensive search of the CSD (Section 9.2) reveals just one other structure in which  $\alpha$ -tapes adopt a non-parallel arrangement: form II of tolbutamide (CSD refcode ZZZPUS05), a highly polymorphic mono(urea) used in hypoglycaemia treatment.<sup>58</sup>

Structures **X** and **XI** are the only examples of three-dimensional hydrogen bonding networks in this study. In structures **I-IX**, lamellae may be categorised according to the presence of asymmetry between the upper and lower faces. Whereas bis(urea) networks in structure **IX** are the most dramatically asymmetric, structure **VII** also displays an uneven packing arrangement: half of the picolyl groups on one lamellar face lie roughly parallel to the lamella, while all of those on the opposite side adopt an extended conformation. Similarly, structure **III** contains two symmetry-independent  $\alpha$ -tapes, which occur on different sides of the lamellar plane. In all other systems, the faces of lamellae are symmetry equivalent. It is hypothesised that the symmetries of the crystalline systems are shared by the solution-phase lamellae from which they develop. As in micellar assemblies,<sup>59</sup> asymmetric features may favour high-curvature aggregate morphologies, causing fibrous structures to be favoured over crystalline materials under certain self-assembly conditions.

#### 2.2.4 Gelation vs crystallisation

Gels of small molecules are typically prepared by cooling a solution of the gelator beyond the point of saturation. Although compounds **2.1** and **2.2** dissolve readily in a number of solvents upon heating, cooling or evaporation of the solutions produces crystalline precipitates instead of gels. By contrast, **2.3** forms

gels in nitrobenzene if its concentration exceeds the critical gelator concentration (CGC) of 0.5% (w/v) (Fig. 46). Gelation of 1% (w/v) solutions typically occurs over 10-20 minutes, whereas 0.5% (w/v) solutions form weak or partial gels over 1-2 hours. Crystals of the hydrated nitrobenzene solvate **IX** occur concomitantly within the gels and are usually small and polycrystalline in nature. Crystallisation is relatively slow and leads to a marked increase in opacity as the gel is left to stand.

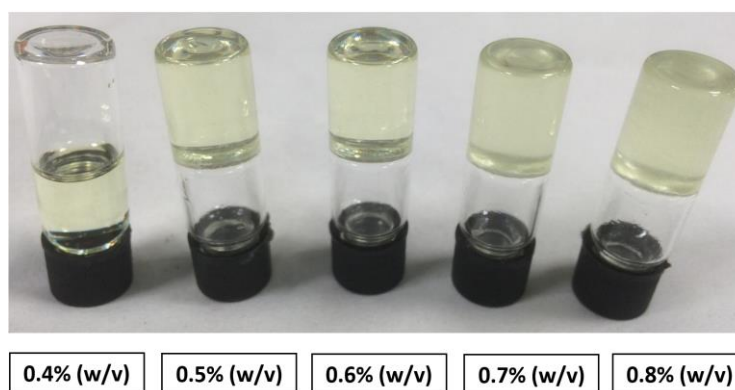


**Fig. 46** Results of gelation trials after six hours with varying concentrations of **2.3** in nitrobenzene under ambient air. In the absence of added water, the CGC of the system is 0.5% (w/v). Crystals are observed in all gels but become more abundant at higher concentrations, resulting in a marked increase in opacity between 0.5 and 0.8% (w/v).

The nitrobenzene solvate of **2.3**, structure **IX** is a hydrated system, in which water contributes hydrogen bonds to bridge the picolyl groups of neighbouring lamellae. Given that hydration is expected to favour multilayer assemblies by strengthening interlamellar interactions, the competition between gelation and crystallisation in this system is likely to be influenced by the availability of water. Systematic testing reveals that a 1% (w/v) solution of **2.3** can only undergo gelation at water concentrations less than 0.3% (w/v). This threshold scales roughly linearly with the quantity of gelator, reaching values of 0.5 and 0.7% (w/v) respectively for gelator concentrations of 2 and 3% (w/v). Thus, it can be deduced that inhibiting gel formation requires around six water molecules per molecule of gelator, corresponding to 25 times the quantity that may be incorporated into crystals. Precipitates above the CGC of the gelator tend to consist of small plates or polycrystalline materials, regardless of whether gelation takes place. In a 0.2% (w/v) solution, however, the presence of up to 1% (w/v) of water typically results in large plates suitable for analysis by single-crystal X-ray diffraction (SC-XRD; Fig. 47). Higher water concentrations cause the size and quality of crystals to be

markedly reduced, while concentrations significantly below 0.2% (w/v) do not induce observable precipitation.

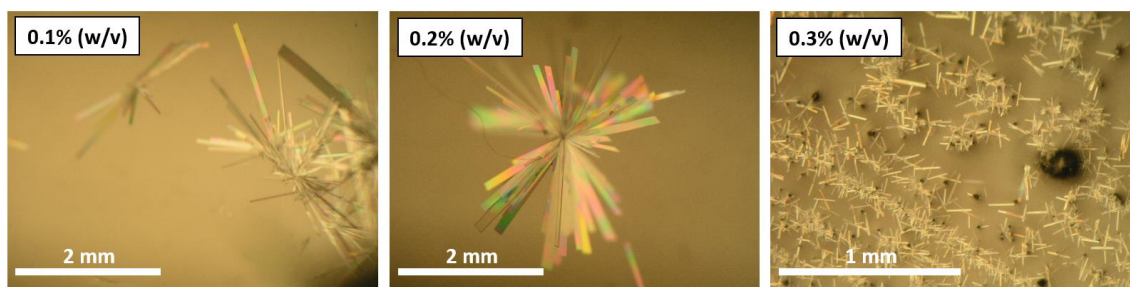


**Fig. 47** Effect of gelator concentration on crystal size in solutions of **2.3** in nitrobenzene with 0.8% (w/v) water. The largest crystals are observed at concentrations of 0.2% (w/v), but crystals of similar size may be obtained from 0.1% (w/v) solutions after several days. Increasing the concentration to 0.3% (w/v) results in microcrystalline deposits not suitable for analysis by SC-XRD.

The microstructures of the nitrobenzene gels of **2.3** were examined by scanning electron microscopy (SEM). SEM images of the platinum-coated xerogels reveal a network of unbranched fibres and entrapped rod- and plate-shaped microcrystals (Figs. 48a and 48b). The diameters of the fibres are variable with a maximum value in the region of 60 nm. The majority of fibres consist of approximately monodisperse fibrils 20 nm in thickness. Given that a small fraction of fibres are thicker and more crystalline in appearance, it is possible that aggregation of the bis(urea) affords a variety of assemblies, diverging from the lamellar crystal structure in a continuous fashion.<sup>17</sup> A fibrous material also occurs in nitromethane alongside octahedral single crystals (Figs. 48c and 48d). The nitromethane solvate of **2.3**, structure **X**, displays a more isotropic habit than the nitrobenzene solvate due to the presence of a three-dimensional network of  $\alpha$ -tapes. Likewise, the fibres in this system are shorter and less abundant, and coalesce into a gelatinous precipitate of isolated clusters rather than a sample-spanning gel.

The rheological properties of the nitrobenzene gel of **2.3** were characterised by oscillatory shear rheometry. The stress-strain profile of a 2% (w/v) gel at an oscillation frequency  $\omega = 1$  Hz reveals the expected viscoelastic behaviour at low shear stresses, marked by a storage modulus  $G'$  one order of magnitude larger than the loss modulus  $G''$  (Fig. 49a). The material exhibits an initial  $G'$  value of 21-25 kPa and undergoes liquefaction at a yield stress of approximately 240 Pa, which are typical values for a moderately rigid small-molecule gel. The frequency

response of the material is also characteristic of a true gel:  $G'$  is almost independent of  $\omega$ , as predicted by the soft glassy rheological (SGR) model of shear deformation (Fig. 49b).<sup>60</sup>

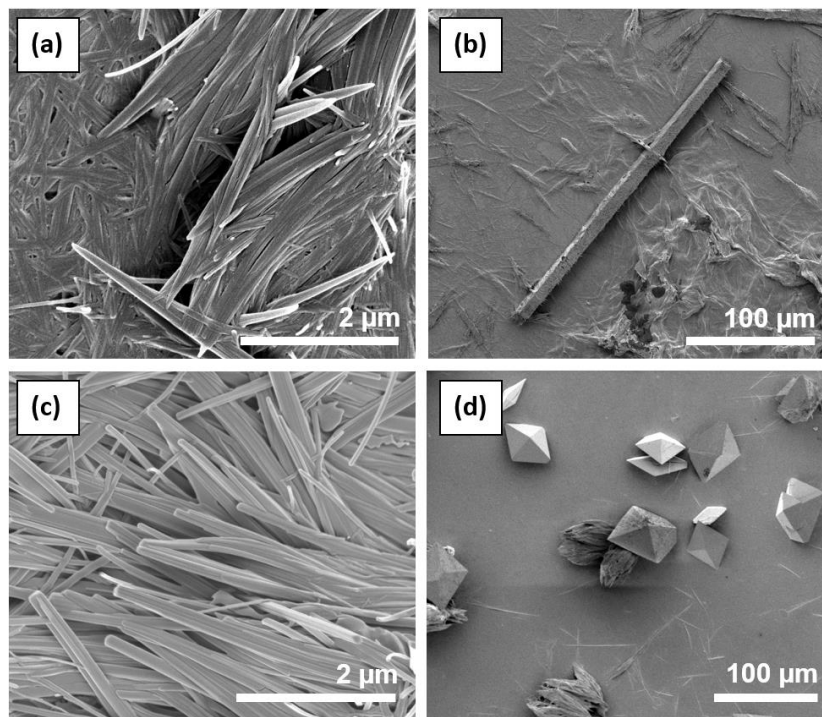


**Fig. 48** SEM micrographs of platinum-coated xerogels prepared from 1% (w/v) gels of **2.3**. Fibres in the nitrobenzene gel (a) entrap rod-shaped crystals of solvate **IX** (b). Fibres in the nitromethane partial gel are shorter but of similar diameter (c), while concomitant crystals of the **2.3** nitromethane solvate **X** exhibit an octahedral habit (d).

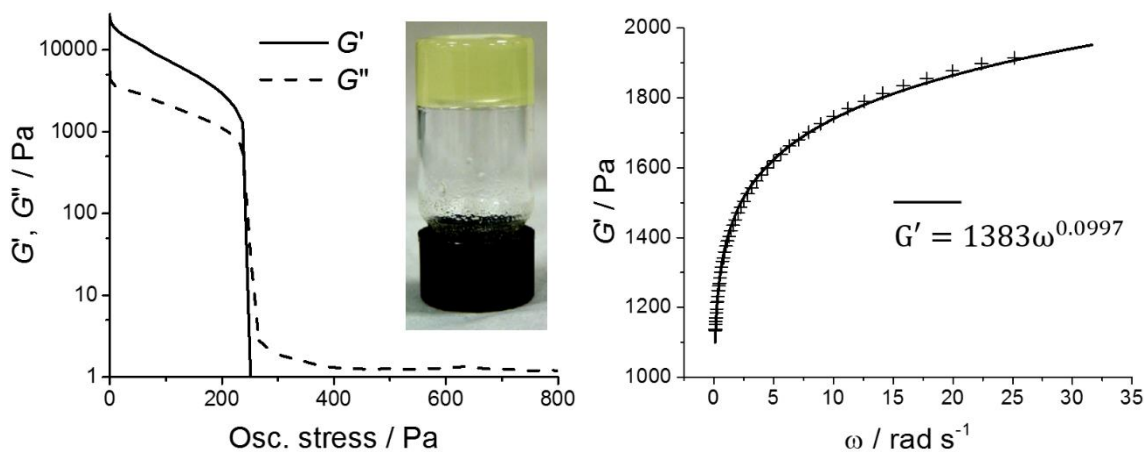


**Fig. 49** Oscillatory stress sweep (a) and frequency sweep (b) profiles of gels of **2.3** in nitrobenzene. The gelator concentrations in (a) and (b) are 2 and 1 % (w/v) respectively. The gel passes the inversion test (inset) but collapses spontaneously on standing, perhaps due to ongoing crystallisation.

Nitrobenzene gels of **2.3** are metastable under ambient conditions and, in 2 cm<sup>3</sup> vials, tend to collapse over several days. Intriguingly, however, this process is

greatly accelerated if the gel is prepared in a larger vial. In other small-molecule systems, relationships between aggregation outcome and container size have been linked to variations in nucleation rate and fibre density.<sup>61</sup> To monitor this effect in a quantitative fashion, 3 cm<sup>3</sup> of a 1% (w/v) solution were added directly to a mould on the rheometer stage at 20 °C, and subjected to a shear stress of 1 Pa with  $\omega = 1$  Hz.  $G'$  increased for approximately 10 minutes but decreased spontaneously thereafter, suggesting that disruption of the gel coincides with the increased precipitation of crystalline material (Fig. 50). Notably, the gel may be regenerated after collapse via heating-cooling cycles in a sealed vial. Thus, destabilisation of the gel is not attributable to the gradual uptake of environmental water, as this would lead to a permanent loss of gelation behaviour.

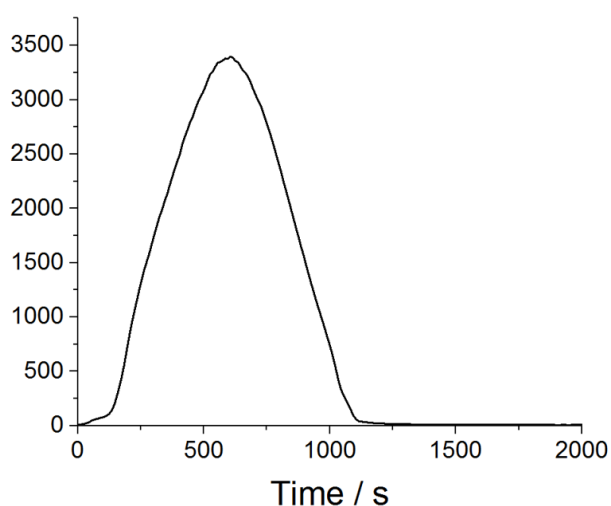


**Fig. 50** Changes in  $G'$  during gelation of nitrobenzene by 1% (w/v) **2.3** on the Peltier plate at 20 °C, with  $\omega = 1$  Hz and an applied stress of 1 Pa. Spontaneous collapse of the gel is indicated by a sharp decrease in  $G'$  beyond 600 s, and appears to coincide with increased crystallisation.

### 2.2.5 Lamellar self-assembly

A requirement for the formation of fibrous gels is that self-assembly occur preferentially in one or two directions. Lamellar networks of bis(urea)s are likely to adopt this mode of aggregation, as crystal growth generates new urea-urea motifs only if it occurs parallel to the lamellar plane. To gauge the effect of this anisotropy, crystallites of between 1200 and 3600 molecules were analysed by atomistic MD simulations in GROMACS 4.6.2<sup>62</sup> using the General Amber Force Field (GAFF)<sup>63</sup> implemented in the Antechamber package.<sup>64</sup> The initial structures were obtained from SC-XRD data, bounded with a 50 nm cubic periodic box and

subjected to an initial energy minimisation step via a steepest-descent procedure. Production runs were performed in a vacuum using a constant- $NVT$  ensemble and a 1 fs time step, with random initial velocities assigned according to a Maxwell distribution at 300 K. The temperature was controlled via a Berendsen thermostat with a time constant of 0.1 ps.<sup>65</sup> Although it fails to generate a correct canonical ensemble, the Berendsen thermostat was chosen as it effects efficient convergence of both temperature and potential energy, allowing the dynamics of many systems to be compared under isothermal conditions over extended timescales.

For each model crystallite, an initial equilibration was performed over 150 ps under constant- $NVT$  conditions. The simulation was then continued for an additional 150 ps, recording the potential energy of the system at 5 ps intervals. The mean potential energy over the final 150 ps period was equated to the equilibrium energy of the crystallite,  $E_{\text{tot}}$ . The energy of each crystal face,  $E_{\text{face}}$ , was estimated by measuring the change in  $E_{\text{tot}}$  upon varying the number of unit cells along the face normal axis. In a crystallite of  $N$  layers, there are  $(N-1)$  interfaces between layers. Thus, the value of  $E_{\text{face}}$  may be calculated from the gradient of the straight line obtained by plotting  $E_{\text{tot}}/N$  against  $1/N$  (Fig. 51). The remaining energy in each layer,  $E_{\text{bulk}}$ , comprises the internal energy of the bulk lattice and surface energies of the edge faces, and largely determines the intercept value:

$$\frac{E_{\text{tot}}}{N} = \frac{-E_{\text{face}}}{N} + (E_{\text{bulk}} + E_{\text{face}}) \quad (1)$$

To obtain a measure of the surface energy,  $\gamma$ ,  $E_{\text{face}}$  must be divided by twice the area of the crystal face, since increasing  $N$  by one removes a free surface from both the original crystallite and the additional layer. It is possible that such values could be estimated more quickly by subtracting the energy of the simulated crystal bulk from that of a surface slab.<sup>25</sup> An advantage of the approach in this study is that increasing  $N$  resembles the actual process of aggregation. Furthermore, the discrete crystallites are closer analogues to real assemblies than an infinite periodic lattice, and the calculation of a gradient through multiple points allows the precision of  $\gamma$  to be easily assessed.

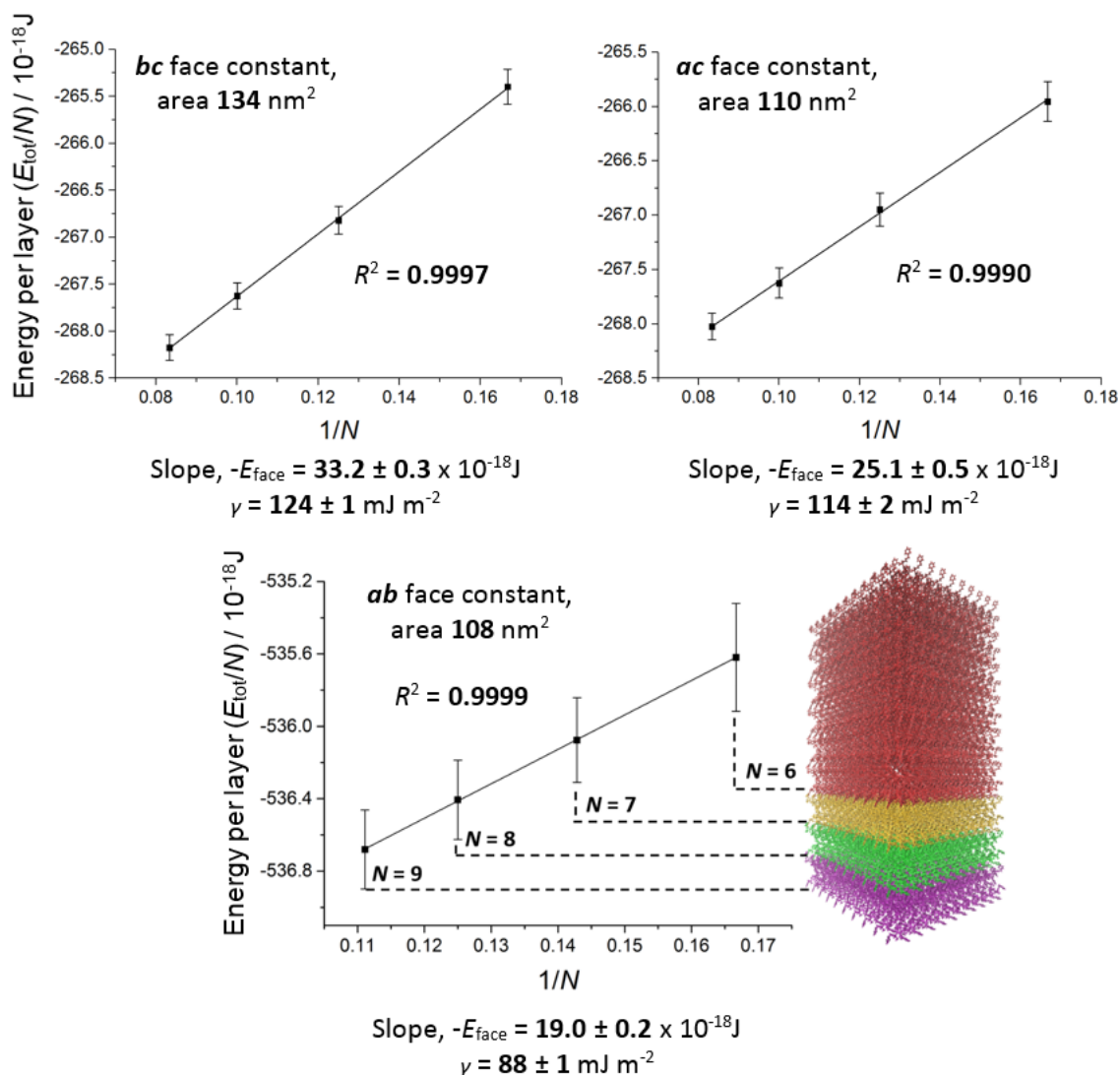


**Fig. 51** Plots to determine surface energies of the *bc*, *ac* and *ab* lattice planes of structure **II**. Energies are equal to the average potential energies of model crystallites over 150 ps after 150 ps equilibration under constant-*NVT* conditions at 300 K. Two crystallite dimensions are kept constant in each case; the constant cell dimensions are  $(a,b,c) = (10,10,5)$ . Error bars indicate the standard deviation of the energy values over the final 150 ps of each 300 ps simulation. The linear trend line was fitted by least-squares analysis and exhibits an  $R^2$  of 0.9998, with an error in the gradient of 0.004%. The smallest model crystallite for the simulation of the (001) face, shown in red, consists of 6 lamellae with 400 molecules per lamella. Illustrated in other colours are the seventh, eighth and ninth layers added to generate larger model crystallites. Trend lines were fitted in Origin.

It is relatively difficult to obtain reliable estimates of  $\gamma$  for crystallites containing loosely bound solvent, or for pairs of parallel crystal faces that are not symmetry equivalent. For simplicity, therefore,  $\gamma$  values were estimated for structure **II**, which consists of non-solvated lamellae with no polar axes. Although the molecules in this structure show no gelation capability, they exhibit supramolecular motifs comparable to those of structure **IX**, which is thought to



resemble the gel fibrils formed by **2.3** in nitrobenzene. Four data points were obtained for each lattice vector, and  $E_{\text{tot}}$  was calculated as the average energy of 100 points spanning 150 ps, with a step size of 1 fs and 150 ps of equilibration time (Fig. 51). Along (100) and (010), the vectors parallel to the lamellar plane,  $\gamma$  values of  $124 \pm 1$  and  $114 \pm 2$   $\text{mJ m}^{-2}$  were obtained. The similarity in these values is unsurprising given that layers of molecules along both lattice vectors interact via strong urea-urea hydrogen bonds. By contrast, the lamellar plane itself is decorated with picolyl moieties, and half of these form picolyl-urea hydrogen bonds with neighbouring lamellae. The corresponding  $\gamma$  value,  $88 \pm 1$   $\text{mJ m}^{-2}$ , is 23-29% smaller than the values for the other crystal faces. These results support the hypothesis that bis(urea)s self-assembling in the absence of strong solvent-gelator interactions can produce isolated monolayers well suited to gel formation. More polar solvents are expected to competitively bind to surface urea groups, producing more isotropic  $\gamma$  values and a stronger tendency for three-dimensional self-assembly. Nonetheless, estimates of  $\gamma$  in vacuum correctly predict the largest and smallest faces of the plate-shaped crystals, which correspond to the (001) and (100) faces respectively of the bis(urea) lamellae (Fig. 52).

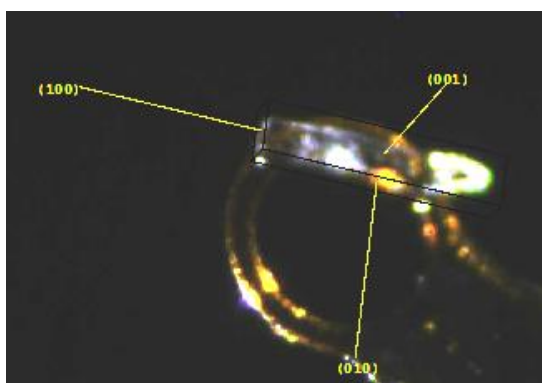


**Fig. 52** Single crystal of **2.2** from acetonitrile (dimensions  $0.49 \times 0.22 \times 0.10$   $\text{mm}^3$ ), from which structure **II** was determined by SC-XRD. The indexed faces (100), (010) and (001) display areas 0.022, 0.050 and 0.11  $\text{mm}^2$  respectively. The relative size of the faces match the order predicted by surface energy calculations, suggesting that crystal faces decorated with urea moieties remain the dominant growth surfaces even when solvent is present.

### 2.2.6 Scrolling simulations

For each crystal structure in this study, the folding behaviour of a single bis(urea) lamella was assessed by means of MD simulations. The model lamellae consisted of 600 molecules and were simulated in a vacuum at 300 K for 1500 ps,



under the constant-*NVT* conditions previously discussed. The size and timeframe of the system were chosen to minimise computational cost: the simulations capture all major structural changes, and the lamellae are sufficiently large to avoid significant edge effects. Solvent was omitted in order to assess how lamellae deform in response to internal stresses alone. Although the models do not account for effects such as viscosity, hydrophobicity and solvent-urea hydrogen bonding, the results illustrate the impact of key structural variables on lamellar morphology and provide a simple baseline for understanding the deformation pathways of more realistic, explicit-solvent simulations.

The bending modulus of a sheet scales roughly as the cube of its thickness  $\tau$ .<sup>66</sup> Thus, it was expected that thinner lamellae would undergo folding more readily and attain larger curvatures at equilibrium. The value of  $\tau$  cannot be gauged directly from the spacing of lamellae in a crystal,  $d_{\text{layer}}$ , as this distance is strongly influenced by interdigitation and the presence of solvent. A more reliable value may be arrived at by noting that bis(urea) molecules in the non-solvated structures **I-III** occupy a roughly constant volume  $V_{\text{mol}} = 620 \pm 10 \text{ \AA}^3$ . Accordingly,  $\tau$  may be equated to  $V_{\text{mol}}/A_{\text{mol}}$ , where  $A_{\text{mol}}$  is the area per molecule in the lamella. It is clear from the simulation results that this analysis offers only a weak indication of lamellar flexibility (Fig. 53). For example, lamellae from structures **IV**, **VI** and **VIII**, display nearly identical values of  $\tau$ , but produce starkly different outcomes in their folding simulations.

The simulations show that large, global curvatures occur only if the faces of the lamella are structurally dissimilar. Lamellae in structure **IX** display marked asymmetry between their upper and lower faces and undergo extensive folding when simulated, attaining an equilibrium radius of curvature of roughly 2 nm. Furthermore, if the lamella is sufficiently large,<sup>68, 69</sup> the system exhibits scrolling behaviour, wherein the upper face of one part of the lamella is layered onto the lower face of a separate region. It is thought that this process resembles the dynamics of lamellae in solution, and is responsible for the formation of gel fibres alongside crystals of structure **IX**.

The outcome of scrolling is likely dependent on the geometric details of the lamella involved. As predicted by models of uniform sheets,<sup>70</sup> the time for equilibration scales with the dimensions of the system, as folding begins at the

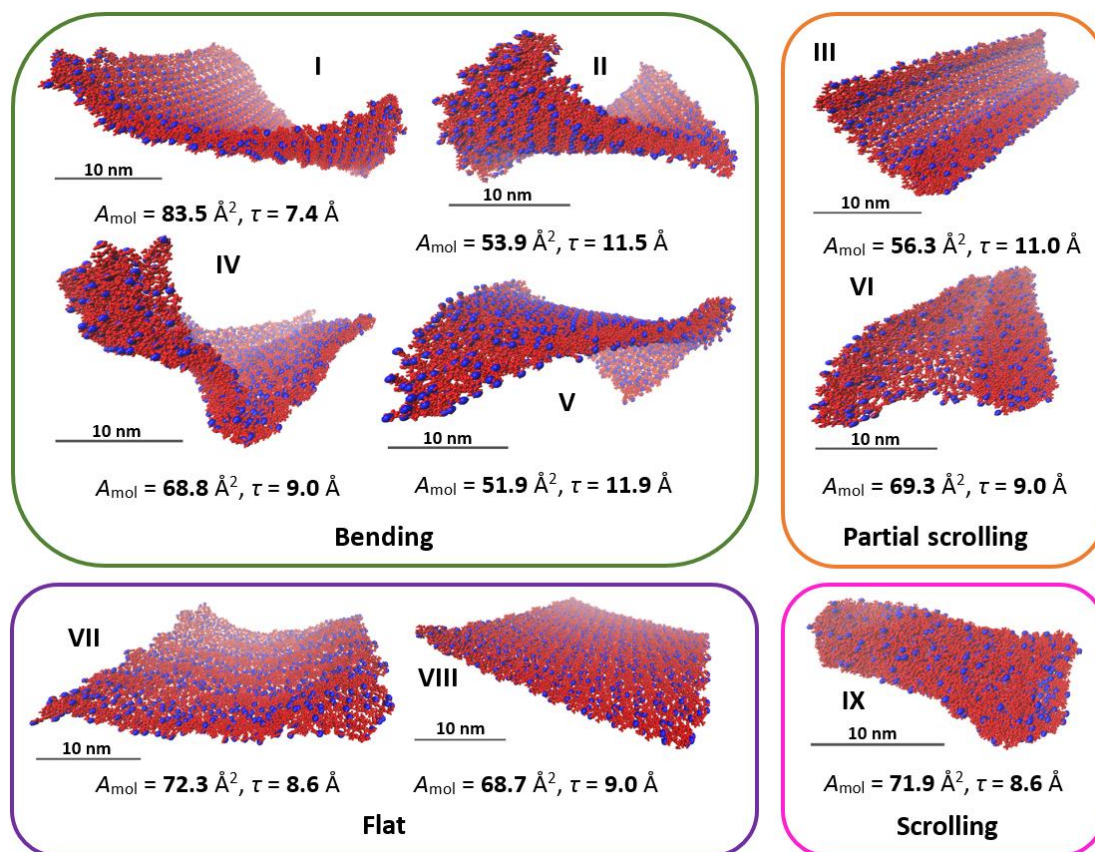


**Fig. 53** Final frames from 1500 ps MD simulations of lamellar bis(urea) networks from structures I-IX. Simulations were performed in a vacuum at 300 K, with the temperature controlled via a Berendsen thermostat. To highlight the end groups of the molecules, nitrogen atoms in the picolyl groups are shown as blue spheres with a 1.3  $\text{\AA}$  radius and all other atoms as red spheres with a 0.6  $\text{\AA}$  radius. Lamellae were constructed based on atomic positions calculated from the SC-XRD structures and equilibrated via a steepest-descent procedure prior to the production run. The morphologies displayed for structures III and VI were obtained after equilibrating the model lamellae within four-layer crystallites at 300 K (see text). All images are representative of the lamellar morphology after equilibration, once all significant large-scale deformation has taken place. Values of  $A_{\text{mol}}$  were obtained from the crystal structures and  $\tau$  was estimated as

$$V_{\text{mol}}/A_{\text{mol}} \text{ with } V_{\text{mol}} = 620 \text{ \AA}^3.$$

edges of lamella and produces only small displacements nearer the centre of the sheet. The rate of scrolling, meanwhile, is roughly constant at 10 nm ns<sup>-1</sup> and does not vary significantly with the dimensions of the lamella. Unexpectedly, the axis of curvature is at 90° to the  $\alpha$ -tape axis, and the face with the highest concentration of end groups forms the internal surface of the resulting fibril. The onset of scrolling, in which the lamella comes into contact with itself, is marked by a sharp decrease in potential energy and acceleration of folding (Fig. 54a). However, the process is not accompanied by any significant increase in hydrogen bonding (Fig. 54b), suggesting that van der Waals forces and non-directional polar

interactions are the major contributors to stabilisation. As observed in scrolling assemblies of amphiphilic copolymers, the decrease in energy exceeds the available thermal energy but is much less than the fusion energy of the system, so scrolling may proceed irreversibly without disrupting the hydrogen bonding network.<sup>71</sup>

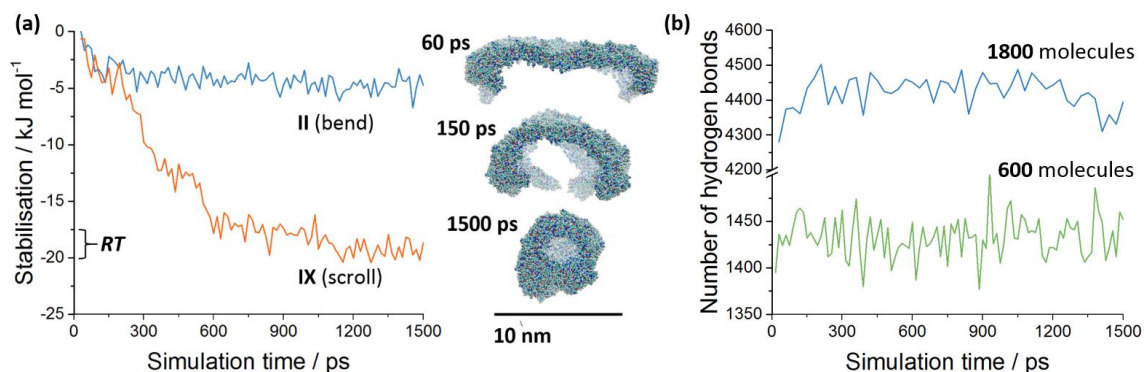


**Fig. 54** As a result of scrolling, a 600-molecule lamella from structure **IX** experiences far greater stabilisation than a non-scrolling lamella of equal size from structure **II** (a). Scrolling is largely complete after 600 ps, producing a fibril roughly 7 nm in diameter. The lamella displays an average of 1433 hydrogen bonds during this process (b), with a standard deviation of just 22 (1.5%). A lamella with three times as many molecules behaves in a similar fashion, even though the scrolling process does not reach completion within 1500 ps: the average number of hydrogen bonds is 4422 (2.46 per molecule), with a standard deviation of 47 (1.1%). Stabilisations are calculated relative to the maximum recorded energy values after 30 ps of simulation time, to allow the systems to equilibrate under constant-*NVT* conditions. Hydrogen bonds are recorded if the donor-acceptor distance is within 3.2 Å and the bond angle within 30° of 180°. Changing these cutoff parameters significantly alters the mean hydrogen bond populations but only weakly affects the standard deviations and overall trends.

Simulations of scrolling represent a simple and appealing model for the initial stages of fibril formation. Folding and growth of a lamella occur concurrently, so a fibril is likely to develop if the structure reaches an appreciable size before further layers are added. In nitrobenzene solutions of **2.3**, it is proposed that scrolling and stacking of lamellae occur at similar rates, such that the competing processes of gelation and crystallisation are simultaneously observed. Comparable concomitant fibre growth alongside crystals of structure **X** at first seems surprising, as the bis(urea) molecules in this system are linked by a three-dimensional arrangement of hydrogen bonds. However, the bis(urea) network of structure **X** can be obtained by a continuous distortion of [AABB] lamellae, in which only one face is decorated with picolyl groups (Fig. 55). MD simulations

reveal that one such lamella can undergo spontaneous scrolling to form a fibril structure. As in the nitrobenzene system, the axis of curvature lies perpendicular to the  $\alpha$ -tapes, and picolyl groups are located mostly on the inside of the fibril. It is proposed that self-assembly in nitromethane initially generates [AABB] lamellae, which can either develop into fibrils or undergo stacking and recombination to form a three-dimensional network. According to this model, the balance between gelation and crystallisation is determined by the relative rates of scrolling and stacking and may be highly solvent-dependent. For example, no concomitant gel is observed alongside the acetonitrile solvate **XI**, even though this structure and the nitromethane solvate **X** are isomorphous materials.

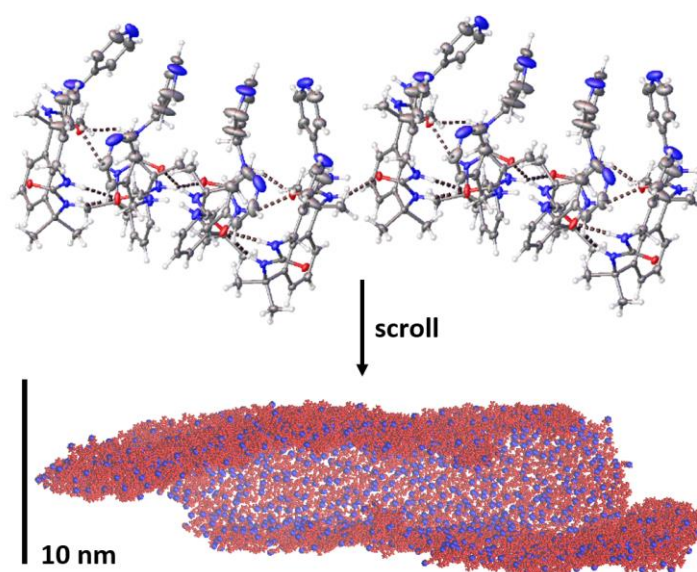


**Fig. 55** The three-dimensional network of  $\alpha$ -tapes in structures **X** and **XI** can be divided into lamellae with an [AABB] repeat unit. Like those from structure **IX**, the lamellae are highly asymmetric and display scrolling behaviour in MD simulations.

Scrolling of lamellae is driven by an internal pressure resulting from structural asymmetry. The lack of gel formation in most of the systems studied may be linked to the abundance of crystal structures comprising symmetric lamellae. MD simulations confirm that lamellae with faces that are symmetry equivalent show no significant bias in their axis of curvature or folding direction. Indeed, even thin lamellae such as those of structure **I** tend to adopt crumpled or saddle-like morphologies,<sup>72</sup> and are thus deformed too little for scrolling behaviour to arise. Stabilisation due to folding is typically comparable to *RT* (Fig. 54), and the incidence of multiple axes of curvature can further limit stabilisation. Crystallisation in such systems likely represents a favourable outcome, as there

are no self-contacts within the lamellae to obstruct the growth of multilayer deposits.

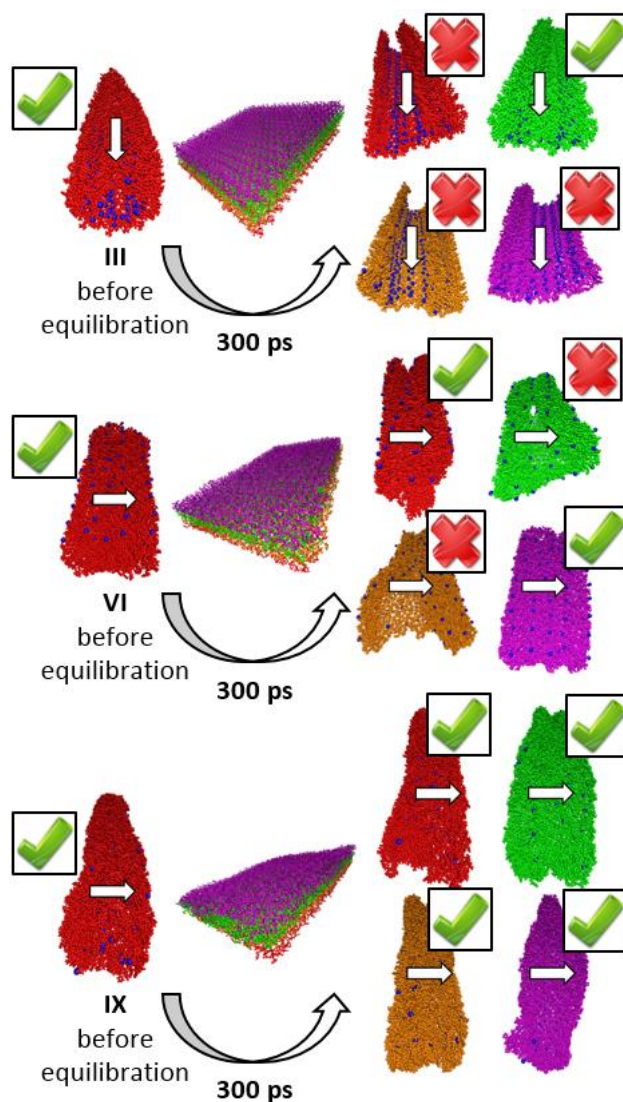


**Fig. 56** Folding of 600-molecule lamellae from structures **III**, **VI** and **IX** after 1500 ps. Lamellae were equilibrated for 300 ps as part of a four-layer crystallite before undergoing folding in isolation. To illustrate the direction of folding, one picolyl nitrogen atom of the repeat unit is represented as a blue sphere of radius 1.3 Å, while the other atoms are represented as spheres of radius 0.6 Å. Arrows indicate the axis of  $\alpha$ -tapes in the folded lamellae (i.e. parallel or perpendicular to the fold axis) and ticks and crosses denote whether complete and partial scrolling respectively.

It is worth emphasising that lamellar asymmetry, while necessary for scrolling, does not guarantee that such deformations will take place. Picolyl groups in structure **IV**, for example, are distributed unevenly between the two sides of the lamellar network, but lamellae are not sufficiently flexible for scrolling to arise. Conversely, MD simulations may predict scrolling due to asymmetric features that would not persist prior to crystallisation. It was noted that lamellae from structures **III** and **VI** resemble those of structure **IX** in their folding behaviour,

despite only small differences in molecular packing between their upper and lower faces (Fig. 56). To test whether these slight asymmetries could impact the dynamics of lamellae in solution, crystallites consisting of four lamellae in a vacuum were allowed to equilibrate at 300 K for 300 ps. This procedure enables the molecules to access a range of conformations, but constrains the overall lamellae to remain approximately planar. Subsequent simulations of each equilibrated lamella in isolation reveal more localised folding, with complete scrolling occurring in only a fraction of cases. By contrast, pre-equilibration of lamellae from structure **IX** does not affect their scrolling behaviour. The results suggest that a lamella in solution could not retain the geometric asymmetries of structures **III** and **VI**, and so would not be predisposed to significant scrolling. The polar distribution of picolyl groups in structure **IX**, however, represents a topological asymmetry, which cannot be removed without disassembling the lamellae. Given the mobility of molecules in solution, only topological asymmetries need be considered when predicting scrolling behaviour in real supramolecular systems.

### 2.2.7 Schematic model

Scrolling of bis(urea) lamellae is analogous to the spontaneous curvature of micelle assemblies.<sup>59</sup> The two faces of a lamella occupy equal areas in the crystal structure but become more compact once neighbouring layers are removed. Interdigitation of lamellae in structure **IX**, for example, serves to fill the space between picolyl groups on the lamellar surface, so these groups must pack more closely when only one lamella is present (Fig. 57). Bending occurs because one face of the lamella contracts more than the other. The axis of curvature is likely to lie parallel or perpendicular to the  $\alpha$ -tapes since the groups either side of these axes are approximately symmetric. In addition, it is favourable for only one axis of curvature to exist, as bending about a second axis would cause stretching of the lamella and produce a high-energy dislocation where the axes intersect.<sup>73</sup> It is worth noting that folding in other systems may occur about an axis not parallel to one of the lamella edges. Such processes tends to produce a helical morphology,<sup>66</sup> but may ultimately give rise to hollow cylindrical fibrils if the pitch of the helix is less than or equal to the width of the lamella.<sup>74</sup>



The geometry of scrolling plays an important role in determining the physical properties of a gel fibril. Supramolecular motifs that are aligned with the fold axis may contribute more strongly to tensile strength,<sup>75</sup> and the moieties decorating the outer surface of the scrolled lamella are largely responsible for its adsorption behaviour.<sup>76, 77</sup> Models of uniform lamellae show that the axis of curvature is determined by the relative lengths of the lamella edges.<sup>70, 78</sup> However, real bis(urea) lamellae are not isotropic, and the simulations reveal that the favoured axis is that which offers the least resistance to bending deformations. Differences in the scrolling behaviour of lamellae from structures **III** and **VI** before and after equilibration suggests that the geometry of scrolling is strongly influenced by molecular packing. Effects of this nature have been observed in supramolecular assemblies of rod-coil molecules, which adopt tubular morphologies only for particular combinations of in-plane bending moduli and respond sensitively to changes in molecular structure.<sup>43, 79</sup>

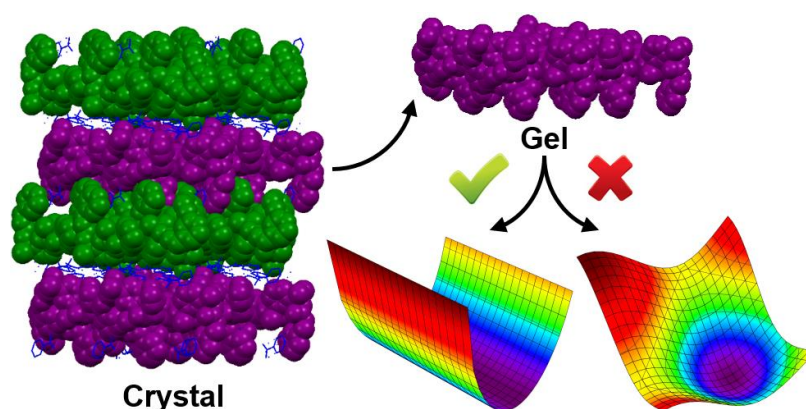


**Fig. 57** Lamellae in structure **IX** are arranged as symmetric bilayers. The faces of a single lamella, however, are asymmetric and must occupy different areas for optimal packing of the surface moieties. Thus, lamellae fold such that the face with the largest area is presented on the outer surface of the final structure. Cylindrical folding (left) can occur isotropically, as indicated by the uniform network of contour lines in the schematic illustration. By contrast, folding along two or more axes (right) leads to stretching of the surface and is energetically disfavoured.

Although fibrils similar to those formed in simulations may form the basis of a fibrous aggregate, they are between two and three times narrower than the majority of fibrils observed in SEM images. Wider structures could arise through continued scrolling about the fibril circumference or accretion of additional layers to an existing fibril. It is worth noting that the equilibrium curvature of scrolled lamella represents the most stable morphology, in which the intermolecular forces within and between the lamella are

optimally balanced. Since increasing the fibril diameter reduces the curvature of the outer layer, each new layer is further from its energetic minimum. Thus, it is likely that lamellae beyond a critical radius will detach from the fibril to gain further stabilisation via scrolling (Fig. 15a). This hypothesis is supported by SEM images of the materials, which reveal little variation in fibril thickness (Fig. 15b). Similar mechanisms have been proposed to explain the monodispersity of asbestos chrysotile needles<sup>44</sup> and, perhaps more strikingly, the inability of cylindrical objects to support climbing plants below a threshold helical radius (Fig. 15c).<sup>80</sup> Given the simplicity and generality of the underlying physics, scrolling may represent an important step in the self-assembly of many supramolecular gelators, including amyloidogenic peptides and micelle-forming amphiphilic species.

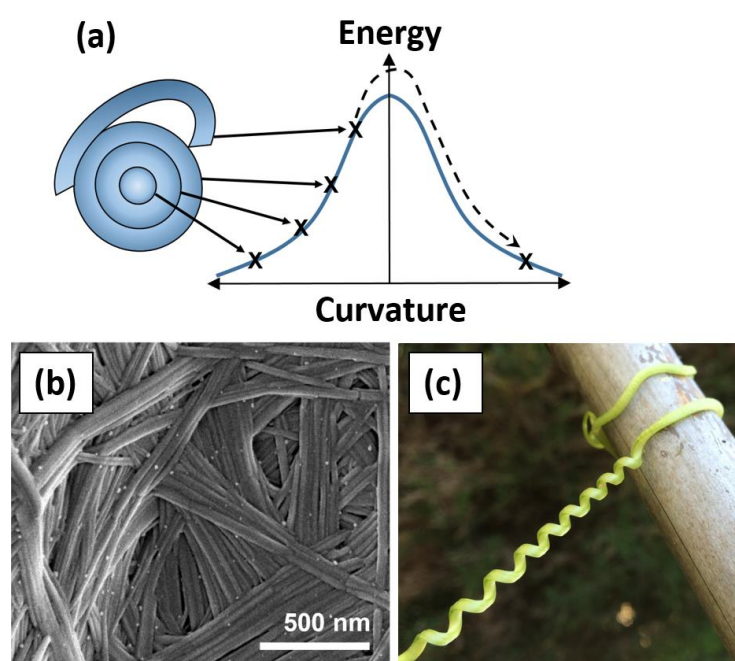


**Fig. 58** Schematic energy plot (a) for concentric layered lamellae, illustrating how the decreasing local curvature with increasing radius leads to detachment of lamellae beyond a threshold fibre thickness. This phenomenon is potentially responsible for the uniformity of fibres in nitrobenzene gels of **2.3** (b), and also underlies the inability of twining plants to wind around columns much larger than their helical diameter (c).

## 2.3 Conclusions

Bis(urea)s are among the most popular examples of LMWGs, owing to their peptidomimetic characteristics and potent gelation capacities in a range of organic solvents. The arrangement of hydrogen bonds in crystalline bis(urea)s is highly sensitive to both the solvent environment and end-group structure. SC-XRD



studies have revealed that a series of picolyl-functionalised bis(urea)s form lamellar  $\alpha$ -tape networks with a wide range of topologies. However, fibrous aggregates are observed only alongside crystals in which the bis(urea) lamellae are topologically asymmetric. The competition between two- and three-dimensional self-assembly is decided largely by the relative surface energies of the crystal faces, which can be estimated through MD simulations of model assemblies. Crystallisation is favoured by factors that reduce this anisotropy, such as polar solvents that provide strong interlayer interactions and competitively bind to growing  $\alpha$ -tapes. Gelation, meanwhile, occurs if multilayer aggregation is outpaced by the growth and scrolling of isolated monolayers. Computational analysis of lamellae represents a simple, general and reliable method for predicting and analysing the scrolling behaviour of hydrogen bonding LMWGs. This approach may offer useful insights into a crucial but underexplored stage of gel formation and aid the identification of effective LMWGs from crystallographic data.

## 2.4 References

1. H. Q. Xu, J. Song, T. Tian and R. X. Feng, *Soft Matter*, 2012, **8**, 3478-3486.
2. P. Dastidar, *Chem. Soc. Rev.*, 2008, **37**, 2699-2715.
3. M. A. Rogers, S. Abraham, F. Bodondics and R. G. Weiss, *Cryst. Growth Des.*, 2012, **12**, 5497-5504.
4. J. H. van Esch and B. L. Feringa, *Angew. Chem. Int. Edit.*, 2000, **39**, 2263-2266.
5. J. H. Fuhrhop, P. Schnieder, J. Rosenberg and E. Boekema, *J. Am. Chem. Soc.*, 1987, **109**, 3387-3390.
6. M. O. M. Piepenbrock, G. O. Lloyd, N. Clarke and J. W. Steed, *Chem. Commun.*, 2008, **23**, 2644-2646.
7. M. A. Rogers and A. G. Marangoni, *Langmuir*, 2009, **25**, 8556-8566.
8. A. Vidyasagar and K. M. Sureshan, *Angew. Chem. Int. Edit.*, 2015, **54**, 12078-12082.
9. G. R. Desiraju, *J. Chem. Soc. Chem. Commun.*, 1991, 426-428.
10. L. Infantes, L. Fabian and W. D. S. Motherwell, *Crystengcomm*, 2007, **9**, 65-71.
11. A. Bajpai, H. S. Scott, T. Pham, K. J. Chen, B. Space, M. Lusi, M. L. Perry and M. J. Zaworotko, *IUCrJ*, 2016, **3**, 430-439.
12. K. M. Steed and J. W. Steed, *Chem. Rev.*, 2015, **115**, 2895-2933.
13. D. Bardelang, M. Giorgi, V. Hornebecq, A. Stepanov, E. Rizzato, M. B. Zaman, G. Chan, O. Ouari and P. Tordo, *RSC Adv.*, 2012, **2**, 5605-5609.
14. G. H. Li, Y. Y. Hu, J. F. Sui, A. X. Song and J. C. Hao, *Langmuir*, 2016, **32**, 1502-1509.
15. D. Braga, S. d'Agostino, E. D'Amen and F. Grepioni, *Chem. Commun.*, 2011, **47**, 5154-5156.
16. Y. J. Wang, L. M. Tang and J. Yu, *Cryst. Growth Des.*, 2008, **8**, 884-889.
17. J. X. Cui, Z. H. Shen and X. H. Wan, *Langmuir*, 2010, **26**, 97-103.
18. K. M. Anderson, G. M. Day, M. J. Paterson, P. Byrne, N. Clarke and J. W. Steed, *Angew. Chem. Int. Edit.*, 2008, **47**, 1058-1062.

19. K. A. Houton, K. L. Morris, L. Chen, M. Schmidtman, J. T. A. Jones, L. C. Serpell, G. O. Lloyd and D. J. Adams, *Langmuir*, 2012, **28**, 9797-9806.
20. R. J. Davey, S. L. M. Schroeder and J. H. ter Horst, *Angew. Chem. Int. Ed.*, 2013, **52**, 2166-2179.
21. D. E. Braun, P. G. Karamertzanis and S. L. Price, *Chem. Commun.*, 2011, **47**, 5443-5445.
22. S. Wu, J. Gao, T. J. Emge and M. A. Rogers, *Soft Matter*, 2013, **9**, 5942-5950.
23. B. G. Xing, C. W. Yu, K. H. Chow, P. L. Ho, D. G. Fu and B. Xu, *J. Am. Chem. Soc.*, 2002, **124**, 14846-14847.
24. A. M. Belenguer, G. I. Lampronti, A. J. Cruz-Cabeza, C. A. Hunter and J. K. M. Sanders, *Chem. Sci.*, 2016, **7**, 6617-6627.
25. S. H. Yoo, T. Eom, S. Kwon, J. Gong, J. Kim, S. J. Cho, R. W. Driver, Y. Lee, H. Kim and H. S. Lee, *J. Am. Chem. Soc.*, 2015, **137**, 2159-2162.
26. J. Kowalczyk, A. Rachocki, M. Bielejewski and J. Tritt-Goc, *J. Colloid Interface Sci.*, 2016, **472**, 60-68.
27. J. Kowalczyk, M. Bielejewski, A. Łapiński, R. Luboradzki and J. Tritt-Goc, *J. Phys. Chem. B*, 2014, **118**, 4005-4015.
28. C. X. Zhang, T. R. Zhang, N. Ji, Y. Zhang, B. L. Bai, H. T. Wang and M. Li, *Soft Matter*, 2016, **12**, 1525-1533.
29. W. Dzwolak, *Chirality*, 2014, **26**, 580-587.
30. H. Kumari, S. R. Kline, S. R. Kennedy, C. Garvey, C. L. Raston, J. L. Atwood and J. W. Steed, *Chem. Commun.*, 2016, **52**, 4513-4516.
31. H. Kumari, S. E. Armitage, S. R. Kline, K. K. Damodaran, S. R. Kennedy, J. L. Atwood and J. W. Steed, *Soft Matter*, 2015, **11**, 8471-8478.
32. B. Ozgur and M. Sayar, *J. Phys. Chem. B*, 2016, **120**, 10243-10257.
33. K. Ogata, W. Uchida and S. Nakamura, *J. Phys. Chem. B*, 2014, **118**, 14353-14365.
34. S. W. Benner and C. K. Hall, *J. Phys. Chem. B*, 2016, **120**, 7253-7264.
35. C. F. Luo, M. Kroger and J. U. Sommer, *Macromolecules*, 2016, **49**, 9017-9025.
36. J. A. Anderson and A. Travesset, *Macromolecules*, 2006, **39**, 5143-5151.
37. D. M. Rutkowski, O. D. Velev, S. H. L. Klapp and C. K. Hall, *Soft Matter*, 2016, **12**, 4932-4943.
38. M. A. Horsch, Z. Zhang and S. C. Glotzer, *Nano Lett.*, 2006, **6**, 2406-2413.
39. T. Perez, Y. Liu, W. Li, J. D. Gunton and A. Chakrabarti, *Langmuir*, 2011, **27**, 11401-11408.
40. M. Grünwald, S. Tricard, G. M. Whitesides and P. L. Geissler, *Soft Matter*, 2016, **12**, 1517-1524.
41. S. J. Marrink, J. Risselada and A. E. Mark, *Chem. Phys. Lipids*, 2005, **135**, 223-244.
42. M. J. Stevens, *J. Chem. Phys.*, 2004, **121**, 11942-11948.
43. D. J. Hong, E. Lee, H. Jeong, J. Lee, W. C. Zin, T. D. Nguyen, S. C. Glotzer and M. Lee, *Angew. Chem. Int. Edit.*, 2009, **48**, 1664-1668.
44. B. Lotz and S. Z. D. Cheng, *Polymer*, 2005, **46**, 577-610.
45. W. Humphrey, A. Dalke and K. Schulten, *J. Molec. Graphics*, 1996, **14**, 33-38.
46. J. van Esch, S. De Feyter, R. M. Kellogg, F. De Schryver and B. L. Feringa, *Chem. Eur. J.*, 1997, **3**, 1238-1243.
47. P. Byrne, D. R. Turner, G. O. Lloyd, N. Clarke and J. W. Steed, *Cryst. Growth Des.*, 2008, **8**, 3335-3344.
48. R. Custelcean, *Chem. Commun.*, 2008, DOI: 10.1039/B708921J, 295-307.
49. L. S. Reddy, S. K. Chandran, S. George, N. J. Babu and A. Nangia, *Cryst. Growth Des.*, 2007, **7**, 2675-2690.
50. A. Cayuela, S. R. Kennedy, M. L. Soriano, C. D. Jones, M. Valcárcel and J. W. Steed, *Chem. Sci.*, 2015, **6**, 6139-6146.
51. L. Meazza, J. A. Foster, K. Fucke, P. Metrangolo, G. Resnati and J. W. Steed, *Nat. Chem.*, 2013, **5**, 42-47.
52. M. O. M. Piepenbrock, N. Clarke and J. W. Steed, *Soft Matter*, 2010, **6**, 3541-3547.

53. A. M. Todd, K. M. Anderson, P. Byrne, A. E. Goeta and J. W. Steed, *Cryst. Growth Des.*, 2006, **6**, 1750-1752.
54. J. Bernstein, R. E. Davis, L. Shimoni and N. L. Chang, *Angew. Chem. Int. Edit.*, 1995, **34**, 1555-1573.
55. M. F. Geer, M. D. Smith and L. S. Shimizu, *Crystengcomm*, 2011, **13**, 3665-3669.
56. C. R. Groom, I. J. Bruno, M. P. Lightfoot and S. C. Ward, *Acta Crystallogr. Sect. B*, 2016, **72**, 171-179.
57. K. Fucke, G. J. McIntyre, M. H. Lemée-Cailleau, C. Wilkinson, A. J. Edwards, J. A. K. Howard and J. W. Steed, *Chem. Eur. J.*, 2015, **21**, 1036-1047.
58. S. Thirunahari, S. Aitipamula, P. S. Chow and R. B. H. Tan, *J. Pharm. Sci.*, 2010, **99**, 2975-2990.
59. J. N. Israelachvili, D. J. Mitchell and B. W. Ninham, *J. Chem. Soc., Faraday Trans. II*, 1976, **72**, 1525-1568.
60. P. Terech, D. Pasquier, V. Bordas and C. Rossat, *Langmuir*, 2000, **16**, 4485-4494.
61. B. Yuan, X. Y. Liu, J. L. Li and H. Y. Xu, *Soft Matter*, 2011, **7**, 1708-1713.
62. D. Van der Spoel, E. Lindahl, B. Hess, G. Groenhof, A. E. Mark and H. J. C. Berendsen, *J. Comput. Chem.*, 2005, **26**, 1701-1718.
63. D. A. Case, T. E. Cheatham, T. Darden, H. Gohlke, R. Luo, K. M. Merz, A. Onufriev, C. Simmerling, B. Wang and R. J. Woods, *J. Computat. Chem.*, 2005, **26**, 1668-1688.
64. J. M. Wang, W. Wang, P. A. Kollman and D. A. Case, *J. Mol. Graphics Modell.*, 2006, **25**, 247-260.
65. H. J. C. Berendsen, J. P. M. Postma, W. F. Vangunsteren, A. DiNola and J. R. Haak, *J. Chem. Phys.*, 1984, **81**, 3684-3690.
66. S. Armon, H. Aharoni, M. Moshe and E. Sharon, *Soft Matter*, 2014, **10**, 2733-2740.
67. T. M. Birshtein, P. A. Lakovlev, V. M. Arnoskov, F. A. M. Leermakers, E. B. Zhulina and O. V. Borisov, *Macromolecules*, 2008, **41**, 478-488.
68. J. Bae, T. Ouchi and R. C. Hayward, *ACS Appl. Mater. Interfaces*, 2015, **7**, 14734-14742.
69. A. A. Evans, S. E. Spagnolie, D. Bartolo and E. Lauga, *Soft Matter*, 2013, **9**, 1711-1720.
70. G. Stoychev, S. Zakharchenko, S. Turcaud, J. W. C. Dunlop and L. Ionov, *ACS Nano*, 2012, **6**, 3925-3934.
71. H. M. Xiong, C. K. Chen, K. Lee, R. M. Van Horn, Z. Liu, B. Ren, R. P. Quirk, E. L. Thomas, B. Lotz, R. M. Ho, W. B. Zhang and S. Z. D. Cheng, *Macromolecules*, 2011, **44**, 7758-7766.
72. L. Radzihovsky and J. Toner, *Phys. Rev. Lett.*, 1995, **75**, 4752-4755.
73. E. Cerda, S. Chaieb, F. Melo and L. Mahadevan, *Nature*, 1999, **401**, 46-49.
74. J. H. Jung, S. H. Lee, J. S. Yoo, K. Yoshida, T. Shimizu and S. Shinkai, *Chem. Eur. J.*, 2003, **9**, 5307-5313.
75. S. Paavilainen, J. L. McWhirter, T. Rog, J. Jarvinen, I. Vattulainen and J. A. Ketoja, *Nord. Pulp Paper Res. J.*, 2012, **27**, 282-286.
76. K. Y. Liu, L. Y. Meng, S. L. Mo, M. M. Zhang, Y. Y. Mao, X. H. Cao, C. H. Huang and T. Yi, *J. Mater. Chem. C*, 2013, **1**, 1753-1762.
77. J. C. Wu, T. Yi, T. M. Shu, M. X. Yu, Z. G. Zhou, M. Xu, Y. F. Zhou, H. J. Zhang, J. T. Han, F. Y. Li and C. H. Huang, *Angew. Chem. Int. Edit.*, 2008, **47**, 1063-1067.
78. S. Alben, B. Balakrishnan and E. Smela, *Nano Lett.*, 2011, **11**, 2280-2285.
79. M. Bowick, M. Falcioni and G. Thorleifsson, *Phys. Rev. Lett.*, 1997, **79**, 885-888.
80. A. Goriely and S. Neukirch, *Phys. Rev. Lett.*, 2006, **97**, 184302.

### 3. Stick or twist: the role of surface packing in the photoreactivity of switchable gelators

#### 3.1 Background

One of the major advantages of small-molecule gels over polymeric materials is their sensitivity to environmental stimuli. In many cases, subjecting the materials to moderate changes in temperature allows gel-sol and sol-gel transitions to be induced in a reversible manner. In addition, photoswitchable responses may be realised by functionalising the LMWGs with reactive moieties such as azobenzenes, spiropyrans and dithienylethenes.<sup>1</sup> Modulating the physical characteristics of a gel via remote physical stimuli allows the material to behave as a sensor or logic gate,<sup>2</sup> with potential applications in catalysis,<sup>3,4</sup> drug delivery<sup>5,6</sup> and optical devices.<sup>7</sup>

Salicylidene-anilines, otherwise known as anils, are stimuli-sensitive chromophores which exhibit particularly diverse optical characteristics when incorporated into an aggregate.<sup>8</sup> Thermochromic anils undergo a heat-induced intramolecular proton transfer, wherein the colourless or yellow enol isomer converts to an orange or red *cis*-keto form (Fig. 59).<sup>9</sup> Photochromic transitions, meanwhile, involve excited state intramolecular proton transfer (ESIPT) under UV illumination, followed by a *cis-trans* isomerisation to generate the red *trans*-keto form.<sup>10</sup> Compared with the dissolved species, anils in the solid-state undergo more prolonged optical changes due to the enhanced lifetimes of their isomerisation products. Indeed, the half-life of the *trans*-keto form is typically milliseconds in solution but may extend to minutes, days or even months in crystals and other solid media.<sup>11, 12</sup> Photoreactivity is greatest in low-density systems that can accommodate large conformational changes, whereas thermochromic behaviour is most frequently exhibited by anils with limited flexibility in the solid state.<sup>13</sup>

Anils and related moieties have been employed as molecular switches in a number of LMWGs.<sup>14-16</sup> Photoisomerisation of anils is possible in the gel state, and may be accompanied by aggregation-induced changes such as increased fluorescence or red-shifted absorption.<sup>15</sup> Cooling an anil gel can lead to decolourisation through depopulation of the *cis*-keto isomer, whilst heating

typically triggers a gel-sol transition to restore the optical characteristics of the dissolved material.<sup>17</sup> An anil gel may exhibit stimuli-sensitivity comparable to that of the solid phase but retain the solvent-dependent properties of a compound in solution. Furthermore, the material may prove multiaddressable, with properties that can be adjusted via mechanical treatments, variation of the gelator concentration or addition of ions and other guest species.<sup>17-19</sup>

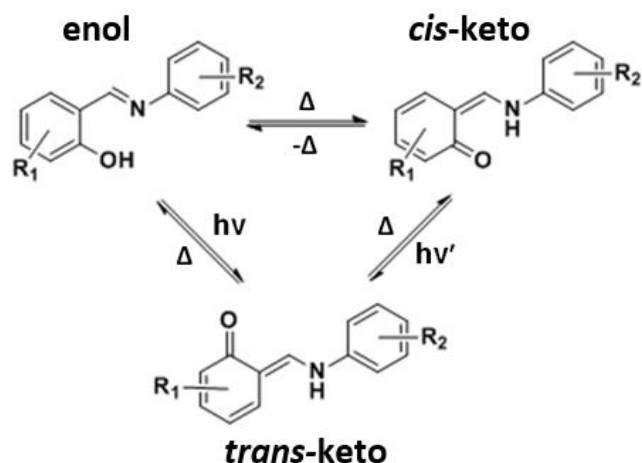


**Fig. 59** Isomerisation pathways of *N*-salicylidene anilines. The feasibility of these reactions in the solid state varies depending on the identities of  $R_1$  and  $R_2$  and the molecular packing arrangement.

Predicting the behaviour anils and other molecular switches after aggregation can be challenging. A popular approach is to simulate reactions in the solid state, to explore the effects of intermolecular interactions on the mobility and stability of the reacting species. The energy of the switchable moiety is typically estimated via a quantum mechanical method such as density functional theory (DFT), wherein the molecular orbitals are calculated by iterative minimisation of an energy functional with respect to a model electron density.<sup>20</sup> The remainder of the molecule is analysed by means of less computationally expensive molecular mechanics (MM) calculations. As in MD simulations, bond lengths, angles, torsions and non-bonded contacts are modelled using classical force expressions, and varied to identify the minimum-energy geometry for each step in the reaction pathway.

Photoreaction simulations of azobenzenes and stilbenes highlight the importance of steric effects in the feasibility of isomerisation. In the gas phase, sterically bulky stilbenes display only slightly enhanced activation barriers for

rotation about the alkene moiety.<sup>21</sup> In the solid state, however, more dramatic differences are observed: SC-XRD studies reveal that unsubstituted stilbenes can isomerise freely at room temperature, while those with  $\alpha$ -chloro or methyl substituents are conformationally locked.<sup>22</sup> Simulations of azobenzenes and azobiphenyls in self-assembled monolayers (SAMs) suggest that quantum yields are reduced due to inhibition of torsions around the central double bond, even though the lifetimes of excited states are significantly extended.<sup>23</sup> Substituents on the reactive moiety may obstruct the reaction by limiting the mobility of the aromatic rings, which must rotate in-phase with the N-N bond for the reaction to be favoured.<sup>24</sup> Conversely, the activation barrier for isomerisation may be lowered by line defects or neighbouring molecules in the *cis* conformation.<sup>25</sup> Models of cooperative switching are supported by scanning tunnelling microscopy (STM) images of pure *cis* domains after the irradiation of azobiphenyl SAMs.<sup>26</sup> Likewise, STM images of *cis*- and *trans*-rich domains may be matched to predicted low-energy packing arrangements, in order to identify the true two-dimensional unit cells of the immobilised molecules and refine computational models of the *trans-cis* trajectory.<sup>27</sup>

The steric factors governing the reactivities of anils in the solid state are comparable to those affecting azobenzenes and stilbenes. Close packing forces the molecules to adopt an extended conformation throughout the reaction, so isomerisation must proceed via a pedal-like motion about the imine moiety.<sup>22, 28</sup> MD simulations involving a DFT treatment of a crystalline anil reveal that ESIPT proceeds over 25 fs, while the subsequent *cis-trans* transformation requires several hundred femtoseconds to reach completion.<sup>20</sup> Analysis of the surrounding enol molecules reveals only small displacements during the isomerisation process. However, photoreaction is demonstrably inhibited in more sterically crowded systems, and displays significant yield enhancements when molecules are functionalised with bulky substituents to minimise packing density.<sup>29</sup>

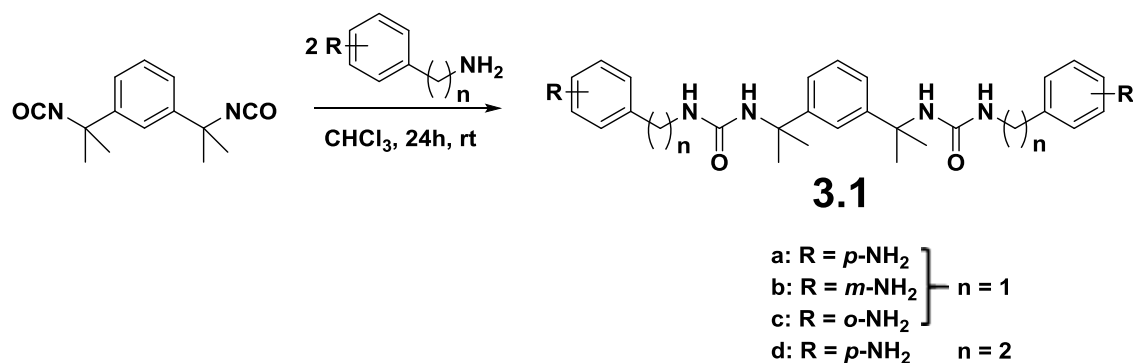
Although reported anil-based LMWGs show some diversity in their structures and solid-state behaviour, there have been few systematic attempts to explore the effects of substituents and molecular configuration on the outcome of self-assembly. In this investigation, comparisons were made between twelve anils featuring the same bis(urea) spacer, including a number of isomers with only

small differences in connectivity. It was found that both photochromism and gel-forming abilities are strongly affected by structural modifications, and may be predicted or explained by means of crystallographic studies and MM calculations. The results illustrate the impact of small changes in molecular packing on the physical properties of an LMWG, and could inform future attempts to design effective gelators with enhanced switchable characteristics.

## 3.2 Results and discussion

### 3.2.1 Synthesis and crystallisation

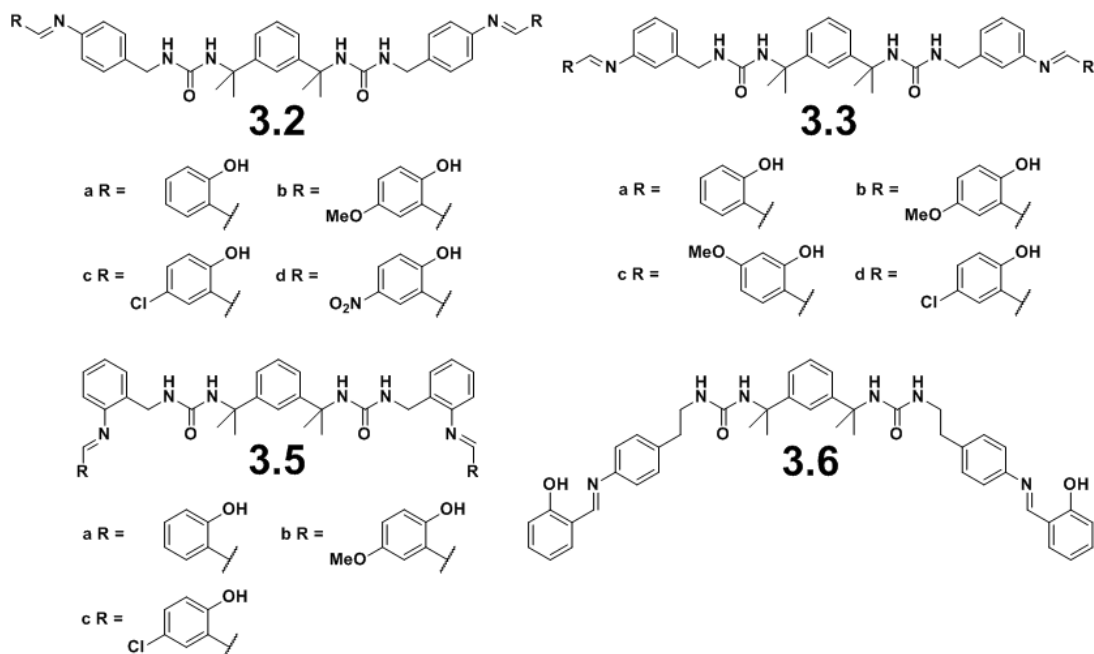
Anil-functionalised bis(urea)s were synthesised via a two-step procedure. In the first step, 1,3-bis(1-isocyanato-1-methylethyl)benzene was reacted with excess benzylamine or 4-(2-aminoethyl)aniline at room temperature to produce diamine intermediates **3.1a-d**. These reactions proceed chemoselectively due to the weaker reactivities of the aniline groups relative to the primary amines.



In the next stage, the diamines were reacted with excess salicylaldehyde in methanol. The products crystallise on formation and were further purified by washing with methanol. Compounds **3.2b**, **3.3b**, **3.3c**, **3.4a**, **3.4b** and **3.4c** form single crystals, while the other derivatives are deposited as microcrystalline precipitates.

### 3.2.2 Crystal structures

All of the diamine intermediates except **3.1c** were recrystallised by slow evaporation of methanol, ethanol, 1-propanol, acetonitrile and nitromethane solutions to yield single crystals of sufficient quality for analysis by SC-XRD (Table 3). The crystal structures of **3.1a**, **3.1b** and **3.1d**, structures **XII**, **XIII** and **XIV** respectively, consist of molecules linked by continuous urea-urea tape motifs,



with N-O contacts in the range 2.83–2.91 Å. However, while the ureas in structures **XII** and **XIII** interact via single hydrogen bonds, half of the urea NH groups in structure **XIV** are incorporated into bifurcated  $R_2^1(6)$  motifs.<sup>30</sup> Moreover, the tapes in structure **XIV** display an unusual configuration: urea groups are arranged into a three-dimensional network hydrogen bonding network, wherein molecules sharing a pair of  $\alpha$ -tapes are separated by three urea-urea interactions (Fig. 60). If tape-sharing molecules are assigned a common letter, the repeat unit of the network is denoted [ABCD]. By contrast, structures **XII** and **XIII** both consist of [AB] networks, wherein molecules adopt a “brick-wall” arrangement and are connected via a two-dimensional array of hydrogen bonds. An analysis of bis(urea) structures in the CSD (section 9.2) reveals just one reported instance of the [ABCD] repeat unit,<sup>31</sup> compared with ten examples of the [AB] topology.

	<b>3.1a (XII)</b>	<b>3.1b (XIII)</b>	<b>3.1d (XIV)</b>	<b>3.1a·0.15MeOH (XV)</b>
<b>Formula</b>	C <sub>28</sub> H <sub>36</sub> N <sub>6</sub> O <sub>2</sub>	C <sub>28</sub> H <sub>36</sub> N <sub>6</sub> O <sub>2</sub>	C <sub>30</sub> H <sub>40</sub> N <sub>6</sub> O <sub>2</sub>	C <sub>28</sub> H <sub>36</sub> N <sub>6</sub> O <sub>2</sub> ·0.15(CH <sub>4</sub> O)
<b>Formula weight</b>	488.63	488.63	516.68	493.43
<b>Space group</b>	<i>P</i> 2 <sub>1</sub> / <i>n</i>	<i>P</i> 2 <sub>1</sub> / <i>c</i>	<i>P</i> 2 <sub>1</sub> 2 <sub>1</sub> 2 <sub>1</sub>	<i>P</i> 2 <sub>1</sub> / <i>c</i>
<b><i>a</i> / Å</b>	14.004(4)	9.3810(7)	12.467(6)	22.1743(15)
<b><i>b</i> / Å</b>	9.395	11.5374(8)	13.096(5)	9.3575(7)
<b><i>c</i> / Å</b>	20.286	24.2145(17)	17.297(9)	27.1514(18)
<b><math>\beta</math> / °</b>	103.797(11)	94.551(2)	90	111.730(2)
<b><i>V</i> / Å<sup>3</sup></b>	2592(1)	2612.5(3)	2824(2)	5233.5(6)
<b><i>Z</i></b>	4	4	4	8
<b><i>D</i><sub>calc</sub> / g cm<sup>-3</sup></b>	1.252	1.242	1.215	1.253
<b><i>R</i><sub>int</sub></b>	0.1174	0.0677	0.1191	0.1158
<b><i>R</i><sub>1</sub> [<i>I</i> ≥ 2<math>\sigma</math> (<i>I</i>)]</b>	0.0644	0.0467	0.0697	0.0705
<b>w<i>R</i><sub>2</sub> [all data]</b>	0.1517	0.1246	0.1877	0.1795

**Table 3** Summary of crystallographic data for diamines **3.1a**, **3.1b** and **3.1d**.



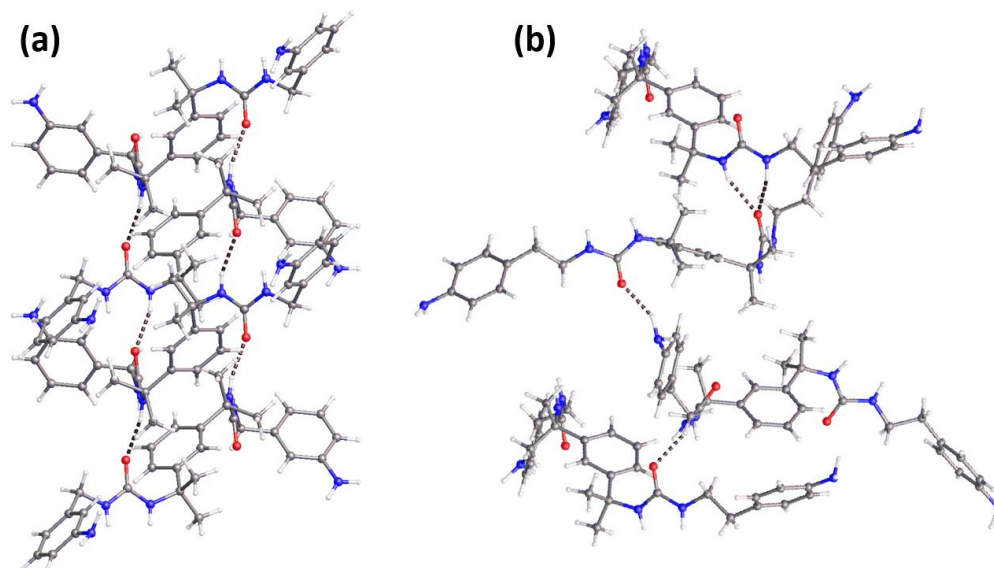


**Fig. 60** Molecules in structure **XIII** (a) form lamellar networks with an [AB] repeat unit. Urea groups interact via single hydrogen bonds, and the amine groups do not participate in any significant supramolecular motifs. By contrast, structure **XIV** (b) displays a three-dimensional [ABCD] network of urea-urea interactions. There are examples of both single and bifurcated urea-urea interactions, in addition to a bifurcated amine-urea-urea hydrogen bonding motif.

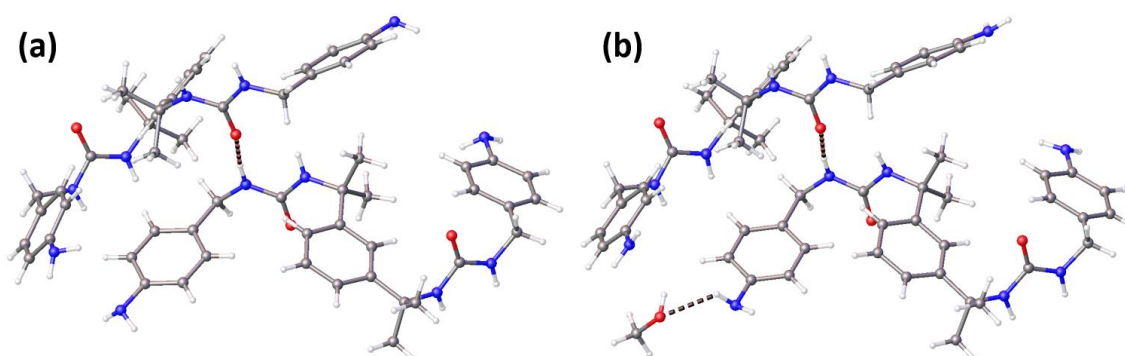


**Fig. 61** In crystals of structure **XII** (a), obtained from ethanol, 1-propanol, acetonitrile and nitromethane, molecules interact via single urea-urea hydrogen bonds (N-O contact 2.910(3) Å). Crystallisation from methanol affords an almost identical structure **XV** (b). However, one end group is disordered over two sites, due to the presence of a methanol guest molecule with approximately 30% occupancy. The methanol forms a hydrogen bond with one of the amine groups (N-O contact 2.894(1) Å), which in the non-solvated system does not participate in any significant supramolecular motifs.

With the exception of one amine-urea hydrogen bond in structure **XIV** (N-O contact 3.004(1) Å), the end groups of the bis(urea) molecules in structures **XII**, **XIII** and **XIV** are not involved in any significant supramolecular motifs. Moreover, compounds **3.1b** and **3.1c** were not observed to produce crystalline solvates: crystals of the bis(urea)s from a range of polar solvents was always found to exhibit the non-solvated structures **XIII** and **XIV**. Interestingly, however,

crystallisation of compound **3.1a** from methanol affords a partial methanol solvate, structure **XV**, in which a guest methanol molecule with 30% occupancy forms a hydrogen bond (N-N contact 2.894(1) Å) to one of the four symmetry independent amine groups (Fig. 61). Despite lowering the symmetry of the structure, the inclusion of the solvent only slightly alters the molecular conformation, suggesting that a single-crystal-to-single-crystal transformation may readily take place. Indeed, repeat SC-XRD experiments reveal that drying the crystals under ambient air for one week results in complete conversion to structure **XII**. This structure is highly stable and does not revert to structure **XV** when re-immersed in methanol.

Compounds **3.2b**, **3.3b**, **3.3c**, **3.4a**, **3.4b** and **3.4c** formed single crystals when synthesised in methanol, ethanol and 1-propanol (Table 4). However, only compounds **3.3b**, **3.3c**, **3.4a** and **3.4c** formed crystals of sufficient quality for complete structure solutions to be obtained. The structures of **3.3b**, **3.3c** and **3.4a** obtained from methanol (**XVI**, **XVII** and **XVIII**, respectively) are non-solvated. Conversely, the crystals of **3.4c** from wet ethanol were found to exhibit a hydrate structure, **XIX**. In addition to one well-resolved water molecule, the structure contains one disordered water molecule per bis(urea), which was masked in the final structure solution. Single crystals of **3.4c** were also generated from methanol, but the crystals were of insufficient quality for reliable unit cell parameters to be obtained.

	<b>3.3b (XVI)</b>	<b>3.3c (XVII)</b>	<b>3.4a (XVIII)</b>	<b>3.4c·H<sub>2</sub>O (XIX)</b>
<b>Formula</b>	C <sub>44</sub> H <sub>48</sub> N <sub>6</sub> O <sub>6</sub>	C <sub>44</sub> H <sub>48</sub> N <sub>6</sub> O <sub>6</sub>	C <sub>42</sub> H <sub>44</sub> N <sub>6</sub> O <sub>4</sub>	C <sub>42</sub> H <sub>44</sub> N <sub>6</sub> O <sub>5</sub> Cl <sub>2</sub>
<b>Formula weight</b>	756.88	756.88	696.83	783.73
<b>Space group</b>	<i>P</i> 2 <sub>1</sub> / <i>c</i>	<i>P</i> 2 <sub>1</sub>	<i>P</i> 2 <sub>1</sub>	<i>P</i> 2 <sub>1</sub> / <i>c</i>
<b><i>a</i> / Å</b>	9.2360(5)	9.5488(3)	8.8878(4)	13.681(6)
<b><i>b</i> / Å</b>	12.4214(7)	11.1690(5)	12.2631(6)	19.626(8)
<b><i>c</i> / Å</b>	34.2801(19)	18.9636(8)	16.6716(8)	15.388(6)
<b><math>\alpha</math> / °</b>	90	90	90	90
<b><math>\beta</math> / °</b>	94.062(4)	99.544(3)	93.251	99.688(4)
<b><math>\gamma</math> / °</b>	90	90	90	90
<b><i>V</i> / Å<sup>3</sup></b>	3922.9(4)	1994.48(14)	1814.15(15)	4073(3)
<b><i>Z</i></b>	4	2	2	4
<b><i>D</i><sub>calc</sub> / g cm<sup>-3</sup></b>	1.282	1.260	1.276	1.278
<b><i>R</i><sub>int</sub></b>	0.0917	0.0673	0.1730	0.0607
<b><i>R</i><sub>1</sub> [<i>I</i> ≥ 2σ(<i>I</i>)]</b>	0.0777	0.0627	0.0750	0.0874
<b><i>wR</i><sub>2</sub> [all data]</b>	0.1687	0.1214	0.1932	0.2641

**Table 4** Summary of crystallographic data for anils **3.3b**, **3.3c**, **3.4a** and **3.4c**. Data listed for structure **XIX** correspond to the structure solution in which one disordered water molecule is masked. The formula unit given is that of the monohydrate system represented in the final crystal structure.

All of the anil structures consist of lamellar [AB] networks with anil moieties symmetrically distributed between the upper and lower faces (Fig. 62). Tapes in structures **XVI**, **XVII** and **XVIII** are composed solely of urea-urea motifs, while those in structure **XIX** comprise discrete pairs of interacting urea groups linked via bridging water molecules. The unusual pattern of interactions in structure **XIX** allows the bis(urea) spacers to lie more parallel to the lamellar plane. This mode of packing reduces the thickness of the structure and expands the area available per anil group,  $A_{\text{mol}}$ , by nearly 40% relative to the other anil structures **XVI-XVIII**. It is possible that the steric bulk of the chlorinated anil groups and conformational rigidity of the spacer moiety prevent effective crystallisation of pure **3.4c**. Forming thinner lamellae in combination with space-filling guest molecules is favourable, as this arrangement relieves steric clashes between adjacent end groups and enables the bis(urea) molecules to adopt a more stable conformation.

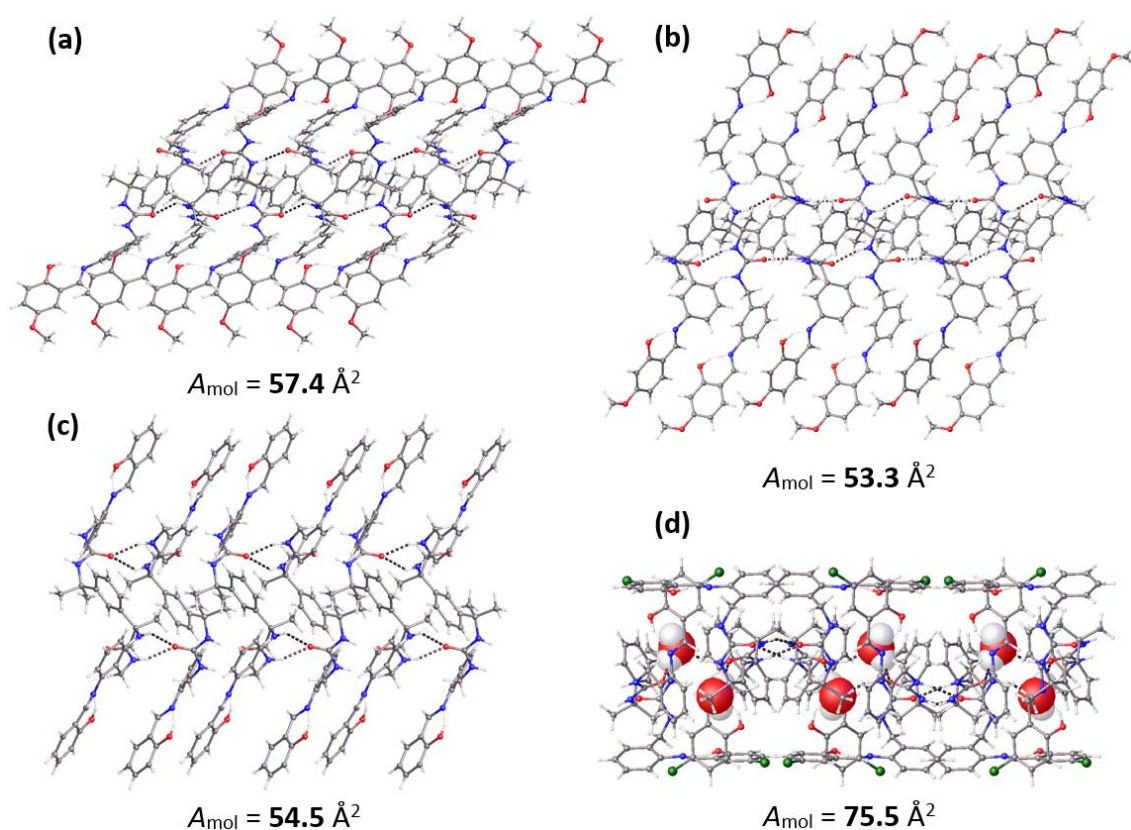


**Fig. 62** Bis(urea) molecules in structures **XVI** (a), **XVII** (b) and **XVIII** (c) form similar two-dimensional hydrogen bonding networks, and are aligned at a steep angle to the lamellar plane.

Lamellae in structure **XIX**, however, are relatively narrow (d). This packing mode greatly increases the area available for each anil group on the lamellar surface ( $A_{\text{mol}}$ ), and is made possible by the presence of bridging water molecules (shown in space-filling representation) between urea groups.

### 3.2.3 Gelation behaviour

The gelation capacities of the anils were tested by dissolving the compounds in a range of hot organic solvents and cooling the solutions to room temperature (Table 5). Nearly all of the anils derived from compounds **3.1a**, **3.1b** and **3.1d** were found to be effective gelators in di- and trichlorobenzenes with CGCs of approximately 0.1% (w/v). Although gelators derived from **3.1a** are the most effective at low concentrations, those based on **3.1b** and **3.1d** are more versatile, forming gels in toluene and, in some cases, nitrobenzene. By contrast, anil derivatives of **3.1c** are non-gelating in all of the solvents tested. The structure of the end group is less significant, but appears to have some influence on the range of solvents gelled. For example, the 5-chlorosalicylaldehyde derivative **3.2c** is able to form gels in a wider range of solvents than analogues with electron-donating substituents, but replacing the chloro substituent with a more electron-withdrawing nitro group serves to limit gel formation to polar solvents such as nitrobenzene.

	1,2-dichlorobenzene		1,2,4-trichlorobenzene	Toluene	Nitrobenzene
	0.1% (w/v)	1% (w/v)	1% (w/v)	1% (w/v)	1% (w/v)
<b>3.2a</b>	<b>G<sup>T</sup></b>	<b>G<sup>O</sup></b>	<b>G<sup>O</sup></b>	P	P
<b>3.2b</b>	<b>G<sup>T</sup></b>	<b>G<sup>O</sup></b>	<b>G<sup>O</sup></b>	P	P
<b>3.2c</b>	<b>G<sup>T</sup></b>	<b>G<sup>O</sup></b>	<b>G<sup>O</sup></b>	P	<b>G<sup>O</sup></b>
<b>3.2d</b>	S	GP	GP	P	<b>G<sup>T</sup></b>
<b>3.3a</b>	GP	<b>G<sup>C</sup></b>	<b>G<sup>C</sup></b>	<b>G<sup>O</sup></b>	P
<b>3.3b</b>	S	<b>G<sup>C</sup></b>	<b>G<sup>C</sup></b>	<b>G<sup>O</sup></b>	P
<b>3.3c</b>	GP	<b>G<sup>O</sup></b>	<b>G<sup>O</sup></b>	<b>G<sup>O</sup></b>	P
<b>3.3d</b>	<b>G<sup>T</sup></b>	<b>G<sup>O</sup></b>	<b>G<sup>O</sup></b>	<b>G<sup>O</sup></b>	P
<b>3.4a</b>	S	P	P	P	P
<b>3.4b</b>	S	P	P	P	P
<b>3.4c</b>	S	P	P	P	P
<b>3.5</b>	<b>PG<sup>T</sup></b>	<b>G<sup>O</sup></b>	<b>G<sup>O</sup></b>	<b>G<sup>O</sup></b>	<b>G<sup>C</sup></b>

**Table 5** Results of gelation trials for anil-functionalised bis(urea)s. Observations were made after heating solutions in 2 cm<sup>3</sup> sealed vials and allowing the materials to cool to room temperature for one hour. Results are marked with a letter corresponding to the aggregation outcome: G = gel (highlighted in bold), PG = partial gel, GP = gelatinous precipitate, P = precipitate and S = solution. Superscripts are used to denote the appearance of gels: C = clear (transparent), T = translucent and O = opaque.

The structures and morphologies of the gels were analysed by SEM and powder X-ray diffraction (PXRD). For both experiments, xerogels were prepared

by drying thin layers of 1% (w/v) gels under air at room temperature. The SEM micrographs reveal that all of the gels analysed consist of uniform 30 nm-wide fibrils, assembled into fibre bundles with thicknesses of up to several hundred nanometres (Fig. 63). By contrast, precipitates of **3.3c** from 1,2-dichlorobenzene consist of irregularly shaped particles tens of micrometres in diameter, which

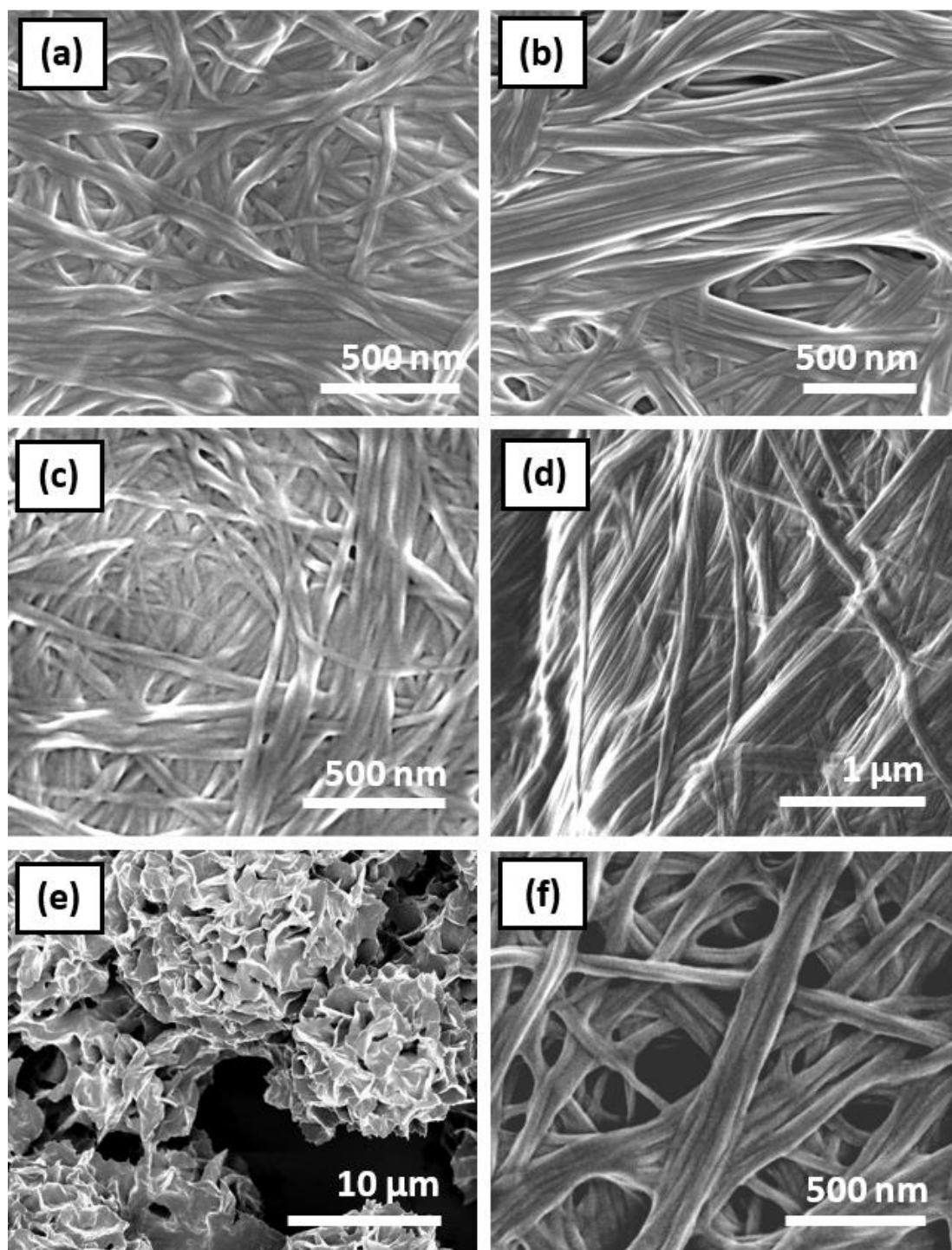


**Fig. 63** SEM micrographs of dried aggregates prepared from 1% (w/v) gels or suspensions of **3.2a** in 1,2-dichlorobenzene (a), **3.2b** in 1,2-dichlorobenzene (b), **3.3b** in toluene (c), **3.3c** in 1,2-dichlorobenzene (d), **3.4c** in 1,2-dichlorobenzene (e) and **3.5** in toluene (f).

cannot assemble into a continuous aggregate network. The PXRD patterns for a selection of the gels (Fig. 64) display a series of broad peaks in the range  $2\theta = 2.5$ – $22.5^\circ$ , which may be indexed to Miller indices of the form  $(h00)$ . Such a distribution of reflections is characteristic of a lamellar structure with limited long-range order and a relatively large interlayer spacing. The calculated lamella thicknesses, 20–23 Å, are comparable with the lengths of the molecules, indicating that the gelators adopt extended conformations and are oriented roughly perpendicular to the lamellar plane. That this packing arrangement is similar to the structures observed by SC-XRD indicates that gelation proceeds via a similar self-assembly mechanism, but produces a more disordered material due to a higher frequency of defects in the developing aggregate.

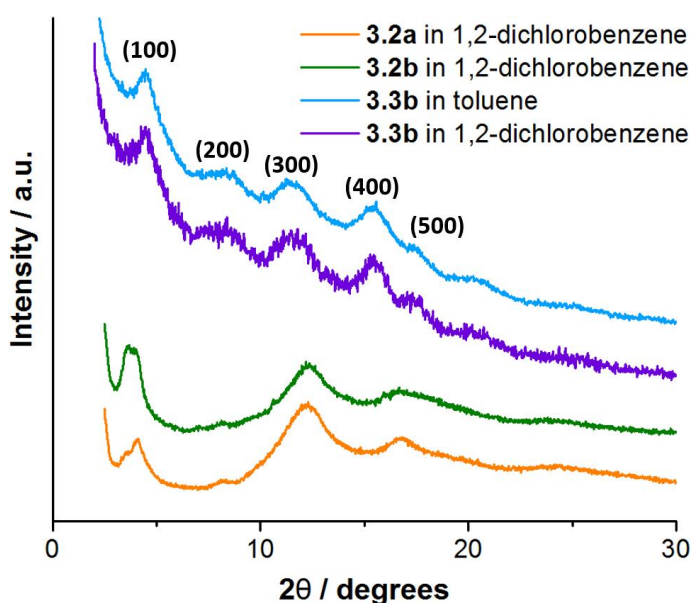


**Fig. 64** PXRD data for gels of **3.2a**, **3.2b** and **3.3b** in toluene and/or 1,2-dichlorobenzene, after drying in ambient air for six hours. The patterns can be indexed to lamellar structures.

The rheological properties of the anil gels were tested by oscillatory shear rheometry. The stress-sweep profile of a 1% (w/v) gel of **3.2a** in 1,2-dichlorobenzene (Fig. 65a) reveals that  $G'$  is an order of magnitude larger than  $G''$ , as is typical for a gel-phase material. A plateau  $G'$  value of 25 kPa indicates that the gel is moderately rigid, while a relatively high yield stress of 150–160 Pa suggests that it is also mechanically stable. Frequency sweep experiments confirm that  $G'$  values for the anil gels scale slowly with the frequency of the applied stress  $\omega$  in accordance with a power law relationship, as predicted by the soft glassy rheological (SGR) model for fibrous gels (Fig. 65b).<sup>32</sup> However, the physical



properties of the gels vary significantly depending on the structure of the gelator and the solvent used (Fig. 65c). At a gelator concentration of 1% (w/v) compound **3.5** produces the strongest gels in 1,2-dichlorobenzene, exhibiting a plateau  $G'$  value of 64 kPa and yield stress of 700-750 Pa. Compound **3.3a**, in contrast, forms weak gels in both toluene and 1,2-dichlorobenzene, displaying  $G'$  values of just 400 and 60 Pa respectively and yield stresses of less than 10 Pa. Substitution of the anil affects the strength of the gel and also its appearance, with electron-withdrawing substituents generally shifting the colour of the material from yellow to orange (Fig. 65d). For a given solvent system, it is notable that weaker gels are generally more transparent, perhaps due to the presence of narrower fibres that buckle more easily when stress is applied.<sup>33-35</sup>

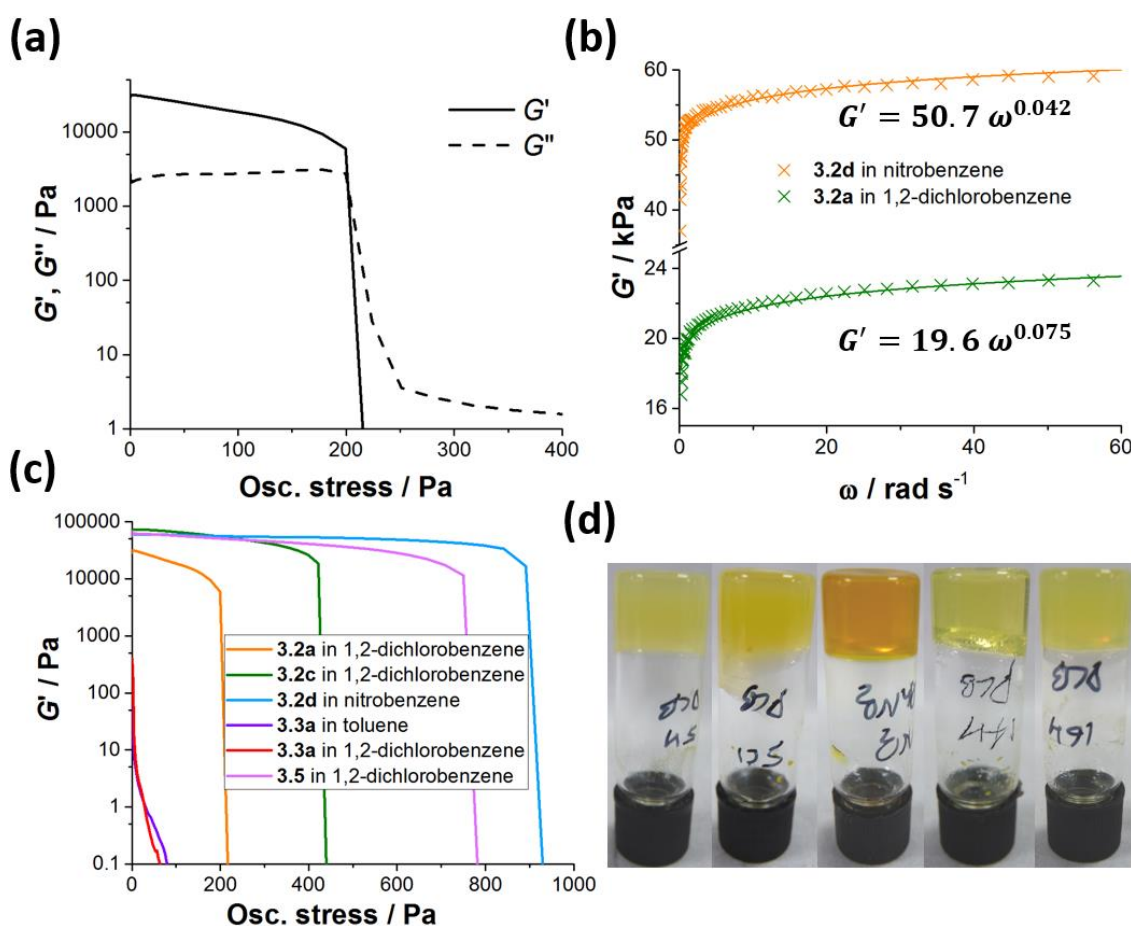


**Fig. 65** Oscillatory shear experiments at 10 °C reveal that a 1% (w/v) gel of **3.2a** in 1,2-dichlorobenzene responds as expected to changes in the applied stress at a frequency  $\omega$  of 1 Hz (a), and to changes in  $\omega$  at a constant stress of 1 Pa (b). Changing the gelator structure and/or solvent can dramatically alter both the rheological properties of the gel (c) and its colour and transparency (d). The photographs depict typical 1% (w/v) gels of (left to right) **3.2a** in 1,2-dichlorobenzene, **3.2c** in 1,2-dichlorobenzene, **3.2d** in nitrobenzene, **3.3a** in 1,2-dichlorobenzene and **3.5** in 1,2-dichlorobenzene.

While SEM micrographs suggest that gels of the anils consist of uniform fibres with little or no branching, it is possible that the microstructures of the materials are altered when they are dried and coated prior to analysis. To gain further insight into the structure of the wet gels, the variation in  $G$  for a gel of **3.2c** in 1,2-dichlorobenzene was monitored throughout the course of aggregation. A low gelator concentration of 0.1% (w/v) was used to maximise the time for gel formation, and the applied stress was restricted to 1 Pa in order to avoid significant disruption of the developing material. Following an induction period of approximately six minutes, during which time the temperature of the gel is equilibrating to that of the Peltier plate (10 °C), the data conform closely to the expected linear trend when plotted as an Avrami plot (Fig. 66).<sup>36-38</sup> The slope of this line is termed the Avrami constant, and may be treated as an estimate of the fractal dimension of the forming gel network. The calculated Avrami constant of  $1.274 \pm 0.003$  is close to 1.0, the characteristic value for ideal one-dimensional assemblies, and is thus consistent with a model of fibrous aggregation and a sparse distribution of permanent or branch points.

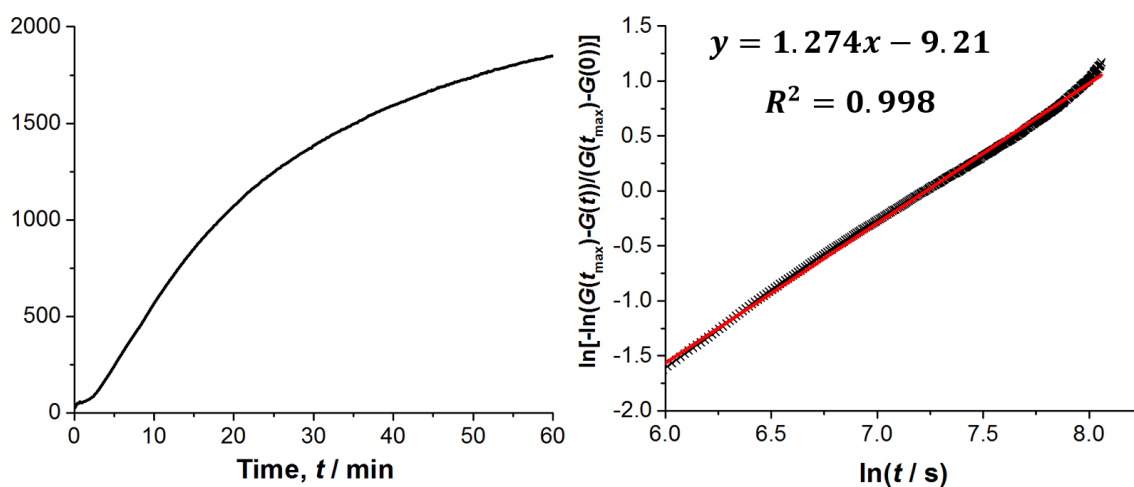


**Fig. 66** Formation of a 0.1% (w/v) gel of **3.2c** in 1,2-dichlorobenzene at 10 °C was monitored with an applied stress of 1 Pa and frequency of 1 Hz (a). Gel strength plateaus after approximately one hour (a). Fitting the trend in  $G$  to an Avrami expression with  $G(0) = 0$  Pa yields an Avrami exponent of  $1.359 \pm 0.005$ . This value can be interpreted as an estimate of the fractal dimension of the gel network,  $D_f$ , and is thus indicative of weakly branched fibrous aggregates.



### 3.2.4 Photoreactivity in crystals

The crystalline anils show substantial variation in their susceptibility to photoisomerisation. After illumination with a 30 mW 405 nm laser for one minute, compounds **3.3b** and **3.5** undergo a pronounced colour change from yellow/orange to red, and return to their original colour after 3-4 minutes (Fig. 67a). Weak chromic responses are also observed in compounds **3.2a**, **3.3a** and **3.3c** (Fig. 67b), while all of the other analogues are completely non-photochromic. The key factors influencing photoreactivity are the configuration of the spacer and substitution pattern of the anil end group. Switching occurs most commonly in anils derived from compounds **1b** and **1d**. In addition, stronger responses are observed in species based on unsubstituted salicylaldehyde, which are likely to encounter less steric hindrance during *cis-trans* isomerisation in the solid state.

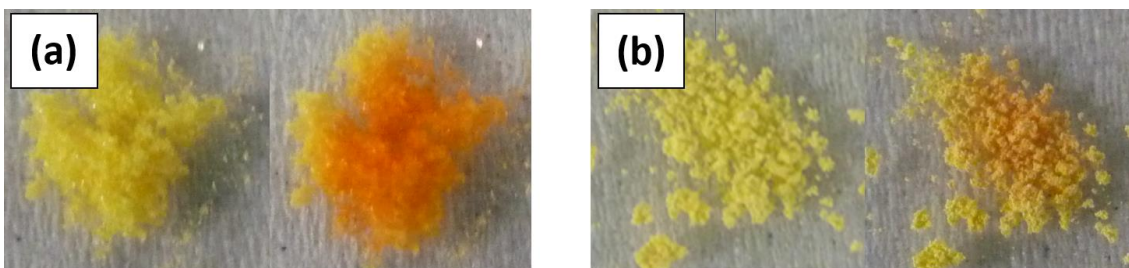


**Fig. 67** Strong photochromic response in solid **3.3b** after irradiation with a 30 mW 405 nm laser for one minute (a), and the weaker response of solid **3.3a** (b). Compound **3.5** displays behaviour similar to that of **3.3b**, while **3.2a** and **3.3c** resemble **3.3a**. The other anils are non-photochromic.

To quantify differences in their photochromic behaviour, compounds **3.2a**, **3.3a**, **3.4a** and **3.5** were analysed by diffuse-reflectance UV-vis (DRUV) spectroscopy after illumination with UV light (Fig. 68). In agreement with visual observations, the DRUV spectra for **3.3a** do not exhibit any significant changes after UV treatment. However, for **3.2a**, **3.3a** and **3.5**, reflectance over the wavelength range 450-600 nm decreases slightly, producing a corresponding increase in the Kubelka-Munk function, an estimate of absorbance.<sup>39</sup> This change may be attributed to an increase in the concentration of the *trans*-keto isomer, while a subsequent decrease in absorbance results from relaxation to the ground-state enol form.<sup>8</sup> Surprisingly, the spectral changes after illumination are largest for compound **3.3a** and relatively small for **3.5**, which produces the strongest chromic response when irradiated with a 405 nm laser. This discrepancy is likely

due to the difference in the light sources used, and suggests that **3.3a** undergoes isomerisation more readily than the other photochromic analogues at shorter excitation wavelengths.

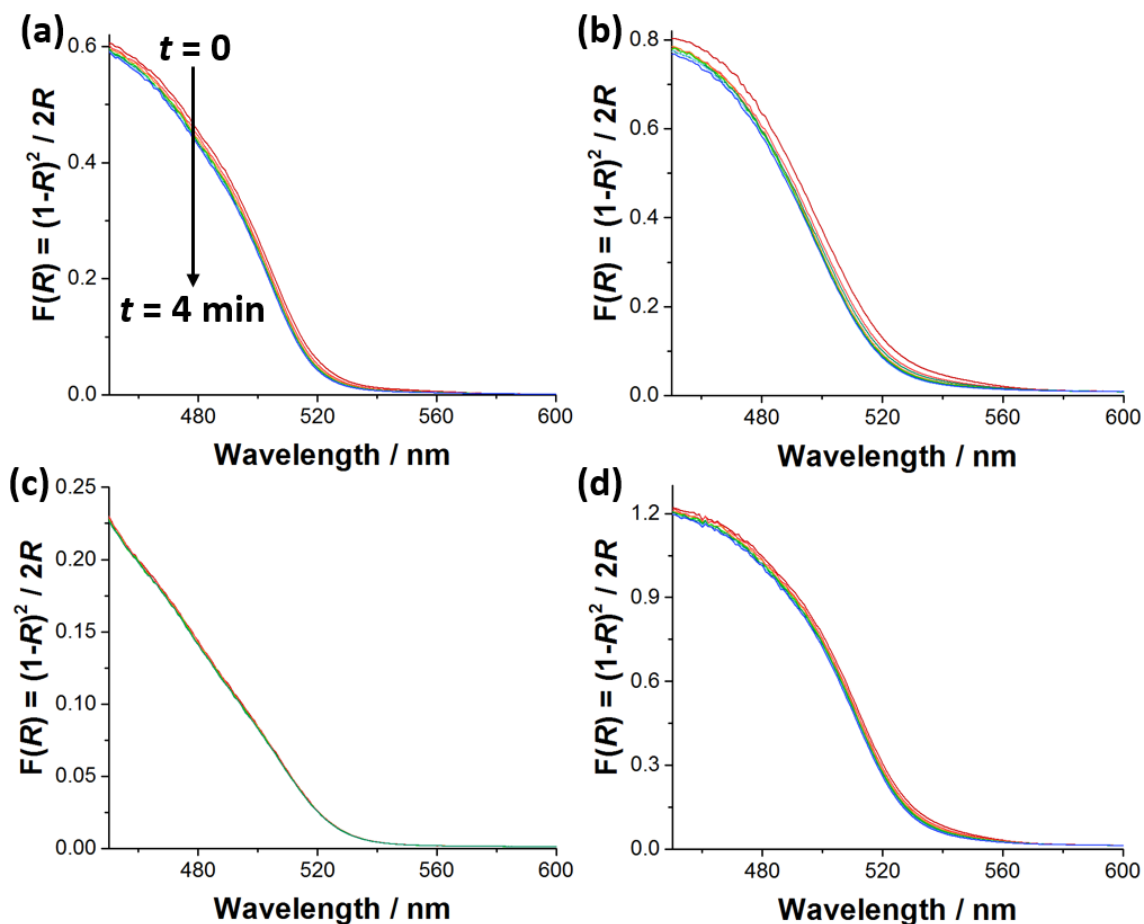


**Fig. 68** DRUV spectra of solid compounds **3.2a** (a), **3.3a** (b), **3.4a** (c) and **3.5**, over a wavelength range corresponding to the absorbance contributions of keto isomers. The solids were illuminated with a high-intensity UV lamp for 10 minutes immediately before analysis, and the relaxation process was monitored by repeat measurements over a four-minute time period. Reflectance data  $R$  were converted to approximate absorbance values via the Kubelka-Munk function  $F(R)$ .

Photoisomerisation involves excitation of the anil in its enol or *cis*-keto form, followed by a non-radiative transition to the  $S_1$  state of the trans-keto structure.<sup>8</sup> Thus, structural changes may lead to lower reactivity if they increase the energy of the  $S_1 \leftarrow S_0$  transition or reduce the stability of the keto species in their excited states. To test this possibility, model compounds corresponding to the end groups of the bis(urea)s were compared by means of DFT calculations. Analysis of the simplified systems was preferred in order to reduce computational cost and minimise the confounding effects of molecular flexibility and multiple isomerising

functionalities. The ground-state energies of the systems were estimated using the B3LYP functional<sup>40</sup> and cc-pVDZ basis set,<sup>41</sup> which was found to produce more physical (planar) aromatic ring geometries than the Pople basis set 6-31+G\*<sup>42</sup> and yield similar results to the larger correlation-consistent basis set cc-pVTZ. A full transition-dipole analysis was not attempted, but the excitation energies of the molecules in each isomeric state may be approximately equated to the HOMO-LUMO gap, which is altered by a substantial amount when isomerisation takes place.

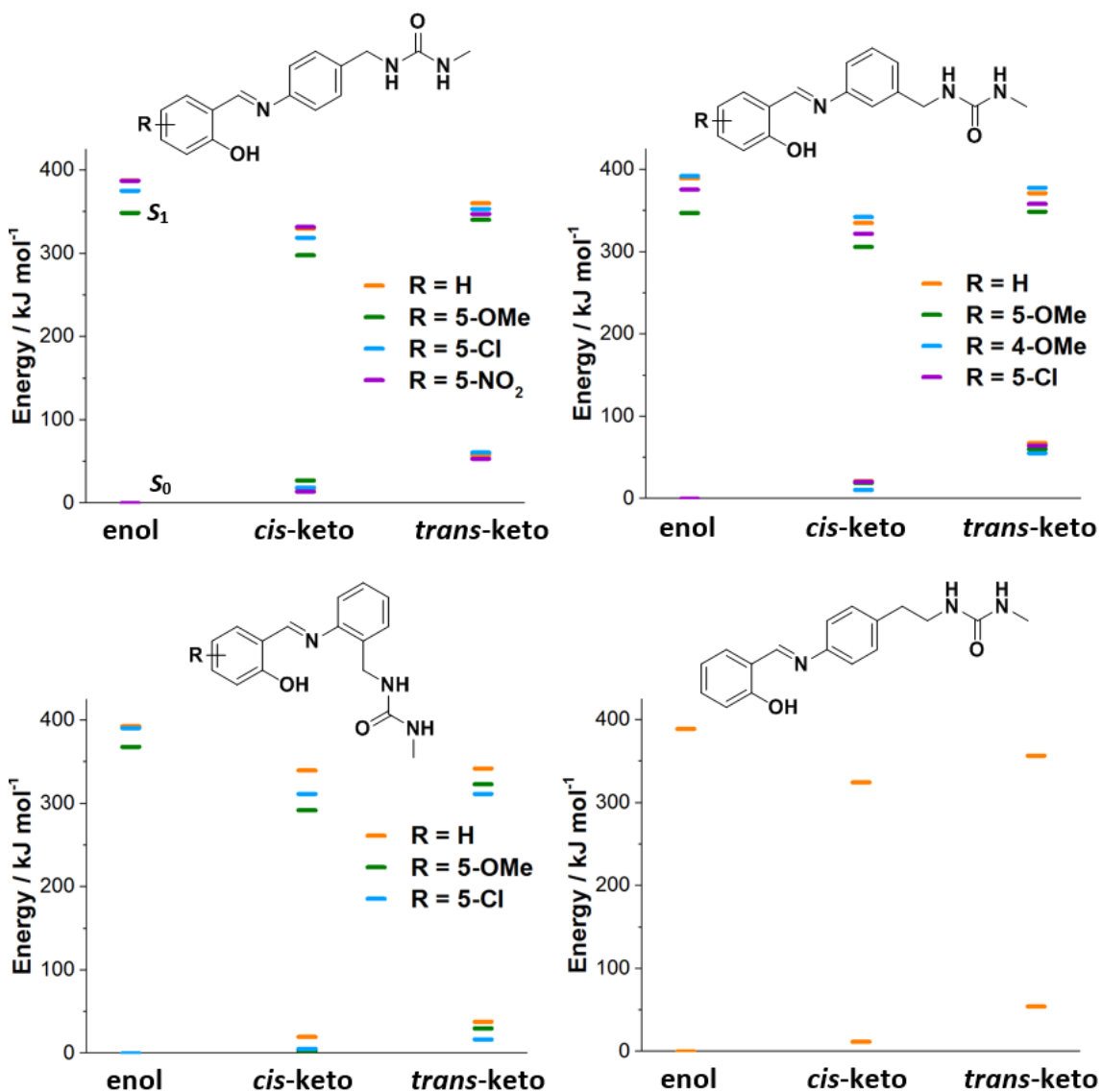


**Fig. 69** DFT energies of the enol, *cis*-keto and *trans*-keto forms of model anils in their ground state ( $S_0$ ) and after excitation ( $S_1$ ). The energies of the  $S_1$  states are estimated from the calculated differences between the HOMO and LUMO. While the *cis*-keto isomer is less stable than the enol form in the ground state, the relative stabilities of the isomers is reversed after excitation, such that tautomerisation in the  $S_1$  state is strongly favoured. Calculations were performed with the B3LYP functional and cc-pVDZ basis set.

The results of the DFT calculations reveal that substitution of the anil has a more significant effect on the arrangement of energy levels than the configuration of the bis(urea) spacer (Fig. 69). In particular, introducing a 5-methoxy group results in a large decrease in the LUMO energies of the enol and *cis*-keto forms, increasing the energy required to access the  $S_1$  state of the *trans*-keto isomer. Analogues with 5-chloro substituents experience a similar effect of smaller magnitude, while unsubstituted anils tend to exhibit the highest orbital energies in both the ground and excited states. There is no clear trend between the electronic configuration of the anils and their observed susceptibility to photoisomerisation. Thus, it may be concluded that the chromic responses of the anils are largely dictated by their packing arrangement, rather than the direct effects of particular structural features on the energy of the molecule.

In order to convert to the *trans*-keto form, an anil must be sufficiently mobile to undergo a *cis-trans* isomerisation. The reaction typically proceeds via a pedal-like motion, in which the relative positions of the aromatic rings remain approximately constant.<sup>28</sup> It is noted that while the bis(urea)s in this study form lamellar assemblies with the same  $\alpha$ -tape topology, the arrangement of anil moieties on the surface of the crystal is strongly dependent on the structures of the end group and the bis(urea) spacer (Fig. 70). To determine whether these differences in packing can account for the variation in photochromic behaviour, the isomerisation process was modelled by molecular mechanics (MM), using the Forcite module in BIOVIA Materials Studio with the cvff force-field<sup>43</sup> and Gasteiger charges.<sup>44</sup> The calculations were performed on supercells generated from SC-XRD coordinates, comprising three lamellae with four repeat units along each axis of the lamellar plane. Periodic boundary conditions were imposed parallel to the lamellae, and the crystal surface simulated by interfacing the model supercell with a vacuum slab 40 Å in thickness. One anil group on the surface was converted manually to the *cis*-keto form and the geometry of the system optimised without constraints. Subsequently, harmonic force restraints of 1000 kcal Å<sup>-1</sup> were imposed on the two torsion angles between the imine and the attached aromatic rings,  $\phi_A$  and  $\phi_B$ , to generate an energy scan over the range  $30^\circ < \phi_A < 400^\circ$ . The pedal-like motion of the isomerisation was achieved by incrementing  $\phi_A$  and  $\phi_B$

by equal amounts in opposite directions, with a step size of  $2.5^\circ$  ensuring smooth changes in geometry for most of the trajectory.

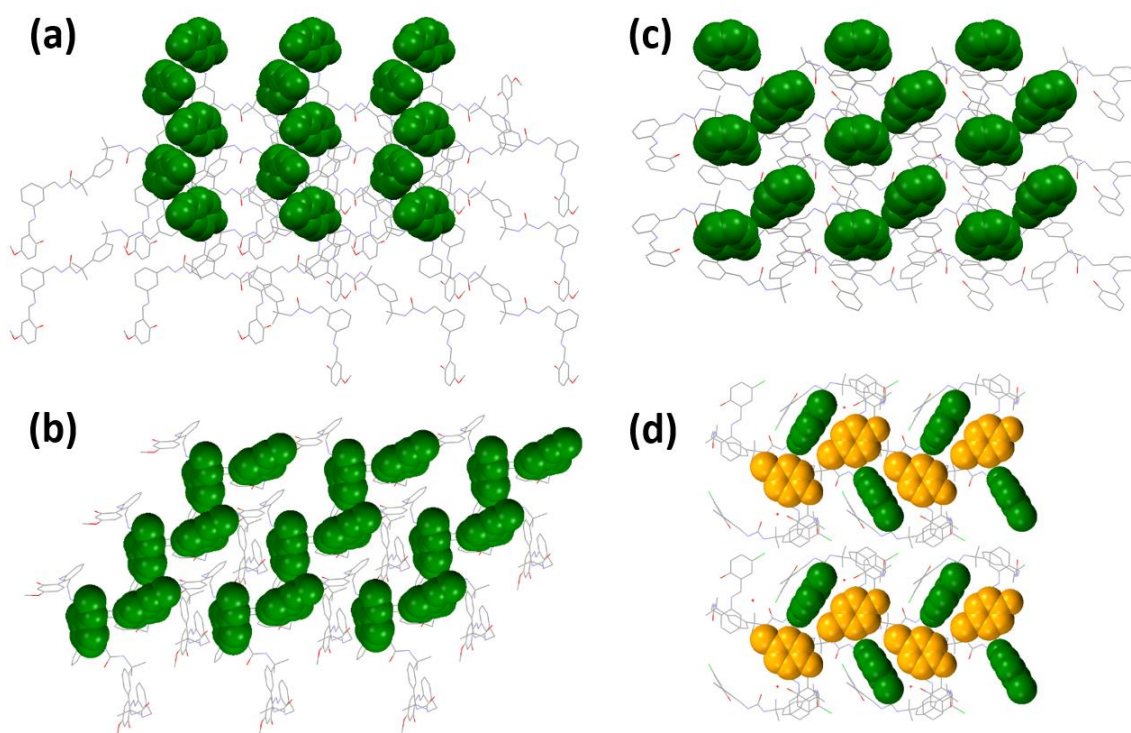


**Fig. 70** Arrangements of anil groups in the lamellar planes of structures **XVI** (a), **XVII** (b), **XVIII** (c) and **XIX** (d). Lamellae lie parallel to the (001) plane in (a)-(c) and the (100) plane in (d). The feasibility of isomerisation in (a)-(c) could be captured by modelling a single anil group, as there are no significant conformational differences between the moieties after the initial geometry optimisation. However, anil groups in structure **XIX** may lie approximately parallel or perpendicular to the lamellar plane, as highlighted in orange and green respectively. Thus, it was necessary to model two different anil rotations in (d) in order to capture the full range of dynamic possibilities.

The MM models reveal that full rotations of the anil moiety are geometrically feasible in all of the crystals studied, with activation barriers  $E_A$  less than the energy of the radiation,  $295 \text{ kJ mol}^{-1}$  (Fig. 71). However,  $E_A$  values for most of the systems lie in the range  $185\text{--}205 \text{ kJ mol}^{-1}$ , approaching or even exceeding the value for a molecule of **3.4c** in the bulk crystal lattice ( $200 \text{ kJ mol}^{-1}$ ). The anil groups of **3.3b**, conversely, can undergo a *cis-trans* transformation by overcoming a barrier of just  $162 \text{ kJ mol}^{-1}$ . In addition, the energy of the molecule in the *trans* geometry is only  $7 \text{ kJ mol}^{-1}$  higher than that of the *cis* form, while the energy differences for **3.3c**, **3.4a** and **3.4c** are  $11$ ,  $23$  and  $19\text{--}21 \text{ kJ mol}^{-1}$  respectively. MM calculations do not account for changes in electronic energy when photoisomerisation takes place. Nonetheless, the analysis suggests that the *trans*

isomer of **3.3b** is kinetically more accessible, and can be accommodated more readily within the crystal surface structure. These results are in good agreement with the empirical observations: **3.3b** is strongly photoresponsive, while **3.3c** reacts weakly and the other derivatives display no significant photochromic behaviour.

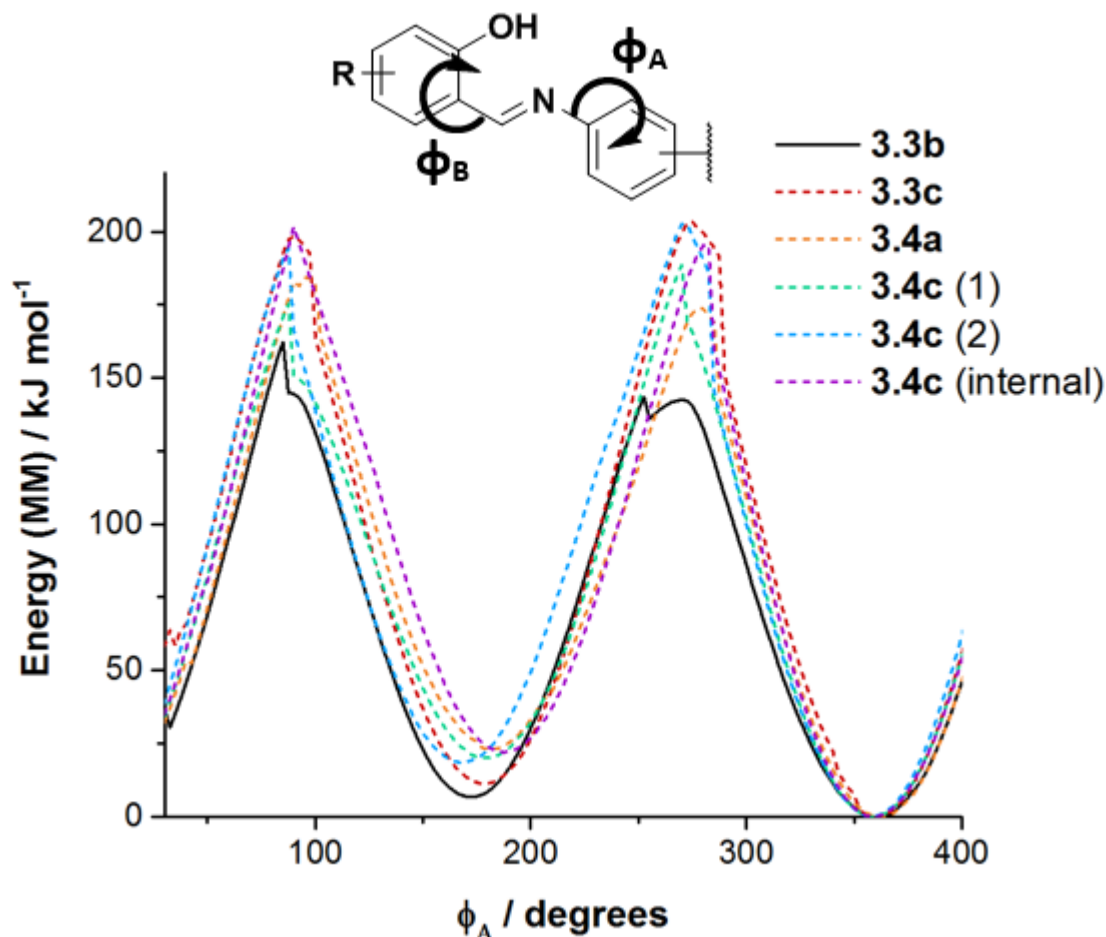


**Fig. 71** MM energy profiles for the rotation of *cis*-keto anil groups on the surface of energy-minimised model crystallites. Calculations were performed using the Forcite module of BIVOLA Materials Studio 2016 using a cvff force-field, Gasteiger charges and a medium-quality convergence threshold. The rotations were simulated using a harmonic force restraint to increase  $\phi_A$  in steps of  $2.5^\circ$ , and a second restraint to alter  $\phi_B$  by the same amount in the opposite direction. The process was repeated for the two symmetry inequivalent anil groups of **3.4c**, which exhibit different orientations relative to the crystal surface: the rotating ring in **3.4c** (1) lies roughly parallel to the lamellar plane, while the ring in **3.4c** (2) is almost perpendicular to it. In addition, an energy profile was calculated for an anil group on the internal surface of the outermost lamella in structure **XIX**, in order to gauge the effect of close packing on the magnitude of the activation barrier. Rotation of anil groups in **3.3b** was found to occur most readily, suggesting that this material displays a stronger photochromic response than the other systems due to a lack of steric hindrance during the *cis-trans* isomerisation.

### 3.2.5 Photoreactivity in gels

Optical changes during gel formation provide information about the self-assembly pathway. In their 0.1% (w/v) 1,2-dichlorobenzene gels, diluted to 0.03% (w/v) in additional solvent, anils **3.2a**, **3.3a** and **3.5** exhibit absorption and fluorescence signals at longer wavelengths than the corresponding 0.03% (w/v) methanol solutions (Fig. 71). Red-shifted absorption is characteristic of J-aggregation, wherein rod-shaped molecules align end-to-end with little  $\pi$ -stacking.<sup>45, 46</sup> Thus, the UV-vis results are consistent with the evidence from PXRD (Fig. 64, section 3.2.3) that molecules self-assemble into lamellar hydrogen bonding networks similar to those observed in single-crystal structures. The large difference in wavelength between the absorbance and fluorescence maxima is attributable to non-radiative relaxation of the excited chromophore, due to tautomerisation in the  $S_1$  state. The magnitude of this difference, known as the Stokes shift, lies consistently in the range 190-220 nm, and is therefore comparable to shifts reported for other ESIPT-active LMWGs.<sup>10, 47, 48</sup>

In contrast to the solid anils, irradiation of the gels with UV light does not result in a visible photochromic transition. The lack of observable photoreactivity is unlikely to result from the filtering effect of the liquid in the gels, since all of the solvents used are largely transparent to light of this wavelength. However, the greater mobility of molecules in a gel may lead to higher rates of non-radiative relaxation and lower yields of the *trans*-keto form. Solvent may facilitate non-radiative  $S_1 \rightarrow S_0$  transitions and increase the flexibility of anils on the aggregate surface, by disrupting urea-urea interactions to create transient defects in the hydrogen bonding network. The fact that absorption and emission signals in the gels are blue-shifted relative to the solid anils supports this hypothesis (Fig. 72), as it indicates that molecules in these aggregates are less closely packed than those of the crystalline materials. Likewise, the absence of a large absorption band between 400 and 550 nm in the gels suggests that the keto species are relatively unstable, so less likely to reach the concentrations necessary to produce a visible chromic response.



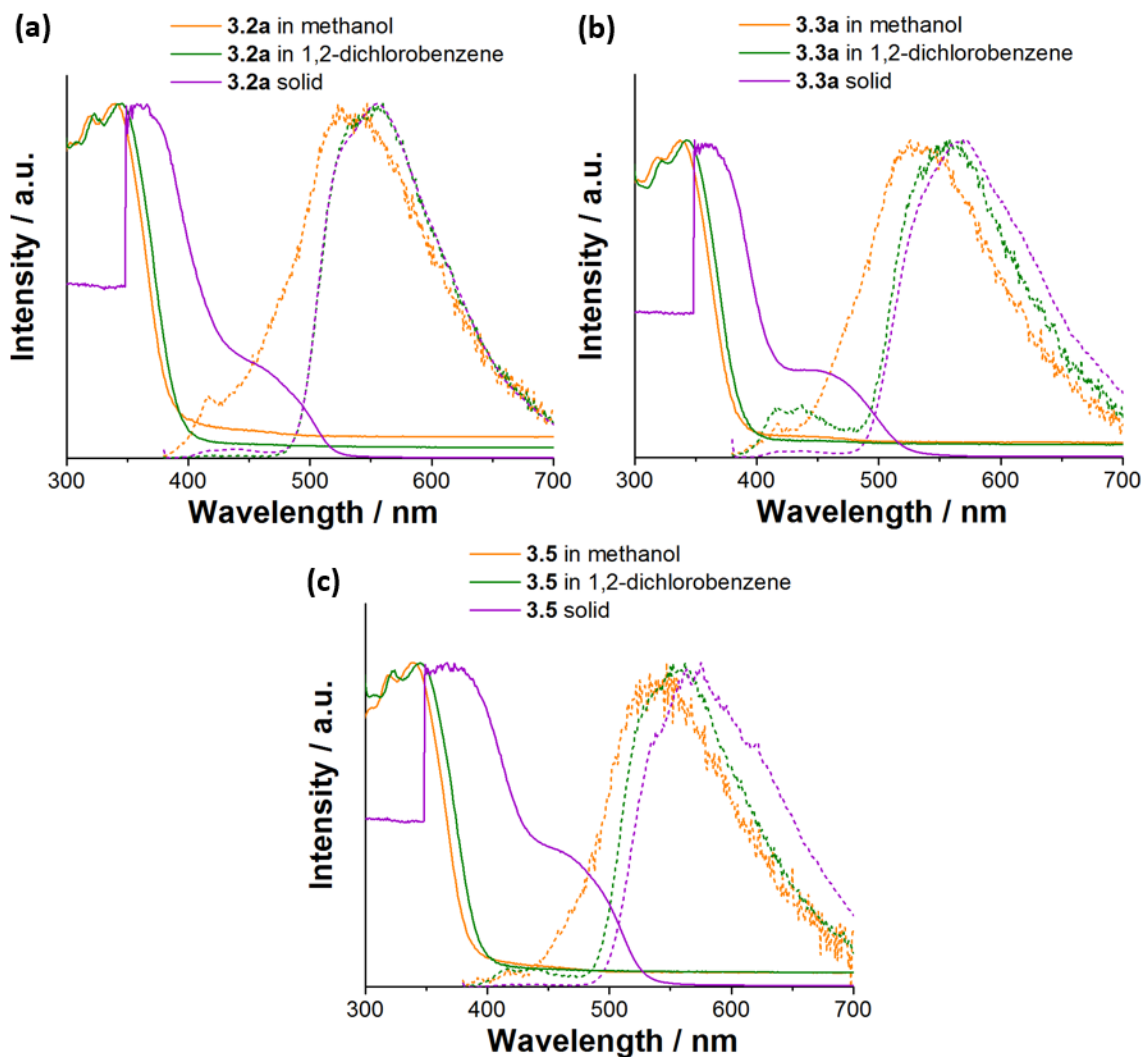


**Fig. 72** Absorption (solid lines) and emission (dashed lines) spectra of **3.2a** (a), **3.3a** (b) and **3.4** (c) as solid materials, 1,2-dichlorobenzene gels and methanol solutions. Absorbance values for solid materials were calculated from DRUV spectra via the Kubelka-Munk function. Fluorescence and absorption spectra for the gels and solutions were recorded at concentrations of 0.1 and 0.03% (w/v) respectively. For ease of comparison, spectra are normalised to produce the same maximum intensities.

*Cis-trans* isomerisations of the surface anil groups may also be directly inhibited by interactions with solvent. It is possible that solvent molecules provide transient steric hindrance by occupying space between the gelator molecules, or alters the mode of packing to increase steric crowding around the reacting imine moiety. Insights into the structures of solvated bis(urea) assemblies may be obtained from co-crystals of the compounds with the corresponding salicylaldehydes. Like the solvents used in gel formation, salicylaldehydes are unable to form strong homomeric interactions due to a lack of available hydrogen bonding groups. Thus, crystals of salicylaldehydes display a range of molecular



arrangements and can often exist in a number of polymorphic forms. Typical modes of packing are illustrated by the two known crystal structures of 5-nitrosalicylaldehyde. Crystals of form II were obtained in this investigation, by slowly evaporating the filtrate collected during the synthesis of compound **3.2d** (Table 6). Molecules in this system, structure **XX**, are arranged in well-defined, evenly spaced layers and interact via  $\pi$ - $\pi$  stacking interactions, with centroid-to-centroid distances of 3.7117(3) Å (Fig. 73). By contrast, form I (CSD refcode DUJBUG<sup>49</sup>) displays more varied  $\pi$ - $\pi$  contacts: relatively short centroid-to-centroid distances of 3.582(2) Å occur alternately with wider separations of 3.857(2) Å. In addition, while stacked rings in form II differ in orientation by 102°, those in form I are exactly antiparallel. It is hypothesised that the alignment of rings in form II provides a poorer match between opposite partial charges, but results in a competitively stable structure due to the more uniform spacing along the continuous  $\pi$ - $\pi$  stacking motifs.

	5-nitrosalicylaldehyde ( <b>XX</b> )	5-methoxysalicylaldehyde ( <b>XXI</b> )	<b>3.3b</b> ·0.25(C <sub>8</sub> H <sub>8</sub> O <sub>2</sub> ) ( <b>XXII</b> )
<b>Formula</b>	C <sub>7</sub> H <sub>5</sub> NO <sub>4</sub>	C <sub>8</sub> H <sub>8</sub> O <sub>3</sub>	C <sub>184</sub> H <sub>200</sub> N <sub>24</sub> O <sub>27</sub>
<b>Formula weight</b>	167.12	152.14	3179.67
<b>Space group</b>	<i>P</i> 2 <sub>1</sub> / <i>c</i>	<i>P</i> 2 <sub>1</sub> / <i>c</i>	<i>P</i> 2 <sub>1</sub>
<b><i>a</i> / Å</b>	7.9232(6)	8.4167(4)	36.612(11)
<b><i>b</i> / Å</b>	12.7353(10)	9.8009(5)	11.348(4)
<b><i>c</i> / Å</b>	7.4143(6)	8.9328(5)	40.926(12)
<b><math>\alpha</math> / °</b>	90	90	90
<b><math>\beta</math> / °</b>	114.125(3)	95.9351(19)	96.89(2)
<b><math>\gamma</math> / °</b>	90	90	90
<b><i>V</i> / Å<sup>3</sup></b>	628.79(9)	732.93(7)	16881(9)
<b><i>Z</i></b>	4	4	4
<b><i>D</i><sub>calc</sub> / g cm<sup>-3</sup></b>	1.626	1.379	1.251
<b><i>R</i><sub>int</sub></b>	0.0769	0.0358	0.1671
<b><i>R</i><sub>1</sub> [<i>I</i> ≥ 2σ(<i>I</i>)]</b>	0.0806	0.0544	0.1209
<b><i>wR</i><sub>2</sub> [all data]</b>	0.2151	0.1595	0.3564

**Table 6** Summary of crystallographic data for salicylaldehydes and a co-crystal of 5-methoxysalicylaldehyde with **3.3b**.

Despite the lack of strong intermolecular interactions in their crystal structures, the majority of salicylaldehydes are solids at room temperature. The 5-methoxy derivative is a notable exception, and thus a good candidate for incorporation into alternative solid forms under ambient conditions. Given that the crystal structure of 5-methoxysalicylaldehyde had not been determined previously, attempts were made to obtain single crystals of the compound for analysis by SC-XRD. Freezing the liquid by rapid cooling to -20 °C results in a poor-

quality, polycrystalline material. However, adding these crystals as seeds to 5-methoxysalicylaldehyde slightly below its melting point (4 °C) allows for the formation of larger, good-quality crystals with a block-shaped habit. The crystal structure of the compound, structure **XXI**, displays layers of molecules with an uneven spacing, as observed in the form I structure of 5-nitrosalicylaldehyde. However, each aromatic ring forms only one significant  $\pi$ - $\pi$  stacking motif, with a relatively long centroid-to-centroid distance of 3.9064(8) Å. The lack of interactions between layers is the likely cause of the material's low melting point, and may be attributed to the non-planarity of the methoxy substituent, which prevents neighbouring molecules from adopting the eclipsed configurations necessary for  $\pi$ - $\pi$  stacking to take place.

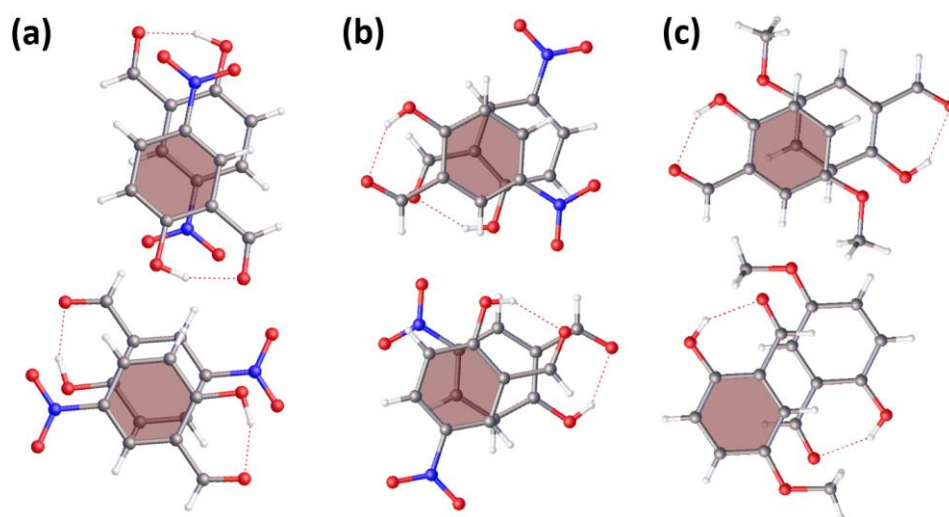


**Fig. 73** Stacking motifs in form I (a) of 5-nitrosalicylaldehyde (CSD refcode DUJBUG<sup>49</sup>) and a second polymorph, form II (structure **XX**), obtained in this study (b). Crystals of 5-methoxysalicylaldehyde (structure **XXI**) display far weaker  $\pi$ - $\pi$  stacking interactions (c), as it is less favourable for neighbouring rings to adopt eclipsed configurations. Rings in two layers of the structures are shown, with those in the upper layer shaded for clarity.

Co-crystallisation of compound **3.3b** with 5-methoxysalicylaldehyde was achieved by storing a saturated ethanol solution of the bis(urea) with a large excess of the salicylaldehyde for one month. The co-crystals could also be obtained from 1-propanol under the same conditions, but attempts to replicate the process in methanol, acetonitrile and nitromethane were not successful. A poor-quality structure of the co-crystal, structure **XXII**, was obtained by SC-XRD. The asymmetric unit of the crystal structure consists of eight molecules of **3.3b** and two of the salicylaldehyde. As in structure **XVI**, the bis(urea) molecules form

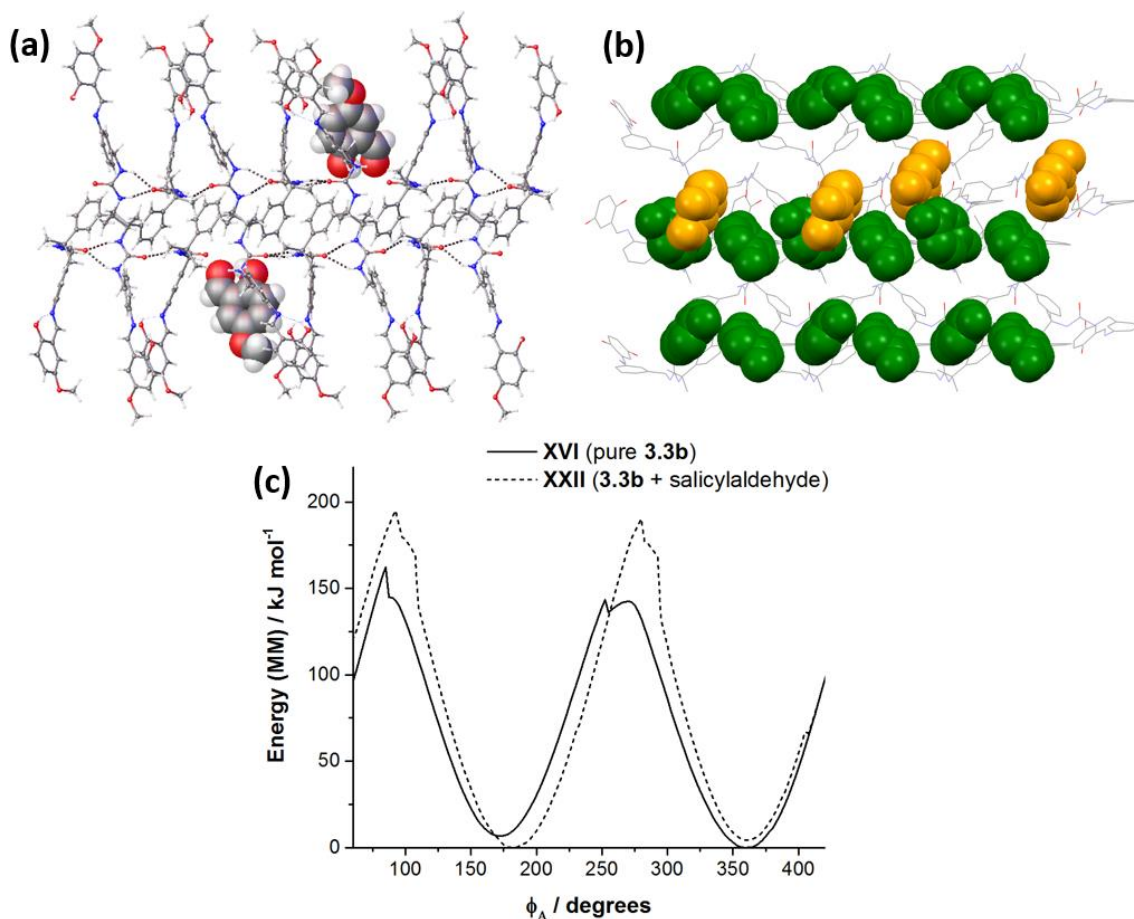


**Fig. 74** In co-crystal structure **XXII**, molecules of 5-methoxysalicylaldehyde (shown in space-fill representation) occupy space between the anil groups of **3.3b** (a). When compared with crystals of the pure anil (structure **XVI**), it is apparent that the presence of the guest (shown in orange) results in a loss of symmetry and alters the arrangement of anil groups (shown in green) on the lamellar surface (b). MM calculations suggest that anil groups in structure **XXII** are less able to undergo *cis-trans* isomerisations than those in structure **XVI**, due to increased steric hindrance around the imine moiety (c). It should be noted that the area per anil group is significantly reduced: structure **XVI** exhibits an  $A_{\text{mol}}$  value of  $57.4 \text{ \AA}^2$ , the value for structure **XXII** is 10% lower at just  $51.9 \text{ \AA}^2$ .

symmetric lamellar  $\alpha$ -tape networks with an [AB] repeat unit (Fig. 74a). The molecules of salicylaldehyde are not involved in any significant supramolecular motifs, but occupy spaces between the anil groups to produce an arrangement markedly different to that of the pure system (Fig. 74b). MM calculations indicate that anil groups closest to the guest species on the surface of a model crystal undergo *cis-trans* transformations less readily than the anil groups in structure **XVI** (Fig. 74c): the activation barrier for the pedal-like motion is higher by  $14 \text{ kJ mol}^{-1}$ , and similar to the value for the non-photochromic structure **XIX**. Unfortunately, it was not possible to ascertain whether the photochromic

behaviour of pure **3.3b** is retained in the co-crystal, as the crystals could not be prepared in sufficient quantities for their optical properties to be reliably assessed.

Studies of crystal formation in supramolecular gels have revealed that chemical interactions of the guest species with the LMWG can influence both the structure and the habit of the material formed.<sup>50-52</sup> Indeed, a promising strategy is to develop LMWGs with end groups that are structurally similar to the crystallising molecule, in order to template the development of particular nuclei.<sup>53, 54</sup> Structure **XXII** represents one of the first direct observations of a pharmaceutically active<sup>55</sup> compound co-assembling with a tailored LMWG in the solid state. The work clearly demonstrates that even weakly interacting guests may be incorporated into a gelator aggregate, and suggests that such non-gelating additives could be used to tune the physical properties of supramolecular gels for practical applications.

### 3.3 Conclusions

The arrangement of molecules following self-assembly is an important factor governing the solid-state reactivity of molecular switches. Isomerisation of anil groups between the enol and *trans*-keto forms involves only small changes in conformation, but is nonetheless strongly influenced by the environment of the reacting moiety. Indeed, adjusting the spacer configuration of anil-substituted bis(urea)s can lead to marked changes in their susceptibility to photochromic transitions, as well as significant variations in gelation capacity. DFT calculations indicate that the transition energy for the switching process is only weakly affected by the substitution patterns of the salicylidene and aniline rings. However, molecular mechanics models of single-crystal X-ray structures reveal that rotations of surface anil groups are highly sensitive to the mode of packing: depending on the arrangement of molecules around the reacting moiety, the activation barrier may be as low as that of the free species or comparable to the value for a molecule in the bulk. It is demonstrated that one derivative exhibits more pronounced chromic behaviour than most other analogues due to a lack of steric crowding in the region of the imine group. Moreover, co-assembly of the compound with the corresponding salicylaldehyde significantly alters the

arrangement of surface anil groups, suggesting that the optical properties of the system might be tuned without modifications to the molecular structure. These observations demonstrate the extent to which solvent-gelator interactions might perturb the pathway for isomerisation, providing a rational explanation for the lack of chromic behaviour in the bis(urea) gels. In addition, the work illustrates the largescale impact of guest species on the structure of gelator assemblies, and the potential usefulness of co-gelators and other additives for optimising the reactivity of molecular switches in supramolecular gels.

### 3.4 References

1. C. D. Jones and J. W. Steed, *Chem. Soc. Rev.*, 2016, **45**, 6546-6596.
2. J. Andréasson and U. Pischel, *Chem. Soc. Rev.*, 2010, **39**, 174-188.
3. D. D. Díaz, D. Kühbeck and R. J. Koopmans, *Chem. Soc. Rev.*, 2011, **40**, 427-448.
4. B. Escuder, F. Rodríguez-Llansola and J. F. Miravet, *New J. Chem.*, 2010, **34**, 1044-1054.
5. H. J. Moon, D. Y. Ko, M. H. Park, M. K. Joo and B. Jeong, *Chem. Soc. Rev.*, 2012, **41**, 4860-4883.
6. A. R. Hirst, B. Escuder, J. F. Miravet and D. K. Smith, *Angew. Chem. Int. Edit.*, 2008, **47**, 8002-8018.
7. D. Buenger, F. Topuz and J. Groll, *Prog. Polym. Sci.*, 2012, **37**, 1678-1719.
8. E. Hadjoudis and I. M. Mavridis, *Chem. Soc. Rev.*, 2004, **33**, 579-588.
9. F. Robert, P. L. Jacquemin, B. Tinant and Y. Garcia, *Crystengcomm*, 2012, **14**, 4396-4406.
10. J. E. Kwon and S. Y. Park, *Adv. Mater.*, 2011, **23**, 3615-3642.
11. M. Ziółek, G. Burdziński and A. Douhal, *Photochem. Photobiol. Sci.*, 2012, **11**, 1389-1400.
12. F. Robert, A. D. Naik, B. Tinant, R. Robiette and Y. Garcia, *Chem. Eur. J.*, 2009, **15**, 4327-4342.
13. F. Robert, A. D. Naik, F. Hidara, B. Tinant, R. Robiette, J. Wouters and Y. Garcia, *Eur. J. Org. Chem.*, 2010, 621-637.
14. S. Datta and S. Bhattacharya, *Chem. Commun.*, 2012, **48**, 877-879.
15. P. Chen, R. Lu, P. C. Xue, T. H. Xu, G. J. Chen and Y. Y. Zhao, *Langmuir*, 2009, **25**, 8395-8399.
16. P. Xue, R. Lu, G. Chen, Y. Zhang, H. Nomoto, M. Takafuji and H. Ihara, *Chem. Eur. J.*, 2007, **13**, 8231-8239.
17. L. B. Zang, H. X. Shang, D. Y. Wei and S. M. Jiang, *Sens. Actuators, B*, 2013, **185**, 389-397.
18. Q. X. Jin, L. Zhang, X. F. Zhu, P. F. Duan and M. H. Liu, *Chem. Eur. J.*, 2012, **18**, 4916-4922.
19. J. K. H. Hui, Z. Yu, T. Mirfakhrai and M. J. MacLachlan, *Chem. Eur. J.*, 2009, **15**, 13456-13465.
20. M. A. Kochman, A. Bil and C. A. Morrison, *Phys. Chem. Chem. Phys.*, 2013, **15**, 10803-10816.
21. S. P. Kwasniewski, J. P. François and M. S. Deleuze, *J. Phys. Chem. A*, 2003, **107**, 5168-5180.
22. J. Harada and K. Ogawa, *Cryst. Growth Des.*, 2014, **14**, 5182-5188.
23. E. Titov, G. Granucci, J. P. Götzte, M. Persico and P. Saalfrank, *J. Phys. Chem. Lett.*, 2016, **7**, 3591-3596.

24. J. A. Gámez, O. Weingart, A. Koslowski and W. Thiel, *J. Chem. Theory Comput.*, 2012, **8**, 2352-2358.
25. V. Cantatore, G. Granucci, G. Rousseau, G. Padula and M. Persico, *J. Phys. Chem. Lett.*, 2016, **7**, 4027-4031.
26. G. Pace, V. Ferri, C. Grave, M. Elbing, C. von Hänisch, M. Zharnikov, M. Mayor, M. A. Rampi and P. Samori, *Proc. Natl. Acad. Sci. U.S.A.*, 2007, **104**, 9937-9942.
27. S. Pipolo, E. Benassi and S. Corni, *Langmuir*, 2013, **29**, 10505-10512.
28. J. Harada, H. Uekusa and Y. Ohashi, *J. Am. Chem. Soc.*, 1999, **121**, 5809-5810.
29. I. O. Staehle, B. Rodríguez-Molina, S. I. Khan and M. A. Garcia-Garibay, *Cryst. Growth Des.*, 2014, **14**, 3667-3673.
30. J. Bernstein, R. E. Davis, L. Shimoni and N. L. Chang, *Angew. Chem. Int. Edit.*, 1995, **34**, 1555-1573.
31. A. Pramanik, T. H. Russ, D. R. Powell and M. A. Hossain, *Acta Crystallogr. Sect. E.*, 2012, **68**, 18.
32. P. Terech and R. G. Weiss, *Chem. Rev.*, 1997, **97**, 3133-3159.
33. M. Jaspers, M. Dennison, M. F. J. Mabesoone, F. C. MacKintosh, A. E. Rowan and P. H. J. Kouwer, *Nat. Commun.*, 2014, **5**, 5808.
34. C. E. Stanley, N. Clarke, K. M. Anderson, J. A. Elder, J. T. Lenthall and J. W. Steed, *Chem. Commun.*, 2006, **30**, 3199-3201.
35. L. J. Gibson and M. F. Ashby, *Proc. R. Soc. London, A*, 1982, **382**, 43-49.
36. C. X. Zhang, T. R. Zhang, N. Ji, Y. Zhang, B. L. Bai, H. T. Wang and M. Li, *Soft Matter*, 2016, **12**, 1525-1533.
37. J. Málek, *Thermochim. Acta*, 2000, **355**, 239-253.
38. M. Avrami, *J. Chem. Phys.*, 1939, **7**, 1103-1112.
39. M. L. Myrick, M. N. Simcock, M. Baranowski, H. Brooke, S. L. Morgan and J. N. McCutcheon, *Appl. Spectrosc. Rev.*, 2011, **46**, 140-165.
40. A. D. Becke, *J. Chem. Phys.*, 1993, **98**, 1372-1377.
41. T. H. Dunning, *J. Chem. Phys.*, 1989, **90**, 1007-1023.
42. W. J. Hehre, R. Ditchfield and J. A. Pople, *J. Chem. Phys.*, 1972, **56**, 2257-2261.
43. P. Dauber-Osguthorpe, V. A. Roberts, D. J. Osguthorpe, J. Wolff, M. Genest and A. T. Hagler, *Proteins*, 1988, **4**, 31-47.
44. T. A. Halgren, *J. Comput. Chem.*, 1996, **17**, 520-552.
45. F. Würthner, T. E. Kaiser and C. R. Saha-Möller, *Angew. Chem. Int. Edit.*, 2011, **50**, 3376-3410.
46. M. Kasha, *Radiat. Res.*, 1963, **20**, 55-70.
47. Y. Qian, S. Y. Li, Q. Wang, X. H. Sheng, S. K. Wu, S. Q. Wang, J. Li and G. Q. Yang, *Soft Matter*, 2012, **8**, 757-764.
48. M. K. Nayak, *J. Photochem. Photobiol., A*, 2011, **217**, 40-48.
49. H. Tanak, M. Macit, M. Yavuz and S. Isik, *Acta Crystallogr. Sect. E.*, 2009, **65**, O3056-U3275.
50. C. Ruiz-Palomero, S. R. Kennedy, M. L. Soriano, C. D. Jones, M. Valcárcel and J. W. Steed, *Chem. Commun.*, 2016, **52**, 7782-7785.
51. D. K. Kumar and J. W. Steed, *Chem. Soc. Rev.*, 2014, **43**, 2080-2088.
52. J. A. Foster, M. O. M. Piepenbrock, G. O. Lloyd, N. Clarke, J. A. K. Howard and J. W. Steed, *Nat. Chem.*, 2010, **2**, 1037-1043.
53. J. A. Foster, K. K. Damodaran, A. Maurin, G. M. Day, H. P. G. Thompson, G. J. Cameron, J. C. Bernal and J. W. Steed, *Chem. Sci.*, 2017, **8**, 78-84.
54. A. Dawn, K. S. Andrew, D. S. Yufit, Y. X. Hong, J. P. Reddy, C. D. Jones, J. A. Aguilar and J. W. Steed, *Cryst. Growth Des.*, 2015, **15**, 4591-4599.
55. O. I. Shadyro, V. L. Sorokin, G. A. Ksendzova, O. V. Savinova, S. N. Samovich, N. I. Pavlova, G. I. Polozov and E. I. Boreko, *Pharm. Chem. J.*, 2016, **50**, 156-158.

## 4. Bis(urea) gelators: a designer's guide

### 4.1 Background

Despite an abundance of insights into the self-assembled structures of small-molecule gels, identifying new LMWGs prior to experimental testing remains a challenge.<sup>1</sup> Gelation ability is dictated by a large number of parameters, which vary in importance depending on the LMWG involved. For example, strong hydrogen bond acceptors such as anions, pyridines and carboxylic acids are often found to reduce the gelation capacities of bis(urea) gelators, by inhibiting the formation of  $\alpha$ -tape motifs.<sup>2,3</sup> In some systems, however, species of this type may facilitate gel formation by giving rise to additional continuous hydrogen bonding motifs,<sup>4,5</sup> or link mono(urea)s into dimeric assemblies with improved gelation properties.<sup>6</sup> A further complication is that the presence of  $\alpha$ -tapes is not always associated with gel formation. Competition between gelation and crystallisation processes is common,<sup>7</sup> and may be strongly influenced by environmental variables such as temperature, pH and solvent composition.<sup>8</sup>

To be able to engineer LMWGs with minimal reliance on serendipity and empirical optimisation, it is essential to understand all of the factors contributing to gel formation. A promising strategy is to correlate the structures of urea-containing species in the Cambridge Structural Database<sup>9</sup> (CSD) with the incidence of commonly occurring supramolecular motifs (Fig. 75a). A survey of version 5.36 of the CSD (Section 9.2) reveals 1568 unique and well-resolved structures of acyclic disubstituted ureas, of which 980 (63%) are based on mono(urea)s, 214 (14%) on bis(urea)s, and 267 (17%) on small molecules with between three and 18 urea groups (Fig. 75b). The remaining 107 structures (7%) consist of coordination polymers, which in all cases incorporate ligands with one, two or three urea groups. Surprisingly, urea-urea interactions are observed in just 648 (41%) of the structures and tape motifs in 385 (25%), suggesting that a large proportion of urea-based systems in the literature are not compatible with gel formation (Fig. 75d).

A benefit of the urea group is that it reliably adopts one of two stable conformations,<sup>10</sup> each of which is associated with a predictable and well-defined hydrogen bonding motif (Fig. 75c).<sup>11</sup> The *syn-syn* conformer, in which both O-C-

N-H torsion angles are approximately  $180^\circ$ , typically interacts via  $R_2^1(6)$  urea-urea synthons.<sup>12, 13</sup> In the *syn-anti* conformer, meanwhile, one of the urea substituents is oriented  $180^\circ$  to the carbonyl group, and  $R_2^2(8)$  synthons are often observed.<sup>14</sup> While both urea conformers may be incorporated into continuous hydrogen bonding tape motifs, it is the *syn-syn* conformer that gives rise to the  $\alpha$ -tapes usually associated with gel formation. The stabilities of the conformers are dictated by the urea substituents and solvent environment but rarely differ to a substantial degree. Indeed, the antidiabetic drug glimepiride, a sulfonyl mono(urea), adopts different conformations in its two polymorphic forms (refcodes TOHBUN01 and TOHBUN02).<sup>15, 16</sup> Likewise, there are five bis(urea) structures in the CSD featuring urea groups in both conformations,<sup>13, 17-20</sup> and even one example (FANWIB<sup>13</sup>) in which interactions between the different conformers give rise to a single hydrogen bonding tape motif.

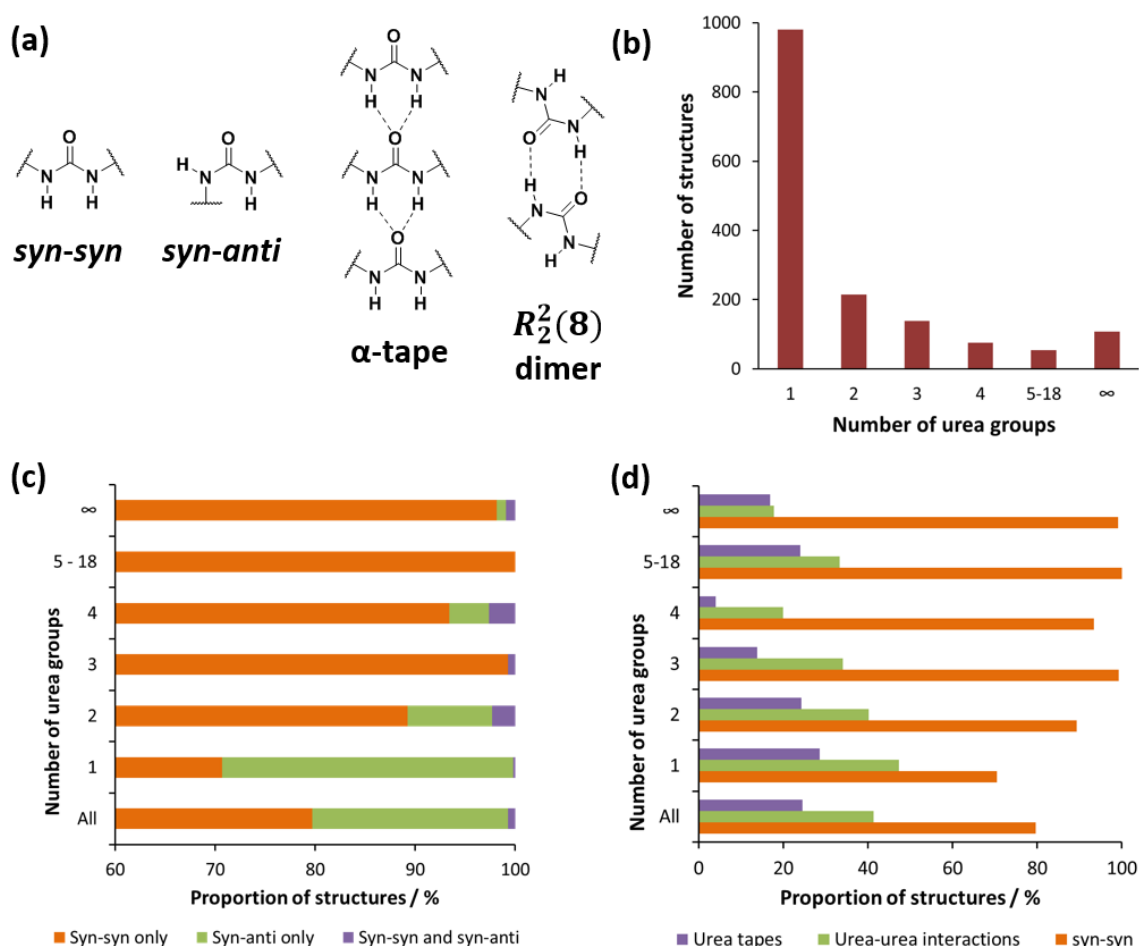


**Fig. 75** Common urea conformers and supramolecular motifs (a) and frequencies of urea-based structures in the CSD (version 5.36) as a function of the number of urea groups (b). *Syn-syn* conformers are present in most of the structures (c), but urea-urea interactions are observed in less than half (d).



Predicting the outcome of urea self-assembly can be problematic. Like many LMWGs, urea-based gelators are often highly flexible, so can exist in a large number of low-energy molecular conformations.<sup>14, 21-24</sup> Some researchers have attempted to reduce the computational cost of crystal structure prediction by basing candidate structures on the results of geometry optimisation calculations in the gas phase.<sup>21</sup> A drawback of this approach is that it overlooks situations where a less favourable conformation gives rise to a more favourable packing mode or supramolecular motif. Among mono(urea)s, for example, 71% of structures feature *syn-syn* urea groups but only 39% of these display urea-urea motifs. By contrast, ureas in the *syn-anti* conformation interact relatively frequently in the crystalline phase, displaying urea-urea motifs in 67% of cases.

Tape motifs account for 97% of interactions between crystalline *syn-syn* mono(urea)s, and approximately 92% of these may be categorised as ideal  $\alpha$ -tapes consisting only of well-defined  $R_2^1(6)$  urea-urea synthons. Owing to their rigid and continuous structure,  $\alpha$ -tapes impose a number of constraints on the crystallisation outcome. In particular, tapes in most crystal structures lie parallel to a cell axis, so the corresponding unit cell parameter must equal an integer multiple of the urea-urea repeat distance. An analysis of tape-containing mono(urea) structures reveals a high frequency of cell dimensions near 4.6 and 9.2 Å, while structures lacking tapes conform to a broader distribution of cell parameters (Fig. 76). Based on these results, the mean repeat distance of the  $\alpha$ -tape may be estimated as 4.65 Å, in agreement with observations from individual single-crystal structures and STM investigations.<sup>25</sup> A statistical analysis suggests that the presence of a cell axis 4.4-4.9 Å in length (the approximate width of the peak in the probability density distribution) is sufficient to identify  $\alpha$ -tapes in 43% of mono(urea) structures, with a false positive rate of just 15%. An axis of 8.8-9.7 Å, meanwhile, is associated with real  $\alpha$ -tapes in 42% of cases. In combination, these observations could act as a positive test for  $\alpha$ -tapes with 76% sensitivity and 80% specificity, providing useful structural information for systems that cannot be fully characterised by SC-XRD. It is worth noting that the cell parameters of bis(urea) crystals display comparable trends, although axes of 4.6 Å are far less common and parameters around 9 and 18 Å more frequently observed.

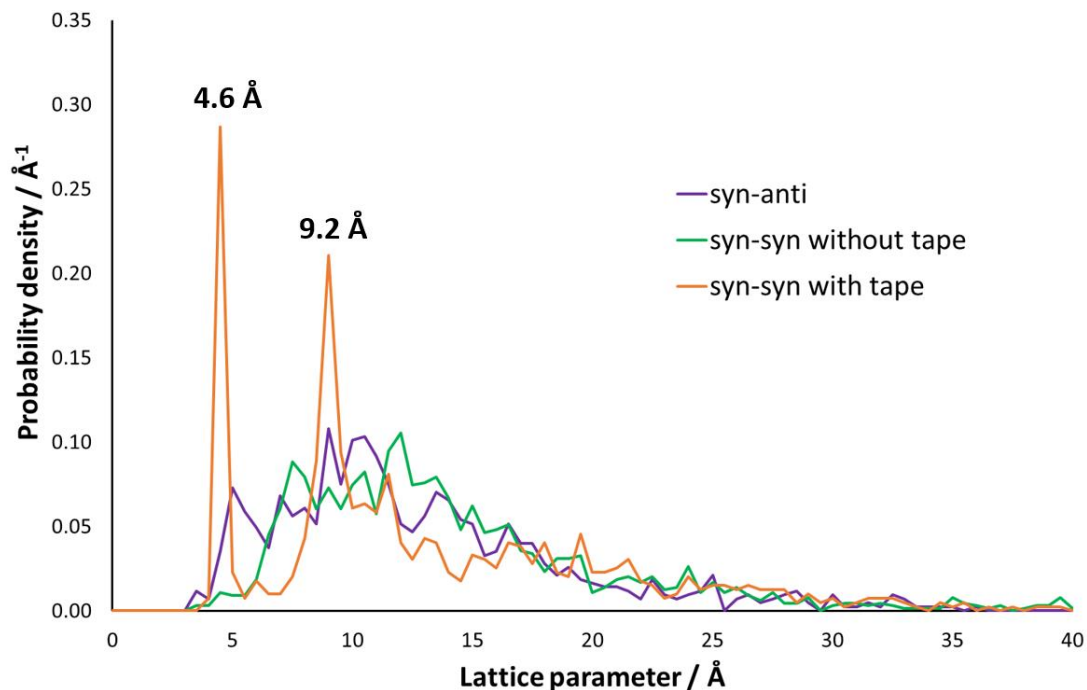


**Fig. 76** Probability of observing particular lattice parameters for structures with different urea conformers and supramolecular motifs. The probability density is calculated such that the area under the curve over an interval of 0.5 Å (units Å<sup>-1</sup> x Å) yields the fraction of lattice parameters within that range.

When designing urea-based LMWGs, it would be useful to be aware of factors that promote or inhibit  $\alpha$ -tape formation (Fig. 77). Among mono(urea)s, urea groups in the *syn-anti* conformation are often involved in intramolecular hydrogen bonds with neighbouring moieties. For example, compounds containing a carbonyl group adjacent to the urea are observed in 33% of the surveyed *syn-anti* systems, and are predictive of a *syn-anti* conformation in 94% of cases. Other electron-withdrawing substituents and heteroatoms  $\alpha$  to the urea group are also disproportionately common within the *syn-anti* population. Crystals of the *syn-syn* conformer with  $\alpha$ -tape networks are most strongly favoured by ureas with two alkyl substituents. By contrast, *syn-syn* ureas with no tape motifs may be targeted by avoiding alkyl substituents<sup>3, 26</sup> or, more reliably, through the inclusion of ions. Indeed, salts account for 37% of *syn-syn* structures lacking tape motifs, whereas *syn-anti* and tape-containing *syn-syn* structures contain ions in just 7.4 and 4.2% of cases respectively. Non-ionic hydrogen bonding species such as water and methanol affect the incidence of  $\alpha$ -tapes in a similar fashion, occurring in *syn-syn* structures without tapes between three and five times more frequently than would be expected by chance.

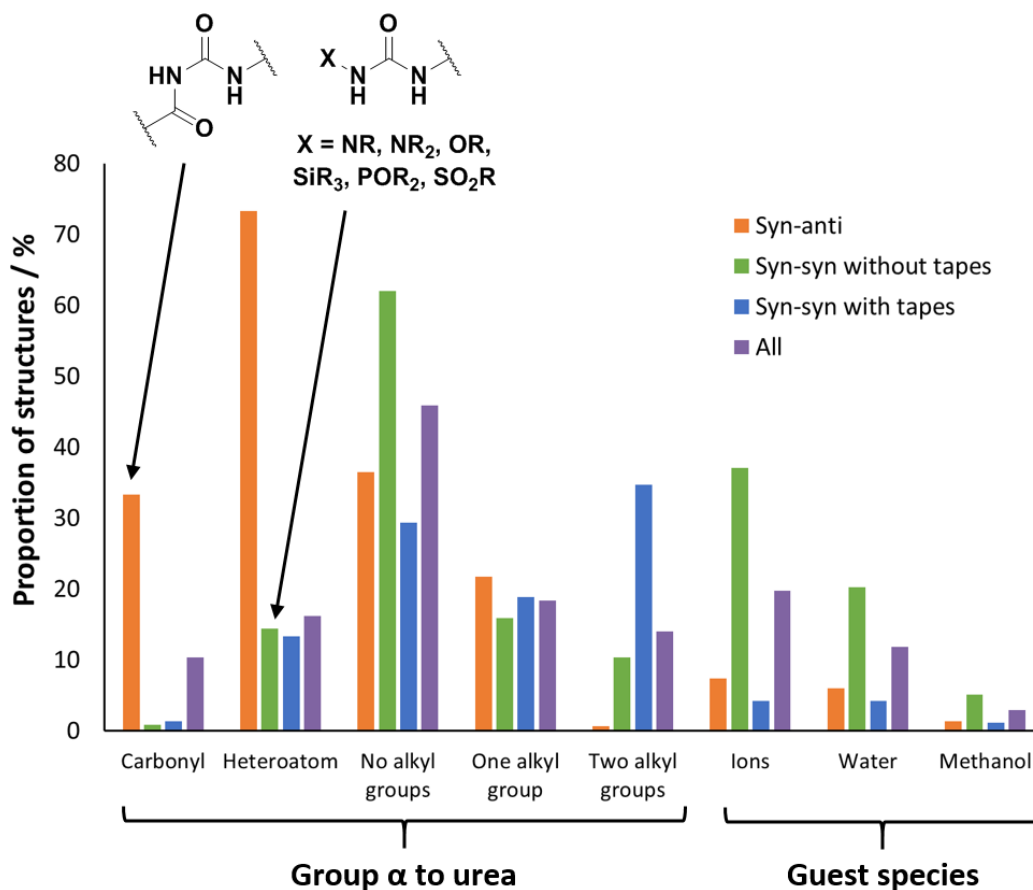


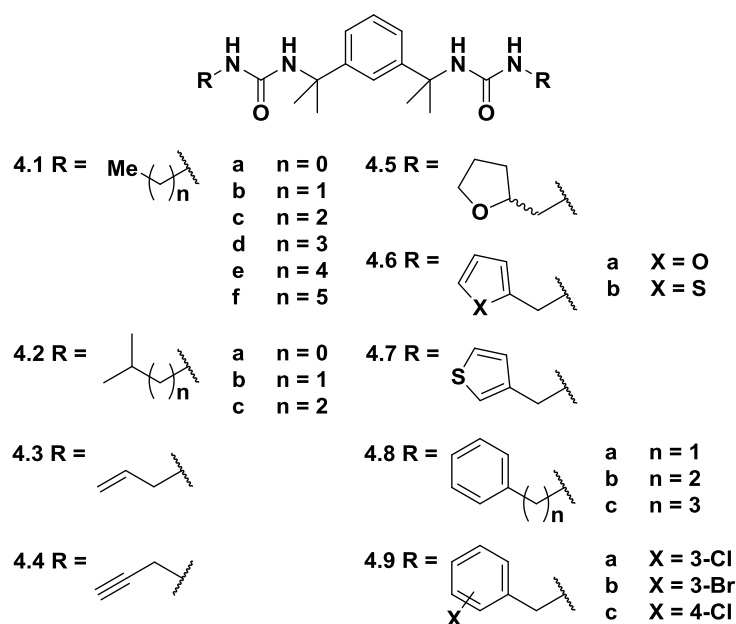
**Fig. 77** Frequency of key structural features and guest species in mono(urea) systems with different urea conformers and hydrogen bonding motifs.

The aim of this investigation was to correlate the gelation properties of bis(urea)s with the arrangements of molecules in their single-crystal structures. Systems containing  $\alpha$  tapes were targeted by avoiding ionic species and molecules capable of intramolecular hydrogen bonding. In addition, the spacer and end group were chosen to place  $sp^3$  carbon sites  $\alpha$  to the urea group, as structures of this type are the most compatible with  $\alpha$ -tape formation. Compounds derived from 1,3-bis(1-isocyanato-1-methylethyl)benzene<sup>27-30</sup> and an aliphatic amine were found to crystallise readily from a range of polar solvents and display interesting diversity in their self-assembly behaviour. Gel formation was shown to be strongly linked to the presence of lamellar hydrogen bonding networks in the corresponding crystal structures, and could be predicted in some cases via MD simulations of isolated assemblies in the gas phase. The study illustrates the utility of structure-property correlations in the design and identification of effective LMWGs, and highlights a number of general principles that could inform future investigations of urea-based crystals and soft materials.

## 4.2 Results and discussion

### 4.2.1 Synthesis and crystallisation

Bis(urea)s with different end groups were prepared by reacting 1,3-bis(1-isocyanato-1-methylethyl)benzene with a range of aliphatic amines in excess. Most of the compounds precipitate on formation and can be purified by washing with chloroform. Recrystallisation of the compounds was performed by slow cooling hot solutions of the compounds in methanol, and yielded good-quality crystals suitable for SC-XRD analysis for all derivatives except **4.1e**, **4.1f** and **4.7** (Table 7). Compound **4.5** was synthesised as a mixture of diastereomers, but a crystal structure was acquired for the *meso* form only. Conversely, two polymorphs each of compounds **4.2a** (structures **XXVII** and **XXVIII**), **4.4** (structures **XXXII** and **XXXIII**) and **4.6b** (structures **XXXV** and **XXXVI**) were obtained. Structures **XXXII** and **XXXV** could be crystallised reproducibly from solutions of compounds **4.4** and **4.6b** in methanol, while the polymorphs **XXXIII** and **XXXVI** were isolated from ethanol and 1-propanol respectively. Both polymorphs of **4.2a** were crystallised from methanol, but the monoclinic structure **XXVIII** was found to be a “disappearing” polymorph:<sup>31</sup> the material was obtained only once by slow recrystallization, and all subsequent trials in methanol and other solvents always yielded the tetragonal system **XXVII**. Comparison of the bis(urea) structures reveals a number of common features (section 4.2.2), which in some cases correlate with the gelation behaviour of the compounds in a range of substituted aromatic solvents (section 4.2.3).



#### 4.2.2 Structural trends

The bis(urea) crystals can be subdivided according to the symmetry and dimensionality of their  $\alpha$ -tape networks. Of the 21 crystal structures obtained, 18 consist of lamellar hydrogen bonding networks with [AB] or [AABB] repeat units. In nine of these systems, the end groups of the bis(urea) molecules are distributed symmetrically between the two faces of the lamellar plane. Asymmetric lamellar structures (Fig. 78) mostly exhibit larger areas per molecule,  $A_{\text{mol}}$ , than their symmetric counterparts (Fig. 79), but end groups are accommodated on just one face of the lamellae so occupy a smaller area overall. Indeed, the area per end group in symmetric lamellae (53-64 Å<sup>2</sup>) is 32-60% larger than that in asymmetric systems (36-40 Å<sup>2</sup>). The weaker steric constraints of symmetric lamellae mean that they are particularly common among bis(urea)s with relatively bulky or inflexible end groups. For example, lamellae in the structure of the *i*-pentyl derivative **4.2c** (**XXX**) are symmetric, while those in the structure of the smaller *i*-butyl analogue **4.2b** (**XXIX**) are asymmetric. The *n*-alkyl derivatives **4.1a**, **4.1b**, **4.1c** and **4.1d** (structures **XXIII**, **XXIV**, **XXV** and **XXVI** respectively) all produce asymmetric lamellae and compounds with benzylic end groups, such as **4.8a**, **4.8b**, **4.8c** and **4.9a** (structures **XXXVIII**, **XXXIX**, **XL** and **XLI** respectively), generally give rise to symmetric assemblies. Compound **4.9b** is a notable outlier, as its structure (**XLII**) exhibits asymmetric lamellae despite the presence of bulky bromo-substituted benzyl end groups. Conversely, the propargyl derivative **4.4** forms symmetric lamellae in one of its polymorphs (**XXXII**) even though the alkyne end group is relatively small. It is worth noting that molecules with less bulky end groups tend to lie more parallel to the lamellar plane, so the symmetric lamellae formed by **4.2a** (in structure **XXVIII**) and **4.4** display large values of  $A_{\text{mol}}$  comparable to those of asymmetric structures.

All of the asymmetric lamellae consist of relatively simple [AB] hydrogen bonding networks. Accommodating bulky end groups in a close-packed layered structure is more difficult, and symmetric lamellae may therefore exhibit more unusual network topologies. However, for analogues with very sterically demanding end groups, forming lamellar assemblies at all is geometrically unfeasible. These compounds may still interact via  $\alpha$ -tape motifs, but the tapes are arranged into three-dimensional networks with relatively complex repeat

units (Fig. 80). Topologies of this nature account for 6% of the bis(urea) structures in the literature, and occur in three (14%) of the structures in this study. Networks with the most common non-lamellar repeat unit, [ABCD], are observed in the structure of **4.3 (XXXI)** and one of the polymorphs of **4.2a (XXVII)**. By contrast, the structure of compound **4.9c (XLIII)** displays the unprecedented repeat unit [ABABCD<sub>2</sub>CD]. It is likely that the complexity of the repeat unit increases as the end group becomes more difficult to accommodate within a continuous network of parallel  $\alpha$ -tapes. Such networks are poorly compatible with gel formation, as the surfaces of the aggregates are similar in energy and unlikely to propagate in an anisotropic fashion.

	<b>4.1a (XXIII)</b>	<b>4.1b (XXIV)</b>	<b>4.1c (XXV)</b>	<b>4.1d (XXVI)</b>	<b>4.2a (XXVII)</b>
<b>Formula</b>	C <sub>16</sub> H <sub>26</sub> N <sub>4</sub> O <sub>2</sub>	C <sub>18</sub> H <sub>30</sub> N <sub>4</sub> O <sub>2</sub>	C <sub>20</sub> H <sub>34</sub> N <sub>4</sub> O <sub>2</sub>	C <sub>22</sub> H <sub>38</sub> N <sub>4</sub> O <sub>2</sub>	C <sub>20</sub> H <sub>34</sub> N <sub>4</sub> O <sub>2</sub>
<b>Formula weight</b>	306.41	334.46	362.51	390.56	362.51
<b>Space group</b>	<i>C2/c</i>	<i>C2</i>	<i>P2</i>	<i>Pbca</i>	<i>P4<sub>3</sub>2<sub>1</sub>2</i>
<b><i>a</i> / Å</b>	25.0139(13)	18.0134(12)	9.1013(9)	8.9115(2)	11.000(2)
<b><i>b</i> / Å</b>	9.1736(3)	13.8756(7)	7.1705(9)	16.2345(3)	11.000(2)
<b><i>c</i> / Å</b>	16.0505(7)	18.0080(13)	16.298(3)	32.4328(7)	18.106(4)
<b><math>\beta</math> / °</b>	103.464(4)	117.631(9)	91.805(12)	90	90
<b><i>V</i> / Å<sup>3</sup></b>	3581.9(3)	3987.7(5)	1063.1(3)	4692.17(17)	2190.7(11)
<b><i>Z</i></b>	8	8	2	8	4
<b><i>D</i><sub>calc</sub> / g cm<sup>-3</sup></b>	1.136	1.114	1.132	1.106	1.099
<b><i>R</i><sub>int</sub></b>	0.0463	0.0710	0.1162	0.1116	0.0726
<b><i>R</i><sub>1</sub> [<i>I</i> ≥ 2σ (<i>I</i>)]</b>	0.0539	0.0883	0.0984	0.0637	0.0682
<b>w<i>R</i><sub>2</sub> [all data]</b>	0.1377	0.1340	0.2246	0.1738	0.1835
	<b>4.2a (XXVIII)</b>	<b>4.2b (XXIX)</b>	<b>4.2c (XXX)</b>	<b>4.3 (XXXI)</b>	
<b>Formula</b>	C <sub>20</sub> H <sub>34</sub> N <sub>4</sub> O <sub>2</sub>	C <sub>22</sub> H <sub>38</sub> N <sub>4</sub> O <sub>2</sub>	C <sub>24</sub> H <sub>42</sub> N <sub>4</sub> O <sub>2</sub>	C <sub>20</sub> H <sub>30</sub> N <sub>4</sub> O <sub>2</sub>	
<b>Formula weight</b>	362.51	390.56	418.62	358.48	
<b>Space group</b>	<i>P2<sub>1</sub>/c</i>	<i>Pna2<sub>1</sub></i>	<i>P2<sub>1</sub></i>	<i>P2<sub>1</sub>2<sub>1</sub>2<sub>1</sub></i>	
<b><i>a</i> / Å</b>	13.876(4)	9.2810(3)	9.3073(16)	10.5775(13)	
<b><i>b</i> / Å</b>	18.058(4)	16.7231(6)	23.098(4)	10.8913(11)	
<b><i>c</i> / Å</b>	17.452(3)	14.7367(5)	11.788(2)	17.9211(18)	
<b><math>\beta</math> / °</b>	93.691(15)	90	90.039(2)	90	
<b><i>V</i> / Å<sup>3</sup></b>	4363.9(18)	2287.25(14)	2534.3(8)	2064.6(4)	
<b><i>Z</i></b>	8	4	4	4	
<b><i>D</i><sub>calc</sub> / g cm<sup>-3</sup></b>	1.104	1.134	1.097	1.153	
<b><i>R</i><sub>int</sub></b>	0.1102	0.1099	0.0463	0.0569	
<b><i>R</i><sub>1</sub> [<i>I</i> ≥ 2σ (<i>I</i>)]</b>	0.0778	0.0670	0.0442	0.0573	
<b>w<i>R</i><sub>2</sub> [all data]</b>	0.2129	0.1176	0.1073	0.1427	
	<b>4.4 (XXXII)</b>	<b>4.4 (XXXIII)</b>	<b>meso-4.5 (XXXIV)</b>	<b>4.6a (XXXV)</b>	
<b>Formula</b>	C <sub>20</sub> H <sub>26</sub> N <sub>4</sub> O <sub>2</sub>	C <sub>20</sub> H <sub>26</sub> N <sub>4</sub> O <sub>2</sub>	C <sub>24</sub> H <sub>38</sub> N <sub>4</sub> O <sub>4</sub>	C <sub>24</sub> H <sub>30</sub> N <sub>4</sub> O <sub>4</sub>	
<b>Formula weight</b>	354.45	354.45	446.58	438.52	
<b>Space group</b>	<i>P2<sub>1</sub>2<sub>1</sub>2<sub>1</sub></i>	<i>Pc</i>	<i>P2<sub>1</sub>/n</i>	<i>Pca2<sub>1</sub></i>	
<b><i>a</i> / Å</b>	15.7089(7)	6.8841(6)	9.3681(10)	9.0107(6)	
<b><i>b</i> / Å</b>	17.8992(8)	8.9554(8)	11.5545(13)	15.7046(11)	
<b><i>c</i> / Å</b>	6.9256(3)	16.1358(14)	22.951(3)	16.3185(11)	
<b><math>\beta</math> / °</b>	90	90.154(3)	96.273(4)	90	
<b><i>V</i> / Å<sup>3</sup></b>	1947.32(15)	994.77(15)	2469.5(5)	2309.2(3)	
<b><i>Z</i></b>	4	2	4	4	
<b><i>D</i><sub>calc</sub> / g cm<sup>-3</sup></b>	1.209	1.183	1.201	1.261	
<b><i>R</i><sub>int</sub></b>	0.0305	0.0421	0.0984	0.1029	
<b><i>R</i><sub>1</sub> [<i>I</i> ≥ 2σ (<i>I</i>)]</b>	0.0304	0.0901	0.1123	0.0593	
<b>w<i>R</i><sub>2</sub> [all data]</b>	0.0769	0.2529	0.2976	0.1191	

	<b>4.6b (XXXVI)</b>	<b>4.6b (XXXVII)</b>	<b>4.8a (XXXVIII)</b>	<b>4.8b (XXXIX)</b>
<b>Formula</b>	C <sub>24</sub> H <sub>30</sub> N <sub>4</sub> O <sub>2</sub> S <sub>2</sub>	C <sub>24</sub> H <sub>30</sub> N <sub>4</sub> O <sub>2</sub> S <sub>2</sub>	C <sub>28</sub> H <sub>34</sub> N <sub>4</sub> O <sub>2</sub>	C <sub>30</sub> H <sub>38</sub> N <sub>4</sub> O <sub>2</sub>
<b>Formula weight</b>	470.64	470.64	458.59	486.64
<b>Space group</b>	<i>Pna</i> 2 <sub>1</sub>	<i>P</i> 2 <sub>1</sub> / <i>c</i>	<i>P</i> 2 <sub>1</sub> / <i>n</i>	<i>Pbca</i>
<b><i>a</i> / Å</b>	9.2052(9)	20.8584(11)	13.7268(5)	41.500(3)
<b><i>b</i> / Å</b>	16.6153(16)	12.8685(6)	9.3304(3)	13.8787(10)
<b><i>c</i> / Å</b>	31.583(3)	9.1945(6)	19.7303(6)	9.2292(7)
<b><math>\beta</math> / °</b>	90	97.234(5)	97.330(3)	90
<b><i>V</i> / Å<sup>3</sup></b>	4830.6(8)	2448.3(2)	2506.33(14)	5315.7(7)
<b><i>Z</i></b>	12	4	4	8
<b><i>D</i><sub>calc</sub> / g cm<sup>-3</sup></b>	1.420	1.277	1.215	1.216
<b><i>R</i><sub>int</sub></b>	0.0904	0.1308	0.0755	0.1356
<b><i>R</i><sub>1</sub> [<i>I</i> ≥ 2σ (<i>I</i>)]</b>	0.0554	0.0829	0.0627	0.0617
<b><i>wR</i><sub>2</sub> [all data]</b>	0.1514	0.1844	0.1316	0.1277
	<b>4.8c (XL)</b>	<b>4.9a (XLI)</b>	<b>4.9b (XLII)</b>	<b>4.9c (XLIII)</b>
<b>Formula</b>	C <sub>32</sub> H <sub>42</sub> N <sub>4</sub> O <sub>2</sub>	C <sub>28</sub> H <sub>32</sub> N <sub>4</sub> O <sub>2</sub> Cl <sub>2</sub>	C <sub>28</sub> H <sub>32</sub> N <sub>4</sub> O <sub>2</sub> Br <sub>2</sub>	C <sub>28</sub> H <sub>32</sub> N <sub>4</sub> O <sub>2</sub> Cl <sub>2</sub>
<b>Formula weight</b>	514.70	527.47	616.39	527.47
<b>Space group</b>	<i>P</i> 2 <sub>1</sub>	<i>P</i> 2 <sub>1</sub> / <i>c</i>	<i>Cc</i>	<i>P</i> 2 <sub>1</sub> 2 <sub>1</sub> 2 <sub>1</sub>
<b><i>a</i> / Å</b>	9.0390(4)	9.0025(7)	20.4713(12)	11.3349(5)
<b><i>b</i> / Å</b>	24.3503(10)	11.9075(8)	16.1223(9)	13.8795(6)
<b><i>c</i> / Å</b>	13.6232(5)	25.3236(17)	9.1809(5)	34.8860(13)
<b><math>\beta</math> / °</b>	92.280(2)	91.255(3)	112.567(2)	90
<b><i>V</i> / Å<sup>3</sup></b>	2996.1(2)	2714.0(3)	2798.1(3)	5488.4(4)
<b><i>Z</i></b>	4	4	4	8
<b><i>D</i><sub>calc</sub> / g cm<sup>-3</sup></b>	1.141	1.291	1.463	1.277
<b><i>R</i><sub>int</sub></b>	0.0455	0.1048	0.0401	0.2337
<b><i>R</i><sub>1</sub> [<i>I</i> ≥ 2σ (<i>I</i>)]</b>	0.0497	0.0469	0.0392	0.1021
<b><i>wR</i><sub>2</sub> [all data]</b>	0.1255	0.1141	0.0839	0.2662

**Table 7** Summary of crystallographic data for bis(urea)s in this study. Visual examination, PLATON CheckCIF tests<sup>32</sup> and analysis of *E*-value statistics confirm the assignment of structures **XXIV**, **XXV**, **XXXIII** and **XLII** to the low-symmetry space groups *P*2, *C*2, *P**c* and *C**c* respectively.

Although the crystal structure of an LMWG can provide useful insight into the molecular arrangements of its supramolecular gels,<sup>24, 33</sup> it should be noted that gelator aggregates are often highly polymorphic in nature.<sup>21, 23</sup> Polymorphism in bis(urea) systems is particularly likely if the molecules are functionalised with end groups of intermediate size and flexibility, and may result from variation in the connectivity or symmetry of the  $\alpha$ -tape assemblies. Compound **4.2a**, which features a sterically demanding *i*-propyl group adjacent to the urea, can form both lamellar and non-lamellar  $\alpha$ -tape networks (structures **XXVII** and **XXVIII** respectively). By contrast, compound **4.4** forms two lamellar polymorphs which exhibit similar layer thicknesses and *A*<sub>mol</sub> values, even though one (structure **XXXII**) comprises symmetric [AABB] lamellae (Fig. 81a) and the other (structure **XXXIII**) asymmetric [AB] assemblies (Fig. 81b). Compound **4.6b** also produces two polymorphic lamellar structures, **XXXVI** (Fig. 81c) and **XXXVII** (Fig. 81d), which differ in the symmetry of their end group distributions. In this case, however, the asymmetric system, structure **XXXVI**, displays a much larger value of *A*<sub>mol</sub> (76.5

Å<sup>2</sup>) than the symmetric form, structure **XXXVII** (59.2 Å<sup>2</sup>). Moreover, structure **XXXVII** displays one of just three examples of syn-parallel tapes in this study (Figs. 81e and 81f), while structure **XXXVI** comprises a more usual antiparallel tape arrangement.

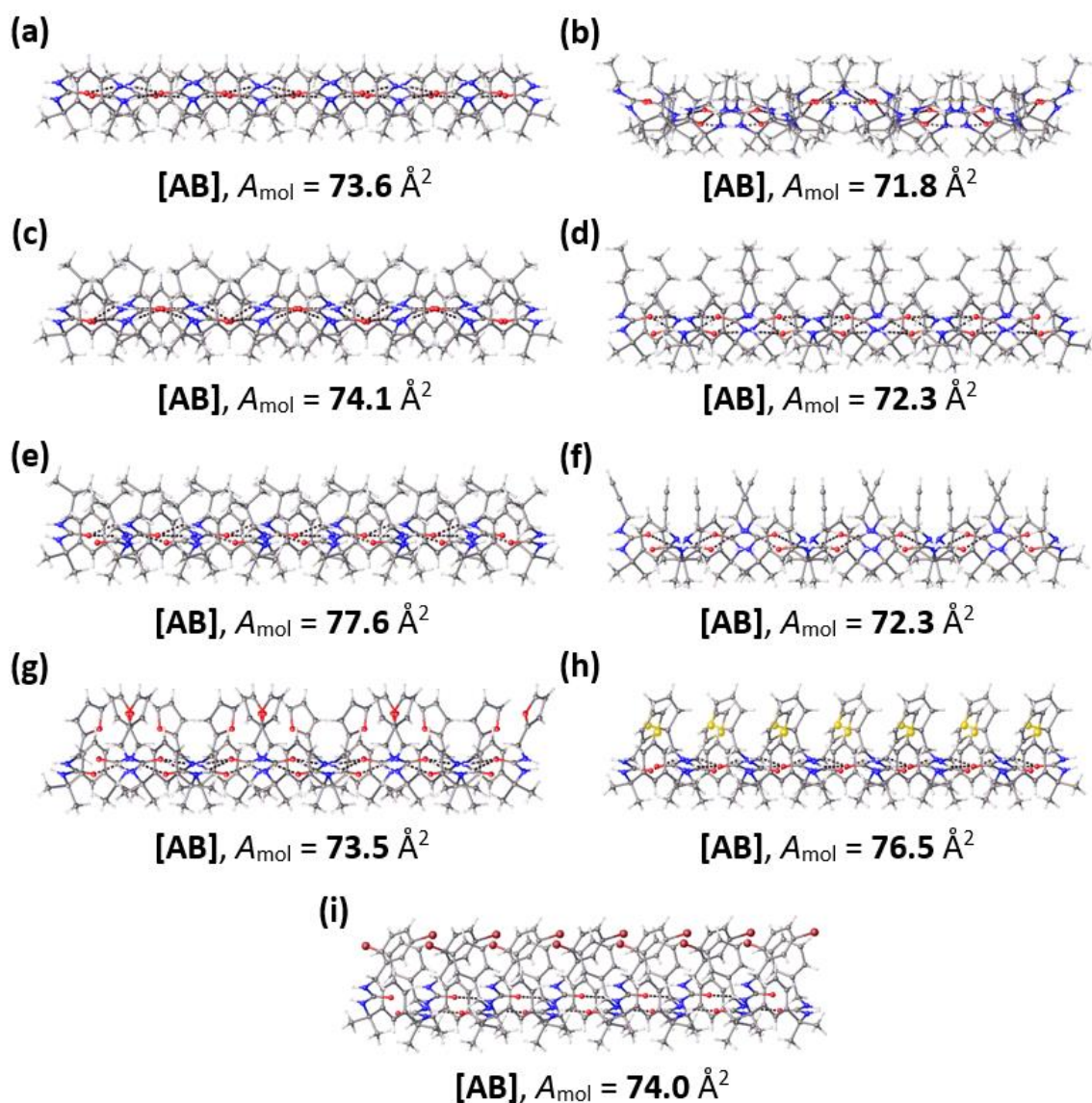


**Fig. 78** Asymmetric lamellae in the crystal structures of (a) **4.1a** (structure **XXIII**), (b) **4.1b** (**XXIV**), (c) **4.1c** (**XXV**), (d) **4.1d** (**XXVI**), (e) **4.2b** (**XXIX**), (f) **4.4** (**XXXIII**), (g) **4.6a** (**XXXV**), (h) **4.6b** (**XXXVI**) and (i) **4.9b** (**XLII**).



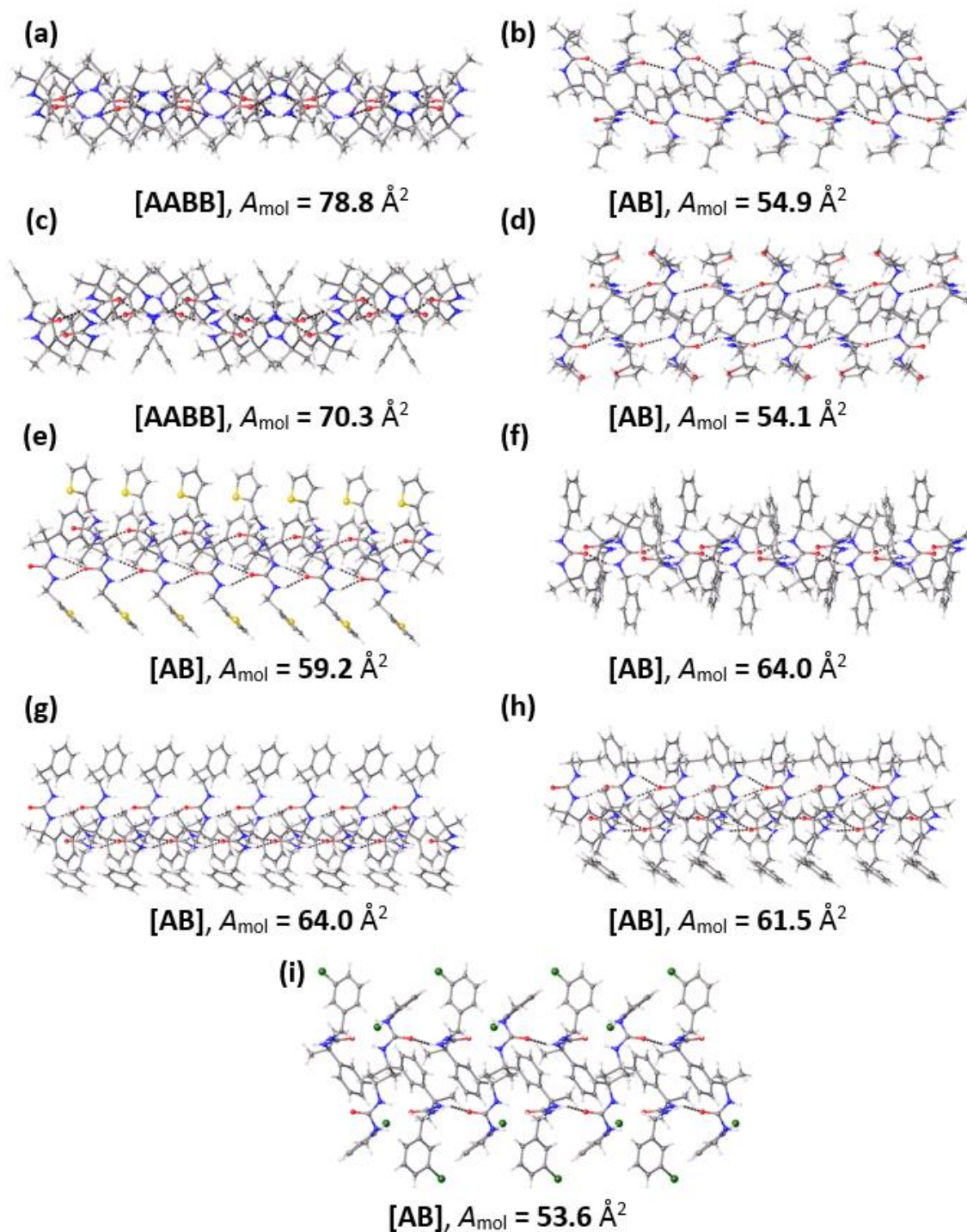


**Fig. 79** Symmetric lamellae in the crystal structures of (a) **4.2a** (structure **XXVIII**), (b) **4.2c** (**XXX**), (c) **4.4** (**XXXII**), (d) *meso*-**4.5** (**XXXIV**), (e) **4.6b** (**XXXVII**), (f) **4.8a** (**XXXVIII**), (g) **4.8b** (**XXXIX**), (h) **4.8c** (**XL**) and (i) **4.9a** (**XLI**).

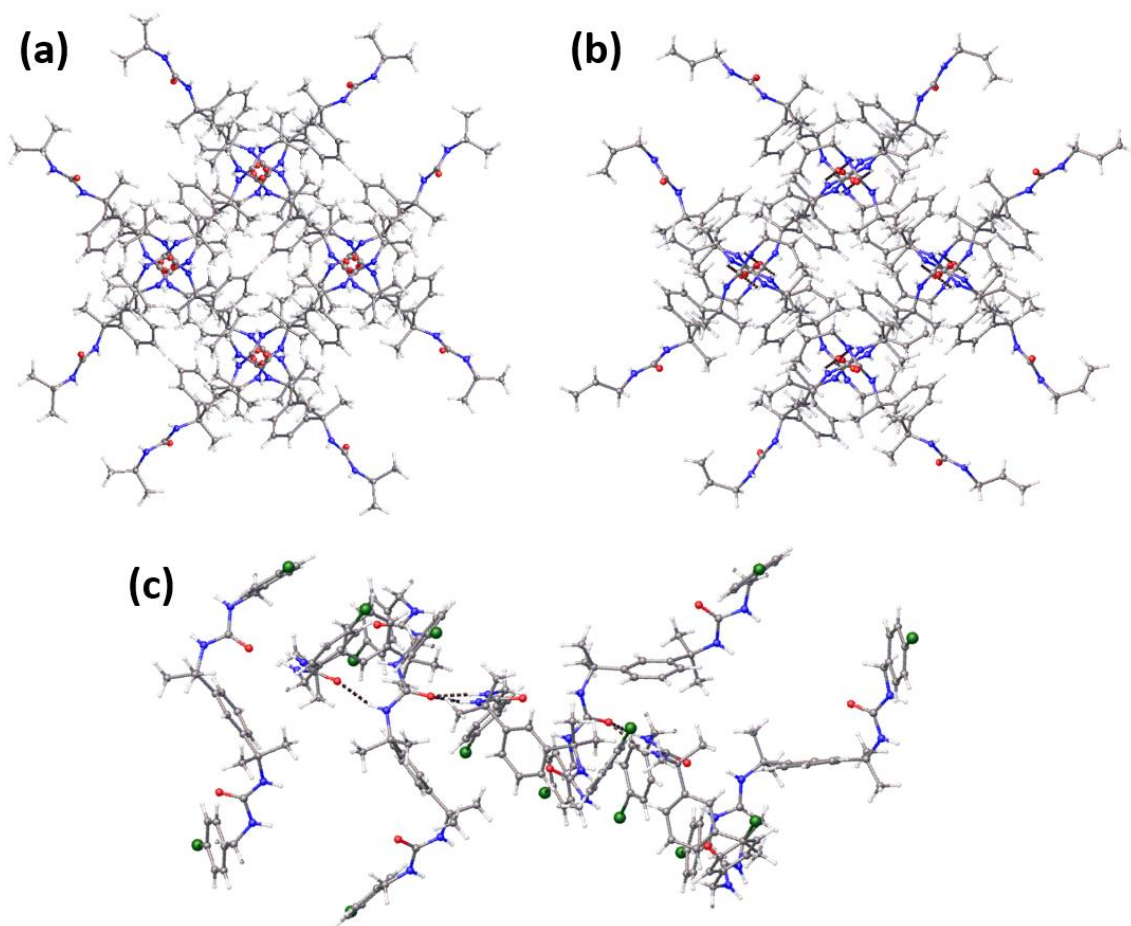


**Fig. 80** [ABCD]  $\alpha$ -tape networks formed by compounds **4.2a** (a) and **4.3** (b) (structures **XXVIII** and **XXXI** respectively), viewing down the tape axes, and [ABABCD]  $\alpha$ -tape network formed by compound **4.9c** (c) in structure **XLIII**.

A key factor influencing the packing of the bis(urea) crystals is the conformation of the spacer moiety. This may be described in terms of  $\phi_1$  and  $\phi_2$ , the two C-C-C-N torsion angles between the central aromatic ring and nearest alkyl-urea bonds (Fig. 82). Due to the structural symmetry of the spacer, all possible combinations of  $\phi_1$  and  $\phi_2$  lie in the range  $0^\circ \leq \phi_2 \leq 180^\circ$ , within a triangular region in a plot of  $\phi_2$  against  $\phi_1$  described by the lines  $\phi_2 = \phi_1$  and  $\phi_2 = 360^\circ - \phi_1$ . Conformations with mirror symmetry are situated on the line  $\phi_2 = \phi_1$ , while the line  $\phi_2 = 360^\circ - \phi_1$  corresponds to conformations that are rotationally ( $C_2$ ) symmetric.

To identify the most stable conformations of the bis(urea) spacer, energies were computed for a molecule of compound **4.1a** with varying combinations of  $\phi_1$  and  $\phi_2$ . The calculations were performed in Gaussian 09 using DFT, with the B3LYP functional<sup>34</sup> and cc-PVDZ basis set.<sup>35</sup> The chosen basis set yields energy values similar to those obtained using the Pople basis set 6-31+G\*,<sup>36</sup> but was

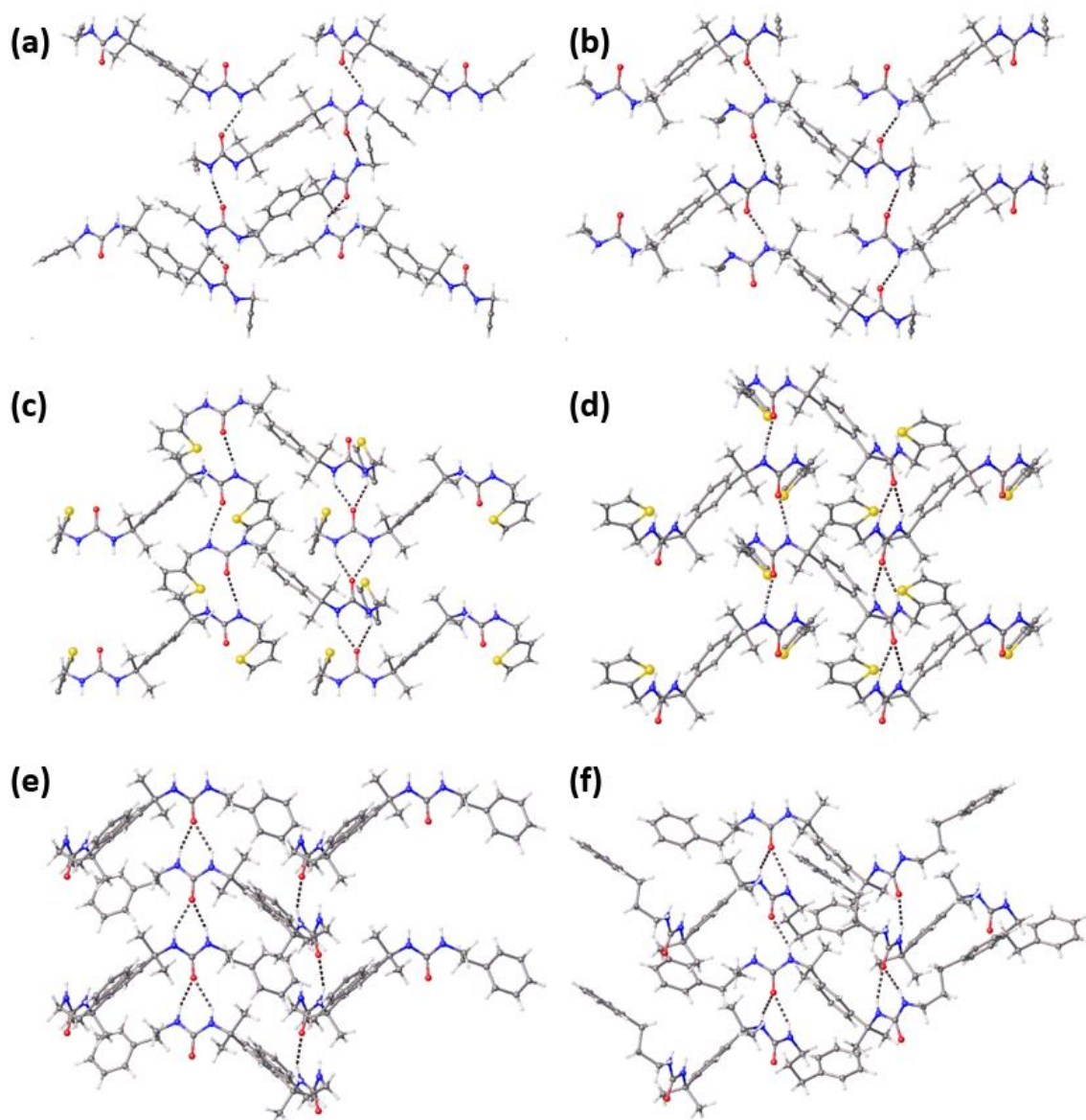


**Fig. 81** Different  $\alpha$ -tape network topologies observed in lamellar bis(urea) crystal structures. Structure **XXXII** (a) consists of molecules of **4.4** in a symmetric [AABB] arrangement, while its polymorph structure **XXXIII** (b) comprises asymmetric lamellae with the more common [AB] repeat unit. Structures **XXXVI** (c) and **XXXVII** (d) both display [AB] lamellae, but the constituent molecules of **4.6b** are packed differently in the two cases. In structure **XXXVI**, neighbouring  $\alpha$ -tapes are antiparallel, and molecules lie in the plane of the lamella with end groups oriented in the same direction. By contrast, the tapes in structure **XXXVII** are syn-parallel and molecules are positioned at an angle to the lamellar plane, producing a symmetric end group arrangement. Syn-parallel tapes are also observed in the symmetric lamellae formed by compounds **4.8b** (e) and **4.8c** (f), in structures **XXXIX** and **XL** respectively.

found to produce aromatic ring conformations closer to the expected planar geometry. For each  $10^\circ$  increment in  $\phi_2$  between 0 and  $180^\circ$ ,  $\phi_1$  was increased from 0 to  $360^\circ$  in steps of  $10^\circ$ , and a geometry optimisation performed on the remainder of the molecule. The final energy landscape was constructed by

comparing the results for equivalent combinations of  $\phi_1$  and  $\phi_2$  and retaining those that were lowest in energy. The calculations reveal a difference of 26.6 kJ mol<sup>-1</sup> between the least and most stable conformations, with a standard deviation of 4.4 kJ mol<sup>-1</sup>, and suggest that conformations with  $\phi_1$  and/or  $\phi_2$  close to 90° are most strongly disfavoured (Fig. 84). Interestingly, a similar analysis of the phenyl bis(urea) analogue produces an almost identical energy landscape, indicating that the identity of the end group has a negligible effect on the conformation of the spacer in the gas phase.

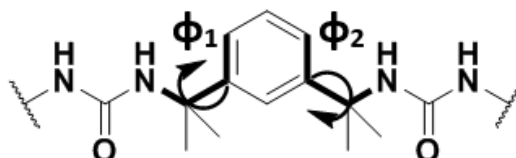


**Fig. 82** The conformation of the methylated *m*-xylylene spacer is specified by two torsion angles,  $\phi_1$  and  $\phi_2$ .

The importance of the spacer conformation on the stability of crystalline bis(urea)s may be deduced by comparing the calculated minimum-energy combinations of  $\phi_1$  and  $\phi_2$  with the torsion angles measured in single-crystal structures. For this analysis, it is useful to include the bis(urea) structures investigated in Chapters 2 and 3, in addition to the structures of other analogues reported in the literature (Fig. 83).<sup>14, 21, 27-30, 37</sup> A plot of the data (Fig. 84) displays three well-defined clusters corresponding to groups of crystal structures with differing characteristics. Cluster A includes most of the structures with  $\alpha$ -tape networks, and particularly those with [AB] repeat units. Both torsion angles lie within 60° of 0°, and the spacer is either rotationally symmetric or nearly so. Cluster B encompasses the remaining tape-containing systems, which typically feature syn-parallel  $\alpha$ -tapes or unusual lamellar repeat units. One torsion angle lies within the range spanned by Cluster A, while the other is close to 180°. Finally, Cluster C comprises all of the structures that do not feature  $\alpha$ -tapes, and is characterised by two torsion angles within 60° of 180°. The existence of well-defined clusters in the conformational landscape can likely be attributed to the steric bulk and inflexibility of the methylated *m*-xylylene spacer, and may be responsible for the strong tendency of the bis(urea)s to form crystalline materials.



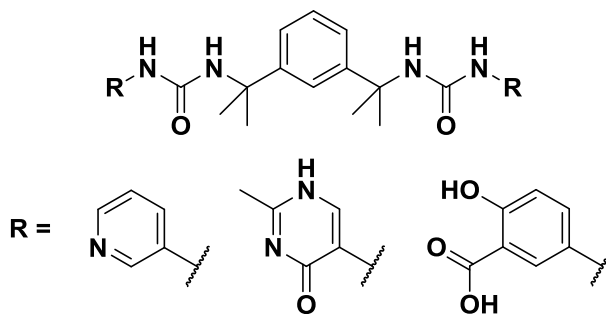


**Fig. 83** Bis(urea)s based on 1,3-bis(1-isocyanato-1-methylethyl)benzene with previously reported crystal structures. The CSD refcodes of the structures are GUDKAR, GUDKEV, JEMQOI, NEJVII, NUTFOZ, NUTFUF, RUSLAU, QENGAS, QENGEW, URIZIF, URIZOL, XOPTUS, XOPVAA and XOPVEE.

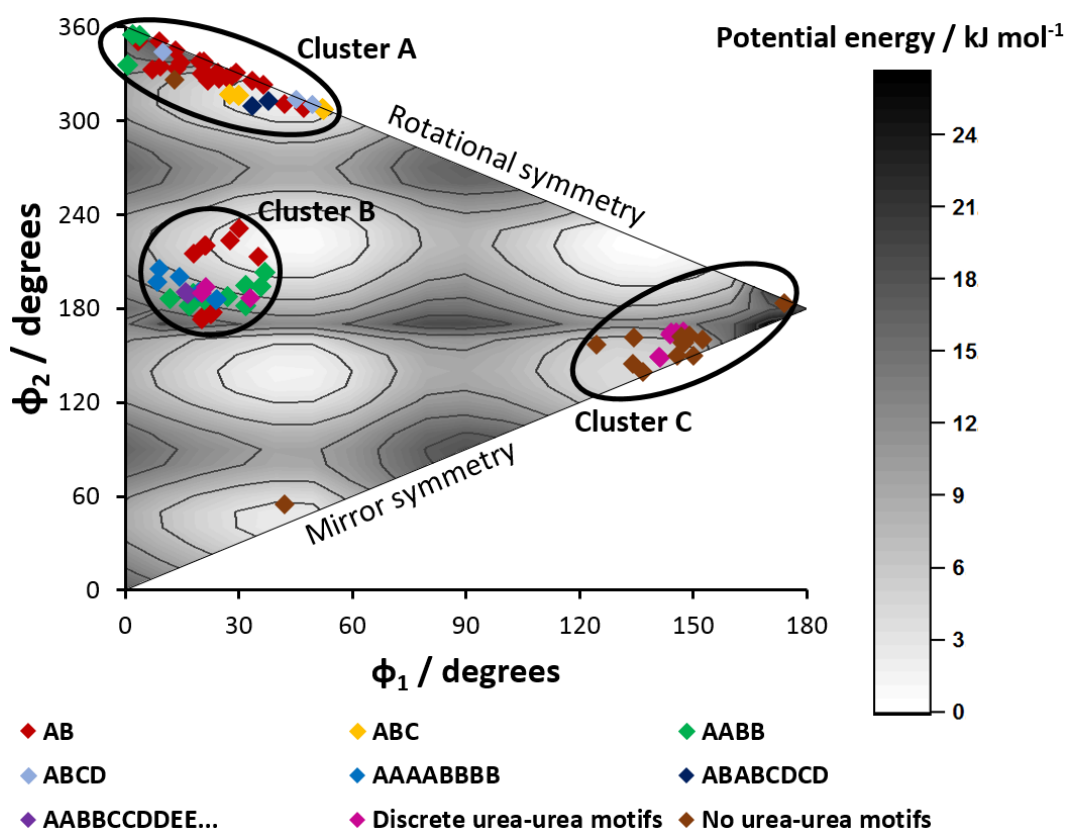


**Fig. 84** DFT energy map of bis(urea) spacer conformations, specified by torsion angles  $\phi_1$  and  $\phi_2$ . Calculations were performed for all possible combinations ( $\phi_1$ ,  $\phi_2$ ), and the lowest energy for each set of degenerate geometries is plotted. The values of  $\phi_1$  and  $\phi_2$  observed in crystal structures are grouped into three distinct clusters (A, B and C), but these only approximately coincide with local minima in the energy landscape. SC-XRD data are coloured to indicate the existence of urea-urea motifs and, where applicable, the topology of the  $\alpha$ -tape network.

The DFT analysis predicts some major features of the conformational landscape, such as a lack of structures in the ranges  $60^\circ < \phi_2 < 120^\circ$ ,  $60^\circ < \phi_1 < 120^\circ$ , and  $240^\circ < \phi_1 < 300^\circ$ . However, it is clear that supramolecular interactions and packing considerations may compensate for a lack of conformational stability

and introduce structural constraints not addressed by calculations in the gas phase. For example, a number of data points in Cluster B and on the edges of Cluster A are situated near local maxima in the calculated energy landscape, and there are no examples of structures with mirror-symmetric spacers, despite an abundance of minima on the line  $\phi_2 = \phi_1$ . These observations indicate that it is not reasonable to base crystal structure predictions for flexible bis(urea)s on geometry optimisations in the gas phase, contrary to the claims of a recent computational study.

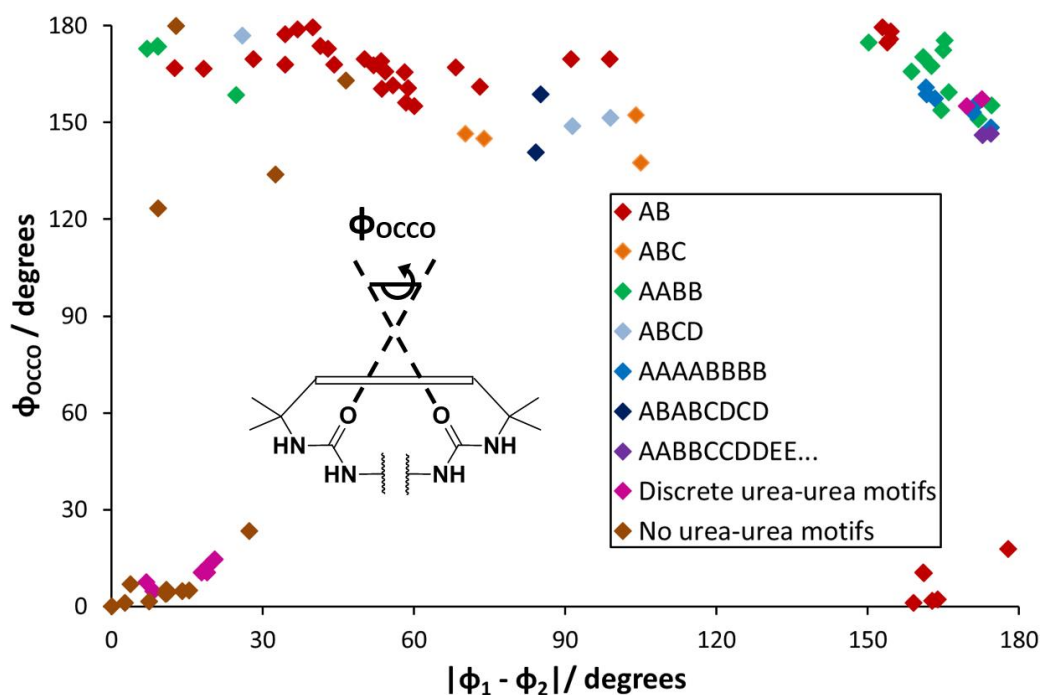


**Fig. 85** Orientations of urea groups and substituents in crystal structures of bis(urea)s with a common methylated *m*-xylylene spacer, specified by the torsion angles  $\phi_{\text{OCCO}}$  and  $|\phi_1 - \phi_2|$ .

The conformational analysis of bis(urea) molecules may be extended by considering the relative orientations of the urea moieties (Fig. 85). Although the presence of multiple flexible bonds between the two C=O bonds limits the utility of the O-C---C-O torsion angle,  $\phi_{\text{OCCO}}$ , the sterically hindered spacer is sufficiently rigid for this parameter to offer a meaningful indication of the urea conformations. As expected, almost all of the structures in Clusters A and B lie in the range  $150^\circ < \phi_{\text{OCCO}} \leq 180^\circ$ , due to the antiparallel arrangement of neighbouring  $\alpha$ -tapes. By contrast, the urea groups of structures in Cluster C typically satisfy either  $0^\circ \leq \phi_1 < 25^\circ$  or  $105^\circ < \phi_{\text{OCCO}} < 135^\circ$ . For structures without tapes, the difference in torsion angles,  $|\phi_1 - \phi_2|$ , is always less than  $30^\circ$ . Tape-

containing structures, however, can display any value of  $|\phi_1 - \phi_2|$  outside of the range 105-155°. Combinations of torsion angles giving  $|\phi_1 - \phi_2| > 155^\circ$  are almost always associated with structures in Cluster B. These display syn-parallel  $\alpha$ -tapes ( $\phi_{\text{occo}} > 155^\circ$ ), large lamellar ([AABB] or [AAAABBBB]) repeat units or bulky end groups.

#### 4.2.3 Gelation behaviour

The gelation properties of the bis(urea) compounds in this investigation were tested by cooling hot 1% (w/v) solutions in a range of solvents (Table 8). Preliminary trials revealed that the solvents amenable to gel formation can be organised into three distinct classes of differing polarities, with the solvents in each class producing similar aggregation outcomes. The least polar solvents, toluene and xylenes, are gelled by a number of analogues with extended alkyl and benzylic end groups. Many of these gelators are also able to gel solvents in the more polar second class, di- and trichlorobenzenes, although the CGCs of these systems tend to be slightly higher. Finally, a small number of compounds form gels in nitrobenzene, representing a third class of significantly more polar solvents. There are two bis(urea) analogues with gelation capacities in all three solvent classes, 17 that form gels in one or two classes, and nine that appear to be completely non-gelating. Most of the gelators exhibit CGCs in the range 0.5-1.0% (w/v). For example, toluene solutions of **4.8c**, 1,2-dichlorobenzene solutions of **4.6a** and nitrobenzene solutions of **4.1a** and **4.4** undergo complete gelation if their concentrations exceed 0.5, 0.9, 0.7 and 0.9% (w/v) respectively. At lower concentrations, only a small number of compounds are able to form sample-spanning gels. The CGCs for the anil species **3.2a-c**, **3.3a-d** and **3.5** in 1,2-dichlorobenzene are typically in the region of 0.1% (w/v), and the *n*-alkyl derivatives **4.1d-f** produce weak gels at concentrations of 0.05% (w/v).

The gelation trials reveal that even small variations in the end group structure can lead to dramatic differences in aggregation behaviour. Notably, the methyl derivative **4.1a** forms gels only in nitrobenzene, but analogues with longer *n*-alkyl end groups form gels in the less polar solvents toluene and 1,2-dichlorobenzene. Likewise, gel formation by the 3-chlorobenzyl analogue **4.9a** occurs most readily in 1,2-dichlorobenzene, while the 4-chlorobenzyl analogue **4.9c** behaves as a

gelator primarily in nitrobenzene. A clear trend is that compounds with more flexible and extended end groups are more likely to display gelation behaviour. For example, compounds **4.1b**, **4.1c** and **4.8a** are non-gelators, but analogues **4.1d-f**, **4.8b** and **4.8c** feature longer alkyl chains and are able to form gels in a range of solvents.

	1,2-dichlorobenzene	nitrobenzene	nitromethane	acetonitrile	toluene
<b>2.1</b>	P	X <sup>P</sup>	X <sup>N</sup>	μX <sup>N</sup>	I
<b>2.2</b>	P	μX + X <sup>N</sup>	X <sup>P/N</sup>	X <sup>P</sup>	I
<b>2.3</b>	P	<b>G<sup>T</sup></b> + X <sup>R</sup>	GP + X <sup>B</sup>	X <sup>B</sup>	I
<b>3.1a</b>	P	P	X <sup>R</sup>	X <sup>R</sup>	I
<b>3.1b</b>	P	P	X <sup>B</sup>	X <sup>P</sup>	I
<b>3.1c</b>	P	P	P	P	I
<b>3.1d</b>	P	P	X <sup>P</sup>	X <sup>P</sup>	I
<b>4.1a</b>	GP	<b>G<sup>T</sup></b>	P	P	I
<b>4.1b</b>	PG <sup>C</sup>	GP	μX <sup>N</sup>	μX <sup>N</sup>	I
<b>4.1c</b>	PG <sup>C</sup>	GP	P	P	I
<b>4.1d</b>	<b>G<sup>C</sup></b>	GP	GP	P	<b>G<sup>C</sup></b>
<b>4.1e</b>	<b>G<sup>C</sup></b>	GP	GP	GP	<b>G<sup>C</sup></b>
<b>4.1f</b>	<b>G<sup>C</sup></b>	GP	GP	GP	<b>G<sup>C</sup></b>
<b>4.2a</b>	P	P	X <sup>P/N</sup>	P	I
<b>4.2b</b>	P	P	P	P	<b>G<sup>T</sup></b>
<b>4.2c</b>	<b>G<sup>T</sup></b>	P	μX <sup>N</sup>	μX <sup>N</sup>	<b>G<sup>T</sup></b>
<b>4.3</b>	P	P	μX <sup>B</sup>	X <sup>B</sup>	I
<b>4.4</b>	P	<b>G<sup>C</sup></b>	P	P	P
<b>4.5</b>	<b>G<sup>C</sup></b>	PG <sup>C*</sup>	P	P	<b>G<sup>C</sup></b>
<b>4.6a</b>	<b>G<sup>T</sup></b>	P	P	P	P
<b>4.6b</b>	GP	<b>G<sup>T</sup></b>	μX + X <sup>P/R</sup>	X <sup>P/R</sup>	<b>G<sup>O</sup></b>
<b>4.7</b>	<b>G<sup>T</sup></b>	<b>G<sup>T</sup></b>	X <sup>B</sup>	X <sup>B</sup>	P
<b>4.8a</b>	P	P	X <sup>P</sup>	X <sup>P/N</sup>	P
<b>4.8b</b>	<b>G<sup>T</sup></b>	PG <sup>T</sup>	P	P	<b>G<sup>O</sup></b>
<b>4.8c</b>	<b>G<sup>C</sup></b>	P	P	P	<b>G<sup>O</sup></b>
<b>4.9a</b>	<b>G<sup>T</sup></b>	P	P	X <sup>P</sup>	PG <sup>O</sup>
<b>4.9b</b>	<b>G<sup>T</sup></b>	P	P	μX <sup>B</sup>	<b>G<sup>O</sup></b>
<b>4.9c</b>	PG <sup>T</sup>	<b>G<sup>T</sup></b>	μX <sup>R</sup>	μX <sup>R</sup>	P

**Table 8** Results of gelation experiments for bis(urea) compounds with a common spacer but different end groups. Observations were made after heating 1% (w/v) solutions in 2 cm<sup>3</sup> sealed vials and allowing the materials to cool to room temperature for one hour. Results are marked with a letter corresponding to the aggregation outcome: G = gel (highlighted in bold), PG = partial gel, X = crystal, μX = microcrystals, GP = gelatinous precipitate and P = precipitate.

Superscripts are used to denote the appearance of gels and crystals: for gels, C = clear (transparent), T = translucent and O = opaque, while for crystals, B = blocks, N = needles, P = plates and R = rods. An asterisk is used to denote materials prepared from an 8% (w/v) solution, in order to exceed the solubility limit of the bis(urea) compound.



The rheological properties of the gels were analysed by means of oscillatory shear experiments. In all of the gels studied,  $G'$  is an order of magnitude larger than  $G''$  at low stresses, and collapse of the material occurs above a well-defined yield stress (Fig. 86a). Moreover, there is a gradual rise in  $G'$  with increasing frequency  $\omega$ , as expected for fibrous gels (Fig. 86b). The properties of the gels may be tuned by altering either the structure of the gelator or the solvent being gelled (Fig. 86c). For example, compound **4.1d** produces stronger gels at 1% (w/v) in 1,2-dichlorobenzene than in toluene, with plateau  $G'$  values of 130 and 21 kPa and yield stresses of 850-900 and 420-450 Pa respectively. Gels of **4.2c** and **4.6a** in this solvent, however, are significantly less robust: the  $G'$  values are just 570 and 170 Pa, and the yield stresses are less than 30 Pa. Nitrobenzene gels also tend to be relatively weak. Compound **4.1a** forms a nitrobenzene gel with a plateau  $G'$  of 11 kPa and yield stress of 70-75 Pa, and nitrobenzene gels of a other derivatives were found to collapse too readily to be reliably analysed (Fig. 86d).

To gain insight into the structural differences underlying the variation in rheological properties, xerogels were prepared from a selection of 1% (w/v) gels and analysed by SEM. The micrographs reveal that the microstructures of gels in toluene and 1,2-dichlorobenzene are remarkably similar: in all cases, the materials consist of uniform, unbranched fibres 20-30 nm in diameter (Fig. 87). This result suggests that the strengths of the gels are determined by the density and connectivity of the fibre network over larger length-scales. However, it is also possible that structural changes during drying of the gels renders the images unrepresentative of the wet materials. Indeed, SEM micrographs show that xerogels prepared from gels of **4.6b** and **4.7** in nitrobenzene consist entirely of microcrystalline particles, indicating that preparation of the sample leads to quantitative recrystallization of the gel assemblies (Fig. 88). Interestingly, microcrystals in the precipitates of **4.1e** and **4.2a**, from nitrobenzene and 1,2-dichlorobenzene respectively, are more fibrous in nature but do not give rise to a sample-spanning gel. It is likely that these aggregates are too short and rigid to generate an extended, interconnected network capable of percolating the system and immobilising the solvent.

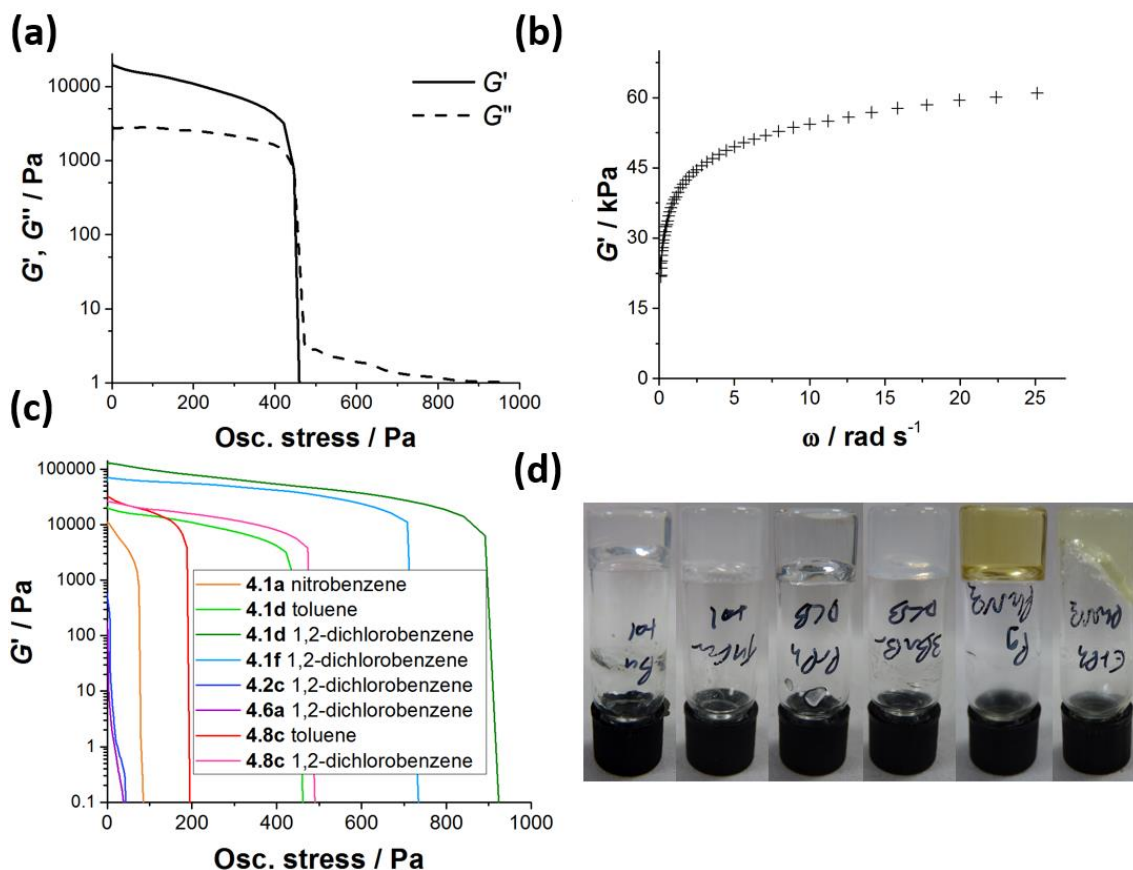


**Fig. 86** Oscillatory shear rheometry experiments for a gel of **4.1d** in toluene show that  $G'$  is an order of magnitude larger than  $G''$  below the yield stress of 420-450 Pa (a), and rises slowly with increasing shear frequency  $\omega$  (b). This behaviour is typical of a moderately strong fibrous gel. The yield stress and plateau  $G'$  value are strongly dependent on the gelator structure and the solvent properties (c). Varying the gelator and solvent also affects the transparency of the gel (d). The photographs depict typical gels of (left to right) **4.1d** in toluene, **4.5** in toluene, **4.8c** in 1,2-dichlorobenzene, **4.9b** in 1,2-dichlorobenzene, **4.4** in nitrobenzene and **4.8b** in nitrobenzene. All gels were prepared from 1% (w/v) solutions and analysed at 10 °C. A constant frequency of 1 Hz was used in shear stress experiments and a constant stress of 1 Pa in the frequency profile.

It is interesting to note that the ethyl and *n*-propyl bis(urea) derivatives, compounds **4.1b** and **4.1c**, show little gelation capacity even though the other *n*-alkyl analogues form strong gels in at least one solvent class. Intriguingly, differences in self-assembly behaviour are also observed in the crystal structures of these compounds. In crystals of the methyl and *n*-butyl analogues **4.1a** and **4.1d**, structures **XXIII** and **XXVI**, the interacting faces of adjacent lamellae are structurally equivalent (Fig. 89). However, in crystals of **4.1b** and **4.1c**, structures **XXIV** and **XXV**, lamellae are stacked in a polar fashion, such that each face of a lamella differs from the face with which it interacts. It is possible that gelation by compounds **4.1b** and **4.1c** is less favourable because the interfaces between

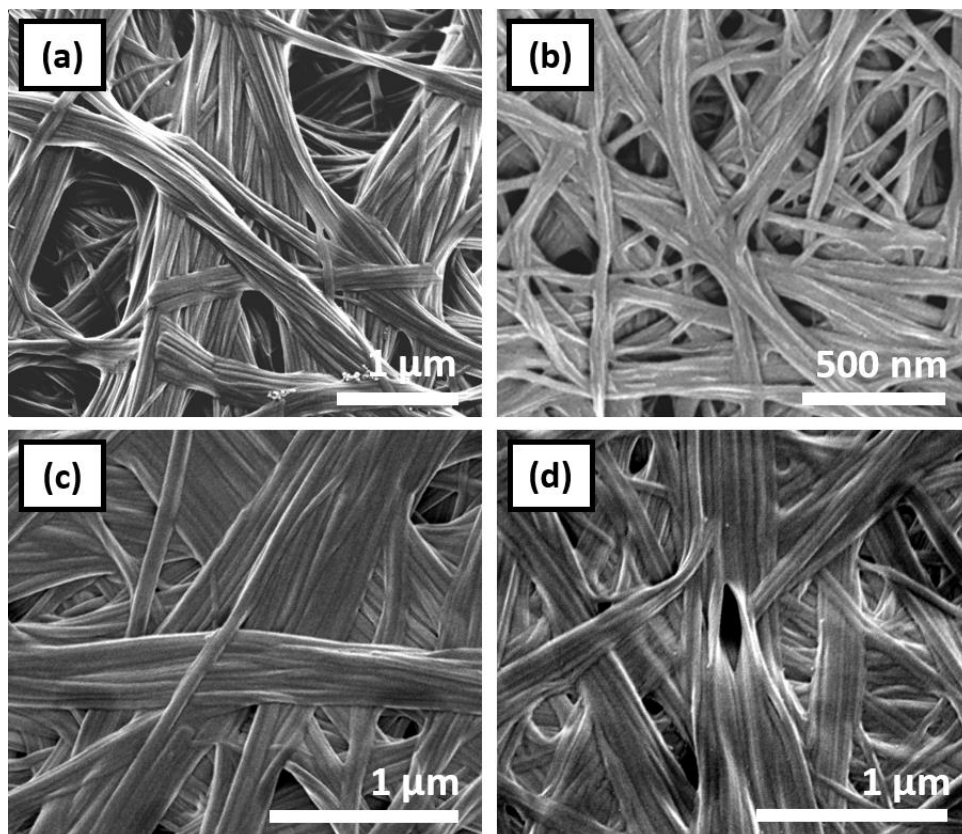


**Fig. 88** SEM micrographs of xerogels prepared from 1% (w/v) gels of **4.1d** (a), **4.2b** (b) and **4.8b** in toluene (c), and **4.8b** in 1,2-dichlorobenzene (d).

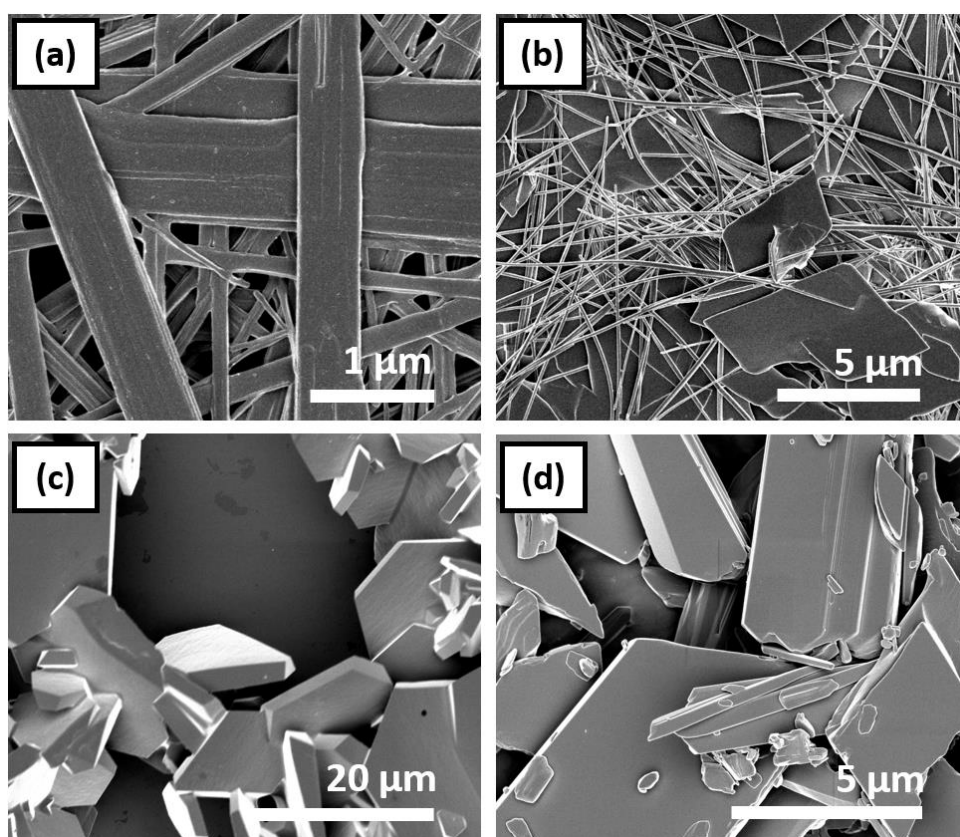


**Fig. 89** SEM micrographs of precipitates of **4.1e** from nitrobenzene (a) and **4.2a** from 1,2-dichlorobenzene (b) and xerogels from 1% (w/v) gels of **4.6b** (c) and **4.7** (d) in nitrobenzene.

lamellae are of higher energy, allowing crystal growth to occur more readily. To test this hypothesis, the surface energies of structures **XXIII**, **XXV**, and **XXVI** were evaluated via MD simulations, according to the method outlined in Chapter 2. The simulations were performed in GROMACS 4.6.2<sup>38</sup> using the General Amber Force Field (GAFF)<sup>39</sup> implemented in the Antechamber package. Model crystallites with varying numbers of layers,  $N$ , were simulated in a vacuum at 300 K, controlled via a Berendsen thermostat. The crystallites consisted of between 16 and 40 lamellae, with each layer spanning 49-70 unit cells. The energy of each crystallite,  $E_{\text{tot}}$ , was calculated as the average potential energy of the system over 150 ps, after equilibration for an equal period of time. The energy of each face,  $E_{\text{face}}$ , was estimated from a plot of  $E_{\text{tot}}/N$  against  $1/N$ , in accordance with the equation:

$$\frac{E_{\text{tot}}}{N} = \frac{-E_{\text{face}}}{N} + (E_{\text{bulk}} + E_{\text{face}}) \quad (1)$$

Four crystallites were simulated for each crystal face, and the surface energy  $\gamma$  evaluated by dividing the estimate for  $E_{\text{face}}$  by the area of the face. For structures **XXIII** and **XXVI**, the process was repeated with two different arrangements of lamellae in order to obtain estimates of  $\gamma$  for the two different lamellar surfaces (Fig. 90a). In structure **XXV**, the interfaces between lamellae involve surfaces of differing composition, so the corresponding estimates of  $\gamma$  represent the average surface energies of the lamellar surfaces. The results (Fig. 90b) reveal that the surfaces perpendicular to the bis(urea) lamellae are similar in energy for structures **XXIII** and **XXV**. In structure **XXVI**, however, there is a significant difference: the surface perpendicular to the  $\alpha$ -tape axis ( $x$  in Fig. 90b) is slightly lowered in energy relative to the other systems, while the surface parallel to the tape axis ( $y$ ) is 10-22% higher. The surface parallel to the lamellar plane ( $z$ ) displays the lowest value of  $\gamma$  in all of the systems. It is evident that surfaces decorated with alkyl end groups (the  $z$  planes of **4.1a** (2) and **4.1d** (2)) interact more strongly than those without (the  $z$  planes of **4.1a** (1), **4.1c** and **4.1d** (1)). However, the average surface energy of the lamellar plane is only weakly affected by the structure of the end group and the mode of packing. Thus, the weaker gelation capacities of **4.1c** and the analogous species **4.1b** cannot be attributed to increased stacking of the bis(urea) lamellae. This conclusion is supported by the

observation that compounds **4.2b**, **4.4** and **4.9b** are effective gelators, despite forming polar stacks of lamellae similar to those of structures **XXIV** and **XXV**.

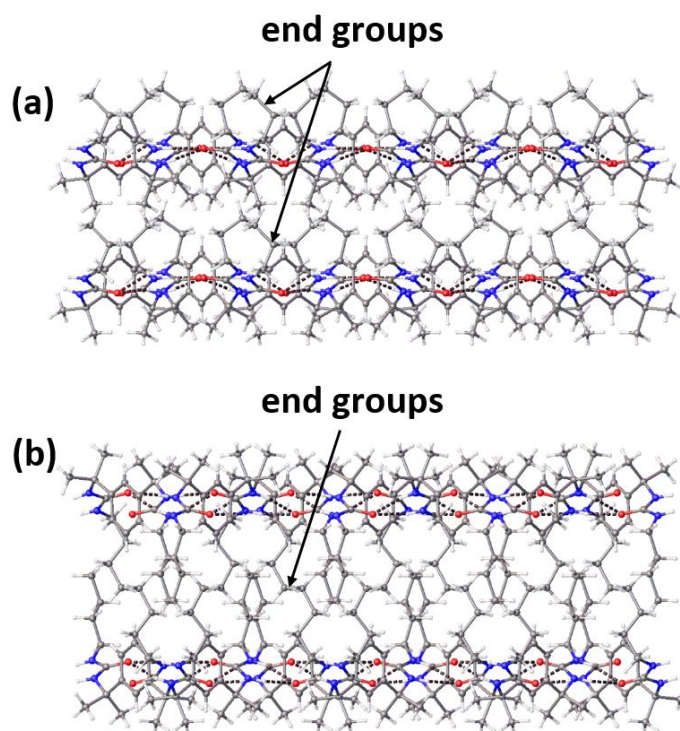


**Fig. 89** Polar stacking of lamellae in structure **XXV** (a) and non-polar stacking in structure **XXVI** (b).

In order to better understand the structural features responsible for the high gelation capacities of particular *n*-alkyl derivatives, single crystals and toluene xerogels of **4.1d** were analysed by PXRD and solid-state  $^{13}\text{C}$  NMR spectroscopy. Broad peaks in the PXRD pattern of the xerogel do not match reflections in the single-crystal pattern, suggesting that the arrangements of molecules in the two materials are significantly different (Fig. 91). Intriguingly, heating at 100 °C for two days causes the reflections of the xerogel to become sharper, indicating that recrystallisation has taken place. The solid-state NMR spectra confirm that the alkyl end groups in the heated material and parent xerogel experience similar local environments, but are packed differently to those in the single crystals (Fig. 92a). It is noted that the terminal methyl resonances of **4.1d** in its single crystals occur at higher chemical shifts than those of crystalline **4.1b** and **4.1c**, even though increasing the length of the alkyl end group separates this site from the deshielding urea moieties (Fig. 92b). This result supports the hypothesis that the polar stacking of lamellae in structures **XXIV** and **XXV** leads to greater shielding of the alkyl carbon nuclei than the non-polar arrangement of structure **XXVI**. Thus, the observed decrease in  $\delta_{\text{C}}$  for the xerogel of **4.1d** is consistent with molecules

self-assembling in a polar fashion, as might be expected if lamellar assemblies scroll into fibrous architectures. It is possible that **4.1b** and **4.1c** do not give rise to gels because crystals of these compounds are also formed via a polar layering mechanism, so conversion of nascent gel aggregates into a microcrystalline precipitate can take place more readily during the self-assembly process.

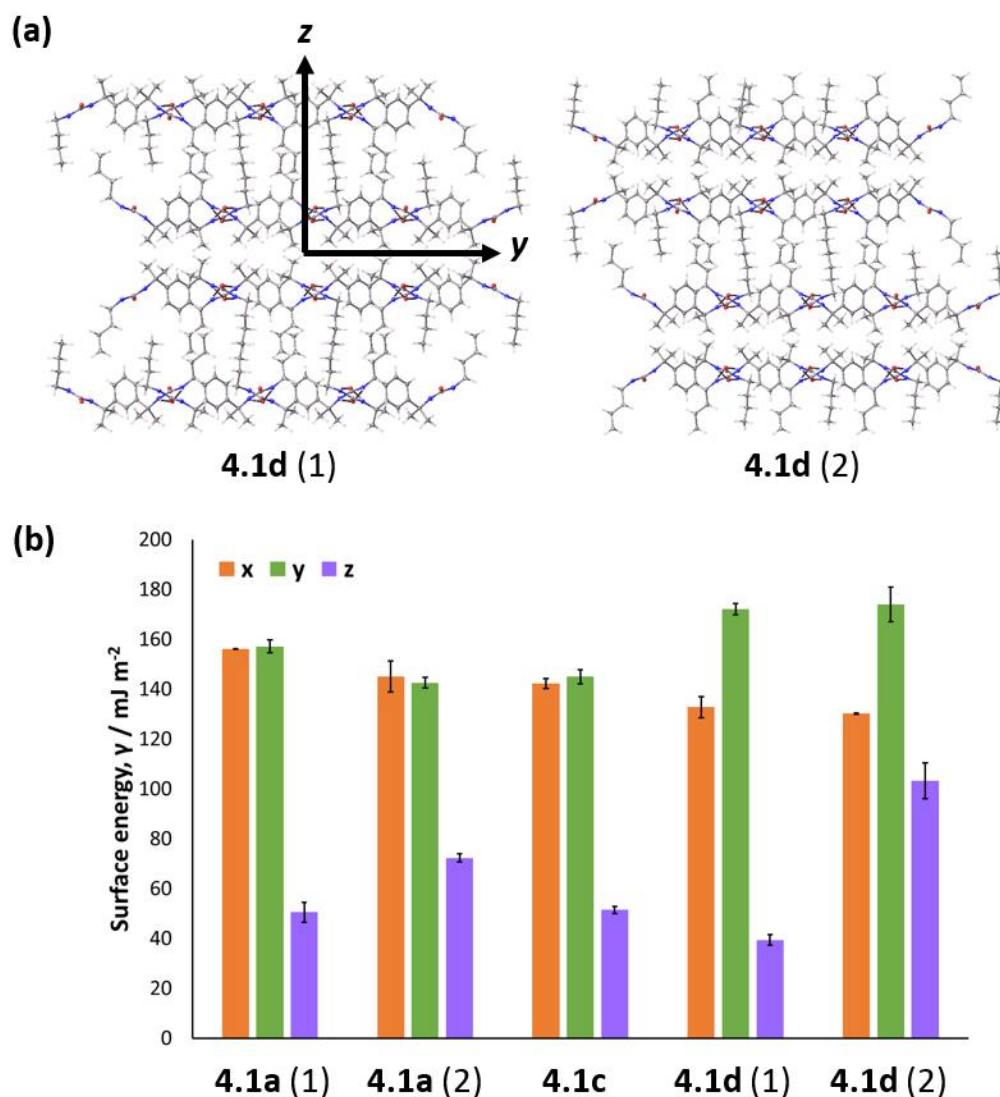


**Fig. 90** Crystallites of **4.1d** (structure **XXVI**) can exhibit two different faces parallel to the lamellar plane (normal axis  $z$ ), depending on the orientation of the last layer deposited (a). These structures, labelled **4.1d (1)** and **4.1d (2)**, were analysed separately in surface energy calculations. Crystallites of **4.1a** (structure **XXIII**) were treated analogously, but crystallites of **4.1c** consist of a polar lamellar arrangement so could only be modelled in a single configuration. Estimates of surface energy,  $\gamma$ , derived from MD simulations under constant- $NVT$  conditions in a vacuum (b) show significant variation in the faces perpendicular to  $y$  and  $z$  and smaller differences in the values perpendicular to the  $\alpha$ -tape axis,  $x$ . Values of  $E_{\text{tot}}$  were calculated as the average potential over 150 ps after 150 ps of equilibration time. For each system, mean values of  $\gamma$  and standard errors were obtained by linear regression analysis of four simulations.



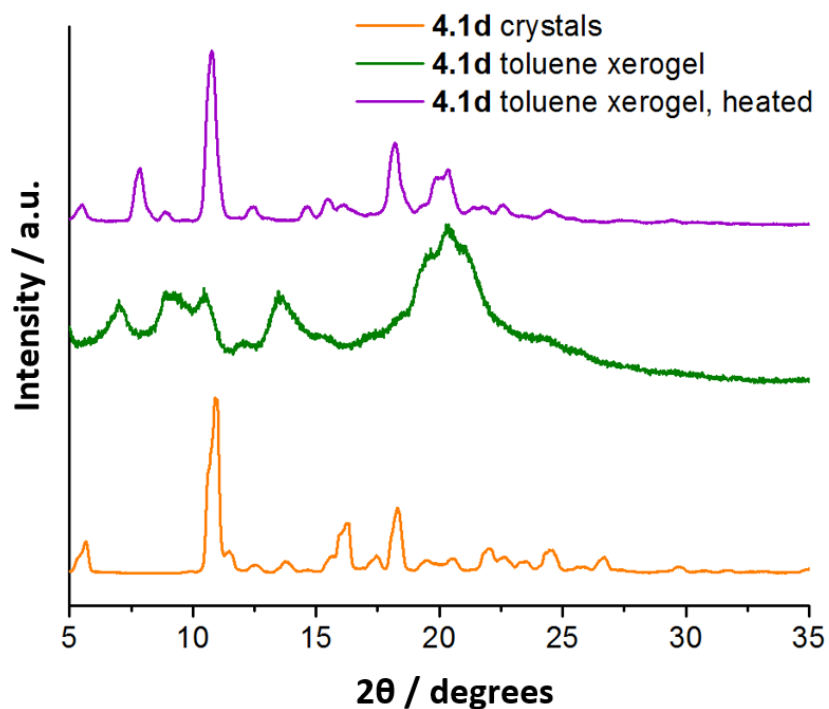


**Fig. 91** PXRD patterns for ground single crystals of **4.1d**, a dried 1% (w/v) gel of **4.1d** in toluene, and the same xerogel after heating at 100 °C for 48 h.

#### 4.2.4 Scrolling pathways

MD simulations of bis(urea) lamellae may help to predict and rationalise gelation characteristics, by offering useful insights into the mechanism of self-assembly. In particular, such simulations highlight the possibility of scrolling behaviour, wherein lamellae in solution fold into stable unbranched fibrils. Model lamellae of 600 molecules were constructed using the atomic coordinates of single-crystal structures and simulated in a vacuum at a temperature of 300 K, controlled via a Berendsen thermostat. Simulations were conducted over 500 ps, as this short time period was found to be sufficient to detect the incidence and direction of scrolling, and capture all major morphological changes involved.

The simulation results reveal that many lamellae adopt similar scrolled morphologies despite substantial differences in their bis(urea) end groups. Indeed, scrolling can occur in all systems with an asymmetric distribution of end groups between the two lamellar surfaces. By contrast, symmetric lamellar assemblies of molecules **4.2c**, **4.5**, **4.8a** and **4.9a** undergo relatively little deformation within the simulation timescale (Fig. 93). The bending modulus of the structure is important, as scrolling requires a radius of curvature that is comparable in magnitude to the lamella thickness. Simulations of multilayer

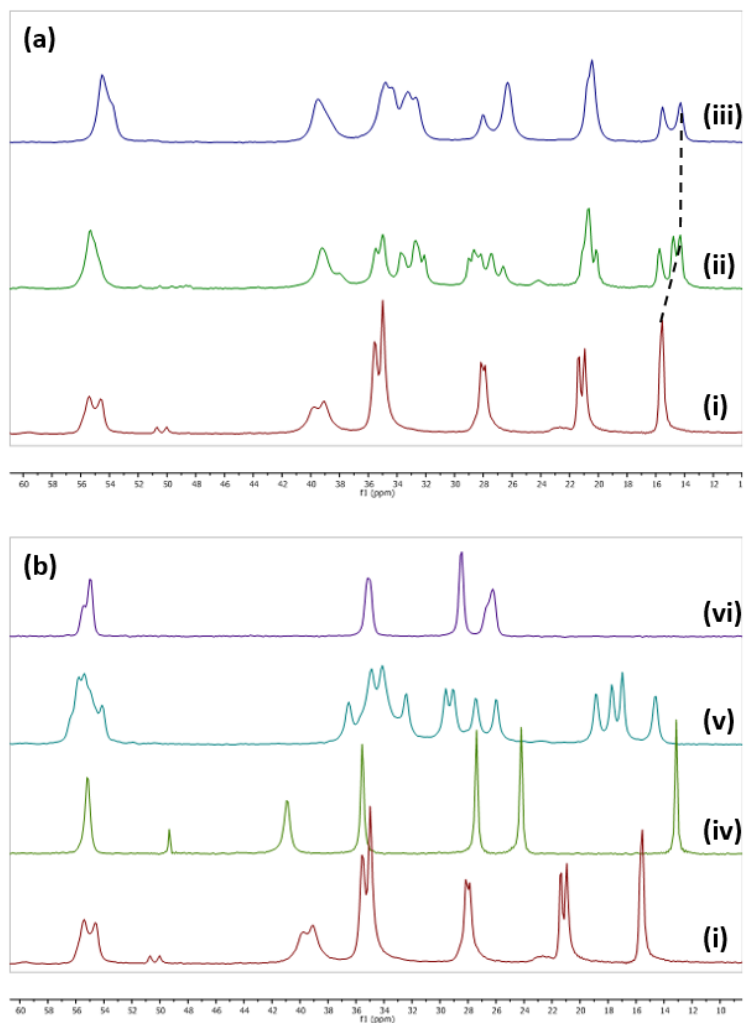


**Fig. 92** Solid-state <sup>13</sup>C NMR spectra in the sp<sup>3</sup> region (δ<sub>c</sub> = 10-60 ppm) for bis(urea) crystals and gels of **4.1d** (a). The spectrum for single crystals of **4.1d**, structure **XXVI** (i), displays sharp doublet peaks corresponding to the two halves of the molecule in the asymmetric unit. The xerogel prepared from a 1% (w/v) gel in toluene (ii) also produces sharp resonances, indicative of locally ordered and immobile assemblies, but there are a wider range of peaks due to the greater variety of conformations present. Heating the xerogel to 100 °C or 48 h leads to coalescence of the signals, suggesting that recrystallisation has taken place. The terminal methyl resonances of the xerogel and recrystallised solid are shifted up-field relative to that of the single crystals. Similar shielding is observed in the terminal methyl resonances of **4.1c** (iv) and **4.1b** (v) in their single crystals, which consist of asymmetric lamellae with a common orientation (b). By contrast, lamellae in crystals of compound **4.1a** (vi) are stacked in a non-polar fashion, and the terminal methyl resonance is strongly deshielded. Thus, the results support the hypothesis that gels of **4.1d** consist of lamellar assemblies in a polar stacked arrangement.

assemblies based on lamellae from structure **XXIII** in a polar stacking arrangement indicate that the radius of curvature is approximately proportional to the cube of the number of layers: for systems of one and three lamellae, the minimum observed radii are 2.5 and 70 nm respectively (Fig. 94). Furthermore, stacking of



lamellae may eliminate the asymmetry of the system, such that a bias in curvature can no longer arise. These observations suggest that fibril formation is possible only if molecules self-assemble into single expanded lamellae, which undergo scrolling before the onset of multilayer aggregation.

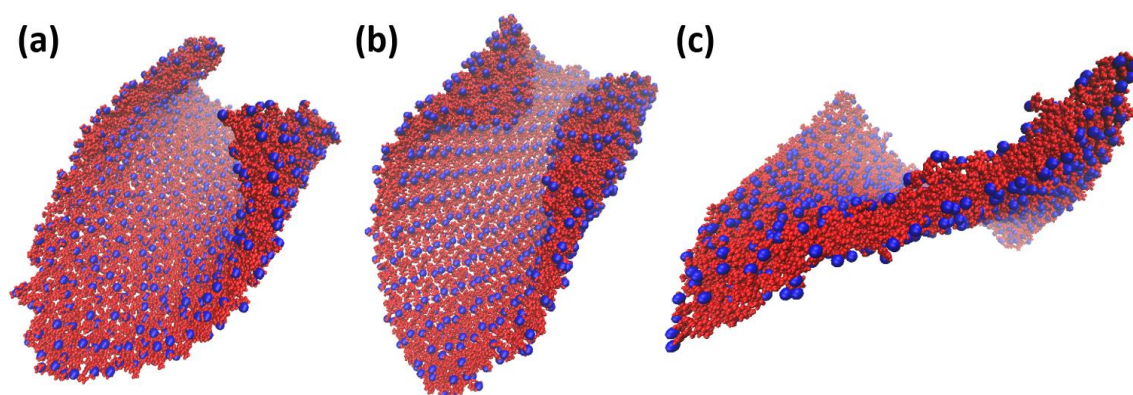


**Fig. 93** Final frames from 500 ps MD simulations of non-scrolling lamellae in a vacuum at 300 K. The lamellae consist of molecules of **4.2c** (a), **4.8a** (b) and **4.9a** (c), and were simulated from initial coordinates extracted from crystal structures **XXX**, **XXXVIII** and **XLI** respectively. One atom in each end group is shown as a blue sphere of radius 1.3 Å and all other atoms are shown as red spheres of radii 0.7 Å.

Although there is little variation in the gross morphologies of scrolled lamellae, the direction of scrolling depends strongly on the identity of the bis(urea) end group (Fig. 95). The bis(urea) network might naively be expected to fold about an axis parallel to the  $\alpha$ -tapes, with the end groups presented to the outside of the resulting fibril. This pattern of deformation matches that observed in lamellar assemblies of compounds **4.1a**, **4.1b**, **4.1c**. However, the axis of scrolling in lamellae from structures lies perpendicular to the  $\alpha$ -tapes, and folding occurs such that end groups are concentrated within the fibril interior. With the exception of **4.1a**, all compounds that form crystal structures with a non-polar arrangement of stacked lamellae undergo scrolling in this fashion. Differences in the scrolling pathway cannot be attributed to the geometry of the  $\alpha$ -tape network, as exchanging the *n*-butyl end groups in a lamella from structure **XXVI** with methyl substituents results in scrolling behaviour characteristic of lamellae from structure **XXIII**. It may be deduced that the axis and direction of scrolling are closely linked, and that folding occurs to strengthen the interactions between moieties on the lamellar surface. Regardless of the folding pathway, scrolling

produces a stabilisation of approximately 26-34 kJ mol<sup>-1</sup>, exceeding the decrease in energy in non-scrolling systems by one order of magnitude (Fig. 95d).

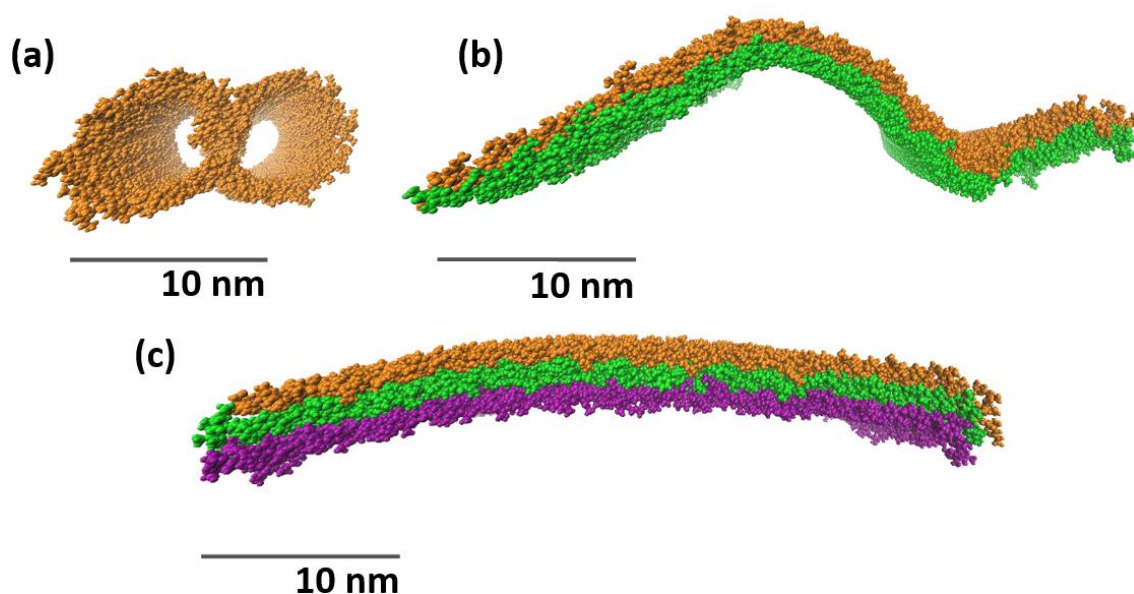


**Fig. 94** Effect of increasing lamellar thickness on the maximum attainable radius of curvature. Monolayers of **4.1a** from structure **XXIII** (a) undergo scrolling readily, but polar stacks of two (b) and three (c) lamellae bend relatively little due to their large bending moduli. All images represent the final frames of 500 ps MD simulations in a vacuum at 300 K.

In many cases, the simulation results are in strong agreement with the outcomes of gelation trials. For example, the models indicate that the asymmetric lamellae formed by compounds **4.1a**, **4.1d**, **4.2b**, **4.4**, **4.6a** and **4.6b** are highly susceptible to scrolling, and therefore highly compatible with gel formation. Likewise, the crystal structures of compounds with little or no gelation capacity (namely **2.1**, **2.2**, **3.1a**, **3.1b**, **3.1d**, **4.2a**, **4.3** and **4.8a**) form symmetric lamellae or three-dimensional hydrogen bonding networks, in which spontaneous scrolling cannot occur. It should be noted, however, that compounds **4.2c**, **4.5**, **4.8b**, **4.8c** and **4.9a** and the anils **3.2a-d**, **3.3a-d** and **3.5** are effective gelators despite the presence of symmetric lamellae in their crystal structures. One possible explanation is that the molecular arrangements in these crystals represent patterns of self-assembly that are not representative of the gel-phase aggregates. Compounds **4.9a** and **4.9c**, in particular, might undergo gelation by forming lamellae similar to those of the bromo analogue **4.9b** in structure **XLII**. Alternatively, gelation may be associated with an abundance of local disorder and structural defects, which could lead to scrolling even in largely symmetric lamellae

by enabling the transient formation of asymmetric features. Such a mechanism is thought to contribute to the gelation capacities of compounds **4.8b** and **4.8c**, as the spacer groups in these compounds adopt less favourable conformations in the crystal phase (structures **XXXIX** and **XL** respectively) and are thus more likely to explore a range of packing modes when forming lamellae in solution.

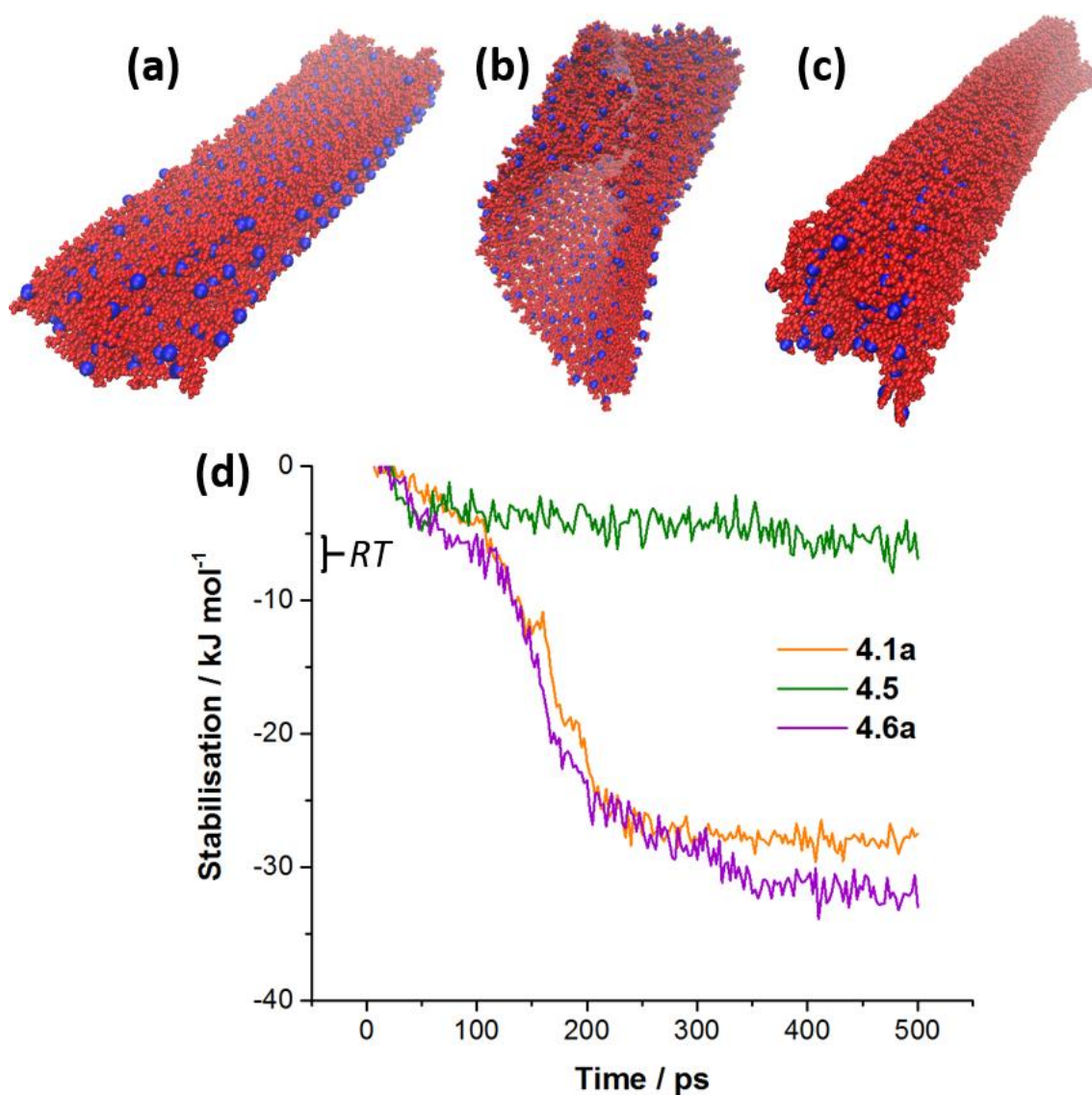


**Fig. 95** MD simulations in a vacuum at 300 K reveal that lamellar assemblies of compound **4.1a** (a) scroll with the end groups orientated outwards and the fold axis parallel to the  $\alpha$  tapes. Asymmetric lamellae of compound **4.6a** scroll in the opposite direction with the fold axis perpendicular to the tape axis (c), while symmetric lamellae of compound **4.5** (b) undergo limited folding in a random direction. The energy profiles for the simulations (d) reveal that **4.1a** and **4.6a** experience similar stabilisation through scrolling, but lamellae of **4.5** decrease in energy by just 4-6 kJ mol<sup>-1</sup>. The simulation frames shown represent the geometries of the systems after 500 ps, and stabilisations are calculated relative to the energy after 20 ps equilibration time. One atom in each end group is shown as a blue sphere with radius 1.3 Å, and all other atoms are shown as red spheres with radii 0.7 Å.

### 4.3 Conclusions

There have been many attempts to predict and rationalise the formation of supramolecular gels based on the crystal structures of the molecules involved. An analysis of 21 bis(urea)s with a shared spacer moiety reveals that derivatives capable of gel formation self-assemble into hydrogen bonding networks with a number of common features. In particular, the ureas typically interact to form a lamellar arrangement of  $\alpha$ -tape motifs, and display enhanced gelation capacities if the faces of these lamellae are structurally asymmetric. The tendency to form asymmetric lamellae is linked to the topology of the  $\alpha$ -tape network and the geometry of the spacer, factors which are in turn governed by the flexibility and steric bulk of the bis(urea) end groups. MD simulations of isolated lamellae suggest that gel fibrils form through spontaneous scrolling, and that the direction and axis of folding are dependent on the structures of moieties decorating the lamellar surfaces. Given that scrolling can occur only in the absence of multilayer aggregation, and that crystal structures are not always representative of the assemblies formed in solution, fibril formation is often highly solvent-sensitive and difficult to predict. Nonetheless, the likelihood of gelation may be increased by choosing end groups that are compatible with an asymmetric lamellar network and avoiding factors that inhibit  $\alpha$ -tape formation, such as substituents capable of ionisation or intramolecular hydrogen bonding. The results illustrate the impact of molecular packing on the dynamics of self-assembly and highlight the importance of symmetry and topology in dictating the morphology of an aggregate. These insights could facilitate the design of more effective urea-based gelators and offer general guidance for the development of other hydrogen bonding molecules with targeted, practically useful self-assembly outcomes.

### 4.4 References

1. J. H. van Esch and B. L. Feringa, *Angew. Chem. Int. Edit.*, 2000, **39**, 2263-2266.
2. G. O. Lloyd, M. O. M. Piepenbrock, J. A. Foster, N. Clarke and J. W. Steed, *Soft Matter*, 2012, **8**, 204-216.
3. P. Byrne, D. R. Turner, G. O. Lloyd, N. Clarke and J. W. Steed, *Cryst. Growth Des.*, 2008, **8**, 3335-3344.
4. S. J. James, A. Perrin, C. D. Jones, D. S. Yufit and J. W. Steed, *Chem. Commun.*, 2014, **50**, 12851-12854.
5. Y. H. Chen, N. Ballard and S. A. F. Bon, *Polym. Chem.*, 2013, **4**, 387-392.

6. A. E. Hooper, S. R. Kennedy, C. D. Jones and J. W. Steed, *Chem. Commun.*, 2016, **52**, 198-201.
7. K. A. Houton, K. L. Morris, L. Chen, M. Schmidtman, J. T. A. Jones, L. C. Serpell, G. O. Lloyd and D. J. Adams, *Langmuir*, 2012, **28**, 9797-9806.
8. A. Vidyasagar and K. M. Sureshan, *Angew. Chem. Int. Edit.*, 2015, **54**, 12078-12082.
9. C. R. Groom, I. J. Bruno, M. P. Lightfoot and S. C. Ward, *Acta Crystallogr. Sect. B-Struct. Sci. Cryst. Eng. Mat.*, 2016, **72**, 171-179.
10. J. T. Lenthall, J. A. Foster, K. M. Anderson, M. R. Probert, J. A. K. Howard and J. W. Steed, *Crystengcomm*, 2011, **13**, 3202-3212.
11. A. Masunov and J. J. Dannenberg, *J. Phys. Chem. B*, 2000, **104**, 806-810.
12. J. Bernstein, R. E. Davis, L. Shimon and N. L. Chang, *Angew. Chem. Int. Edit.*, 1995, **34**, 1555-1573.
13. D. R. Turner, B. Smith, A. E. Goeta, I. R. Evans, D. A. Tocher, J. A. K. Howard and J. W. Steed, *Crystengcomm*, 2004, **6**, 633-641.
14. B. J. B. Folmer, R. P. Sijbesma, H. Kooijman, A. L. Spek and E. W. Meijer, *J. Am. Chem. Soc.*, 1999, **121**, 9001-9007.
15. I. Ilić, R. Dreu, M. Burjak, M. Homar, J. Kerč and S. Srčić, *Int. J. Pharm.*, 2009, **381**, 176-183.
16. W. Grell, R. Hurnaus, G. Griss, R. Sauter, E. Rupprecht, M. Mark, P. Luger, H. Nar, H. Wittneben and P. Müller, *J. Med. Chem.*, 1998, **41**, 5219-5246.
17. G. Brancatelli, C. Capici, G. Gattuso, S. Geremia, A. Notti, S. Pappalardo, M. F. Parisi, S. Sortino and E. Vittorino, *Chem. Asian J.*, 2012, **7**, 50-54.
18. P. Curinova, M. Pojarova, J. Budka, K. Lang, I. Stibor and P. Lhotak, *Tetrahedron*, 2010, **66**, 8047-8050.
19. K. Yabuuchi, E. Marfo-Owusu and T. Kato, *Org. Biomol. Chem.*, 2003, **1**, 3464-3469.
20. P. S. Corbin, S. C. Zimmerman, P. A. Thiessen, N. A. Hawryluk and T. J. Murray, *J. Am. Chem. Soc.*, 2001, **123**, 10475-10488.
21. J. A. Foster, K. K. Damodaran, A. Maurin, G. M. Day, H. P. G. Thompson, G. J. Cameron, J. C. Bernal and J. W. Steed, *Chem. Sci.*, 2017, **8**, 78-84.
22. P. Brocorens, M. Linares, C. Guyard-Duhayon, R. Guillot, B. Andrioletti, D. Suhr, B. Isare, R. Lazzaroni and L. Bouteiller, *J. Phys. Chem. B*, 2013, **117**, 5379-5386.
23. D. J. Adams, K. Morris, L. Chen, L. C. Serpell, J. Bacsá and G. M. Day, *Soft Matter*, 2010, **6**, 4144-4156.
24. K. M. Anderson, G. M. Day, M. J. Paterson, P. Byrne, N. Clarke and J. W. Steed, *Angew. Chem. Int. Edit.*, 2008, **47**, 1058-1062.
25. J. van Esch, S. De Feyter, R. M. Kellogg, F. De Schryver and B. L. Feringa, *Chem. Eur. J.*, 1997, **3**, 1238-1243.
26. L. S. Reddy, S. K. Chandran, S. George, N. J. Babu and A. Nangia, *Cryst. Growth Des.*, 2007, **7**, 2675-2690.
27. A. Cayuela, S. R. Kennedy, M. L. Soriano, C. D. Jones, M. Valcárcel and J. W. Steed, *Chem. Sci.*, 2015, **6**, 6139-6146.
28. L. Meazza, J. A. Foster, K. Fucke, P. Metrangolo, G. Resnati and J. W. Steed, *Nat. Chem.*, 2013, **5**, 42-47.
29. M. O. M. Piepenbrock, N. Clarke and J. W. Steed, *Soft Matter*, 2010, **6**, 3541-3547.
30. A. M. Todd, K. M. Anderson, P. Byrne, A. E. Goeta and J. W. Steed, *Cryst. Growth Des.*, 2006, **6**, 1750-1752.
31. J. D. Dunitz and J. Bernstein, *Acc. Chem. Res.*, 1995, **28**, 193-200.
32. A. Spek, *Acta Cryst. Sect. D*, 2009, **65**, 148-155.
33. J. X. Cui, Z. H. Shen and X. H. Wan, *Langmuir*, 2010, **26**, 97-103.
34. A. D. Becke, *J. Chem. Phys.*, 1993, **98**, 1372-1377.
35. T. H. Dunning, *J. Chem. Phys.*, 1989, **90**, 1007-1023.
36. W. J. Hehre, R. Ditchfield and J. A. Pople, *J. Chem. Phys.*, 1972, **56**, 2257-2261.
37. M. O. M. Piepenbrock, K. M. Anderson, B. C. R. Sansam, N. Clarke and J. W. Steed, *Crystengcomm*, 2009, **11**, 118-121.

38. D. Van der Spoel, E. Lindahl, B. Hess, G. Groenhof, A. E. Mark and H. J. C. Berendsen, *J. Comput. Chem.*, 2005, **26**, 1701-1718.
39. D. A. Case, T. E. Cheatham, T. Darden, H. Gohlke, R. Luo, K. M. Merz, A. Onufriev, C. Simmerling, B. Wang and R. J. Woods, *J. Computat. Chem.*, 2005, **26**, 1668-1688.

## 5. Targeting gelation over crystallisation in the self-assembly of linear tris(urea)s

### 5.1 Background

The gelation capacities of hydrogen bonding molecules are often strongly dependent on their conformational flexibility. A lack of long-range order is a common feature of gel aggregates, and one more likely to arise if the gelator can access a wide range of conformations. Moreover, disorder in the gelator assemblies may correlate with the frequency of branching in the resulting fibres, which can strongly influence the rheological properties of the bulk material. Unfortunately, predicting self-assembly outcomes for potential LMWGs can be challenging, due to the existence of multiple packing modes with similarly low potential energies.<sup>1-3</sup> A promising alternative strategy is to correlate the observed solid-state characteristics of the molecules with their interactions and dynamic behaviour in solution, probed via techniques such as neutron scattering and NMR spectroscopy.<sup>4-9</sup> Studies of this nature could aid the development of novel LMWGs and shed light on related biological aggregation pathways, such as the self-assembly of amyloid fibrils from misfolded proteins and soluble oligopeptides.<sup>10</sup>

Urea-based LMWGs represent a useful alternative to amide-based systems, as they typically form more robust supramolecular motifs and are thus more tolerant of extreme pH values and highly polar solvents.<sup>11</sup> Linear oligo(urea)s are close structural analogues of peptide systems with a similar tendency to form helical foldamers and other fibrous assemblies,<sup>12, 13</sup> and potential applications in anion binding,<sup>14-17</sup> intracellular DNA delivery,<sup>18</sup> peptide stabilisation<sup>19</sup> and antibacterial treatments.<sup>13, 20, 21</sup> A number of studies have demonstrated that multipodal oligo(urea)s can act as effective gelators, producing rigid trichelate complexes, dimeric capsules or columnar discotic assemblies.<sup>22-26</sup> By contrast, investigations of linear oligo(urea)s focus largely on the intramolecular hydrogen bonding of extended helicates,<sup>27, 28</sup> and seldom address their capacity for gel formation. One reason for this discrepancy is that multipodal species can often be synthesised in one or two steps, whereas the production of a linear analogue can require a relatively challenging, multi-step procedure. The principal difficulty

is that each reaction to extend the oligomer must preserve free amine sites for further urea couplings. Each intermediate in the process must therefore possess two or more amine groups, with countermeasures to eliminate the risk of polymeric side products.

Linear tris(urea)s were chosen as the focus of this study, as investigations into the self-assembly properties of these species are particularly rare. Indeed, only five (4%) of the 138 distinct and well-resolved tris(urea) crystal structures in version 5.36 of the CSD<sup>29</sup> (namely DUVLEM,<sup>17</sup> GERVUW,<sup>28</sup> REPQOU,<sup>27</sup> ZATBON<sup>16</sup> and ZATBUT) consist of linear molecules, compared with 25 (33%) of the 75 tetrakis(urea) structures and 35 (65%) of the 54 other oligo(urea) structures (Section 9.2). Arguably the most straightforward route to linear tris(urea)s is via the condensation of carbohydrazide with two equivalents of an isocyanate.<sup>30</sup> The products of this reaction, however, possess limited flexibility and are necessarily symmetric, exhibiting little variation in their self-assembly behaviour. A more versatile strategy is to construct ureas sequentially by reacting a difunctional reagent with one equivalent of its coupling partner. For example, Mousseau *et al.* achieved single substitution of a secondary diamine with phenyl isocyanate, generating a mono(urea) intermediate that could be further reacted with a diisocyanate to yield a tetrakis(urea).<sup>12</sup> Likewise, Kim *et al.* employed a Sonogashira reaction to couple ureas with iodoaryl and alkyne end groups, producing oligomers with between three and five monomeric units.<sup>15</sup> The main disadvantage of this approach is that selectivity depends strongly on the reaction conditions, and multiply substituted by-products may be difficult to avoid. Although mixtures of products may be separated by chromatographic techniques in some cases,<sup>21</sup> the poor solubilities and similar  $R_f$  values of oligo(urea)s may necessitate time-consuming optimisation of the purification process.

One way to produce oligo(urea)s more selectively is to make use of isocyanates or isocyanate equivalents with masked or protected amine groups.<sup>31</sup> Such species may react with an amine to generate the first urea linkage, and subsequently undergo deprotection to yield a new amine reactant for the second coupling step. Wu *et al.* produced anion-binding foldamers with up to six urea groups by coupling anilines with nitrophenyl isocyanates, reducing the nitro moieties and repeating the process.<sup>16, 32</sup> Similarly, Pendem *et al.* constructed a



variety of chiral hexakis(urea)s via iterative coupling of *N*-alkyl *O*-succinimidyl carbamates with reducible azide or Boc-protected amine groups.<sup>27</sup> The latter approach has been utilised in a convergent fashion to generate oligo(urea)s with as many 20 urea groups,<sup>33</sup> and may be modified for compatibility with solid-phase techniques,<sup>34, 35</sup> or to introduce alternative linkages such as amides, carbamates and thioureas.<sup>27</sup>

A clear drawback of most oligo(urea) syntheses is the need for multiple stages of deprotection. The preparation of protected substrates can in some cases prove difficult, and the conditions for their removal may limit the range of tolerated substituents. A key finding of this investigation is that tris(urea)s may be generated from unprotected diamines, by employing reaction conditions that promote the precipitation of singly coupled products. Exploiting the contrasting reactivities of aryl and alkyl amines allows benzylamines to be linked in a chemoselective fashion.<sup>36</sup> In addition, it is sometimes possible to isolate the precursor to urea formation in which, remarkably, both isocyanate equivalents and unreacted amine groups are present. These frustrated intermediates offer access to tris(urea) scaffolds with a wide range of connectivities. Positional isomers of oligo(urea)s can, like their peptide analogues, adopt starkly different conformations in solution, and exhibit useful diversity in their gelation abilities and aggregate morphologies.

## 5.2 Results and discussion

### 5.2.1 Synthesis

Tris(urea)s were synthesised from a range of amine-functionalised mono(urea) intermediates. In the simplest case, a symmetrical mono(urea) with two aniline functionalities is prepared via the homocoupling of a benzylamine with half an equivalent of 1,1'-carbonyldiimidazole (CDI, Fig. 96a).<sup>21, 37, 38</sup> Although the reactivity of CDI is similar to that of other amine coupling agents, its mechanism of action displays a number of advantages. Firstly, the carbonylimidazole intermediate is relatively stable in the presence of even moderate concentrations of water,<sup>39</sup> so does not undergo appreciable hydrolysis in undried solvents. Secondly, the reaction avoids the generation of problematic by-products, such as the pungent and toxic methanethiol gas liberated during the

analogous reaction of *S,S'*-dimethyl dithiocarbonate (Fig. 96b).<sup>36</sup> Thirdly, the leaving group in the reaction, imidazole, facilitates further coupling by acting as a base ( $pK_a$  7.05 in water<sup>40</sup>), and is too weak a nucleophile to displace other functionalities in the amine substrate. By contrast, methanethiol is a relatively strong nucleophile under basic conditions, and the acidity of *N*-hydroxysuccinimide ( $pK_a$  6.0<sup>41</sup>), produced during the reaction of *N,N'*-disuccinimidyl carbonate (Fig. 96c), can lead to deactivation of the reacting amine.

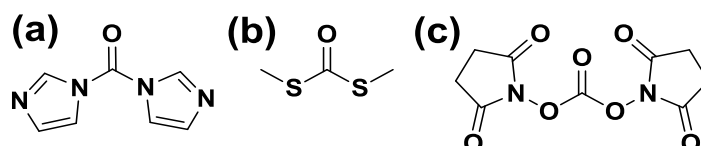
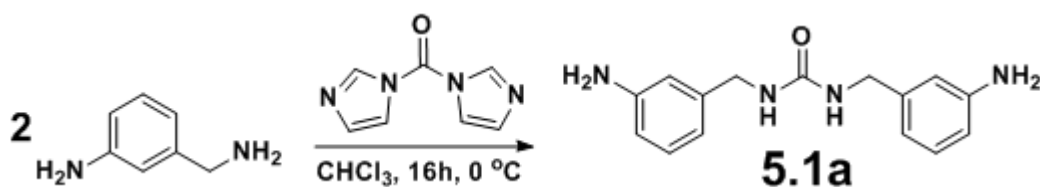


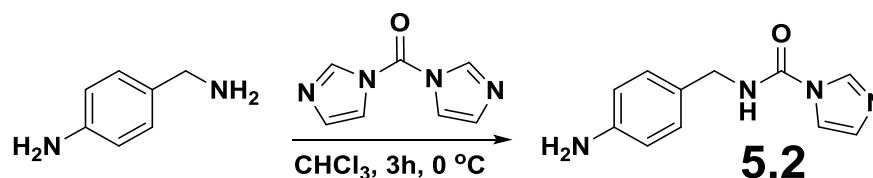
**Fig. 96** Common coupling agents for the synthesis of ureas and peptides: (a) CDI, (b) *S,S'*-dimethyl dithiocarbonate and (c) *N,N'*-disuccinimidyl carbonate.

Benzylamines are coupled chemoselectively by CDI due to the differing reactivities of the primary amine and aniline sites. However, mixing the reagents in chloroform or dichloromethane at room temperature does not produce a pure product: the precipitated solid contains an oligomeric component, generated via a CDI-mediated coupling of the target compound with one or more equivalents of additional amine. In the homocoupling of 3-aminobenzylamine, this problem may be circumvented by adding a CDI solution dropwise to a stirred solution of the amine at 0 °C. Chloroform or dichloromethane are the most suitable solvents for the reaction, as they readily dissolve both reactants but allow the mono(urea) product, **5.1a**, to precipitate on formation. In addition, the immiscibility of the solvents with water aids in minimising the loss of CDI, which is easily hydrolysed in wet solvents.

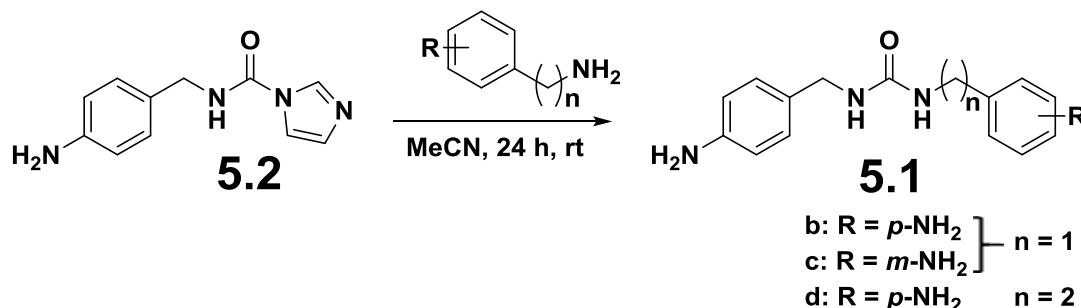


Although 4-aminobenzylamine is less susceptible than the 3-isomer to oligomerisation, homocoupling of the molecule with CDI at room temperature still results in a slightly impure product. Interestingly, adding the CDI solution dropwise to a solution of the amine at 0 °C does not yield the mono(urea) as the

major product, even when more than two equivalents of amine are used. Instead, the product is the carbonylimidazole intermediate of the CDI coupling, **5.2**, which precipitates before nucleophilic attack by the amine is able to take place. This species is stable in the solid state for several months under ambient conditions, despite possessing a moderately nucleophilic aniline group in addition to the electrophilic carbonyl moiety.



Compound **5.2** may be reacted with alkyl amines to produce a wide variety of mono(urea)s. In particular, mono(urea) diamines may be prepared by adding the intermediate to acetonitrile solutions of primary amines with additional aniline moieties. The symmetrical compound **5.1b** and its less symmetrical analogues **5.1c** and **5.1d** were synthesised as crystalline materials by reacting **5.2** with 4-aminobenzylamine, 3-aminobenzylamine and 4-(2-aminoethyl)aniline respectively. All of the compounds crystallise on formation, and may be further purified by recrystallization from hot methanol, yielding single crystals suitable for analysis by SC-XRD (Table 9). The structures of **5.1a**, **5.1b** and **5.1d**, labelled **XLIV**, **XLV** and **XLVI** respectively, all consist of non-solvated diamine molecules. Structures **XLV** and **XLVI** exhibit a  $Z'$  value of 1, while molecules in structure **XLIV** are located on a two-fold rotation axis so contribute only half a molecule to the asymmetric unit. The mono(urea)s interact to form  $\alpha$ -tape motifs, and are oriented such that the end groups on each side of a tape exhibit the same configuration (Fig. 97). Interestingly, hydrogen bonds between the amine groups of **5.1b** and **5.1c** in structures **XLIV** and **XLV** are relatively long (N-N contacts 3.316(2) and 3.158(4) Å respectively) and the end groups of **5.1d** in structure **XLVI** are not involved in any significant supramolecular motifs.



In the absence of protecting groups, tris(urea)s prepared via the CDI coupling of aminobenzylamines must always incorporate a urea moiety with two  $\alpha$  methylene sites, as the more reactive alkyl amine groups are the first to react. One way to synthesise tris(urea)s with alternative connectivity is to introduce the terminal urea groups of the target compound first, by reacting an isocyanate with an excess of the aminobenzylamine. The benzyl-functionalised mono(urea) **5.3** was synthesised via the addition of benzyl isocyanate to a stirred dichloromethane solution of 1.2 equivalents of 4-aminobenzylamine at 0 °C. It is worth noting that compound **5.3** may also be obtained by reacting **5.2** with benzylamine in acetonitrile. However, the selectivity of this reaction is slightly inferior, as the product is moderately soluble in the reaction solvent and can thus react with another equivalent of **5.2** to generate an oligomeric material.

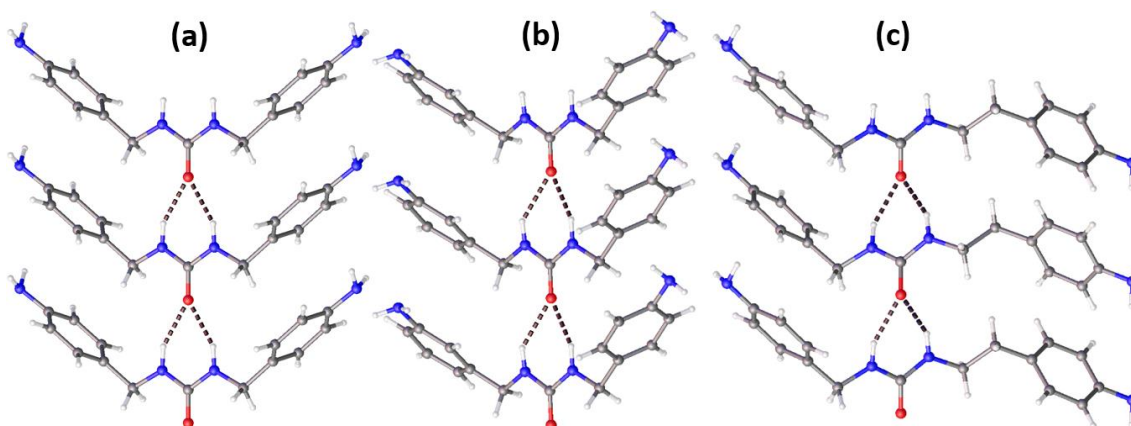
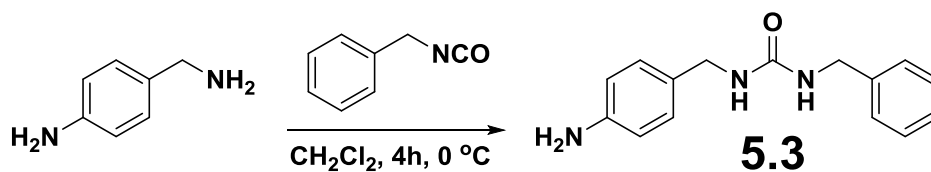


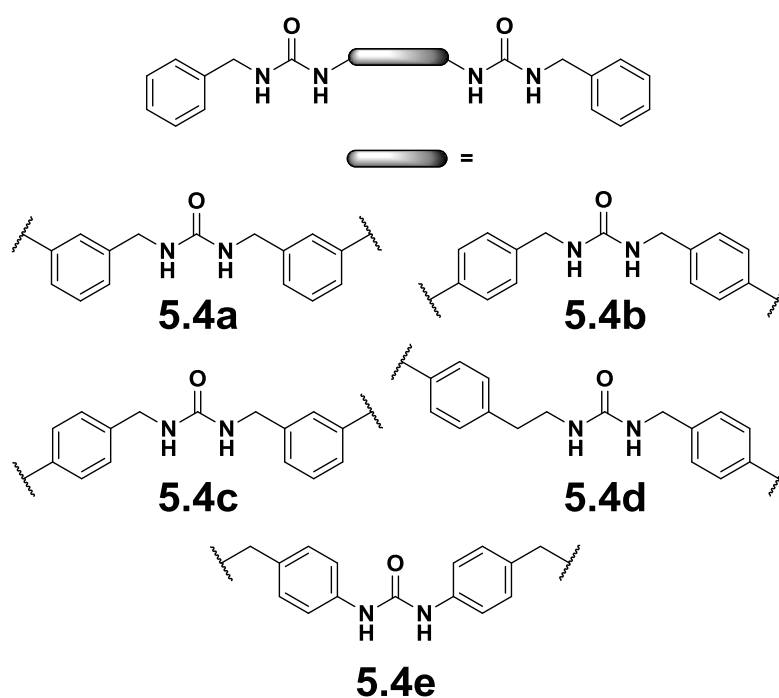
**Fig. 97** Arrangement of urea-urea hydrogen bonds between molecules of **5.1b**, **5.1c** and **5.1d** in structures **XLIV** (a), **XLV** (b) and **XLVI** (c) respectively.

	<b>5.1b (XLIV)</b>	<b>5.1c (XLV)</b>	<b>5.1d (XLVI)</b>
<b>Formula</b>	C <sub>15</sub> H <sub>18</sub> N <sub>4</sub> O	C <sub>15</sub> H <sub>18</sub> N <sub>4</sub> O	C <sub>16</sub> H <sub>20</sub> N <sub>4</sub> O
<b>Formula weight</b>	270.33	270.33	284.36
<b>Space group</b>	C2/c	C2	Pbca
<b>a / Å</b>	22.2703(16)	23.2045(18)	11.9119(6)
<b>b / Å</b>	4.5802(3)	4.6253(4)	8.5202(5)
<b>c / Å</b>	13.9016(10)	14.3611(11)	29.5884(15)
<b><math>\beta</math> / °</b>	106.252(2)	118.572(3)	90
<b>V / Å<sup>3</sup></b>	1361.33(16)	1353.63(19)	3003.0(3)
<b>Z</b>	4	4	8
<b>D<sub>calc</sub> / g cm<sup>-3</sup></b>	1.319	1.326	1.258
<b>R<sub>int</sub></b>	0.0411	0.0504	0.0942
<b>R<sub>1</sub> [<math>I \geq 2\sigma(I)</math>]</b>	0.0499	0.0508	0.0522
<b>wR<sub>2</sub> [all data]</b>	0.1451	0.1294	0.1277

**Table 9** Summary of crystallographic data for diamines **5.1b**, **5.1c** and **5.1d**.



Tris(urea)s are prepared from the diamine intermediates **5.1a-d** by refluxing the compounds in acetonitrile with two equivalents of an isocyanate. Benzyl end groups were targeted in this study, as preliminary work revealed that tris(urea)s of this type display interesting diversity in their self-assembly behaviour. All of the compounds, **5.4a-d**, may be purified by sonication in hot methanol. A fifth benzyl tris(urea) analogue, **5.4e**, was synthesised via the homocoupling of **5.3** in refluxing acetonitrile with half an equivalent of CDI.



### 5.2.2 Self-assembly behaviour

The gelation capacities of tris(urea)s **5.4a-e** were tested by sonicating and heating 1% (w/v) suspensions of the compounds in a range of organic solvents (Table 10). Neither water nor most organic solvents were capable of dissolving the materials to a significant extent. However, solutions could be obtained upon heating in a number of highly polar solvents. Cooling the solutions usually resulted in precipitation, but translucent gels of compounds **5.4a** and **5.4c** were observed in pyridine, cyclohexanone, benzyl alcohol, 3-chloro-1-propanol and acetic acid after standing for several hours at room temperature. In addition, it was possible to generate partial gels from a DMF solution of **5.4a** by exposure to diethyl ether

vapour under ambient conditions over one day. The gels are typically weak and can be disrupted easily by gentle warming or mechanical disturbance.

The rheological properties of the tris(urea) gels were further analysed by oscillatory shear rheometry (Fig. 98). The gels could not be prepared reliably on the rheometer *in situ*, so were pre-formed in 7 cm<sup>3</sup> vials and left to stand for three hours before being transferred to the Peltier plate. In stress sweep experiments, a 1% (w/v) gel of **5.4a** in cyclohexanone exhibits a plateau  $G'$  value of 13 kPa and a yield stress of 175-190 Pa.  $G'$  exceeds  $G''$  by an order of magnitude, and increases slowly with the shear frequency  $\omega$  in accordance with the expected power law relationship.<sup>42</sup> These properties are characteristic of a moderately strong fibrous gel. However, the rheological properties are highly solvent-dependent: partial gels prepared by diffusion of diethyl ether into a DMF solution are slightly stronger, while those formed in benzyl alcohol and 3-chloro-1-propanol are significantly weaker. Compound **5.4c** gels similar solvents to **5.4a**, but the materials were found to be too mechanically unstable for rheometric testing to be reliably performed.

SEM was used to investigate the microstructures of the as-synthesised tris(urea)s and the aggregates produced in gelation trials. Micrographs of as-synthesised **5.4b**, **5.4d** and **5.4e** and the precipitates from polar solvents display a range of plate-, rod- and ribbon-shaped aggregates (Fig. 99), which cannot give rise to a stable gel network. By contrast, synthesis of **5.4a** (Fig. 100a) in acetonitrile generates a gelatinous precipitate, comprising a uniform network of fibres 15-30 nm in diameter. Interestingly, xerogels prepared from 1% (w/v) gels of **5.4a** in 3-chloro-1-propanol (Fig. 100b) and by diffusion of ether vapour into DMF (Fig. 100c) are similar in appearance. Assuming the observed fibre networks are representative of those in the parent materials, it may be concluded that differences in the strength and opacity of the gels is due to slight variation in fibre density and connectivity. Compound **5.4c** also forms a gelatinous precipitate consisting of fibrous aggregates when synthesised in acetonitrile (Fig. 100d). However, these structures are less extended and more particulate than fibres in the pyridine (Fig. 100e) and acetic acid (Fig. 100f) gels, so less capable of generating a highly interconnected sample-spanning network.

	Pyridine	Cyclohexanone	Benzyl alcohol	3-chloro-1-propanol	Acetic acid	DMF	DMF + ether
<b>5.4a</b>	<b>G<sup>T</sup></b>	<b>G<sup>T</sup></b>	<b>PG<sup>T</sup></b>	<b>G<sup>T</sup></b>	GP	S	<b>PG<sup>C</sup></b>
<b>5.4b</b>	P	P	P	S	P	S	P
<b>5.4c</b>	<b>G<sup>T</sup></b>	<b>PG<sup>T</sup></b>	<b>PG<sup>T</sup></b>	S	<b>PG<sup>T</sup></b>	S	P
<b>5.4d</b>	P	P	P	P	P	P	P
<b>5.4e</b>	GP	P	P	S	P	P	P

**Table 10** Results of gelation trials for benzyl-functionalised linear tris(urea)s **5.4a-e**. Observations were made after heating 1% (w/v) solutions in 2 cm<sup>3</sup> sealed vials and allowing the materials to cool to room temperature for six hours. Results are marked with a letter corresponding to the aggregation outcome: G = gel (highlighted in bold), GP = gelatinous precipitate, P = precipitate and S = solution. Superscripts are used to denote the appearance of gels: C = clear (transparent), T = translucent and O = opaque.

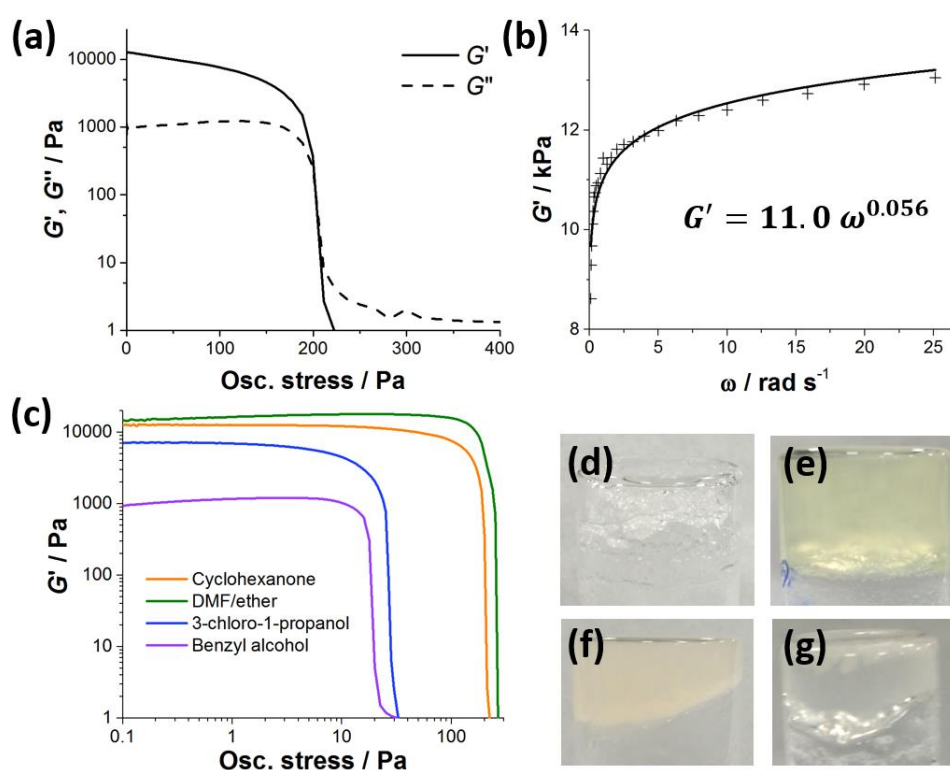


**Fig. 98** Stress sweep (a) and frequency sweep (b) profiles of a gel of **5.4a** in cyclohexanone display behaviour typical of a fibrous gel. Gels prepared by cooling a hot cyclohexanone solution of **5.4a** or exposing a DMF solution to ether vapour display plateau  $G'$  values of 13 and 17 kPa and yield stress of 175-190 and 200-220 Pa respectively (c). By contrast, gels in 3-chloro-1-propanol and benzyl alcohol are much weaker: the plateau  $G'$  values of the materials are 7 and 1 kPa, and the yield stresses just 24-26 and 16-18 Pa respectively. The solvent used also affects the appearance of the gel. Partial gels of **5.4a** prepared in DMF by vapour diffusion (d) are transparent, while gels in 3-chloro-1-propanol (e), benzyl alcohol (f), pyridine (g) and cyclohexanone are translucent. All gels were prepared using 1% (w/v) gelator solutions and analysed at 17 °C. Stress sweeps were conducted with a frequency of 1 Hz and frequency sweeps with a stress of 1 Pa.

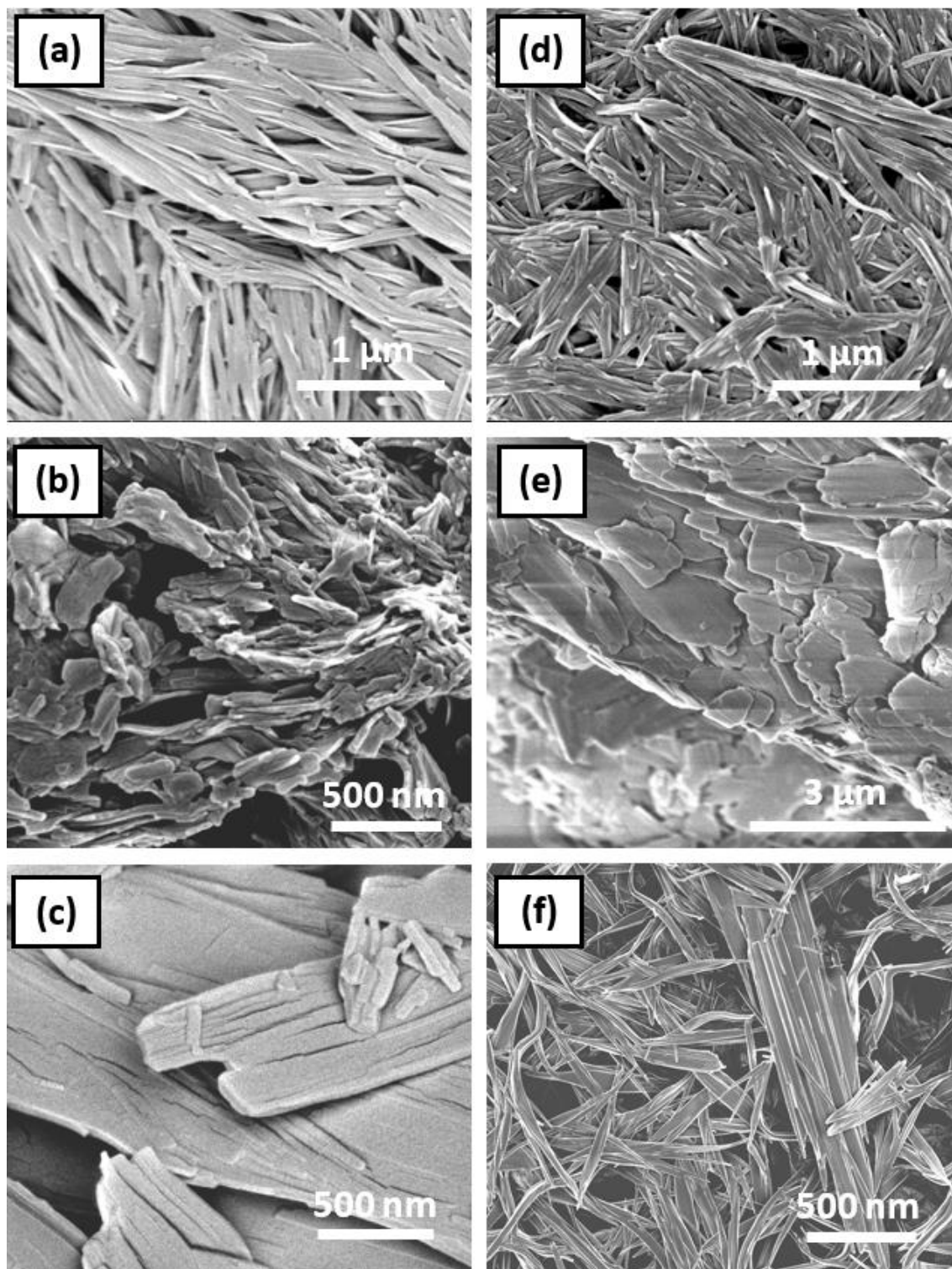


**Fig. 99** SEM micrographs of aggregates in as-synthesised **5.4b** (a), **5.4d** (b) and **5.4e** (c) and in precipitates of **5.4b**, **5.4d** and **5.4e** from 1% (w/v) solutions in pyridine, DMF and benzyl alcohol respectively. Aggregates of **5.4b** exhibit a consistent rod-like fibrous morphology, but these structures are not sufficiently extended and entangled for gelation to take place. The as-synthesised solid forms of **5.4d** and **5.4e** both consist of particulate aggregates that are highly crystalline in appearance. While the microstructure of **5.4d** is preserved following precipitation, **5.4e** forms ribbon-like fibres in a number of solvents. These aggregates greatly increase the viscosity of the sol but do not give rise to a stable gel network.



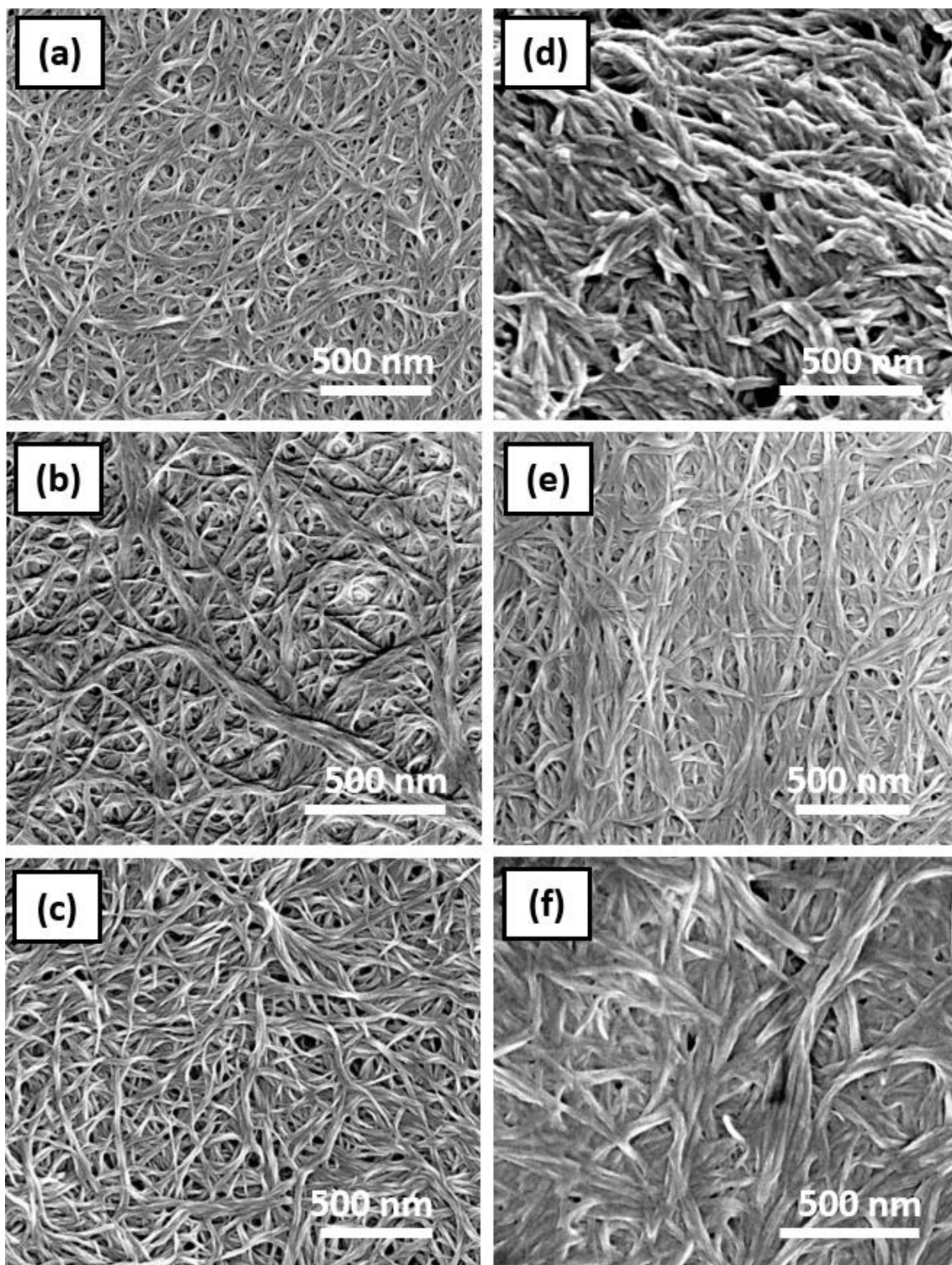


**Fig. 100** SEM micrographs of fibrous aggregates in as-synthesised **5.4a** (a) and xerogels prepared from 1% (w/v) gels in 3-chloro-1-propanol (b) and DMF/ether (c). The fibres are more extended and uniform in structure than those of as-synthesised **5.4c**. However, gels of **5.4c** in pyridine (e) and acetic acid (f) display similar interconnected fibre networks.

To gain further insight into the structural differences between the tris(urea) aggregates, PXRD data were obtained for the as-synthesised solids and a selection of air-dried precipitates and gels (Fig. 101). All of the patterns can be indexed to

lamellar structures with relatively large interlayer spacings, giving rise to approximately evenly spaced ( $h00$ ) reflections over the range  $2\theta = 3-18^\circ$ . The calculated  $d$ -spacings for these reflections lie in the range 25-31 Å, and are approximately equal to the lengths of the extended molecules. Thus, it is likely that the molecules adopt open-chain conformations and are oriented perpendicular to the lamellar planes with little interdigitation. Moreover, additional strong reflections beyond  $2\theta = 18.8^\circ$  suggest that molecules interact via  $\alpha$ -tapes in the plane of the lamellae, as the  $d$ -spacings of 4.5-4.7 Å are equal to the urea-urea separation in an ideal  $R_2^1(6)$  motif. The relative broadness of peaks in the patterns of **5.4a** and **5.4c** indicates that lamellae in these structures exhibit less long-range order, due to incorporation into narrow, high-curvature fibrous assemblies. That the patterns for solid **5.4a** and its gels are similar supports the conclusion that it is the connectivity of fibres rather than their molecular arrangements that leads to variability in gel formation.

Although the PXRD patterns suggest that all of the tris(urea)s form lamellar assemblies, the conformations and interactions of molecules within these lamellae may differ. Indeed, the relatively large  $d$ -spacings of **5.4b** and **5.4e** indicate that these molecules adopt almost fully extended conformations and are oriented perpendicular to the lamellar plane with little interdigitation. This conclusion is supported by geometry optimisations of model assemblies, which reveal that the measured  $d$ -spacing for **5.4b** is close to the maximum possible value for a single layer of molecules regardless of the relative orientations of neighbouring  $\alpha$ -tapes (Fig. 101a,b). Conversely, the unexpectedly narrow interlayer spacing of **5.4d**, nominally the longest molecule in this study, demonstrates that increasing the flexibility of the molecule by the inclusion of an additional methylene group allows lamellae to pack more closely together. It is interesting to note that gel formation is not necessarily associated with large differences in the thickness of lamellae. Nonetheless, peaks in the patterns of **5.4a** and **5.4c** are far wider than can be explained by Scherrer broadening alone, suggesting that the separation of layers may vary by several Å between different aggregate domains.

FT-IR spectra of the as-synthesised materials provide further evidence that variation of the molecular structure has a significant impact on self-assembly

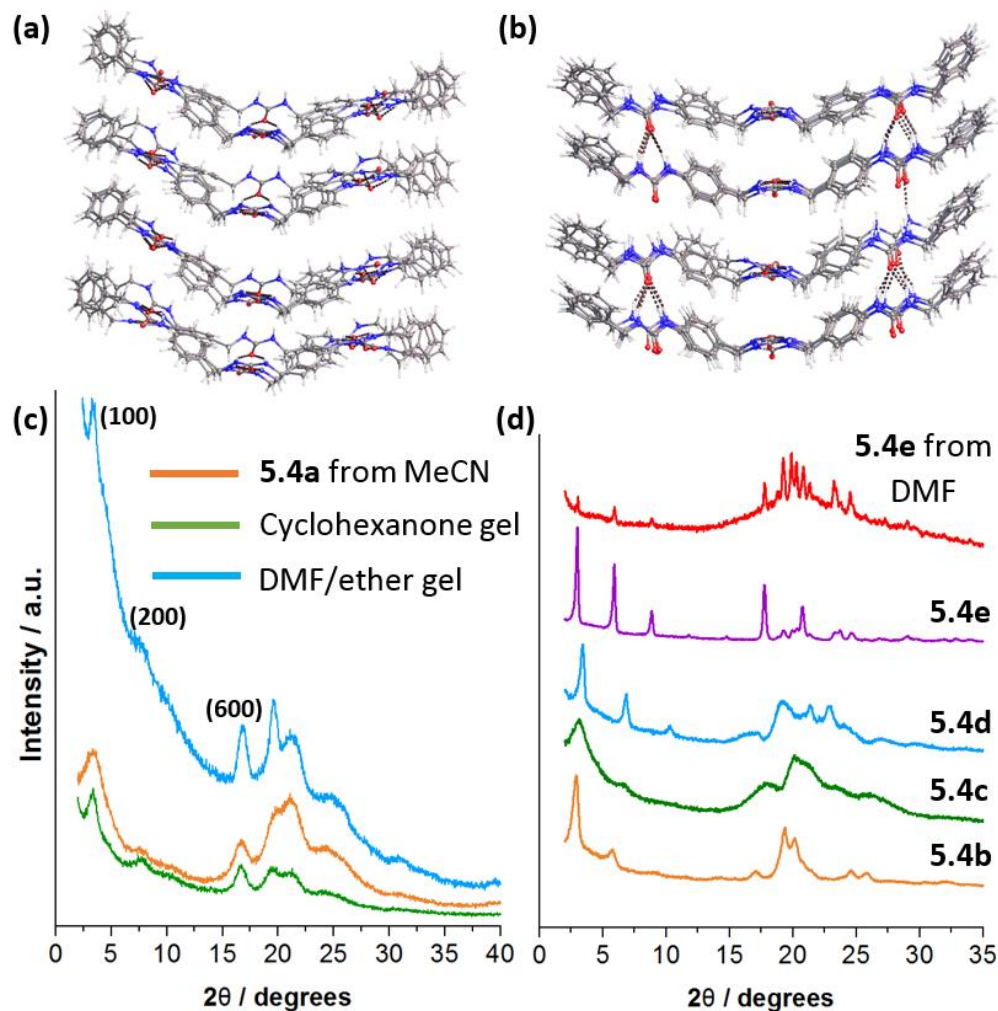


**Fig. 101** Simulated lamellar networks of **5.4b**, generated in SCIGRESS 3.0.0 by geometry optimisation of a 4x4 lattice in MO-G<sup>43</sup> using AM1 parameters.<sup>44</sup> Lamellae in which all  $\alpha$ -tapes are parallel (a) appear slightly more disordered than those containing a two-dimensional network of perpendicular tapes (b). PXRD patterns for as-synthesised solid **5.4a** and dried 1% (w/v) gels prepared in cyclohexanone and in DMF by vapour diffusion display broad peaks at consistent values of  $2\theta$  (c). Peaks in the PXRD pattern of as-synthesised **5.4c** are similarly broad, while the non-gelating derivatives **5.4b**, **5.4d** and **5.4e** give sharp peaks indicative of long-range order (d). All of the patterns may be indexed to a lamellar structure. The  $d$ -spacings for as-synthesised **5.4a**, **5.4b**, **5.4c**, **5.4d** and **5.4e** are 26.8, 30.7, 28.4, 25.8 and 29.9 Å respectively.

Notably, the  $d$ -spacing for **5.4b** is close to the thicknesses of the simulated lamellae (approximately 30 Å in both cases), suggesting that real assemblies consist of similarly extended molecules lying perpendicular to the lamellar plane with little interdigitation between layers.

behaviour (Fig. 102). In all cases, the data are consistent with the formation of strong urea-urea interactions, as the urea NH stretch, CO stretch (amide I band) and NH bend (amide II band) occur at substantially lower frequencies than would be expected in the absence of hydrogen bonding.<sup>45, 46</sup> However, the dominant NH stretching frequencies of the gelators **5.4a** and **5.4c** are 4-9 cm<sup>-1</sup> higher than those

of non-gelators **5.4b** and **5.4d**, which contain similarly functionalised urea moieties. In addition, the amide II frequencies are higher than those of the non-gelators by 2-10  $\text{cm}^{-1}$ . These observations are indicative of slightly weaker hydrogen bonding in the gelator aggregates, which may be attributed to the lower packing efficiency and more disordered arrangement of the molecules involved. It is interesting to note that while **5.4e** exhibits the greatest degree of long range order in PXRD, its FT-IR spectrum displays a small amide I band at the relatively high frequency of  $1693\text{ cm}^{-1}$ . It is possible that a proportion of carbonyl groups, most likely those of the central urea group, cannot be incorporated into  $\alpha$ -tapes due to steric hindrance by the neighbouring aryl groups and/or intramolecular aryl C-H---O=C hydrogen bonding.

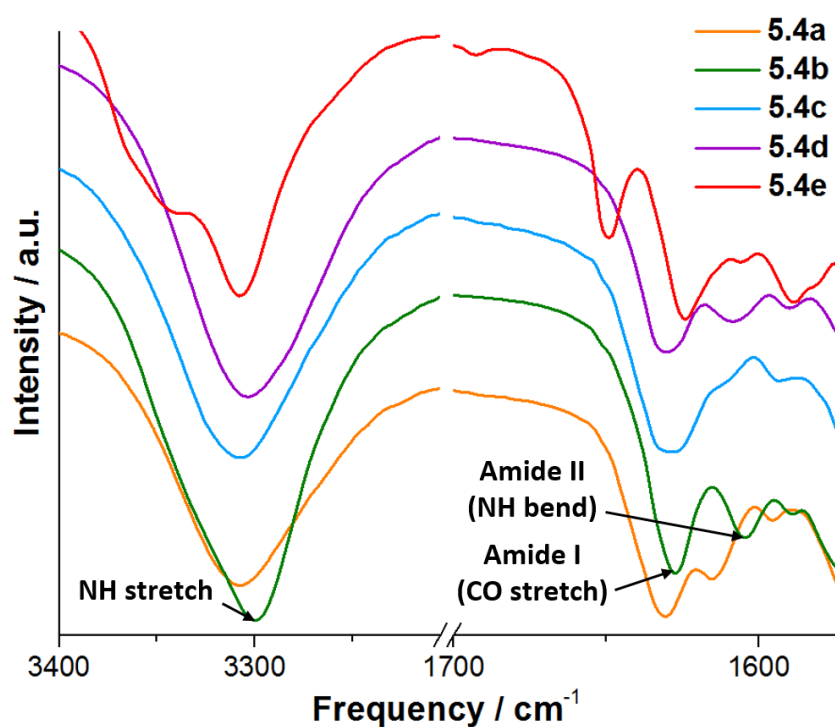


**Fig. 102** FT-IR spectra of as-synthesised solid forms of **5.4a-e**. For **5.4a**, **5.4b**, **5.4c**, **5.4d** and **5.4e**, the dominant NH stretching frequencies are, respectively, 3308, 3300, 3309, 3304 and 3308  $\text{cm}^{-1}$ ; the amide I frequencies, 1631, 1627, 1628, 1630 and 1624  $\text{cm}^{-1}$ ; and the amide II frequencies, 1615, 1605, 1611, 1609 and 1606  $\text{cm}^{-1}$ . Compound **5.4e** exhibits an additional NH stretch at  $3339\text{ cm}^{-1}$ , corresponding to the aryl-substituted central urea group. This functionality also gives rise to an amide I band at  $1649\text{ cm}^{-1}$ , with a small contribution at  $1693\text{ cm}^{-1}$  that may be attributed to carbonyl groups not involved in hydrogen bonding. The presence of non-interacting urea groups in this material is surprising given the lack of disorder evident in the PXRD data. It is possible that the central urea groups are less able to form strong urea-urea interactions due to the large steric bulk and inflexibility of the attached aryl moieties, and possible presence of competing intramolecular aryl C-H---O=C hydrogen bonds.

### 5.2.3 Solution-state conformations

Analysis of tris(urea)s **5.4a-e** in the solid state suggests that the molecules do not undergo intramolecular hydrogen bonding to adopt a folded conformation. This is unexpected, as even short oligo(urea)s have been found to form helical foldamers both before and after crystallisation.<sup>16, 17, 27, 28</sup> It is possible that intramolecular hydrogen bonds are feasible in solution but are removed in favour of intermolecular interactions when self-assembly takes place. To test this hypothesis, the geometries of the molecules were optimised by DFT calculations in the gas phase, using the B3LYP functional<sup>47</sup> and 6-31+G\* basis set.<sup>48</sup> Each molecule was first modelled in an open-chain, flexible conformation, to obtain an estimate of the minimum potential energy in the absence of hydrogen bonding. Subsequently, the conformation was altered to bring the carbonyl oxygen of one terminal urea group into contact with a hydrogen atom of the other, and a second geometry optimisation performed. The difference between the two calculated energies,  $\Delta E_{U-U}$ , represents an estimate of the change in potential energy due to intramolecular urea-urea hydrogen bonding. This calculation takes into account the destabilisation of the molecule as torsion angles are displaced from their equilibrium values. It should be noted, however, that the calculations are performed in the gas phase at 0 K, so do not incorporate solvation effects or the decrease in entropy resulting from the loss of conformational freedom when a hydrogen bond is formed. Notwithstanding these limitations, trends in the results offer a useful indication of the relative stabilities of the hydrogen bonded conformers, as the tris(urea)s display comparable numbers of flexible torsion angles and are unlikely to vary greatly in their potential for solvation.

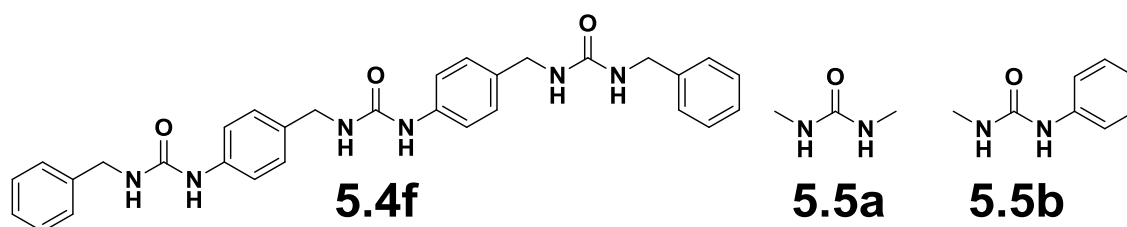


**Fig. 103** DFT calculations were used to obtain  $\Delta E_{U-U}$  and  $\Delta E_{U-Cl}$  values for the hypothetical tris(urea) **5.4f** and model mono(urea)s **5.5a** and **5.4b**. The mono(urea)s were chosen to explore the effects of alkyl and aryl substituents on the interaction energies, and to probe the stabilities of 2:1 urea-chloride complexes in the absence of conformational strain.

The results of the DFT calculations indicate that the energy of an intramolecular hydrogen bond is strongly dependent on the molecular configuration. Comparison of the  $\Delta E_{U-U}$  values, including the energy for the hypothetical tris(urea) analogue **5.4f** (Fig. 103), reveals that the stabilities of the hydrogen bonded species decrease in the order **5.4d**  $\approx$  **5.4c** > **5.4b**  $\approx$  **5.4e** > **5.4a**  $\gg$  **5.4f** (Fig. 104). A key factor dictating the feasibility of hydrogen bonding is the conformation of the central urea group. Compound **5.4a** displays a positive value of  $\Delta E_{U-U}$  because interactions between the terminal urea groups require the third urea to adopt a highly unfavourable *anti-anti* conformation. The other molecules can undergo intramolecular hydrogen bonding with all of the urea groups in the relatively stable *syn-syn* conformation. It must be noted, however, that conformational strain elsewhere in the molecule can also lead to dramatic destabilisation of the hydrogen bonded system. In particular, **5.4c** and **5.4e** display strained urea-methylene C-N-C bond angles of 88 and 123° respectively, and the bond between one aromatic ring and its urea substituent in **5.4f** is bent 12° out of the plane of the ring. Even in the most stable hydrogen bonded system, **5.4d**, the value of  $\Delta E_{U-U}$  is 29-44% smaller than the energies calculated for dimers of **5.5a** and **5.5b**, which can interact without deviating from the most stable molecular geometries.

Probing the stability of intramolecular urea-urea hydrogen bonds by NMR is difficult, as the formation of these interactions is concentration-independent and, in the presence of a polar solvent, only weakly influences the  $^1\text{H}$  chemical shift of the urea protons. The feasibility of the interaction may be qualitatively assessed, however, via proxy measurements of anion binding constants in solution. In order to act as a chelating ligand, a tris(urea) must adopt a conformation only slightly less strained than the C-shaped geometry required for intramolecular hydrogen bonding. Anion binding to urea groups is typically strong,<sup>14, 15, 49</sup> and can be readily analysed by measuring the changes in chemical shift when a tetrabutylammonium (TBA) salt of the anion is added in aliquots to a urea solution of fixed concentration.<sup>50</sup>

The gas-phase stabilities of the 1:1 chloride complexes of compounds **5.4a-f** were estimated via a DFT method analogous to that previously described (Fig. 105). To assess the impact of conformational strain on the energies of the

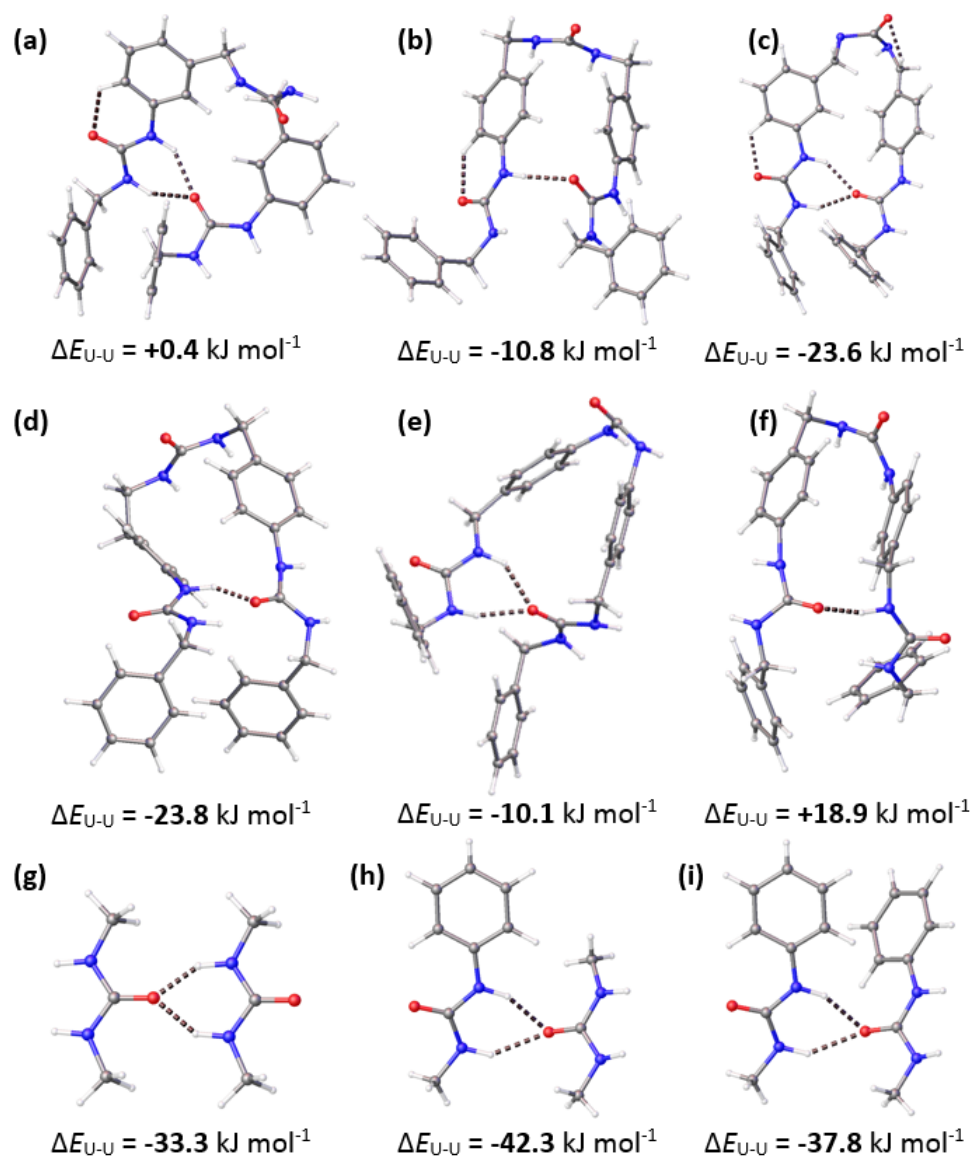


**Fig. 104** DFT optimised geometries and urea-urea hydrogen bonding energies of **5.4a** (a), **5.4b** (b), **5.4c** (c), **5.4d** (d), **5.4e** (e) and **5.4f** (f), and the model mono(urea) dimers (**5.5a**)<sub>2</sub> (g), (**5.5a**)(**5.5b**) (h) and (**5.5b**)<sub>2</sub> (i). Calculations were performed with the B3LYP functional and 6-31+G\* basis set. Where two bonding topologies are possible, the most stable calculated outcome is shown.

tris(urea) systems, 1:2 complexes of chloride ions with the mono(urea)s **5.5a** and **5.5b** were also analysed. Variation in the total urea-chloride binding energy,  $\Delta E_{U-Cl}$ , approximately matches the trend in  $\Delta E_{U-U}$ : stability decreases in the order **5.4d**  $\approx$  **5.4c** > **5.4b** > **5.4a**  $\gg$  **5.4f**  $\approx$  **5.4e**. Generally, larger values of  $\Delta E_{U-Cl}$  are displayed by molecules that can establish three or four hydrogen bonds to the chloride ion, while compounds that form just one or two bonds (namely **5.4a** and **5.4f**) give rise to less favourable complexes. Compound **5.4e** represents an exception, as the formation of four significant N-H---Cl contacts requires highly strained urea-aryl



C-N-C bond angles of 106 and 136°. It is interesting to note that the most stable tris(urea) complex exhibits a  $\Delta E_{U-Cl}$  value just 6% lower than that of the most stable mono(urea) system, and exceeds the stability of the least stable mono(urea) complex by 25 kJ mol<sup>-1</sup> (14%). This similarity suggests that the chelation of chloride ions introduces much less strain than intramolecular hydrogen bonding. Nonetheless, a plot of  $\Delta E_{U-U}$  against  $\Delta E_{U-Cl}$  for the tris(urea) systems reveals a moderately strong positive correlation (Fig. 106) encompassing all of the analogues except **5.4e**, confirming the validity of the chloride binding model for determining the likely stability of the urea-urea motif.

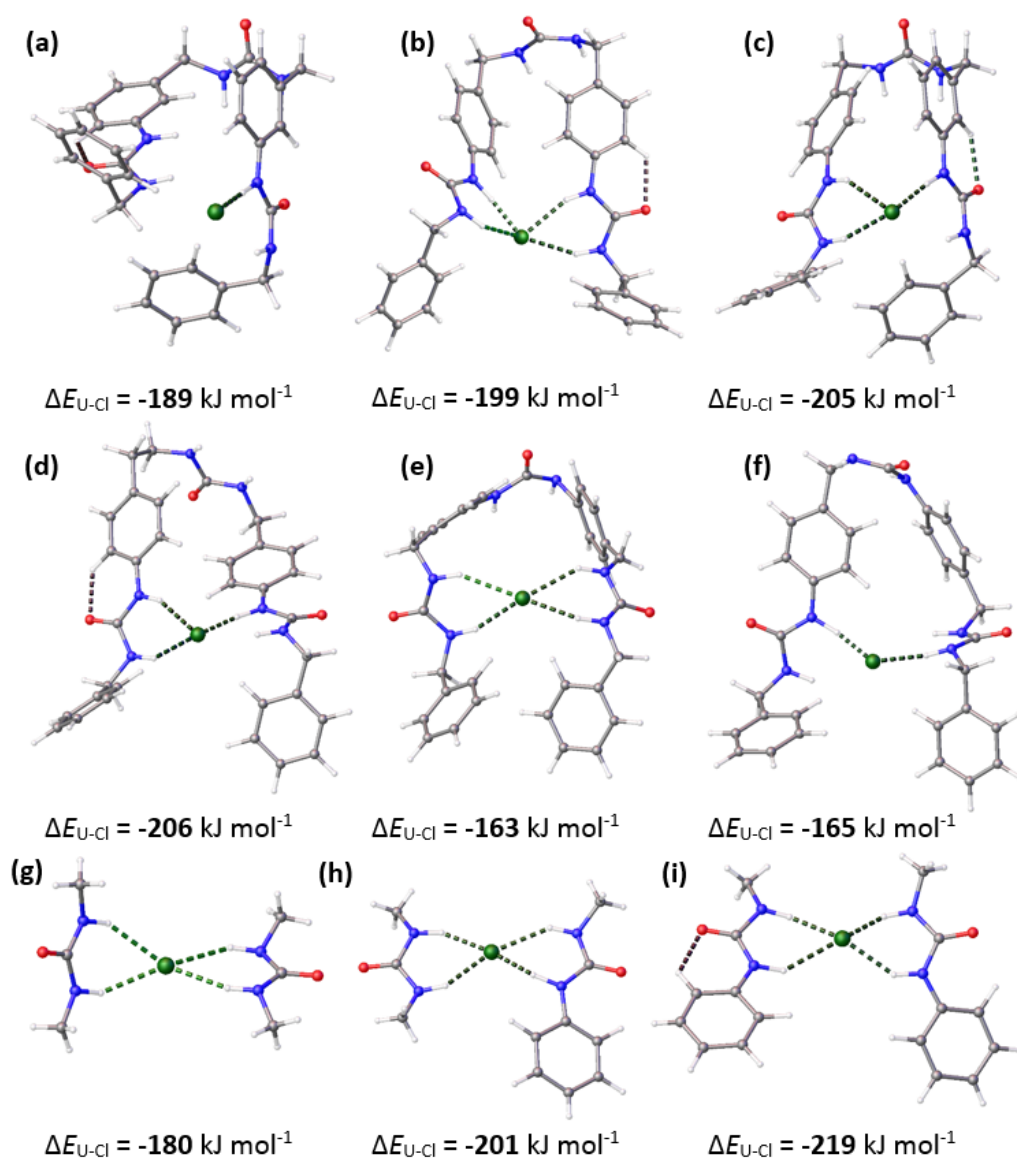


**Fig. 105** DFT optimised geometries and formation energies for 1:1 chloride complexes of **5.4a** (a), **5.4b** (b), **5.4c** (c), **5.4d** (d), **5.4e** (e) and **5.4f** (f). The stabilities of model 1:2 chloride-mono(urea) complexes [(**5.5a**)<sub>2</sub>Cl]<sup>-</sup> (g), [(**5.5a**)(**5.5b**)Cl]<sup>-</sup> (h) and [(**5.5b**)<sub>2</sub>Cl]<sup>-</sup> (i) were also calculated. Hydrogen bonds are marked if the N-H...Cl contact distance is less than 2.6 Å.



The chloride binding constants of tris(urea)s **5.4a-e** in DMSO were measured by NMR titration experiments. Chloride ions were added as the TBA salt to 20 mM solutions of the ureas in DMSO- $d_6$  to achieve chloride/urea molar ratios ranging from 0 to 10 (Fig. 107). Job plots for **5.4a** and **5.4e**, constructed by varying the chloride/urea molar ratio while keeping the sum of the concentrations constant,<sup>51</sup> reveal that the species bind the anions with a 1:1 stoichiometry. Thus, the titration data were fitted to 1:1 binding isotherms, yielding estimates for the urea-chloride binding constant  $K_{11}$ . Unexpectedly, the measurements indicate that complexes of **5.4e** with chloride ions are the most stable ( $K_{11} = 35 \pm 2$ ), while  $K_{11}$  values for the other compounds all lie in the range 8.5-13.5. The lack of correlation between calculated  $\Delta E_{U-Cl}$  values and the experimental data suggests that the tris(urea)s in DMSO are largely non-chelating. It may be inferred that intramolecular hydrogen bonding is also unlikely, and that molecules generally adopt open-chain conformations comparable to those of the aggregated species. This result highlights the importance of spacer flexibility in determining the self-assembly pathways of extended hydrogen bonding molecules, and could serve as a useful point of reference for the design of oligo(urea)s with improved gelation and anion-binding characteristics.

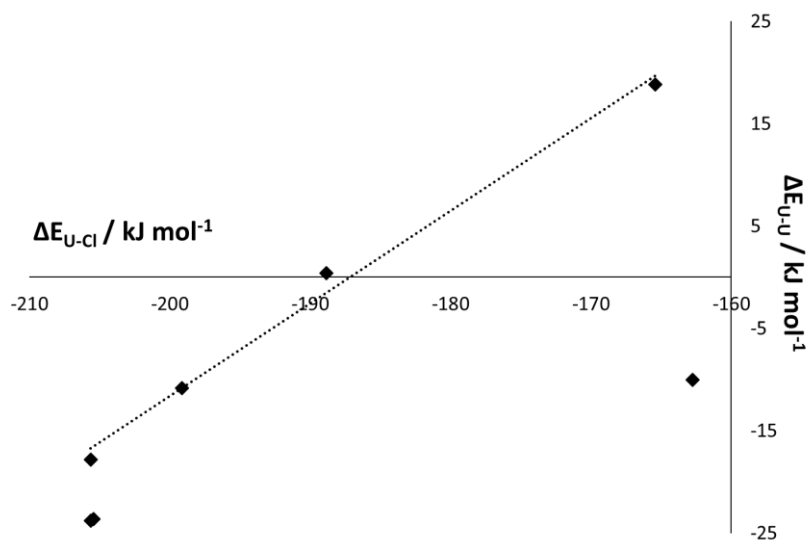


**Fig. 106** Comparison of the DFT intramolecular urea-urea hydrogen bonding energies,  $\Delta E_{U-U}$ , of compounds **5.4a-f** with the formation energies of their 1:1 urea-chloride complexes,  $\Delta E_{U-Cl}$ . Energies for the two possible intramolecular hydrogen bonding configurations of compound **5.4d** are displayed as both are energetically feasible. Four points belonging to compounds **5.4a**, **5.4b**, **5.4d** and **5.4f** exhibit an almost exactly linear trend, with  $R^2 = 0.99$ .

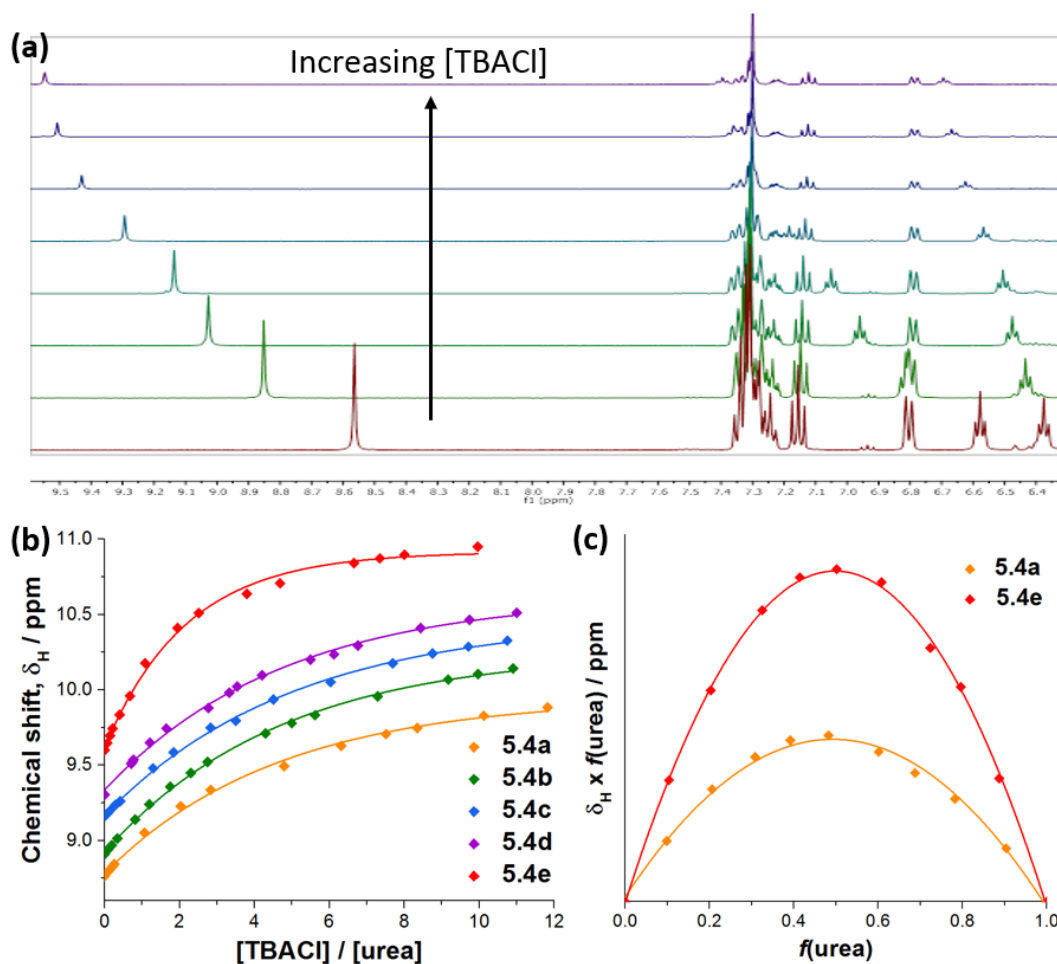


**Fig. 107**  $^1\text{H}$  NMR spectra for compound **5.4a** in  $\text{DMSO-}d_6$  with varying quantities of added TBACl (a). Increasing the chloride concentration results in large down-field shifts in the urea signals. Chloride ions produce similar shifts in the spectra for compounds **5.4a-d** (b), suggesting that there is little variation in the chloride binding constants of these species. However, the shifts for **5.4e** begin to plateau at lower chloride/urea ratios, indicating that coordination of chloride in this system occurs far more readily. Job plots of **5.4a** and **5.4e** (c) display maxima when  $f(\text{urea}) = [\text{urea}]/([\text{urea}] + [\text{TBACl}]) = 0.5$ . Thus, the data are fitted to 1:1 binding isotherms. The binding constants,  $K_{11}$ , of **5.4a**, **5.4b**, **5.4c**, **5.4d** and **5.4e** were calculated to be  $13.3 \pm 0.5$ ,  $10.0 \pm 0.1$ ,  $8.7 \pm 0.2$ ,  $10.9 \pm 0.3$  and  $35 \pm 2$  respectively. For clarity, the titration curves in (b) are separated by increasing the chemical shifts of **5.4b**, **5.4c**, **5.4d** and **5.4e** by 0.25, 0.5, 0.75 and 1.0 respectively.

### 5.3 Conclusions

Predicting the arrangement of molecules within aggregates of LMWGs is a challenging task, due to the conformational flexibility of the species in solution and the disordered nature of the materials formed. A combination of DFT and NMR titration results reveal that the outcome of self-assembly in tris(urea) systems is strongly dependent on the molecular configuration. Comparing the chloride binding constants for five structural variants, including four isomeric

species, suggests that chelation of the anion via the two terminal urea groups introduces too much strain to represent the dominant mode of coordination. Thus, molecules are likely to adopt open-chain conformations, as observed in PXRD data for the gels and solid materials. All of the aggregates analysed consist of lamellar assemblies. However, spacer moieties that result in more bent and asymmetrical open-chain geometries are more strongly associated with gel formation, due to the inability of the molecules to adopt close-packed arrangements with extensive long-range order. The novel synthetic strategies presented allow these spacers to be adjusted in a modular fashion, and may therefore be exploited to tune the self-assembly behaviour of a tris(urea) for particular applications. Overall, the results illustrate the importance of molecular shape effects in the design of effective LMWGs, highlight the strengths and limitations of solution-state studies in predicting gel formation, and reveal general synthetic routes to oligo(urea) compounds for use as gelators, peptide analogues and anion-binding agents.

## 5.4 References

1. J. A. Foster, K. K. Damodaran, A. Maurin, G. M. Day, H. P. G. Thompson, G. J. Cameron, J. C. Bernal and J. W. Steed, *Chem. Sci.*, 2017, **8**, 78-84.
2. D. J. Adams, K. Morris, L. Chen, L. C. Serpell, J. Bacsá and G. M. Day, *Soft Matter*, 2010, **6**, 4144-4156.
3. K. M. Anderson, G. M. Day, M. J. Paterson, P. Byrne, N. Clarke and J. W. Steed, *Angew. Chem. Int. Edit.*, 2008, **47**, 1058-1062.
4. S. R. Kennedy, A. Miquelot, J. A. Aguilar and J. W. Steed, *Chem. Commun.*, 2016, **52**, 11846-11849.
5. N. Steinke, R. J. Gillams, L. C. Pardo, C. D. Lorenz and S. E. McLain, *Phys. Chem. Chem. Phys.*, 2016, **18**, 3862-3870.
6. H. Kumari, S. E. Armitage, S. R. Kline, K. K. Damodaran, S. R. Kennedy, J. L. Atwood and J. W. Steed, *Soft Matter*, 2015, **11**, 8471-8478.
7. R. J. Davey, S. L. M. Schroeder and J. H. ter Horst, *Angew. Chem. Int. Ed.*, 2013, **52**, 2166-2179.
8. B. J. B. Folmer, R. P. Sijbesma, H. Kooijman, A. L. Spek and E. W. Meijer, *J. Am. Chem. Soc.*, 1999, **121**, 9001-9007.
9. J. Shang, Q. Gan, S. J. Dawson, F. Rosu, H. Jiang, Y. Ferrand and I. Huc, *Org. Lett.*, 2014, **16**, 4992-4995.
10. D. M. Ke, C. L. Zhan, X. Li, X. Wang, Y. Zeng and J. N. Yao, *J. Colloid Interface Sci.*, 2009, **337**, 54-60.
11. M. de Loos, B. L. Feringa and J. H. van Esch, *Eur. J. Org. Chem.*, 2005, 3615-3631.
12. J. J. Mousseau, L. Y. Xing, N. Tang and L. A. Cuccia, *Chem. Eur. J.*, 2009, **15**, 10030-10038.

13. A. Violette, S. Fournel, K. Lamour, O. Chaloin, B. Frisch, J. P. Briand, H. Monteil and G. Guichard, *Chem. Biol.*, 2006, **13**, 531-538.
14. V. Diemer, L. Fischer, B. Kauffmann and G. Guichard, *Chem. Eur. J.*, 2016, **22**, 15684-15692.
15. M. J. Kim, H. W. Lee, D. Moon and K. S. Jeong, *Org. Lett.*, 2012, **14**, 5042-5045.
16. B. Wu, C. D. Jia, X. L. Wang, S. G. Li, X. J. Huang and X. J. Yang, *Org. Lett.*, 2012, **14**, 684-687.
17. C. Jia, B. Wu, S. Li, Z. Yang, Q. Zhao, J. Liang, Q.-S. Li and X.-J. Yang, *Chem. Commun.*, 2010, **46**, 5376-5378.
18. C. Douat, C. Aisenbrey, S. Antunes, M. Decossas, O. Lambert, B. Bechinger, A. Kichler and G. Guichard, *Angew. Chem. Int. Edit.*, 2015, **54**, 11133-11137.
19. J. Fremaux, L. Mauran, K. Pulka-Ziach, B. Kauffmann, B. Odaert and G. Guichard, *Angew. Chem. Int. Edit.*, 2015, **54**, 9816-9820.
20. C. Aisenbrey, N. Pendem, G. Guichard and B. Bechinger, *Org. Biomol. Chem.*, 2012, **10**, 1440-1447.
21. H. Z. Tang, R. J. Doerksen and G. N. Tew, *Chem. Commun.*, 2005, 1537-1539.
22. M. Yamanaka, T. Nakagawa, R. Aoyama and T. Nakamura, *Tetrahedron*, 2008, **64**, 11558-11567.
23. C. E. Stanley, N. Clarke, K. M. Anderson, J. A. Elder, J. T. Lenthall and J. W. Steed, *Chem. Commun.*, 2006, **30**, 3199-3201.
24. J. J. van Gorp, J. Vekemans and E. W. Meijer, *J. Am. Chem. Soc.*, 2002, **124**, 14759-14769.
25. M. de Loos, A. G. J. Ligtenbarg, J. van Esch, H. Kooijman, A. L. Spek, R. Hage, R. M. Kellogg and B. L. Feringa, *Eur. J. Org. Chem.*, 2000, 3675-3678.
26. J. J. González, R. Ferdani, E. Albertini, J. M. Blasco, A. Arduini, A. Pochini, P. Prados and J. de Mendoza, *Chem.-Eur. J.*, 2000, **6**, 73-80.
27. N. Pendem, Y. R. Nelli, C. Douat, L. Fischer, M. Laguerre, E. Ennifar, B. Kauffmann and G. Guichard, *Angew. Chem. Int. Edit.*, 2013, **52**, 4147-4151.
28. B. Legrand, C. André, E. Wenger, C. Didierjean, M. C. Averlant-Petit, J. Martinez, M. Calmes and M. Amblard, *Angew. Chem. Int. Edit.*, 2012, **51**, 11267-11270.
29. C. R. Groom, I. J. Bruno, M. P. Lightfoot and S. C. Ward, *Acta Crystallogr. Sect. B*, 2016, **72**, 171-179.
30. N. Roy, E. Buhler and J. M. Lehn, *Chem. Eur. J.*, 2013, **19**, 8814-8820.
31. E. Valeur and M. Bradley, *Chem. Soc. Rev.*, 2009, **38**, 606-631.
32. P. J. Yang, J. M. Wang, C. D. Jia, X. J. Yang and B. A. Wu, *Eur. J. Org. Chem.*, 2013, 3446-3454.
33. J. Fremaux, L. Fischer, T. Arbogast, B. Kauffmann and G. Guichard, *Angew. Chem. Int. Edit.*, 2011, **50**, 11382-11385.
34. A. Violette, N. Lancelot, A. Poschalko, M. Piotto, J. P. Briand, J. Raya, K. Elbayed, A. Bianco and G. Guichard, *Chem. Eur. J.*, 2008, **14**, 3874-3882.
35. G. Guichard, V. Semetey, M. Rodriguez and J. P. Briand, *Tetrahedron Lett.*, 2000, **41**, 1553-1557.
36. M. K. Leung, J. L. Lai, K. H. Lau, H. H. Yu and H. J. Hsiao, *J. Org. Chem.*, 1996, **61**, 4175-4179.
37. P. A. Duspara, M. S. Islam, A. J. Lough and R. A. Batey, *J. Org. Chem.*, 2012, **77**, 10362-10368.
38. J. A. Grzyb and R. A. Batey, *Tetrahedron Lett.*, 2008, **49**, 5279-5282.
39. R. K. Sharma and R. Jain, *Synlett*, 2007, 603-606.
40. H. Walba and R. W. Isensee, *J. Org. Chem.*, 1961, **26**, 2789-2791.
41. D. E. Ames and T. F. Grey, *J. Chem. Soc.*, 1955, 631-636.

42. P. Terech, D. Pasquier, V. Bordas and C. Rossat, *Langmuir*, 2000, **16**, 4485-4494.
43. J. J. P. Stewart, *Quant. Chem. Prog. Exch.*, 1990, **10**, 86.
44. M. J. S. Dewar, E. G. Zoebisch, E. F. Healy and J. J. P. Stewart, *J. Am. Chem. Soc.*, 1985, **107**, 3902-3909.
45. C. S. Paik Sung, T. W. Smith and N. H. Sung, *Macromolecules*, 1980, **13**, 117-121.
46. C. G. Cannon, *J. Phys. Chem.*, 1976, **80**, 1247-1248.
47. A. D. Becke, *J. Chem. Phys.*, 1993, **98**, 1372-1377.
48. W. J. Hehre, R. Ditchfield and J. A. Pople, *J. Chem. Phys.*, 1972, **56**, 2257-2261.
49. G. O. Lloyd, M. O. M. Piepenbrock, J. A. Foster, N. Clarke and J. W. Steed, *Soft Matter*, 2012, **8**, 204-216.
50. P. Thordarson, *Chem. Soc. Rev.*, 2011, **40**, 1305-1323.
51. J. S. Renny, L. L. Tomasevich, E. H. Tallmadge and D. B. Collum, *Angew. Chem. Int. Ed.*, 2013, **52**, 11998-12013.

## 6. Braided helices and lily pad gels: controlling hierarchical self-assembly over a range of length scales

### 6.1 Background

The gelation behaviour of LMWGs is commonly attributed to specific supramolecular interactions. Hydrogen bonding of amides and ureas, for example, drives anisotropic aggregation by producing tape motifs along a single axis,<sup>1</sup> and amphiphilic gelators commonly assemble into highly extended tubular micelles.<sup>2</sup> Although these processes are important, it must be noted that the appearance and mechanical properties of supramolecular gels can be strongly influenced by self-assembly on a larger scale.<sup>3</sup> In amyloids, for example there is evidence that amyloid fibrils form helical bundles more readily if they are left-handed,<sup>4</sup> but that chirality inversion is possible when multiple left-handed bundles are intertwined.<sup>5</sup> Interactions between fibrils could affect their ability to propagate, and are therefore an important consideration in the study of prion diseases and other protein misfolding pathologies.<sup>6</sup>

Ordered assemblies of entangled fibres have been observed in a wide range of polymeric systems. In nearly all instances, the fibres involved exhibit pronounced twisted morphologies.<sup>7</sup> Such structures are typically described as cylindrical helices or coils, which exhibit zero Gaussian curvature and a constant separation from the central screw axis, or twisted ribbons, wherein the screw axis coincides with the midline of the fibre.<sup>8</sup> In practice, the shapes of fibres often lie between these extremes, and can vary in response to environmental factors such as solvent, pH, temperature and guest inclusion.<sup>8-10</sup> Twisting on a molecular scale may arise if the self-assembling species favour an offset stacking arrangement,<sup>11</sup> or due to a stress imbalance between the edges or faces of a lamella, caused by topological asymmetry of the surface residues.<sup>12</sup> Coiling may also serve to strengthen interactions between non-adjacent sections of a chain<sup>13-15</sup> or reduce the area exposed to solvent, such that surface energy<sup>16</sup> and excluded volume effects<sup>17</sup> are minimised. Since the strain due to curvature scales with the radius of the structure, twisted fibres tend to be relatively narrow and monodisperse.<sup>8, 18</sup> The pitch-to-radius ratio is similarly conserved, and dictated principally by

packing constraints,<sup>14, 15, 17</sup> the elastic moduli of the fibre<sup>8, 19</sup> and its interactions with solvent during self-assembly.<sup>8</sup>

Twisted fibres in Nature exhibit a wide range of morphologies, and such diversity is further evident at a superstructural level.<sup>20</sup> Interactions between non-adjacent helices typically arise through matching of grooves and ridges, and are thus highly sensitive to the handedness and orientations of adjacent fibres.<sup>21-23</sup> In general, a close-packed, aligned fibre network necessitates an alternating pattern of left- and right-handed helices, but homochiral associations are common in supercoiled DNA and a number of peptides, and may be promoted by functional group complementarity and electrostatic effects.<sup>21, 24-27</sup> By contrast, reported instances of entangled helices almost exclusively involve fibres of like chirality. It has been postulated that entanglement proceeds via a ratchet-like mechanism, in which one fibre is driven to coil around another as it transitions between high- and low-pitch geometries.<sup>28</sup> Entanglements are thus particularly likely among helices that are compact yet extensible, with grooves that are sufficiently wide to accommodate an intercalating fibre.

Controlling the entanglement of twisted fibres may allow the properties of fibrous materials to be usefully modulated. For example, solutions of a poly(diacetylene) with chiral side chains were found to change from blue-purple to red-violet upon acidification, due to a transition from right-handed quadruple helices to left-handed double helices.<sup>29</sup> Helical bundles also contribute to the unusual strain-stiffening behaviour of biological polymers such as actin, collagen and fibrin,<sup>30</sup> and may be exploited to generate synthetic polymer hydrogels with biomimetic mechanical characteristics.<sup>31</sup> It must be noted, however, that the entanglements of simple helical bundles represent sliding, dynamic junctions<sup>32</sup> which may be lost due to unwinding of the fibrils under tensile stress. More permanent connections, analogous to the mechanical bonds of catenanes and rotaxanes,<sup>33</sup> could be achieved by assembling the fibres into more complex braided networks.<sup>34-36</sup> Braids, also known as plaits and sinnets, are an important component of ropes, decorative structures and other man-made objects,<sup>37</sup> but occur relatively rarely in Nature<sup>35, 36</sup> and are particularly uncommon on the colloidal scale. In this study, a variety of braids with nanoscale dimensions were prepared via the self-assembly of helical fibrils in gels of an achiral LMWG. The

aim of the investigation was to determine the impact of helix chirality on braid formation and the effects of the resulting structures on the connectivity of the overall fibre network. Braid theory<sup>38</sup> was used to categorise the braiding patterns and rationalise differences between homochiral and heterochiral fibre interactions. Furthermore, a simple chiral templating method was employed to produce pure samples of right-handed helices, allowing the influence of chirality on the aggregate microstructure to be directly ascertained.

Fibrous aggregates are not the only structures capable of large-scale self-assembly. Structural order may also occur *via* the spontaneous organisation of micelles, microdroplets and solid colloidal particles.<sup>39-41</sup> Hexagonal and columnar lattices of surfactant assemblies have been widely exploited as soft-matter templates for mesoporous silicas and other solid frameworks.<sup>42</sup> Periodic arrangements of hard polymer aggregates, meanwhile, may be formed by evaporating suspensions of monodisperse colloids,<sup>43, 44</sup> or through the action of capillary forces<sup>45-47</sup> or magnetism<sup>48-50</sup> on floating particle arrays. Close-packed colloidal crystals have been used to achieve hierarchical porosity in heterogeneous catalysts<sup>51</sup> and to generate structural colour in thin-film displays based on swelling polymer hydrogels.<sup>52</sup> In addition, ordered microemulsion droplets can serve as reaction vessels<sup>53, 54</sup> and crystallisation media,<sup>55, 56</sup> or as abiotic analogues of cellular clusters to model differentiation and other biological processes.<sup>57, 58</sup>

Spatially resolved supramolecular aggregates can sometimes be obtained through localised changes to the self-assembly environment. Aggregation of LMWGs may proceed non-uniformly if the rate of reagent mixing is substantially less than the rate of aggregation.<sup>59</sup> Acid-induced self-assembly can be driven electrochemically such that aggregates are confined to the surface of the driving electrode.<sup>60</sup> Similarly, LMWGs containing photoswitchable moieties such as azobenzenes, spiropyrans and DTEs may form patterns of gel and sol phases matching zones of illumination.<sup>61, 62</sup> Region-specific gelation can be used to control viscosity and diffusion rates, modulate the catalytic activities of immobilised enzymes, or retard the movement of large molecules and colloidal particles.<sup>63</sup> Moreover, a localised gel may adsorb solutes from the surrounding liquid, allowing the species to be extracted via standard filtration methods.<sup>64-67</sup>



A general principle underlying spatial resolution in gels is that gel formation and/or disassembly must occur under non-equilibrium conditions. Regions of high aggregate density may reflect a gradient in pH, temperature, light intensity or gelator concentration. A straightforward approach is to add a preformed gel to an immiscible liquid medium. For example, Yan *et al.* showed that heptane gels of a cholesteryl LMWG can be dispersed in aqueous solutions by shaking, but reform upon demixing of the two liquid phases.<sup>64</sup> Alternatively, hierarchical structures may be generated on the boundary of two solutions by inducing aggregation before mixing can occur. In one notable study, Capito *et al.* manufactured polymer sacs by depositing aqueous hyaluronic acid into a solution of an oppositely charged amphiphilic peptide.<sup>68</sup> Initial nanofibre aggregates of the peptide were found to act as a barrier through which the polysaccharide could reptate, providing nucleation sites for new peptide fibrils perpendicular to the original layer.

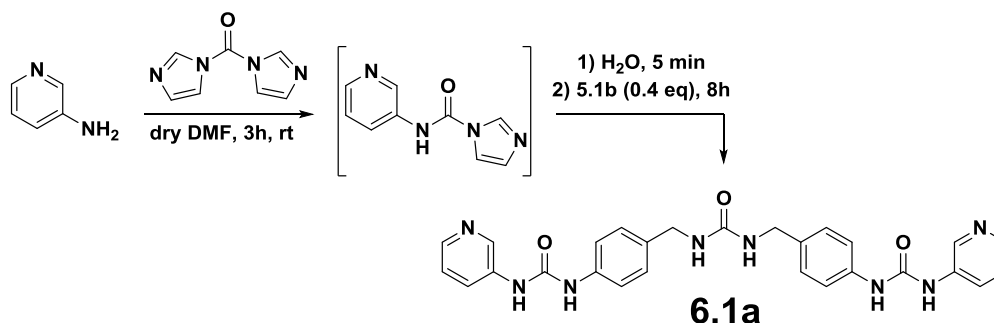
Another simple method for generating non-equilibrium conditions for gel formation is to introduce a secondary solvent into the gelator solution. In this study, the diffusion of anti-solvent vapour into a solution of nickel(II) chloride and a pyridyl-functionalised tris(urea) was found to give rise to monodisperse interfacial microdroplets, which fuse via the “Cheerios effect” to produce a floating spheroidal metallogel.<sup>69</sup> The resulting gel, termed a “lily pad gel”, grows until its weight can no longer be counterbalanced by surface tension.<sup>70</sup> This process offers insight into the surface properties of the tris(urea) aggregate and also serves to extract significant quantities of metal from solution, allowing the material to be manually isolated without filtration or bulk solution processing.

## 6.2 Results and discussion

### 6.2.1 Synthesis

To investigate the effect of the number of urea groups on self-assembly behaviour, two oligo(urea)s of differing length were synthesised via a series of CDI coupling reactions. The molecules were functionalised with 3-picolyl groups, as comparable bis(urea) analogues have been found to display interesting variation in their supramolecular interactions and are usefully responsive to metal coordination.<sup>71-73</sup> Tris(urea) **6.1a** was prepared by reacting diamine **5.3** with the

carbonylimidazole derivative of 3-aminopyridine, generated *in situ* with a slight excess of CDI. To avoid oligomeric by-products, unreacted CDI must be quenched with water before the diamine is added to the reaction mixture. This countermeasure is viable because CDI is readily hydrolysed in the presence of water, whereas the coupling intermediate is stable for several minutes under the same conditions. The difference in reactivities also limits the potential for homocoupling of 3-aminopyridine, which would reduce the yield of the tris(urea) in the subsequent step.



To synthesise the pentakis(urea) analogue **6.1b**, it is necessary to make use of a protected amine substrate. Moreover, it is advantageous to construct the central urea moiety in the final step, as this approach prevents the formation of a mono-substituted tetrakis(urea). In the first step, *N*-Boc-protected 4-aminobenzylamine is reacted with the carbonylimidazole intermediate of 3-aminopyridine, generated *in situ* as before. The resulting mono(urea) **6.2** is deprotected with trifluoroacetic acid to afford the benzylammonium trifluoroacetate salt **6.3**, which is coupled to a further equivalent of 4-aminobenzylamine in the form of the carbonylimidazole intermediate **5.2**. Finally, homocoupling of the bis(urea) **6.4** is achieved using half an equivalent of CDI. Following a series of washings with DMF and hot methanol, both **6.1a** and **6.1b** are pure but for trace amounts (approximately 0.06 equivalents) of DMF, which bind too strongly to the oligo(urea)s to be easily removed by drying.

## 6.2.2 Gelation behaviour

Compounds **6.1a** and **6.1b** differ greatly in their capacity for gel formation. The materials are insoluble in most organic solvents, including the highly polar liquids benzyl alcohol, cyclohexanone, pyridine and acetic acid. However, both **6.1a** and **6.1b** dissolve in hot DMF, with solubility limits of 1.0 and 0.2% (w/v) respectively

at room temperature. While **6.1a** precipitates on standing, **6.1b** forms weak gels with gelation times ranging from several hours for a 0.5% (w/v) solution to one week for a solution at the CGC (0.2% (w/v)). Oscillatory shear rheometry experiments at 22 °C reveal that  $G'$  is an order of magnitude larger than  $G''$  at zero stress and is roughly constant over a wide range of frequencies (Fig. 108). Gels are typically very weak, and easily disrupted by mechanical disturbance.

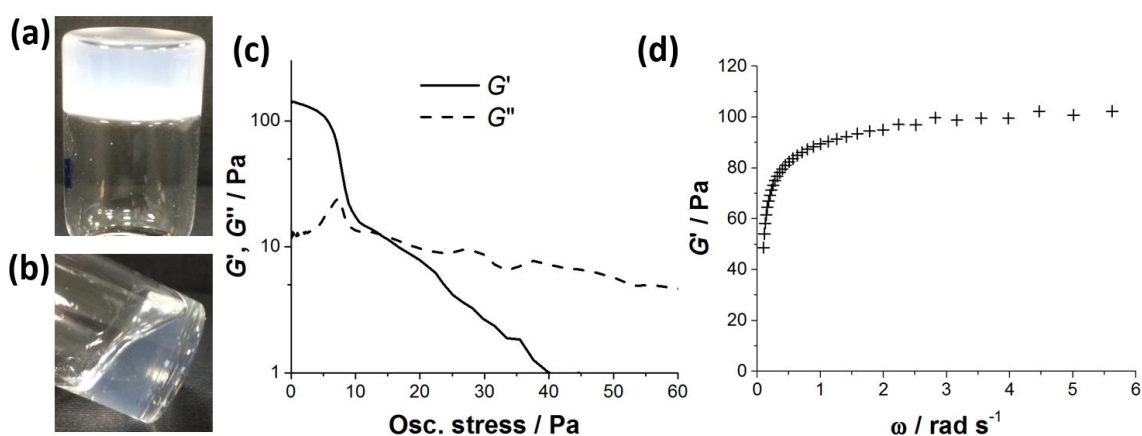
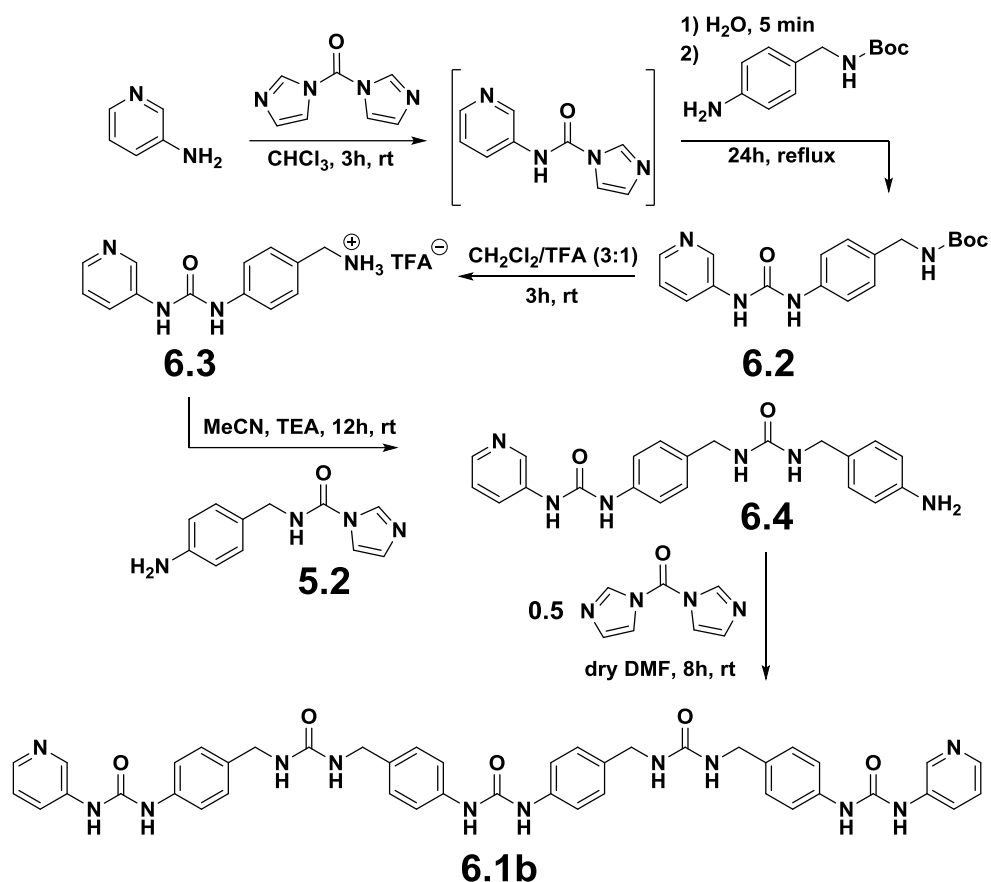


**Fig. 108** Typical gels of **6.1b** in DMF at concentrations of 0.4% (a) and 0.2% (w/v) (b). As expected,  $G'$  for a 0.3% (w/v) gel at 22 °C exceeds  $G''$  by an order of magnitude at low stresses (c), and is roughly constant over a wide range of frequencies (d). The gel is very weak, exhibiting a yield stress of approximately 7 Pa. Gels are typically translucent due to partial precipitation of the gelator, and become more opaque with increasing concentration.

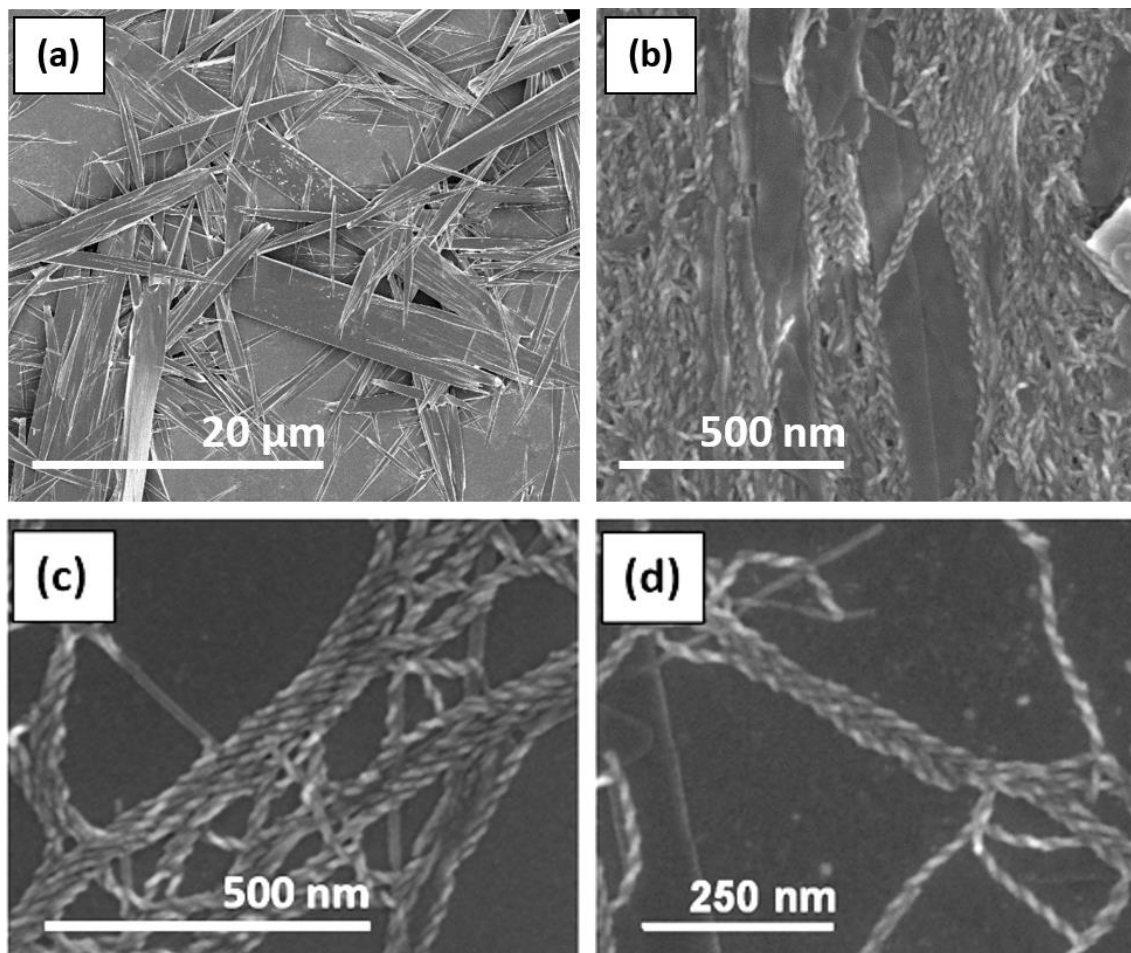


**Fig. 109** SEM micrographs of a dried precipitate of **6.1a** (a) and xerogel of **6.1b** (b) from DMF. Helices in the **6.1b** gel form large helical bundles (c) and a variety of flat braided networks (d).

SEM micrographs reveal marked microstructural differences between the aggregates of **6.1a** and **6.1b**. Precipitates of **6.1a** consist of flat ribbons with variable widths and typical thickness of 200-250 nm (Fig. 109a). By contrast, gels of **6.1b** contain a mixture of 100-150 nm-wide ribbons and highly monodisperse helical fibrils, with a diameter and pitch of 16 and 35 nm respectively (Fig. 109b). Helices of like chirality intertwine to form helical bundles with an estimated maximum size of 10-13 fibrils, corresponding to an overall fibre thickness of 25-30 nm (Fig. 109c). In addition, a significant fraction of fibrils are incorporated into highly ordered flat braids, which sometimes reach 60 nm in width and exhibit complex arrangements of more than a dozen helices (Fig. 109d). Although individual fibrils are unbranched, the splitting and recombination of helical bundles and braided assemblies gives rise to an interconnected network of fibres with pseudo-permanent branch points. It is likely that the structure of this

network depends on the chirality of the component helices, which in turn dictates the possible topologies of the braided aggregates.

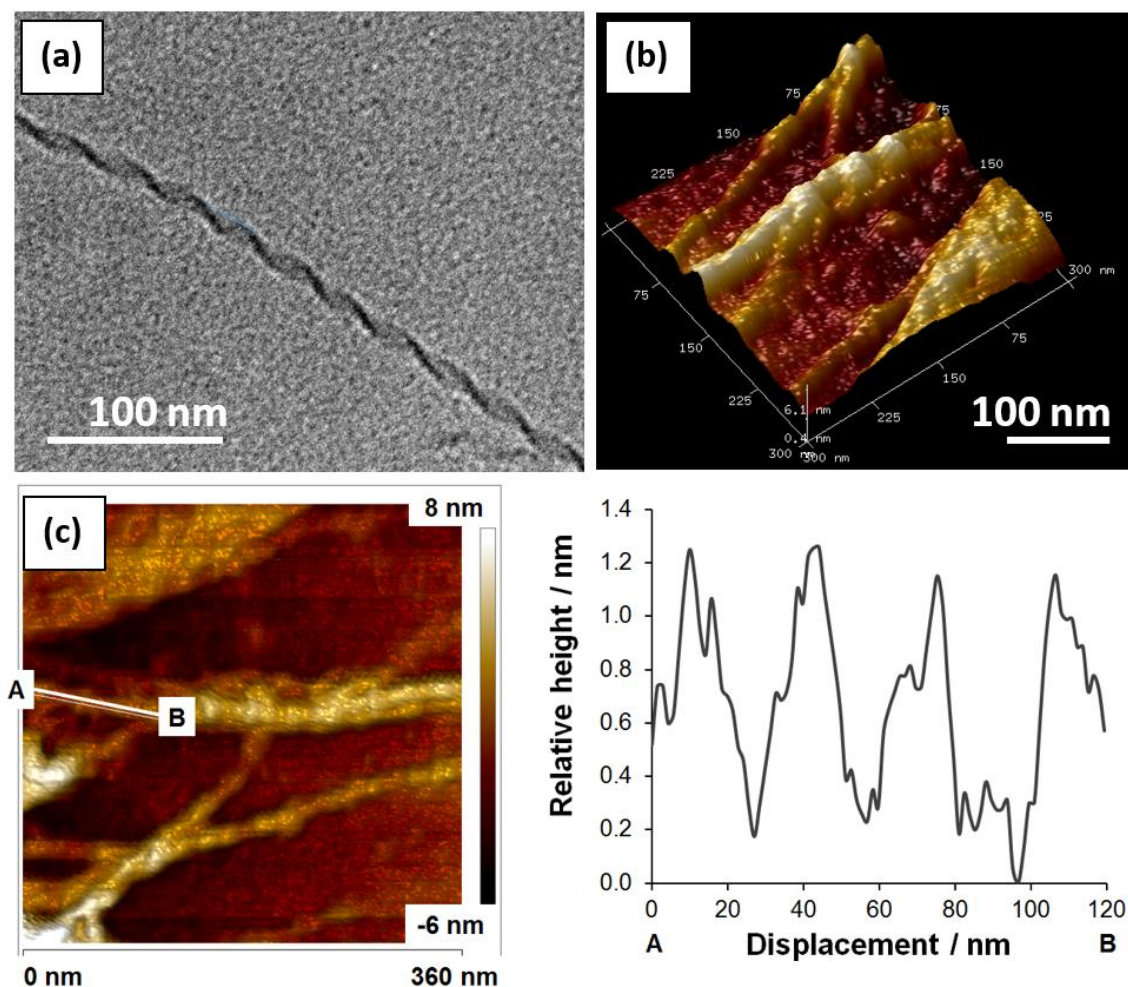


**Fig. 110** TEM (a) and AFM (b) images of single helices in a DMF gel of **6.1b**. Height profiles from AFM (c) reveal a periodic variation in fibril thickness of 1.0-1.1 nm along the helix axis.

To obtain higher-resolution images of the helical fibrils, the materials were analysed by transmission electron microscopy (TEM) and atomic force microscopy (AFM). The TEM micrographs reveal that helices consist of single twisted ribbons (Fig. 110a). Moreover, the AFM data indicate that the fibril thickness decreases by 1.0-1.1 nm between the highest and lowest points, with no variation suggestive of multiple separate fibrous components (Fig. 110b,c). The fibril appears to be moderately flexible, displaying significant variations in pitch over the range 32-40 nm, but the handedness of the structure is generally conserved over the entirety of its length. Exceptions may arise in parts of a fibril connecting two braided structures or other large aggregates. Chirality inversion can occur locally in such cases due to the inability of the fibril to twist in response to changes

in tension. This phenomenon, known as a curvature-to-writhe instability or helix perversion, can be demonstrated on a larger scale using twisted objects such as telephone wires, and is also a common feature of bacterial flagella, umbilical cords and tendril-bearing climbing plants.<sup>74</sup>

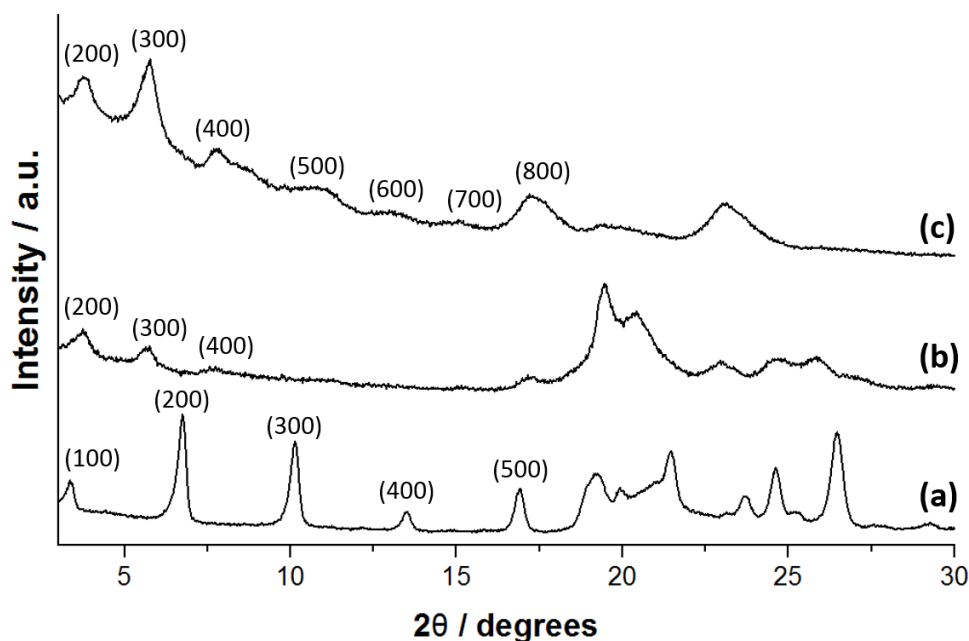


**Fig. 111** PXR D patterns for a precipitate of **6.1a** from DMF (a), solid as-synthesised **6.1b** (b) and a dried 0.4% (w/v) gel of **6.1b** in DMF (c) can all be indexed to a lamellar structure. The  $d$ -spacings for **6.1a** and **6.1b** are calculated to be  $26.2 \pm 0.2$  and  $46.5 \pm 0.5$  Å respectively. In both cases, these values are approximately equal to the length of one extended oligo(urea) molecule. It should be noted that reflections at  $2\theta = 18.8$ - $19.7^\circ$  correspond to a  $d$ -spacing of 4.5-4.7 Å, which likely corresponds to the distance between urea groups in the  $\alpha$ -tapes of the lamellar assemblies. The low intensity of these reflections in (c) suggests that these lamellae are more disordered than those in (b), perhaps due to a relative lack of thick multilayer crystallites.

It is apparent that elongating an oligo(urea) enhances its ability to form fibrous assemblies. To rationalise this trend, dried aggregates of **6.1a** and **6.1b** from DMF were analysed by powder X-ray diffraction (PXR D). For both systems, the diffraction patterns correspond to a lamellar structure with an interlayer distance comparable to the length of the extended molecule (Fig. 111). This result is consistent with the plate-like microstructure displayed by aggregates of **6.1a** in SEM micrographs. However, the helical assemblies in gels of **6.1b** cannot be responsible for the reflections observed, as AFM measurements of the fibril thickness are approximately three times smaller than the calculated  $d$ -spacing. The diffraction pattern of the gels can thus be solely attributed to the larger, non-



fibrous aggregates also present within the materials. It is possible that the molecules in the fibrils form narrower layers by adopting folded conformations stabilised by intramolecular hydrogen bonds. Such structures would resemble peptide  $\beta$ -sheets, which are typically (but not exclusively<sup>24</sup>) responsible for amyloid formation.<sup>75</sup> Intriguingly, amyloid fibrils are often similar in morphology to the fibrils reported here, and exhibit a similar tendency to self-assemble into larger fibres.<sup>4-6</sup> Insights gained in this study might therefore aid our understanding of protein aggregation, which plays a central role in a number of important biological processes.

### 6.2.3 Helix braiding

Braiding of helices produces highly ordered structures with a well-defined periodic topology. In this sense, the braids in gels of **6.1b** resemble two-dimensional colloidal crystals, such as the close-packed arrangements of polymer spheres produced by controlled drying of aqueous suspensions.<sup>43</sup> However, the entanglements in a braid do not arise through the random aggregation of separate particles, but are generated via the supramolecular equivalent of an intramolecular reaction, incorporating structural components that are already present within the material. Furthermore, defects during aggregation can arise relatively readily, as each new entanglement in a braid prevents those before it from being removed or altered. Braiding may thus be compared to the formation of mechanical bonds in catenanes and molecular knots.<sup>33, 34, 76</sup> The ability of helices to form extended braids despite these constraints suggests that the pattern of entanglements is tightly controlled by interhelical interactions. The frequency of defects may be inferred from the mesh size of the gel, as fibrils not integrated correctly into a developing braid are likely to give rise to branch points in the resulting fibre network (Fig. 112). Given that fibre branching is crucial for the production of a robust gel,<sup>72</sup> the weakness of the gels in this study could suggest that branch points are distributed relatively sparsely, due to the abundance of highly extended braids with few errors in their periodic structures.

To better understand the braiding process, it is necessary to catalogue the network topologies of the braids observed. In braid theory, a braid is represented as a series of aligned strands numbered in order, left to right, according to their

position before a crossing is made (Fig. 113).<sup>38</sup> Crossings are denoted by letters corresponding to the identity of the leftmost strand involved, and upper and lower cases are used to indicate if the crossing is left- or right-handed respectively. The braid word of a braid is the series of letters needed to describe the sequence of crossings in the repeat unit. For example, the braid word  $(ab)$  describes a right-handed triple helix, and  $(aB)$  a three-strand Brunnian braid, which converts to separate, non-entangled strands if any one strand is removed.<sup>36, 77</sup> A braid may be described by multiple equivalent braid words, as the sequence of certain groups of crossings may be altered without affecting the resulting structure. Similarly, it is possible to construct a braid word that appears more complicated than the true repeat unit, as rearranging the sequence allows certain left-handed crossings to be cancelled by their right-handed counterparts. The two key rules are that non-consecutive letters of any case may be swapped, and that groups of the form  $(x_1x_2x_1)$  and  $(x_2x_1x_2)$  are equivalent provided  $x_1$  and  $x_2$  are consecutive letters of the same case. Thus  $(Ac) = (cA)$  but  $(ab) \neq (ba)$ , and  $(aba) = (bab)$  but  $(Aba) \neq (abA)$  and  $(aca) \neq (cac)$ . The utility of these relations may be illustrated by noting that the braid  $(bCBCbacab)$  simplifies to a double helix, via the sequence  $(bCBCbacab) \rightarrow (bBCBbaca) \rightarrow (Caca) \rightarrow (aCca) \rightarrow (aa)$ .

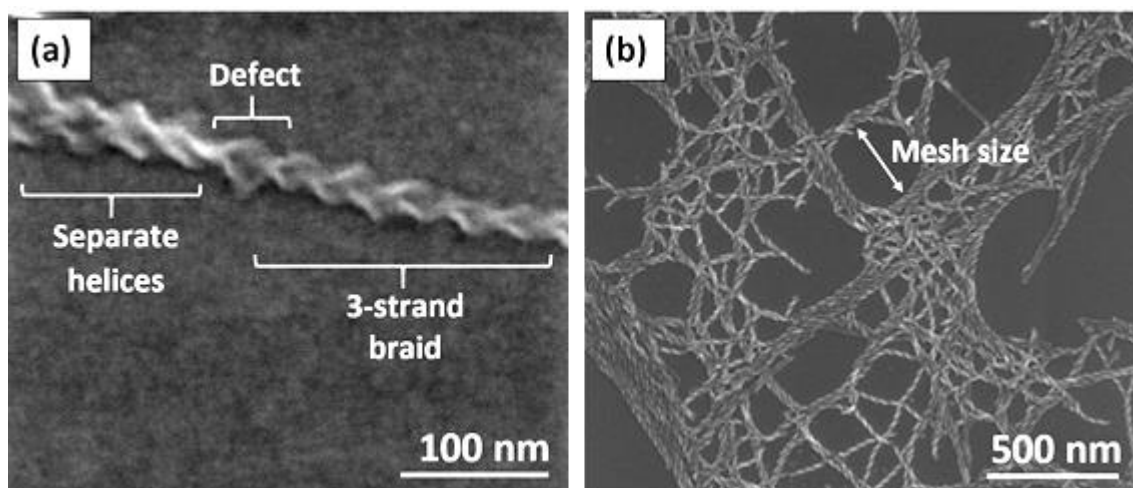


**Fig. 112** Branch points in braided fibres arise due to defects in the pattern of entanglements. For example, a three-strand Brunnian braid may separate into separate helices if the necessary crossing does not arise (a). The frequency of branch points determines the mesh size (b), which strongly influences the rheological properties of the bulk gel. The mesh size in gels of **6.1b** is highly variable but may be increased on average by the presence of heterochiral helices, which give rise to complex flat braids more prone to defect formation.



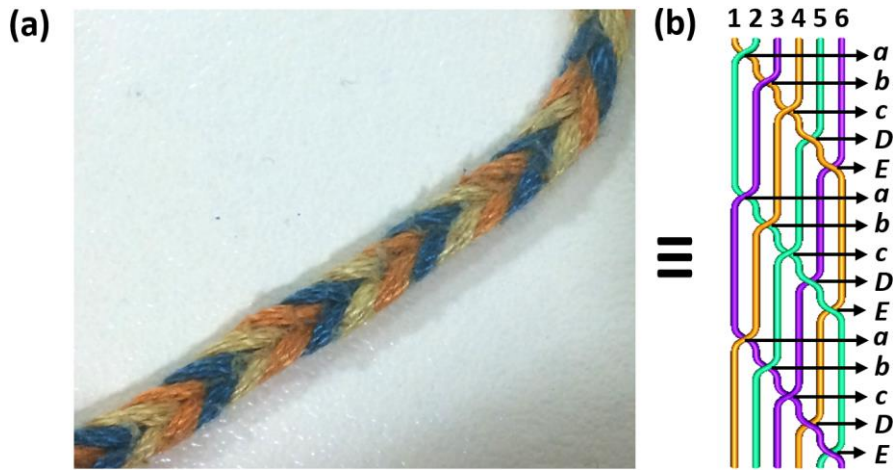


**Fig. 113** A braid consisting of three nested right-handed double helices (a) and the braid theory representation of half a repeat unit (b). Strands are numbered 1 to 6 from left to right after each junction, and crossings are denoted with the letters *a*, *b*, *c*, *d* or *e* if the leftmost strand involved is strand 1, 2, 3, 4 or 5 respectively. A lower case letter is used if the crossing is right-handed (i.e. the left strand passes underneath the right) and a capital letter if it is left-handed. In the braid shown, strands with the same colour exhibit only right-handed crossings, while strands of different colour alternate between left- and right-handed crossings and are therefore not entangled. For example, strand 2 (as defined at the top of the diagram) always passes over strands 1 and 6 and beneath strands 3 and 4. Noted that the braid word for homochiral nested double helices always takes the form  $(abc\dots m\dots XYZ)$ , where the case of the central crossing *m* describes the handedness of the double helices.

In gels of **6.1b**, it was noted that heterochiral braids do not form unless three or more helices are present. In addition, the majority of braids are relatively simple and highly symmetrical, as the pattern of crossings is the same for each helix. Based on these observations, it was postulated that braid formation is subject to three rigid structural constraints. Firstly, the braid must be representable by a braid word with an equal number of crossings for each strand (Rule 1). Secondly, strands must exhibit equivalent or mirror symmetric patterns of crossings, such that the helical pitch remains uniform along the length of the braid (Rule 2). Finally, fibrils may become entangled only via crossings that match their natural helical handedness (Rule 3). Under these rules, heterochiral braids can arise only if strands of opposite handedness are linked by an alternating pattern of left- and right-handed crossings. Pairwise entanglements between left- and right-handed helices are thus prohibited unless one helix undergoes a change in handedness.<sup>5, 78</sup> While such chirality inversions have been observed in SEM

images (Fig. 114a), it is far more common for heterochiral fibrils to retain their handedness and diverge from each other after a crossing takes place (Fig. 114b).

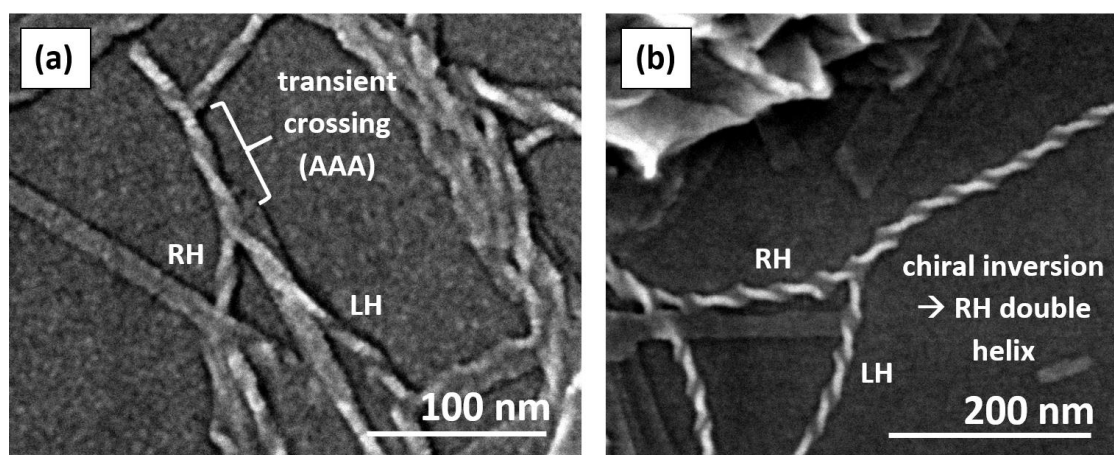


**Fig. 114** SEM micrographs illustrating intersections between left-handed (LH) and right-handed (RH) helices in a DMF gel of **6.1b**. Short sequences of crossings are possible (a), but extended ordered braids do not occur unless an odd number of fibrils are involved. In some cases, chirality inversion may produce a homochiral system, allowing helical bundles to form (b).

It is trivial to show that the only allowed braid with two strands is the double helix, while three strands may form either a triple helix or a Brunnian braid. For four strands, the number of possibilities is significantly greater. An exhaustive survey of the 186 braid words satisfying Rule 1, excluding mirror images (of which there are 168), reveals five distinct structures that are feasible under the proposed constraints (Table 11). The braid words of two structures are notably less complex, comprising four repetitions of the same three crossings. Remarkably, the simplicity of the braid word correlates strongly with the frequency of the braids in SEM images (Fig. 115). Helical bundles such as double and quadruple helices are common, and nested homochiral double helices are also sometimes observed. Three-strand Brunnian braids, the braid equivalent<sup>79</sup> of a Borromean link,<sup>77, 80</sup> may be either homochiral or heterochiral, and account for the vast majority of braids between helices of different handedness. These trends were detected consistently in over 15 different samples, which were each imaged over three regions several hundred micrometres apart. The inability of helices to form braids with larger repeat units is unsurprising given that the crossings of each fibril are prescribed by neighbouring entanglements, producing a periodic structure in a manner resembling a cellular automaton.<sup>81, 82</sup> The handedness of a

crossing is dictated solely by the group of crossings immediately surrounding it, and these are unlikely to encode sufficient information to template a complex arrangement of crossings in a reliable fashion.

Braid	Braid word of repeat unit	Chiral?
<b>2-strand</b> Double helix	$a^2$	Yes
<b>3-strand</b> Triple helix	$(ab)^3$	Yes
3-strand Brunnian braid	$(aB)^3$	No
<b>4-strand</b> Quadruple helix	$(abc)^4$	Yes
Nested double helices (homochiral)	$(abC)^4$	Yes
Nested double helices (heterochiral), I	$aBcaBcAbCAbC$	No
Nested double helices (heterochiral), II	$abCAbcABcaBC$	No
4-strand Brunnian braid	$AbcABcaBcAbC$	No

**Table 11** Allowed braids with two, three and four strands. A braid is chiral if the pattern of crossings is non-superimposable with its mirror image, regardless of the handedness of the individual strands. Chiral braids often consist of homochiral helices, but this is not always the case: a 2-helix with two Brunnian strands, for example, need only comprise two helices of the same handedness. Braids are favoured if they consist of equivalent strands with a simple repeat unit. Of the 186 possible 4-strand braid words satisfying Rule 1 (excluding mirror images), 79 satisfy Rule 3, but only a small fraction of these consist of entangled strands with equivalent crossings (Rule 2). Note that a four-strand braid word does not always represent a true four-strand braid, as one or more strands may be removable without affecting the braid topology.

A notable feature of most of the observed braids is that they consist only of helices with the same handedness. The relative absence of heterochiral braids can partly be explained by more closely examining the braid words of the structures allowed. For braids of  $n$  strands with  $(n-1)$  crossings in their repeat units, pairs of strands may be labelled  $O$  if they exhibit no entanglements,  $R$  if they exhibit only right-handed crossings and  $L$  if the crossings are all left-handed. In this manner, the patterns of crossings in the braid may be illustrated in a table, with each row and column pertaining to the pairwise interactions of a particular strand (Fig.

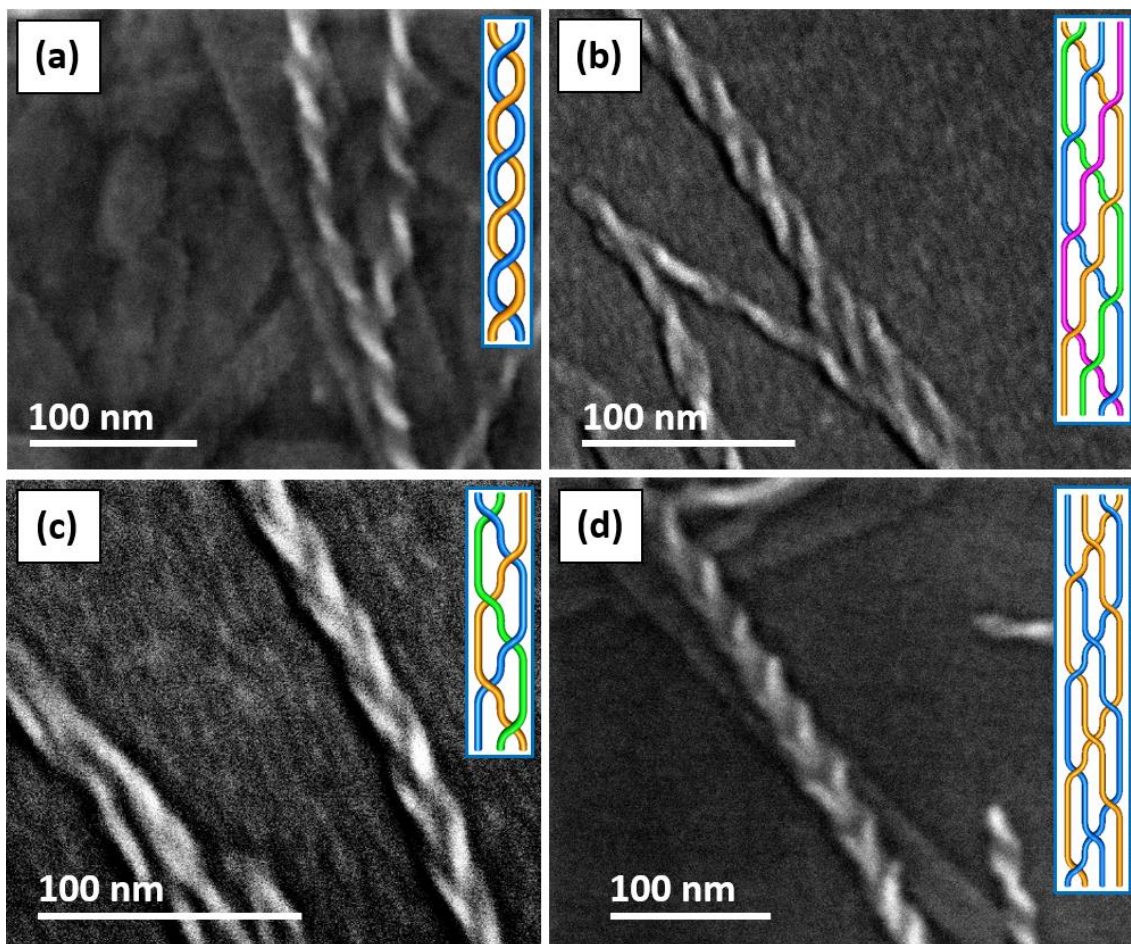


**Fig. 115** SEM micrographs of dried gels of **6.1b**, illustrating the observed variations in braiding patterns. Double helices (a) are the most common structure observed, but larger helical bundles such as quadruple helices (b) are also abundant. The majority of well-defined heterochiral braids are three-strand Brunnian braids (c). These are often visually similar to nested double helices (d), which display a simple repeat unit only if the double helices are of the same chirality.

116). It can be seen that only one row of the table need be specified, as each subsequent row can be generated by shifting the entries in the row above one column to the right. Furthermore, the first row of the table may be deduced by simple inspection of the corresponding braid word. For a braid word of  $(n-1)$  crossings, corresponding to a braid of  $n$  strands, a value of 0 is recorded in the  $j$ th column if the  $(j-1)$ th and  $(n-j+1)$ th crossings differ in case. If the crossings are of the same case, values of  $R$  and  $L$  are entered for crossings that are mutually right- and left-handed respectively. For example, the six-strand braid word  $(aBcdE)$  produces the row  $(00R00)$ , indicating that each strand winds in a right-handed fashion about one strand and forms no entanglements with the remaining four. It is clear that a braid with an even number of strands and a repeat unit of  $(n-1)$  crossings cannot be Brunnian, as the  $(n-j+1)$ th and  $(j-1)$ th crossings are identical

for  $j = n/2$ . Thus, it is not possible for an even number of heterochiral fibrils to form braids with a simple repeat unit. Large heterochiral braids probably develop through the merging of even-stranded homochiral and odd-stranded heterochiral braids, as this is the only mechanism by which the structure can grow without the need for an even-stranded heterochiral intermediate.

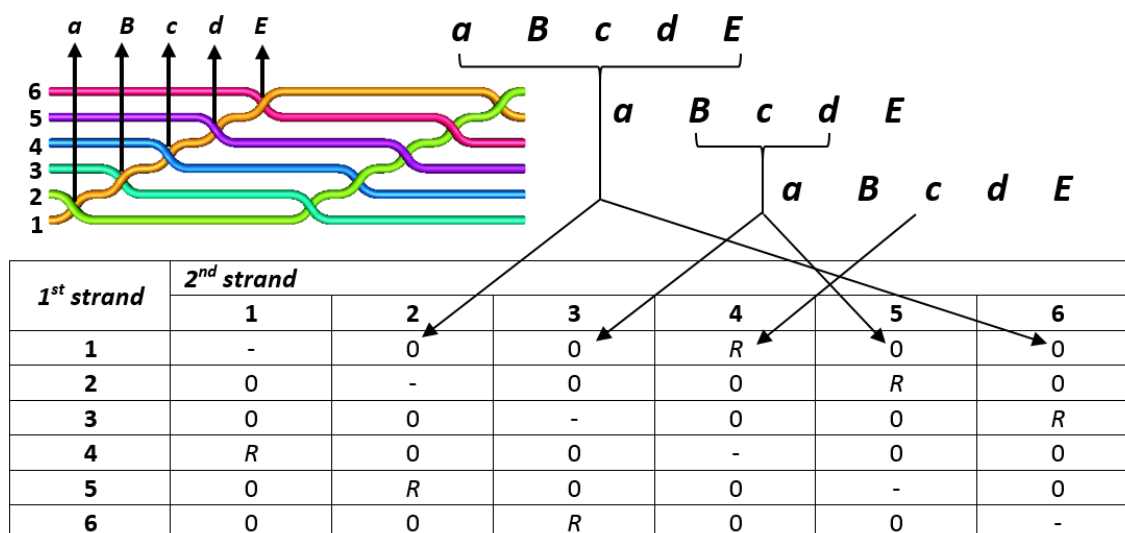


**Fig. 116** Illustration of the method by which braid words may be used to derive the pattern of pairwise entanglements for a braid of  $n$  strands with  $(n-1)$  crossings in the repeat unit. If the first crossing is of a different case than the last, an entry of 0 is recorded in the second cell of the first row of the table. If they are of the same case, an entry of  $R$  is recorded if the crossings are right-handed and an entry of  $L$  if they are left-handed. This process is repeated for the second and second-to-last entries, the third and third-to-last entries, and so on. Subsequent rows are generated by shifting all entries in the row above one cell to the right. Note that braid words with an odd number of crossings, corresponding to an even number of strands, must give rise to at least one entry of  $R$  or  $L$  in each row since the central crossing is already matched with itself.

An advantage of studying braids based on an achiral LMWG is that the chirality of the system may be strongly influenced by the addition of a chiral template.<sup>83-</sup><sup>85</sup> Aggregates of **6.1b** were found to be highly susceptible to this effect: gels consisting exclusively of right-handed helices can be prepared simply by filtering the precursor solution through cotton wool, and sometimes form without prior treatment due to trace chiral materials in the ambient environment. Circular dichroism (CD) spectra of the templated gels confirm the presence of net chirality, displaying a signal at 315 nm that is absent in the spectra of the non-templated gels and a control sample of DMF filtered through cotton wool (Fig. 117). Heating the materials beyond 50 °C results in a marked reduction in the CD signal,



suggesting that the supramolecular helices undergo dissolution and/or chiral inversion once this temperature is reached.

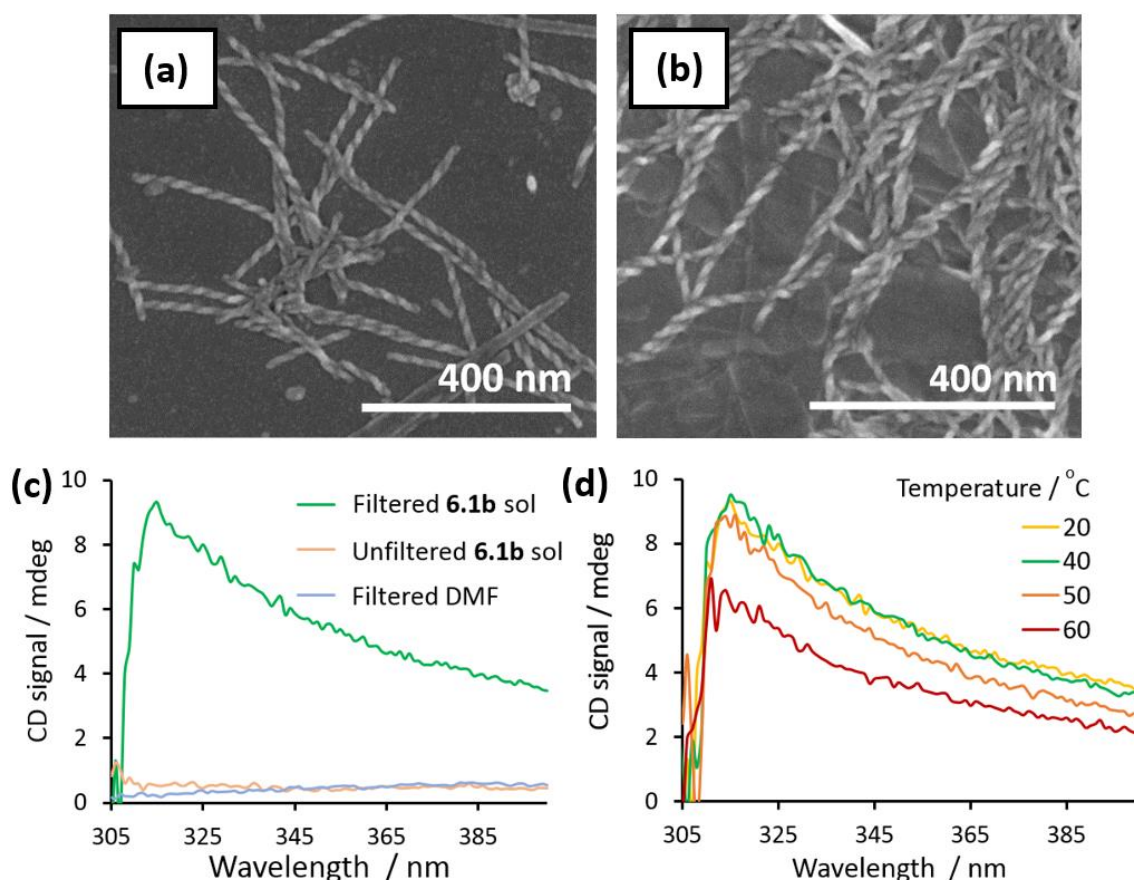


**Fig. 117** Since gelator **6.1b** is achiral, SEM images of its gels typically display an equal mixture of left- and right-handed helices (a). However, filtering the hot gelator sol through cotton wool results in a gel consisting only of right-handed helices (b). The presence of net chirality is indicated by a signal in the CD spectrum of a 0.4% (w/v) gel diluted to 0.1% (w/v) in DMF (c). This signal is absent from the spectra for the mixed-chirality gel and a control sample of DMF filtered through cotton wool. Incubating the gel at 40 °C for 30 minutes has no effect on the CD signal, but successive 30 minute incubations at 50 and 60 °C cause the intensity of the signal to gradually decrease. This suggests that heating the gel to 50 °C and above is sufficient to induce dissolution or chiral inversion of the helical fibrils.

Symmetry breaking in achiral systems can occur via a number of different mechanisms.<sup>86</sup> Chiral amplification during aggregate formation has previously been attributed to the Adam effect, in which the propagation of small numbers of primary nuclei produces a skewed distribution of chiral products.<sup>87-89</sup> Such a process is unlikely to be the cause of chirality in this system, however, as networks of purely left-handed helices have never been observed. It is possible that an excess of right-handed fibrils arises due to a chiral bias introduced during

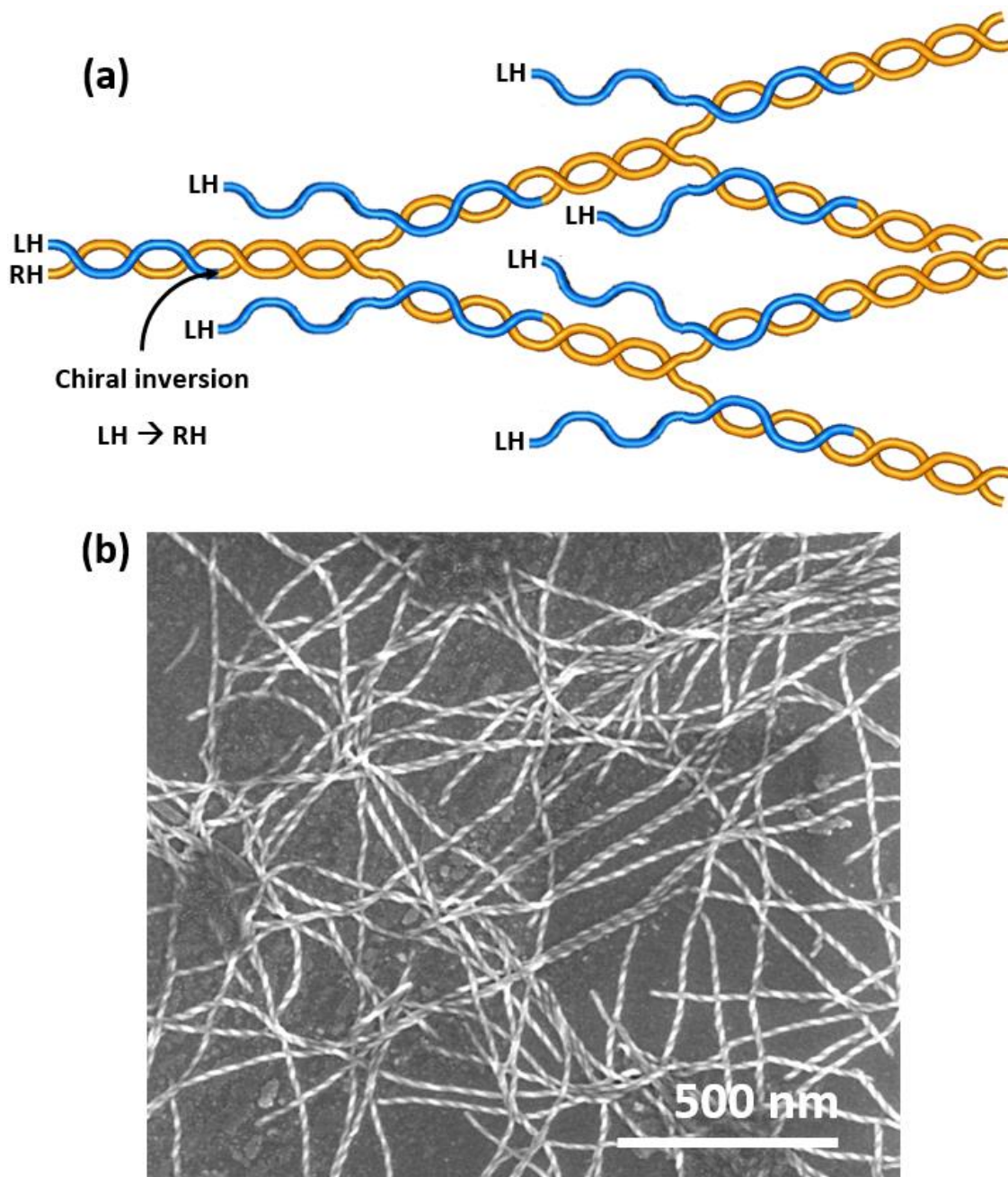


**Fig. 118** Schematic illustration of chiral enrichment through a braiding mechanism (a). When two helices of opposite handedness are entangled, one may undergo a chiral inversion such that a double helix can form. The chirality of one fibril can propagate exponentially, since each helix it templates can participate in further chiral inversion events. Thus, a small excess of right-handed helices (orange strands) can ultimately give rise to a gel in which no left-handed helices (blue strands) are observed. In SEM micrographs of air-dried xerogels prepared from 0.4% (w/v) DMF solutions of **6.1b** filtered through cotton wool (b), left-handed fibrils are rarely visible. Similar SEM images have been obtained for gels with concentrations spanning the range 0.2-0.6% (w/v). secondary nucleation.<sup>83</sup> However, the ability of helices to undergo inversions in chirality when entangled with fibrils of opposite handedness (Fig. 114b) suggests that chiral enrichment could take place after helix formation via a similar

mechanism. Since the handedness of each helix can propagate via entanglements with other helices, only trace quantities of the chiral impurity are needed: the optical activity of the “sergeant” material is translated to a small group of pentakis(urea) “soldier” fibrils, which subsequently induce chirality in the rest of the helix population.<sup>90</sup> Moreover, examples of the less abundant enantiomorph may be completely removed from the system, as each helix templated can itself induce chirality through additional interhelical interactions (Fig. 118).<sup>91</sup> This “majority rules” effect resembles the propagation of prion proteins, which are thought to replicate in an exponential fashion due to the breakage or separation of bundled fibril assemblies.<sup>92</sup>

The ability to generate gels of varying chiral purity could allow the physical properties resulting from homo- and heterochiral braiding patterns to be directly compared. Since they cannot form cylindrical bundle structures, heterochiral braids tend to be flatter, and their relative complexity and inability to incorporate an even number of strands mean that they are also likely to be shorter, narrower and less abundant. Studies of semi-flexible helical polymers have shown that the shear modulus of a gel,  $G$ , scales non-linearly with the thickness and persistence length of the constituent fibres.<sup>31, 93, 94</sup> Thus, gels of mixed chirality are expected to be less stiff than those containing only homochiral braids. Conversely, it is possible that the presence of heterochiral braids will serve to lower the CGC, as such structures are more highly branched and incorporate less gelator per unit length. Moreover, the increased likelihood of defects in heterochiral systems could result in a greater population of free fibril ends, producing higher rates of secondary nucleation. Unfortunately, preliminary work has shown that the rheological differences of chirally templated and mixed chirality gels cannot be assessed reliably, due to the weakness of the materials and confounding influence of non-fibrous aggregates.

#### 6.2.4 Lilypad gelation

Pyridyl groups were incorporated into compounds **6.1a** and **6.1b** to allow their self-assembly properties to be controlled via metal coordination. In preliminary tests, it was found that metallo gels could not be prepared via the direct addition of transition metal salts to solutions of the compounds. However, gelation may



be induced by introducing diethyl ether vapour into a DMF solution containing an equimolar mixture of the oligo(urea) and a nickel(II) halide. Intriguingly, the gel is produced as a floating aggregate with a well-defined spheroidal morphology. This body, termed a lilypad gel, grows via the fusion of monodisperse microparticles 5  $\mu\text{m}$  in diameter, which initially self-assemble into a membrane-like particle raft that can be lifted intact from the liquid-vapour interface (Fig. 119).<sup>95, 96</sup> The hexagonal close-packed structure of the membrane may be attributed to the “Cheerios effect”, whereby particles on a liquid or soft elastic surface are drawn together due to the surface tension of the meniscus between them.<sup>44, 69</sup> Similar processes have been observed in floating and suspended particles over a variety of length scales, and exploited to generate two-dimensional colloidal crystals with a range of packing symmetries.<sup>43, 44, 97</sup>

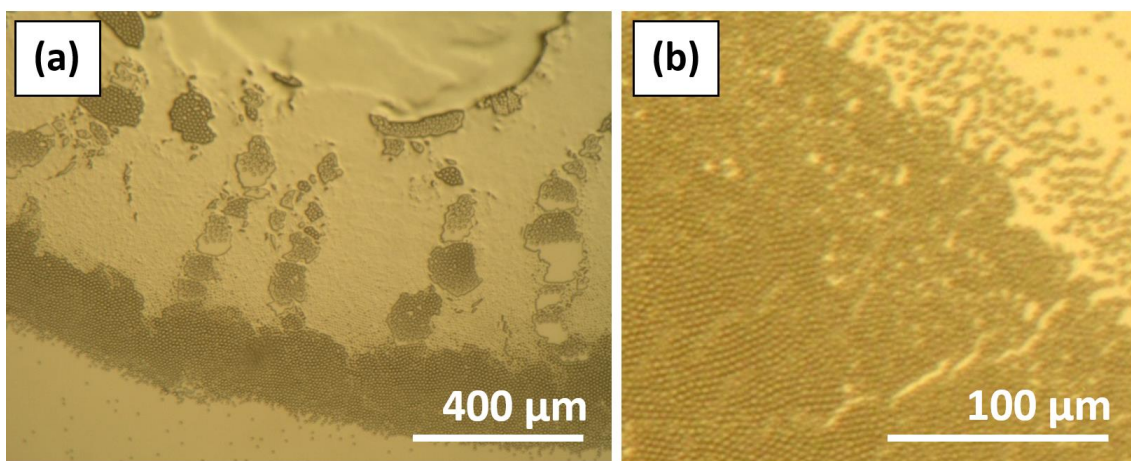


**Fig. 119** Exposure of a 0.5% (w/v) solution of **6.1a** in DMF ( $2\text{ cm}^3$ ) to diethyl ether vapour results in aggregation at the liquid-vapour interface. The fusion of monodisperse microparticles gives rise to a spheroidal gel with a maximum radius on the order of 1 mm (a). The formation of a meniscus between pairs of microparticles gives rise to an attractive force, such that the particles coalesce into a hexagonal close-packed lattice (b).

Since the density of a lilypad gel,  $\rho_{\text{gel}}$ , exceeds that of the underlying sol,  $\rho_{\text{sol}}$ , it can only grow until the weight of material exceeds the upwards force due to surface tension (Fig. 120). This system represents an unusual example of a Rayleigh-Taylor instability, in which layers of immiscible and incompressible fluids interpenetrate due to the greater density of the upper phase.<sup>95, 96, 98</sup> For gels of **6.1a** and **6.1b**, the difference in densities ( $\rho_{\text{gel}} - \rho_{\text{sol}}$ ) lies in the range 160-200  $\text{kg m}^{-3}$ , and the structure reaches a maximum radius  $R_{\text{end}}$  of between 0.78 and 0.90

mm. Once  $R_{\text{end}}$  is reached, further growth results in sinking of the gel. However, the gel may remain connected to material remaining at the surface via an extensible ligament, which typically stretches by 2-2.5 mm and remains at this length for several minutes before yielding takes place. This stalling behaviour cannot result from the equalisation of gravitational and surface energies, as both contributions scale approximately linearly with the length of the ligament. Elastic potential energy, by contrast, increases in proportion to the square of the extension, so may counterbalance the weight of the gel as the ligament length approaches a critical value.<sup>96, 99, 100</sup> It is worth noting that the equilibrium extension is sensitive to the experimental conditions, as visual observations indicate that the gel becomes stiffer the longer it resides at the liquid-vapour interface.

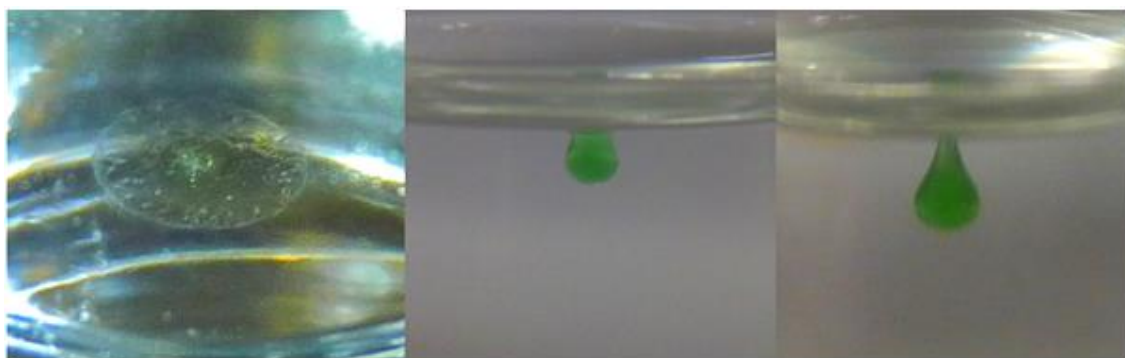


**Fig. 120** A lily pad gel grows at the centre of a colourless membrane, formed by the coalescence of self-assembled monodisperse microparticles. Growth continues until the weight of the gel is no longer supported by surface tension, whereupon the material sinks and stretches to form a ligament. Maximum radii of 0.78-0.90 mm are typical. Extension of the ligament often stalls at a typical length of 2 mm due to the viscoelastic nature of the material.

Since lily pad gelation takes place in a multicomponent system under non-equilibrium conditions, the results of the process can be highly variable. In solutions of **6.1a**, increasing the concentration of the LMWG causes the gels to form more rapidly and attain a larger final diameter. Compound **6.1b**, however, tends to precipitate rapidly upon exposure to the anti-solvent, so gives rise to relatively small gels that are unlikely to separate from the surface of the sol. As the radius of the gel approaches  $R_{\text{end}}$ , sinking may occur spontaneously and unpredictably in response to mechanical disturbances or other small changes in the physical environment. In addition, aggregation can sometimes result in two or more lily pad gels, which grow simultaneously in a symmetrical pattern about

the liquid meniscus. Surprisingly, all of these observations may be rationalised by means of a simple geometric model of the gelation process (Fig. 121). The solution is represented as a homogeneous liquid of density  $\rho_{\text{sol}}$ , with a planar interface intersecting a uniform gel of density  $\rho_{\text{gel}}$ . The gel represents a fraction of a sphere with radius  $R$  and a centre located a perpendicular distance  $fR$  from the liquid-vapour interface, where  $-1 < f < 1$ . At each stage of growth, the observed value of  $f$  is that which produces a local minimum in the total potential energy of the system,  $E$ . This approach reproduces the key features of the gelation process and avoids the pitfalls of classical force-based models, which often suppose that the gel forms a complete sphere and require the geometry of the interfacial phase boundaries to be accurately known.<sup>96, 101</sup>

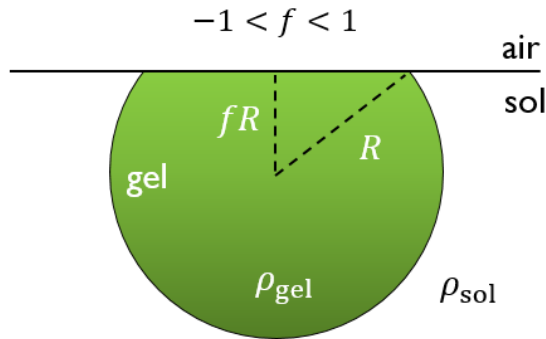


**Fig. 121** Geometric model of lily pad gel, from which general expressions for the pattern of growth may be derived. The gel is represented as a spherical cap intersected with a planar interface. Note that  $\rho_{\text{gel}} > \rho_{\text{sol}}$ .

It can be shown (Section 9.1) that the total potential energy of the system,  $E$ , is given by:

$$E = \frac{\pi g \rho R^4}{12} (f - 3)(f + 1)^3 + \pi R^2 (1 + f) (\gamma_{\text{vap}} (1 - f) + 2\gamma_{\text{sol}}) \quad (2)$$

where  $\rho = (\rho_{\text{gel}} - \rho_{\text{sol}})$ ,  $g$  is the acceleration due to gravity and  $\gamma_{\text{sol}}$  and  $\gamma_{\text{vap}}$  the surface energies of the gel-sol and gel-vapour interfaces respectively. The first term in equation (2) represents the gravitational potential energy, while the later terms are the interaction energies of the gel with the vapour and solution. For realistic values of  $R$ ,  $\rho$ ,  $\gamma_{\text{sol}}$  and  $\gamma_{\text{vap}}$ , the system exhibits small Bond numbers over a wide range in  $f$ .<sup>95</sup> Thus, the surface energy terms are between one and two orders of magnitude larger than the gravitational energy, and exert a far stronger influence on the morphology of the gel. The term in  $\gamma_{\text{sol}}$  is particularly important,

as it is typically accounts for the majority of the surface energy contribution. In addition, this term passes through a local minimum as  $f$  is varied for a fixed gel volume  $V$ , and is therefore solely responsible for the equilibrium stabilities of spherical cap morphologies.

The optimal value of  $f$  is determined by minimisation of  $E$  at constant volume. This yields the expression:

$$V = 2\sqrt{6}\pi \left(\frac{2-f}{1+f}\right) \left(\frac{f\gamma_{\text{sol}} - \gamma_{\text{vap}}}{\rho g}\right)^{3/2} \quad (3)$$

Rearranging equation (3) reveals a linear relationship between  $\gamma_{\text{sol}}$  and  $\gamma_{\text{vap}}$ :

$$\gamma_{\text{vap}} = f\gamma_{\text{sol}} - \frac{\rho g}{2} \left(\frac{1}{\sqrt{3}\pi} \left(\frac{1+f}{2-f}\right) V\right)^{2/3} = f\gamma_{\text{sol}} + c \quad (4)$$

It can be seen from these equations that physical values of  $V$  and  $f$  are only possible for the full duration of growth if  $\gamma_{\text{sol}} > 0$  and  $|\gamma_{\text{vap}}| < \gamma_{\text{sol}}$ . In a plot of  $\gamma_{\text{sol}}$  against  $\gamma_{\text{vap}}$ , a combination of  $\gamma_{\text{sol}}$  and  $\gamma_{\text{vap}}$  is allowed only if it lies in the quadrant bounded by the lines  $\gamma_{\text{vap}} = \gamma_{\text{sol}}$  and  $\gamma_{\text{vap}} = -\gamma_{\text{sol}}$  and bisected by the positive x-axis. This observation offers a partial explanation for the apparent rarity of lily pad gels: though the gel-vapour surface energy is only weakly constrained, associations between the gel and the sol must be unfavourable on the bulk scale. The use of an anti-solvent may promote lily pad gelation by reducing the strength of solvent-gelator interactions, such that aggregation is more likely to be localised at the surface of the solution.

Although the above results do not account for elasticity or local variations in material density, they may nonetheless provide realistic estimates for the physical parameters of a lily pad gel system. Equation (4) may be used to predict the growth profile of a gel with known surface characteristics, or deduce the values of  $\gamma_{\text{sol}}$  and  $\gamma_{\text{vap}}$  from observations of the gel morphology. In a plot of  $\gamma_{\text{vap}}$  against  $\gamma_{\text{sol}}$ , straight lines intersect combinations of surface energies which, for a given value of  $f$ , exhibit the same gel volume (Fig. 122). The gradient of the line connecting the origin and the point  $(\gamma_{\text{sol}}, \gamma_{\text{vap}})$  is equal to the ratio  $(\gamma_{\text{vap}}/\gamma_{\text{sol}})$ , and corresponds to the value of  $f$  at the beginning of gel growth. Likewise, the intercept of the line with gradient  $f = 1$  that passes through  $(\gamma_{\text{sol}}, \gamma_{\text{vap}})$  may be used to calculate the volume of the gel when it becomes fully spherical in shape. If  $\gamma_{\text{vap}}$

$\geq 0$ , this volume defines the maximum size of the gel when sinking takes place. For gels with  $\gamma_{\text{vap}} < 0$ , however, there exists a critical value of  $f$ ,  $f_{\text{end}}$ , beyond which the energy of the system  $E$  exhibits no local minimum. Maximising  $V$  with respect to  $f$  yields an expression for  $f_{\text{end}}$ :

$$f_{\text{end}} = \frac{1}{2} \left( -1 + \sqrt{9 + 8 \frac{\gamma_{\text{vap}}}{\gamma_{\text{sol}}}} \right) \quad (5)$$

The maximum volume of the gel,  $V_{\text{end}}$ , may be calculated by substituting this expression into equation (3). Coordinates of constant  $V_{\text{end}}$  and the corresponding radii  $R_{\text{end}}$  are specified by curved lines in the plot of  $\gamma_{\text{sol}}$  against  $\gamma_{\text{vap}}$ . It is worth noting that the value of  $f_{\text{end}}$  is determined only by the ratio  $(\gamma_{\text{vap}}/\gamma_{\text{sol}})$ , so observations of the final gel morphology may allow relative values for the gel surface energies to be accurately deduced.

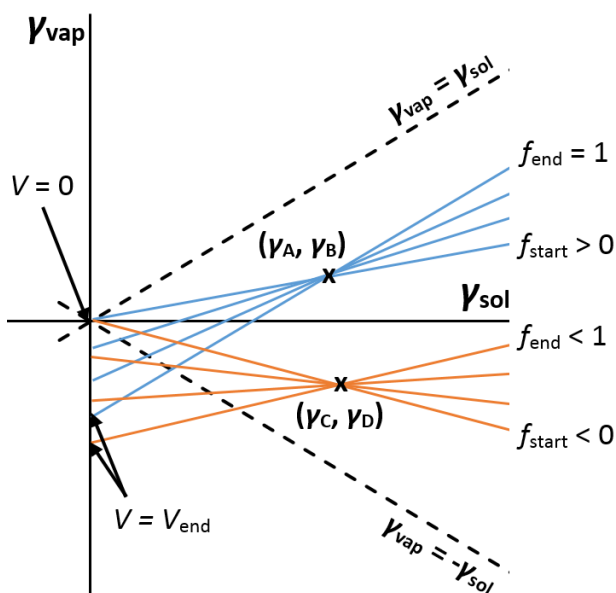


**Fig. 122** Schematic surface energy plot for two hypothetical lilypad gels with  $(\gamma_{\text{sol}}, \gamma_{\text{vap}}) = (\gamma_A, \gamma_B)$  and  $(\gamma_C, \gamma_D)$ , with  $\gamma_A, \gamma_B, \gamma_C > 0$  and  $\gamma_D < 0$ . For each gel, lines intersecting the surface energy coordinates describe the geometry of the gel as it grows. The shape of the gel is given by the slope of the line  $f$ , and the volume may be calculated from the y-intercept. The maximum volume,  $V_{\text{end}}$ , of the gel at  $(\gamma_A, \gamma_B)$  is indicated by the line of gradient  $f = 1$ . However, the maximum volume of  $f$  for the gel at  $(\gamma_A, \gamma_B)$  is less than 1, as there is no local minimum in the energy of the gel for  $f > f_{\text{end}}$ . Note that only surface energy combinations between the dashed lines can give rise to lilypad gels, and that  $V_{\text{end}}$  may be increased by increasing  $\gamma_{\text{sol}}$  or making  $\gamma_{\text{vap}}$  more negative.

Equations (2)-(5) were used to estimate the physical properties of a lilypad gel generated from an equimolar mixture of **6.1a** and nickel(II) chloride in DMF. The

experiment was performed at 20 °C with a 0.5% (w/v) gelator solution in a 7 cm<sup>3</sup> glass vial, enclosed by a 28 cm<sup>3</sup> vial containing 2 cm<sup>3</sup> of diethyl ether. Values of  $R_{\text{end}}$  and  $f_{\text{end}}$  were obtained from a combination of *in situ* optical microscopy and side-on visual observations, while  $\rho$  was estimated after eight hours by weighing the gel and a 0.1 cm<sup>3</sup> sample of the sol from close to the interface. The measurement of  $f_{\text{end}} = 0.47 \pm 0.7$  corresponds to a ratio  $(\gamma_{\text{vap}}/\gamma_{\text{sol}}) = -0.65 \pm 0.07$ , while the values  $R_{\text{end}} = 0.84 \pm 0.6$  mm and  $\rho = 180 \pm 20$  kg m<sup>-3</sup> yield absolute values for  $\gamma_{\text{vap}}$  and  $\gamma_{\text{sol}}$  of  $0.4 \pm 0.1$  and  $-0.25 \pm 0.05$  mJ m<sup>-2</sup> respectively. Although the errors in these results are relatively large, it is clear that the signs of the surface energies and their orders of magnitude may be reliably determined. That the values of  $\gamma_{\text{vap}}$  and  $\gamma_{\text{sol}}$  are much smaller than typical surface energies for liquid-vapour and liquid-solid interfaces (15-30 mJ m<sup>-2</sup> for organic solvents under air<sup>102</sup> and 5-50 mJ m<sup>-2</sup> for water on organic polymers<sup>103</sup>) suggests that the solution component of the gel accounts for a substantial fraction of the total volume, and is similar in composition to the surrounding sol.

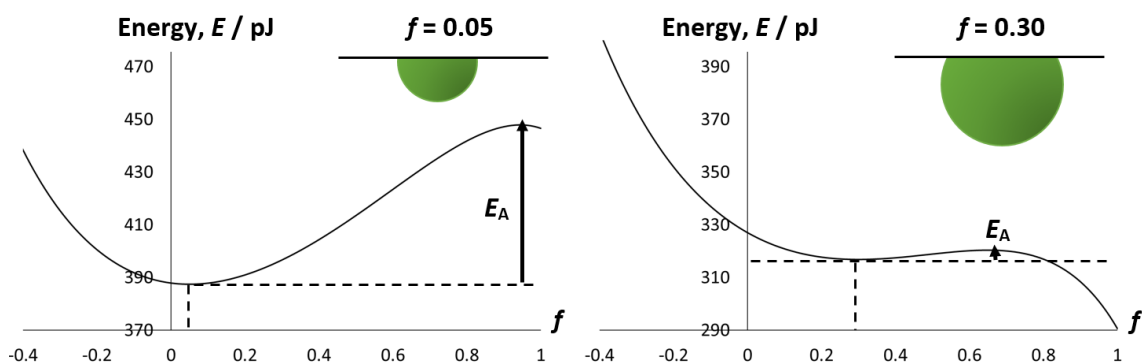


**Fig. 123** Energy profiles for lilypad gels with  $\rho = 180$  kg m<sup>-3</sup>,  $\gamma_{\text{sol}} = 0.40$  mJ m<sup>-2</sup> and  $\gamma_{\text{vap}} = -0.26$  mJ m<sup>-2</sup>. Schematic diagrams of the gel geometries are exaggerated for clarity. The observed values of  $f$  at a given volume  $V$  occur at the local minimum of the energy plot. At  $f = 0.05$ , the gel is moderately stable: the activation barrier to reach  $f = 1$ ,  $E_A$ , is 60.5 pJ, and spans a range in  $f$  of 0.91. The gel with  $f = 0.3$ , however, exhibits a much smaller  $E_A$  of 3.5 pJ. Furthermore, surmounting the activation barrier requires a relatively small change in geometry, since the  $f$  values at the minimum and maximum differ by just 0.35. Thus, this gel is significantly more likely to sink before further growth can take place.

It has been observed that lilypad gels sometimes form as multiple spheroidal bodies with similar maximum volumes. This outcome may be explained by noting that growth of the gel beyond  $f_{\text{end}}$  cause the energy of the system to increase, so continuing aggregation can only be accommodated by the formation of a separate

gel. Interestingly, for gels with  $\gamma_{\text{vap}} < 0$ , the expression for  $E$  also contains a local maximum at a value of  $f$  between  $f_{\text{end}}$  and 1 for all  $f > 0$  (Fig. 123). The minimum and maximum in  $E$  are separated by an activation barrier,  $E_A$ , which decreases in magnitude as the gel grows larger. Thus, lily pad gels with  $f > 0$  and  $\gamma_{\text{vap}} < 0$  are metastable: given sufficient energy, they may deform beyond the local maximum in  $E$  and thereafter relax into a spherical geometry. For a typical gel in this study,  $E_A$  is approximately 40 pJ at  $f = 0.1$ , but decreases to around 3 pJ at  $f = 0.3$  and just 0.005 pJ at  $f = 0.45$ . The sharp reduction of the activation barrier on approaching  $f_{\text{end}}$  greatly increases the probability of ligament formation, as even slight environmental changes can provide the energy required for sinking to take place.

The localised formation of metallo gels at the interface of a solution could potentially be exploited for the facile sequestration of dissolved metals. To assess the feasibility of this approach, lily pad gels were prepared from 0.5% (w/v) solutions of **6.1a** in DMF with equimolar quantities of nickel(II) chloride and analysed by a variety of techniques. The FT-IR spectra of the gels indicate a high concentration of **6.1a**, but the characteristic signals of this species are significantly different to those of the pure compound (Fig. 124a). In particular, the carbonyl stretch at  $1654\text{ cm}^{-1}$  in the spectrum of **6.1a** is shifted to a higher frequency of  $1710\text{ cm}^{-1}$ , suggesting the bond strength has been altered substantially due to incorporation of the molecule into a nickel(II) complex. X-ray photoelectron spectroscopy (XPS) measurements on the vacuum-dried gel support this conclusion, as the presence of shake-up peaks in the Ni 2p region are diagnostic of a paramagnetic octahedral complex (Fig. 125).<sup>104</sup> SEM micrographs reveal a lack of discernible microstructure in the bulk of the material (Fig. 124b). However, fibrous structures are visible within desiccation cracks, suggesting that the nickel(II) complexes give rise to polymeric assemblies that densely entangle to form a homogeneous aggregate.

Comparison of the signal intensities in XPS spectra can offer an approximate indication of elemental concentrations within the gel. Summing the integrals of the Ni 2p, Cl 2p, O 1s, N 1s and C 1s regions for the vacuum-dried gel suggests a total Ni concentration of  $4.8 \pm 0.3\text{ wt.}\%$  and a C/Ni atomic ratio of  $55 \pm 3$ . The surface-sensitive nature of XPS means that results may vary significantly depending on the distribution of elements with depth. Nonetheless, the



measured C/Ni ratio closely matches the expected ratio of 54 for a 1:2 nickel(II)-tris(urea) complex. It can thus be deduced that the tris(urea) accounts for most of the organic component of the gel, and occupies four of the six coordination sites of the nickel(II) complexes. It should be noted that repeat experiments employing two equivalents of nickel(II) chloride were attempted, but did not produce consistent differences in the growth profiles of the lilypad gels.

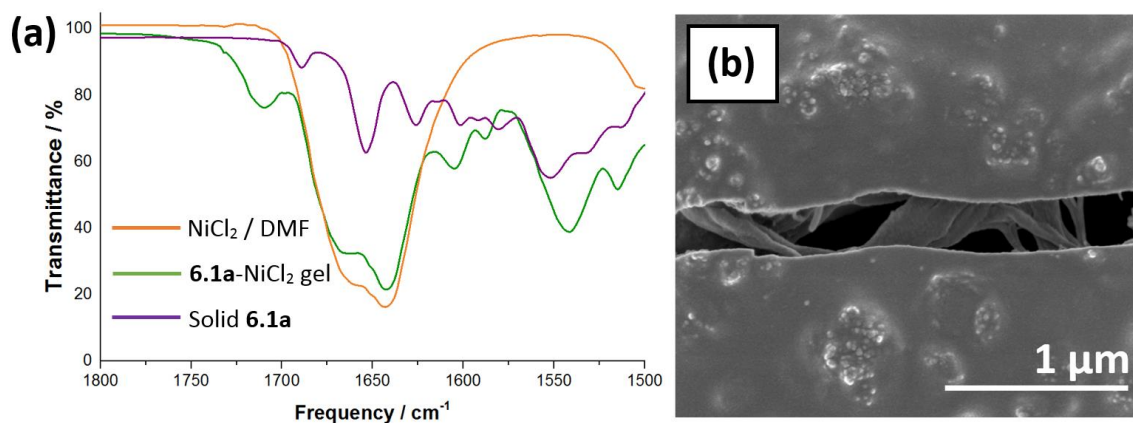


**Fig. 124** FT-IR spectrum (a) and SEM micrograph (b) of a dried lilypad gel prepared from **6.1a** and NiCl<sub>2</sub> in DMF. The FT-IR spectrum (green line) is plotted with the spectra of pure **6.1a** (purple line) and a concentrated DMF solution of NiCl<sub>2</sub> (orange line).

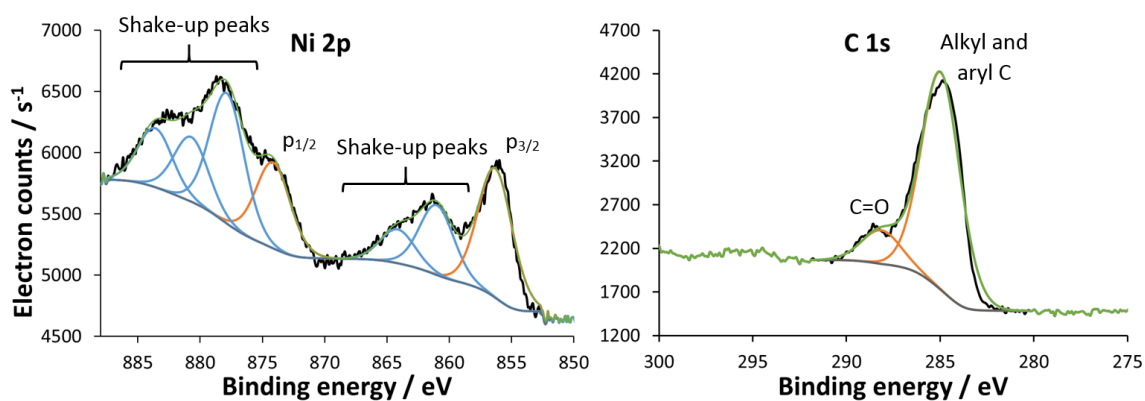


**Fig. 125** XPS spectra of a vacuum-dried lilypad gel prepared from a 0.5% (w/v) solution of **6.1a** in DMF with an equimolar quantity of NiCl<sub>2</sub>. Shake-up peaks in the Ni 2p region occur due to excitation of ionised atoms by outgoing electrons, and exhibit a high intensity characteristic of a paramagnetic electron configuration. The C 1s region also displays a satellite peak, which may be attributed to the carbon atoms of carbonyl groups in DMF and the tris(urea) ligand.

Further quantitative measurements of the gel composition were obtained by thermogravimetric analysis (TGA) of the wet, as-synthesised gel under a nitrogen atmosphere (Fig. 126a). An initial mass loss of 41% below 150 °C is attributed to the removal of weakly bound solvent, while a subsequent decrease of 47%



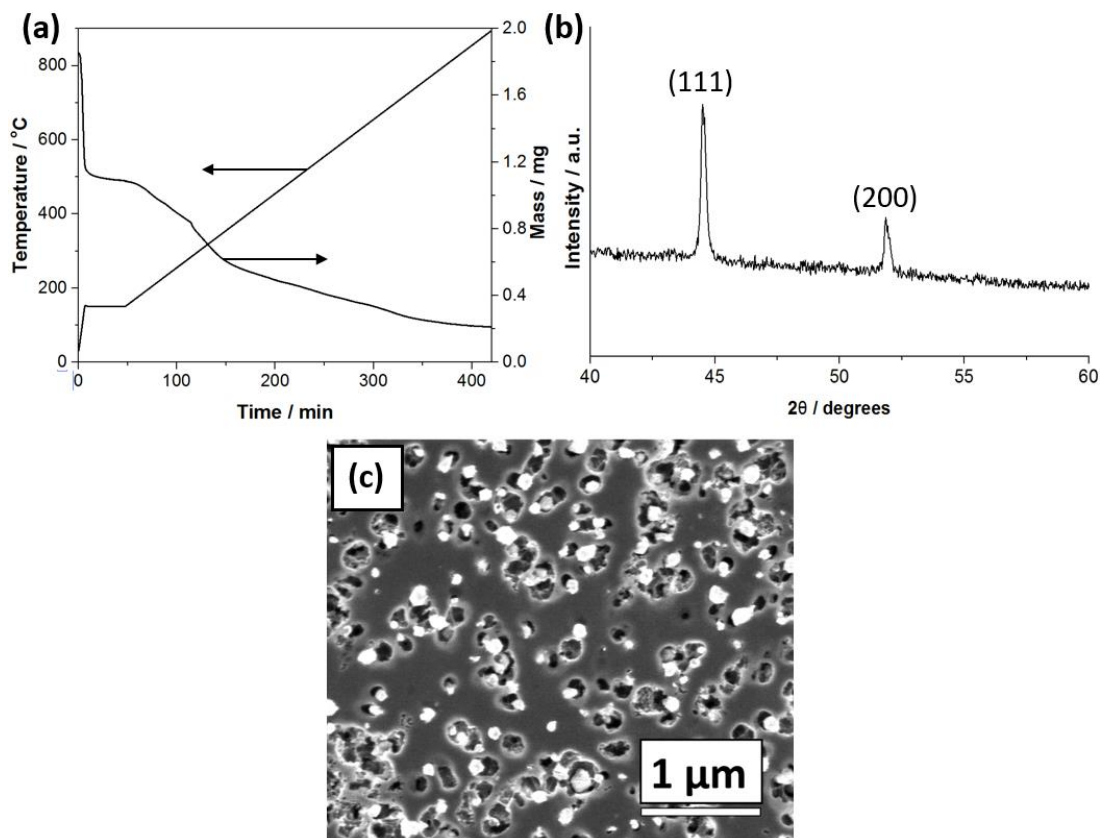


**Fig. 126** The TGA thermogram for a lilypad gel prepared from a solution of **6.1a** and NiCl<sub>2</sub> in DMF shows that only 41% of the material is weakly bound solvent (a). Decomposition at high temperatures results in further mass loss of 47%. The PXRD pattern of the pyrolysate, which represents 12% of the original gel mass, displays reflections characteristic of elemental nickel (b). SEM reveals a porous network of homogeneous material.

between 150 and 900 °C corresponds to decomposition of the metal complexes. The measured solvent content is at least one order of magnitude smaller than that of a typical supramolecular gel, and therefore consistent with the high aggregate density observed in SEM experiments. SEM images of the black powder remaining after pyrolysis display a uniform network of 100-300 nm pores, suggesting that the organic component of the original gel is also homogeneously distributed (Fig.126c). Peaks at  $2\theta = 44.5$  and  $51.9^\circ$  in the PXRD pattern of the pyrolysate match the (111) and (200) reflections of elemental nickel (Fig. 126b). However, analysis of pyrolysed elastomer-metal halide mixtures has shown that carbonaceous material often accounts for 20-40 % of the residue mass.<sup>105</sup> Inductively coupled plasma mass spectrometry (ICP-MS) data indicate total nickel concentrations in the dry and pyrolysed gels of  $5.37 \pm 0.6$  and  $35.5 \pm 0.3$  wt.% respectively, in agreement with the estimate from XPS analysis. The metal content of a lilypad gel represents just 1.5-2.0 % of the total quantity of nickel(II)

chloride but exceeds the concentration of the sol by a factor of 15-20, and may be harvested manually without any further processing of the parent solution.

## 6.3 Conclusions

Compounds with multiple urea functionalities can form a variety of highly ordered structures with length scales ranging from molecular monolayers to macroscopic colloidal aggregates. In all cases, self-organisation depends on the intrinsic symmetries of the underlying physical processes. Helical fibrils in gels of pentakis(urea) **6.1b** form complex braids due to the topological constraints governing interhelical interactions. Braid theory may be employed to rationalise the dominant patterns of fibre entanglements, and highlight general rules applicable to other networks of helical fibres. It has been demonstrated, for example, that braids of heterochiral helices are likely to exhibit more varied arrangements of crossings, and become particularly complex if even numbers of strands are involved. Remarkably, these conclusions may be tested by preparing populations of helices of a single handedness, through chiral templating of the gelator sol. The insights gained could aid the understanding of analogous peptide aggregates, and facilitate the development of supramolecular gels with biomimetic microstructures and rheological characteristics.

Lilypad gelation represents another interesting and unprecedented example of hierarchical self-assembly. The use of non-equilibrium conditions leads to the formation of a spatially resolved aggregate, via the fusion of a self-assembling lattice of monodisperse colloidal particles. A simple geometric model allows the growth profile of the gel to be accurately predicted, and yields reasonable estimates for the surface energies of the system based largely on the evidence of visual observations. The phenomenon effectively illustrates how unusual self-assembly pathways may be accessed via simple perturbations to the physical environment. Moreover, such processes may prove practically useful, since they enable the partial sequestration of dissolved metals with minimal handling of the bulk solution. The results of this study could inform future investigations of interfacial processes and serve as a starting point for the development of more versatile lilypad gelators, with material characteristics better suited to real-world applications.

## 6.4 References

1. M. de Loos, B. L. Feringa and J. H. van Esch, *Eur. J. Org. Chem.*, 2005, 3615-3631.
2. P. Terech and R. G. Weiss, *Chem. Rev.*, 1997, **97**, 3133-3159.
3. G. M. Whitesides and B. Grzybowski, *Science*, 2002, **295**, 2418-2421.
4. D. Kurouski, X. F. Lu, L. Popova, W. Wan, M. Shanmugasundaram, G. Stubbs, R. K. Dukor, I. K. Lednev and L. A. Nafie, *J. Am. Chem. Soc.*, 2014, **136**, 2302-2312.
5. I. Usov, J. Adamcik and R. Mezzenga, *ACS Nano*, 2013, **7**, 10465-10474.
6. W. Dzwolak, *Chirality*, 2014, **26**, 580-587.
7. E. Yashima, N. Ousaka, D. Taura, K. Shimomura, T. Ikai and K. Maeda, *Chem. Rev.*, 2016, **116**, 13752-13990.
8. S. Armon, H. Aharoni, M. Moshe and E. Sharon, *Soft Matter*, 2014, **10**, 2733-2740.
9. S. Yagai, M. Gushiken, T. Karatsu, A. Kitamura and Y. Kikkawa, *Chem. Commun.*, 2011, **47**, 454-456.
10. Y. Qiao, Y. Y. Lin, Z. Y. Yang, H. F. Chen, S. F. Zhang, Y. Yan and J. B. Huang, *J. Phys. Chem. B*, 2010, **114**, 11725-11730.
11. J. C. Hu, W. F. Kuang, K. Deng, W. J. Zou, Y. W. Huang, Z. X. Wei and C. F. J. Faul, *Adv. Funct. Mater.*, 2012, **22**, 4149-4158.
12. B. Lotz and S. Z. D. Cheng, *Polymer*, 2005, **46**, 577-610.
13. M. A. Miller and D. J. Wales, *J. Phys. Chem. B*, 2005, **109**, 23109-23112.
14. S. Przybył and P. Pierański, *Eur. Phys. J. E*, 2001, **4**, 445-449.
15. A. Maritan, C. Micheletti, A. Trovato and J. R. Banavar, *Nature*, 2000, **406**, 287-290.
16. S. Yang, L. Z. Zhao, C. Z. Yu, X. F. Zhou, J. W. Tang, P. Yuan, D. Y. Chen and D. Y. Zhao, *J. Am. Chem. Soc.*, 2006, **128**, 10460-10466.
17. Y. Snir and R. D. Kamien, *Science*, 2005, **307**, 1067-1067.
18. Y. Yang, Y. J. Zhang and Z. X. Wei, *Adv. Mater.*, 2013, **25**, 6039-6049.
19. D. S. Chung, G. B. Benedek, F. M. Konikoff and J. M. Donovan, *Proc. Natl. Acad. Sci. U. S. A.*, 1993, **90**, 11341-11345.
20. M. A. Mateos-Timoneda, M. Crego-Calama and D. N. Reinhoudt, *Chem. Soc. Rev.*, 2004, **33**, 363-372.
21. Y. Timsit and P. Várnai, *PLoS One*, 2010, **5**, 1-12.
22. M. Boncheva, D. A. Bruzewicz and G. M. Whitesides, *Langmuir*, 2003, **19**, 6066-6071.
23. C. Chothia, M. Levitt and D. Richardson, *J. Mol. Biol.*, 1981, **145**, 215-250.
24. E. Tayeb-Fligelman, O. Tabachnikov, A. Moshe, O. Goldshmidt-Tran, M. R. Sawaya, N. Coquelle, J.-P. Colletier and M. Landau, *Science*, 2017, **355**, 831-833.
25. F. Xu, I. J. Khan, K. McGuinness, A. S. Parmar, T. Silva, N. S. Murthy and V. Nanda, *J. Am. Chem. Soc.*, 2013, **135**, 18762-18765.
26. A. G. Cherstvy, *J. Phys. Chem. B*, 2008, **112**, 12585-12595.
27. D. Walther, F. Eisenhaber and P. Argos, *J. Mol. Biol.*, 1996, **255**, 536-553.
28. F. V. de Abreu, R. G. Dias and C. von Ferber, *Soft Matter*, 2008, **4**, 731-734.
29. J. Weiss, E. Jahnke, N. Severin, J. P. Rabe and H. Frauenrath, *Nano Lett.*, 2008, **8**, 1660-1666.
30. R. H. Pritchard, Y. Y. Huang and E. M. Terentjev, *Soft Matter*, 2014, **10**, 1864-1884.
31. M. Jaspers, M. Dennison, M. F. J. Mabesoone, F. C. MacKintosh, A. E. Rowan and P. H. J. Kouwer, *Nat. Commun.*, 2014, **5**, 5808.
32. Y. Okumura and K. Ito, *Adv. Mater.*, 2001, **13**, 485-487.
33. G. Gil-Ramírez, D. A. Leigh and A. J. Stephens, *Angew. Chem. Int. Edit.*, 2015, **54**, 6110-6150.
34. C. Alvaríño, D. Simond, P. M. Lorente, C. Besnard and A. F. Williams, *Chem. Eur. J.*, 2015, **21**, 8851-8858.
35. G. P. Yang, L. Hou, X. J. Luan, B. A. Wu and Y. Y. Wang, *Chem. Soc. Rev.*, 2012, **41**, 6992-7000.
36. J. P. Zhang, X. L. Qi, C. T. He, Y. Wang and X. M. Chen, *Chem. Commun.*, 2011, **47**, 4156-4158.

37. C. W. Ashley, *The Ashley Book of Knots*, Doubleday, 1944.
38. E. Artin, *Ann. Math.*, 1947, **48**, 101-125.
39. M. Grünwald, S. Tricard, G. M. Whitesides and P. L. Geissler, *Soft Matter*, 2016, **12**, 1517-1524.
40. A. B. Subramaniam, M. Abkarian and H. A. Stone, *Nat. Mater.*, 2005, **4**, 553-556.
41. E. Kumacheva, P. Garstecki, H. K. Wu and G. M. Whitesides, *Phys. Rev. Lett.*, 2003, **91**, 4.
42. D. Y. Zhao, J. L. Feng, Q. S. Huo, N. Melosh, G. H. Fredrickson, B. F. Chmelka and G. D. Stucky, *Science*, 1998, **279**, 548-552.
43. K. P. Velikov, C. G. Christova, R. P. A. Dullens and A. van Blaaderen, *Science*, 2002, **296**, 106-109.
44. P. A. Kralchevsky and N. D. Denkov, *Curr. Opin. Colloid Interface Sci.*, 2001, **6**, 383-401.
45. I. A. Larmour, G. C. Saunders and S. E. J. Bell, *Angew. Chem. Int. Edit.*, 2008, **47**, 5043-5045.
46. A. L. Rogach, D. V. Talapin, E. V. Shevchenko, A. Kornowski, M. Haase and H. Weller, *Adv. Funct. Mater.*, 2002, **12**, 653-664.
47. N. Bowden, F. Arias, T. Deng and G. M. Whitesides, *Langmuir*, 2001, **17**, 1757-1765.
48. R. Chinomona, J. Lajeunesse, W. H. Mitchell, Y. Yao and S. E. Spagnolie, *Soft Matter*, 2015, **11**, 1828-1838.
49. N. Vandewalle, N. Obara and G. Lumay, *Eur. Phys. J. E*, 2013, **36**, 6.
50. M. Giersig and M. Hilgendorff, *J. Phys. D*, 1999, **32**, L111-L113.
51. J. Dhainaut, J. P. Dacquin, A. F. Lee and K. Wilson, *Green Chem.*, 2010, **12**, 296-303.
52. K. Ueno, K. Matsubara, M. Watanabe and Y. Takeoka, *Adv. Mater.*, 2007, **19**, 2807-2812.
53. T. Dwars, E. Paetzold and G. Oehme, *Angew. Chem. Int. Edit.*, 2005, **44**, 7174-7199.
54. F. M. Menger and A. R. Elrington, *J. Am. Chem. Soc.*, 1991, **113**, 9621-9624.
55. R. Muñoz-Espí, Y. Mastai, S. Gross and K. Landfester, *Crystengcomm*, 2013, **15**, 2175-2191.
56. M. Li, H. Schnablegger and S. Mann, *Nature*, 1999, **402**, 393-395.
57. J. M. P. Gutierrez, T. Hinkley, J. W. Taylor, K. Yanev and L. Cronin, *Nat. Commun.*, 2014, **5**, 8.
58. N. Tompkins, N. Li, C. Girabawe, M. Heymann, G. B. Ermentrout, I. R. Epstein and S. Fraden, *Proc. Natl. Acad. Sci. U.S.A.*, 2014, **111**, 4397-4402.
59. K. L. Morris, L. Chen, J. Raeburn, O. R. Sellick, P. Cotanda, A. Paul, P. C. Griffiths, S. M. King, R. K. O'Reilly, L. C. Serpell and D. J. Adams, *Nat. Commun.*, 2013, **4**, 1480.
60. J. Raeburn, B. Alston, J. Kroeger, T. O. McDonald, J. R. Howse, P. J. Cameron and D. J. Adams, *Mater. Horiz.*, 2014, **1**, 241-246.
61. J. J. D. de Jong, P. R. Hania, A. Pugžlys, L. N. Lucas, M. de Loos, R. M. Kellogg, B. L. Feringa, K. Duppen and J. H. van Esch, *Angew. Chem. Int. Edit.*, 2005, **44**, 2373-2376.
62. M. Moriyama, N. Mizoshita, T. Yokota, K. Kishimoto and T. Kato, *Adv. Mater.*, 2003, **15**, 1335-1338.
63. S. Matsumoto, S. Yamaguchi, S. Ueno, H. Komatsu, M. Ikeda, K. Ishizuka, Y. Iko, K. V. Tabata, H. Aoki, S. Ito, H. Noji and I. Hamachi, *Chem. Eur. J.*, 2008, **14**, 3977-3986.
64. J. L. Yan, J. Liu, H. R. Lei, Y. Kang, C. Zhao and Y. Fang, *J. Colloid Interface Sci.*, 2015, **448**, 374-379.
65. H. Q. Wang, W. L. Xu, S. S. Song, L. Feng, A. X. Song and J. C. Hao, *J. Phys. Chem. B*, 2014, **118**, 4693-4701.
66. Q. Y. Cheng, D. Zhou, Y. Gao, Q. Chen, Z. Zhang and B. H. Han, *Langmuir*, 2012, **28**, 3005-3010.
67. B. Adhikari, G. Palui and A. Banerjee, *Soft Matter*, 2009, **5**, 3452-3460.
68. R. M. Capito, H. S. Azevedo, Y. S. Velichko, A. Mata and S. I. Stupp, *Science*, 2008, **319**, 1812-1816.
69. D. Vella and L. Mahadevan, *Am. J. Phys.*, 2005, **73**, 817-825.
70. A. Chakrabarti and M. K. Chaudhury, *Langmuir*, 2014, **30**, 4684-4693.

71. L. Meazza, J. A. Foster, K. Fucke, P. Metrangolo, G. Resnati and J. W. Steed, *Nat. Chem.*, 2013, **5**, 42-47.
72. M. O. M. Piepenbrock, N. Clarke and J. W. Steed, *Soft Matter*, 2010, **6**, 3541-3547.
73. A. M. Todd, K. M. Anderson, P. Byrne, A. E. Goeta and J. W. Steed, *Cryst. Growth Des.*, 2006, **6**, 1750-1752.
74. T. McMillen and A. Goriely, *J. Nonlinear Sci.*, 2002, **12**, 241-281.
75. A. W. P. Fitzpatrick, G. T. Debelouchina, M. J. Bayro, D. K. Clare, M. A. Caporini, V. S. Bajaj, C. P. Jaroniec, L. C. Wang, V. Ladizhansky, S. A. Müller, C. E. MacPhee, C. A. Waudby, H. R. Mott, A. De Simone, T. P. J. Knowles, H. R. Saibil, M. Vendruscolo, E. V. Orlova, R. G. Griffin and C. M. Dobson, *Proc. Natl. Acad. Sci. U.S.A.*, 2013, **110**, 5468-5473.
76. K. E. Horner, M. A. Miller, J. W. Steed and P. M. Sutcliffe, *Chem. Soc. Rev.*, 2016, **45**, 6432-6448.
77. P. Byrne, G. O. Lloyd, N. Clarke and J. W. Steed, *Angew. Chem. Int. Edit.*, 2008, **47**, 5761-5764.
78. S. I. Sakurai, S. Ohsawa, K. Nagai, K. Okoshi, J. Kumaki and E. Yashima, *Angew. Chem. Int. Edit.*, 2007, **46**, 7605-7608.
79. J. W. Alexander, *Proc. Natl. Acad. Sci. U.S.A.*, 1923, **9**, 93-95.
80. K. S. Chichak, S. J. Cantrill, A. R. Pease, S. H. Chiu, G. W. V. Cave, J. L. Atwood and J. F. Stoddart, *Science*, 2004, **304**, 1308-1312.
81. J. Holden and L. Holden, *Bridges Finland Conference Proc.*, 2016, 127-134.
82. E. Jen, *Commun. Math. Phys.*, 1988, **118**, 569-590.
83. S. Azeroual, J. Surprenant, T. D. Lazzara, M. Kocun, Y. Tao, L. A. Cuccia and J. M. Lehn, *Chem. Commun.*, 2012, **48**, 2292-2294.
84. J. J. D. de Jong, T. D. Tiemersma-Wegman, J. H. van Esch and B. L. Feringa, *J. Am. Chem. Soc.*, 2005, **127**, 13804-13805.
85. H. von Berlepsch, S. Kirstein and C. Böttcher, *J. Phys. Chem. B*, 2003, **107**, 9646-9654.
86. A. R. A. Palmans and E. W. Meijer, *Angew. Chem. Int. Edit.*, 2007, **46**, 8948-8968.
87. Y. Saito and H. Hyuga, *Rev. Mod. Phys.*, 2013, **85**, 603-621.
88. Z. El-Hachemi, J. Q. Crusats, J. M. Ribo and S. Veintemillas-Verdaguer, *Cryst. Growth Des.*, 2009, **9**, 4802-4806.
89. D. K. Kondepudi, R. J. Kaufman and N. Singh, *Science*, 1990, **250**, 975-976.
90. L. J. Prins, P. Timmerman and D. N. Reinhoudt, *J. Am. Chem. Soc.*, 2001, **123**, 10153-10163.
91. B. M. W. Langeveld-Voss, R. J. M. Waterval, R. A. J. Janssen and E. W. Meijer, *Macromolecules*, 1999, **32**, 227-230.
92. J. Masel, V. A. A. Jansen and M. A. Nowak, *Biophys. Chem.*, 1999, **77**, 139-152.
93. M. L. Gardel, J. H. Shin, F. C. MacKintosh, L. Mahadevan, P. Matsudaira and D. A. Weitz, *Science*, 2004, **304**, 1301-1305.
94. F. C. Mackintosh, J. Kas and P. A. Janmey, *Phys. Rev. Lett.*, 1995, **75**, 4425-4428.
95. S. G. Jones, N. Abbasi, A. Ahuja, V. Truong and S. S. H. Tsai, *Phys. Fluids*, 2015, **27**, 8.
96. M. Abkarian, S. Protiere, J. M. Aristoff and H. A. Stone, *Nat. Commun.*, 2013, **4**, 8.
97. V. N. Manoharan, M. T. Elsesser and D. J. Pine, *Science*, 2003, **301**, 483-487.
98. H. J. Kull, *Phys. Rep.-Rev. Sec. Phys. Lett.*, 1991, **206**, 197-325.
99. E. B. Burov and R. Molnar, *Earth Planet. Sci. Lett.*, 2008, **275**, 370-381.
100. L. B. Smolka and A. Belmonte, *J. Non-Newton. Fluid Mech.*, 2003, **115**, 1-25.
101. D. Vella, D. G. Lee and H. Y. Kim, *Langmuir*, 2006, **22**, 5979-5981.
102. N. A. Lange and J. A. Dean, *Lange's Handbook of Chemistry*, McGraw-Hill, 1967.
103. D. K. Owens and R. C. Wendt, *J. Appl. Polym. Sci.*, 1969, **13**, 1741-&.
104. M. C. Biesinger, B. P. Payne, L. W. M. Lau, A. Gerson and R. S. C. Smart, *Surf. Interface Anal.*, 2009, **41**, 324-332.
105. M. Berger and T. A. Manuel, *J. Polym. Sci. Part B - Polym. Lett.*, 1964, **2**, 873-876.

## 7. Closing remarks

### 7.1 Conclusions

Hierarchical aggregates can form via a number of self-assembly mechanisms. In order to predict and design the properties of LMWGs, it is necessary to understand how particular interactions on a molecular scale give rise to the fibrous structures responsible for gelation. In this investigation, it has been established that fibrils of uniform diameter may emerge from the spontaneous scrolling of lamellar bis(urea) assemblies. Scrolling behaviour is primarily associated with molecules that self-assemble into asymmetric lamellae with relatively weak interlayer interactions. Thus, crystal structures of a candidate LMWG provide a useful indication as to whether scrolling is likely, and serve as a useful starting point for probing the dynamics of fibril formation in MD simulations.

Correlations between the gelation capacity of a compound and its crystallisation behaviour demonstrate the importance of topological features, such as the symmetry and  $\alpha$  tape arrangement of a bis(urea) lamella, in determining the outcome of hierarchical self-assembly. Within networks of helical fibrils, comparable topological constraints in the patterning of physical junctions can result in self-organisation on a larger scale. Studies of a pentakis(urea) LMWG reveal that helices of like chirality may intertwine to form wide helical bundles, while heterochiral helices must form relatively narrow and complex flat braided architectures. Moreover, it has been shown that trace chiral additives may cause an achiral LMWG to form pure homochiral braided helices, thus altering the microstructure and bulk physical properties of the resulting gel. Braiding represents a general but relatively unexplored mechanism of colloidal crystallisation, with potentially important implications for the study of biological soft matter and amyloid-related disorders such as Alzheimer's disease.

The pathway of self-assembly is a key consideration in the development of practically useful supramolecular gels, as functionality often depends on the surface properties of the gelator aggregates. Physical characteristics can sometimes be inferred from the crystal structure of the LMWG. The photoreactivities of anil-functionalised bis(urea)s in the solid state, for example, was found to correlate with steric crowding of surface anil moieties, which could be quantitatively assessed via MM models. In other systems, rationalising the behaviour of a self-assembled material may require a combination of insights from microscopy, crystallography and bulk characterisation

techniques. Studies of tris(urea)s before and after aggregation suggest that molecules adopt extended conformations in solution and self-assemble into lamellar structures that are seldom compatible with gel formation. However, incorporating a metal coordination site into the LMWG allows a metallogel to be formed under vapour diffusion conditions. Hierarchical organisation is observed over visible length scales: the gel grows as a well-defined spheroid at the liquid-vapour interface via the coalescence of monodisperse microparticles into a close-packed structure. This process may be exploited for the facile sequestration of dissolved metals, and offers a clear illustration of how the surface energies of supramolecular assemblies can strongly dictate the mode of aggregation.

## 7.2 Further work

The simulations of lamellar folding presented in this study represent a useful starting point for predicting the gelation properties of LMWGs from crystallographic data. The method could be further validated by calculating the charges and intermolecular forces of the bis(urea) assemblies at a higher level of theory. Fidelity to real self-assembly processes could be improved by evaluating the dynamics of the system in an implicit or atomistic solvent under constant-NPT conditions. In addition, it would be beneficial to develop a coarse-grained model of the lamellae that could accurately replicate the results of atomistic simulations. This would allow for the analysis of larger systems, such as fibrils consisting of multiple layers, and highlight effects of key structural parameters on the ability of lamellae to exhibit scrolling behaviour.

Rationalising the surface properties of fibrous gel aggregates remains a difficult task. Single-crystal structures and molecular mechanics simulations of anil-functionalised bis(urea)s offer valuable insight into the chromic properties of these species in the solid state. However, it is unclear whether the results of the computational work are truly representative of real isomerisation processes, or applicable to other photoreactive LMWGs. Furthermore, the work offers limited assistance in the development of gels with improved switchable characteristics, since the arrangement of molecules on the surface of a gel fibre is unlikely to resemble that of a crystalline material. These shortcomings could be addressed by incorporating disorder and surface curvature into the model bis(urea) assemblies, and simulating a larger population of reacting chromophores with transition probabilities estimated via DFT calculations.

There is much still to be learned about the self-assembly pathways of linear tris(urea)s. While NMR studies and DFT calculations provide indirect evidence as to how these molecules behave in solution, the process of self-assembly could be probed more directly by means of SANS experiments, MD simulations and UV-vis studies of fluorescent analogues. Altering the end groups of the compounds and the conditions for aggregation could facilitate the isolation of good-quality single crystals, allowing the interactions between tris(urea)s to be precisely determined. Moreover, synthesising a wider range of tris(urea) derivatives would aid the development of more detailed structure-property relationships, which could be used to design or predict the characteristics of new tris(urea) LMWGs.

The utility of oligo(urea)s as analogues for amyloidogenic peptides is one of the key findings of this investigation. The compounds presented form a range of unusual hierarchical aggregates which illustrate the importance of colloidal self-assembly in determining the bulk properties of a supramolecular gel. However, these species are poorly soluble in most organic solvents and give rise to heterogeneous materials that can be difficult to analyse. Adjusting the structures of the oligo(urea)s or introducing alternative hydrogen bonding functionalities could lead to more versatile gels that are easier to tune and physically characterise. A particular aim is to gain a better understanding of lily pad gelation and develop compounds that can undergo this process in aqueous solutions, for application in wastewater remediation and the recovery and separation of dissolved metal ions. Furthermore, it would be useful to undertake kinetic studies of helix braiding, elucidate the mechanism of chiral templating and quantify the effects of different braiding patterns on rheological behaviour. Such insights could inform models of helix-helix interactions in biological systems, and aid the development of treatments for protein misfolding disorders such as Alzheimer's disease.



## 8. Experimental

### 8.1 Compositional analysis

#### Elemental analysis and mass spectrometry

Electrospray-ionisation mass spectra of intermediates and bis(urea) products were obtained from dilute ( $1 \text{ mg ml}^{-1}$ ) samples in methanol using a TQD mass spectrometer (Waters Ltd.), while oligo(urea)s were analysed in filtered methanol/DMSO (4:1) solutions using an LCT Premier (Waters) high-resolution spectrometer. Elemental analysis was conducted on dried materials using an Exeter CE-440 Elemental Analyser.

#### XPS spectra of lily pad gels

Lily pad gels were prepared by exposing a 0.5% (w/v) solution of **6.1a** in DMF ( $2 \text{ cm}^3$ ) to vapour from  $2 \text{ cm}^3$  of diethyl ether. The ether reservoir was stored in a sealed  $28 \text{ cm}^3$  vial and surrounded an open  $7 \text{ cm}^3$  vial containing the DMF solution. To obtain XPS spectra of the nickel(II) metallogel of **6.1a** (Chapter 6), a sample was deposited on a silicon wafer and dried in air under vacuum for 2 weeks. The analysis was performed by Dr Aled Lewis at Swansea University under ultrahigh-vacuum conditions (base pressure  $4 \times 10^{-10}$  mbar) using a VG Escalab MkII with charge neutralisation and a monochromatic Al X-ray source, emission settings of 375 W and 25 mA and pass energies of 80 and 20 eV for the wide and narrow scans respectively. Spectra were analysed in CasaXPS 2.3.18 with binding energies referenced against the lowest-energy C 1s signal at 285 eV. Narrow scans in the Ni 2p, Cl 2p, O 1s, N 1s and C 1s regions were fitted with Shirley backgrounds, GL(30) peak shapes and equal full-width-half-maxima for each element analysed. Compositions were calculated with custom relative sensitivity factors for the instrument used, and errors were estimated by making reasonable adjustments to the region boundaries and refitting the data.

#### TGA and ICP-MS analysis of lily pad gels

Thermogravimetric analysis of the wet gel was performed under nitrogen using a TA Instruments TGA Q500 with a sample gas flow rate of  $60 \text{ ml min}^{-1}$ . The

mass of non-coordinated solvent was measured with a 25 °C min<sup>-1</sup> ramp to 150 °C followed by isothermal heating until no further mass loss was detected. Pyrolysis was subsequently performed by increasing the temperature to 900 °C at a rate of 2 °C min<sup>-1</sup>. ICP-MS data for gel samples before and after pyrolysis were obtained using a Thermo Scientific X-Series ICP-MS, previously optimised for Ni isotopes 58, 60, 61 and 62 to maximise sensitivity and minimise oxide interference. Samples corresponding to approximately 2 mg of wet gel were transferred to PFA vials, dried in air for 24 hours and dissolved in concentrated analytical grade nitric acid (Romil) over 24 hours at 20 °C. The solutions were diluted 100-fold in 3% nitric acid prior to analysis. Measurements were calibrated against an external 1000 ppm Ni reference standard (Romil). The close agreement between isotopes confirmed the absence of significant spectral interference, while analysis of procedural blanks indicated that no Ni was present in the reagents used.

## 8.2 Single-crystal X-ray diffraction

Crystals of suitable quality for single-crystal X-ray diffraction were obtained by cooling hot solutions to room temperature and leaving the samples to stand for 1-2 days. Different crystallisation conditions were employed for each compound series.

### Chapter 2

Crystals of the dihydrate of **2.2**, structure **V**, were obtained from an 8% (w/v) solution of **2.2** in methanol, and all picoline solutions were prepared at concentrations of 12% (w/v). The hydrated nitrobenzene solvate of **2.3**, structure **IX**, was obtained from a 0.2% (w/v) nitrobenzene solution with a water concentration of 0.8% (w/v), to maximise crystal size and avoid concomitant gel formation. All other solutions were prepared at concentrations of 1% (w/v), and solvents were used as received without further purification.

### Chapter 3

Non-solvated crystals of diamine **3.1a** (structure **XII**) were obtained by slow evaporation of a 1% (w/v) ethanol solution under ambient conditions, while crystals of **3.1b** and **3.1d** (structures **XII** and **XIV** respectively) were obtained from

methanol by the same procedure. Crystallisation of **3.1a** by slow evaporation of a 1% (w/v) solution yielded a partial methanol solvate (structure **XV**). The anils **3.3b**, **3.3c**, **3.4a** and **3.4c** (structures **XVI**, **XVII**, **XVIII** and **XIX** respectively) crystallised on formation in static 0.8-1.0% (w/v) methanol solutions at room temperature. Single crystals of compounds **3.2b** and **3.4b** were similarly formed, but these were of insufficient quality for complete structure solutions to be obtained. Crystals of 5-nitrosalicylaldehyde (structure **XX**) were produced serendipitously after the filtrate from the synthesis of compound **3.2d**, collected without concentration *in vacuo*, was allowed to slowly evaporate at room temperature. Crystals of 5-methoxysalicylaldehyde (structure **XXI**) were acquired by freezing the pure liquid at -20 °C, and using the resulting microcrystals (<1 mg) to seed a second sample of the material at 4 °C. Finally, a co-crystal of **3.3b** with 5-methoxysalicylaldehyde (structure **XXII**) was obtained by synthesising the anil with a large excess (4 equivalents) of the salicylaldehyde in ethanol or 1-propanol and storing the concentrated and filtered reaction mixture for 1 month at room temperature.

#### Chapter 4

Crystals were obtained by slow, partial evaporation of 1% (w/v) solutions under ambient conditions. Crystals of **4.2b** (structure **XXIX**) were obtained from ethanol, and polymorphs of **4.4** (structure **XXXIII**) and **4.6b** (structure **XXXVII**) from ethanol and 1-propanol respectively. Methanol was used as the solvent for all other crystallisations.

#### Chapter 5

Diamines **5.1b**, **5.1c** and **5.1d** (structures **XLIV**, **XLV** and **XLVI** respectively) crystallised on formation in dry acetonitrile at room temperature, and were recrystallised from hot methanol.

#### Diffraction experiments

Single-crystal diffraction data for structures **VII**, **XIX**, **XXX** and **XL** were collected at 120 K on a three-circle diffractometer with Pilatus 2M photon-counting detector at station I19 of the Diamond Light Source synchrotron (undulator,  $\lambda = 0.6889 \text{ \AA}$ ,  $\omega$ -scan, 1.0°/frame). Diffraction data for structures **XVII**,

**XXIII**, **XXIV** and **XXV** were collected at 120 K on an Oxford Diffraction Xcalibur (MoK $\alpha$ ,  $\lambda = 0.71073$  Å, CCD detector). All other diffraction data were collected at 120 K on a Bruker D8 Venture (CMOS area detector). Structure **XVIII** was solved using CuK $\alpha$  radiation ( $\lambda = 1.54178$  Å) while for the other structures MoK $\alpha$  radiation ( $\lambda = 0.71073$  Å) was used. Data were processed using the Bruker APEX II software and solved and refined using the SHELX suite of programs<sup>1</sup> in Olex2.<sup>2</sup>

### 8.3 Powder X-ray diffraction

Xerogels were prepared by applying 1% (w/v) gels to a silicon sample plate and drying the materials in ambient air for 6 hours. Experiments were performed at 20 °C using a PANalytical Empyrean diffractometer fitted with a copper tube operated at 40 kV and 40 mA (unsplit K $\alpha$ 1+K $\alpha$ 2 doublet, mean wavelength  $\lambda = 154.19$  pm). A 1/8° fixed divergence slit, 1/4° antiscatter slit and 10 mm mask were mounted in the primary beam path, and a Ni filter and 7.5 mm antiscatter slit in the diffracted beam. 0.04 rad axial Soller slits were used in both beam paths. Detection was performed with a PIXcel (PANalytical) 1D scanning line detector with 255 active channels. Scans were typically conducted over a 2 $\theta$  range of 2-40° with a step size of 0.02626° and a scan speed of 0.0112°/s.

### 8.4 Rheometry

Oscillatory rheometry measurements were performed using a TA Instruments AR 2000 on a rough Peltier plate with a 25 mm rough plate geometry and 2.5 mm gap. Samples were prepared by boiling gelator solutions in sealed 7 cm<sup>3</sup> vials. In Chapters 3 and 4, the hot solutions were poured into a 25 mm cylindrical glass mould on the Peltier plate and the gels allowed to form over 30 minutes prior to analysis. The materials were cooled to 10 °C throughout formation and analysis in order to minimise evaporation of the gel solvent. In Chapters 2, 5 and 6, however, the gels could not be formed *in situ*; thus, the gels were generated in sealed vials and transferred to a cylindrical mould on the Peltier plate at 17 or 22 °C, to achieve a total volume of 3 cm<sup>3</sup>. In Chapter 2, gels were produced at room temperature over 1 hour, while gels in Chapters 5 and 6 were left to stand for 3 days before analysis. The gels were equilibrated for 30 minutes at the experiment temperature before removing the mould and initiating the analysis. Frequency sweep experiments were performed with a constant applied stress of 1 Pa,

and stress sweep experiments with a constant frequency of 1 Hz. Time sweep experiments were performed without removing the glass mould, and with a fixed stress and frequency of 1 Pa and 1 Hz respectively. It is worth noting that the use of non-standard conditions in the time sweep profiles introduces a constant scaling factor into the values of  $G$ . This error limits the usefulness of the absolute values of  $G'$  and  $G''$ , but has no effect on the ratio  $G'/G''$  or the value of the gradient in Avrami plots.

## 8.5 Microscopy

SEM samples were prepared on silicon wafers, dried in air for 2 days, and coated with 2 nm of platinum using a Cressington 328 Ultra High Resolution EM Coating System. The images were obtained using an FEI Helios NanoLab DualBeam microscope in immersion mode, with beam settings of 1.5 kV and 0.17 nA. TEM samples were prepared on copper support grids, dried in air for 1 hour and imaged in high-resolution mode using a JEOL 2100F FEG TEM, fitted with a Gatan 914 High Tilt Tomography holder. The temperature was maintained at -65 °C by cryo-cooling with liquid nitrogen, and monitored using a Gatan 900 SmartSet controller. AFM samples were prepared on silicon support chips, dried for 2 days and imaged with a Bruker MultiMode MM8 Atomic Force Microscope, used in ScanAsyst mode with a resolution of 256 lines. A NanoWorld NCR arrow probe was used with a resonant frequency of 285 kHz and nominal force constant of 42 N m<sup>-1</sup>.

## 8.6 NMR spectroscopy

### Solution-state spectra

Solution-state NMR spectra were recorded in DMSO- $d_6$  using a Bruker Avance 400 without an internal reference. The concentrations of samples were typically in the range 1-2% (w/v). NMR titrations (Chapter 5) were performed using DMSO- $d_6$  solutions with a fixed urea concentration of 20 mM and varying concentrations of tetrabutylammonium chloride. Using the same urea stock solution, three solutions were prepared with chloride/urea ratios of 0, 1 and 10. A minimum quantity (approximately 700 mg) of each solution was added to an NMR tube, and the concentration of chloride increased or decreased in stages by the addition of weighed aliquots (typically 60-250 mg) of another solution. Binding isotherms

were fitted via a non-linear regression analysis using the online software BindFit.<sup>3</sup> Job plot measurements were performed in an analogous fashion, by mixing urea and chloride solutions of equal concentration.

#### Solid-state spectra

Solid-state <sup>13</sup>C spectra were recorded at 100.63 MHz using a Bruker Avance III HD spectrometer and a 4 mm (rotor o.d.) magic-angle spinning probe. They were obtained using cross-polarisation with a 1 s recycle delay, 10 ms contact time, at ambient probe temperature (approximately 25 °C) and at a sample spin-rate of 10 kHz. Between 3000-3600 repetitions were accumulated. Spectral referencing was with respect to an external sample of neat tetramethylsilane.

## 8.7 UV-vis and FT-IR spectroscopy

#### Absorbance spectra

Absorbance spectra of anil solutions and gels (Chapter 3) were recorded under ambient conditions using an ATi Unicam UV2-100 UV-vis spectrometer with a data interval of 1 nm and scan speed of 120 nm min<sup>-1</sup>. Methanol solutions were prepared at concentrations of 0.03% (w/v), while gels in 1,2-dichlorobenzene were prepared at concentrations of 0.1% (w/v) and diluted to obtain uniform 0.03% (w/v) suspensions. All samples were analysed in a de-mountable quartz cuvette with a path length of 1 mm.

#### Fluorescence spectra

Fluorescence spectra of anils were measured in solutions, gels and the solid state under ambient conditions using a Horiba Jobin Yvon SPEX Fluorolog 3-22 spectrofluorimeter. The experiments were performed in front-face mode with an excitation wavelength of 370 nm. Gels and solutions were prepared with concentrations of 0.1% (w/v), and solids were ground before analysis. Solids were analysed in a de-mountable quartz cuvette with a path length of 1 mm, and solutions and gels in a quartz cuvette with a path length of 1 cm.

## Diffuse reflectance spectra

Diffuse reflectance measurements of solid anils were performed at Swansea University using a spring-loaded powder cell loaded into an Agilent Cary 100 UV-Vis spectrophotometer, referencing the spectra to a Labsphere Spectralon diffuse reflectance standard. The spectra were recorded between wavelengths of 450 nm and 600 nm, using a step size of 1 nm and a scan rate of 300 nm min<sup>-1</sup>. The effect of UV illumination on absorbance properties was determined by treating the materials with a UV lamp for 10 minutes prior to analysis.

## CD spectra

CD spectra for DMF gels of **6.1b** were recorded at room temperature using a Jasco J-810 spectropolarimeter. Gels were prepared with concentrations of 0.4% (w/v), diluted to 0.1% (w/v) with DMF and transferred to a quartz cuvette with a path length of 1 cm. The analysis was performed in high-sensitivity mode with 5 accumulations, a scan speed of 50 nm min<sup>-1</sup> and a data pitch of 1 nm. To test the effect of heating on supramolecular chirality, measurements were performed on gel samples incubated for 30 minutes in an oil bath at a variety of temperatures.

## FT-IR spectra

Infrared spectra were measured using a PerkinElmer Spectrum Two spectrometer fitted with the ATR accessory. Data were recorded between 450 and 4000 cm<sup>-1</sup> with 4 accumulations.

## 8.8 Computational work

### Molecular dynamics

MD simulations were performed in GROMACS 4.6.2<sup>4</sup> using the General Amber Force Field (GAFF)<sup>5</sup>. The Antechamber package<sup>6</sup> was used to assign bonded and non-bonded interaction parameters, and calculate atomic charges via the semi-empirical AM1 method with bond charge correction (AM1-BCC).<sup>7</sup> The initial structures were obtained from single-crystal data, bounded with a 50 nm cubic periodic box and subjected to an initial energy minimisation step via a steepest-descent procedure. Production runs were performed in the absence of solvent

using a constant-*NVT* ensemble, with random initial velocities assigned according to a Maxwell distribution at 300 K. The temperature was controlled via a Berendsen thermostat with a time constant of 0.1 ps.<sup>8</sup> Although it fails to generate a correct canonical ensemble, the Berendsen thermostat was chosen as it effects efficient convergence of both temperature and potential energy, allowing the dynamics of many large assemblies to be compared under isothermal conditions over extended timescales. Folding simulations were carried out for 1500 ps with a time step of 1 fs, while surface energy calculations were based on 150 ps simulations of model crystallites after equilibration under constant-*NVT* conditions for 150 ps. Surface energies were calculated by varying the length of one axis in the model crystallites, which were otherwise constructed with standard dimensions of 10 x 10 x 5 unit cells for structure **II**, 7 x 7 x 16 unit cells for structure **XXV** and 7 x 7 x 4 unit cells for structures **XXIII** and **XXVI**. No bond or angle constraints were applied. The neighbour list was updated every five steps with a cut-off distance of 0.9 nm, while cut-off distances of 1.4 and 1.5 nm were used for the van der Waals and electrostatic interactions respectively. Electrostatics were calculated using the reaction-field method with a relative dielectric constant of 1 inside the reaction field and 78 beyond the cut-off distance.

### Molecular mechanics

Molecular mechanics models of anil crystallites (Chapter 3) were constructed and analysed using the Forcite module in BIOVIA Materials Studio 2016. Calculations were performed on a supercell derived from the single-crystal structure, consisting of three lamellae with four repeat units along each axis of the lamellar plane. The crystal was cleaved to produce a surface parallel to the lamellae and appended to a vacuum slab 40 Å in thickness. The system was modelled with the cvff force-field<sup>9</sup> and Gasteiger charges.<sup>10</sup> One surface anil moiety was converted manually to the *cis*-keto form, and a geometry optimisation performed without restraints. To map the energy profile of the anil rotation, the system was re-optimised with harmonic force constants of 1000 kcal Å<sup>-1</sup> mol<sup>-1</sup> to restrain the torsion angles describing the imine conformation,  $\phi_A$  and  $\phi_B$ , to selected values. A pedal motion was simulated by varying  $\phi_A$  and  $\phi_B$  in 2.5°



increments in opposite directions and re-optimising the geometry after each rotation step. Geometry optimisations were performed with Ewald summation of the van der Waals and electrostatic forces and a medium-quality convergence threshold.

### DFT calculations

DFT calculations were performed in Gaussian 09 using the B3LYP functional<sup>11</sup> and Berny optimisation algorithm, with redundant internal coordinates and default settings for the convergence thresholds.<sup>12</sup> In Chapters 3 and 4, analyses were conducted using the cc-pVDZ basis set,<sup>13</sup> as this was found to produce more realistic (planar) aromatic ring geometries than the more commonly used Pople basis sets.<sup>14</sup> However, the cc-pVDZ basis set does not include a diffuse component, and incorporating such functions by switching to the aug-cc-pVDZ basis set resulted in an unacceptable increase in computation time. Thus, hydrogen bonding energies in Chapter 6 were treated using the 6-31+G\* basis set, which better accounts for the diffuse nature of polar interactions.<sup>15</sup> Physically reasonable starting coordinates were produced in SCIGRESS 3.0.0 by geometry optimisation in MO-G<sup>16</sup> using AM1 parameters.<sup>17</sup> Conformational energy landscapes (Chapter 4) were constructed by optimising the geometry with no fixed variables, then repeating the optimisation with fixed values of selected torsion angles.

## 8.9 Synthesis

Reagents and solvents were purchased from commercial sources and used without further purification. Reagent and solvent quantities detailed in the general procedures are typical, but the actual masses used may deviate from these values by a constant scaling factor of 0.5-1.5. Yields are scaled according to the reagent quantities listed.

### General procedure for bis(urea) synthesis

Compounds **2.1-2.3**, **3.1a-d**, and **4.1-4.9** were synthesised by the addition of 1,3-bis(1-isocyanato-1-methylethyl)benzene (0.1 cm<sup>3</sup>, 0.43 mmol) to a stirred solution of the necessary amine (0.97 mmol) in chloroform (20 cm<sup>3</sup>) under air at

20 °C. The reaction mixture was left to stand for 24 hours at 20 °C then concentrated *in vacuo* and filtered under suction. The collected solids were washed with chloroform (2 x 20 cm<sup>3</sup>) and dried in a drying pistol.

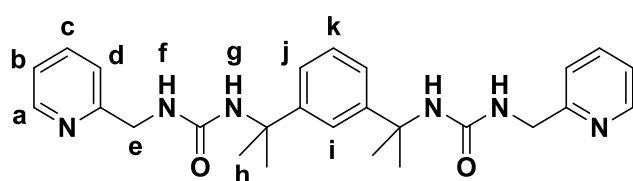
#### General procedure for anil synthesis

Compounds **3.2a-d**, **3.3a-d**, **3.4a-c** and **3.5** were synthesised by the addition of the necessary salicylaldehyde (0.48 mmol) to a stirred solution of **3.1a**, **3.1b**, **3.1c** or **3.1d** (0.20 mmol) in methanol (15 cm<sup>3</sup>) at 20 °C. The reaction mixture was left to stand under air for 24 hours at 20 °C then concentrated *in vacuo* and filtered under suction. The resulting crystalline materials were washed with cold methanol (2 x 10 cm<sup>3</sup>) and dried in a drying pistol.

#### General procedure for benzyl tris(urea) synthesis

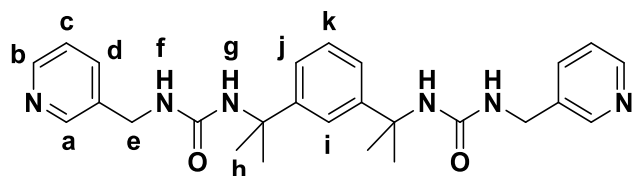
Compounds **5.4a-e** were synthesised by the addition of benzyl isocyanate (0.2 cm<sup>3</sup>, 1.6 mmol) to a stirred solution of **5.1a**, **5.1b**, **5.1c** or **5.1d** (0.70 mmol) in dry acetonitrile (50 cm<sup>3</sup>) under nitrogen at 80 °C. The reaction mixture was stirred for 24 hours at 80 °C, then left to stand under nitrogen for 12 hours at 20 °C. The resulting solids were collected under suction and washed with hot acetonitrile (3 x 50 cm<sup>3</sup>). The product was sonicated in hot methanol (20 cm<sup>3</sup>), filtered, washed with methanol (2 x 50 cm<sup>3</sup>) and dried under air at 80 °C for 24 hours.

#### Compound 2.1



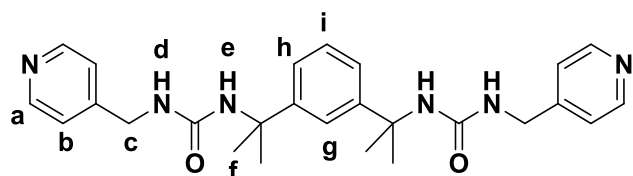
Compound **2.1** was obtained as a white solid (155 mg, 0.34 mmol, 78%), *m/z* (ESI-MS) 461.7 [M+H]<sup>+</sup>, 483.7 [M+Na]<sup>+</sup>. Elem. Anal. Calc. (%) (C<sub>26</sub>H<sub>32</sub>N<sub>6</sub>O<sub>2</sub>) C 67.80, H 7.00, N 18.25; Found (%) C 67.39, H 6.98, N 18.15. <sup>1</sup>H NMR (400 MHz, DMSO-*d*<sub>6</sub>) δ 8.49 (ddd, *J* = 4.8, 1.8, 1.0 Hz, 2H, *a*), 7.74 (dt, *J* = 7.7, 1.8 Hz, 2H, *c*), 7.38 (t, *J* = 2.1 Hz, 1H, *i*), 7.31 – 7.18 (m, 4H, *b*, *d*), 7.18 (m, 3H, *j*, *k*), 6.52 (s, 2H, *g*), 6.44 (t, *J* = 5.9 Hz, 2H, *f*), 4.25 (d, *J* = 5.9 Hz, 4H, *e*), 1.53 (s, 12H, *h*). <sup>13</sup>C{<sup>1</sup>H} NMR (101 MHz, DMSO) δ 160.30, 157.49, 149.11, 148.85, 137.03, 127.70, 122.80, 122.30, 121.77, 121.24, 54.80, 45.06, 30.64.

### Compound 2.2



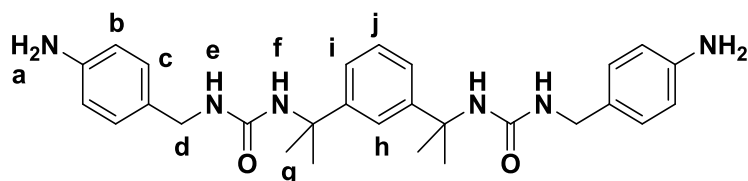
Compound **2.2** was obtained as a white solid (164 mg, 0.36 mmol, 82%),  $m/z$  (ESI-MS) 461.8  $[M+H]^+$ , 483.7  $[M+Na]^+$ . Elem. Anal. Calc. (%) ( $C_{26}H_{32}N_6O_2$ ) C 67.80, H 7.00, N 18.25; Found (%) C 67.50, H 6.98, N 18.22.  $^1H$  NMR (400 MHz, DMSO- $d_6$ )  $\delta$  8.52 – 8.33 (m, 4H, *a, b*), 7.61 (dt,  $J = 7.8, 2.1$  Hz, 2H, *d*), 7.36 (t,  $J = 2.1$  Hz, 1H, *i*), 7.32 (ddd,  $J = 7.8, 4.7, 0.9$  Hz, 2H, *c*), 7.16 (m, 3H, *j, k*), 6.38 (s, 2H, *g*), 6.35 (t,  $J = 6.0$  Hz, 2H, *f*), 4.18 (d,  $J = 6.0$  Hz, 4H, *e*), 1.52 (s, 12H, *h*).  $^{13}C\{^1H\}$  NMR (101 MHz, DMSO)  $\delta$  157.48, 148.94, 148.82, 148.26, 136.94, 135.14, 127.73, 123.79, 122.80, 121.70, 54.82, 40.70, 30.58.

### Compound 2.3



Compound **2.3** was obtained as a white solid (172 mg, 0.37 mmol, 86%),  $m/z$  (ESI-MS) 461.7  $[M+H]^+$ , 483.7  $[M+Na]^+$ . Elem. Anal. Calc. (%) ( $C_{26}H_{32}N_6O_2$ ) C 67.80, H 7.00, N 18.25; Found (%) C 67.52, H 7.01, N 18.18.  $^1H$  NMR (400 MHz, DMSO- $d_6$ )  $\delta$  8.52 – 8.41 (m, 4H, *a*), 7.39 (t,  $J = 2.2$  Hz, 1H, *g*), 7.26 – 7.08 (m, 7H, *b, h, i*), 6.46 (s, 2H, *e*), 6.39 (t,  $J = 6.1$  Hz, 2H, *d*), 4.18 (d,  $J = 6.1$  Hz, 4H, *c*), 1.54 (s, 12H, *f*).  $C\{^1H\}$  NMR (101 MHz, DMSO)  $\delta$  157.47, 150.74, 149.81, 148.82, 127.76, 122.82, 122.26, 121.69, 54.82, 42.05, 30.59.

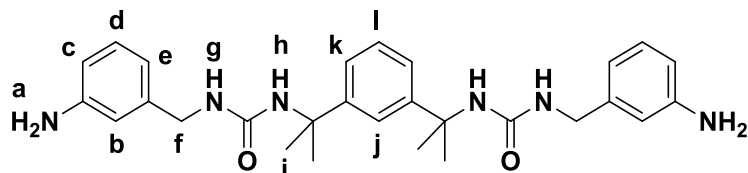
### Compound 3.1a



Compound **3.1a** was obtained as a white solid (177 mg, 0.36 mmol, 84%),  $m/z$  (ESI-MS) 489.9  $[M+H]^+$ , 510.9  $[M+Na]^+$ , 977.6  $[2M+H]^+$ , 999.0  $[2M+Na]^+$ .  $^1H$  NMR (400 MHz, DMSO- $d_6$ )  $\delta$  7.38 (t,  $J = 2.0$  Hz, 1H, *h*), 7.30 – 7.07 (m, 3H, *i, j*), 6.90 (d,  $J$

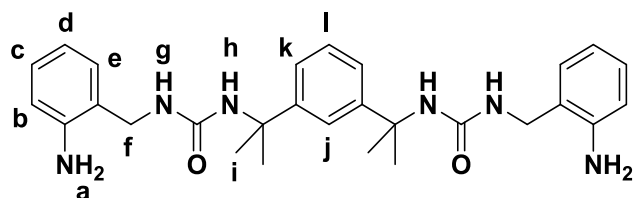
= 8.3 Hz, 4H, *b*), 6.51 (d, *J* = 8.3 Hz, 4H, *c*), 6.22 (s, 2H, *f*), 6.03 (t, *J* = 5.6 Hz, 2H, *e*), 4.93 (s, 4H, *a*), 3.96 (d, *J* = 5.6 Hz, 4H, *d*), 1.54 (s, 12H, *g*). <sup>13</sup>C NMR (101 MHz, DMSO-*d*<sub>6</sub>) δ 157.49, 148.97, 147.81, 128.44, 128.08, 127.68, 122.81, 121.80, 114.18, 54.75, 42.89, 30.67. Elem. Anal. Calc. (%) (C<sub>28</sub>H<sub>36</sub>N<sub>6</sub>O<sub>2</sub>) C 68.83, H 7.43, N 17.20; Found (%) C 68.74, H 7.40, N 17.16.

### Compound 3.1b



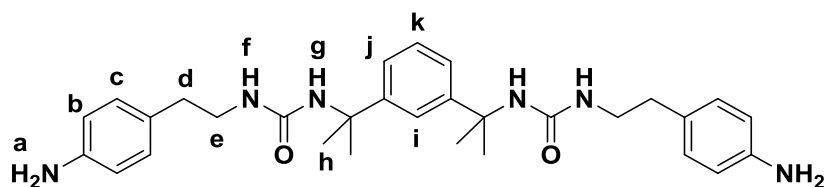
Compound **3.1b** was obtained as a white solid (201 mg, 0.41 mmol, 95%), *m/z* (ESI-MS) 511.7 [M+Na]<sup>+</sup>. <sup>1</sup>H NMR (400 MHz, DMSO-*d*<sub>6</sub>) δ 7.38 (t, *J* = 2.1 Hz, 1H, *j*), 7.26 – 7.14 (m, 3H, *k, l*), 6.94 (t, *J* = 7.6 Hz, 2H, *d*), 6.48 – 6.34 (m, 6H, *b, c, e*), 6.25 (s, 2H, *h*), 6.13 (t, *J* = 5.8 Hz, 2H, *g*), 4.99 (s, 4H, *a*), 4.00 (d, *J* = 5.8 Hz, 4H, *f*), 1.55 (s, 12H, *i*). <sup>13</sup>C NMR (101 MHz, DMSO-*d*<sub>6</sub>) δ 157.48, 149.04, 148.94, 141.73, 129.18, 127.77, 122.86, 121.79, 115.00, 113.06, 112.79, 54.77, 43.39, 30.65. Elem. Anal. Calc. (%) (C<sub>28</sub>H<sub>36</sub>N<sub>6</sub>O<sub>2</sub>) C 68.83, H 7.43, N 17.20; Found (%) C 68.47, H 7.39, N 16.93.

### Compound 3.1c



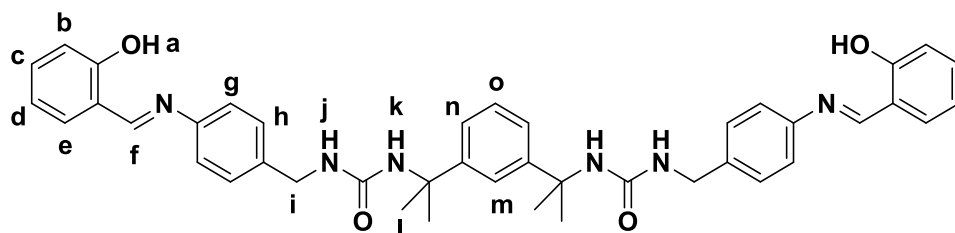
Compound **3.1c** was obtained as a white solid (118 mg, 0.24 mmol, 55%), *m/z* (ESI-MS) 489.7 [M+H]<sup>+</sup>, 511.7 [M+Na]<sup>+</sup>. <sup>1</sup>H NMR (400 MHz, DMSO-*d*<sub>6</sub>) δ 7.34 (t, *J* = 2.0 Hz, 1H, *j*), 7.26 – 7.14 (m, 3H, *k, l*), 6.94 (t, *J* = 7.6 Hz, 2H, *c*), 6.47 – 6.34 (m, 6H, *b, d, e*), 6.25 (s, 2H, *h*), 6.13 (t, *J* = 5.8 Hz, 2H, *g*), 4.99 (s, 4H, *a*), 4.00 (d, *J* = 5.8 Hz, 4H, *f*), 1.55 (s, 12H, *i*). <sup>13</sup>C NMR (101 MHz, DMSO-*d*<sub>6</sub>) δ 157.88, 148.81, 146.76, 129.28, 128.12, 127.74, 123.95, 122.80, 121.68, 116.01, 114.89, 54.80, 40.03, 30.61. Elem. Anal. Calc. (%) (C<sub>28</sub>H<sub>36</sub>N<sub>6</sub>O<sub>2</sub>) C 68.83, H 7.43, N 17.20; Found (%) C 68.55, H 7.33, N 17.06.

### Compound 3.1d



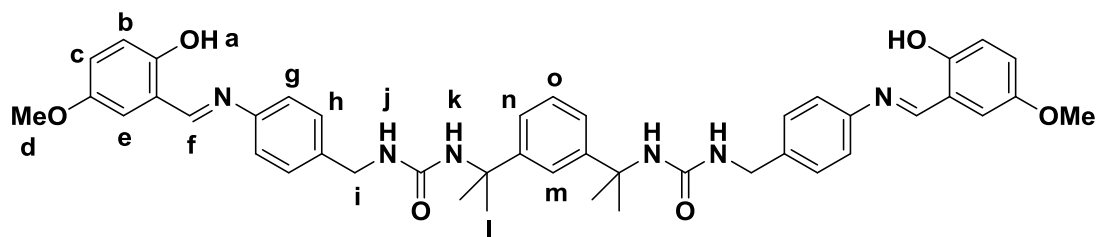
Compound **3.1d** was obtained as a white solid (206 mg, 0.40 mmol, 92%),  $m/z$  (ESI-MS) 539.8  $[M+2Na-H]^+$ .  $^1H$  NMR (400 MHz, DMSO- $d_6$ )  $\delta$  7.33 (t,  $J = 1.9$  Hz, 1H, *i*), 7.19 (dd,  $J = 6.4, 2.4$  Hz, 1H, *k*), 7.13 (dd,  $J = 6.4, 1.8$  Hz, 2H, *j*), 6.83 (d,  $J = 8.3$  Hz, 4H, *c*), 6.49 (d,  $J = 8.3$  Hz, 4H, *b*), 6.22 (s, 2H, *g*), 5.72 (t,  $J = 5.7$  Hz, 2H, *f*), 3.06 (dt,  $J = 5.7, 7.2$  Hz, 4H, *e*), 2.45 (t,  $J = 7.2$  Hz, 4H, *d*), 1.51 (s, 12H, *h*).  $^{13}C$  NMR (101 MHz, DMSO- $d_6$ )  $\delta$  157.50, 148.96, 147.16, 129.44, 127.70, 127.00, 122.76, 121.78, 114.44, 54.68, 41.51, 35.95, 30.69. Elem. Anal. Calc. (%) ( $C_{30}H_{40}N_6O_2$ ) C 69.74, H 7.80, N 16.27; Found (%) C 69.24, H 7.78, N 16.04.

### Compound 3.2a



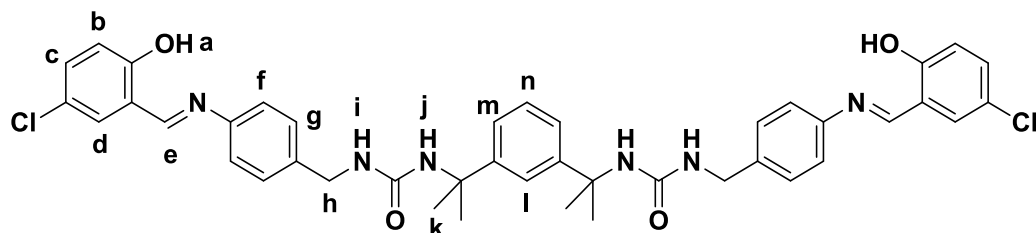
Compound **3.2a** was obtained as a yellow solid (112 mg, 0.16 mmol, 79%),  $m/z$  (ESI-MS) 696.7  $[M+H]^+$ , 718.7  $[M+Na]^+$ .  $^1H$  NMR (400 MHz, DMSO- $d_6$ )  $\delta$  13.18 (s, 2H, *a*), 8.95 (s, 2H, *f*), 7.65 (dd,  $J = 7.7, 1.8$  Hz, 2H, *e*), 7.46 – 7.34 (m, 7H, *c, g, m*), 7.31 (d,  $J = 8.4$  Hz, 4H, *h*), 7.27 – 7.15 (m, 3H, *n, o*), 7.03 – 6.93 (m, 4H, *b, d*), 6.36 (s, 2H, *k*), 6.32 (t,  $J = 5.9$  Hz, 2H, *j*), 4.19 (d,  $J = 5.9$  Hz, 4H, *i*), 1.55 (s, 12H, *l*).  $^{13}C$  NMR (101 MHz, DMSO- $d_6$ )  $\delta$  163.37, 160.74, 157.52, 148.90, 146.89, 140.53, 133.64, 132.96, 128.44, 127.78, 122.84, 121.79, 121.68, 119.77, 119.58, 117.04, 54.84, 42.65, 30.65. Elem. Anal. Calc. (%) ( $C_{42}H_{44}N_6O_4$ ) C 72.39, H 6.36, N 12.06; Found (%) C 71.95, H 6.35, N 12.13.

### Compound 3.2b



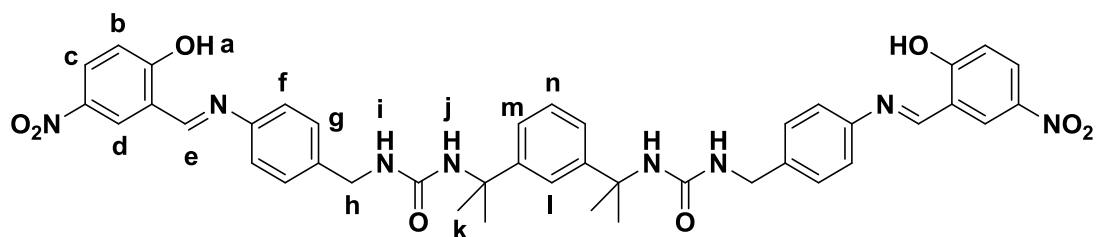
Compound **3.2b** was obtained as pale orange plate-shaped crystals (76 mg, 0.10 mmol, 49%),  $m/z$  (ESI-MS) 757.6  $[M+H]^+$ , 778.6  $[M+Na]^+$ .  $^1H$  NMR (400 MHz, DMSO- $d_6$ )  $\delta$  12.53 (s, 2H, *a*), 8.92 (s, 2H, *f*), 7.40 (t,  $J = 2.0$  Hz, 1H, *m*), 7.35 (d,  $J = 8.5$  Hz, 4H, *g*), 7.31 (d,  $J = 8.5$  Hz, 4H, *h*), 7.25 (d,  $J = 3.1$  Hz, 2H, *e*), 7.23 – 7.16 (m, 3H, *n, o*), 7.04 (dd,  $J = 8.9, 3.1$  Hz, 2H, *c*), 6.91 (d,  $J = 8.9$  Hz, 2H, *b*), 6.36 (s, 2H, *k*), 6.32 (t,  $J = 6.0$  Hz, 2H, *j*), 4.20 (d,  $J = 6.0$  Hz, 4H, *i*), 3.75 (s, 6H, *d*), 1.55 (s, 12H, *l*).  $^{13}C$  NMR (101 MHz, DMSO- $d_6$ )  $\delta$  162.90, 157.52, 154.77, 152.32, 148.90, 147.17, 140.47, 128.45, 127.78, 122.84, 121.78, 121.63, 120.85, 119.64, 117.90, 115.57, 56.02, 54.84, 42.65, 30.65. Elem. Anal. Calc. (%) ( $C_{44}H_{48}N_6O_6$ ) C 69.82, H 6.39, N 11.10; Found (%) C 69.50, H 6.37, N 11.01.

### Compound 3.2c



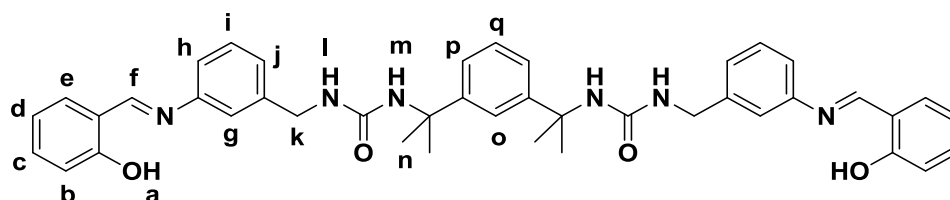
Compound **3.2c** was obtained as a yellow solid (127 mg, 0.17 mmol, 81%),  $m/z$  (ESI-MS) 766.2  $[M+H]^+$ , 786.5  $[M+Na]^+$ .  $^1H$  NMR (400 MHz, DMSO- $d_6$ )  $\delta$  13.12 (s, 2H, *a*), 8.94 (s, 2H, *e*), 7.75 (d,  $J = 2.7$  Hz, 2H, *d*), 7.44 (dd,  $J = 8.8, 2.7$  Hz, 2H, *c*), 7.41 – 7.29 (m, 9H, *f, g, l*), 7.27 – 7.15 (m, 3H, *m, n*), 7.00 (d,  $J = 8.8$  Hz, 2H, *b*), 6.36 (s, 2H, *j*), 6.32 (t,  $J = 6.0$  Hz, 2H, *i*), 4.20 (d,  $J = 6.0$  Hz, 4H, *h*), 1.55 (s, 12H, *k*).  $^{13}C$  NMR (101 MHz, DMSO- $d_6$ )  $\delta$  161.85, 159.39, 157.52, 148.90, 146.68, 140.91, 133.08, 131.44, 128.46, 127.78, 122.98, 122.84, 121.74, 121.67, 121.06, 119.07, 54.84, 42.64, 30.64. Elem. Anal. Calc. (%) ( $C_{42}H_{42}N_6O_4Cl_2$ ) C 65.88, H 5.53, N 10.98; Found (%) C 62.66, H 5.25, N 10.47.

### Compound 3.2d



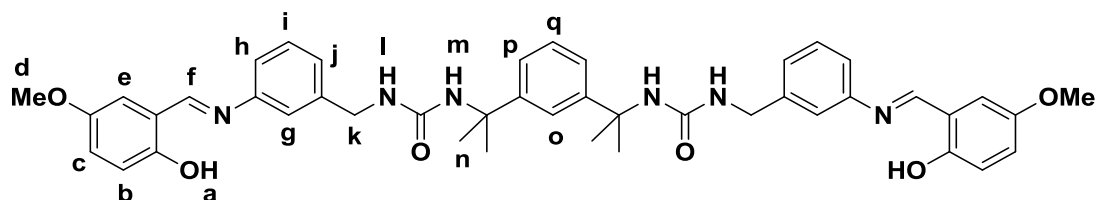
Compound **3.2d** was obtained as an orange solid (115 mg, 0.15 mmol, 71%), *m/z* (ESI-MS) 489.1  $[M+5H-2(CHPh(OH)NO_2)]^+$ , 510.9  $[M+4H+Na-2(CHPh(OH)NO_2)]^+$ , 637.8  $[M+3H-(CHPh(OH)NO_2)]^+$ , 660.0  $[M+2H+Na-(CHPh(OH)NO_2)]^+$ .  $^1H$  NMR (400 MHz, DMSO-*d*<sub>6</sub>)  $\delta$  14.55 (s, 2H, *a*), 9.17 (s, 2H, *e*), 8.66 (d, *J* = 2.9 Hz, 2H, *d*), 8.25 (dd, *J* = 9.2, 2.9 Hz, 2H, *c*), 7.44 (d, *J* = 8.4 Hz, 4H, *f*), 7.41 (t, *J* = 2.1 Hz, 1H, *l*), 7.34 (d, *J* = 8.4 Hz, 4H, *g*), 7.25 – 7.15 (m, 3H, *m*, *n*), 7.10 (d, *J* = 9.2 Hz, 2H, *b*), 6.37 (s, 2H, *j*), 6.34 (t, *J* = 6.0 Hz, 2H, *i*), 4.21 (d, *J* = 6.0 Hz, 4H, *h*), 1.56 (s, 12H, *k*).  $^{13}C$  NMR (101 MHz, DMSO-*d*<sub>6</sub>)  $\delta$  167.70, 161.43, 157.55, 148.90, 144.91, 141.50, 139.40, 128.99, 128.79, 128.51, 127.79, 122.85, 121.79, 121.71, 118.88, 118.84, 54.85, 42.63, 30.64. Elem. Anal. Calc. (%) (C<sub>42</sub>H<sub>42</sub>N<sub>8</sub>O<sub>8</sub>) C 64.11, H 5.38, N 14.24; Found (%) C 63.80, H 5.37, N 14.25.

### Compound 3.3a



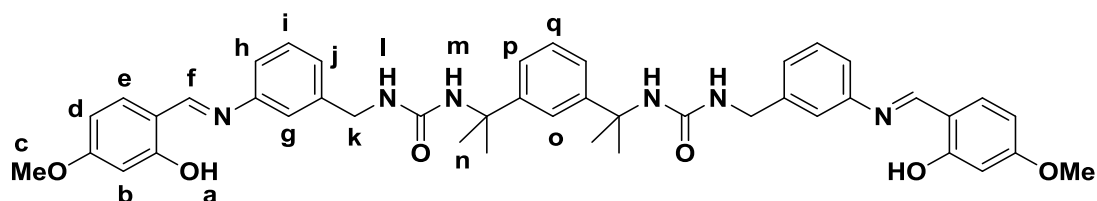
Compound **3.3a** was obtained as a yellow solid (122 mg, 0.18 mmol, 86%), *m/z* (ESI-MS) 698.0  $[M+H]^+$ , 719.2  $[M+Na]^+$ .  $^1H$  NMR (400 MHz, DMSO-*d*<sub>6</sub>)  $\delta$  13.10 (s, 2H, *a*), 8.94 (s, 2H, *f*), 7.66 (dd, *J* = 8.0, 1.6 Hz, 2H, *e*), 7.47 – 7.33 (m, 5H, *c*, *i*, *o*), 7.32 – 7.22 (m, 4H, *g*, *h*), 7.22 – 7.12 (m, 5H, *j*, *p*, *q*), 7.04 – 6.95 (m, 4H, *b*, *d*), 6.36 (s, 2H, *m*), 6.34 (t, *J* = 6.0 Hz, 2H, *l*), 4.21 (d, *J* = 6.0 Hz, 4H, *k*), 1.52 (s, 12H, *n*).  $^{13}C$  NMR (101 MHz, DMSO-*d*<sub>6</sub>)  $\delta$  163.74, 160.75, 157.50, 148.86, 148.53, 143.13, 133.75, 132.95, 129.79, 127.69, 125.96, 122.76, 121.74, 120.67, 119.90, 119.75, 119.62, 119.52, 117.07, 54.81, 42.83, 30.64. Elem. Anal. Calc. (%) (C<sub>42</sub>H<sub>44</sub>N<sub>6</sub>O<sub>4</sub>) C 72.39, H 6.36, N 12.06; Found (%) C 72.07, H 6.34, N 11.85.

### Compound 3.3b



Compound **3.3b** was obtained as orange-yellow plate-shaped crystals (113 mg, 0.15 mmol, 73%),  $m/z$  (ESI-MS) 758.0  $[M+H]^+$ , 779.9  $[M+Na]^+$ .  $^1H$  NMR (400 MHz, DMSO- $d_6$ )  $\delta$  12.43 (s, 2H, *a*), 8.91 (s, 2H, *f*), 7.44 – 7.34 (m, 3H, *i*, *o*), 7.29 – 7.20 (m, 6H, *e*, *g*, *h*), 7.20 – 7.12 (m, 5H, *j*, *p*, *q*), 7.05 (dd,  $J = 8.9, 3.1$  Hz, 2H, *c*), 6.92 (d,  $J = 8.9$  Hz, 2H, *b*), 6.36 (s, 2H, *m*), 6.33 (t,  $J = 6.0$  Hz, 2H, *l*), 4.21 (d,  $J = 6.0$  Hz, 4H, *k*), 3.75 (s, 6H, *d*), 1.52 (s, 12H, *n*).  $^{13}C$  NMR (101 MHz, DMSO- $d_6$ )  $\delta$  163.24, 157.49, 154.77, 152.33, 148.86, 148.83, 143.11, 129.79, 127.68, 125.90, 122.76, 121.73, 120.98, 120.63, 119.64, 119.48, 117.93, 115.48, 56.00, 54.80, 42.84, 30.63. Elem. Anal. Calc. (%) (C<sub>44</sub>H<sub>48</sub>N<sub>6</sub>O<sub>6</sub>) C 69.82, H 6.39, N 11.10; Found (%) C 69.77, H 6.42, N 11.08.

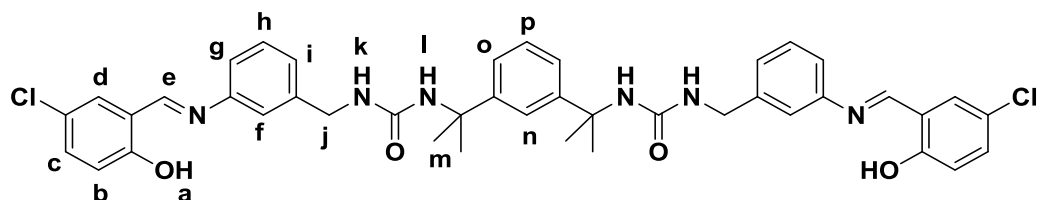
### Compound 3.3c



Compound **3.3c** was obtained as bright yellow plate-shaped crystals (118 mg, 0.16 mmol, 76%),  $m/z$  (ESI-MS) 779.8  $[M+Na]^+$ .  $^1H$  NMR (400 MHz, DMSO- $d_6$ )  $\delta$  13.71 (s, 2H, *a*), 8.85 (s, 2H, *f*), 7.53 (d,  $J = 8.7$  Hz, 2H, *e*), 7.42 – 7.33 (m, 3H, *i*, *o*), 7.28 – 7.20 (m, 4H, *g*, *h*), 7.20 – 7.11 (m, 5H, *j*, *p*, *q*), 6.57 (dd,  $J = 8.6, 2.5$  Hz, 2H, *d*), 6.51 (d,  $J = 2.5$  Hz, 2H, *b*), 6.36 (s, 2H, *m*), 6.33 (t,  $J = 6.0$  Hz, 2H, *l*), 4.20 (d,  $J = 6.0$  Hz, 4H, *k*), 3.81 (s, 6H, *c*), 1.52 (s, 12H, *n*).  $^{13}C$  NMR (101 MHz, DMSO- $d_6$ )  $\delta$  163.25, 157.51, 154.80, 152.35, 148.87, 148.84, 143.12, 129.79, 127.70, 125.91, 122.77, 121.75, 120.98, 120.64, 119.65, 119.50, 117.94, 115.50, 56.01, 54.82, 42.86, 30.64. Elem. Anal. Calc. (%) (C<sub>44</sub>H<sub>48</sub>N<sub>6</sub>O<sub>6</sub>) C 69.82, H 6.39, N 11.10; Found (%) C 69.69, H 6.42, N 11.18.

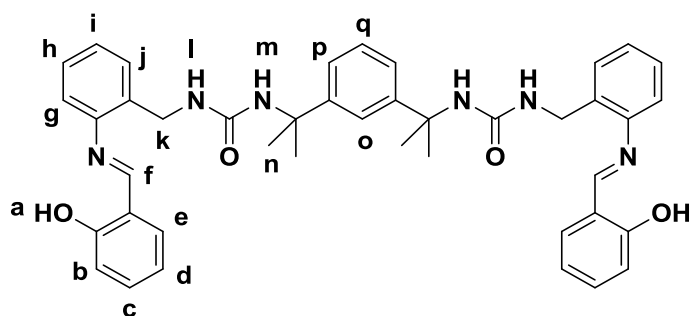


### Compound 3.3d



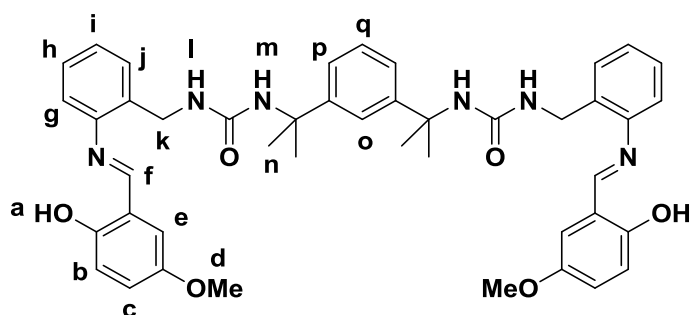
Compound **3.3d** was obtained as an orange-yellow solid (137 mg, 0.18 mmol, 88%),  $m/z$  (ESI-MS) 649.9  $[M-CH_2Ph(OH)Cl+3H+Na]^+$ , 780.3  $[M+Na]^+$ .  $^1H$  NMR (400 MHz, DMSO- $d_6$ )  $\delta$  13.03 (s, 2H, *a*), 8.92 (s, 2H, *e*), 7.75 (d,  $J = 2.7$  Hz, 2H, *d*), 7.49 – 7.33 (m, 5H, *c, h, n*), 7.30 – 7.12 (m, 9H, *f, g, i, o, p*), 7.01 (d,  $J = 8.9$  Hz, 2H, *b*), 6.36 (s, 2H, *l*), 6.33 (d,  $J = 6.1$  Hz, 2H, *k*), 4.21 (d,  $J = 5.9$  Hz, 4H, *j*), 1.52 (s, 12H, *m*).  $^{13}C$  NMR (101 MHz, DMSO- $d_6$ )  $\delta$  162.18, 159.38, 157.49, 148.86, 148.38, 143.19, 133.20, 131.37, 129.82, 127.68, 126.24, 123.03, 122.75, 121.75, 121.08, 120.79, 119.50, 119.09, 54.80, 42.82, 30.64. Elem. Anal. Calc. (%) ( $C_{42}H_{42}N_6O_4Cl_2$ ) C 65.88, H 5.53, N 10.98; Found (%) C 65.68, H 5.55, N 10.90.

### Compound 3.4a



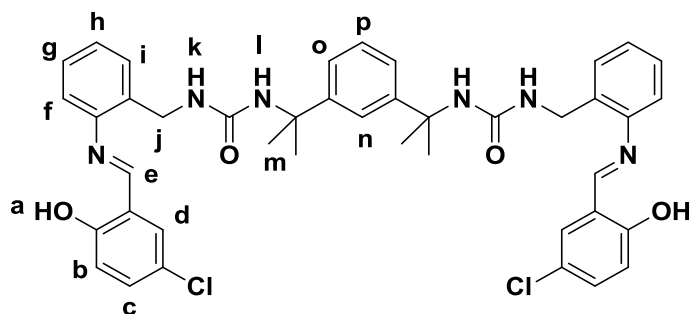
Compound **3.4a** was obtained as a pale yellow solid (116 mg, 0.17 mmol, 82%),  $m/z$  (ESI-MS) 719.9  $[M+Na]^+$ .  $^1H$  NMR (400 MHz, DMSO- $d_6$ )  $\delta$  12.93 (s, 2H, *a*), 8.88 (s, 2H, *f*), 7.69 (dd,  $J = 7.6, 1.8$  Hz, 2H, *e*), 7.44 (ddd,  $J = 8.2, 7.4, 1.7$  Hz, 2H, *g*), 7.39 – 7.23 (m, 9H, *c, h, i, j, o*), 7.19 – 7.12 (m, 3H, *p, q*), 7.04 – 6.95 (m, 4H, *b, d*), 6.40 (s, 2H, *m*), 6.23 (t,  $J = 5.9$  Hz, 2H, *l*), 4.29 (d,  $J = 5.9$  Hz, 4H, *k*), 1.52 (s, 12H, *n*).  $^{13}C$  NMR (101 MHz, DMSO- $d_6$ )  $\delta$  163.85, 160.69, 157.46, 148.85, 146.78, 134.74, 133.80, 133.01, 128.28, 128.00, 127.72, 127.17, 122.84, 121.74, 119.99, 119.60, 118.63, 117.04, 54.80, 30.58. Elem. Anal. Calc. (%) ( $C_{42}H_{44}N_6O_4$ ) C 72.39, H 6.36, N 12.06; Found (%) C 71.88, H 6.44, N 11.92.

### Compound 3.4b



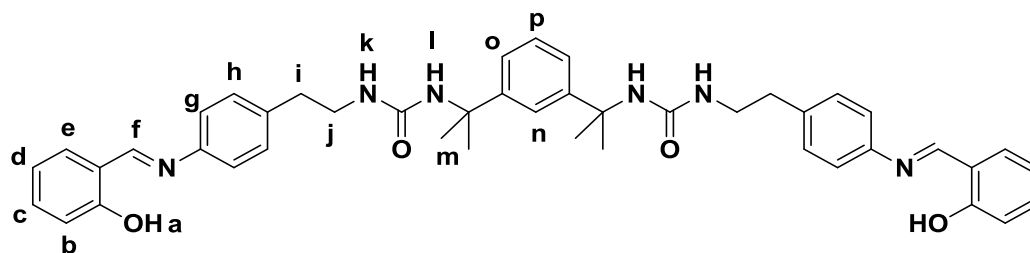
Compound **3.4b** was obtained as orange plate-shaped crystals (109 mg, 0.14 mmol, 70%),  $m/z$  (ESI-MS) 779.8  $[M+Na]^+$ .  $^1H$  NMR (400 MHz, DMSO- $d_6$ )  $\delta$  12.29 (s, 2H, *a*), 8.84 (s, 2H, *f*), 7.41 – 7.32 (m, 5H, *g, i, o*), 7.32 – 7.23 (m, 6H, *e, h, j*), 7.20 – 7.13 (m, 3H, *p, q*), 7.06 (dd,  $J = 8.9, 3.1$  Hz, 2H, *c*), 6.92 (d,  $J = 8.9$  Hz, 2H, *b*), 6.40 (s, 2H, *m*), 6.23 (t,  $J = 5.9$  Hz, 2H, *l*), 4.28 (d,  $J = 5.9$  Hz, 4H, *k*), 3.76 (s, 6H, *d*), 1.52 (s, 12H, *n*).  $^{13}C$  NMR (101 MHz, DMSO- $d_6$ )  $\delta$  163.32, 157.47, 154.75, 152.37, 148.86, 147.02, 134.77, 128.28, 127.98, 127.73, 127.12, 122.84, 121.75, 121.00, 119.89, 118.51, 117.91, 115.70, 56.07, 54.80, 30.59. Elem. Anal. Calc. (%) ( $C_{44}H_{48}N_6O_6$ ) C 69.82, H 6.39, N 11.10; Found (%) C 69.43, H 6.41, N 10.79.

### Compound 3.4c



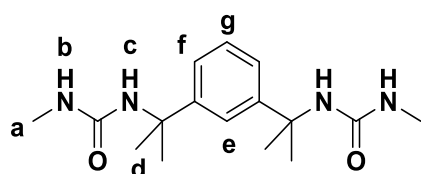
Compound **3.4c** was obtained as yellow plate-shaped crystals (113 mg, 0.15 mmol, 72%),  $m/z$  (ESI-MS) 764.4  $[M-H]^-$ , 765.6  $[M+H]^+$ , 787.8  $[M+Na]^+$ .  $^1H$  NMR (400 MHz, DMSO- $d_6$ )  $\delta$  12.83 (s, 2H, *a*), 8.85 (s, 2H, *e*), 7.80 (d,  $J = 2.7$  Hz, 2H, *d*), 7.46 (dd,  $J = 8.8, 2.7$  Hz, 2H, *c*), 7.40 – 7.24 (m, 9H, *f, g, h, i, n*), 7.19 – 7.09 (m, 3H, *o, p*), 7.06 – 6.97 (m, 2H, *b*), 6.38 (s, 2H, *l*), 6.23 (t,  $J = 5.9$  Hz, 2H, *k*), 4.28 (d,  $J = 5.9$  Hz, 4H, *j*), 1.51 (s, 12H, *m*).  $^{13}C$  NMR (101 MHz, DMSO- $d_6$ )  $\delta$  162.18, 159.29, 157.44, 148.85, 146.71, 134.88, 133.24, 131.38, 130.69, 128.33, 128.12, 127.73, 127.44, 123.07, 122.84, 121.75, 121.36, 119.08, 118.61, 54.80, 30.58. Elem. Anal. Calc. (%) ( $C_{42}H_{42}N_6O_4Cl_2$ ) C 65.88, H 5.53, N 10.98; Found (%) C 65.68, H 5.56, N 11.05.

### Compound 3.5



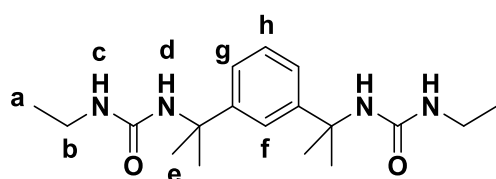
Compound **3.5** was obtained as a yellow solid (116 mg, 0.16 mmol, 78%),  $m/z$  (ESI-MS) 748.2  $[M+Na]^+$ .  $^1H$  NMR (400 MHz, DMSO- $d_6$ )  $\delta$  13.22 (s, 2H, *a*), 8.97 (s, 2H, *f*), 7.65 (dd,  $J = 7.7, 1.8$  Hz, 2H, *e*), 7.46 – 7.33 (m, 7H, *c, g, n*), 7.32 – 7.25 (d,  $J = 8.4$  Hz, 4H, *h*), 7.23 – 7.10 (m, 3H, *o, p*), 7.04 – 6.93 (m, 4H, *b, d*), 6.25 (s, 2H, *l*), 5.82 (t,  $J = 5.8$  Hz, 2H, *k*), 3.20 (dt,  $J = 7.1, 5.8$  Hz, 4H, *j*), 2.69 (t,  $J = 7.1$  Hz, 4H, *i*), 1.53 (s, 12H, *m*).  $^{13}C$  NMR (101 MHz, DMSO- $d_6$ )  $\delta$  163.23, 160.75, 157.50, 148.94, 146.41, 139.32, 133.59, 132.98, 130.18, 127.73, 122.79, 121.81, 121.76, 119.79, 119.56, 117.03, 54.72, 41.00, 36.26, 30.66. Elem. Anal. Calc. (%) (C<sub>44</sub>H<sub>48</sub>N<sub>6</sub>O<sub>4</sub>) C 72.90, H 6.67, N 11.59; Found (%) C 72.74, H 6.71, N 11.50.

### Compound 4.1a



Compound **4.1a** was obtained as a white solid (125 mg, 0.41 mmol, 94%),  $m/z$  (ESI-MS) 329.6  $[M+Na]^+$ , 341.8  $[M+Cl]^-$ .  $^1H$  NMR (400 MHz, DMSO- $d_6$ )  $\delta$  7.34 (t,  $J = 1.9$  Hz, 1H, *e*), 7.23 – 7.08 (m, 3H, *f, g*), 6.17 (s, 2H, *c*), 5.65 (q,  $J = 4.6$  Hz, 2H, *b*), 2.49 (d,  $J = 4.6$  Hz, 6H, *a*), 1.52 (s, 12H, *d*).  $^{13}C$  NMR (101 MHz, DMSO- $d_6$ )  $\delta$  158.20, 148.92, 127.70, 122.82, 121.84, 54.68, 30.59, 26.49. Elem. Anal. Calc. (%) (C<sub>16</sub>H<sub>26</sub>N<sub>4</sub>O<sub>2</sub>) C 62.72, H 8.55, N 18.29; Found (%) C 62.56, H 8.52, N 18.11.

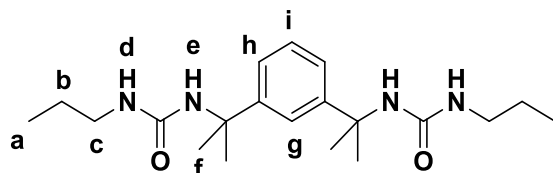
### Compound 4.1b



Compound **4.1b** was obtained as a white solid (129 mg, 0.38 mmol, 89%),  $m/z$  (ESI-MS) 357.6  $[M+Na]^+$ .  $^1H$  NMR (400 MHz, DMSO- $d_6$ )  $\delta$  7.34 (t,  $J = 1.8$  Hz, 1H, *f*),

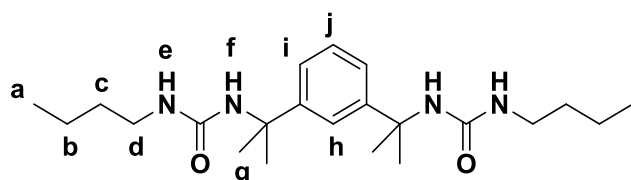
7.23 – 7.10 (m, 3H, *g, h*), 6.12 (s, 2H, *d*), 5.73 (t, *J* = 5.6 Hz, 2H, *c*), 2.94 (dq, *J* = 7.2, 5.6 Hz, 4H, *b*), 1.52 (s, 12H, *e*), 0.96 (t, *J* = 7.2 Hz, 6H, *a*). <sup>13</sup>C NMR (101 MHz, DMSO-*d*<sub>6</sub>) δ 157.52, 148.95, 127.70, 122.76, 121.79, 54.67, 34.16, 30.64, 16.23. Elem. Anal. Calc. (%) (C<sub>18</sub>H<sub>30</sub>N<sub>4</sub>O<sub>2</sub>) C 64.64, H 9.04, N 16.75; Found (%) C 64.37, H 8.92, N 16.63.

#### Compound 4.1c



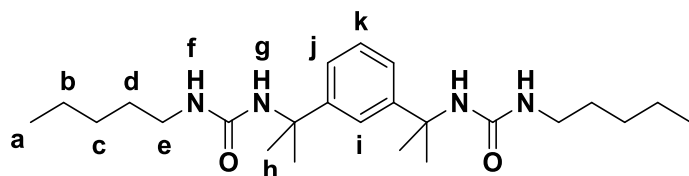
Compound **4.1c** was obtained as a white solid (120 mg, 0.33 mmol, 76%), *m/z* (ESI-MS) 461.7 [M+H]<sup>+</sup>, 483.7 [M+Na]<sup>+</sup>. <sup>1</sup>H NMR (400 MHz, DMSO-*d*<sub>6</sub>) δ 7.34 (t, *J* = 1.8 Hz, 1H, *g*), 7.23 – 7.11 (m, 3H, *h, i*), 6.14 (s, 2H, *e*), 5.79 (t, *J* = 5.8 Hz, 2H, *d*), 2.89 (dt, *J* = 7.0, 5.8 Hz, 4H, *c*), 1.52 (s, 12H, *f*), 1.34 (tq, *J* = 7.4, 7.0 Hz, 4H, *b*), 0.82 (d, *J* = 7.4 Hz, 6H, *a*). <sup>13</sup>C NMR (101 MHz, DMSO-*d*<sub>6</sub>) δ 157.61, 148.97, 127.69, 122.75, 121.77, 54.65, 41.15, 30.63, 23.76, 11.81. Elem. Anal. Calc. (%) (C<sub>20</sub>H<sub>34</sub>N<sub>4</sub>O<sub>2</sub>) C 66.26, H 9.45, N 15.46; Found (%) C 66.40, H 9.43, N 15.46.

#### Compound 4.1d



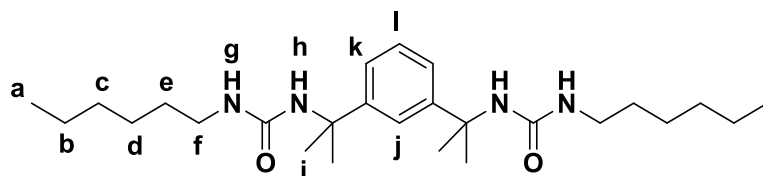
Compound **4.1d** was obtained as a white solid (152 mg, 0.39 mmol, 90%), *m/z* (ESI-MS) 413.8 [M+Na]<sup>+</sup>. <sup>1</sup>H NMR (400 MHz, DMSO-*d*<sub>6</sub>) δ 7.33 (t, *J* = 1.8 Hz, 1H, *h*), 7.20 – 7.08 (m, 3H, *i, j*), 6.12 (s, 2H, *f*), 5.75 (t, *J* = 5.7 Hz, 2H, *e*), 2.92 (dt, *J* = 6.3, 5.7 Hz, 4H, *d*), 1.51 (s, 12H, *g*), 1.38 – 1.18 (m, 8H, *b, c*), 0.95 – 0.73 (m, 6H, *a*). <sup>13</sup>C NMR (101 MHz, DMSO-*d*<sub>6</sub>) δ 157.59, 148.97, 127.68, 122.75, 121.75, 54.65, 38.96, 32.71, 30.63, 19.99, 14.17. Elem. Anal. Calc. (%) (C<sub>22</sub>H<sub>38</sub>N<sub>4</sub>O<sub>2</sub>) C 67.66, H 9.81, N 14.35; Found (%) C 67.40, H 9.72, N 14.27.

### Compound 4.1e



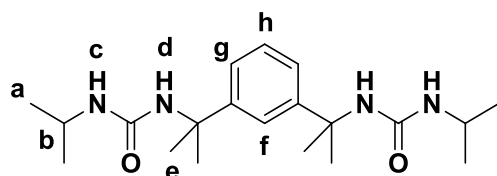
Compound **4.1e** was obtained as a white solid (140 mg, 0.33 mmol, 77%),  $m/z$  (ESI-MS) 419.6  $[M+H]^+$ , 441.8  $[M+Na]^+$ .  $^1H$  NMR (400 MHz, DMSO- $d_6$ )  $\delta$  7.34 (t,  $J$  = 2.0 Hz, 1H, *i*), 7.22 – 7.10 (m, 3H, *j*, *k*), 6.12 (s, 2H, *g*), 5.76 (t,  $J$  = 5.7 Hz, 2H, *f*), 2.91 (dt,  $J$  = 6.6, 5.7 Hz, 4H, *e*), 1.51 (s, 12H, *h*), 1.39 – 1.13 (m, 12H, *b*, *c*, *d*), 0.88 (s, 6H, *a*).  $^{13}C$  NMR (101 MHz, DMSO- $d_6$ )  $\delta$  157.60, 148.97, 127.67, 122.76, 121.78, 54.67, 39.28, 30.65, 30.25, 29.10, 22.36, 14.43. Elem. Anal. Calc. (%) ( $C_{24}H_{42}N_4O_2$ ) C 68.86, H 10.11, N 13.38; Found (%) C 68.69, H 10.11, N 13.33.

### Compound 4.1f



Compound **4.1f** was obtained as a white solid (171 mg, 0.38 mmol, 88%),  $m/z$  (ESI-MS) 469.8  $[M+Na]^+$ .  $^1H$  NMR (400 MHz, DMSO- $d_6$ )  $\delta$  7.33 (t,  $J$  = 2.0 Hz, 1H, *j*), 7.22 – 7.10 (m, 3H, *k*, *l*), 6.13 (s, 2H, *h*), 5.76 (t,  $J$  = 5.7 Hz, 2H, *g*), 2.91 (dt,  $J$  = 6.4, 5.7 Hz, 4H, *f*), 1.51 (s, 12H, *i*), 1.38 – 1.15 (m, 16H, *b*, *c*, *d*, *e*), 0.85 (s, 6H, *a*).  $^{13}C$  NMR (101 MHz, DMSO- $d_6$ )  $\delta$  157.58, 148.96, 127.65, 122.75, 121.77, 54.66, 39.31, 31.52, 30.65, 30.54, 26.53, 22.57, 14.39. Elem. Anal. Calc. (%) ( $C_{26}H_{46}N_4O_2$ ) C 69.91, H 10.38, N 12.54; Found (%) C 69.70, H 10.22, N 12.42.

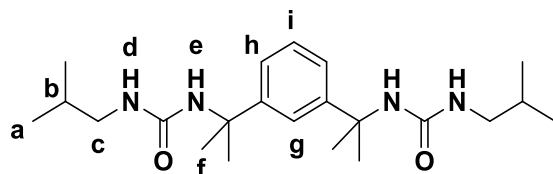
### Compound 4.2a



Compound **4.2a** was obtained as a white solid (128 mg, 0.35 mmol, 81%),  $m/z$  (ESI-MS) 362.0  $[M-H]^-$ , 385.7  $[M+Na]^+$ , 397.8  $[M+Cl]^-$ .  $^1H$  NMR (400 MHz, DMSO- $d_6$ )  $\delta$  7.34 (t,  $J$  = 1.8 Hz, 1H, *f*), 7.23 – 7.10 (m, 3H, *g*, *h*), 6.05 (s, 2H, *d*), 5.64 (d,  $J$  = 7.7 Hz, 2H, *c*), 3.58 (dspt,  $J$  = 7.7, 6.6 Hz, 2H, *b*), 1.51 (s, 12H, *e*), 1.00 (d,  $J$  = 6.6 Hz,

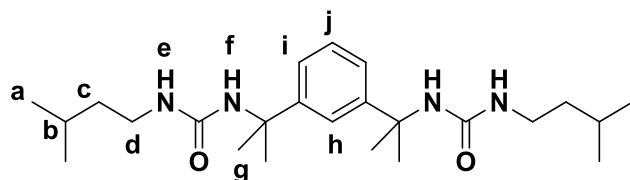
12H, *a*).  $^{13}\text{C}$  NMR (101 MHz,  $\text{DMSO-}d_6$ )  $\delta$  157.03, 148.99, 127.70, 122.73, 121.77, 79.65, 54.68, 40.95, 30.69, 23.77. Elem. Anal. Calc. (%) ( $\text{C}_{20}\text{H}_{34}\text{N}_4\text{O}_2$ ) C 66.26, H 9.45, N 15.46; Found (%) C 66.22, H 9.46, N 15.42.

#### Compound 4.2b



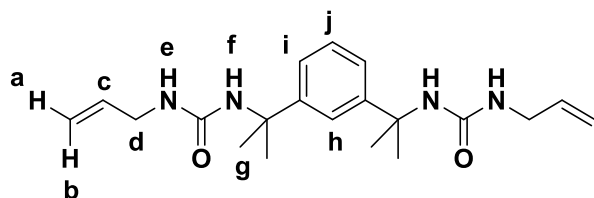
Compound **4.2b** was obtained as a white solid (134 mg, 0.34 mmol, 79%),  $m/z$  (ESI-MS) 389.9  $[\text{M-H}]^-$ , 413.7  $[\text{M+Na}]^+$ , 425.7  $[\text{M+Cl}]^-$ .  $^1\text{H}$  NMR (400 MHz,  $\text{DMSO-}d_6$ )  $\delta$  7.34 (t,  $J = 1.9$  Hz, 1H, *g*), 7.23 – 7.10 (m, 3H, *h, i*), 6.15 (s, 2H, *e*), 5.83 (t,  $J = 5.9$  Hz, 2H, *d*), 2.76 (dd,  $J = 6.2, 5.9$  Hz, 4H, *c*), 1.64 – 1.53 (m, 2H, *b*), 1.52 (s, 12H, *f*), 0.82 (d,  $J = 6.7$  Hz, 12H, *a*).  $^{13}\text{C}$  NMR (101 MHz,  $\text{DMSO-}d_6$ )  $\delta$  157.62, 148.99, 127.69, 122.76, 121.76, 54.64, 46.91, 30.64, 29.17, 20.50. Elem. Anal. Calc. (%) ( $\text{C}_{22}\text{H}_{38}\text{N}_4\text{O}_2$ ) C 67.66, H 9.81, N 14.35; Found (%) C 67.52, H 9.75, N 14.29.

#### Compound 4.2c



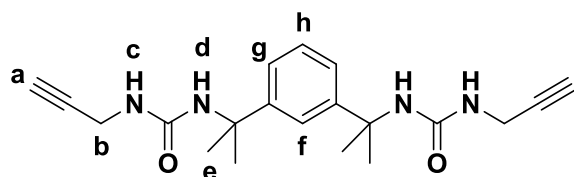
Compound **4.2c** was obtained as a white solid (117 mg, 0.28 mmol, 64%),  $m/z$  (ESI-MS) 417.9  $[\text{M-H}]^-$ , 441.9  $[\text{M+Na}]^+$ , 454.0  $[\text{M+Cl}]^-$ .  $^1\text{H}$  NMR (400 MHz,  $\text{DMSO-}d_6$ )  $\delta$  7.33 (t,  $J = 1.8$  Hz, 1H, *h*), 7.20 – 7.11 (m, 3H, *i, j*), 6.11 (s, 2H, *f*), 5.73 (t,  $J = 5.7$  Hz, 2H, *e*), 2.94 (dt,  $J = 7.7, 5.7$  Hz, 4H, *d*), 1.64 – 1.54 (m, 2H, *b*), 1.51 (s, 12H, *g*), 1.23 (dt,  $J = 7.7, 7.0$  Hz, 4H, *c*), 0.85 (d,  $J = 6.6$  Hz, 12H, *a*).  $^{13}\text{C}$  NMR (101 MHz,  $\text{DMSO-}d_6$ )  $\delta$  157.58, 148.98, 127.69, 122.76, 121.76, 54.68, 39.63, 37.53, 30.65, 25.58, 22.89. Elem. Anal. Calc. (%) ( $\text{C}_{24}\text{H}_{42}\text{N}_4\text{O}_2$ ) C 68.86, H 10.11, N 13.38; Found (%) C 68.64, H 10.09, N 13.32.

### Compound 4.3



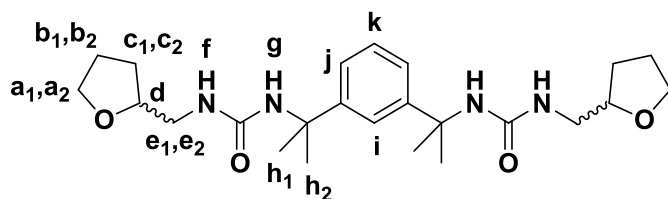
Compound **4.3** was obtained as a white solid (149 mg, 0.42 mmol, 96%),  $m/z$  (ESI-MS) 357.8  $[M-H]^-$ , 381.7  $[M+Na]^+$ .  $^1H$  NMR (400 MHz,  $DMSO-d_6$ )  $\delta$  7.35 (t,  $J = 1.9$  Hz, 1H, *h*), 7.22 – 7.12 (m, 3H, *i, j*), 6.26 (s, 2H, *f*), 5.90 (t,  $J = 5.9$  Hz, 2H, *e*), 5.80 (ddt,  $J = 17.2, 10.2, 5.0$  Hz, 2H, *c*), 5.12 (dq,  $J = 17.2, 1.8$  Hz, 2H, *b*), 5.01 (dq,  $J = 10.2, 1.8$  Hz, 2H, *a*), 3.58 (ddt,  $J = 5.9, 5.0, 1.8$  Hz, 4H, *d*), 1.53 (s, 12H, *g*).  $^{13}C$  NMR (101 MHz,  $DMSO-d_6$ )  $\delta$  157.31, 148.88, 137.39, 127.74, 122.81, 121.78, 114.59, 54.74, 41.77, 30.59. Elem. Anal. Calc. (%) ( $C_{20}H_{30}N_4O_2$ ) C 67.01, H 8.44, N 15.63; Found (%) C 66.71, H 8.38, N 15.53.

### Compound 4.4



Compound **4.4** was obtained as a white solid (148 mg, 0.42 mmol, 96%),  $m/z$  (ESI-MS) 353.6  $[M-H]^-$ , 377.6  $[M+Na]^+$ , 389.9  $[M+Cl]^-$ .  $^1H$  NMR (400 MHz,  $DMSO-d_6$ )  $\delta$  7.34 (t,  $J = 1.7$  Hz, 1H, *f*), 7.26 – 7.10 (m, 3H, *g, h*), 6.32 (s, 2H, *d*), 6.09 (t,  $J = 5.7$  Hz, 2H, *c*), 3.74 (dd,  $J = 5.7, 2.5$  Hz, 4H, *b*), 3.04 (t,  $J = 2.5$  Hz, 2H, *a*), 1.53 (s, 12H, *e*).  $^{13}C$  NMR (101 MHz,  $DMSO-d_6$ )  $\delta$  156.90, 148.67, 127.80, 122.87, 121.79, 83.01, 72.96, 54.92, 30.51, 28.93. Elem. Anal. Calc. (%) ( $C_{20}H_{26}N_4O_2$ ) C 67.77, H 7.39, N 15.81; Found (%) C 67.25, H 7.35, N 15.73.

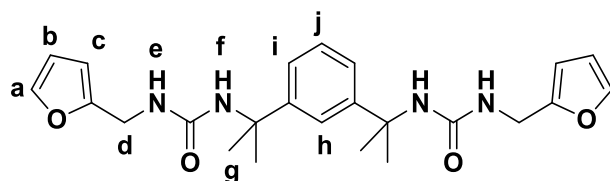
### Compound 4.5



Compound **4.5** was synthesised from racemic tetrahydrofurfurylamine as a mixture of diastereomers. The product was obtained as a white solid (120 mg, 0.27 mmol, 62%),  $m/z$  (ESI-MS) 447.8  $[M+H]^+$ , 470.0  $[M+Na]^+$ .  $^1H$  NMR (400 MHz,

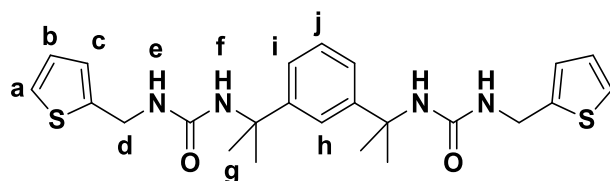
DMSO-*d*<sub>6</sub>)  $\delta$  7.33 (t,  $J$  = 1.9 Hz, 1H, *i*), 7.22 – 7.10 (m, 3H, *j*, *k*), 6.32 (s, 2H, *g*), 5.89 (t,  $J$  = 5.9 Hz, 2H, *f*), 3.81 – 3.69 (m, 4H, *a*<sub>1</sub>, *d*), 3.61 (dt,  $J$  = 6.9, 6.4 Hz, 2H, *a*<sub>2</sub>), 3.12 – 3.01 (m, 2H, *e*<sub>2</sub>), 3.00-2.90 (m, 2H, *e*<sub>1</sub>), 1.81 (m, 6H, *b*<sub>1</sub>, *b*<sub>2</sub>, *c*<sub>2</sub>), 1.52 (s, 6H, *h*<sub>2</sub>), 1.51 (s, 6H, *h*<sub>1</sub>), 1.50 – 1.41 (m, 2H, *c*<sub>1</sub>). <sup>13</sup>C NMR (101 MHz, DMSO-*d*<sub>6</sub>)  $\delta$  157.57, 148.92, 127.67, 122.73, 121.75, 78.50, 67.60, 54.68, 43.38, 30.75, 30.72, 30.54, 30.51, 28.55, 25.83. Elem. Anal. Calc. (%) (C<sub>24</sub>H<sub>38</sub>N<sub>4</sub>O<sub>4</sub>) C 64.55, H 8.58, N 12.55; Found (%) C 64.17, H 8.46, N 12.23.

#### Compound 4.6a



Compound **4.6a** was obtained as a white solid (195 mg, 0.36 mmol, 83%), *m/z* (ESI-MS) 461.7 [M+Na]<sup>+</sup>. <sup>1</sup>H NMR (400 MHz, DMSO-*d*<sub>6</sub>)  $\delta$  7.56 (dd,  $J$  = 1.8, 0.9 Hz, 2H, *a*), 7.35 (t,  $J$  = 1.9 Hz, 1H, *h*), 7.21 – 7.06 (m, 3H, *i*, *j*), 6.38 (dd,  $J$  = 3.1, 1.8 Hz, 2H, *b*), 6.30 (s, 2H, *f*), 6.19 (t,  $J$  = 5.8 Hz, 2H, *e*), 6.17 (dd,  $J$  = 3.1, 0.9 Hz, 2H, *c*), 4.13 (d,  $J$  = 5.8 Hz, 4H, *d*), 1.53 (s, 12H, *g*). <sup>13</sup>C NMR (101 MHz, DMSO-*d*<sub>6</sub>)  $\delta$  157.14, 154.21, 148.76, 142.27, 127.75, 122.83, 121.77, 110.83, 106.46, 54.82, 36.52, 30.53. Elem. Anal. Calc. (%) (C<sub>24</sub>H<sub>30</sub>N<sub>4</sub>O<sub>4</sub>) C 65.73, H 6.90, N 12.78; Found (%) C 65.69, H 6.92, N 12.81.

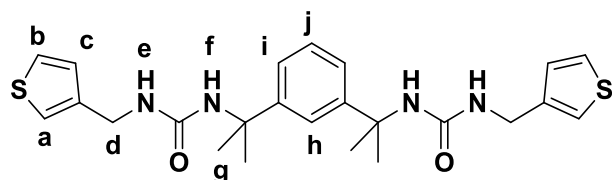
#### Compound 4.6b



Compound **4.6b** was obtained as a white solid (184 mg, 0.39 mmol, 90%), *m/z* (ESI-MS) 493.8 [M+Na]<sup>+</sup>. <sup>1</sup>H NMR (400 MHz, DMSO-*d*<sub>6</sub>)  $\delta$  7.39 – 7.33 (m, 3H, *a*, *h*), 7.23 – 7.12 (m, 3H, *i*, *j*), 6.98 – 6.88 (m, 4H, *b*, *c*), 6.32 (t,  $J$  = 6.0 Hz, 2H, *e*), 6.31 (s, 2H, *f*), 4.32 (d,  $J$  = 6.0 Hz, 4H, *d*), 1.54 (s, 12H, *g*). <sup>13</sup>C NMR (101 MHz, DMSO-*d*<sub>6</sub>)  $\delta$  157.15, 148.76, 144.95, 127.73, 127.06, 125.03, 124.93, 122.85, 121.77, 54.86, 38.26, 30.60. Elem. Anal. Calc. (%) (C<sub>24</sub>H<sub>30</sub>N<sub>4</sub>O<sub>2</sub>S<sub>2</sub>) C 61.25, H 6.42, N 11.90; Found (%) C 61.27, H 6.40, N 11.90.

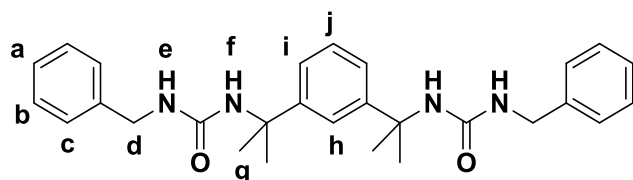


### Compound 4.7



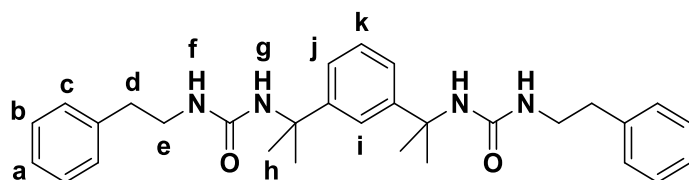
Compound **4.8** was obtained as a white solid (164 mg, 0.35 mmol, 80%), *m/z* (ESI-MS) 493.6 [M+Na]<sup>+</sup>. <sup>1</sup>H NMR (400 MHz, DMSO-*d*<sub>6</sub>) δ 7.47 (dd, *J* = 4.9, 2.9 Hz, 2H, *b*), 7.37 (t, *J* = 1.9 Hz, 1H, *h*), 7.25 – 7.13 (m, 5H, *a*, *i*, *j*), 6.99 (dd, *J* = 4.9, 1.3 Hz, 2H, *c*), 6.28 (s, 2H, *f*), 6.20 (t, *J* = 5.9 Hz, 2H, *e*), 4.13 (d, *J* = 5.9 Hz, 4H, *d*), 1.54 (s, 12H, *g*). <sup>13</sup>C NMR (101 MHz, DMSO-*d*<sub>6</sub>) δ 157.41, 148.87, 142.47, 127.81, 127.74, 126.66, 122.84, 121.76, 121.32, 54.77, 38.72, 30.60. Elem. Anal. Calc. (%) (C<sub>24</sub>H<sub>30</sub>N<sub>4</sub>O<sub>2</sub>S<sub>2</sub>) C 61.25, H 6.42, N 11.90; Found (%) C 60.90, H 6.41, N 11.84.

### Compound 4.8a



Compound **4.8a** was obtained as a white solid (117 mg, 0.26 mmol, 59%), *m/z* (ESI-MS) 457.9 [M-H]<sup>-</sup>, 481.7 [M+Na]<sup>+</sup>, 506.2 [M+Cl]<sup>-</sup>. <sup>1</sup>H NMR (400 MHz, DMSO-*d*<sub>6</sub>) δ 7.40 (t, *J* = 1.9 Hz, 1H, *h*), 7.35 – 7.26 (m, 4H, *b*), 7.26 – 7.14 (m, 9H, *a*, *c*, *i*, *j*), 6.32 (s, 2H, *f*), 6.27 (t, *J* = 6.0 Hz, 2H, *e*), 4.16 (d, *J* = 5.9 Hz, 4H, *d*), 1.55 (s, 12H, *g*). <sup>13</sup>C NMR (101 MHz, DMSO-*d*<sub>6</sub>) δ 157.51, 148.90, 141.48, 128.65, 127.73, 127.35, 126.96, 122.83, 121.75, 54.79, 42.99, 30.63. Elem. Anal. Calc. (%) (C<sub>28</sub>H<sub>34</sub>N<sub>4</sub>O<sub>2</sub>) C 73.33, H 7.47, N 12.22; Found (%) C 73.24, H 7.46, N 12.22.

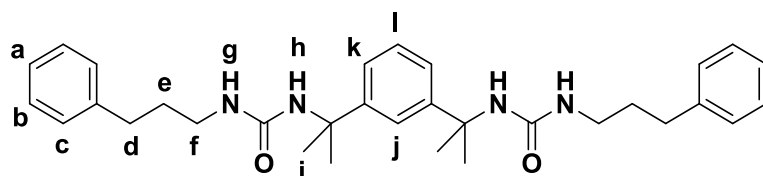
### Compound 4.8b



Compound **4.8b** was obtained as a white solid (185 mg, 0.38 mmol, 87%), *m/z* (ESI-MS) 509.8 [M+Na]<sup>+</sup>, 521.9 [M+Cl]<sup>-</sup>. <sup>1</sup>H NMR (400 MHz, DMSO-*d*<sub>6</sub>) δ 7.34 (t, *J* = 1.9 Hz, 1H, *i*), 7.33 – 7.26 (m, 4H, *b*), 7.23 – 7.16 (m, 7H, *a*, *c*, *k*), 7.16 – 7.11 (m, 2H, *j*), 6.24 (s, 2H, *g*), 5.80 (t, *J* = 5.8 Hz, 2H, *f*), 3.17 (dt, *J* = 7.2, 5.8 Hz, 4H, *e*), 2.64

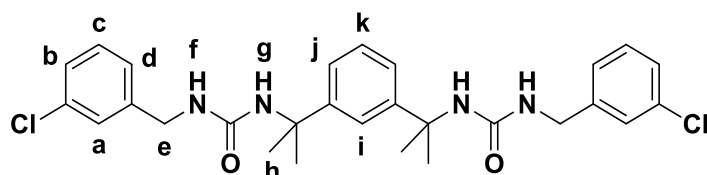
(t,  $J = 7.2$  Hz, 4H, d), 1.52 (s, 12H, h).  $^{13}\text{C}$  NMR (101 MHz,  $\text{DMSO-}d_6$ )  $\delta$  157.49, 148.93, 140.23, 129.10, 128.74, 127.71, 126.41, 122.77, 121.78, 54.70, 41.04, 36.72, 30.66. Elem. Anal. Calc. (%) ( $\text{C}_{30}\text{H}_{38}\text{N}_4\text{O}_2$ ) C 74.04, H 7.87, N 11.51; Found (%) C 73.80, H 7.88, N 11.45.

#### Compound 4.8c



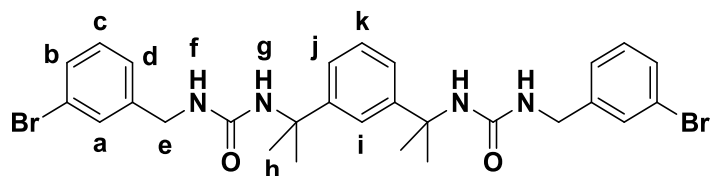
Compound **4.8c** was obtained as a white solid (177 mg, 0.34 mmol, 79%),  $m/z$  (ESI-MS) 513.9  $[\text{M-H}]^-$ , 537.8  $[\text{M}+\text{Na}]^+$ .  $^1\text{H}$  NMR (400 MHz,  $\text{DMSO-}d_6$ )  $\delta$  7.35 (t,  $J = 1.9$  Hz, 1H, j), 7.32 – 7.23 (m, 4H, b), 7.22 – 7.09 (m, 9H, a, c, k, l), 6.16 (s, 2H, h), 5.86 (t,  $J = 5.7$  Hz, 2H, g), 2.94 (dt,  $J = 6.6, 5.7$  Hz, 4H, f), 2.55 (t,  $J = 8.1$  Hz, 4H, d), 1.68 – 1.58 (tt,  $J = 8.1, 6.6$  Hz, 4H, e), 1.51 (s, 12H, i).  $^{13}\text{C}$  NMR (101 MHz,  $\text{DMSO-}d_6$ )  $\delta$  157.59, 148.95, 142.26, 128.71, 127.70, 126.12, 125.99, 122.77, 121.77, 54.69, 38.90, 32.96, 32.41, 30.64. Elem. Anal. Calc. (%) ( $\text{C}_{32}\text{H}_{42}\text{N}_4\text{O}_2$ ) C 74.67, H 8.23, N 10.89; Found (%) C 74.65, H 8.22, N 10.88.

#### Compound 4.9a



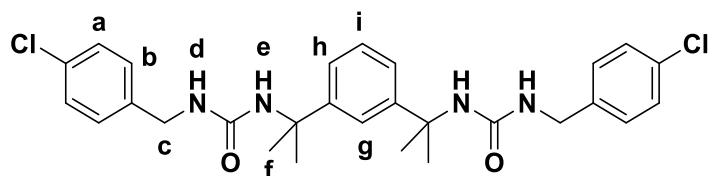
Compound **4.9a** was obtained as a white solid (211 mg, 0.40 mmol, 92%),  $m/z$  (ESI-MS) 549.7  $[\text{M}+\text{Na}]^+$ .  $^1\text{H}$  NMR (400 MHz,  $\text{DMSO-}d_6$ )  $\delta$  7.38 – 7.25 (m, 7H, a, b, c, i), 7.24 – 7.07 (m, 5H, d, j, k), 6.38 (s, 2H, g), 6.35 (t,  $J = 6.0$  Hz, 2H, f), 4.16 (d,  $J = 6.0$  Hz, 4H, e), 1.53 (s, 12H, h).  $^{13}\text{C}$  NMR (101 MHz,  $\text{DMSO-}d_6$ )  $\delta$  157.45, 148.84, 144.37, 133.39, 130.50, 127.72, 127.06, 126.84, 125.97, 122.76, 121.72, 54.83, 42.44, 30.64. Elem. Anal. Calc. (%) ( $\text{C}_{28}\text{H}_{32}\text{N}_4\text{O}_2\text{Cl}_2$ ) C 63.76, H 6.11, N 10.62; Found (%) C 63.77, H 6.08, N 10.63.

### Compound 4.9b



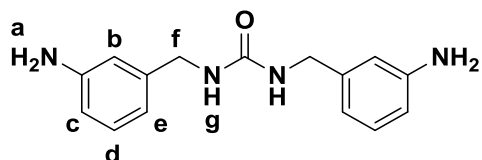
Compound **4.9b** was obtained as a white solid (233 mg, 0.38 mmol, 87%),  $m/z$  (ESI-MS) 642.1  $[M+Na]^+$ .  $^1H$  NMR (400 MHz, DMSO- $d_6$ )  $\delta$  7.45 – 7.38 (m, 4H, *a*, *b*), 7.35 (t,  $J$  = 2.0 Hz, 1H, *i*), 7.30 – 7.12 (m, 7H, *c*, *d*, *j*, *k*), 6.38 (s, 2H, *g*), 6.34 (t,  $J$  = 6.0 Hz, 2H, *f*), 4.16 (d,  $J$  = 6.0 Hz, 4H, *e*), 1.53 (s, 12H, *h*).  $^{13}C$  NMR (101 MHz, DMSO- $d_6$ )  $\delta$  157.44, 148.83, 144.64, 130.82, 129.96, 129.74, 127.76, 126.38, 122.74, 122.07, 121.72, 54.84, 42.40, 30.65. Elem. Anal. Calc. (%) ( $C_{28}H_{32}N_4O_2Br_2$ ) C 54.56, H 5.23, N 9.09; Found (%) C 54.65, H 5.25, N 9.10.

### Compound 4.9c



Compound **4.9c** was obtained as a white solid (188 mg, 0.36 mmol, 82%),  $m/z$  (ESI-MS) 529.7  $[M+H]^+$ , 543.6  $[M+Na]^+$ .  $^1H$  NMR (400 MHz, DMSO- $d_6$ )  $\delta$  7.39 – 7.32 (m, 5H, *a*, *g*), 7.24 (d,  $J$  = 8.5 Hz, 4H, *b*), 7.22 – 7.12 (m, 3H, *h*, *i*), 6.35 (s, 2H, *e*), 6.31 (t,  $J$  = 6.0 Hz, 2H, *d*), 4.14 (d,  $J$  = 6.0 Hz, 4H, *c*), 1.52 (s, 12H, *f*).  $^{13}C$  NMR (101 MHz, DMSO- $d_6$ )  $\delta$  157.45, 148.84, 140.69, 131.42, 129.19, 128.55, 127.74, 122.80, 121.71, 54.80, 42.33, 30.60. Elem. Anal. Calc. (%) ( $C_{28}H_{32}N_4O_2Cl_2$ ) C 63.76, H 6.11, N 10.62; Found (%) C 63.74, H 6.11, N 10.63.

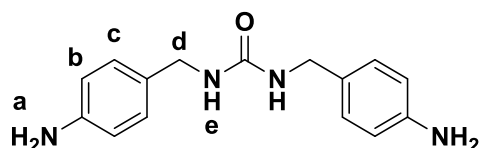
### Compound 5.1a



A solution of CDI (310 mg, 1.9 mmol) in dry chloroform (25 cm<sup>3</sup>) was added dropwise over 30 minutes to a stirred solution of 3-aminobenzylamine (528 mg, 4.3 mmol) in chloroform (35 cm<sup>3</sup>) under nitrogen at 0 °C. The reaction mixture was stirred for 16 hours under nitrogen at 0 °C then concentrated *in vacuo*. The resulting white solid was collected under suction and washed with chloroform (2

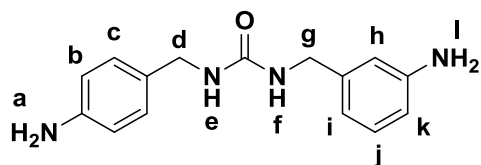
x 20 cm<sup>3</sup>). Compound **5.1a** was obtained as a white solid (457 mg, 1.7 mmol, 88%), m/z (ESI-MS) 271.6 [M+H]<sup>+</sup>, 541.1 [2M+H]<sup>+</sup>. <sup>1</sup>H NMR (400 MHz, DMSO-*d*<sub>6</sub>) δ 6.94 (t, *J* = 7.7 Hz, 2H, *d*), 6.47 (t, *J* = 1.9 Hz, 2H, *b*), 6.41 (m, 4H, *c*, *e*), 6.20 (t, *J* = 5.8 Hz, 2H, *g*), 5.01 (s, 4H, *a*), 4.08 (d, *J* = 5.8 Hz, 4H, *f*). <sup>13</sup>C NMR (101 MHz, DMSO-*d*<sub>6</sub>) δ 158.42, 149.06, 141.72, 129.15, 115.08, 113.05, 112.80, 43.73. Elem. Anal. Calc. (%) (C<sub>15</sub>H<sub>18</sub>N<sub>4</sub>O) C 66.64, H 6.71, N 20.73; Found (%) C 66.23, H 6.69, N 20.78.

#### Compound 5.1b



Compound **5.2** (399 mg, 1.8 mmol) was added to a solution of 4-aminobenzylamine (0.26 cm<sup>3</sup>, 2.3 mmol) in dry acetonitrile (10 cm<sup>3</sup>) under nitrogen at 20 °C and sonicated briefly with gentle warming to dissolve. The reaction mixture was left to stand under nitrogen at 20 °C for 24 hours. The resulting crystalline material was collected under suction, washed with acetonitrile (20 cm<sup>3</sup>) and recrystallized from hot methanol. Compound **5.1b** was obtained as large colourless needle-shaped crystals (341 mg, 1.3 mmol, 68%), m/z (ESI-MS) 271.0 [M+H]<sup>+</sup>, 293.0 [M+Na]<sup>+</sup>, 541.6 [2M+H]<sup>+</sup>, 563.8 [2M+Na]<sup>+</sup>. <sup>1</sup>H NMR (400 MHz, DMSO-*d*<sub>6</sub>) δ 6.91 (d, *J* = 8.3 Hz, 2H, *c*), 6.50 (d, *J* = 8.3 Hz, 2H, *b*), 6.04 (t, *J* = 5.8 Hz, 1H, *e*), 4.93 (s, 2H, *a*), 4.03 (d, *J* = 5.8 Hz, 2H, *d*). <sup>13</sup>C NMR (101 MHz, DMSO-*d*<sub>6</sub>) δ 158.42, 147.82, 128.54, 128.04, 114.17, 43.27. Elem. Anal. Calc. (%) (C<sub>15</sub>H<sub>18</sub>N<sub>4</sub>O) C 66.64, H 6.71, N 20.73; Found (%) C 66.41, H 6.65, N 20.91.

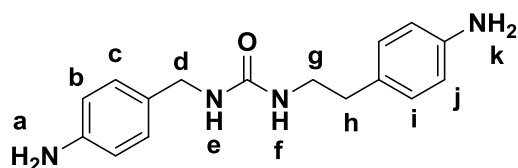
#### Compound 5.1c



Compound **5.2** (204 mg, 0.95 mmol) was added to a solution of 3-aminobenzylamine (155 mg, 1.3 mmol) in dry acetonitrile (10 cm<sup>3</sup>) under nitrogen at 20 °C and sonicated briefly with gentle warming to dissolve. The reaction mixture was left to stand under nitrogen at 20 °C for 24 hours. The reaction mixture was concentrated *in vacuo*, and the resulting crystalline material was collected under suction, washed with acetonitrile (20 cm<sup>3</sup>) and recrystallized from

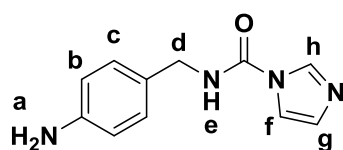
hot methanol. Compound **5.1c** was obtained as colourless crystals (123 mg, 0.45 mmol, 48%),  $m/z$  (ESI-MS) 271.2  $[M+H]^+$ , 293.2  $[M+Na]^+$ , 541.3  $[2M+H]^+$ , 563.6  $[2M+Na]^+$ .  $^1H$  NMR (400 MHz, DMSO- $d_6$ )  $\delta$  7.02 – 6.84 (m, 3H, *c, j*), 6.51 (d,  $J = 8.4$  Hz, 1H, *i*), 6.47 – 6.29 (m, 4H, *b, h, k*), 6.15 (t,  $J = 5.9$  Hz, 1H, *f*), 6.08 (t,  $J = 5.7$  Hz, 1H, *e*), 5.00 (s, 2H, *l*), 4.93 (s, 2H, *a*), 4.07 (d,  $J = 5.9$  Hz, 2H, *g*), 4.04 (d,  $J = 5.7$  Hz, 2H, *d*).  $^{13}C$  NMR (101 MHz, DMSO- $d_6$ )  $\delta$  158.41, 149.06, 147.85, 141.76, 129.13, 128.58, 127.97, 115.04, 114.17, 113.03, 112.78, 43.69, 43.32. Elem. Anal. Calc. (%) ( $C_{15}H_{18}N_4O$ ) C 66.64, H 6.71, N 20.73; Found (%) C 66.42, H 6.68, N 20.90.

#### Compound 5.1d



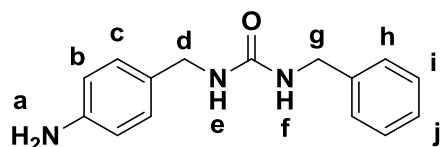
Compound **5.2** (145 mg, 0.67 mmol) was added to a solution of 4-(2-aminoethyl)aniline (105 mg, 0.77 mmol) in dry acetonitrile (10 cm<sup>3</sup>) under nitrogen at 20 °C and sonicated briefly with gentle warming to dissolve. The reaction mixture was left to stand under nitrogen at 20 °C for 24 hours. The resulting crystalline material was collected under suction, washed with acetonitrile (20 cm<sup>3</sup>) and recrystallized from hot methanol. Compound **5.1d** was obtained as large colourless needle-shaped crystals (135 mg, 0.47 mmol, 71%),  $m/z$  (ESI-MS) 285.2  $[M+H]^+$ , 307.5  $[M+Na]^+$ , 570.3  $[2M+H]^+$ , 591.3  $[2M+Na]^+$ .  $^1H$  NMR (400 MHz, DMSO- $d_6$ )  $\delta$  6.89 (d,  $J = 8.3$  Hz, 2H, *c*), 6.84 (d,  $J = 8.3$  Hz, 2H, *i*), 6.51 (d,  $J = 8.3$  Hz, 2H, *b*), 6.49 (d,  $J = 8.3$  Hz, 2H, *j*), 6.09 (t,  $J = 5.7$  Hz, 1H, *e*), 5.74 (t,  $J = 5.7$  Hz, 1H, *f*), 4.92 (s, 2H, *a*), 4.84 (s, 2H, *k*), 4.00 (d,  $J = 5.7$  Hz, 2H, *d*), 3.14 (dt,  $J = 7.2, 5.7$  Hz, 2H, *g*), 2.48 (d,  $J = 7.2$  Hz, 2H, *h*).  $^{13}C$  NMR (101 MHz, DMSO- $d_6$ )  $\delta$  158.37, 147.78, 147.14, 129.45, 128.52, 128.07, 127.00, 114.44, 114.15, 43.19, 41.89, 35.93. Elem. Anal. Calc. (%) ( $C_{16}H_{20}N_4O$ ) C 67.58, H 7.09, N 19.70; Found (%) C 67.35, H 7.05, N 19.65.

#### Compound 5.2



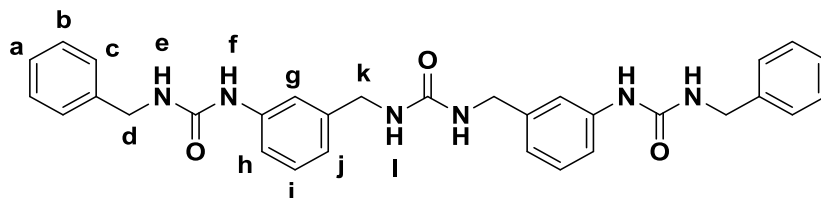
A solution of CDI (1.410 g, 8.6 mmol) in dry chloroform (25 cm<sup>3</sup>) was added dropwise over 30 minutes to a stirred solution of 4-aminobenzylamine (1 cm<sup>3</sup>, 8.8 mmol) in chloroform (35 cm<sup>3</sup>) under nitrogen at 0 °C. The reaction mixture was stirred for 3 hours under nitrogen at 0 °C. The resulting white solid was collected under suction and washed with chloroform (2 x 20 cm<sup>3</sup>). Compound **5.2** was obtained as a white solid (1.609 g, 7.4 mmol, 86%). <sup>1</sup>H NMR (400 MHz, DMSO-*d*<sub>6</sub>) δ 8.88 (t, *J* = 5.7 Hz, 1H, *e*), 8.26 (t, *J* = 1.2 Hz, 1H, *h*), 7.70 (t, *J* = 1.5 Hz, 1H, *f*), 7.03 (t, *J* = 1.5 Hz, 1H, *g*), 7.01 (d, *J* = 8.4 Hz, 2H, *c*), 6.53 (d, *J* = 8.4 Hz, 2H, *b*), 4.93 (s, 2H, *a*), 4.28 (d, *J* = 5.7 Hz, 2H, *d*). <sup>13</sup>C NMR (101 MHz, DMSO-*d*<sub>6</sub>) δ 149.19, 148.37, 136.40, 129.99, 128.93, 125.63, 117.02, 114.17, 43.82. Elem. Anal. Calc. (%) (C<sub>11</sub>H<sub>12</sub>N<sub>4</sub>O) C 61.10, H 5.59, N 25.91; Found (%) C 60.32, H 5.54, N 25.90.

### Compound 5.3



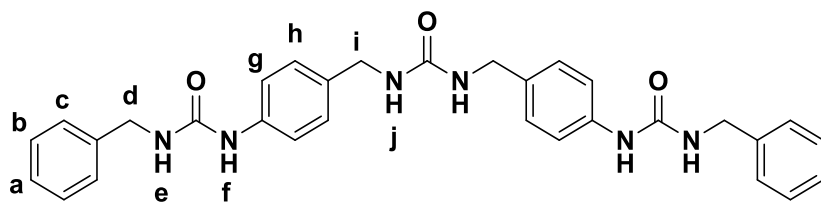
Benzyl isocyanate (0.9 cm<sup>3</sup>, 7.3 mmol) was added to a stirred solution of 4-aminobenzylamine (1 cm<sup>3</sup>, 8.8 mmol) in dichloromethane (100 cm<sup>3</sup>) under nitrogen at 0 °C. The reaction mixture was stirred under nitrogen at 0 °C for 4 hours. The resulting precipitate was filtered under suction, washed with dichloromethane (3 x 20 cm<sup>3</sup>) and recrystallised from hot methanol. Compound **5.3** was obtained as an off-white solid (1.612 g, 6.3 mmol, 87%), *m/z* (ESI-MS) 256.5 [M+H]<sup>+</sup>, 278.1 [M+Na]<sup>+</sup>. <sup>1</sup>H NMR (400 MHz, DMSO-*d*<sub>6</sub>) δ 7.36 – 7.28 (m, 2H, *i*), 7.28 – 7.18 (m, 3H, *h*, *j*), 6.92 (d, *J* = 8.4 Hz, 2H, *c*), 6.51 (d, *J* = 8.4 Hz, 2H, *b*), 6.32 (t, *J* = 6.1 Hz, 1H, *f*), 6.17 (t, *J* = 5.8 Hz, 1H, *e*), 4.94 (s, 2H, *a*), 4.23 (d, *J* = 6.0 Hz, 2H, *g*), 4.04 (d, *J* = 5.7 Hz, 2H, *d*). <sup>13</sup>C NMR (101 MHz, DMSO-*d*<sub>6</sub>) δ 158.48, 147.86, 141.43, 128.66, 128.55, 127.97, 127.45, 126.99, 114.16, 43.40, 43.32. Elem. Anal. Calc. (%) (C<sub>15</sub>H<sub>17</sub>N<sub>3</sub>O) C 70.56, H 6.71, N 16.46; Found (%) C 70.36, H 6.61, N 16.41.

### Compound 5.4a



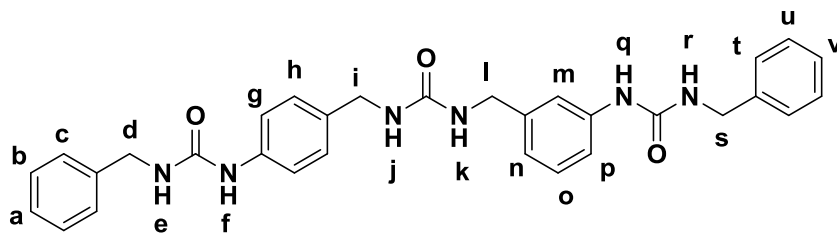
Compound **5.4a** was obtained as a white solid (301 mg, 0.56 mmol, 76%),  $m/z$  (ESI-MS) 537.26  $[M+H]^+$ .  $^1H$  NMR (400 MHz, DMSO- $d_6$ )  $\delta$  8.56 (s, 1H, *f*), 7.39 – 7.20 (m, 7H, ArH), 7.16 (t,  $J = 7.8$  Hz, 1H, *i*), 6.81 (dt,  $J = 7.8, 1.2$  Hz, 1H, *j*), 6.58 (t,  $J = 6.0$  Hz, 1H, *e*), 6.38 (t,  $J = 6.0$  Hz, 1H, *l*), 4.30 (d,  $J = 5.9$  Hz, 2H, *d*), 4.18 (d,  $J = 5.9$  Hz, 2H, *k*).  $^{13}C$  NMR (101 MHz, DMSO- $d_6$ )  $\delta$  158.44, 155.66, 141.81, 140.88, 140.84, 129.00, 128.76, 127.55, 127.17, 120.37, 116.80, 116.48, 43.57, 43.18. Elem. Anal. Calc. (%) ( $C_{31}H_{32}N_6O_3$ ) C 69.38, H 6.01, N 15.66; Found (%) C 69.19, H 6.01, N 15.66.

### Compound 5.4b



Compound **5.4b** was obtained as a white solid (296 mg, 0.55 mmol, 75%),  $m/z$  (ESI-MS) 537.26  $[M+H]^+$ .  $^1H$  NMR (400 MHz, DMSO- $d_6$ )  $\delta$  8.51 (s, 2H, *f*), 7.41 – 7.18 (m, 14H, *a, b, c, g*), 7.11 (d,  $J = 8.5$  Hz, 4H, *h*), 6.57 (t,  $J = 6.0$  Hz, 2H, *e*), 6.27 (t,  $J = 5.9$  Hz, 2H, *j*), 4.30 (d,  $J = 5.9$  Hz, 4H, *d*), 4.14 (d,  $J = 5.9$  Hz, 4H, *i*).  $^{13}C$  NMR (101 MHz, DMSO- $d_6$ )  $\delta$  158.45, 155.68, 140.83, 139.48, 133.86, 128.75, 127.96, 127.58, 127.16, 118.07, 43.21, 43.07. Elem. Anal. Calc. (%) ( $C_{31}H_{32}N_6O_3$ ) C 69.38, H 6.01, N 15.66; Found (%) C 68.99, H 6.00, N 15.79.

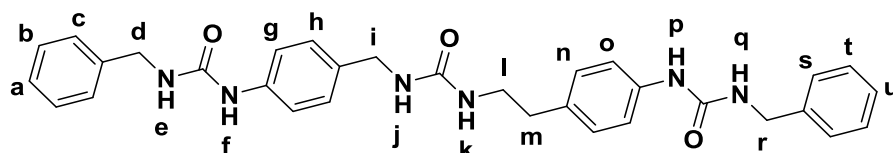
### Compound 5.4c



Compound **5.4c** was obtained as a white solid (321 mg, 0.60 mmol, 81%),  $m/z$  (ESI-MS) 537.26  $[M+H]^+$ ,  $[M+Na]^+$ .  $^1H$  NMR (400 MHz, DMSO- $d_6$ )  $\delta$  8.56 (s, 1H, *q*), 8.50

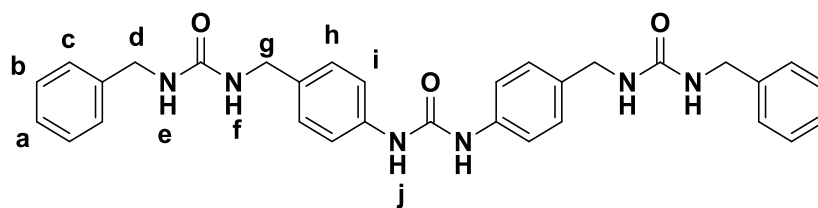
(s, 1H, f), 7.39 – 7.04 (m, 17H), 6.80 (dt,  $J = 7.7, 1.2$  Hz, 1H), 6.58 (t,  $J = 5.9$  Hz, 2H), 6.30 (t,  $J = 5.9$  Hz, 1H), 4.30 (dd,  $J = 6.0, 3.7$  Hz, 4H), 4.16 (dd,  $J = 10.6, 5.9$  Hz, 4H).  $^{13}\text{C}$  NMR (101 MHz,  $\text{DMSO-}d_6$ )  $\delta$  158.45, 155.70, 155.66, 141.86, 140.91, 140.84, 139.49, 133.82, 128.97, 128.76, 127.99, 127.59, 127.57, 127.17, 120.34, 118.12, 116.81, 116.48, 43.56, 43.21, 43.11. Elem. Anal. Calc. (%) ( $\text{C}_{31}\text{H}_{32}\text{N}_6\text{O}_3$ ) C 69.38, H 6.01, N 15.66; Found (%) C 69.06, H 5.96, N 15.80.

#### Compound 5.4d



Compound **5.4d** was obtained as a white solid (279 mg, 0.24 mmol, 72%),  $m/z$  (ESI-MS) 551.28  $[\text{M}+\text{H}]^+$ .  $^1\text{H}$  NMR (400 MHz,  $\text{DMSO-}d_6$ )  $\delta$  8.50 (s, 1H, f), 8.47 (s, 1H, p), 7.58 – 6.99 (m, 18H, ArH), 6.57 (t,  $J = 6.1$  Hz, 1H, e), 6.56 (t,  $J = 6.1$  Hz, 1H, q), 6.26 (t,  $J = 5.9$  Hz, 1H, j), 5.84 (t,  $J = 5.7$  Hz, 1H, k), 4.29 (d,  $J = 5.9$  Hz, 4H, d, r), 4.11 (d,  $J = 5.8$  Hz, 2H, i), 3.20 (dt,  $J = 7.6, 5.7$  Hz, 2H, l), 2.60 (t,  $J = 7.2$  Hz, 2H, m).  $^{13}\text{C}$  NMR (101 MHz,  $\text{DMSO-}d_6$ )  $\delta$  158.38, 155.74, 155.70, 140.87, 140.83, 139.45, 138.94, 133.92, 132.75, 129.28, 128.76, 127.96, 127.59, 127.57, 127.17, 127.16, 118.29, 118.08, 43.21, 42.99, 41.62, 35.98. Elem. Anal. Calc. (%) ( $\text{C}_{32}\text{H}_{34}\text{N}_6\text{O}_3$ ) C 69.80, H 6.22, N 15.26; Found (%) C 69.37, H 6.14, N 15.19.

#### Compound 5.4e

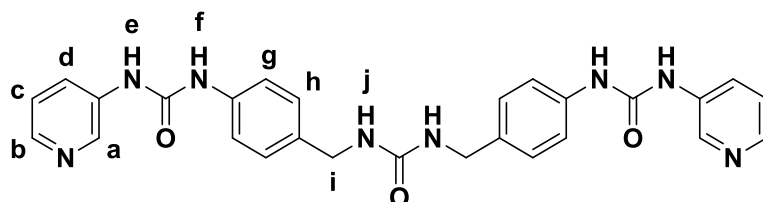


CDI (163 mg, 1.0 mmol) was added to a stirred solution of **5.3** (507 mg, 2.0 mmol) in dry acetonitrile (20  $\text{cm}^3$ ) under nitrogen at 80  $^\circ\text{C}$ . The reaction mixture was stirred under nitrogen at 80  $^\circ\text{C}$  for 24 hours, and the resulting precipitate washed with hot acetonitrile (2 x 20  $\text{cm}^3$ ). The wet crude product was sonicated 3 times with hot methanol (20  $\text{cm}^3$ ), collected under suction and dried at 80  $^\circ\text{C}$  for 24 hours. Compound **5.4e** was obtained as a white solid (436 mg, 0.81 mmol, 82%),  $m/z$  (ESI-MS) 537.26  $[\text{M}+\text{H}]^+$ .  $^1\text{H}$  NMR (400 MHz,  $\text{DMSO-}d_6$ )  $\delta$  8.60 (s, 2H, j), 7.38 (d,  $J = 8.1$  Hz, 4H, i), 7.31 (d,  $J = 7.3$  Hz, 4H, b), 7.26 (m, 6H, a, c), 7.17 (d,  $J = 8.1$  Hz, 4H, h), 6.41 (t,  $J = 6.0$  Hz, 2H, e), 6.37 (t,  $J = 6.0$  Hz, 2H, f), 4.24 (d,  $J = 6.0$  Hz,



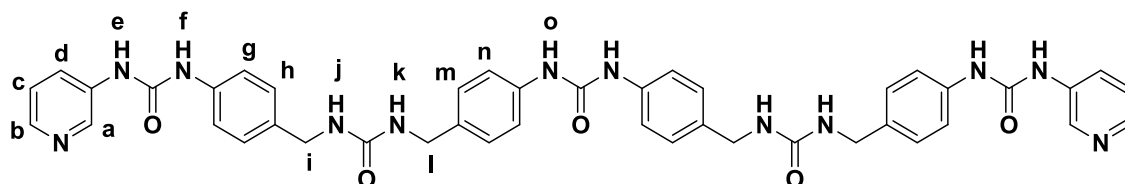
4H, *d*), 4.17 (d, *J* = 6.0 Hz, 4H, *g*). <sup>13</sup>C NMR (101 MHz, DMSO-*d*<sub>6</sub>) δ 158.50, 152.99, 141.38, 138.73, 134.60, 128.66, 128.05, 127.45, 127.00, 118.52, 43.43, 43.08. Elem. Anal. Calc. (%) (C<sub>31</sub>H<sub>32</sub>N<sub>6</sub>O<sub>3</sub>) C 69.38, H 6.01, N 15.66; Found (%) C 69.11, H 5.98, N 15.88.

### Compound 6.1a



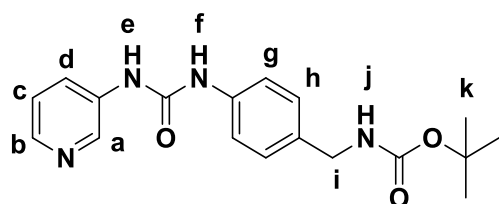
A solution of 3-aminopyridine (563 mg, 6.0 mmol) and CDI (969 mg, 6.0 mmol) in dry DMF (10 cm<sup>3</sup>) was stirred under nitrogen at 20 °C for 3 hours. The reaction mixture was stirred with water (1 cm<sup>3</sup>) under nitrogen for 5 minutes to consume unreacted CDI. Compound **5.1b** (608 mg, 2.2 mmol) was added and the solution stirred under nitrogen at 20 °C for 8 hours. The reaction mixture was concentrated *in vacuo* and the resulting precipitate washed with DMF (2 x 10 cm<sup>3</sup>). To remove singly substituted products, the crude product was dissolved in hot DMF (5 cm<sup>3</sup>) and precipitated by the gradual addition of methanol vapour (5 cm<sup>3</sup>). The resulting solid was washed with DMF (2 x 10 cm<sup>3</sup>), sonicated 3 times with hot methanol (50 cm<sup>3</sup>), collected under suction and dried at 80 °C for 24 hours. Compound **6.1a** was obtained as a white solid (841 mg, 1.6 mmol, 73%), *m/z* (ESI-MS) 511.22 [M+H]<sup>+</sup>. <sup>1</sup>H NMR (400 MHz, DMSO-*d*<sub>6</sub>) δ 8.82 (s, 2H, *e*), 8.78 (s, 2H, *f*), 8.60 (d, *J* = 2.0 Hz, 2H, *a*), 8.19 (dd, *J* = 4.7, 1.5 Hz, 2H, *b*), 7.95 (ddd, *J* = 8.3, 2.7, 1.5 Hz, 2H, *d*), 7.41 (d, *J* = 8.6 Hz, 4H, *g*), 7.31 (ddd, *J* = 8.3, 4.7, 0.7 Hz, 2H, *c*), 7.19 (d, *J* = 8.6 Hz, 4H, *h*), 6.36 (t, *J* = 6.0 Hz, 2H, *j*), 4.18 (d, *J* = 6.0 Hz, 4H, *i*). <sup>13</sup>C NMR (101 MHz, DMSO-*d*<sub>6</sub>) δ 158.51, 153.04, 143.27, 140.52, 138.42, 136.92, 135.00, 128.08, 125.57, 124.04, 118.81, 43.09. Elem. Anal. Calc. (%) (C<sub>27</sub>H<sub>26</sub>N<sub>8</sub>O<sub>3</sub>) C 63.52, H 5.13, N 21.95; Calc. (%) (6.4 · 0.06 DMF, C<sub>27.18</sub>H<sub>26.42</sub>N<sub>8.06</sub>O<sub>3.06</sub>) C 62.67, H 5.40, N 21.78; Found (%) C 62.71, H 4.98, N 21.70.

### Compound 6.1b



CDI (50 mg, 0.31 mmol) was added to a stirred solution of **6.4** (243 mg, 0.62 mmol) in dry DMF (5 cm<sup>3</sup>) under nitrogen at 20 °C. The reaction mixture was left to stand under nitrogen at 20 °C for 8 hours, and the resulting gelatinous precipitate washed with DMF (2 x 2 cm<sup>3</sup>). The wet crude product was sonicated 3 times with hot methanol (20 cm<sup>3</sup>), collected under suction and dried at 80 °C for 24 hours. Compound **6.1b** was obtained as an off-white solid (120 mg, 0.15 mmol, 48%), *m/z* (ESI-MS) 807.34 [M+H]<sup>+</sup>. <sup>1</sup>H NMR (400 MHz, DMSO-*d*<sub>6</sub>) δ 8.83 (s, 2H, e), 8.78 (s, 2H, f), 8.65 – 8.54 (m, 4H, a, o), 8.19 (dd, *J* = 4.7, 1.5 Hz, 2H, b), 7.94 (ddd, *J* = 8.4, 2.6, 1.5 Hz, 2H, d), 7.45 – 7.34 (m, 8H, g, n), 7.31 (ddd, *J* = 8.4, 4.7, 0.7 Hz, 2H, c), 7.22 – 7.08 (m, 8H, h, m), 6.34 (dt, *J* = 6.0, 1.9 Hz, 4H, i), 4.18 (d, *J* = 6.0 Hz, 4H, j), 4.17 (d, *J* = 6.2 Hz, 4H, l). <sup>13</sup>C NMR (101 MHz, DMSO-*d*<sub>6</sub>) δ 158.48, 153.03, 153.00, 143.27, 140.50, 138.74, 138.41, 136.92, 135.00, 134.61, 128.07, 125.56, 124.05, 118.78, 118.54, 43.07. Elem. Anal. Calc. (%) (C<sub>43</sub>H<sub>42</sub>N<sub>12</sub>O<sub>5</sub>) C 64.01, H 5.25, N 20.83; Calc. (%) (6.5 · 0.06 DMF, C<sub>43.18</sub>H<sub>42.42</sub>N<sub>12.06</sub>O<sub>5.06</sub>) C 63.13, H 5.51, N 20.73; Found (%) C 63.11, H 5.26, N 20.51.

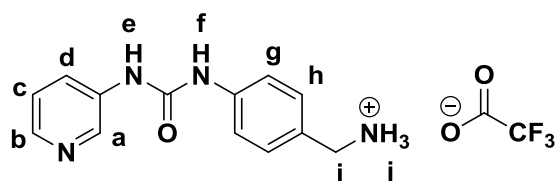
### Compound 6.2



A solution of 3-aminopyridine (770 mg, 8.2 mmol) and CDI (1.340 g, 8.3 mmol) in dry chloroform (60 cm<sup>3</sup>) was stirred under nitrogen at 20 °C for 3 hours. The reaction mixture was stirred with water (1 cm<sup>3</sup>) under nitrogen for 5 minutes to consume unreacted CDI. To the resulting solution, 4-[(N-Boc)aminomethyl]aniline (1.740 g, 7.8 mmol) was added and the reaction mixture stirred at 65 °C for 24 hours. The cooled reaction mixture was extracted with water (3 x 50 cm<sup>3</sup>) and the resulting precipitate collected under suction. The product was washed with water (2 x 50 cm<sup>3</sup>) and dried at 80 °C for 24 hours. Compound **6.2** was obtained as a

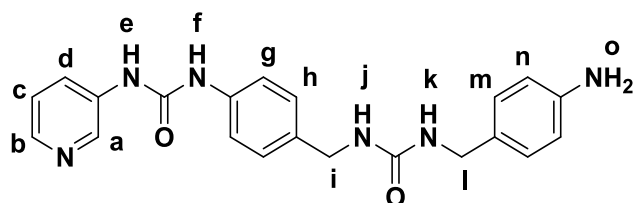
white solid (1.226 g, 3.6 mmol, 46%),  $m/z$  (ESI-MS) 343.1  $[M+H]^+$ , 365.8  $[M+Na]^+$ .  $^1H$  NMR (400 MHz, DMSO- $d_6$ )  $\delta$  8.82 (s, 1H, e), 8.77 (s, 1H, f), 8.60 (d,  $J = 2.5$  Hz, 1H, a), 8.19 (dd,  $J = 4.7, 1.5$  Hz, 1H, b), 7.94 (ddd,  $J = 8.4, 2.6, 1.5$  Hz, 1H, d), 7.40 (d,  $J = 8.6$  Hz, 2H, h), 7.36 – 7.26 (m, 2H, c, j), 7.16 (d,  $J = 8.6$  Hz, 2H, g), 4.06 (d,  $J = 6.2$  Hz, 2H, i), 1.40 (s, 9H, k).  $^{13}C$  NMR (101 MHz, DMSO- $d_6$ )  $\delta$  156.21, 153.03, 143.26, 140.48, 138.43, 136.91, 134.34, 127.97, 125.53, 124.04, 118.79, 78.15, 43.43, 28.73. Elem. Anal. Calc. (%) (C<sub>18</sub>H<sub>22</sub>N<sub>4</sub>O<sub>3</sub>) C 63.14, H 6.48, N 16.36; Found (%) C 63.07, H 6.47, N 16.25.

### Compound 6.3



A solution of **6.2** (931 mg, 2.7 mmol) in a mixture of dichloromethane (16 cm<sup>3</sup>) and trifluoroacetic acid (4 cm<sup>3</sup>) was stirred for 3 hours at 20 °C. The reaction mixture was evaporated to dryness *in vacuo* and excess acid removed by further heating at 80 °C for 24 hours. The resulting solid was recrystallised from hot methanol. Compound **6.3** was obtained as a pale yellow solid (897 mg, 2.5 mmol, 93%),  $m/z$  (ESI-MS) 112.9  $[TFA]^-$ , 243.2  $[M-TFA]^+$ , 355.1  $[M-H]^-$ .  $^1H$  NMR (400 MHz, DMSO- $d_6$ )  $\delta$  10.41 (s, 1H, e), 9.95 (s, 1H, f), 9.07 (d,  $J = 2.4$  Hz, 1H, a), 8.47 (dd,  $J = 5.4, 1.3$  Hz, 1H, b), 8.30 (ddd,  $J = 8.6, 2.4, 1.3$  Hz, 1H, d), 8.13 (s, 3H, j), 7.85 (dd,  $J = 8.6, 5.4$  Hz, 1H, c), 7.57 (d,  $J = 8.6$  Hz, 2H, h), 7.40 (d,  $J = 8.6$  Hz, 2H, g), 3.99 (q,  $J = 5.9$  Hz, 2H, i).  $^{13}C$  NMR (101 MHz, DMSO- $d_6$ )  $\delta$  159.16 (q,  $J = 36$  Hz, CF<sub>3</sub>), 152.74, 139.94, 139.75, 136.57, 132.80, 132.50, 130.13, 128.26, 127.24, 120.71, 118.95, 117.80, 114.90, 111.99, 42.41.

### Compound 6.4



Compound **5.2** (408 mg, 1.9 mmol) was added to a solution of **6.3** (722 mg, 2.0 mmol) and triethylamine (2 cm<sup>3</sup>) in dry acetonitrile (15 cm<sup>3</sup>) under nitrogen at 20 °C and sonicated to dissolve. The reaction mixture was stirred under nitrogen at

20 °C for 12 hours, and the resulting precipitate washed with acetonitrile (3 x 20 cm<sup>3</sup>) and sonicated in hot methanol (20 cm<sup>3</sup>). The product was collected under suction, washed with methanol (2 x 20 cm<sup>3</sup>) and dried at 80 °C for 24 hours. Compound **6.4** was obtained as an off-white solid (493 mg, 1.3 mmol, 67%), m/z (ESI-MS) 391.2 [M+H]<sup>+</sup>, 412.8 [M+Na]<sup>+</sup>. <sup>1</sup>H NMR (400 MHz, DMSO-*d*<sub>6</sub>) δ 8.83 (s, 1H, *e*), 8.78 (s, 1H, *f*), 8.60 (dd, *J* = 2.6, 0.8 Hz, 1H, *a*), 8.19 (dd, *J* = 4.7, 1.5 Hz, 1H, *b*), 7.94 (ddd, *J* = 8.4, 2.7, 1.5 Hz, 1H, *d*), 7.40 (d, *J* = 8.6 Hz, 2H, *g*), 7.31 (ddd, *J* = 8.4, 4.7, 0.8 Hz, 1H, *c*), 7.17 (d, *J* = 8.6 Hz, 2H, *h*), 6.92 (d, *J* = 8.4 Hz, 2H, *m*), 6.51 (d, *J* = 8.4 Hz, 2H, *n*), 6.25 (t, *J* = 5.9 Hz, 1H, *j*), 6.14 (t, *J* = 5.7 Hz, 1H, *k*), 4.94 (s, 2H, *o*), 4.16 (d, *J* = 5.9 Hz, 2H, *i*), 4.04 (d, *J* = 5.7 Hz, 2H, *l*). <sup>13</sup>C NMR (101 MHz, DMSO-*d*<sub>6</sub>) δ 158.44, 153.04, 147.85, 143.26, 140.50, 138.39, 136.92, 135.05, 128.55, 128.06, 127.98, 125.55, 124.05, 118.78, 114.16, 43.31, 43.02. Elem. Anal. Calc. (%) (C<sub>21</sub>H<sub>22</sub>N<sub>6</sub>O<sub>2</sub>) C 64.60, H 5.68, N 21.52; Found (%) C 64.00, H 5.65, N 21.22.

## 8.10 References

1. G. M. Sheldrick, *Acta Crystallogr. Sect. A*, 2015, **71**, 3-8.
2. O. V. Dolomanov, L. J. Bourhis, R. J. Gildea, J. A. K. Howard and H. Puschmann, *J. Appl. Cryst.*, 2009, **42**, 339-341.
3. D. S. Kim, J. Chang, S. Leem, J. S. Park, P. Thordarson and J. L. Sessler, *J. Am. Chem. Soc.*, 2015, **137**, 16038-16042.
4. D. Van der Spoel, E. Lindahl, B. Hess, G. Groenhof, A. E. Mark and H. J. C. Berendsen, *J. Comput. Chem.*, 2005, **26**, 1701-1718.
5. D. A. Case, T. E. Cheatham, T. Darden, H. Gohlke, R. Luo, K. M. Merz, A. Onufriev, C. Simmerling, B. Wang and R. J. Woods, *J. Computat. Chem.*, 2005, **26**, 1668-1688.
6. J. M. Wang, W. Wang, P. A. Kollman and D. A. Case, *J. Mol. Graphics Modell.*, 2006, **25**, 247-260.
7. A. Jakalian, B. L. Bush, D. B. Jack and C. I. Bayly, *J. Comput. Chem.*, 2000, **21**, 132-146.
8. H. J. C. Berendsen, J. P. M. Postma, W. F. Vangunsteren, A. DiNola and J. R. Haak, *J. Chem. Phys.*, 1984, **81**, 3684-3690.
9. P. Dauber-Osguthorpe, V. A. Roberts, D. J. Osguthorpe, J. Wolff, M. Genest and A. T. Hagler, *Proteins*, 1988, **4**, 31-47.
10. T. A. Halgren, *J. Comput. Chem.*, 1996, **17**, 520-552.
11. A. D. Becke, *J. Chem. Phys.*, 1993, **98**, 1372-1377.
12. C. Y. Peng, P. Y. Ayala, H. B. Schlegel and M. J. Frisch, *J. Comput. Chem.*, 1996, **17**, 49-56.
13. T. H. Dunning, *J. Chem. Phys.*, 1989, **90**, 1007-1023.
14. W. J. Hehre, R. Ditchfield and J. A. Pople, *J. Chem. Phys.*, 1972, **56**, 2257-2261.
15. J. G. Hill, *Int. J. Quantum Chem.*, 2013, **113**, 21-34.
16. J. J. P. Stewart, *Quant. Chem. Prog. Exch.*, 1990, **10**, 86.
17. M. J. S. Dewar, E. G. Zoebisch, E. F. Healy and J. J. P. Stewart, *J. Am. Chem. Soc.*, 1985, **107**, 3902-3909.

## 9. Appendices

### 9.1 Derivations

#### Equation 1

The total energy of a crystallite,  $E_{\text{tot}}$ , is the sum of the bulk layer energies  $E_{\text{bulk}}$  and interface energies  $E_{\text{face}}$ . There are  $N$  layers and  $(N - 1)$  interfaces. Thus:

$$E_{\text{tot}} = NE_{\text{bulk}} + (N - 1)E_{\text{face}}$$

Rearranging:

$$E_{\text{tot}} = N(E_{\text{bulk}} + E_{\text{face}}) - E_{\text{face}}$$

Finally:

$$\boxed{\frac{E_{\text{tot}}}{N} = \frac{-E_{\text{face}}}{N} + (E_{\text{bulk}} + E_{\text{face}})} \quad (1)$$

$E_{\text{face}}$  is estimated by plotting  $\frac{E_{\text{tot}}}{N}$  against  $\frac{1}{N}$  and calculating the gradient of the linear trend.

#### Equations 2-5

Lily pad gels are observed to adopt spheroidal morphologies and do not undergo significant stretching for the majority of their growth. Thus, such a gel may be modelled as a spherical cap, representing a fraction of a sphere of radius  $R$ . The width of the vial is much greater than both the depth of the meniscus and the diameter of the gel, so the gel-vapour interface may be approximated by a planar interface at a minimum distance  $fR$  from the centre of the sphere. In this model, the limits  $f = +1$  and  $-1$  correspond to the cases of a spherical gel or no gel respectively. For a spherical cap of height  $H$ , the volume  $V$  is given by:

$$V = \frac{1}{3}\pi H^2(3R - H)$$

For the gel,  $H = R(1 + f)$ . Thus:

$$\begin{aligned} V &= \frac{1}{3}\pi(1 + f)^2 R^2(3R - R(1 + f)) \\ &= \frac{1}{3}\pi R^3(2 + 3f - f^3) \end{aligned}$$

$$= \frac{1}{3}\pi R^3(2 - f)(1 + f)^2$$

By Pythagoras' theorem, the radius of the circular intersection between the sphere and the interface is  $\sqrt{R^2 - (fR)^2} = R\sqrt{1 - f^2}$ . Thus, the area of the gel at the interface,  $A_{\text{vap}}$ , may be expressed:

$$A_{\text{vap}} = \pi R^2(1 - f^2)$$

The area of the gel-sol interface,  $A_{\text{sol}}$ , is given by:

$$A_{\text{sol}} = 2\pi RH = 2\pi R^2(1 + f)$$

The total energy of the system,  $E$ , is equal to the sum of the gravitational potential energy,  $E_g$ , and the surface energies of the gel-vapour and gel-sol interfaces,  $E_{\text{vap}}$  and  $E_{\text{sol}}$  respectively. In order to evaluate  $E_g$ , it is necessary to sum over the contributions of mass elements at a vertical distance  $z$  from the centre of the sphere:

$$\begin{aligned} E'_g &= g(\rho_{\text{gel}} - \rho_{\text{sol}}) \int_{-R}^{fR} \int_0^{2\pi} \int_0^{\sqrt{R^2 - z^2}} zr \, dr \, d\theta \, dz \\ &= \pi g(\rho_{\text{gel}} - \rho_{\text{sol}}) \int_{-R}^{fR} z(R^2 - z^2) \, dz \\ &= \pi g(\rho_{\text{gel}} - \rho_{\text{sol}}) \left[ \frac{z^2}{2} \left( R^2 - \frac{z^2}{2} \right) \right]_{-R}^{fR} \\ &= \frac{\pi g R^4}{4} (\rho_{\text{gel}} - \rho_{\text{sol}}) (2f^2 - f^4 - 1) \end{aligned}$$

Here,  $g$  is the acceleration due to gravity and  $\rho_{\text{gel}}$  and  $\rho_{\text{sol}}$  the densities of the gel and sol respectively. Note that  $\rho_{\text{gel}} > \rho_{\text{sol}}$  and it is assumed that neither value varies with respect to  $z$ . This is approximately true if the range in  $z$  is much smaller than the distance diffused by the antisolvent over the course of gel growth. However, accuracy could be improved by measuring the variation in  $\rho_{\text{sol}}$  with  $z$  and incorporating this function into the integral expression.

The coordinates of the system must be displaced to produce a fixed gravitational potential energy of zero at the gel-vapour interface ( $z = fR$ ):

$$E_g = E'_g - fg\rho RV$$

$$\begin{aligned}
&= \frac{\pi g \rho R^4}{4} (2f^2 - f^4 - 1) - \frac{\pi g \rho R^4}{3} (2f + 3f^2 - f^4) \\
&= \frac{\pi g \rho R^4}{12} (-8f - 6f^2 + f^4 - 3) \\
&= \frac{\pi g \rho R^4}{12} (f - 3)(1 + f)^3
\end{aligned}$$

where  $\rho = (\rho_{\text{gel}} - \rho_{\text{sol}})$ . If  $\gamma_{\text{vap}}$  and  $\gamma_{\text{sol}}$  are the surface energies of the gel-vapour and gel-sol interfaces respectively, the total energy  $E$  is expressed:

$$E = E_g + \gamma_{\text{vap}} A_{\text{vap}} + \gamma_{\text{sol}} A_{\text{sol}}$$

$$E = \frac{\pi g \rho R^4}{12} (f - 3)(f + 1)^3 + \pi R^2 (1 + f) (\gamma_{\text{vap}} (1 - f) + 2\gamma_{\text{sol}}) \quad (2)$$

To determine the optimal value of  $f$  for a given gel mass,  $E$  is differentiated with respect to  $f$  at constant  $V$  and set to zero:

$$\begin{aligned}
\left(\frac{\partial E}{\partial f}\right)_V &= \pi R \left(\frac{\partial R}{\partial f}\right)_V \left( \frac{g \rho R^2}{3} (f - 3)(f + 1)^3 + 2(1 + f)(\gamma_{\text{vap}}(1 - f) + 2\gamma_{\text{sol}}) \right) \\
&+ \pi R^2 \left( \frac{g \rho R^2}{3} (-2 - 3f + f^3) + 2(\gamma_{\text{sol}} - f\gamma_{\text{vap}}) \right) = 0
\end{aligned}$$

Noting the expression for  $V$  and that  $R \neq 0$ :

$$\begin{aligned}
\left(\frac{\partial R}{\partial f}\right)_V (1 + f) \left( \frac{g \rho R^2}{3} (f - 3)(1 + f)^2 + 2(\gamma_{\text{vap}}(1 - f) + 2\gamma_{\text{sol}}) \right) - \frac{g \rho V}{\pi} \\
+ 2R(\gamma_{\text{sol}} - f\gamma_{\text{vap}}) = 0
\end{aligned}$$

From the expression for  $V$ :

$$\begin{aligned}
R &= \left( \frac{3V}{\pi(2 - f)(1 + f)^2} \right)^{1/3} \\
\left(\frac{\partial R}{\partial f}\right)_V &= \left( \frac{3V}{\pi(2 - f)^4(1 + f)^5} \right)^{1/3} (f - 1)
\end{aligned}$$

Thus:

$$\begin{aligned} & \left( \frac{3V}{\pi(2-f)^4(1+f)^2} \right)^{1/3} (f-1) \left( \frac{g\rho}{3} \left( \frac{3V}{\pi(2-f)(1+f)^2} \right)^{2/3} (f-3)(1+f)^2 \right. \\ & \quad \left. + 2(\gamma_{\text{vap}}(1-f) + 2\gamma_{\text{sol}}) \right) - \frac{g\rho V}{\pi} + 2 \left( \frac{3V}{\pi(2-f)(1+f)^2} \right)^{1/3} (\gamma_{\text{sol}} - f\gamma_{\text{vap}}) \\ & = 0 \end{aligned}$$

Setting  $a = (2-f)(1+f)^2$ :

$$\begin{aligned} & \left( \frac{3V}{\pi a} \right)^{1/3} \frac{f-1}{2-f} \left( \frac{g\rho}{3} \left( \frac{3V}{\pi a} \right)^{2/3} (f-3)(1+f)^2 + 2(\gamma_{\text{vap}}(1-f) + 2\gamma_{\text{sol}}) \right) - \frac{g\rho V}{\pi} \\ & \quad + 2 \left( \frac{3V}{\pi a} \right)^{1/3} (\gamma_{\text{sol}} - f\gamma_{\text{vap}}) = 0 \end{aligned}$$

Simplifying and collecting terms:

$$\begin{aligned} & \frac{(f-1)}{(2-f)^2} \left( g\rho(f-3) \left( \frac{aV^2}{3\pi^2} \right)^{1/3} + 2(2-f)(\gamma_{\text{vap}}(1-f) + 2\gamma_{\text{sol}}) \right) - g\rho \left( \frac{aV^2}{3\pi^2} \right)^{1/3} \\ & \quad + 2(\gamma_{\text{sol}} - f\gamma_{\text{vap}}) = 0 \end{aligned}$$

$$bV^{2/3} \left( \frac{(f-1)(f-3)}{(2-f)^2} - 1 \right) = \left( 4 \left( \frac{1-f}{2-f} \right) - 2 \right) \gamma_{\text{sol}} + \left( 2 \frac{(1-f)^2}{2-f} + 2f \right) \gamma_{\text{vap}}$$

where  $b = g\rho \left( \frac{a}{3\pi^2} \right)^{1/3}$ . Solving for  $V$ :

$$\begin{aligned} & bV^{2/3} \left( \frac{f^2 - 4f + 3 - 4 + 4f - f^2}{(2-f)^2} \right) \\ & = \left( \frac{4 - 4f - 4 + 2f}{2-f} \right) \gamma_{\text{sol}} + \left( \frac{2 - 4f + 2f^2 + 4f - 2f^2}{2-f} \right) \gamma_{\text{vap}} \end{aligned}$$

$$bV^{2/3} \left( \frac{-1}{2-f} \right) = -2f\gamma_{\text{sol}} + 2\gamma_{\text{vap}}$$

$$\boxed{V = 2\sqrt{6}\pi \left( \frac{2-f}{1+f} \right) \left( \frac{f\gamma_{\text{sol}} - \gamma_{\text{vap}}}{\rho g} \right)^{3/2}} \quad (3)$$

Rearranging the expression for  $V$  reveals a linear relationship between  $\gamma_{\text{vap}}$  and  $\gamma_{\text{sol}}$ :

$$\boxed{\gamma_{\text{vap}} = f\gamma_{\text{sol}} - \frac{\rho g}{2} \left( \frac{1}{\sqrt{3}\pi} \left( \frac{1+f}{2-f} \right) V \right)^{2/3} = f\gamma_{\text{sol}} + c} \quad (4)$$



Physical solutions  $V > 0$  are possible if and only if  $\gamma_{\text{vap}} < f\gamma_{\text{sol}}$ . As the gel drops,  $f \rightarrow 1$  and  $\gamma_{\text{vap}} < \gamma_{\text{sol}}$ . At the beginning of gel growth,  $V \rightarrow 0$  and the inequality  $f \rightarrow f_{\text{start}} \geq -1$  must hold, such that

$$\left(\frac{\gamma_{\text{vap}}}{\gamma_{\text{sol}}}\right) \rightarrow f_{\text{start}} \geq -1$$

Thus  $\gamma_{\text{vap}} \geq -\gamma_{\text{sol}}$ . Combining these observations, it may be deduced that  $\gamma_{\text{sol}} > 0$  for all  $f$ : lily pad gelation cannot occur if the gel-sol interface displays a negative surface energy. The energy of the gel-vapour interface can be positive or negative, but must not deviate from zero by more than the value of  $\gamma_{\text{sol}}$ . The allowed values of  $(\gamma_{\text{sol}}, \gamma_{\text{vap}})$  may be represented as one quadrant in a plot of  $\gamma_{\text{vap}}$  against  $\gamma_{\text{sol}}$ , bounded by the lines  $\gamma_{\text{vap}} = \gamma_{\text{sol}}$  and  $\gamma_{\text{vap}} = -\gamma_{\text{sol}}$  and bisected by the positive x-axis. For a given value of  $V$  with constant  $\rho g$ , a straight line in the plot intersects all combinations  $(\gamma_{\text{sol}}, \gamma_{\text{vap}})$  that will produce gels of identical shape. The shape is specified by the value  $f$ , given by the gradient of the line, while  $V$  may be determined from the y-intercept. The shape of the gel at the beginning of growth is indicated by the slope,  $f_{\text{start}}$ , of the line connecting  $(\gamma_{\text{sol}}, \gamma_{\text{vap}})$  with the origin. This parameter is given by the ratio of the two surface energies:

$$f_{\text{start}} = \frac{\gamma_{\text{vap}}}{\gamma_{\text{sol}}}$$

If  $\gamma_{\text{vap}} > 0$ , increasing  $f$  always produces a stable morphology with a larger value of  $V$ . The minimum in  $E(f)$  is the only turning point corresponding to a physical value of  $V$ , so  $V(f)$  can be evaluated directly from equation (2). The minimum at  $f = 1$ ,  $V(1)$ , is equal to the maximum volume of the gel at the point of dropping,  $V_{\text{end}}$ , and is represented by the intercept of the line with slope  $f = 1$  that intersects  $(\gamma_{\text{sol}}, \gamma_{\text{vap}})$ :

$$V_{\text{end}} = V(1) = \sqrt{6}\pi \left(\frac{\gamma_{\text{sol}} - \gamma_{\text{vap}}}{\rho g}\right)^{3/2}$$

If  $\gamma_{\text{vap}} < 0$ ,  $V_{\text{end}}$  is significantly greater than  $V(1)$ , and the function  $E(f)$  may contain a local maximum in addition to a minimum. The maximum occurs for all  $V(f) < V(1)$  where  $f > 0$  and always occurs at a value  $f_{\text{max}} < f < 1$ , where  $f_{\text{end}}$  is the value approached as  $V(f) \rightarrow V_{\text{end}}$ . Because  $f_{\text{end}} < 1$ , the system does not form a complete sphere until dropping occurs. This phenomenon is analogous to flocculation: the value of  $f$  at the local minimum is not necessarily the lowest-energy morphology, but the

system is inhibited from reaching  $f = 1$  by an activation barrier  $E_A$ . As  $V$  increases,  $E_A$  decreases, the minimum shifts to a higher value of  $f$  and the minimum and the maximum move closer together. When  $V_{\text{end}}$  is reached, the minimum and maximum converge such that  $E_A = 0$ , and there is a spontaneous transition  $f \rightarrow f_{\text{end}}$  as dropping takes place. For unphysical values of  $V > V_{\text{end}}$ ,  $E$  exhibits only a local maximum, which shifts to higher  $f$  as  $V$  increases and reaches  $f = 1$  at  $V(1)$ . It should be noted that  $V$  is often smaller than  $V_{\text{end}}$  at the point of dropping, as the small magnitude of  $E_A$  in the region of  $V_{\text{end}}$  means that the system is sensitive to even minor inputs of energy or environmental changes.

Calculating  $V_{\text{end}}$  in the case  $\gamma_{\text{vap}} < 0$  is relatively challenging, as the parameter  $f$  in equation (3) specifies the position of the maximum in  $E(f)$  for all  $f > f_{\text{end}}$ . The solution is to maximise  $V$  with respect to  $f$ :

$$\frac{\partial V}{\partial f} = 2\sqrt{6}\pi \left( \left( \frac{-1}{1+f} - \frac{2-f}{(1+f)^2} \right) \left( \frac{f\gamma_{\text{sol}} - \gamma_{\text{vap}}}{\rho g} \right)^{3/2} + \frac{3\gamma_{\text{sol}}}{2\rho g} \left( \frac{2-f}{1+f} \right) \left( \frac{f\gamma_{\text{sol}} - \gamma_{\text{vap}}}{\rho g} \right)^{1/2} \right) = 0$$

The solution  $f\gamma_{\text{sol}} - \gamma_{\text{vap}} = 0$  corresponds to the trivial case  $V = 0$ . For the other solutions:

$$f(1+f)\gamma_{\text{sol}} - 2(\gamma_{\text{sol}} + \gamma_{\text{vap}}) = 0$$

Thus:

$$f = \frac{1}{2} \left( -1 \pm \sqrt{9 + 8 \frac{\gamma_{\text{vap}}}{\gamma_{\text{sol}}}} \right)$$

The negative root in this expression returns an unphysical value  $f < -1$  for all possible negative ratios of  $\gamma_{\text{vap}}$  and  $\gamma_{\text{sol}}$ , so  $f_{\text{end}}$  must correspond to the other solution:

$$\boxed{f_{\text{end}} = \frac{1}{2} \left( -1 + \sqrt{9 + 8 \frac{\gamma_{\text{vap}}}{\gamma_{\text{sol}}}} \right)} \quad (5)$$

It is interesting to note that the value of  $f_{\text{end}}$  depends only on the ratio of the surface energies, so this expression applies generally to all possible physical scenarios where  $\gamma_{\text{vap}} < 0$ . As expected,  $f_{\text{end}} = 1$  for  $\gamma_{\text{vap}} = 0$  and unphysical values  $f_{\text{end}} > 1$  are obtained for  $\gamma_{\text{vap}} > 0$ . Substituting the expression into equation (3):

$$V_{\text{end}}(\gamma_{\text{vap}} < 0)$$

$$= \frac{\sqrt{3}\pi}{4} \left( \frac{3 \sqrt{9 + 8 \frac{\gamma_{\text{vap}}}{\gamma_{\text{sol}}} - 4 \frac{\gamma_{\text{vap}}}{\gamma_{\text{sol}}} - 7}}{\frac{\gamma_{\text{vap}}}{\gamma_{\text{sol}}} + 1} \right) \left( \frac{\gamma_{\text{sol}} \sqrt{9 + 8 \frac{\gamma_{\text{vap}}}{\gamma_{\text{sol}}} - 2\gamma_{\text{vap}} - \gamma_{\text{sol}}}}{\rho g} \right)^{3/2}$$

The growth profile of the gel at fixed values of  $\gamma_{\text{vap}}$  and  $\gamma_{\text{sol}}$  can be evaluated by drawing lines of increasing gradient through the point  $(\gamma_{\text{sol}}, \gamma_{\text{vap}})$ . Conversely, unknown values of  $\gamma_{\text{vap}}$  and  $\gamma_{\text{sol}}$  may be estimated by measuring  $f$  and  $V$  at each stage of gel growth, plotting the corresponding straight lines on the surface energy plot, and identifying the points of intersection for successive lines. If there is no common point of intersection, it may be concluded that  $\rho$ ,  $\gamma_{\text{vap}}$  and/or  $\gamma_{\text{sol}}$  do not remain constant throughout the experiment. It should be noted that the first physical value of  $f$ ,  $f_{\text{start}}$ , corresponds to the gradient of the straight line that intersects both  $(\gamma_{\text{sol}}, \gamma_{\text{vap}})$  and the origin. For  $\gamma_{\text{vap}} > 0$ , all lines with gradients larger than  $f_{\text{start}}$  correspond to energetically accessible morphologies. For  $\gamma_{\text{vap}} < 0$ , however, lines with gradients above  $f_{\text{end}}$  do not correspond to real stages in the gel growth profile. Coordinates of equal  $V_{\text{end}}$  are specified by curved lines in the surface energy plot.

## 9.2 CSD survey

REFCODE	Urea-urea motifs?	REFCODE	Urea-urea motifs?	REFCODE	Urea-urea motifs?
AGOLIS01	Y	IJUXOB	Y	RASGOI	Y
AGOLOY	Y	JEHFAE		RASGUO	
AGOLUE	Y	JEMQOI	Y	RAWBOI	Y
AGOMAL	Y	KASLOH	Y	REMRAD	
AGOMIT	Y	KEVQAF		RENKOM	
ASUQEK	Y	KISNOQ	Y	RETGAA	
AZOMUY	Y	KOCXOQ		REZQUK	
BABHAQ	Y	KOCXUW		REZRAR	
BASXOJ		KOCYAD		REZRIZ	
BAXQAT		LAJDIL		REZRIZ01	
BEHTIT	Y	LARFOB		REZROF	
BEHTOZ	Y	LETLIH	Y	REZRUL	
BIDRUD		LETLON	Y	RIDLUN	
BORQOP	Y	LETLUT		RIYXUU	
BUKSIK	Y	LETMAA		ROCPIJ	Y
CAZBUB	Y	LETMEE		RUSLAU	
CAZCEM	Y	LETMII		RUSPAX	
CIQMEU		LIHYIM	Y	SAGRID	Y
COFKUE	Y	LIHZAF		SAWLAE	
COFLEP	Y	LIHZEJ		SICHOC	
COFLOZ	Y	LIHZIN		SICHUI	
CUCBAD		LIHZOT		SICJAQ	Y
CUTHOQ	Y	LIHZUZ		SIHROS	
DASNUH		LIPBIW	Y	SUBCOJ	
DONQOO		LIPBIW01	Y	SUSPON	Y
DUVZIF	Y	LIPBOC	Y	TOLBUS	
EFIKIO01	Y	LISDIB		TOLCAZ	
EFIKOU	Y	LOBHUH	Y	TOLCED	
EFIKOU02	Y	MEXBIA		TOLCIH	
EFIKUA	Y	MIXFOP		TOLCON	
EJISEW		MIXFUV	Y	TOLCUT	
ELIGAH	Y	MOQNEL	Y	TOLDAA	
EMIRUO		MOWWAY	Y	TORWAZ01	
EQOHIB		MOZJAO	Y	TUJZIJ	
EXESUW	Y	MOZJES	Y	TUJZOP	
EZUKIT01		MUMRER	Y	UJISEM	Y
EZUKOZ01		NADHIL	Y	UJISIQ	
EZUKUF01		NEJVIJ		UJISOW	
FABFAR	Y	NEJVOP	Y	VEGQUV	
FABFEV	Y	NEKZIN		VEGRAC	Y
FABFIZ	Y	NIHROM		VEGREG	Y
FACWIR		NIZHIP	Y	VEGRIK	Y
FACWOX		NOWZEG	Y	VEGROQ	Y
FANWEX		NOWZIK	Y	VEGRUW	Y

FANWIB	Y	NOWZOQ	Y	VIDSOS	
FANWOH		NOWZUW		VIDSUY	
FANWUN		NOXBAF		VIHDAS	
FANXAU		NOXBEJ		VIHDIA	Y
FANXEY	Y	NOXBIN		VIHDOG	
FANXIC	Y	NOXBUZ		VINBEA	
FANXOI		NUPQIA		VINBIE	
FEGVEU		ODAKUB	Y	VINZAV	
FELFAE		ONICUK	Y	VINZAV01	
FELFEI		OQINUY		VINZID	
FELFIM		OQINUY01		VOCYES	
FELFOS		OQINUY02		VOCYIW	
FELGAF		OQPIO	Y	VOCYUI	
FIJNET		PAVMEF		VOMDAD	
FIWBOD	Y	PAVMIJ		VOMDEH	
FIWBUJ	Y	PEFHOY	Y	VUCTUJ	
FONXUC		PEJKIZ	Y	WESVOG	Y
FONYAJ		PEPROS	Y	WIMSES	
FONYEN		PIBKOB	Y	WIMSIW	
FUWHAI	Y	PIBTUQ		WIMSUI	
GAMQER	Y	POGMAB		WIMTAP	Y
GIRYIQ		POHHOK	Y	WOHFEG	Y
GUDKAR		POJNOT		WOHFIK	Y
GUDKEV		PORGOU06	Y	XAFBAK	
GUTBAZ		POXPAU	Y	XERDED	Y
HAFQIQ		POXPEY		XOGBOM	
HAGVER	Y	PUKCOO	Y	XOLJAK	
HAGVOB		QAVQAG		XOLJEO	Y
HAWQEC		QAVQEK		XUFWIG	
HEHRAP	Y	QENGAS	Y	YEKQAI	Y
HEHRET	Y	QENGEW	Y	YOJZUU	
HEKWOL		QIBJAN		YOXQOS	
HICWOH		QOCLAW		YOXQUY	
HIVVOY	Y	QOCLEA		YOXRAF	
HIWPEI	Y	QOXRAY		YOXREJ	
HOMSUZ		QOXREC		YUZHEI	
HOMTIO		QUSBUD	Y	ZAHFUM	Y
HOSNOU		QUSCEO		ZITREB	
IDEMOV	Y	QUSDEP	Y		
IDEMUB	Y	QUSWIM	Y		

**Table A1** Bis(urea) structures in the Cambridge Structural Database (CSD), version 5.37.<sup>9</sup> There are 250 well-defined, inequivalent structures containing exactly two acyclic urea moieties. Of these, 102 (41%) display urea-urea interactions. The majority of urea-urea hydrogen bonds (69 structures, 68%) are found in continuous tape motifs.

REFCODE	Repeat	Pairs of syn-parallel tapes?	Polar space group?	All tapes syn-parallel?
AGOLUE	A			
AGOMAL	A			
AGOMIT	A			
ASUQEK	A			
AZOMUY	A	Y		
BABHAQ	A			
CUTHOQ	A			
EFIKIO01	A		Y	
EFIKOU	A		Y	
EFIKOU02	A		Y	
EFIKUA	A	Y	Y	Y
FABFAR	A			
FABFEV	A	Y		
FABFIZ	A	Y		
FANXIC	A			
FIWBOD	A			
FIWBUJ	A	Y		
FUWHAI	A			
HIWPEI	A	Y	Y	Y
IDEMOV	A			
IDEMUB	A			
LETLON	A	Y		
LIPBIW01	A	Y		
NEJVOP	A			
NOWZEG	A			
NOWZIK	A			
NOWZOQ	A			
ODAKUB	A			
PEJKIZ	A			
RAWBOI	A	Y	Y	Y
ROCPIJ	A		Y	
SICJAQ	A			
VEGRAC	A	Y	Y	Y
VEGREG	A	Y	Y	Y
VEGRIK	A			
WIMTAP	A	Y		
AGOLIS01	AB			
HIVVOY	AB			
MOWWAY	AB	Y	Y	
ONICUK	AB	Y		
PEPROS	AB		Y	
PIBKOB	AB			
UJISEM	AB			
VEGROQ	AB	Y		
VEGRUW	AB	Y		
XOLJEO	AB			

AGOLOY	AABB			
FANWIB	AABB	Y	Y	Y
LETLIH	AABB		Y	
PUKCOO	AABB			
JEMQOI	ABC		Y	
QENGAS	ABC		Y	
LIPBIW	AABC	Y		
SAGRID	ABCD	Y	Y	
BEHTOZ	1 tape	N/A		
IJUXOB	1 tape	N/A	Y	Y
LIPBOC	1 tape	N/A		
NIZHIP	1 tape	N/A		
PORGOU06	1 tape	N/A		
QUSBUD	1 tape	N/A		
QUSDEP	1 tape	N/A		
WOHFIK	1 tape	N/A		
YEKQAI	1 tape	N/A	Y	
ZAHFUM	1 tape	N/A	Y	Y
<b>Total</b>	<b>64</b>	<b>19</b>	<b>19</b>	<b>8</b>

**Table A2** Bis(urea) structures in the CSD (version 5.37) displaying continuous urea-urea tape motifs. Note that only structures occupying one of the 68 polar space groups may exhibit urea tape networks in which all tapes are syn-parallel (i.e. an entry of “Y” in column 5 must be accompanied by entries of “Y” in columns 3 and 4). In networks categorised as “1 tape”, each bis(urea) molecule is involved in only one  $\alpha$  tape, mostly commonly due to the presence of an intramolecular hydrogen bond between the two urea moieties.

Repeat	Total
A	36
AB	10
AABB	4
ABC	2
AABC	1
ABCD	1
1 tape	10

**Table A3** Frequencies of different bis(urea) network topologies in the CSD (version 5.37).

ADEZEP	DOWTAL	KEWSOW	POPMOX	UYUTIS
ADIFAV	DUCSEA	KIDXEC07	POPMUD	VABQUM
AFIPIQ	DUNTUC	KIVLIM	POQYIE	VAPGOI
AFIPIQ01	EGUDIV	KIVLOS	PUCGLR10	VATLIN
AGOKIR	EKAXOD16	KOSHEF	PUQYOQ	VATLOT
AKELIM	EKECAY02	KPRCGM20	PUQYOQ01	VATLUZ
ALEFUT	ELAPIR	KUDZIS	PUQYOQ02	VATMAG
ALEGAA	EMIPW01	KUGCUK	PUQYOQ03	VECSAZ

APUXUF	EPEVEB	LAKXOM	PURTRE	VILLUZ
AQETIZ	EVEQEC	LELROJ	QACLAH	VIMGUV
ASITEC01	EVEQEC01	LIDCEH	QAJSIE	VINYEW
AWUGIJ	EVIQEF	LIDLUH	QAJSOK	VOCBOG
AYUHEI	EYUJEO	LINSEG	QALXAE	VODWER
AZUMIS	FABPUV	LIWBOJ	QALXEI	VORBAF
BAQJUY	FIVRAD	LOFDUH	QANYIO	VUZLIM
BEBLOJ	FUHQEF	LOFFAP	QAZXEU	WEFQAB
BEFSIO	FUZQEX	LOFFIX	QAZXIY	WERTET
BORHAS	GAQQAS	LOFWAG	QEHDUC	WEXBEG
BORHIA	GEJHEJ	LOHSOR	QERXUG	WEXMOD
BORHOG	GIDTIW	LUKHOP	QIBHEO02	WICBAL
BOTRIL10	GIHMER	MAPJOD	QIRJEG	WOGXUM
BPCTHA	GIHMUH	MEXBOG	QIVNUG	WOKNOB
BUDSOJ	GIJVEC	MIXGAC	QUCWOB	WOMGUC
BUFXOP	GIYJEE	MOCNIC	QUCWUH	WOMHAJ
BUXFEG	GOFBEK	MOQNAH	QUCXAO	WOMHEN
BUXFEG01	GOFBIO	NAFVIA	QUCXES	WOYHIB
CABCOX	GORBOE	NAFWAT	QUCXIW	WOYQOQ
CABCUD01	GORBOE01	NAXHUR	QUCXOC	WUNNUP
CBOHAZ04	HABTEJ	NAXJAZ	QUCXUI	WUPYAI
CBOHAZ05	HAMCAB	NAXJON	RABYOJ	XAVNAL
CDSCBA	HANFUY	NAXJUT	RACCOO	XAVWIC
CDSCBB02	HAYRAB	NEMRON	REHFIV	XAYHUA
CDSCBC	HOBXOM	NEPKIE	REHFOB	XAYJAI
CDSCBD	HOBYAZ	NEVXIV	SAKCIQ	XAYSUL
CDSCBE	HODHAK	NICGEL	SERXAO	XELQUB
CEJTEQ	HOFDAI	NICGOV	SISSOE	XENHEE
CEJTIU	HOFKAP	NIDYUW	SOBCUI	XENSOY
CEVSAY	HOGYUZ	NIWFOQ	SOBPEE	XEQDEC
CIDGIH	HYXBUR10	NUCDIY	SOBP EE01	XERDIH
CIGSES	ICAKAY01	NUVCAI	SOBP EE02	XIGLAB
CIJFOS	ICILUC	OBUNAC	SOWQIE	XIVDEN
CIWMEC	IFAFEB	OCAKUZ	SUVGUL	XOWNIH
CIWWEM	IFEPAL	ODOMIE	TAWPUD	XUXNOT
CIZLUS	IHOWEI	OGECIN	TEDBUZ	XUYTUG
CNBPCT	INUGOO	OGIQIF	TEHBIR	YAGWAG
COGNIX	ISAGUF	PACNEO	TEJNEC	YAXZAA
CORZEQ	IWUXAA	PASHUN	TEVMOX	YAYYON
COYNOU	IWUXEE	PAWPAG	TEWJOV	YEJQUZ
CPDPSC11	IZOLIT	PAWXUI	TIRYIC	YIFVIT
CPFBUR01	JAHSUG	PCMTRE10	TOHBUN01	YIHRUC
CUGHUH	JAXGEV	PCTRIB10	TOLMOX	YINCAB
CUQTIR	KABMOR	PELKAT	TOLPUF	YINFOS
CYCOXB	KAJSUK01	PELKEX	UJIHAX	YIVGUG
CYNONB	KARTED	PELKIB	UJOLAH	YOCVOC
DATKAL	KATBIS	PELKOH	URAWUG	YUZHUV
DELRES	KATFAN	PIFZAG	USOCOV	ZEWDUC
DEMDOP	KEMZUZ	PIFZAG01	UXAYAU	ZINCEG



**Table A4** Structures in the CSD (version 5.36) containing *syn-anti* mono(urea)s.

ABIBEU	EXAHEQ	KAZVEN	QEBBOQ	VIPBED01
ACURUN	EZAXOS	KAZWAK	QEMFEU	VIRTUN
ACUSAU	EZAXUY	KEDREQ	QEYBOM	VIXMOF
AGOKOX	FAWZEK	KETSUY	RAVVAN	VIXNAS
AGOLAK	FAWZOU	KOMBEV	RAVVER	VOBNIJ
AGOMEP	FAXBAJ	KOXPIW	REHQUR	VOFDAX
AJUJOF	FAXBIR	KUWHIT	REMWOV	VOHCEC
AJUJUL	FAXBOX	LAXJOK01	REPRUZ	VOKXAW
AKENOU	FEBWUG	LAXJOK02	RESRIR	VOYNUS
AKENUA	FEMQEU	LAXJOK03	RIPBOH	VUFWID
ALOFOW	FEMQIY	LAXJUQ	RISVEW	VUKJIV
APURIN	FEZWUE	LAXKAX	RISWUN	VUSPUV
AQOSAB	FITYAI01	LEPMAU	RIXBEH	VUSQAC
AXAWIG	FODXUT	LIDCAD	ROCNIH	VUZFUS
AZUQOB	FUDJAQ	LIKNEY	ROCPAB	VUZZAS
BAGPII	FUDJIY	LIPBUI	ROFGIE	VUZZUL
BEJTEP	FUDJOE	LIPCAP	ROHKO0	WAMGAU
BESCAD	FUWHIP	LIYLAI	RUJDOP	WARXOC
BIMWUQ	GAKGAA	LIYLEM	SAGXOP02	WARYAP
BOFXOK	GAPJAK	LIYLIQ	SAGXOP03	WEGLUP
BOFXUQ	GASMUJ	LONXIX	SAYQEP01	WEGQEG
BOJTIF	GASNAQ	MAHWAV	SEPQEJ	WEGQIK
BOJTUR	GASNEU03	MAMPUR	SEPTIQ	WEGQUW
BONLAS	GASNIY01	MBECUR	SEPTUC	WESKUB
BOZYOF	GAWZUB	MEHGAH	SIFDER	WESVEW
BUXVAS	GAXBAK	MEKSEA	SILVAK	WESWAT
CAGPIL	GEBFEA	MEPWUZ01	SILVOY	WETDIJ
CAZLEW	GIDTES	MEPXAG	SIQTOD	WICBEP
CBHYZS	GIHKUF	MEPXEK	SLFURE	WICBIT
CEGNOT	GIMROJ10	MEWMOQ01	SOBLUQ	WICNAY
CEKBEB	GIMRUP10	MICZII	SOBNOM	WIGJEC
CIBQIN	GIMSAW10	MIPLUT	SOHNAF	WIVGUF
CILFEJ	GIMSEA10	MIPMAA	SOKVOE	WIXYUZ
CIVRUV01	GOJBUC	MUWQIF	SOQXUR	WIXZAG
CIWNON	GOKXAF	MUWQOL	SUNHUF	WIXZEK
CIWPOP	GOLWUA	MUWQUR	SUZNIL	WIXZIO
CIWVIP	GURHUX	MUZSEG	SUZWOA	WOCFAW
COMZOT	HAFKOO	MXYLUR	TAMSUX	WOCFEA
CONKUM	HAMCEF	NATGIA04	TEPNEH	WOCFIE
CONLEX	HAMCIJ	NEBBIG	TERYIY	WOCFOK
CONMOJ	HASCIN	NEBBOM	TIFLOK	WOCFUQ
CONMUP	HEZTEL	NEBGEH	TIHTIO	WOCLIL
CONNEA	HIFZUR	NEBYID	TIMXIY	WOGZIC
CUCFAH	HIMPEZ	NEBYOJ	TIVMAN	WOGZOI
CUCFEL	HINWAE	NEBZEA	TIVMER	WOGZUO
CUKPUU	HITFOG	NEBZIE	TIVMIV	WOHBAX
DACPEE	HITFUM	NEGCOR	TIVMOB	WOHBEB

DARSIA	HITGAT	NEHHIT	TIVMUH	WOLPUJ
DARSOG	HITGEX	NIPXAN	TIVNAO	WOLQIY
DASYUS	HOMSOT	NIQFID	TIVNES	WOMHIR
DAZJUL	IDUSIK	NODYEM	TIVNIW	WOMHOX
DAZKAS	IFANOU	NUSVIH	TIVNOC	WOMHUD
DAZKEW	IFANUA	NUSVUT	TIVNUI	WOMJAL
DAZKIA	IFOCEM01	OVEBAT	TIVPAQ	WOMJEP
DEZGIA	IKEGIP	OVEBEX	TIVPEU	WOMJIT
DEZGOG	ILICEL	OVEBIB	TIVPIY	WONZAC
DIGBUR	ILICIP	OVEBOH	TIVPOE	WONZIK
DIGCAY	ILIDEM	OVEBUN	TIXKES	WUDMAK
DIGCEC	INUGAZ	OVECAU	TORSEM02	XANPOT
DIGCIG	IQOLEG	OXULOJ	TORSEM03	XATNIQ
DIGCOM	ISODEZ	OXULUP	TOSBUR	XAZGEM
DIGCUS	IXUDIO	OXUMAW	TUJNUH	XEFFAR01
DIGPIU	JANKOY	OXUMEA	TUJPAP	XEWXON
DIGPUG	JEDKIN02	PAMPOK	TUPMAS	XEFEL
DIGQAN	JEDKOT	PAMPUQ	UCOHUQ	XEYUQ
DISBOW	JEDKUZ	PAQLID	UDEJUK	XINHIN
DISBUC	JEDLAG01	PEFGOX	UDEKAR	XOLHIQ
DISVAD	JEDLEK	PEVREP	UDEKEV	XOMBEG
DIVYOY01	JEDSER	PEZDEE	UDEKIZ	XOPKIW
DIWBUI01	JEDSIV	PEZJUA	UJIGUQ	XUCDOO
DIWDAQ02	JEDSOB	PIHFOB	UJIHEB	YAFJOG
DIWDEU02	JEDSUH	PIHLAU	UJIHIF	YEKNUZ
DOJXEG	JEDTAO	PIHLIC	UJIHUR	YEKPAH
DUNXAL	JEDTES	PIHLOI	UJIJAZ	YEKPEL
DUQGOM	JEHFIM	PIHLUO	UJUVEA	YEKPIP
DUTNEM	JODXAC	PIHMAV	UKIFIE	YEKPOV
DUXBOO	JODXEG	PILFUM	ULIXOD	YEKPUB
ECATOT	JOJZOZ	PIXNER	UXIPOH	YEKQEM
ECATUZ	KABCUN	POJNIN	UYOZUE	YIGQAH
ECAVAH	KAQRUR	POKDIC	VACDIO	YITFEN
ECAVEL	KAQSAY	POQVAT	VIJDID	YIXDIT
EHEHEF	KARTAZ	POQYUQ	VIMQEN	ZAQROA
EKEJAF	KARTIH	POYZOT	VIMZAT	
EWEMEY	KAXJAW	POYZUZ	VIMZEX	
EWEMIC	KAXJEA	PPESIR	VIMZIB	
EWOZUL	KAXJIE	PUHHAC	VINBOK	
EXABIO	KAZVAJ	QAZXUK	VIPBED	

**Table A5** Structures in the CSD (version 5.36) containing non-interacting *syn-syn* mono(urea)s.

AGOKUD	FABDUJ	MOQCAX	SIGBUF	WANPEH
AMAFEZ01	FATWAY	MUBHIB	SILTOW	WARWIV
AQASIV	FATWEC	NAXJIH	SILTOW11	WARWOB
AQATIW	FEBXAN	NEBYUP	SILTOW12	WARWUH
AQAVIY	FEYSEJ	NERPUX	SILTUC	WARXAO
AQAWUL	FICKAF	NIJHUJ03	SILTUC01	WARXES

ASITEC	FICTIU	NIJHUJ04	SISSOE01	WARXIW
AZUDAB	FIQSEE	NOEURA	SUZKII	WARXUI
BAHPIK	FOLRUU	NUQFIP	TAPRAD	WARYET
BATQUK	FUDJEU	NUSVAZ	TEPNEH	WARYIX
BEDMIG01	FUMQIN01	NUSVED	TIVPUK	WEGQOQ
BEDMIG02	FUWJAJ	NUSVON	TIVQAR	WEJBUI
BEDMIG03	GAKGAA	NUVRUS	TIVQEV	WESVIA
BEDMIG06	GEKFEJ	ODAKOV	TOHBUN02	WESVUM
BEDMIG07	GIJYUT	ODIRIE	TOSMUR	WESWEX
BEDMIG11	GOKWUY	OJIYAI	TRURET20	WESWOH
BEDMIG12	HAHCOJ	OJOWOA	TUDLUZ	WEVZED
BEDMIG16	HAWLIB	OKOSUD	TUDLUZ01	WEWRAR
BEDMIG18	HEVXAH	OTEBOF	TUHCUV	WIGJIG
BEQNAN	HEZSUA	OZIVAV	TUHPIV	WIXMEW
BOJCUY	HEZTAH	PAYQAI	TUNZAE	WONZEG
BOZZUM	HORPUB	PEFGIR	UCOYAM	XAVNEP
BUVHOP	IFANIO	PIHLEY	UGIWOX	XAYSOF
BUYZIE	IFEHEG	POTLIT	UJOBEA	XEBRUS
CAJQEK	ILICAH	POTLOZ	VAJFUI	XEGDES
CAJQIO	IPPSUR	POZWEG	VALPII	XEWXIH
CAJQOU	IWEHIB	QAXSUD	VALPII01	XINRIV
CAJRAH	IZUVII	QAXSUD01	VAQMIK	XINRIV01
CAJRIP	JADHEC	QAZXOE	VAQMIL	XINRIV02
CEGBAT	JEDRUG	QIYMEQ	VARGIF	XISNUI
CIMKUG	JEDSAN	QONSET	VEGSAD	XIXQOL
COCMEN	JEDTIW	QQQXOK	VEJBOB	XNTLUR
CONKOH	JODVED	QQQAFY01	VEPKIL01	XOMLIV
CONLAT	JUPDED	QQQAGA04	VEPTUG	XOYYEP
CONMID	KAXHUO	RABVIV	VICZIR	XUGNAO
CUNCEU	KEVRAG	RALGAO	VIMYEV	XURBIW
CUSWUJ	LAGKIP	REKDAM	VINZOJ	YALVOX
CYHXUR08	LAGKOV	REKDEQ	VINZUP	YEHHUQ
DATTUN	LAJFAF	RIPBOH01	VIRVAV	YIJBEZ
DATWOK01	LECLEL	RIPBUN	VOFCOK	YIJBID
DCPHUR	LEGZUT	ROCNON	VOFDIF	YIKDAZ
DEDDOG	LENXOT	ROCNUT	VOFDOL	YUNRIJ
DEDFAU	LIDJEP	ROHQAI	VOFFAZ	YUYSAM
DEVVUV	LIWRIT	RULPOD	VOPDUA01	ZINZUR
DIDVES	LIWROZ	SAGXOP01	VOPFAI	ZIPBAB
DPCBHZ	LIWRUF	SARZAM	VOPFEM01	ZIPBEF
DPUREA09	LIWSAM	SARZOA04	VUKHUF	ZIPBIJ
EFETEQ	LIWSEQ	SEPQIN	VUKJAN	ZZZPUS04
EFISOD	MAHWEZ	SEPQOT	VUKJER	ZZZPUS05
ETOBII01	MBZAUR10	SIGBAL	VUSPOP	ZZZPUS10
EYOMAG	MEPXEK01	SIGBEP	VUSQEG	ZZZPUS13
EZAYAF	MILTOS	SIGBIT	WAMXEN	
EZAYEJ	MIXZAV01	SIGBOZ01	WANPAD	

**Table A6** Structures in the CSD (version 5.36) containing interacting *syn-syn* mono(urea)s.

BAWJIU	<b>GERVUW</b>	OHOGO	SASKEE	XAGRUS
BAWJOA	GIXZOD	OHOGUN	TEFZUA	XEW TOK
BAWJUG	GIYCAT	OHOHAU	TEGBAJ	XEWTUQ
BULKUP	GIYCEX	OKOKIJ	TEGBEN	XEUVAY
BULLAW	GIYCIB	OKOKOP	TOMJEM	XIBQEG
BULLEA	GIYCOH	OKOKUV01	TOMJIQ	XIBQIK
CAZCAI	GIYCUN	OLAVIH	TOMMIT	XIDBES
CEVWOQ	GIYDAU	OLAVON	TOMMOZ	XIDBIW
CEVXIL	GIYDEY01	OLAVUT	VAMJUQ	XIDBOC
CITYIO	HANWUQ	OLAWAA	VAMKAX	XUFFEK
CITYOU	HIBPIT	ONERAB	VIFYIU	XUFFIO
DAQWEZ	HIBPOZ	ONEREF	VIFYOA	YACJAP
DAQWID	HIJFOW	ONERIJ	WANKUT	YEMJOQ
DAQWOJ	HIJGAJ	OWISUJ	WANLAA	YIXJAS
DASZAZ	HIJGEN	PUSTIH	WANLEE	YIXJEW
DASZED	ISOWAP	QAMHIV01	WANLII	YIXJIA
DASZIH	ISOWET	QIQSIU	WANLOO	YIXJOG
DIXWIR	IWEHAT	QIQSOA	WANLUU	YIXLAU
DIXWOX	IXEMON	QIQSUG	WANMAB	YOZQIO
DOKDAJ	KECHEG	QOFVIS	WANMEF	YOZQOU
<b>DUVLEM</b>	KEVQEJ	QOFVOY	WANMIJ	YOZROV
EBONUF	KEVQUZ	QOLKIL	WANMOP	YUSDIA
EGUFER	KIKCUE	<b>REPQOU</b>	WANMUV	YUSDOG
EHIXID	MINTUY	RIBKIY	WEWTEX	YUSDUM
FABPOO	NEHGOY	SAKBIR	WIDXEO	<b>ZATBON</b>
FABPUU	OCUPAF	SAKBOX	WITMUJ	<b>ZATBUT</b>
FAFYUI	OCUPEJ	SAKCUE	WITNAQ	
FUXYIH	OCUPIN	SASKAA	WITNEU	

**Table A7** Structures in the CSD (version 5.36) containing tris(urea)s. Structures consisting of linear molecules are highlighted in bold italics; molecules in the remaining structures are multipodal.

AXEYAD	<b>DEXROP</b>	KEYKEG	<b>QIFPUS</b>	VADDAH
AXEYEH	<b>ESICOZ</b>	KICZIG	<b>REPQAG</b>	VATXIX
<b>BEPSOG</b>	<b>ESICUF</b>	LISCAS	<b>REPQUA</b>	VATXUJ
<b>BEPSUM</b>	EZULAM03	LISCIA	SAWLEI	VATYAQ
BEQFUZ	EZULAM05	LISCOG	SAWLIM	VAVCUQ
CONKUN	EZULEQ03	NIJHEU	SAWLOS	VEZPIB
COTBAP	EZULIU	OLAWEE	SIHSAF	VEZQUO
<b>DEXQAA</b>	EZULO04	PEDQUL	SIHSEJ	VEZRAV
<b>DEXQEE</b>	FANXUO	PEDRAS	TEJQOP	WOQCEK
<b>DEXQII</b>	GIVDOF	PEDREW	TIDWEI	XAFCEO
<b>DEXQOO</b>	GUBYIM	<b>PEKZIQ</b>	TISSYI	<b>XAXFUY</b>
<b>DEXQUU</b>	HAGVIV	<b>PEKZOW</b>	TISSOE	XOPVEE
<b>DEXRAB</b>	IFOWEG	PIBKIV	UHEQIH	XUPZEO
<b>DEXRAB01</b>	KEVQIN	<b>QIFPIG</b>	<b>USOJUI</b>	<b>YUBQIW</b>
<b>DEXRIJ</b>	KEVQOT	<b>QIFPOM</b>	<b>UZHIV</b>	<b>ZATCAA</b>

**Table A8** Structures in the CSD (version 5.36) containing tetrakis(urea)s. Structures consisting of linear molecules are highlighted in bold italics; molecules in the remaining structures are multipodal.

AMUVIO01	FEBNOR	<b>MAVSEJ</b>	<b>OJOCO</b>	SUVMIG
<b>BEPRUL</b>	FEBNUX	<b>MAVSIN</b>	PEPNEF	<b>XUNFIW</b>
<b>BEPSAS</b>	FEBPAF	<b>MAVSOT</b>	PEPNIJ	<b>XUNFOC</b>
<b>BEPSEW</b>	FEBPEJ	MOGLIE	<b>PIBFIR</b>	<b>XUNFUI</b>
<b>BEPSIA</b>	<b>GERWAD</b>	NIVFOP01	<b>PIBFOX</b>	<b>XUNGAP</b>
<b>CEXMID</b>	JOGZIQ	<b>OCUNAD</b>	<b>PIBFUD</b>	YAKFOH
<b>CEXMOJ</b>	JOGZOW	<b>OCUNEH</b>	REPMAC	YAZQUL
<b>CEXMUP</b>	LEXMIM	<b>OCUNIL</b>	<b>REPQEK</b>	<b>ZATCEE</b>
CONLAU	<b>MAVROS</b>	<b>OCUNOR</b>	<b>REPQIO</b>	<b>ZATCII</b>
<b>DIJRUL</b>	<b>MAVRUY</b>	<b>OCUNUX</b>	<b>REPPRAH</b>	<b>ZATCOO</b>
FEBNIL	<b>MAVSAF</b>	<b>OJOCIA</b>	SUVMEC	

**Table A9** Structures in the CSD (version 5.36) containing oligomers with five or more urea groups. Structures consisting of linear molecules are highlighted in bold italics; molecules in the remaining structures are multipodal.

CUXBUT	HEKVUQ	LEYWUJ	NOQSOB	SEQGEB
CUXCAA	HEYDEV	LISCEW	NUCFIB	SEQGIF
CUXCEE	HEZLAA	LISCUM	ODAHEI	SEQGOL
CUYWOJ	IPONOQ	LISDAT	ODAHIM	SEQGUR
DEPDAE	JEXNEG	LISDEX	ODAHOS	SEQHAY
DEPDEI	JEYZET	LOFKIC	OWISIX	SETKIM
EHIXOJ	JOHYIP	LOFKOI	OWISOD	SIHRUY
EJISAS	JOHYOV	MEXCAT	PEFGUD	URIZOL
EJISIA	KAJFUY	NANZAE	PEFHAK	VEDYAF
EJISOG	KAJGAF	NANZEI	PEFHEO	VEDYOT
EJISUM	KAJGEJ	NAVWEN	PEFHIS	VEDYUZ
FELFUY	KAJGIN	NAVWIR	PEFHUE	VINBAW
FELJAJ	KAJGOT	NAVWIR02	PEFJAM	WITNIY
GEQTIH	KECHAC	NEMJOF01	PEJVAD	WITNOE
GEQTON	KIKGAO	NEMJUL	PEJVEH	WOCXIW
GEQTUT	KOLNEF	NEMKAS	PEJVOR	WOCXOC
GEQVAB	KOLNIJ	NEMKEW	PEJWAE	XAFCAK
GUBXOR	KOLNOP	NEMKIA	POQTIZ	XAFCIS
GUBXOR01	KOLNUV	NEMKOG	POQTOF	XAFCOY
GUBYAE	KURTUN	NERNOO	PUDRIQ	
GUBYEI	LEYWET	NOGSIL	PUDROW	
HAPHUD	LEYWIX	NOGXEM	PUNRUM	

**Table A10** Structures in the CSD (version 5.36) containing polymeric ureas.

### 9.3 Conference presentations

*Just add water: exploiting hydration to unlock new self-assembly pathways*, Lancaster University, British Crystallographic Association Spring Meeting 2017.

*Braided helices and lily pad gels: controlling hierarchical self-assembly over a range of lengthscales*, University of Newcastle, Chemical Nanoscience Symposium 2017.

*Bis(urea) gelators: a designer's guide*, University of Stellenbosch, South Africa, Newton Fund International PhD Partnering Scheme Miniconference 2016.

*Lamellar urea tape networks as building blocks for crystals and gels*, University of Nottingham, British Crystallographic Association Spring Meeting 2016.

*Gels with sense: supramolecular materials that respond to heat and light*, Flash Talk, University of Glasgow, Macrocyclic and Supramolecular Chemistry Meeting 2013.